Pluviage

tors

Damage
and Fracture
Mechanics

ure Analysis of
gineering Materials and Structures

Damage and Fracture Mechanics

Taoufik Boukharouba • Mimoun Elboujdaini
Guy Pluvinage
Editors

Damage and Fracture Mechanics

Failure Analysis of Engineering Materials
and Structures

Springer

Editors

Taoufik Boukharouba
Dépt. Génie Mécanique & Productique
Université des Sciences et de la
Technologie Houari Boumediene (USTHB)
16111 Algiers
El Alia, Bab Ezzouar, Algeria
t.boukha@gmail.com

Mimoun Elboujdaini
Natural Resources Canada CANMET
Materials Technology Lab.
568 Booth Street
Ottawa, ON K1A 0G1
Canada
melboujd@nrcan.gc.ca

Guy Pluvinage
Université Paul Verlaine - Metz
57012 Metz
France
pluvina@sciences.univ-metz.fr

Printed on acid-free paper

9 8 7 6 5 4 3 2 1

springer.com

Table of Contents

v

Acknowledgments

We would like to thank all of our partners and sponsors of the First African InterQuadrennial ICF Conference "AIQ-ICF2008", which was held in Algiers from 01 till 05 June 2008, for their help to the organization of this scientific event.

Editors' Biographies

Prof. Taoufik Boukharouba

Received his Mechanical Engineering Degree (1987) in Mechanical Engineering from the University of Annaba, his Magister (1991) in Mechanical Engineering from Polytechnic School of Algiers and then his Doctorate (1995) from the University of Metz in France. He joined the staff of Houari Boumédiène Sciences and Technology University, (USTHB) in 1996. He was Director of the Mechanical Institute (IGM of USTHB) from 1998 to 2000. Presently, he is member of the "Haut Conseil Universitaire et de Recherche Algéro-Français (HCUR)". He is president of the Algerian Association of Mechanics and Materials and member of the "Commission Universitaire Nationale (CUN)".

He is supervising many projects on fatigue of materials as well as cooperation projects with CNRS and CMEP with French laboratories.

His research interest is in damage of composite materials and materials in biomechanics. He has published several technical papers. He is a reviewer for many international conferences and he organized the "Congrès de Génie des Procédés" (2000) in Ouargla, the "Congrès Algérien de Mécanique de Construction" (2007) in Algiers and the First African InterQuadrennial ICF Conference "AIQ-ICF2008".

Dr. Mimoun Elboujdaïni

Received his Mechanical Engineering degree and Diplôme d'Etude Approfondie (DEA) at the University of Technology of Compiègne (UTC) in France. He obtained an M.Sc. at physical metallurgy at Ecole Polytechnique of Montreal and his Ph.D. at the Laval University in Canada. In 1989 he joined the CANMET the Materials Technology Laboratory of Natural Resources Canada in Ottawa as research scientist working on many industrial projects and very active in the professional field of pipelines – oil/gas/petrochemical industries and has been participating in many professional organizations such as NACE, CIM, ICF, ECS, ASM, etc.

He leads several Canadian as well as international projects in different fields (hydrogen-induced cracking (H_2S), hydrogen embritlement, stress-corrosion cracking (SCC), galvanizing, liquid metal embritlement, etc.). He has published in excess of 100 technical papers, contributions to chapters in handbook; edited books and over 14 conference proceedings and organized several conference sessions and symposia.

He holds adjunct professorship in the Department of Chemical and Materials Engineering at the University of Alberta and trained and supervised national and foreign Ph.D. students and invited by several universities to serve as external examiner of Ph.D. theses. Selected as Distinguished Lecturer for 2006–2007 by the Canadian Institute of Mining, Metallurgy, and Petroleum (CIM). He also served as a member of organizing committees of several national and international conferences. Invited as Distinguished Speaker in addition received many national and international invitations (e.g.; China, USA, Egypt, Canada, etc) and universities. Organized and chairs several short courses. Presently, is the general Chair (2005–2009) for The Twelfth International Conference on Fracture (ICF12) to be held in Ottawa, Canada in 2009 (www.icf12.com).

Prof. Guy Pluvinage

Received his Doctorat de 3éme cycle in 1967 and his Doctorat d'état in 1973 at the University of Lille in France. He was successively Assistant Professor at Université de Valenciennes (1968–1974) and Professor at Université de Metz since 1974.

He was invited professor at University of Newcastle (Australia), (1982), University of Tokyo (Japon), (1984), University of'Auburn (USA) (1986). He was Director of "Laboratoire de Fiabilité Mécanique" from 1974 to 2002. Vice-President of the University of Metz (Research Council) (1988–1992) and Director of Maison du Pôle Universitaire Européen Nancy-Metz (1996–2003).

His expertise is mainly focused on strength of materials and particularly on fatigue and fracture Mechanics. He has published 167 papers in refereed journals: and 322 published communications to scientific meetings: He is author of several books in French, English and Russian. He is member of the editorial board and reviewer of several journals. He has received several honours and awards: Grand Prix du Centenaire de l'AAUL.

Officier des Palmes Académiques; Professor Honoris Causa University of Miskolc (Hungary); Doctor Honoris Causa Univerity Polytechnic of Tirana (Albania).

Foreword

The First African InterQuadrennial ICF Conference "AIQ-ICF2008" on Damage and Fracture Mechanics – Failure Analysis of Engineering Materials and Structures", Algiers, Algeria, June 1–5, 2008 is the first in the series of InterQuadrennial Conferences on Fracture to be held in the continent of Africa. During the conference, African researchers have shown that they merit a strong reputation in international circles and continue to make substantial contributions to the field of fracture mechanics. As in most countries, the research effort in Africa is undertaken at the industrial, academic, private sector and governmental levels, and covers the whole spectrum of fracture and fatigue.

The AIQ-ICF2008 has brought together researchers and engineers to review and discuss advances in the development of methods and approaches on Damage and Fracture Mechanics. By bringing together the leading international experts in the field, AIQ-ICF promotes technology transfer and provides a forum for industry and researchers of the host nation to present their accomplishments and to develop new ideas at the highest level. International Conferences have an important role to play in the technology transfer process, especially in terms of the relationships to be established between the participants and the informal exchange of ideas that this ICF offers.

Topics covered in AIQ-ICF2008 include: concepts of damage and fracture mechanics of structures, cumulative damage crack initiation, crack growth, residual strength, probability aspects and case histories; macro and micro aspects of fatigue; analytical methods for fatigue life assessment in structures; and applications of linear fracture mechanics to failure analysis and fracture control, fracture toughness and fatigue testing techniques, and environmental effects. These are areas where corrosion scientists, chemists, mechanical, civil, metallurgical and chemical engineers, corrosion prevention and coating specialists, operating and maintenance personnel can unite their efforts to better understand the complexities of these phenomena and develop effective preventive methods. Mechanistic understanding of cracking failures of metals and alloys can be used in conjunction with phenomenological data to identify and quantify the influence of environmental and material parameters. The conference has been devoted to the exchange of ideas and information on the evaluation of materials performance, and the development of advanced materials for resistance to damage and fracture in severe conditions.

Twelve plenary keynote presentations and ten introductory conferences covered a wide range of topics: *Computational Materials Engineering/Modelling; Nanomaterials; Biomaterials/Biomechanics; Pipeline Materials; Stress Corrosion Cracking & Hydrogen Embrittlement; Materials & Joining/Welds; High Strength Steel; Fracture Mechanics; Failure Analysis; Fatigue; Fracture Dynamics, etc…*

As chairs of this conference, we would like to express our thanks to all authors and reviewers who, collectively, have participated in making this conference a success and for their written contributions that make this proceedings volume a valuable record of the recent advances in *Damage and Fracture Mechanics*.

Prof. Taoufik Boukharouba
Dr. Mimoun Elboujdaini
Prof. Guy Pluvinage

Preamble

Ahmed Djebbar, is mathematician with diploma from Université Paris Sud (1972), from Université de Nantes (1990) and from Ecole des Hautes Etudes en Sciences Sociales de Paris (1998). He is Emeritus Professor at Université des Sciences et des Technologies de Lille. (France).

Advisor for Education, Culture and Communication at the Presidency of the Algerian Republic (January, 1992–June, 1992) and minister of Education, of Higher Education and Scientific Research (July, 1992–April, 1994).

He is one of the specialists of the history of sciences and in his assets a dozen works, from which some were translated in several languages. He is one of the specialists of the Arab World whom they consult on questions related to the provision of Arabic and Muslims in science.

We wanted by this preamble just to give a historical overview and not to write the history of sciences and point out the provision of Muslim civilization in sciences and particularly in mechanics object of the First African InterQuadrennial ICF Conference "AIQ-ICF2008".

We apologize to the author for possible errors in the translation of his original text which was sent to us in French language.

The original version of the text is available to anyone who wants to have the original copy.

The Arabic Phase of the Mechanics

For the first time in the history of the *International Congress on Fracture*, the works of the *InterQuadriennal Conference presented in this Book*, take place in the land of Africa, in Algeria precisely, one of the regions of the Maghreb which made its contribution to science and technology within the framework of the Arabian-Moslem civilization. How then omit evoking, even quickly, an important chapter of the history of the mechanics, the least known maybe, which was written within the framework of this civilization. The organizers of this meeting thought of it. A conference on this subject was presented. Here is a modest summary which is essentially homage to these discoverers of the past and to my colleagues specialists of mechanics who, through different roads, immortalize the same scientific adventure.

From the end of the VIIIth century to the middle of the XVIth, a new mechanical tradition, expressing itself essentially in Arabic, developed in the immense space governed in the name of Islam and which extended, in certain times, from

Samarkand to Saragossa and from Palermo to Tombouctou. As quite other scientific activity was practised during this period, the mechanics elaborated at the same time on the theoretical aspect and on the applied one as well, and on both aspects it produces significant results.

The theoretical part of this discipline was integrated into the physics. It concerns the study of statics, of the hydrostatics and the dynamics. Its applied part, which was called "Science of the ingenious processes", is subdivided into three big domains. The first domain is the one of the playful mechanics. It concerns machines and all the realizations which aim at distracting or at amazing the caliphs, the princes and fortunate people. The second corresponds to the utilitarian mechanics which aims at resolving the problems of the everyday life. The third concerns the military technology and, more particularly, the conception of weapons and machines of seat.

In the VIIIth century, we already mastered a set of techniques which served in the various domains which have just been evoked. Some of them were of unknown origin but the others had been used by the Romans, the Byzantine or the Persians. With the advent of the phenomenon of translation, writings dedicated to the mechanics were dug up and translated into Arabic. In our knowledge, they were all written in Greek. Having assimilated the ideas found in these texts, the first Moslem specialists of this domain tried, from the IXth century, to bring improvements and complements among which some were real innovations. But these last ones did not concern the only technical aspect. They also allowed bringing to light new concepts, never applied before. Some of them will be completely put into practice to realize complex systems. Others will stay in the state of ingenious findings and will be exploited only much later when they will be rediscovered in Europe.

It is finally necessary to indicate that the researches in this domain continued until the XVIth century and that they became a reality in numerous publications. The contents of those who reached us reveal a rich tradition which was born in Bagdad but which bloomed in the other metropolises of the Muslim empire, as Damascus, Cordoba and Istanbul [1].

1. The playful mechanics

In this domain, the ancient written heritage which reached the first technicians of the countries of Islam is exclusively Greek. The most important references are the Book of the pneumatic devices and the hydraulic machines of Philon of Byzantium (IIIrd century BC) [2] and the Mechanics of Heron of Alexandria (Ist century BC). After assimilation of the contents of these papers, the first specialists began to conceive new machines. In their research for original ingenious systems, they had the idea to use former principles and to realize combinations of technical constituents, as siphons, valves, airholes, cogwheels, ballcocks and cranks. They

also introduced new principles as that of the conical valve and that of the double concentric siphon.

The oldest Arabic work dealing with this subject is the Book of the ingenious processes of the brothers Banû Mûsâ (IXth century). One hundred of mechanical systems which are described there, 95 are machines [3]. We have no information about the repercussions of this first contribution during the period going from the Xth century to the XIIth century. But it seems that the practices and the knowledge acquired during the first phase remained alive until the publication of the known big second Arabic treaty of mechanics, that of al-Jazarî (XIIth century). This last one indeed makes reference to some of the contributions of his predecessors (others than Banû Mûsâ) by recognizing them the priority in certain innovations. In his work, entitled the *Useful collection of the theory and the practice in the ingenious processes*, he describes about twenty mechanical systems which are grouped together in two big categories: Water jets and musical machines or jugs of liquids [4]. Most of these mechanisms are his own invention. These subjects perpetuate during the centuries and we find them, in the XVIth century, in the work of Taqiy ad-Dîn Ibn Ma' rûf (1585) [5].

Considering the manufacturing costs of these machines, only a comfortable clientele could finance their realization. It was quite found among the caliphs, the local kings, the governors, the princes, the fortunate traders, the notables and, generally speaking, the members of the elite who appreciated this type of entertainment.

2. The civil engineering

It especially concerned the hydraulic problems (harnessing and routing of water) and mills. As we notice it by looking at a map of the Muslim empire, this region of the world had, always, to manage the rarity of the water and the weak flows of most of the rivers. This worrisome situation could only deteriorate with the demographic development of cities, the acclimatization of new subsistence crops and the rise of the standard of living of certain layers of the population. It is necessary to add the water requirements of certain vital sectors of the economy, as the paper industry and the textile industry. All these needs encouraged the research for technical means to pump the water, to store it and to forward it to the places of consumption.

The first known work which looked at some of these problems is the one of al-Jazarî (XIIth century) which was already evoked. We find, in particular, the description of sophisticated systems to raise the water of a river or a well by using the animal or hydraulic force. One of them is a device with pendulum, which uses the principle of the gearing segmentaire. Another system conceived for the same usage would have been the first one to use a crank integrated joined into a machine. The third is a water pump whose conception was quite new for that period because it worked by converting the circular movement in an alternative linear

movement and by use of suction pipes [6]. It is necessary to precise that these models did not stay of simple technological curiosities. Some were realized and their smooth running is attested by their longevity. It is the case of the machine that was built by the middle of the XIIIth century, on the river Yazîd in Syria, the native country of the author, and which worked until the middle of the XXth century [7]. This tradition of engineering continued after al-Jazarî but we have, at the moment, only a single confirming document it and it is issued very late. It is about the *Book of the noble processes on the magnificent instruments* of Taqiy ad-Dîn Ibn Ma' rûf, a mathematician and astronomer native of Damascus. Its contents prolong that of his predecessor, in particular in the field of water pumps [8]. With regard to this and considering the nature of this sector, its vitality is especially attested by hundreds of hydraulic systems which were built almost everywhere in the Muslim empire of which remain vestiges which are still often very lifelike.

As regards the mills which were used in the Muslim empire, we can classify them in several categories according to their size, to their use and to their energy consumption. With regard to the size, it goes from the small mill of farm pulled by a mule to the real complex which worked in Bagdad, and which activated hundred pairs of grindstones at once. Sometimes, mills were distributed in the city as it was the case in Nichapour where 70 devices worked at the same time, and in Fes where there would have been up to 400 devices for the local industry of paper and for the grinding of wheat.

The working of these mills depended on local conditions and on the available energy. So, there were systems activated by hand or by animals, as it was practised well before the advent of Islam. There were also those who used the drainage of river waters and who were fixed to the banks of rivers, to the piles of bridge or who floated on barges, in the middle of the river, as those of Bagdad which used the water of Tigre. From the IXth century, we indicate the increasing use of the wind energy in the windiest regions of the empire, as those of Central Asia. We would have even realized, in the XIth century, around Bassora, mills activated by the tide.

Besides two big domains which have been evoked, the works of mechanics present other ingenious processes for other usages: machines of lifting, systems of ventilation, locks with combinations, automatic lamps and even a roasting spit working with vapor.

3. Instruments to measure the time

The measure of time was a constant concern in the profane and religious everyday life of the societies of the Muslim empire. One of the oldest processes was the gnomon, a simple stalk fixed vertically or horizontally and whose shade indicates the time approximately. As this system could not work at night, we looked for other solutions. The most practised, well before the advent of Islam, is based on the principle of the continuous flow of a liquid (what gave water clocks), or of a

solid enough fluid, as mercury. From the IXth century, the first technicians of the countries of Islam had at their disposal, through the translations, Greek texts giving ingenious solutions of this problem. It is the case of the *Book of the manufacturing of clocks* attributed to Archimède (212 BC) [9]. From there, a powerful tradition developed and certain number of works which reached us testifies of the high degree of ingenuity and of technicality reached by the specialists of this domain.

The oldest known text was published by Andalusian Ibn Khalaf al-Murâdî (XIth century). It is entitled "*The book of the secrets on the results of thoughts*". 19 models of clocks are described there. The one of them announces the hours with lamps which ignite automatically, the other one possesses mirrors which are illuminated, successively, at the end of every hour [10]. At the same time, in Egypt, the big physicist Ibn al-Haytham (1041) described a mechanism giving the hour but its text was not found. From the XIIth century, the treaty of al-Khâzinî reached us, "*The balance of the wisdom*", a chapter of which is dedicated to an original water clock called "*balance of hours*". Some decades later, Ridwân as – Sâ'âtî publishes his Book on the construction of clocks and their use, dedicated to this subject [11]. He describes a monumental clock which his father had built, in 1154, in Damascus and which we had tried to restore repeatedly. It is finally the author who succeeds in restarting it completely in 1203. The information reported by as-Sâ'âtî confirm the continuous character of the tradition of clocks in East and reveal the existence, in the XIIth century, of a real profession specialized in the realization and maintenance of these devices [12]. It is moreover at the same time that al-Jazarî described, in its famous work which we have already evoked, six water clocks and four clocks with candles [13].

After him, and until XVIth century, we do not know works having immortalized this tradition. But there could have been existed specialists whose papers did not reach us or which realized clocks without feeling the need to speak about it. It is probably the case of certain craftsmen of al-Andalus and the Maghreb as authorize us to think of it the testimonies which we have. We know, for example, due to the information contained in the Libros del Saber, drafted by the middle of the XIIIth century at the request of Castillan king Alphonse X (1252–1284) that water clocks and clocks with mercury or with wax candle were used in Andalus before the reconquest of Toledo in 1085 [14]. We also know that in the XIVth century, the engineer Ibn al-Fahhâm, native of Tlemcen, conceived and realized, in Madrasa Bou Inânia of Fes, a clock which would have amazed his contemporaries [15]. The vestiges of this clock are still visible today. We can also see, in the mosque Qarawiyîn of the same city, what stays of a clock, built by 1357 by the mathematician al-Lajâ'î (1370).

It is finally necessary to indicate, the contributions of one of the last representatives of this tradition, Taqiy ad-Dîn Ibn Ma' rûf, who published two works containing descriptions of clocks. In the first one, entitled: *The book of the sublime processes on the magnificent instruments*, he presents hourglasses and water

clocks. The second entitled: *The precious planets for the construction of clocks*, is completely dedicated to the mechanical clocks [16].

4. The military engineering

Since the conquests of the VIIth century, the war instruments of the Moslem armies did not stop perfecting and diversifying. If we are only held in those which were described in the specialized works and in the history books, we count tens more or less sophisticated: handguns (sabres, daggers, javelins), bows, (wooden or steel), crossbows, machines of seat, rams, incendiary bombs, without forgetting artillery and rifles, for the last period of the empire history. The Arabic works dealing with these subjects were not all dug up. Those who were studied take place after the XIIth century but what they describe concerns partially the previous period. It is necessary to clarify that we have, today, two types of works. In the first category, the authors expose, in three big different subjects, all the subjects linked to the art of the war. Both first ones deal with the cavalry and with the technology of bows. It is in the third, reserved for the tactics, for the military organization and for the weapons, that the technological aspects are developed. Beside this category of general works, there were treaties more specialized in particular on the subject which interests us here. The oldest of them is probably the *Book on the war instruments* of the brothers Banû Mûsâ (IXth century) which was not found yet. The most known is the *Elegant book on the mangonneaux* of az-Zaradkâshî (ca. 1462) which is dedicated to catapults and to inflammatory missiles [17].

From a heritage probably of Persian origin, the technicians of the Moslem armies introduced very early the instruments of seat. We indicate their presence in all the important wars until the middle of the XVIth century, date which corresponds to the introduction of artillery in the Ottoman armies and thus giving up the classic shell throwers. The longevity of catapults also explains by their multiple features because various variants were adapted to the nature of missiles: stone coal nuts, arrows, balls of naphte, flares, asphyxiating bombs and even bowls filled with snakes or with scorpions to terrorize the besieged.

At the end of this fast flying over the Arabic mechanical tradition, we can consider that this discipline, by its technological and theoretical contributions at once, not only participated in the extension of the field of the scientific practices, but it also strengthened the links between the learned knowledges and the know-how, allowing these last ones to reach the status of "sciences". It also has, by its ingenious realizations, illustrated this capacity of the specialists of this domain, when the conditions allowed it, to innovate by by-passing various types of obstacles. For these reasons, and independently of its realizations, the Arabic phase of the mechanics is an important link in the long history of the technologies.

References

[1] A. Djebbar: *Une histoire de la science arabe*, Paris, Seuil, 2001, pp. 241–262 (en français).

[2] J. Shawqî: *Les fondements de la mécanique dans les traductions arabes*, Koweït, Fondation pour l'Avancement des Sciences, 1995 (en arabe).

[3] Banû Mûsâ: *Livre des procédés ingénieux*, A.Y. Al-Hassan (édit.), Alep, Institute for the History of Arabic Science, 1981 (en arabe).

[4] Al-Jazarî: *Le recueil utile de la théorie et de la pratique dans l'art des procédés ingénieux*, A.Y. Al-Hassan (édit.), Alep, Institute for the History of Arabic Science, 1979, pp. 223–438 (en arabe).

[5] A.Y. Al-Hassan: *Taqiy ad-Dîn et l'ingénierie mécanique arabe*, Alep, Institute for the History of Arabic Science, 1976 (en arabe).

[6] Al-Jazarî: *Le recueil utile de la théorie et de la pratique ...*, op. cit., pp. 441–465.

[7] A.Y. Al-Hassan and D. Hill: *Sciences et techniques en Islam*, Paris, Edifra-UNESCO, 1991, pp. 44–45.

[8] A.Y. Al-Hassan: *Taqiy ad-Dîn et l'ingénierie mécanique arabe*, op. cit.

[9] D.R. Hill: *Arabic Water-Clocks*, Alep, Institute for the History of Arabic Science, 1981, pp. 15–35.

[10] Op. cit., pp. 36–46.

[11] Ms. Gotha, Ar. 1348.

[12] D.R. Hill: *Arabic Water-Clocks*, op. cit., pp. 69–88.

[13] Al-Jazarî: *Le recueil utile de la théorie et de la pratique*, op. cit., pp. 7–221.

[14] D.R. Hill: *Arabic Water-Clocks*, op. cit., pp. 125–129.

[15] Y. Ibn Khaldûn: *Le souhait des précurseurs sur l'histoire des Abd al-Wadids*, Alger, Bibliothèque Nationale, p. 119.

[16] A.Y. Al-Hassan: *Taqiy ad-Dîn et l'ingénierie mécanique arabe*, op. cit., p. 26.

[17] Az-Zaradkâshî: *Le livre élégant sur les mangonneaux*, Alep, Institute for the History of Arabic Science, 1985.

Determination of the Hardness of the Oxide Layers of 2017A Alloys

Chahinez Fares[1], Taoufik Boukharouba[1], Mohamed El Amine Belouchrani[2], Abdelmalek Britah[3] and Moussa Naït Abdelaziz[4]

[1]Laboratoire de Mécanique Avancée (LMA), faculté GM&GP, l'USTHB, BP 32, 16111 Bab-Ezzouar, Alger Algeria

[2]Laboratoire Génie des Matériaux E.M.P, BP17C, Bordj El Bahri, Alger Algeria

[3]Laboratoire Génie des Matériaux, E.M.P, BP17C, Bordj El Bahri, Alger Algeria

[4]Laboratoire de Mécanique de Lille, Ecole Polytechnique Universitaire de Lille, Cité Scientifique Avenue Paul Langevin 59600 Villeneuve d'Asq, France

Abstract   In order to improve the resistance of materials to surface damage by mechanical and environmental action, considerable research has been conducted to increase the hardness of the surface of mechanical parts. This is achieved, for example, by anodisation of aluminium alloys. The objective of designing films possessing optimum mechanical properties cannot avoid the determination of their hardness as precisely as possible. Unfortunately, direct measurement of film hardness by conventional micro-hardness testing is not possible for a large range of indentation loads because the substrate also participates in the plastic deformation occurring during the indentation process. It is often assumed that this phenomenon, which involves the two materials, begins to be noticeable for loads such that the depth of the indent exceeds one tenth of the film thickness. In this situation, the hardness number is thus the result of the combined substrate and film contributions. In order to determine the true hardness of the film, it is necessary to separate these contributions. Numerous mathematical models were proposed for that purpose on the basis of different assumptions. The objective of the present work is to study hardness response of oxide film developed by sulphuric anodisation on annealing aluminium alloys substrates (2017A) over a range of applied loads. The hardness values were determined experimentally using conventional Vickers microhardness measurements. The results were analysed using the work-of-indentation model for the hardness of coated systems. Both experimental measurements and modelling work in this area will be aimed at obtaining the estimates mechanical properties of oxide layer.

Keywords: Aluminum Alloy, Anodisation, Annealing, Microhardness, Indentation Model.

1. Introduction

According to their excellent mechanical, optical and electrical properties, aluminium oxide thin films are used in a very large range of applications [1–3]. Alumina thin films are currently deposited using methods such anodisation with excellent results.

1

Therefore, research to determine the material properties and the reliability of the Aluminium Anodic Oxide (AAO) structure is currently taking place. Among the various techniques to investigate the material characteristics, the simplest method is the nano-indentation technique, which is based on the application of very low load and continuous measurement of the indenter penetration depth from the surface [4, 5].

When nano-indentation equipment is not available, determination of the intrinsic film hardness requires the analysis of a set apparent hardness values obtained experimentally for different indentation loads using standard micro-indentation equipment. Consequently, numerous models of analysis have been developed in order to extract the true film hardness from standard indentation tests [6–13].

This research investigated the mechanical properties of AAO film developed by sulphuric anodisation on aluminium alloys substrates (2017A) over a range of applied loads. The various influences of the substrate for amorphous alumina thin film were studied by measuring the hardness before and after heat treatment.

2. Model for determining hardness

It is known that, depending on the thickness of the film and on the applied load, indentation measurements give apparent hardness values (H_C), which are the results of contributions, by both the substrate (H_S) and the film (H_F). There is a need therefore to separate these two contributions in order to determine the true hardness of the film.

Whatever many hypotheses, have in common the supposition of a linear additive law for the expression of the composite hardness (H_C), as a function of the film (H_F) and substrate (H_S) hardness, and a contribution coefficient of the film, α. Coefficient α, can take different expressions depending on the hypotheses, physical or empirical, which are stated. Generally these models are written under the following form (see Eq. 1):

$$H_C = H_S + \alpha \cdot \left(H_F - H_S \right) \tag{1}$$

Among predictive models that of Jönsson and Hogmark are still widely used because it is very simple to employ [12]. The original form of the Jönsson and Hogmark model is the following (Eq. 2):

$$H_C = \frac{A_f}{A} H_f + \frac{A_S}{A} H_S \tag{2}$$

where A_f and A_S, are the load-supporting area of the film and the substrate respectively, A is the total projected contact area ($A = A_S + A_F$).

From geometric considerations of the size, Jönsson and Hogmark derived an expression for the composite hardness given by (Eq. 3)

$$H_C = H_S + \left[2C\left(\frac{t}{d}\right) - C^2\left(\frac{t}{d}\right)^2 \right] \cdot \left(H_f - H_S\right) \tag{3}$$

where t is the coating thickness, d is the indentation diagonal and C is a constant dependent on indenter geometry.

The model involves a parameter C which can take two different values depending to the toughness of the film: $C=0.5$ for brittle material, $C=1$ for ductile material. Korsunsky [10, 11] proposed another model for the composite hardness behaviour based on the total energy dissipated in deforming the composite.

The total energy dissipated during composite deformation contains contributions from both the substrate and the coating; however, the division of the energy between coating and substrate varies with the relative indentation depth. The total work is composed of two parts: the plastic work of deformation in the substrate (W_S), and the deformation and fracture energy in the coating (W_F) (see Eq. 4):

$$W_T = W_S + W_F \tag{4}$$

Considering the dependence of individual contributions on the relative indentation depth, coating and substrate properties, and the following expression for H_C can be derived (Eq. 5):

$$H_C = H_S + \frac{H_F - H_S}{1 + k \cdot \beta^2} \tag{5}$$

where $\beta = \delta/t$ denotes the indentation depth normalized with respect to the coating thickness and has been termed the relative indentation depth. δ is the maximum penetration depth, for Vickers indenters, $\delta = d/7$ where d is the indentation diagonal, t presents coating thickness.

The composite hardness H_C can be thought to depend only on the dimensionless parameters k and β, and the hardness difference between the coating and the substrate. The parameter k is proportional to the dimensionless ratio $G_C/H_S t$, and scales inversely with the coating thickness for fracture-dominated cases.

Where G_C denotes the thickness fracture toughness of coatings. The parameter k varies from $(t/0.2)$ for thin coatings to $(t/0.4)$ for thick coatings. The film hardness is obtained for very low relative indentation depth as: $H_C = H_F$ as $\beta \to 0$

3. Experimental methods

3.1. Anodisation process

Specimens of dimensions, $6 \times 0.5 \times 0.5$ cm were machined from 2017A aluminum alloys. The chemical composition of the alloy is given in Table 1. The specimens were annealed at 300°C and cool down at room temperature. This treatment of homogenization is used to eliminate deformations that may have been produced during machining. After this treatment, Anodisations were carried out in thermostatically controlled electrochemical cell (±2°C), using a lead cathode and a heat-treated aluminum alloy anode. Individual specimens were anodized in sulfuric bath (200 g/l H_2SO_4) at constant cell voltage of 12 V for 60 min, at 20°C. After anodising, specimens were washed in distilled water and sealed in boiling water for 60 min at 97°C.

Table 1. Chemical composition of the material used

Al	Cu	Fe	Si	Mn	Mg	Zn	Cr	Ti
Balance	3.5–4.5	Max 0.7	0.2–0.8	0.4–1	0.4–1	0.25	0.1	Traces

3.2. Hardness measurements

Vickers indentations were then performed on the as deposited samples using a High Wood HWDM-1 hardness tester with loads ranging from 25 g to 2 kg. The applied loads ranged from 5 to 15 g were performed with Leitz MM6 micro-hardness tester. Three tests were performed at each load chosen in order to have reasonable confidence in the calculated average hardness value. Film thickness was about 16 μm measured directly by scanning electron microscopy. After indentations were performed with a Vickers diamond pyramid both in uncoated substrates and various coating-substrate composites, and the average values of impression diagonals were recorded, the composite hardness was computed using the formula (Eq. 6):

$$H_V \left\lfloor gf / \mu m^2 \right\rfloor = 1854.4 \cdot P\left[gf\right] / d^2 \left\lfloor \mu m^2 \right\rfloor \tag{6}$$

Figure 1 represents the experimental hardness data calculated by formula (Eq. 6). The fitting models developed by Korsunsky [10, 11], Jönsson and Hogmark [12] are directly applied to the data. For the model of Jönsson et al. We choose a value for C equal to 0.5. The film hardness is then obtained for very low relative indentation depth. In order for the H_F values estimated by the both models to be compared together, we chose to calculate H_F at a ratio of $t/d = 1$. A justification of this procedure is given in the paper published by Lesage et al. [7].

3.3. Structure examination

After anodisation, morphologies of anodic layers were investigated using an Electron Probe MicroAnalyser (EPMA) SX100 from CAMECA, France. All samples were cross-sectioned, embedded in epoxy resin, polished and carbon coated with a Bal-Tec SCD005 sputter coater. Secondary (SE) and back scattered electrons (BSE) images were carried out at 20 kV, 10 nA. Oxygen (O), copper (Cu) and aluminium (Al) X-ray profiles were carried out at 20 k 40 nA, magnesium (Mg), manganese (Mn), and Cu quantifications at 15 kV, 15 nA, and, Al, Cu, Mn and Mg X-ray mappings at 15 kV, 40 nA. Intensity profiles are representative of the concentration of the element present in the oxide film. The quantitative measurements were obtained using standards samples (Al_2O_3, pure Cu, MgO and pure Mn). For profiles, quantifications or mappings, a PC2 crystal was used to detect the O Kα X-ray, a TAP crystal for Al and Mg Kα X-rays and a LiF crystal for Cu and Mn Kα X-rays.

4. Results and discussion

Figure 1 represents the experimental hardness data as a function of normalized depth β (δ/t = d/7t) for the both heat-treated and untreated anodized specimens. The composite hardness of the annealed samples was more important, that is justified because the aluminum alloys of series 2000 were hardened by heat treatment. It's immediately apparent from this figure that there is a transition of behavior; the film indentation response is for β < 0.1 for the both samples.

The results corresponding to the film hardness determined by different models applied, for each sample, are reported in Fig. 2. These figures illustrate the change of film hardness as a function of the normalized depth. The Kornusky et al. model predicts values for the film hardness fairly greater than those obtained with Jönsson and Hogmark model (Table 2).

The hardness of film was obtained from $d/t = 1$. The clean hardness of alumina is very large, one notices for the two samples the same shape of the curves, and the surface part of the layer is, in general, much more to tend that in the vicinity of the barrier layer.

The change of film hardness between untreated and annealed samples showed that hardness was reduced as the porosity increased. The annealed samples present more heterogeneity in the oxide film than untreated ones. Back-scattered electrons (BSE) images (Fig. 3) of the two anodized alloys (annealed or untreated) revealed the presence of cracks on the anodic layers. However, cracks are more important after the annealing heat treatment.
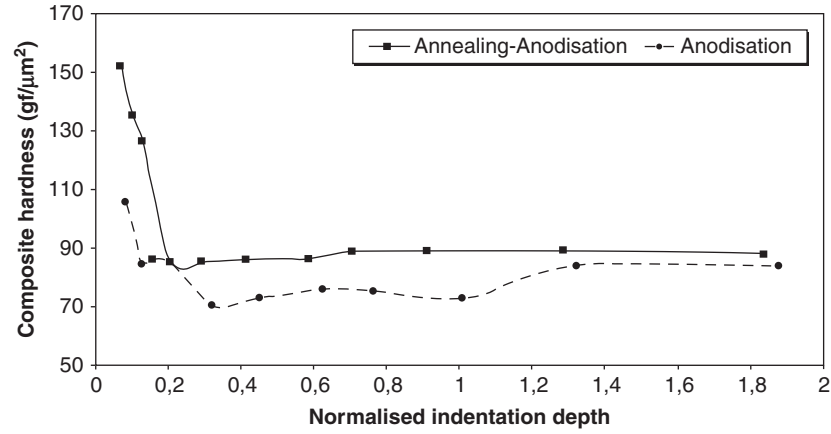
Fig. 1. Composite hardness of aluminium alloys 2017A anodised before and after annealing treatment

Table 2. Hardness of oxide film by Jönsson-Hogmark and Korsunsky models

	H_S	H_F (Jönsson-Hogmark)	H_F (Korsunsky)
Annealing	88.000	118	160
Untreated	75.000	80	100
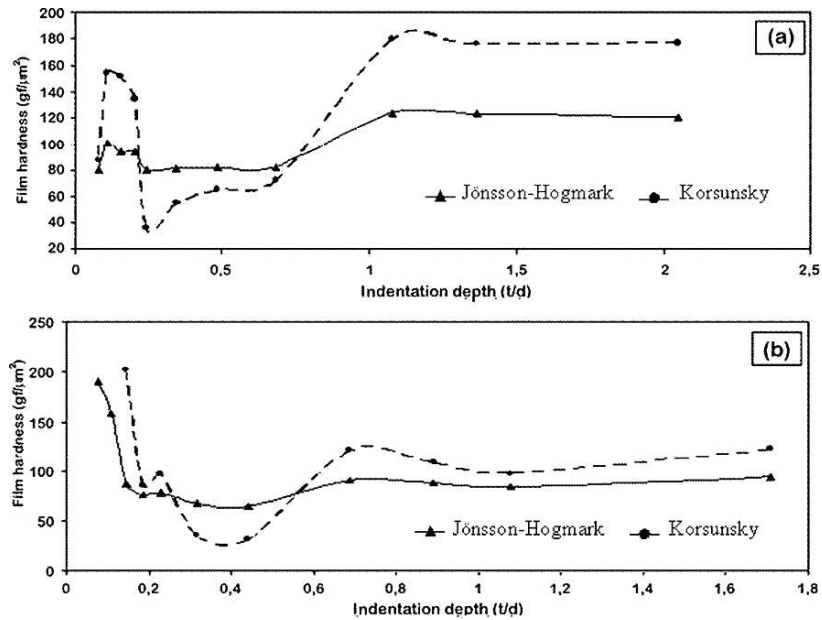
Fig. 2. Comparison of film hardness behavior according to the models of Jönsson-Hogmark and Korsunsky et al. for: (**a**) annealing samples, (**b**) untreated samples

Figure 4 showed that high copper content in the case of the annealing treatment accompanies the presence of defects in the anodic layers. The observed pores are attributed to the preferential dissolution of copper (grain boundary precipitates) during anodizing in sulfuric bath.

Figure 4 illustrates the weight percentage of Mg, Mn and Cu in the sample as a function of depth in the oxide layer for both samples along a same line (as showed in Fig. 3) from the inside of the sample (1) to the edge (2) (oxide layers for both heat treatments). They revealed the presence of very few copper through the whole depth of the film. The copper concentration decreases from the interface to the surface of the oxide layer for the two different heat treatments.
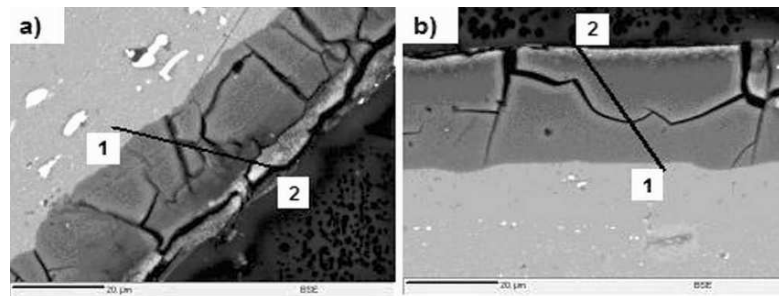
Fig. 3. Micrographs of 2017 alloys anodized for: (**a**) annealed samples, (**b**) untreated samples
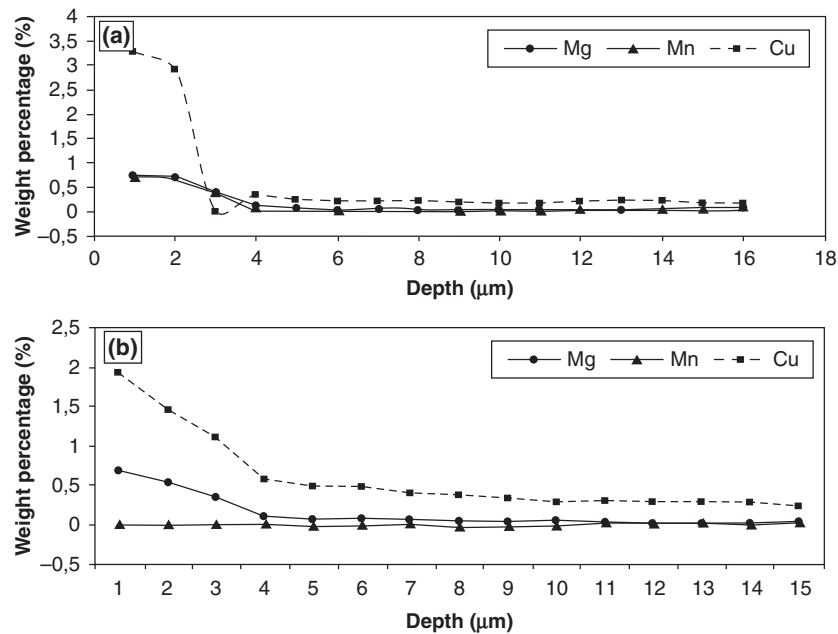
Fig. 4. Weight percentage of element in the oxide layer as function of depth: (**a**) annealed samples, (**b**) untreated samples
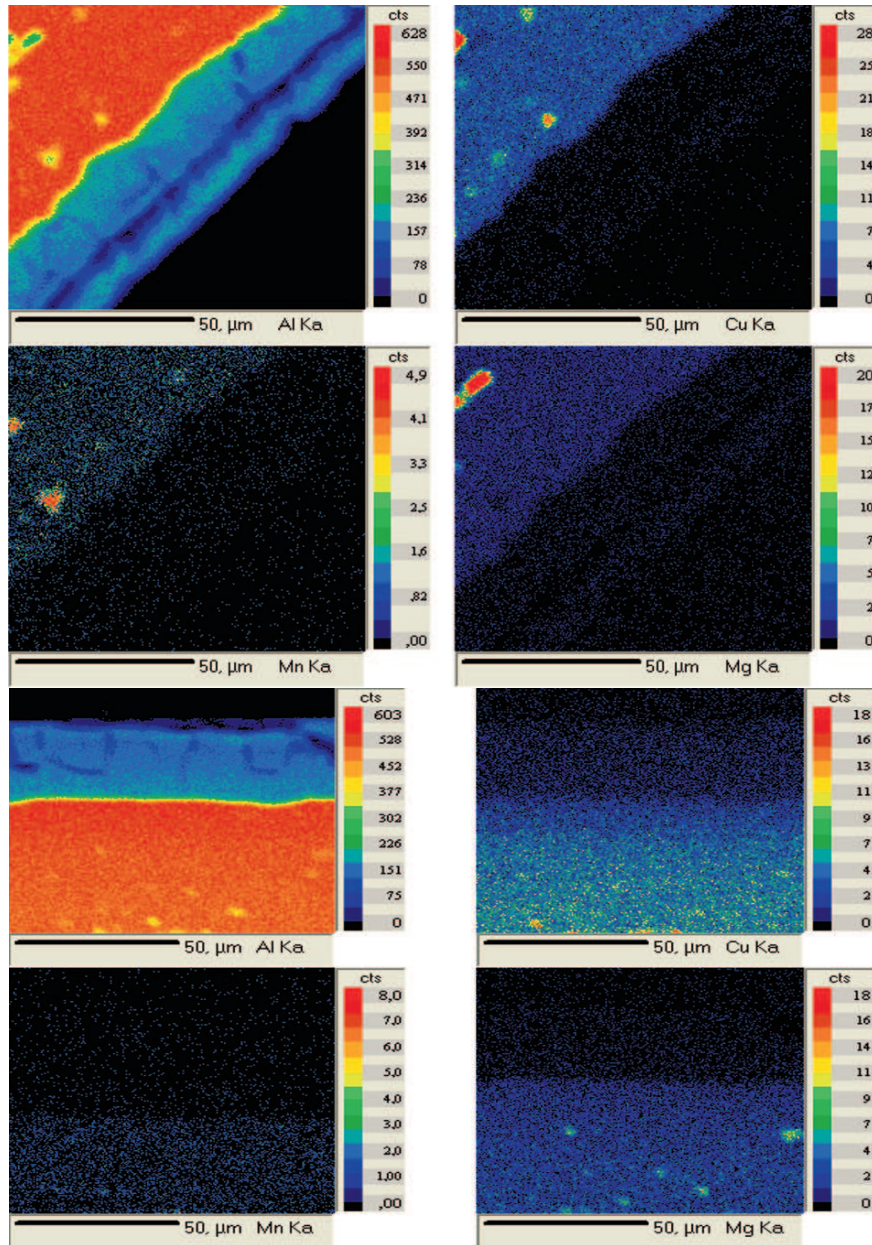
Fig. 5. X-ray cartography of Al, Cu, Mn, and Mg in the oxide layer after: (**a**) annealed samples, (**b**) untreated samples

X-ray cartographies (Fig. 5) of annealed samples showed the presence of a coarse-grained material. The largest coarse-grained materials are made of Al_2Cu.

This phase can affect the morphology of oxide layers (cracks) as showed in Fig. 4. When Al_2Cu particles rich in copper are present as coarse grained, they support micro galvanic coupling between intermetallic particles and the adjacent matrix. Thus, these particles constitute local cathodes, which stimulate the dissolution of the impoverished zone [14].

Then, the intermetallic dissolution during anodisation treatment involves the formation of a heterogeneous surface layer rich in copper. The copper diffusion in this case is more significant because the copper is in the shape of precipitated Al_2Cu in the boundary grains. The precipitation of copper in the form of stable θ-Al_2Cu can impoverish out of copper the close solid solution. In a corrosive medium, the stripped zone will form an anodic way and will dissolve preferentially. Since we apply an anodisation treatment the selective dissolution will incorporate copper to the alumina.

5. Conclusions

In this research, hardness of AAO structures were investigated applying to numerous mathematical models of Jönsson-Hogmark and Korsnusky to the measurement obtained by conventional micro-hardness testing. The various intermetallic compounds, which are present in the substrate, have various shapes, sizes and compositions according to the heat treatment used. Direct oxidation of alloying elements and incorporation oxides into the film during anodisation treatment involves the formation of a heterogeneous surface layer rich in copper and causes modifications in porous film growth, film and microstructure composition which affect the film hardness.

The film hardness obtained by micro-hardness measurements and calculated using Jönsson and Hogmark and Korsunsky models have confirmed that the surface part of the layer is much more to tend that in the vicinity of the barrier layer. Further, when aluminium alloy was annealed, a new intermetallic phase was formed (Al_2Cu) whose the low resistance favours the oxidation and dissolution of these particles, increasing the porosity of the oxide. By consequent the film hardness obtained by the both models are very different in annealed state.

References

[1] Hwang SK, Jeong SH, Hwang HY, Lee OJ, Lee KH (2002) Fabrication of highly ordered pore array in anodic aluminum oxide. Korean J. Chem. Eng. 19/3: 467.
[2] Doener MF, Nix WD (1986) A method for interpreting data from depth-sensing indentation instruments. J. Mater. Res. 1: 601.
[3] Oliver WC, Pharr GM (1992) An improved technique for determining hardness and elastic modulus using load and displacement sensing indentation experiments. J. Mater. Res. 7: 1564.

[4] Zeng K, Chiu CH (2001) An analysis of load–penetration curves from instrumented indentation. Acta Mater. 49: 141.

[5] Musil J, Kunc F, Zeman H, polakova H (2002) Relationships between hardness Young's modulus and elastic recovery in hard nanocomposite coatings. Surf. Coat Technol. 154: 304.

[6] Wen SP, Zong RL, Zeng F, Gao Y, Pan F (2007) Evaluating modulus and hardness enhancement in evaporated Cu/W multilayers. Acta Mater. 55: 345.

[7] Lesage J, Pertuz A, Puchi Carbrera ES, Chicot D (2006) A model to determine the surface hardness of thin films from standard micro-indentation tests. Thin Solid Films 497: 232.

[8] Chicot D, Bénarioua Y, Lesage J (2000) Hardness measurements of Ti and TiC multilayers: a model. Thin Solid Films 359: 228.

[9] Korsunsky AM, McGurk MR, Bull SJ, Page TF (1998) On the hardness of coated systems. Surf. Coat. Technol. 99: 171.

[10] Tuck JR, Korsunsky AM, Davidson RI, Bull SJ, Elliott DM (2000) Modelling of the hardness of electroplated nickel coating on copper substrates. Surf. Coat. Technol. 127: 1.

[11] Ichimura H, Rodriguez FM, Rodrigo A (2000) The composite and film hardness of TiN coatings prepared by cathodic arc evapation. Surf. Coat. Technol. 127: 138.

[12] Jönsson B, Hogmark S (1984) Hardness measurements of thin films. Thin Solid Films 114: 257.

[13] Chicot D, Bemporad E, Galtieri G, Roudet F, Alvisi M, Lesage J (2008) Analysis of data from various indentation techniques for thin films intrinsic hardness modelling. Thin Solid Films 516: 1964–1971.

[14] Fratila-Apachitei LE, Terryn H, Skeldon P, Thompson GE, Duszczyk J, Katgerman L (2004) Influence of substrate microstructure on the growth of anodic oxide layers. Electrochim. Acta 49: 1127.

Effect of Non-Metallic Inclusions on Hydrogen Induced Cracking

Mimoun Elboujdaini and Winston Revie

CANMET Materials Technology Laboratory, Natural Resources Canada, 568 Booth S, Ottawa, Ontario, K1A 0G1, Canada

Abstract   Two types of cracking, namely sulphide stress cracking (SSC) and hydrogen-induced cracking (HIC), were evaluated in linepipe steels using NACE standard solution to establish the metallurgical parameters that control HIC and SSC. Quantitative experiments indicate a threshold hydrogen concentration for HIC below which no cracking will initiate. Propagation of cracks occurs by hydrogen assisted fracture of the matrix surrounding the site where initiation occurs. The HIC susceptibility of steels containing Cr, Ni, and Mo under stress and hydrogen diffusion was been investigated by electrochemical methods. As the content of alloying elements increased, the apparent hydrogen diffusion coefficient (D) and threshold hydrogen permeation rate (J_{th}) for hydrogen embrittlement decreased. Hydrogen content (C_o) in the steel in NACE TM-0177 solutions increased due to decreasing D with increased Cr content, although hydrogen permeability ($J \times L$) decreased, and the susceptibility to sulfide stress cracking (SSC) increased as a result. Moreover, Mo exhibited clear effect of decreasing $J \times L$, and consequently the resistance to SSC improved with increasing Cr content.

1. Introduction

Numerous research results have been published on the hydrogen embrittlement of carbon steel and low-alloy steel. Some common features of HIC are now known: HIC occurs when hydrogen concentration, C_o, in the steel matrix exceeds the threshold hydrogen concentration, C_{th}. The C_{th} might be considered as a parameter unique to a given material [1]. With increased materials strength, threshold hydrogen content (C_{th}) tends to decrease, and threshold stress-intensity factor K_{IH} becomes dependent on hydrogen concentration (C_o) irrespective of material (K_{IH} tends to decrease with increasing hydrogen concentration (C_o)). C_o is known to be dependent on alloy composition, H_2S partial pressure, and pH, whereas C_{th} depends on inclusions and segregation in the matrix [2, 3].

The atomic hydrogen formed at the reacting surface can diffuse into the steel where it may cause embrittlement and/or accumulate at the inclusion/matrix interface, building up pressure that leads to cracking. Two typical types of HIC cracks are shown in Fig. 1, namely, centre line cracks and blister cracks.

Blister cracks are those hydrogen induced cracks that are formed near the surface so that the hydrogen pressure is able to raise the material, developing blisters that are observable on the surface Fig. 1b. The formation of blister cracks seems to be directly related to the type and distribution of non-metallic inclusions in the steel [4].

Fig. 1. Two types of HIC: (**a**) center line cracks; and (**b**) blister crack

Hydrogen sulfide (H_2S) is known to poison the hydrogen recombination reaction, $H \rightarrow H2$, thereby increasing hydrogen absorption in steel. As a consequence, hydrogen sulphide accelerates HIC and SSC in carbon steel and low-alloy steel in sour environments.

In contrast to the research on hydrogen effect in carbon steel and low-alloy steel, research on HIC in chromium steel is sparse. As reported in the literature, chromium steel is highly resistant to CO_2; however, this steel is known to be susceptible to SSC in sour environments, and the influence of H_2S on HIC behaviour of chromium steel has not been systematically explored [5, 6].

The aim of this work is to understand the influence of inclusions, segregation, chemical composition and alloying elements on both HIC and SSC.

2. Experimental procedure

The chemical compositions of the steels used in this study are presented in Table 1.

Table 1. Chemical analysis (wt%)

Steel code	C	Mn	P	S	Si	Cu	Ni	Cr
WC-1	0.105	1.03	0.010	0.0270	0.075	0.20	0.08	0.05
G-2	0.130	1.09	0.012	0.0084	0.165	0.22	0.07	0.06
AM-1	0.120	0.69	0.006	0.0031	0.008	0.33	0.095	0.17
PC-1	0.090	0.73	0.013	0.0036	0.200	0.23	0.08	0.06
CTR-2	0.100	0.84	0.018	0.0013	0.175	0.005	0.25	0.03

2.1. Hydrogen-induced cracking tests

HIC tests were carried out according to NACE standard TM-0284 [7]. The quantity of diffusible hydrogen in the specimens exposed for the 96 h was determined. Coupons were examined for cracks by ultrasonic C-scan before and after hydrogen charging using an Automated Ultrasonic Flaw Imaging System (AUFIS) or "TOMOSCAN".

2.2. Quantitative metallography of inclusions

Metallographic specimens were prepared from sections for many of the linepipe steels, and were examined in the as-polished condition by optical microscopy. Quantitative measurements of inclusion length and volume fractions were obtained using a Leco 2001 Image Analysis System. The inclusion populations in 200 microscopic fields were measured on each metallographic sample to obtain statistically significant data on volume fraction and size of the nonmetallic inclusions present.

3. Results and discussion

3.1. Diffusible hydrogen and threshold hydrogen concentration

The use of C_{th} of a steel as a measure of its resistance to HIC would be a rational alternative to that used in the present NACE standard test. There would be less difficulty in ranking steels in their susceptibility to HIC; also, the C_{th} value of steel can be related directly to the performance of that linepipe steel containing a corrosive sour environment. In such pipe, permeation methods can be used in the

field to determine the maximum concentration of dissolved hydrogen in the wall C_0; HIC should only occur when $C_0 > C_{th}$.

The basic limitation of the metallographic evaluation of HIC could be overcome by using the ultrasonic C-scan test which is rapid and sensitive to determining cracks in samples. However, quantitative data on cracking, such as crack length ratio, are not obtained by this method. Figure 2 shows a typical output from a C-scan test carried out after the steels is exposed to H_2S-saturated solution in the HIC test.
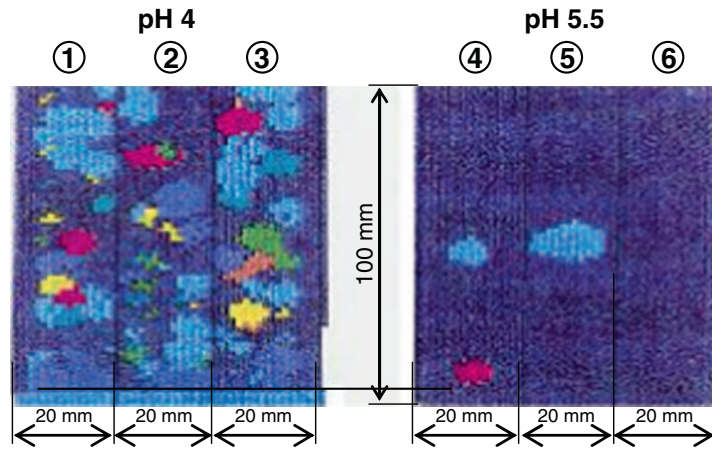
Fig. 2. Ultrasonic C-scan image of six coupons tested in TM-0284 solution: three coupons with significant cracks tested at pH 4, and three coupons no cracking tested at pH 5.5

3.2. Threshold hydrogen concentration, C_{th}, and pH_{th}

Data on threshold hydrogen concentration, C_{th}, and pH_{th} values for linepipe steels of Group #1 in Table 1: WC-1, G-2, AM-1, PC-1, CTR-2 and AM-2 are summarized in Table 2. Also reported in the table is the occurrence of cracking as indicated by ultrasonic C-scans. For each steel the threshold hydrogen concentration, C_{th}, and pH_{th} are arrived at from the data presented in the corresponding table for that steel. It may be noted here that cracking was observed below pH 5 in all but two of the steels. Two steels, CTR-2 and AM-2, did not crack even at pH 1, whereas the other steels showed cracking below pH 5. The most probable mechanism of the accelerating effect of hydrogen sulphide involves the formation of a molecular surface complex (Fe H-S-H)$_{ads}$ which on cathodic polarization leads to formation of hydrogen atoms. Some of the hydrogen atoms may recombine while others diffuse into the metal.

$$Fe + HS \rightarrow Fe \, (HS^-)_{ads} \tag{1}$$

$$Fe(HS^-)_{ads} + H_3O \rightarrow Fe\,(H\text{-}S\text{-}H)_{ads} + H_2O \tag{2}$$

$$Fe\,(H\text{-}S\text{-}H)_{ads} + e^- \rightarrow Fe(HS^-)_{ads} + H_{ads} \tag{3}$$
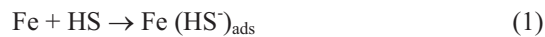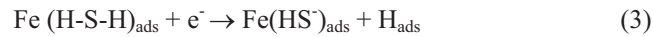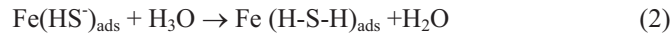
Among the steels studied CTR-2 and AM-2 would be the best choice for use in sour media.

Table 2. Data on threshold pH and hydrogen concentration

	Steels	Thresh pH	Threshold hydrogen concentration mL (STP)/100 g steel	Ca/S ratio	Cracking (Yes/No)
Three samples were tested in each pH	WC-1	5.3	0.3 ± 0.1	0.15	Yes
	G-2	5.3	0.6 ± 0.3	0.50	Yes
	PC-1	5.3	0.4 ± 0.3	0.96	Yes
	AM-1	5.3	1.2 ± 0.4	1.31	Yes
Six samples were tested in each pH	CTR-2	<1.1	$> 1.5 \pm 0.2$	2.62	No
	AM-2	<1.1	$> 2.0 \pm 0.2$	2.50	No

3.3. Significance of inclusions

Scanning electron microscopic examination indicated the presence of cracks as shown in Fig. 3. The EDX microanalysis revealed that the inclusions in cracks are manganese sulphide.

The present investigation shows that MnS inclusions are the dominant initiation sites for cracking. These MnS inclusions provided sites for hydrogen to accumulate, leading to higher HIC susceptibility.

3.4. Mapping by image analysis of linepipe steels

In order to assess the relationship between HIC and non-metallic inclusions and in particular planar arrays of aligned inclusions, it was desired to obtain quantitative metallographic information for the inclusion population in a number of linepipe steels that were assessed for HIC.

This was achieved by image analysis where two types of inclusion geometry were identified and measured separately, namely, long strings of fragmented inclusions and other dispersed inclusions.
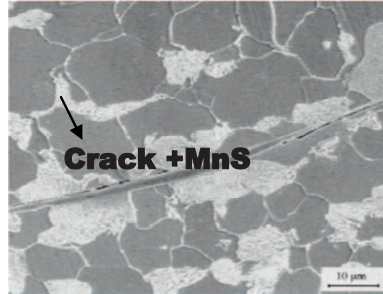
Fig. 3. SEM of coupons tested in sour environment showing massive and elongated non-metallic inclusion (MnS) and cracking surface

3.5. Quantitative metallography

Data on volume percent, average size and length of inclusions were investigated by image analysis and are reported in Table 3. The results are correlated with threshold hydrogen concentration and plotted in Fig. 4. It is clear from this figure that the steel with minimum inclusions has the highest threshold hydrogen concentration and vice versa.

The correlation is shown in Table 3 as a ratio of inclusion volume fraction to that of the WC-1 steel [highest volume fraction (0.387 in Table 3)] versus the ratio of hydrogen threshold concentration to that of AM-2 steel [highest hydrogen threshold concentration (~2.0 mL in Table 3)]. A linear relationship exists between threshold hydrogen concentration ratio and the quantity of inclusions in the steel.
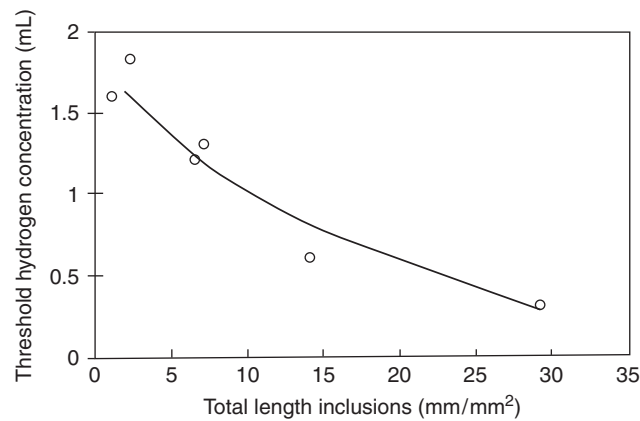
Fig. 4. Effect of the total length inclusions on threshold hydrogen concentration for cracking (C_{th})

Table 3. Linepipe steels data on inclusions

Sample	Vol. %	Average size (Fm)	#/mm^2	Length/mm^2	Threshold hydrogen concentration mL (STP)/100 g
WC-1	0.387	1.73	16963	29.3	0.3
G-2	0.338	2.45	5729	14.1	0.6
AM-1	0.209	3.71	1774	6.5	1.2
PC-1	0.205	4.96	1382	6.9	1.3
CTR-2	0.042	3.25	278	0.9	>1.5
AM-2	0.034	1.41	1614	2.2	>2.0

The size and shape of the inclusions were considered to depend on the Ca/S ratio in steel. The Ca/S ratio in Table 2, showed that a greater ratio of Ca/S decreases the hydrogen damage susceptibility; i.e. steels CTR-2 and AM-2. According to the results, steel susceptibility to SSC and HIC depends on the stress localization around large and hard inclusion particles. This localized stress could exceed the yield strength.

4. Conclusions

There is good correlation between inclusion measurements and HIC. The elongated MnS and planar array of other inclusions are primarily responsible for cracking. Lower volume fractions of inclusions corresponded to higher resistance to HIC. However, the microstructure may also play a role in HIC, in particular, heavily banded microstructures could enhance HIC by providing low fracture resistance paths for cracks to propagate more easily.

References

[1]   Ikeda et al. (1977), Proc. of the 2nd International Conference on Hydrogen in Metals, Paris, 4A-7.
[2]   Tau L, Chan SLI, Shin CS (1996), Effects of anisotropy on the hydrogen diffusivity and fatigue crack propagation of a banded ferrite/pearlite steel, Proc. of the 5th International Conference on Hydrogen Effect in Materials, edited by AW Thompson and NR Moody, The Minerals, Metals and Materials Society, pp. 475.
[3]   Ikeda A, Kaneke T, Hashimoto I, Takeyama M, Sumitomo Y, Yamura T (1983), Proc. of the Symposium on Effect of Hydrogen Sulphide on Steels, 22nd Annual Conference of Metallurgists, August 22–24, Edmonton, Canada, Canadian Institute of Mining and Metallurgy (CIM), Montreal, pp. 1–71.

[4] Elboujdaini M, Revie RW, Shehata MT, Sastri VS. Ramsingh RR (1998), Hydrogen-induced cracking and effect of non-metallic inclusions in linepipe steels, NACE International, Houston, Texas, Paper No. 748.
[5] Turnbull A, Saenz de Santa Maria M, Thomas ND (1989), Corrosion Science, vol. 29, No. 89
[6] Tamaki K, Shimuzu T, Yamane Y (1991), Corrosion/91, Paper 14.
[7] Standard Test Method TM-0284, Test method evaluation of pipeline steels for resistance to stepwise cracking, NACE International, Houston, Texas.

Defect Assessment on Pipe Transporting a Mixture of Natural Gas and Hydrogen

Guy Pluvinage

Laboratoire de Fiabilité Mécanique, ENIM, Ile du Saulcy Metz 57045, France

Abstract   Procedure of defect assessment for steel pipes used for hydrogen or mixture of natural gas and hydrogen is proposed. The hydrogen concentration is controlled by a cathodic polarisation method. Fracture toughness for blunt pipe defect such as dent is measured on "roman tile specimen". It can be determined either critical J parameter or critical notch stress intensity factor. Then the defect assessment is made using a notch modified failure assessment diagramme (NMFAD).

1. Introduction

Nowadays, pipelines for gas and oil transportation are very significant component of national economic infrastructures as well as global. There are the huge plans for installation of new transcontinental pipelines that require of increased attention to their reliable and safe exploitation. In this frame, the hydrogen degradation of pipeline steels is the important problem among other structural integrity problems from the following reasons.

Specific long term exploitation of pipelines promotes of steel hydrogenating process. First of all, pipeline steels encounter hydrogen during transport of sour crude oil and other petroleum products [1]. Moreover, external environmental conditions cause free corroding processes, where hydrogen can evaluate on metal surface as result of cathodic counterpart of the anodic dissolution reaction. This fact has been proved by several studies [2–4]. Also under in-service condition when a cathodic protection system is in place, hydrogen charging of pipeline steels is possible too [4, 5]. As result there is the problem of structural integrity of aging buried pipelines having cathodic protection [5].

Second reason, which increases of attention to the problem hydrogen degradation of pipeline steels, is fact that hydrogen will play a decisive role in a future energy system, when fossil fuels have become scarce and thus expensive and/or unsuitable from ecological reasons. The number of aspects related to the technical feasibility and economics of developing a hydrogen energy infrastructure are presented and discussed in literature during last decades [6, 7]. The possible use of existing pipeline networks for mixtures of natural gas and hydrogen offers a unique and

19

cost-effective opportunity to initiate the progressive introduction of hydrogen as part of the development of a full hydrogen energy system [6, 8].

2. Determination of hydrogen concentration pipelines steels

Hydrogen concentration in metal has been determined on the base of hydrogen discharging process under anodic polarisation with using of hydrogen electrochemical oxidation method proposed in work [9]. Hear, the standard three-electrode electrochemical cell has been used (Fig. 1). The hydrogen discharging of specimen were curried out in 0.2 M NaOH (pH = 12.4) solution under anodic polarisation $E_{anodic} = +168\,mV(SCE)$ during some defined time τ_{dis}. The total quantity of absorbed hydrogen by metal can be defined as (Fig. 2):

$$Q_H^{abs} = \int_0^{\tau_{dis}} \left[I_H\left(\tau\right) - I_{ref}\left(\tau\right) \right] d\tau \quad \text{under } E_{anodic} = \text{const.} \tag{1}$$

where $I_H(\tau)$ is anodic polarisation current for hydrogen charged specimen and $I_{ref}(\tau)$ is anodic polarisation current for specimen without hydrogen (reference curve). Calculation of hydrogen concentration was done according to formula:

$$C_H = \frac{Q_H^{abs}}{zFv} \tag{2}$$

where z is the number of electrons take in reaction; F is the Faraday constant; v is the effective volume of specimen: $C_H \left[\text{mol}/\text{cm}^3 \right]; Q_H^{abs} \left[A.s \right]; \quad z = 1;$ F=9,65×10^4 C/mol; v=0.256cm^3. Process of hydrogen charging of pipeline steels at the given conditions of cathodic polarisation was characterised by following parameters: hydrogen concentration in metal C_H; total quantity of evaluated Q_{ev} and absorbed Q_{abs} hydrogen; averaged meaning of cathodic current density i_c and coefficient of efficiency of hydrogen permeation in metal $k = Q_{abs}/Q_{ev}$.

Comparative assessment of X52, X70 and X100 steels showed that last possesses of highest resistance to hydrogen absorption. The steel X70 is the most sensitive to hydrogen-charging in assigned testing conditions (Fig. 3a). The hydrogen evaluation process is slightly intensive for X100 steel than the for X52 and X70 steels. For all steels, the efficiency of hydrogen permeation in metal is quite low and depends on time of exposition. It can be stated that under $\tau \geq 20$ hours there is the tendency of monotonic decreasing of parameter $k = Q_{abs}/Q_{ev}$ up to level $k = 0.0012 - 0.0024$ (Fig. 3b).
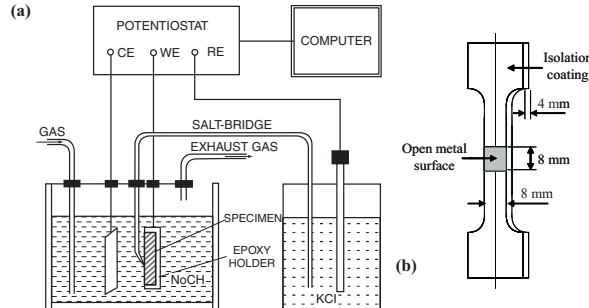
Fig. 1. Schematic view of the electrochemical cell (**a**) and specimen (**b**) for determining of hydrogen discharging current
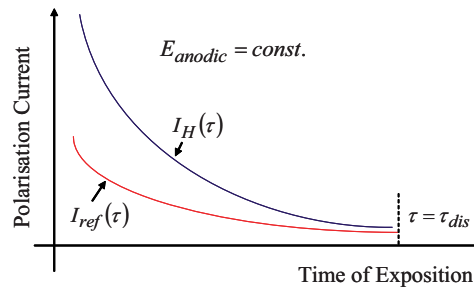
Fig. 2. Schematic view of hydrogen discharging process under anodic polarisation
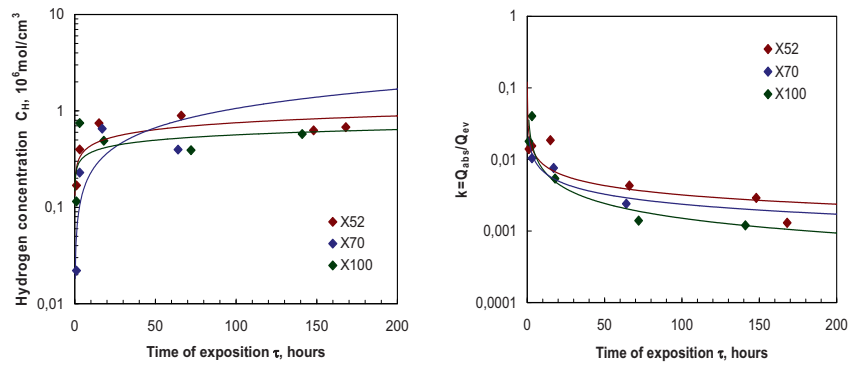
Fig. 3. (**a**) Hydrogen concentration in metal versus time of exposition of unloaded specimens under cathodic polarisation of pipeline steels API X52, X70 and X100. (**b**) Efficiency of hydrogen permeation in metal versus time of exposition of specimens under given cathodic polarisation

Applied stress (gross stress σ_{gross} which corresponds of the internal pressure in pipe under exploitation $p_{exp} = 70$ bar) can intensify the hydrogen charging

process in several times at least. At that, under $\tau \geq 100$ hours the difference between hydrogen concentration in unloaded and stressed metal can exceed more than five times. Based on experimental results; the increasing of hydrogen concentration in metal versus time of exposition of specimens in the hydrogenating conditions can be described by power relation:

$$C_H = A \cdot 10^{-6} \cdot \tau^m \text{ mol/cm}^3 \tag{3}$$

where A and m are constants (Table1).

Table 1. Meanings of constants in formula (3)

Steel	Unloaded metal	Stressed metal
API X52	C_H=0.253 10^{-6} $\tau^{0.24}$	C_H=0.300 10^{-6} $\tau^{0.57}$
API X70	C_H=0.049 10^{-6} $\tau^{0.67}$	C_H=0.400 10^{-6} $\tau^{0.42}$
API X100	C_H=0.200 10^{-6} $\tau^{0.19}$	–

3. Hydrogen embrittlement and brittle to ductile transition with hydrogen concentration

For fracture toughness test the special "Roman tile" [10] specimens were used. The specimens were notched for modeling of the longitudinal external defects under operating internal pressure. Here, should be noted that prevail number of reported studies [11–14] were conducted with using of cathodic charging of hydrogen under high density of polarisation current. Such charging is not truly representative of the hydrogen entry conditions in real operating pipelines, where there is the situation of freely corroding system [15].

This fact was pointed out in work [4]. Accounting the fact that a steady state condition of hydrogen charging cannot be imposed nor obtained in a freely corroding situation, in presented study the following procedure has been made. The specimens were hydrogen charged at some constant potential of polarisation $E_p = const$, which is slightly negative than free corrosion potential for given steel: $E_{cath} = 1000 \text{ mV}(SCE)$ and $E_{corr} = -800 \text{ mV}(SCE)$.

For this experimental procedure the potentiostat VMP [16] has been used. The specimens were immersed into the cell with special NS4 solution and exposed under constant potential of polarisation $E_{cath} = const$.

The surface of auxiliary electrode was parallel to notch plane with some constant distance h. The mutual location of working (specimen) and auxiliary electrodes is given in Fig. 4.

Fig. 4. Mutual location of working electrode (specimen) and auxiliary electrode
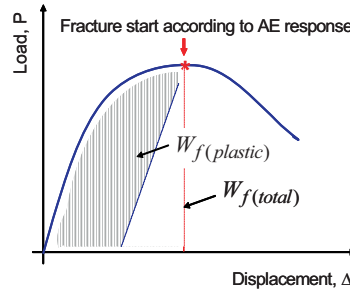
Fig. 5. Scheme of local fracture work determining

During the hydrogen-charging process, the specimens are loaded. The level of load was defined as gross hoop stress σ_{gross} which corresponds of the internal pressure in pipe under exploitation $p_{\exp} = 70$ bar. The hydrogen-charging process was controlled by registration of the cathodic polarisation current $I_{cath}(\tau)$. The total quantity of evaluated hydrogen on metal surface can be assessed as: After assigned exposition under hydrogenating conditions, all specimens were tested to failure under increasing static loading, according to three-point bending scheme. Testing machine INSTRON was used under the constant rate of displacement of grips $d\Delta/d\tau = 0.02\,\text{mm/s}$. The "load displacement" diagram and acoustic emission (AE) signals were simultaneously registered by PC during the tests. The start of fracture process has been defined by acoustic emission method.

$$Q_H^{ev} = \int_0^{\tau_{\exp}} I_{cath}(\tau)d\tau \quad under\ E_{cath} = const. \tag{4}$$

Fracture toughness of notched specimens is given, which reflect of local strength of pipeline steels in presence of hydrogen.

The data were presented as dependencies of total work of local fracture $W_{f(total)}$ emanating from notch or its plastic component $W_{f(plastic)}$ versus time of exposition τ of specimens under hydrogenating conditions. The scheme of determination of parameters $W_{f(total)}$ and $W_{f(plastic)}$ is given in Fig. 5. For steel X52 the value of critical hydrogen concentration is $C_H \geq 4.3.10^{-6}$ mol$/$cm^3 (Fig. 6). The steel X70 is very sensitive to notch effect even in air and the presence of hydrogen strengthens this tendency. The hydrogen concentration about $C_H \geq 2.1.10^{-6}$ mol$/$cm^3 can be considered as critical, because at this conditions the given steel losses in 2.5 times its local strength with comparison of test in air. Therefore, for assigned testing conditions, steel X52 is preferable than steel X70 from the point of view of local strength at notches. It should be stated that definition "critical concentration" is often used in studies of problems of hydrogen in metals and alloys. Although in different works this term has different physical sense. Hydrogen treatment below the "critical" content was found to cause the substantial rearrangement of dislocations and de-cohesion of grain boundaries and in overcritical condition, the formation of micro crevices at the grain and phase boundaries has been occurred. Two characteristic value of hydrogen concentration in metal of pipe may be classified. First one is concentration $C_{H(0)}$, beginning from which hydrogen affects on local strength of material. Second one is critical concentration $C_{H(critical)}$, which causes the significant loss of local fracture resistance of material. This critical hydrogen concentration defines a real brittle to ductile transition.
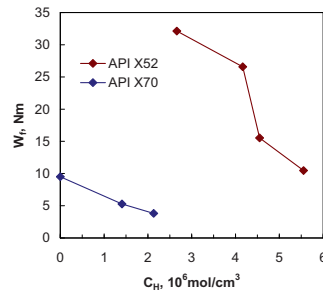
Fig. 6. Comparison of local fracture work emanating from notch in steel API X52 and X70 versus hydrogen concentration in metal

4. Determination of gaz pipe steel fracture toughness in presence of dentes

Stress concentration is considered as the origin in more than 90% of the failures in service.

In Canada it can be seen that the failure caused by corrosion is very important, expressed in 42% cases [15]. In Europe, due to more densely populated area's, the statistics are different; more damage is caused by external interference [16]. A very important fraction of failures is also connected with mechanical damage due to soil digging or excavating by machines. Frequently, notch-like defects are formed in pipelines by machines used in ground removal during construction. Together with cracks caused by stress corrosion, these notches are stress raisers, reducing the material resistance to fatigue and fracture. Therefore, structural integrity of pipelines under various service conditions including the presence of notch-like defects should be evaluated. Therefore it is necessary to measure the pipe steel fracture toughness in a proper way. The concept of the notch stress intensity factor based on the volumetric method has been employed and the corresponding notch fracture toughness $K_{\rho,c}$ was measured. Furthermore, the notch fracture toughness $J_{\rho,c}$ in terms of the J-integral has been determined by means of the load separation method.

The experimental procedure for measurement of the notch fracture toughness of the API 5L X52 steel using a non-standard curved specimen with a notch simulating the expected scratch damage of gas pipelines. The concept of the notch stress intensity factor based on the volumetric method has been employed and the corresponding notch fracture toughness $K_{\rho,c}$ was measured. Furthermore, the notch fracture toughness $J_{\rho,c}$ in terms of the J-integral has been determined by means of the load separation method. The concept of the critical notch stress intensity factor and corresponding local fracture criterion assume that the fracture process requires a certain fracture process volume [8]. This volume is assumed as a cylinder with a diameter called the effective distance. Determination of the effective distance is based on the bi-logarithmic elastic–plastic stress distribution on the continuation of the notch because the fracture process zone is the highest stressed zone. This zone is characterized by an inflexion point in the stress distribution at the limit of zones II and zone III in Fig. 7. This stress distribution is corrected by a weight function in order to take into account the distance from notch tip of the acting point and the stress gradient at this point. The effective distance corresponds is to the inflexion point with the minimum of the relative stress gradient χ which can be written as:

$$\chi(r) = \frac{1}{\sigma_{yy}(r)} \frac{\partial \sigma_{yy}(r)}{\partial r} \tag{5}$$

The effective stress is considered as the average value of the stress distribution within the fracture process zone.

$$\sigma_{eff} = \frac{1}{X_{eff}} \cdot \int_0^{X_{eff}} \sigma_{yy}(r) \cdot \Phi(r) dr \tag{6}$$

Here, σ_{eff}, X_{eff}, $\sigma_{yy}(r)$ and $\Phi(r)$ are effective stress, effective distance, maximum principal stress and weight function, respectively. The notch stress intensity factor is defined as a function of the effective distance and the effective stress [17].

$$K_\rho = \sigma_{eff} \sqrt{2\pi \cdot X_{eff}} \tag{7}$$

where K_ρ is the notch intensity factor, α is a constant. Failure occurs when the notch stress intensity factor K_ρ reaches the critical value, i.e. the notch fracture toughness $K_{\rho,c}$ which reflects the resistance to fracture initiation from the notch tip.
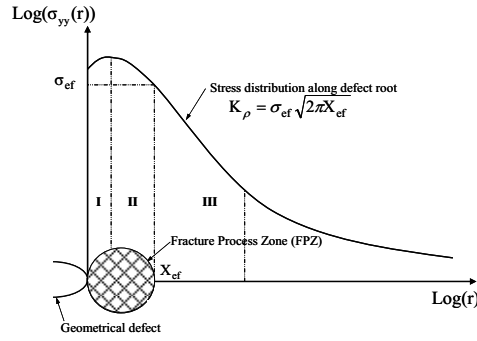
Fig. 7. Schematic distribution of elastic–plastic stress ahead of the notch tip on the line of notch extension and the notch stress intensity concept

The load separation method was adopted to measure the notch fracture toughness in terms of the J-integral. The J-integral can be calculated as the sum of elastic J_e and plastic J_p components [18].

$$J = J_e + J_p = \eta_{el} \frac{A_{el}}{B(W \quad a)} + \eta_{pl} \frac{A_{pl}}{B(W \quad a)} \tag{8}$$

where $E' = \dfrac{E}{1-v^2}$, E is Young's modulus; v is Poisson ratio; η_{el} and η_{pl} are elastic and plastic correction factors, respectively; A_{el}, A_{pl} are elastic and plastic area under the load versus load-line displacement curve, respectively; *W* and *B* are thickness (direction of the notch continuation) and width of the "Roman tile" specimen, respectively; *a* is notch depth in thickness direction. More recognized equation is given by:

$$J = J_e + J_p = \frac{K^2}{E^{'}} + \eta_{pl} \frac{A_{pl}}{B(W-a)} \tag{9}$$

where K is the notch stress intensity factor. Such dividing the J-integral could be useful to analyse a contribution of elastic and plastic J-components in deformation and fracture process. The J-integral can be also written using its energy rate interpretation.

$$J_{pl} = \frac{1}{B} \frac{dA_{pl}}{da} \tag{10}$$

The classical and numerical methods to determine η_{pl}-factors are based on the energy rate interpretation of the J-integral for a body with a crack. In this case, from Eqs. (9) and (10) the η_{pl}-factor is found to be:

$$\eta_{pl} = -\frac{(W-a)}{A_{pl}} \frac{dA_{pl}}{da} = \frac{b}{A_{pl}} \frac{dA_{pl}}{da} \tag{11}$$

where $W - a = b$ is remaining ligament length, $A_{pl} = \int_0^{\upsilon_{pl}} Pd\upsilon$. In the Eq. (11) the value of P represents the load applied during the test and the value of v_{pl} is the plastic load-line displacement. The procedure of calculating the η_{pl}-factor can be also based on the load separation method. The method assumes that the load can be represented as a product of two functions, namely, a crack geometry function G and a material deformation function H, it is assumed the load to be in the form:

$$P = G\left(\frac{b}{W}\right) \cdot H \cdot \left(\frac{\upsilon_{pl}}{W}\right) \tag{12}$$

Using this load separation form, it is possible from Eqs. (11) and (12) to represent the μ_{pl}-factor as follows:

$$\eta_{pl} = \frac{b}{\int G\left(\frac{b}{W}\right) H\left(\frac{v_{pl}}{W}\right) dv_{pl}} \frac{d\left(\int G\left(\frac{b}{W}\right) H\left(\frac{v_{pl}}{W}\right) dv_{pl}\right)}{db} = b \frac{G'\left(\frac{b}{W}\right)}{G\left(\frac{b}{W}\right)} \tag{13}$$

The load separation concept introduces a separation parameter S_{ij} as the ratio of loads $P(a, v_{pl})$ of same specimens but with two different crack lengths a_i and a_j over the whole domain of the plastic displacement, namely.

$$S_{ij} = \frac{P(a_i, v_{pl})}{P(a_j, v_{pl})}\bigg|_{v_{pl}=const} \tag{14}$$

Substituting Eq. (13) into Eq. (14), we obtain another presentation of the separation parameter S_{ij}:

$$S_{ij}\left(\frac{b_i}{W}\right)\bigg|_{v_{pl}} = \frac{G\left(\frac{b_i}{W}\right)H\left(\frac{v_{pl}}{W}\right)}{G\left(\frac{b_j}{W}\right)H\left(\frac{v_{pl}}{W}\right)}\bigg|_{v_{pl}} = \frac{G\left(\frac{b_i}{W}\right)}{G\left(\frac{b_j}{W}\right)}\bigg|_{v_{pl}} = const \tag{15}$$

It was suggested that for a given material in the separation region, the $S_{ij}\left(\frac{b_i}{W}\right)$ parameter as a function of remaining ligament b_i determined at constant plastic load-line displacement can be fitted with a power law $G\left(\frac{b}{W}\right) = C\left(\frac{b}{W}\right)^{\eta_{pl}}$, i.e.

$$S_{ij}\left(\frac{b_i}{W}\right)\bigg|_{v_{pl}} = \frac{C\left(\frac{b_i}{W}\right)^{\eta_{pl}}}{C\left(\frac{b_j}{W}\right)^{\eta_{pl}}}\bigg|_{v_{pl}} = A_m\left(\frac{b_i}{W}\right)^{\eta_{pl}} \tag{16}$$

where C is a constant. Thus, the slope of the $S_{ij}(b/W)$ curve is the η_{pl}-factor in Eq. (16). The results of the notch fracture toughness $J_{\rho,c}$ as a function of the notch aspect ratio are presented in Fig. 9. It can be seen that the value of $J_{\rho,c}$ increases with the decrease of the notch aspect ratio.

Thus, the present results on the notch fracture toughness of the API 5L X52 steel can be used in the modified failure assessment diagram for structural integrity assessment of gas pipelines damaged by scratches.
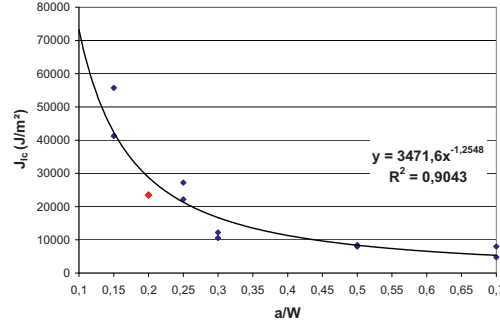
Fig. 8. Dependence of the notch fracture toughness $J_{p,c}$ of the "Roman tile" specimens of the API 5L X52 steel pipe versus the notch aspect ratio. The value of $J_{p,c}$ for $a/W = 0.2$ was represented as a result of the tests of 11 specimens

5. The use of a modified failure assessment diagram for notches and dentes

The critical non dimensional stress intensity k_r^c and critical non dimensional loading parameter L_r^c delineate the critical design curve according to the available codes, e.g., EPRI, RCC-MR, R6 and SINTAP This curve depicts the integrity area as the area under the interpolation curve between critical points (0,1) and (1,0). The non dimensional crack driving force k_r and non dimensional applied stress L_r are primarily defined as the ratio of applied stress intensity factor, K_{app}, to the fracture toughness of material, K_c^*.

$$k_r = \frac{K_{app}}{K_c^*} \tag{17}$$

The British Standard (BS) is firstly improved the FAD diagram by introducing the J integral or crack opening displacement as

$$k_r = \sqrt{\frac{J_{app}}{J_{mat}}} \quad or \quad k_r = \sqrt{\frac{\delta_{app}}{\delta_{mat}}} \tag{18}$$

where, J_{app}, δ_{app} are the applied J integral and crack opening displacement and J_{mat} and δ_c are fracture toughness in terms of critical value of J integral or critical crack opening displacement of the material. For notch and dents problems, the k_r parameter is defined from the notch stress intensity factor.

$$k_r = \frac{K_{\rho,app}}{K_{\rho,c}} \tag{19}$$

where $K_{\rho,c}$ is the critical notch stress intensity factor. Non dimensional stress L_r is described as the ratio of the gross stress σ_g over flow stress (chosen as yield stress σ_Y, ultimate stress; σ_U or classical flow stress $R_c = (\sigma_Y + \sigma_U)/2$).

$$L_r = \frac{\sigma_g}{R_c} \tag{20}$$

The critical assessment points leading to fracture yield an assessment inter-polation curve between two specific or reference limit states: brittle fracture [$k_r = 1$; $L_r = 0$]; plastic collapse [$k_r = 0$; $L_r = 1$]. The assessment point of a component can be highlighted by a point of coordinates k_r^* and L_r^*. If this point is inside the boundary lines of the diagram which is limited by the interpolation curve; the structure is safe. If not, failure occurs, and the assessment point is situated outside of the interpolation curve (Fig. 9).

As illustrated in Fig. 9, the safety factor is denoted using ratio OC over OA for chosen assessment point. According to the codes safety factor consideration, the assessment point is positioned within the acceptable zone of the FAD and the structure fulfils the required conditions for practical engineering applications. The interpolation curve in terms of non dimensional load is given by the level 1 SINTAP formula:

$$f(L_r) = \frac{1}{\sqrt{\left[1 + \frac{L_r^2}{2}\right]}} . \left[0.3 + 0.7 \exp\left(-0.6 . L_r^6\right)\right] \quad 0 \le L_r \le L_{r,\max} \tag{21}$$

$$L_{r,\max} = 1 + \left[\frac{150}{\sigma_y}\right]^{2.5} \tag{22}$$

The safety factor can be defined from the Fracture Analysis Diagram (FAD), starting with the assumption that the defect will not extend under applied loading. It is presented in Fig. 10 that the safety factor can be defined on the radial straight line in the form of the ratio $F_S = $ OB/OA. Figure 10 gives an example of safety factor resulting from the presence of a notch in a gin a gas pipe under a service pressure of 70 bars.
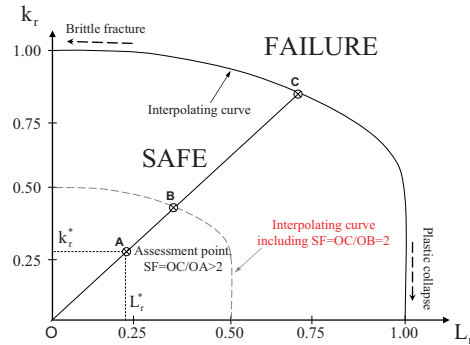
Fig. 9. Typical failure assessment diagram (FAD) indicating safe, failure zone and desirable assessment point
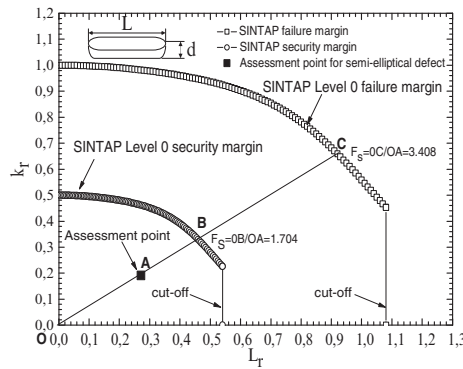
Fig. 10. Modified failure assessment diagram and safety factor associated with defect geometry and internal pressure. Central long notch (t = 6.1 mm, d = t/2, d/L=0.1, ρ = 0.15 mm)

6. Conclusions

Special attention needs to be paid for defect assessment for pipes transporting pure hydrogen or a mixture of natural gas and hydrogen. This is necessary due to hydrogen embrittlement above a critical hydrogen concentration which is relatively low and decreases with the steel yield stress. A special procedure is also necessary for determining fracture toughness in pipe in radial direction due to surface curvature. The use of roman tile specimen is recommended.

Then the Modified Notch failure assessment diagramme can be used to determine the safety factor associated with dent geometry and service pressure.

References

[1] Azevedo C. Failure analysis of a crude oil pipeline. Engineering Failure Analysis 14 (2007) 978–994.

[2] Cheng Y.F., Niu L. Mechanism for hydrogen evolution reaction on pipeline steel in near-neutral pH solution. Electrochemistry Communications 9 (2007) 558–562.

[3] Cheng Y.F. Fundamentals of hydrogen evolution reaction and its implications on near-neutral pH stress corrosion cracking of pipelines. Electrochimica Acta 52 (2007) 2661–2667.

[4] Dey S., Mandhyan A.K., Sondhi S.K., Chattoraj I. Hydrogen entry into pipeline steel under freely corroding conditions in two corroding media. Corrosion Science 48 (2006) 2676–2688.

[5] Shipilov S.A., May I.L. Structural integrity of aging buried pipelines having cathodic protection. Engineering Failure Analysis 13 (2006) 1159–1176.

[6] Yurum C.R. (ed.) Hydrogen energy systems: production and utilisation of hydrogen and future aspects. Kluwer Academic Publisher, the Netherlands (1995), 352p.

[7] Hanneken J.W. Hydrogen in metals and other materials: a comprehensive reference to books, bibliographies, workshops and conferences. International Journal of Hydrogen Energy 24, No. 10 (1999) 1005–1026.

[8] Ibeh B., Gardner C., Ternan M. Separation of hydrogen from a hydrogen/methane mixture using a PEM fuel cell. International Journal of Hydrogen Energy 32 (2007) 908–914.

[9] Yan M., Weng Y. Study on hydrogen absorption of pipeline steel under cathodic charging. Corrosion Science 48 (2006) 432–444.

[10] Adib-Ramezani H., Jeong J., Pluvinage G. Structural integrity evaluation of X52 gas pipes subjected to external corrosion defects using the SINTAP procedure. International Journal of Pressure Vessels and Piping 83 (2006) 420–432.

[11] Hardie D., Charles E.A., Lopez A.H. Hydrogen embrittlement of high strength pipeline steels. Corrosion Science 48 (2006) 4378–4385.

[12] Torres-Islas A., Salinas-Bravo V.M., Albarran J.L., Gonzalez-Rodriguezd J.G. Effect of hydrogen on the mechanical properties of X-70 pipeline steel in dilutedNaHCO3 solutions at different heat treatments. International Journal of Hydrogen Energy 30 (2005) 1317–1322.

[13] Zhang T., Chu W.Y., Gao K.W., Qiao L.J. Study of correlation between hydrogen-induced stress and hydrogen embrittlement. Materials Science and Engineering A347 (2003) 291–299.

[14] Cheng Y.F. Analysis of electrochemical hydrogen permeation through X-65 pipeline steel and its implications on pipeline stress corrosion cracking. International Journal of Hydrogen Energy 32 (2007) 1269–1276.

[15] Li M.C., Cheng Y.F. Mechanistic investigation of hydrogen-enhanced anodic dissolution of X-70 pipe steel and its implication on near-neutral pH SCC of pipelines. Electrochimica Acta 52 (2007) 8111–8117.

[16] Rapport de l'enquête MH-2-95, Fissuration par corrosion sous tension des oléoducs et gazoducs canadiens, Office National d'Energie (1996), Canada. 16th EGIG report 1970–2004, December 2005, "Gas Pipeline Incidents", Doc. Number EGIG 05.R.0002

[17] Akourri O., Louah M., Kifani A., Gilgert G., Pluvinage G. The effect of notch radius on fracture toughness J_{IC}. Eng Fract Mech 65 (2000) 491–505.

[18] SINTAP: Structural integrity assessment procedure. Final report E-U project BE95-1462. Brite Euram Programme, Brussels, 1999.

Reliability Analysis of Low Alloy Ferritic Piping Materials

A. Guedri[1, 4], B. Merzoug[2], Moe Khaleel[3] and A. Zeghloul[4]

[1]Department of Maintenance, University Center of Souk Ahras, Algeria

[2]University of Badji Mokhtar, Algeria

[3]PNNL Laboratory, PO Box 999, 902 Battelle Boulevard, Richland, WA 99352, USA

[4]LPMM Laboratory, UMR CNRS 7554, Paul Verlaine University, Metz, France

Abstract   The aim of this study is to improving microstructure and mechanical properties of the weldable gas pipeline steel using laboratory mill. To achieve the required microstructure and mechanical properties of thermo mechanically processed HSLA steels, it is necessary to have an idea about the role of composition and process parameters. The large numbers of parameters obtained during the production process in the plant were systematically changed to optimize the strength and toughness properties. The optimized parameters were used for the production of the API X60/X70 steel. However, the controlled cooling after rolling should result in transformed products that provide excellent combination of strength and toughness. The coiling at an appropriate temperature have the advantage of the precipitation strengthening, giving further rise to the high yield strength and also improvement in toughness of the steel. The coiling temperature is a decisive parameter because it determines the beginning of the formation of fine precipitations. Therefore, four different laboratory cooling systems were used, in this study to simulate the rolling conditions of a real industrial Thermomechanically controlled process, as close as possible and to check the possibilities of improving the mechanical properties of the welded pipeline steel.

Keywords: Micro Alloying, TMCP, Controlled Rolling, Controlled Cooling, Processing Parameters, Mechanical Properties.

1. Introduction

Piping systems experience fatigue damage as a result of anticipated plant transients (e.g. rapid cooling of the piping during auxiliary feed water initiation following a scram) and because of unanticipated transients (e.g. check valve leakage) [1]. This paper describes the probabilistic fracture mechanics computer code and structural mechanics modelling approach used to simulate the effects of these cyclic fatigue stresses on the reliability of reactor piping.

Probabilistic fracture mechanics (PFM) calculations often assume that the stress state in the pipe wall is uniform through the wall thickness. This approach is appropriate for stresses as a result of internal pressure and for bending stresses as a

result of the thermal expansion of pipe systems, but does not address through-wall stress gradient as a result of radial thermal gradients or geometric discontinuities [2]. This paper describes modifications to pc-PRAISE to provide capabilities for probabilistic analysis of fatigue-crack initiation and growth. This expanded version of the software is referred to as Version 4.2. The PRAISE code was originally developed to provide a probabilistic treatment of the growth of crack-like weld defects in piping due to cyclic loading [3]. This treatment of fatigue-crack growth was later expanded to include the initiation and growth of stress corrosion cracks [4]. The software was then made to run on a personal computer for ease and economy of use [5]. The purpose of the efforts reported herein is to expand the capabilities of PRAISE to include a probabilistic treatment of fatigue-crack initiation. The current capabilities for analyzing fatigue-crack growth are then used to continue the calculations to crack penetration of the pipe wall. The schematic diagram of the steps in the piping reliability calculations by pc-PRAISE are presented in Fig. 1.
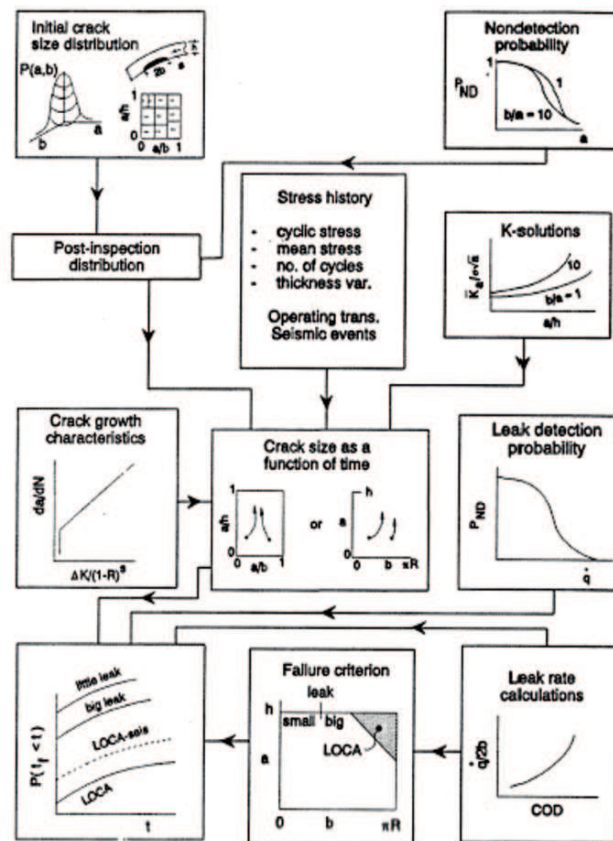
Fig. 1. Schematic diagram of piping failure probability calculation as performed by pc-PRAISE (baseline case)

2. Description of general model

The components of a probabilistic fracture mechanics model of structural reliability that considers the realistic case of two-dimensional cracks are presented in Fig. 1, which also shows the interrelationship of the various components. The approach is applicable to a wide variety of two-dimensional cracks, but the case of semi-elliptical surface cracks of arbitrary aspect ratio in a body of finite thickness will be considered here. Such a crack is shown schematically in the upper left corner of Fig. 1, and is characterized by two dimensions (a) and (b). The model depicted in Fig. 1 is described in detail in [5], so only a brief review will be presented here.

The procedures shown in Fig. 1 are applicable to a given location in a structure, such as a weld of volume V. The as-fabricated crack size distribution is combined with the nondetection probability to provide the post-inspection distribution. The manner in which the cracks that escape detection grow is then calculated by fracture mechanics techniques. The cumulative probability of failure at any time is simply the probability of having a crack at that time equal to or larger than the critical crack size [6].

The crack size distribution at the time of the first in-service inspection (ISI) can be calculated. This pre-inspection distribution is combined with the non-detection probability to provide the post-inspection distribution. Fracture mechanics calculations then proceed up to the next ISI, at which time the procedures are again applied. Calculations of the failure probability for the general model are performed numerically because of the complexity of the fracture mechanics calculations of the growth of two-dimensional cracks as well as the complicated bivariate nature of the crack size distribution [2, 6]. A specific example of results from the general model will be presented later along with a discussion of inputs to the model.

3. Praise modifications to consider fatigue – crack initiation

The Argonne National Laboratory (ANL) crack initiation correlations were for cycles for the tensile load to drop by 25%. This corresponds to a crack of approximately 3 mm depth (0.12 in.) [7, 8]. The specimen size was assumed to be about 2 in. (51.76 mm) gouge length. The fatigue tests were performed under fully reversed loading (i.e., a mean load of zero).

The subroutine provided by the Pacific Northwest National Laboratory (PNNL) already had size-effect and surface-finish adjustments, but a single factor was considered to account for size regardless of size. The subroutine provides cycles to initiation for a given probability of initiation and set of conditions (material, cyclic stress, strain rate, oxygen level, and sulfur content). The relations, "should not be extrapolated beyond a probability of 0.02%" [7, 8]; hence, they are not suitable for initiation probabilities below about 2.10^{-4}.

Modifications were made to pc-PRAISE to consider the initiation of cracks and their subsequent growth to become through-wall. For initiation, the PNNL subroutine for initiation was used in conjunction with Monte Carlo simulation to estimate the probability of initiation as a function of time. The subroutine provides results for a constant stress amplitude, whereas the stress histories to be considered have cyclic stresses of different amplitudes. The Miner's rule was used to account for these more complex stress histories. The cycles per year are equal to the cycles per 40-year life divided by 40; that is, the cycling rate is considered to be constant. A description of each transient is usually provided. Since multiple initiation sites are employed, some adjustment should be made to the size/surface finish compensations made by ANL. A portion of the size/surface finish effect introduced by ANL is removed by multiplying each sampled initiation time by a constant between 1 (using the ANL size/surface finish factor) and 4 (using the ANL laboratory specimen correlations). Tire distribution of initiation time is determined for each of the specimens in a component. The initiation times in each specimen can either be independent or dependent. If dependent and no stress gradient, then each specimen will initiates a crack at the same time. This results in initiated cracks being as long as the component, such as completely around the circumference for a girth weld in a pipe. This leads to all leaks being double-ended pipe breaks. Hence, independent initiation is believed to be the most realistic.

4. Praise modifications for crack growth and linking of multiple cracks

Once a crack initiates, pc-PRAISE calculates its subsequent growth. An initiated crack is considered to be 3 mm (0.12 in.) deep. It is still necessary to specify the surface length $2b_0$ of the initiated crack. Although cracks that grow from a small defect will tend to be nearly semi-circular ($b_0/a_0 = 1$), the median length of an initiated crack is taken to be 7.6 mm (0.3 in.). This is believed to be conservative. The initial length is taken to be a random variable. The value of b_0 itself could be the random variable, and this is one alternative that was considered.

Taking b_0 to be lognormal with a median value of 7.6 mm (0.30 in.), it is then only necessary to define the shape parameter, in order to define the complete distribution. A couple of items of interest in the distribution of b_0 [2] are

1. The probability that (b/a) at initiation is less than 1, which is physically unrealistic because the crack would then be tunnelling into the specimen.
2. The probability that $2b_0$ would be greater than the "specimen" size of 50.76 mm (2 in.).

Multiple cracks can initiate in a component and then grow to perhaps eventually coalesce. The criteria for linking of multiple cracks are already in pc-PRAISE to account for multiple initiations of stress corrosion cracks [4, 5]. The

criteria are based on procedures in the American Society of Mechanical Engineers (ASME) Boiler and Pressure Vessel Code.

5. Correlations between initiation and growth properties

It is conceivable that there is a correlation between the initiation and growth properties of the material. That is, if the crack-initiation characteristics are poor, then the growth characteristics are also poor. Pc-PRAISE provides for treating these properties as either independent or correlated.

If they are correlated, then the one minus the sampled random number used for the initiation simulations is used for the growth relation.

6. Modification of fatigue crack growth relations for ferritic material

The fatigue-crack-growth characteristics for ferritic steels that are built into pc-PRAISE are for LWR environments. At very high values of ΔK, the crack growth relation falls below the air line for this material, which is physically unrealistic. For ferritic steel in air, the crack growth rate is given by:

$$\frac{da}{dN} = C(\Delta K)^{3.726} \tag{1}$$

The exponent 3.726 comes from the ASME Boiler and Pressure Vessel Code. No effect of R is considered for growth in air. C for the ASME air line is 2.67×10^{-11}, which is an upper-bound value. Consider C to be log normally distributed with the ASME value being at the 95th percentile.

The scatter in air will be less than in water. Therefore, the shape parameter, μ, used in pc-PRAISE will be less than for values for water. Taking μ to be the smallest value used in the treatment in pc-PRAISE for water provides a value of 0.542. Once is fixed, the median value of C can be evaluated, which leads to $C_{50} = 1.10 \times 10^{-11}$.

To analyze fatigue crack growth in ferritic materials in water, a sample is drawn for the fatigue crack growth rate in water. The same random number is used to sample the fatigue crack growth rate in air. The crack growth rate is then taken to be the largest of the two.

7. Example

The example problem of the previous section was analyzed using 18 initiation sites with a multiplier on t, of 3 and using $(b_0–a_0)$ as the random variable describing the size of the initiated cracks.

8. Probability result

In addition to probability of crack initiation, the probability of a leak (through-wall crack), is evaluated. Analyses were performed for no circumferential variation of the stresses. The results provide information on the relative leak-to-break probability for situations with and without variations of stress on the surface. Such information is useful in leak-before-break assessments.

For no circumferential stress variation, the stresses were taken to be axisymmetric, and the results are for times extending to 60 years. Figure 2 provides a plot of these results. No results are plotted for the Double-Ended Pipe Break (DEPB) probability because no such failures occurred in the 100 trials performed. Provisions were added to the pc-PRAISE output to summarize the linking of cracks, which is described here. The results for this example problem with no stress gradient are considered.

Figure 3 provides an example of the information in pc-PRAISE on crack initiations, and a summary of crack initiation and linking. Such results are printed out for each evaluation time that is a multiple of 10. Hence, the crack-linking information is printed out for 20, 40, 50 and 60 years. Table1 includes the crack-linking information at 60 years. The results are summarized on a crack-by-crack basis, so information is lost regarding cracks on a weld-by-weld (trial-by-trial) basis.
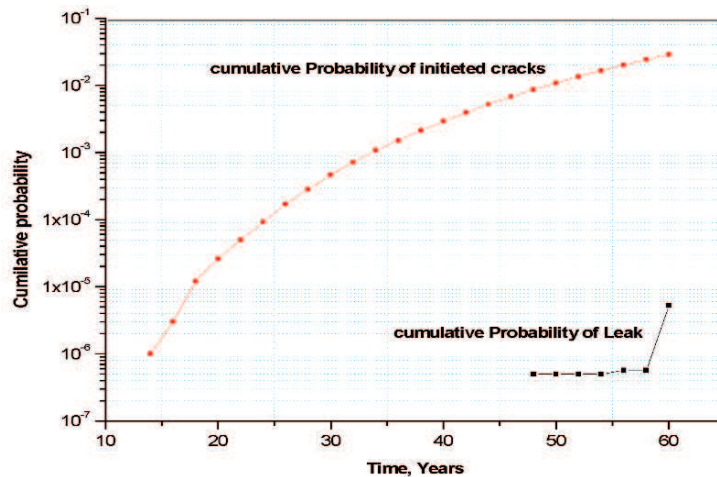
Fig. 2. Cumulative failure probability as functions of time

The effects of the number of initiated cracks sites are shown in Fig. 4, and the benefit effect of (ISI) are shown in Fig. 5. Cracks in the depth range of 0.95 < a/h < 99% are mostly through-wall cracks, which are of particular interest. Table entries for this range of depths provide information on the length distribution of through-wall cracks and how many cracks linked to form them. Any cracks that grew to become leaks before 60 years also appear in the Table 1.
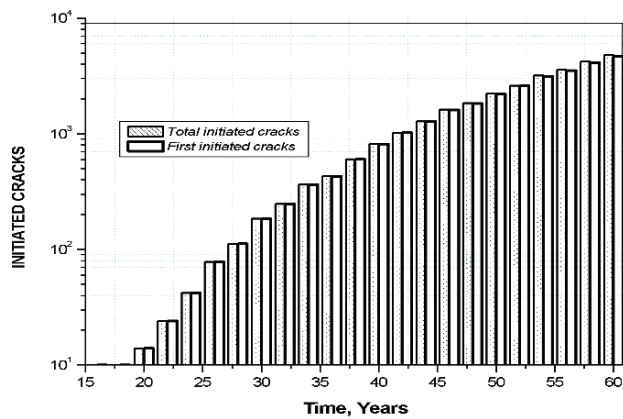
Fig. 3. Crack initiation information from pc-Praise

Table 1. Example of crack-linking information printed out in pc-Praise at Time60 Years

```
At time (yrs)    60.00

   .00< a/h <=   .30

% circumf.  [ ALL ]|[  1 ][  2 ][  3 ][  4 ][  5 ]

   .0- 20.0  28924|  28923      1      0      0      0
  20.0- 40.0      0|      0      0      0      0      0

   .30< a/h <=   .60

% circumf.  [ ALL ]|[  1 ][  2 ][  3 ][  4 ][  5 ]

   .0- 20.0    361|    360      1      0      0      0
  20.0- 40.0      0|      0      0      0      0      0

   .60< a/h <=   .80

% circumf.  [ ALL ]|[  1 ][  2 ][  3 ][  4 ][  5 ]

   .0- 20.0     26|     26      0      0      0      0
  20.0- 40.0      0|      0      0      0      0      0

   .80< a/h <=   .95

% circumf.  [ ALL ]|[  1 ][  2 ][  3 ][  4 ][  5 ]
   .0- 20.0     10|     10      0      0      0      0
  20.0- 40.0      0|      0      0      0      0      0

   .95< a/h <= 99.00

% circumf.  [ ALL ]|[  1 ][  2 ][  3 ][  4 ][  5 ]

   .0- 20.0     13|     13      0      0      0      0
  20.0- 40.0      1|      1      0      0      0      0
```
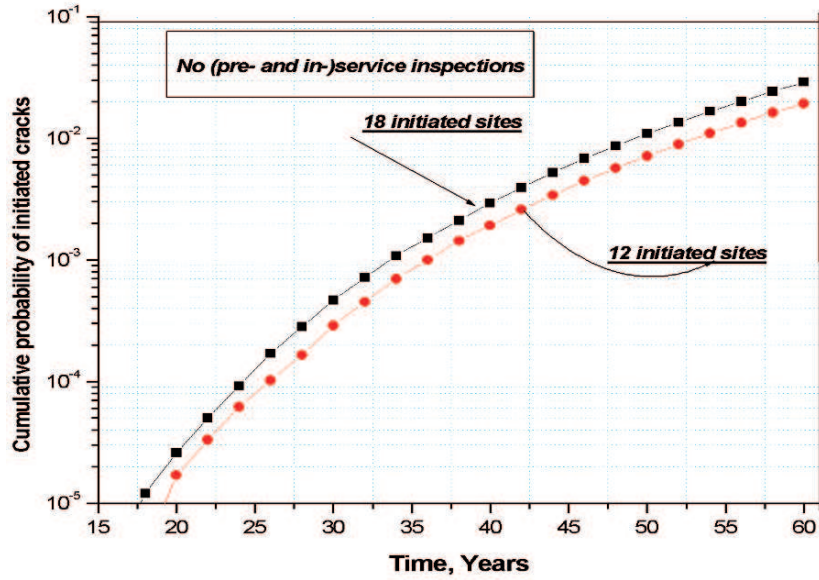
Fig. 4. Effect of initiation site number on the cumulative failure probability
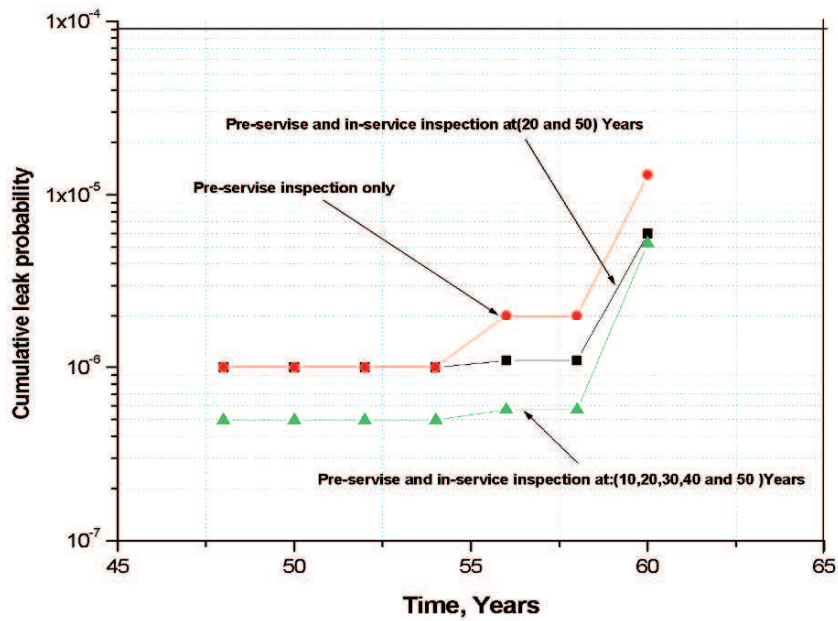
Fig. 5. Effect of pre-service and in-service inspection on the cumulative failure probability

Table 2 summarizes results on a weld-by-weld (trial-by-trial) basis. The number of individual cracks involved is not given, but only the sum of the surface lengths.

Table 2. Crack size data sorted on a weld by weld basis 60 years

	>0	>0.3h	>0.6h	>0.8h	>.95h
0 - 20%	28945	410	49	23	13
20-40%	1	1	1	1	1

9. Conclusions

A probabilistic fracture mechanics model of structural reliability is summarized that considers cracks to be two-dimensional such as semi-elliptical surface cracks. The model uses a fatigue initial crack and crack growth model to grow pre-existing, semi-elliptical, fabrication defects. Critical flaw sizes for pipe breaks are based on a net section collapse criteria of fracture.

Numerical results obtained for a weld in a large reactor pipe are then presented for randomly distributed material properties. As a conclusion, using the initiation only show a weakly cumulative probability of leak in the ferritic components, one may say it will be better to combine the effect of the initiation with a pre-existing crack.

References

[1] Khaleel, M.A. and F.A. Simonen, 1994. A Parametric Approach to Predicting the Effects of Fatigue on Piping Reliability. ASME PVP Vol. 288 Service Experience and Reliability Improvement: Nuclear, Fossil and Petrochemical Plants, Vol. 1, pp. 117–125.

[2] Khaleel, M.A. and F.A. Simonen, 2000. Effects of Alternative Inspection Strategies on Piping Reliability. Nuclear Engineering and Design 197, pp. 115–140.

[3] Harris, D.O., E.Y. Lim, and D.D. Dedhia, 1981. Probability of Pipe Fracture in the primary Coolant Loop of a PWR Plant, Vol. 5: Probabilistic Fracture Mechanics NUREG/CR-2189. US Nuclear Regulatory Commission, Washington, DC.

[4] Harris, D.O., D.D. Dedhia, E.D. Eason, and S.P. Patterson, 1986. Probability of Failure in BWR Reactor Coolant Piping, NUREG/CR-4792, Vol. 3. US Nuclear Regulatory Commission, Washington, DC.

[5] Harris, D.O., D.D. Dedhia, and S.C. Lu, 1992. Theoretical and User's Manual for pc-PRAISE, A Probabilistic Fracture Mechanics Computer Code for Pipe Reliability Analysis. NUREG: CR-5864, UCRL-ID-109798. US Nuclear Regulatory Commission, Washington, DC.

[6] Harris, D.O. and E.Y. Lim, 1983. Applications of a Probabilistic Fracture Mechanics Model to the Influence of In-Service Inspection on Structural Reliability, Probabilistic Fracture Mechanics and Fatigue Methods: Applications for Structural Design and Maintenance. ASTM STP 798, J.M. Bloom and J.C. Ekvall, Eds., American Society for Testing and Materials, pp. 19–41.

[7] Keisler, J.M. and O.K. Chopra, 1995. Statistical Analysis of Fatigue Strain-Life Data for Carbon and Low-Alloy Steels, Risk and Safety Assessment: Where Is the balance? ASME PVP-vol296/SERA-Vol. 3, pp. 355–366.

[8] Keisler, J.M. and O.K. Chopra, and W.J. Shack, 1996. Statistical for Estimating Fatigue Strain-Life Behavior of pressure Boundary Materials in Light water Reactor Environments. Nuclear Engineering and Design, Vol. 167, pp. 129–154.

Experimental Characterization and Effect of the Triaxiality on the Behavior of the HDPE

K. Hachour[1], R. Ferhoum[1], M. Aberkane[1], F. Zairi[2] and M. Nait Abdelaziz[2]

[1]Laboratoire d'Energétique Mécanique et Matériaux. Faculté du Génie de la Construction. Université Mouloud Mammeri, BP 17 RP Tizi-Ouzou 15000, Algéria

[2] Laboratoire de Mécanique de Lille UMR CNRS 8707 Polytech'lille, Cité Scientifique-Avenue Paul Langevin 59655 Villeneuve d'Ascq Cedex, France

Abstract   In this work, a particular interest is granted to the effect of triaxial stress states on the behaviour of the HDPE in uniaxial tensile test. To investigate this effect, tensile tests were performed using notched round bars with four different notch radii (2, 4, 10 and 80 mm). These tests were achieved on an Instron testing machine at constant strain-rate 10-3 s-1 and at ambient temperature. The measure of the local strain is done from the minimal cross-section diameter. We get then the transverse strain. The curves of behaviour deducted of these tests show that the yield stress (defined at the maximal strength point on the conventional stress–strain curve) of the material increases with the reduction of the notch radii. This tendency is due to the fact that the triaxial stress increases with the reduction of the notch radii.

Keywords: HDPE, Damage, Triaxiality, Vidéo-Traction.

1. Introduction

The first studies of the plastic behavior of the semi-crystallines polymers, achieved in the 60 years, were based on nominal laws that don't take into account the plastic instabilities (necking) occurring during the distortion. The following studies tried to establish the true plastic behavior of the material and to characterize the micro-mechanisms of distortion that controls it.

During tensile tests, the necking leads a considerable modification of the triaxial stress that affects on their turn the experimental measures of the stress and the necessary strain for the characterization of these materials.

For the isochores strain (to constant volume), this triaxiality is corrected by a factor given by Bridgman [1]. On the other hand the polymers are subject to phenomena of plastic damage that increase their specific volume [2].

In this work we examine the effect of the stress triaxiality on the behavior of the HDPE diabolo specimens during uniaxial tensil tests.

2. Experimental procedure

2.1. Material

The HDPE studied in this paper is furnished in a first time as granules, imported by the CHIALLI Company (Algeria) and extruded in order to manufacture tubes of different diameters. The specimens are cuts as parallelepipeds from these tubes in the axial sense (see Fig. 1), and machined as notched round bars specimens with four different curvature radius (see Fig. 2). This geometry permits to localize the necking in the zone of minimal cross-section diameter [3].
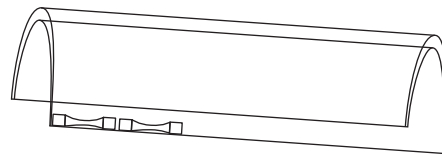
Fig. 1. Cutting sense of the specimens in HDPE tube

D : specimen diameter
r : notch radius
   of curvature
l : notch length
d : notch hole diameter
L : specimen length

Type 1 : r = 2 ; l = 3,87
Type 2 : r = 4 ; l = 7,42
Type 3 : r = 10 ; l = 13,23
Type 4 : r = 80 ; l = 39,69

D=10 ; **L**=66 ; **d**=5 For all specimens
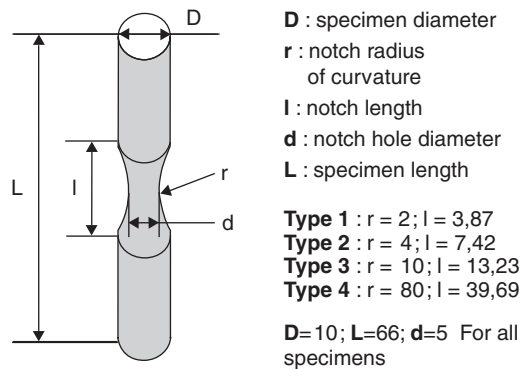
Fig. 2. Notched round bars specimens dimensions

2.2. Tensile tests

Uniaxial tensile tests are conducted at a room temperature on an Instron computer-controlled tension machine on the four kinds (Type 1, 2, 3 and 4) of specimens considered in our tests. The strain rate is imposed constant and equal to $\dot{\varepsilon} = 10^{-3}\,\mathrm{s}^{-1}$. Three (03) tests are made for every type of specimen (notch radii), giving a total of 12 tests.

The local deformations in a representative volume element (RVE) are measured with an intelligent optical extensometer by the video-traction technique developed by the team of Professor G'SELL [4, 5] and marketed by the Appolor® society. A digital video camera analyzes the relative displacements of markers printed on the tensile specimens. Mechanical data analysis, stress and strain, are measured in real time, while the axial strain is dynamically regulating at a constant rate.

3. Experimental results

The videoTraction tests provide the true stress versus true strain curves from local measures. The analysis system marks the minimal diameter of the notch and therefore, the variation of the diameter. We obtain then the transverse strain. Through this test, the software analyzes and records permanently the following data:

- The applied axial strength
- The time
- The minimal diameter
- The transverse deformation at the minimal diameter
- The axial true stress that takes into account the section reduction of the specimen

During the tests, the deformation of specimen exhibit "diffuse" necking which is greatly localized (see Figs. 3 and 4).
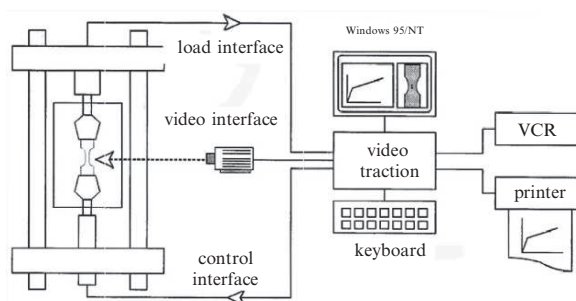
Fig. 3. Videotraction system
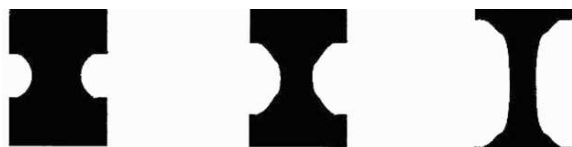
Fig. 4. Necking formation in specimens during tensile test

The curves representing the evolution of the true stress according to the true strain have the same evolution for each type of specimen (see Fig. 5). They present three stages:

(a) Viscoélastic stage due to the successive mechanisms [6, 7]:

  • The deformation of VanderWalls strips
  • Conformations change of the chains in the amorphous phase
  • The inter lamellar sliding

(b) The second stage is characterized by a small but significant reduction of the stress.

(c) The third stage corresponds to the hardening of the material.
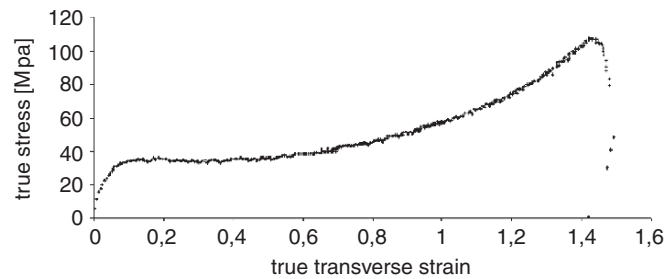
Fig. 5. Tensile test performed at $\dot{\varepsilon} = 10^{-3}\,\mathrm{s}^{-1}$ and at room temperature on notched round bars specimen (type1)

Figure 6 shows the influence of the notch radius on the behavior of the HDPE during the uniaxial tensile tests. Indeed, the yield stress increases with the reduction of notch radius (Fig. 7). It passes from 36.36 MPa for a radius equal to 2 mm, to 25.04 MPa for radius equal to 80 mm. The correspondent limit true strain decreases from 0.12 to 0.053. This tendency is due to the fact that the stress triaxility increases with the reduction of notch radius.
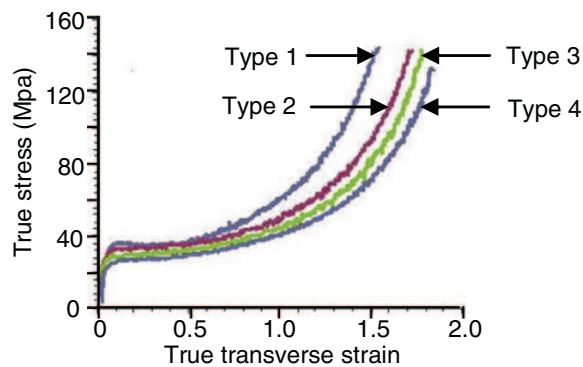
Fig. 6. True stress–strain curves measured in video-controlled tests
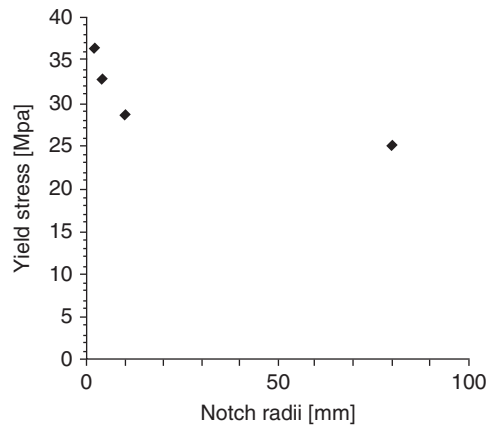
Fig. 7. Trixiality influence on the yield stress

4. Conclusions

The mechanical behavior of the polyethylene during tensile tests presented three (03) stages before the specimens rupture: a viscoélastic stage, a plasticity stage followed by a hardening of the material.

The effect of the triaxiality was verified. Indeed, the tensile tests showed that the yield stress increases with the reduction of notch radii. Also, the stage of plastic hardening of the material during these tests generally occurs when the notch radius is weak.

The variation of the volume during these tests was not determined, since we have used notched bars. That imposes the realization of other tests in order to determine the evolution of the porosity during deformation.

References

[1] Bridgman WP (1964). Studies in large plastic flow and fracture with special emphasis on the effects of hydrostatic pressure. Harvard University Press, Cambridge, Mass.
[2] Dahoun A (1992). Déformation plastique et textures cristallines induites dans les polymères semi-cristallins. Thèse de Doctorat, INPL, Nancy.
[3] G'Sell C (1988). Instabilités de déformation pendant l'étirage des polymères solides. Revue de Physique Appliquée, 23, 1085–1101.
[4] G'Sell C, Hiver JM, Dahoun A, Souahi A (1992). Video-controlled tensile testing of polymers and metals beyond the necking point. J. Mater. Sci., 27, 5031–5039.

[5] G'Sell C, Hiver JM, Dahoun A (2002). Experimental characterization of deformation damage in solid polymers under tension and its interrelation with necking. Int. J. Solids Struct., 39, 3857–3872.

[6] G'Sell C, Dahoun A (1994). Evolution of microstructure in semi-crystalline polymers under large plastic deformation. Mater. Sci. Eng., A175, 183–199.

[7] Glenz W, Peterlin A (1971) Plastic deformation of polymers. Peterlin A (ed.) Marcel Dekker, New York, pp 13–29.

Effects of Aggressive Chemical Environments on Mechanical Behavior of Polyethylene Piping Material

Souheila Rehab-Bekkouche, Nadjette Kiass and Kamel Chaoui

LR3MI, Mechanical Engineering Department, Badji Mokhtar University, BP 12, Annaba, 23000, Algeria

Abstract   During the construction process of fluid handling structures, material selection for pipe applications is an important step. Both natural gas and drinkable water are mainly transported in underground polyethylene (PE) pipe networks. It is known that the interaction between materials like HDPE (high density PE) and its service environment represents critical factors of influence on the structure behaviour for short and long terms. The goal of this study is to establish the effect of some chemical agents on the mechanical properties of PE tubes for underground use. The results are discussed basing on the stress–strain curves and according to the mechanical resistance to aggressive environments. It was found that the environments consisting of solvents show degradation of the mechanical properties of tubes and a structural weakening of the rigidity of the system is observed. Organic solvents have significant oxidizing capacity which weakens polyethylene chains, whereas acids such as H_2SO_4 have less influences on the mechanical properties compared to organic solvents. In the case of crude oil, results show moderate effect although it is known to attack many polymers. In the case of solvents, the elasticity modulus is reduced up to 64% for crude oil which represents a serious problem for the underground polyethylene networks. Design equations of such structure should take into account serious adjustments of long term loads when polyethylene is exposed to aggressive environment.

Keywords: Polyethylene, Pipe, Filaments, Stress, Strain, Chemical Agents, Degradation.

1. Introduction

High density polyethylene resins (HDPE) are largely used in distribution and transmission of fluids such as natural gas and water. The choice of polyethylene (PE) for the manufacturing of gas and water distribution networks rises from the many technical and economic advantages presented by such polymeric materials. PE is a resistant and lightweight material, which facilitates the handling operations and implementation for above and underground applications.

PE systems have good corrosion resistance and support efficiently ground movements' effects due to soil instabilities and high temperature gradients overnight. Because of their good resistance to cracking, the PE pipes have a high reliability level for normal conditions of use.

In such cases, their lifespan is estimated at more than 50 years on the basis of bursting tests used to build a regression curve correlating stress level and failure times [1]. Because the creep phenomenon of polymers can be important even at ambient temperature, the effect of deformation on polymers widely differs from that of structural metals as it is not only function of the magnitude of the stress but also of exposure time. Thus, lifetime management of underground pipelines is mandatory for safety and the use of HDPE tubes subjected to internal pressure, external loading and environmental stress cracking agents requires a reliability study in order to define the service limits and the optimal operating conditions.

In a recent work, a reliability-based study of pipe lifetime model was carried out to propose a probabilistic methodology for lifetime model selection and to determine the pipe safety levels as well as the most important parameters for pipeline reliability [2, 3]. Mechanical properties of HDPE tubular structures are the subject of several research works concerning various aspects, such as the variation of the physical and mechanical properties in relation to the molecular structure [4], the applied load patterns [5–7] and the effects of environments during service conditions [8]. These properties can also be influenced by the manufacturing processes, post production treatments and service life of the finished product [9].

The resistance of polymeric materials to chemical agents depends on the nature of polymer as well as additives processed during extrusion [10]. The strongly oxidizing acids may chemically attack plastics, provoke fading and substantially degrade the mechanical properties. The organic liquids such as fuel oils, mineral oils and various organic solvents cause swellings, softening or finally the dissolution of polymer [11]. Another study treated the degradation of the surface active environment with Arkopal in de-ionized water and it was found that failure times of PE pipes increased continuously with the age of the solutions. This is a good indication of how dangerous, could be the exposure to various chemicals. In addition, ranking of several PE pipe materials can be established based on behavior in aggressive environments.

This study presents a new approach to investigate the mechanical heterogeneity through the wall thickness of a high resistance PE pipe and analyses the interaction between the polymer and some chemical environments representing service environment aggressiveness.

2. Experimental approach

2.1. Material

The material used in this study was extruded by STPM CHIALI Co. of Sidi Bel-Abbès (Algeria). The HDPE resin was obtained by addition polymerization, whereas the tubes were manufactured by co-extrusion.

Typical properties of this polymer are provided in Table 1 [12]. External diameter and pipe wall thickness are respectively 113 and 12 mm.

Table 1. Physical properties of HDPE-100

Property	Value
Density	0.95 - 0.98 g/cm^3
MFI	0.75 g/10 min
Back carbon content	2.0 - 2.5%
Toughness	2 - 5 MPa m$^{1/2}$
Vitreous transition temperature	300 (K)
Softening temperature	390 (K)
Thermal expansion coefficient	150 - 300 (m K^{-1})
Oxidation stability	≥20 min
Resistance to cracking in surface-active environment	≤15 mm/day

2.2. Specimen preparation

In order to measure the mechanical properties in every layer within the pipe, it is needed to prepare specimens with the following criteria: (1) the specimens should be directly extracted from the pipe so that to preserves the build-in thermo-mechanical history, (2) they must obey a reproducible preparation methodology and (3) structural morphology disturbances should be kept to minimum through the reduction of contact stresses during the automatic machining operation. Several cutting conditions were tried with a machining program to obtain the most regular filament section.

Filament cutting was performed continuously in the radial direction with 2 mm steel right tool at a low spinning speed of 45 rpm and a constant depth of cut of 0.96 mm/tr. A batch of five continuous filaments and set of three test specimens of dimensions $120 \times 4 \times 0.5$ mm^3 is depicted in Fig. 1a, b.
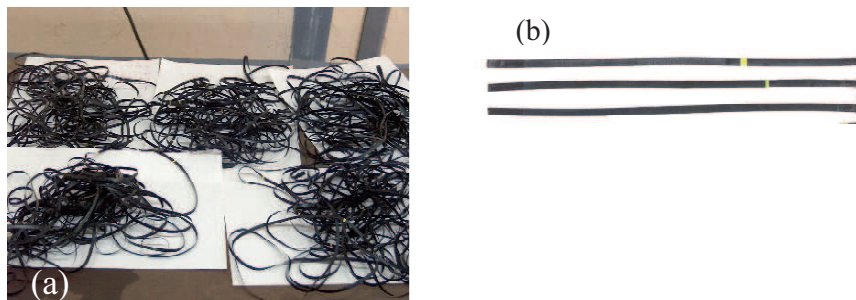
Fig. 1. (a) Machined PE filaments and **(b)** Prepared set of specimens

2.3. Experimental procedure

Test specimens (Fig. 1b) were subjected to tensile loads using a Zwick 1120 universal testing machine on the basis of the general recommendations of ASTM D-638. The TestXpert® software controlled and recorded the output data in real time using a computer interface. The testing speed was 1.66 mm/s and the specimens were immerged solutions for 15 months. In H_2SO_4, crude oil and a mixture of toluene–methanol.

3. Results and discussion

Typical tensile tests are presented in the form of stress-strain curves at constant speed as illustrated in Figs. 2 and 3. Globally, the curves show three distinct zones: (I) elastic, (II) cold drawing and (III) plastic hardening. These curves show that HDPE has elastic–plastic behavior like the majority of polymers and is drastically influenced by chemical environments.
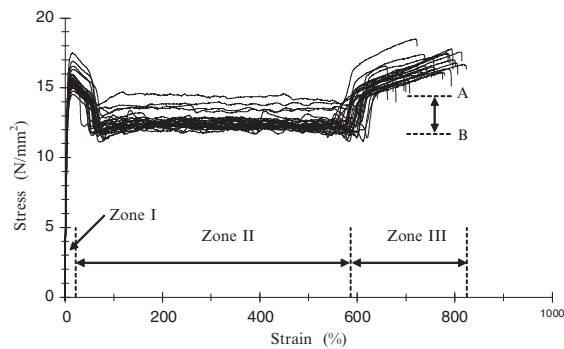
Fig. 2. Stress–strain curves of HDPE-100 in free air
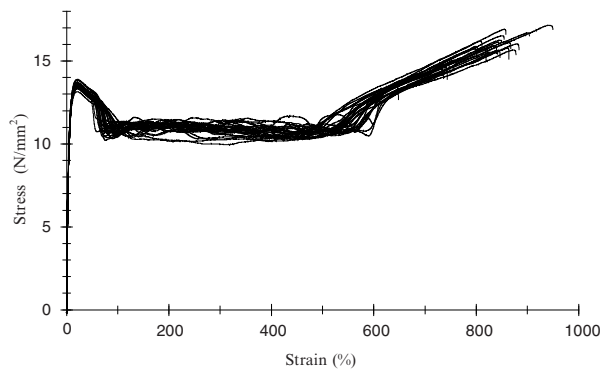
Fig. 3. Stress–strain curves of HDPE-100 in a 50–50% toluene–methanol solution

3.1. Stress strain behavior in air

During and after machining, each HDPE filament is left to deform freely in order to avoid any further effects due to handling. This step is observed in the same way for all specimens and as a result, the inherent manufacturing residual stresses conferred a curly shape which is kept as it is until testing time (Fig. 1b). Stress and deformation values were checked and they are similar to those obtained using standard test specimens.

The spreading of the curves represented by zone II in Fig. 2 is a good indication on how much heterogeneity is contained in a polyethylene pipe wall since all the curves describe the whole pipe wall thickness (from outer to inner layer). The mechanical behavior of HDPE-100 under monotonous traction and which was exposed only to ambient air is depicted in Fig. 2. Three characteristic zones are observed: (I) an elastic zone over less than 25% strain, (II) a zone of drawing propagation which extends roughly over 550% strain and (III) a zone of plastic over-drawing over approximately 250% strain. Zone III is characterized by maximum material orientation and is terminated by tearing.

3.2. Interaction PE with toluene-methanol

Figure 3 presents the interaction of HDPE with a mixture of toluene-methanol which is known to be a good solvent of many materials. It is found that the yield stress is definitely smaller and the thresholds of matter flow (onset of drawing) occurred at slightly more important deformations compared to air results. The drawing phenomenon being located at around 11 MPa is appreciably shortened than that of air. With regard to the onset of plastic hardening, the slope is reduced; i.e. it becomes weaker indicating a direct effect of the mixture of both solvents on the polyethylene structural chains which are now completely oriented around 500% strain up to 900%. The strain at failure reached the 950% limit with less dispersion before rupture.

3.3. Interaction PE with Algerian crude oil

Interaction of HDPE pipe material with crude oil was also studied and substantial decreases in all mechanical properties relating to the state of stress are observed. Indeed, yield stress, drawing stress threshold and average drawing stress are all smaller than those of the air case. The dispersion of the curves obtained for the whole thickness of the tube is rather important especially for zones (II). As an example, the average stress during drawing is spread out between 9.5 and 12.5 MPa, while the nominal breaking stress approaches 19 MPa. A consequent contraction is also noted in the drawing zone which lies over only (~400% strain) to compared to a total of 1000%.

The interaction with crude oil is probably owing to the fact that certain oil fractions might be transported by the gas flow. Moreover, the hardening plastic slope is almost rolled out (distance A–B in Fig. 2) while for both air and toluene-methanol environments the transition is quite drastic.

3.4. Interaction PE with sulfuric acid

In contact with the H^+ ions coming from sulfuric acid, the HDPE presents behaviors contrasting those of crude oil and toluene–methanol environments. The yield stress is comparable with that of the air case. The mean drawing stress is also similar to that of the air (~12.5 MPa) whereas its extent largely exceeds that of the reference case (Fig. 2).

The zone of plastic hardening remains comparable but the strains at failure approaches approximately 1000%, which represents more than 200% compared to the air. It remains much less than that of crude oil environment. Zone III is also characterized by a strong dispersion and the nominal stress at failure is relatively smaller compared to all other cases.

3.5. Mechanical properties evolution across pipe thickness

The change in elastic modulus (E) is depicted in Fig. 4. It is observed that all environments influence negatively the HDPE pipe as compared to air. The most important reduction is associated with crude oil as the change reached more than one third especially at pipe outer and middle regions. Sulfuric acid, crude oil and toluene–methanol solutions affected also the structure reducing E by 36%, 64% and 55%, respectively.

Through the pipe thickness, some fluctuations of E are pointed out but it seems that the lower values are basically at the outer pipe layers. For the yield stress values (Fig. 5), the effect order is inverted as toluene–methanol solution is more aggressive and reduced the elastic limit by 14%. Crude oil remains the most degrading environment for stress values especially at inner pipe layer which presents most critical condition for natural gas distribution networks.

In the case of the nominal drawing stress, definitely toluene–methanol solution is the most aggressive as it lowered the stress level by 16%. The inner layer shows heterogeneous effects dominated by crude oil whereas sulfuric acid is shown to have very minute effect since its curve is overlapping with that of air.

In terms of strain, Fig. 6 illustrates the effects of the environments on the failure strain. It is observed that crude oil has the most preponderant activity as it emerges from the lot with strain at failure 200% higher.
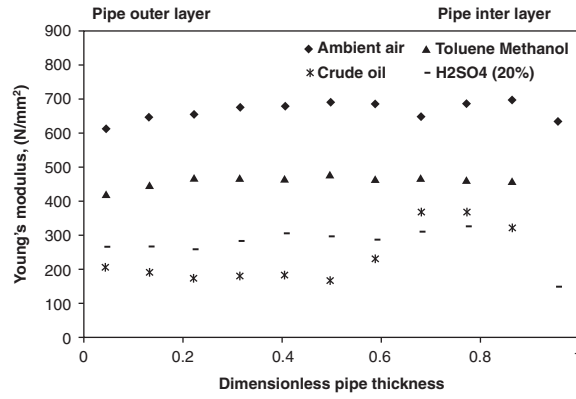
Fig. 4. Young's modulus evolution as a function of pipe thickness
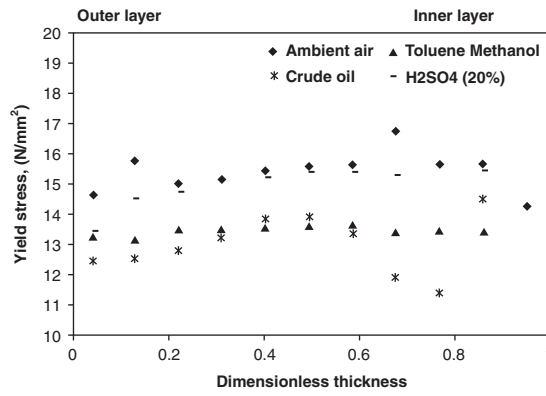
Fig. 5. Changes in yield stress as a function of pipe thickness
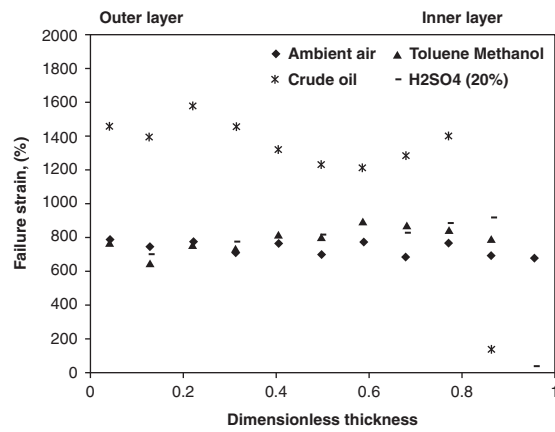
Fig. 6. Evolution of nominal failure strain through pipe thickness

On the other hand, for the drawing extent, it is found that the outer layer present an average value of 600% for most of the environments (Fig. 7). Then, dispersion starts evolving at mid pipe thickness towards the outer layers and the case of crude oil is the striking as $\Delta\varepsilon_{CD}$ fell from 625% to 150%.
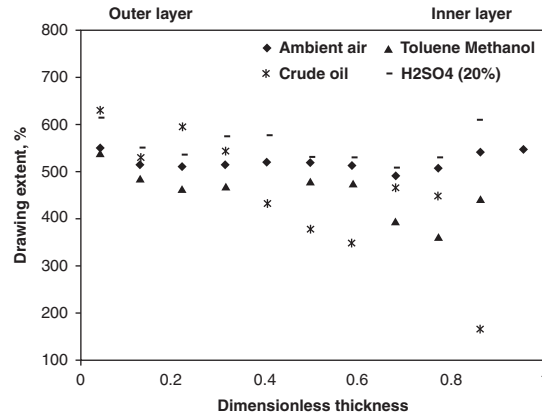
Fig. 7. Evolution of drawing extent through pipe thickness

Table 2 gives a comparison of the values of E, $R_{p0.2}$ (elastic limit at 0.2%), σ_y (maximum yield stress), σ_y (yield strain), ε_{rupt} (strain at failure), σ_{CD} (mean drawing stress) and $\Delta\varepsilon_{CD}$ (extent of drawing in terms of % strain) for the HDPE exposed to considered environments. It can be seen that in term of yield strain, crude oil is allowing the highest value while sulfuric acid exhibits the highest change in cold drawing strains.

It is also noted that the mechanical properties of plastic pipes are strongly influenced by the contact with the chemical agents and swelling plays another role. The resistance of polymeric materials to chemical agents depends on the nature of polymer as well as additives especially anti-oxidants [11].

Table 2. Comparison of mains results

Environment	E N/mm²	$R_{p0.2}$ N/mm²	σ_y (N/mm²)	ε_y (%)	ε_{rupt} (%)	σ_{CD} (N/mm²)	$\Delta\varepsilon_{CD}$ (%)
Air	669.42	6.39	15.33	14.56	737.50	12.22	520.62
Toluene–methanol	461.16	4.29	13.45	19.15	791.74	10.74	452.18
Crude oil	239.82	8.64	13.00	27.95	1245.44	11.02	452.90
H_2SO_4 (20%)	277.36	10.72	15.01	19.32	731.90	12.40	553.50

The results indicate that there is an evolution of properties from the external layer towards the inner layer and this is probably due to crystallinity changes which increase in the same direction [13].

Crude oil and its derivatives should be kept away from HDPE pipes as long term mechanical properties are drastically degraded with exposure time.

4. Conclusions

This study showed that the developed technique of filament machining through HDPE pipe thickness is convenient to highlight extruded material mechanical heterogeneity.

Thus, studying aggressive environments effects is possible using stress strain curves. It is found that toluene–methanol solution is very effective in degrading stress components while sulfuric acid basically affects strain ones.

Crude oil effect is important especially on Young's modulus and on the drawing extend. These changes in mechanical properties are consequences of crystallinity changes imposed by the manufacturing process.

References

[1] C. Munier, E. Gaillard-Devaux, A. Tcharkhchi, J. Verdu, Durability of cross-linked polyethylene pipes under pressure. J. Mater. Sci., 37, 4159–4163 (2002).

[2] R. Khelif, A. Chateauneuf, K. Chaoui, Reliability-based assessment of polyethylene pipe creep lifetime. Int. J. Pres. Ves. Pip., 84 (12), 697–707 (2007).

[3] J.M. Lagaron, N.M. Dixon, W. Reed, J.M. Pastor, B.J. Kip, Morphological characterisation of the crystalline structure of cold-drawn HDPE used as a model material for the environmental stress cracking (ESC) phenomenon. Polymer, 40, 2569–2586 (1999).

[4] L. Hubert, L. David, R. Séguéla, G. Vigier, C. Degoulet, Y. Germain, Physical and mechanical properties of polyethylene for pipes in relation to molecular architecture: I. Microstructure and crystallization kinetics. Polymer, 42 (20), 8425–8434 (2001).

[5] H.B.H. Hamouda, M. Simoes-betbeder, F. Grillon, P. Blouet, N. Billon, R. Piques, Creep damage mechanisms in polyethylene gas pipes. Polymer, 42 (12), 5425–5437 (2001).

[6] J. Christopher, G. Plummer, A. Goldberg, A. Ghanem, Micromechanisms of slow crack growth in polyethylene under constant tensile loading. Polymer, 42 (23), 9551–9564 (2001).

[7] B.-H. Choi, Z. Zhou, A. Chudnovsky, S.S. Stivala, K. Sehanobish, C.P. Bosnyak, Fracture initiation associated with chemical degradation: observation and modelling, Int. J. Solid Struct., 42 (2), 681–695 (2005).

[8] Marilda Munaro, Leni Akcelrud, Polyethylene blends: A correlation study between morphology and environmental resistance. Polym. Degrad. Stabil., 93 (1), 43–49 (2008).

[9] J. Cazenave, B. Sixou, R. Seguela, Structural approaches of polyethylene environmental stress-crack resistance. Oil Gas Sci. Technol. – Rev. IFP, 61, No. 6, 735–742 (2006).

[10] Y. Zhou, X. Lu, Z. Zhou, N. Brown, The relative influence of molecular structure on brittle fracture by fatigue and under constant loads in polyethylene. Polym. Eng. Sci., 36, 2101–2107 (1996).

[11] G. Pinter, M. Haager, R.W. Lang, Influence of nonylphenol–polyglycol–ether environments on the results of the full notch creep test. Polym. Test., 26 (6), 700–710 (2007).

[12] STPM Chiali, Tubes polyéthylène et accessoires. Technical Catalog, Sidi Bel-Abbes, (www.stpm-chiali.com), 2000.

[13] N. Kiass, R. Khelif, L. Boulanouar, K. Chaoui, Experimental approach to mechanical property variability through a high-density polyethylene gas pipe wall. J. Appl. Polym. Sci., 97, 272–281 (2005).

Hydrogen Embrittlement Enhanced by Plastic Deformation of Super Duplex Stainless Steel

A. Elhoud[1], N. Renton[2] and W. Deans[2]

[1]Abalt Solutions Limited, Davidson House, Aberdeen Science and Technology Park, Campus 1, Aberdeen, AB22 8GT, Scotland, UK

[2]University of Aberdeen, School of Engineering, Kings College, Aberdeen, AB24 3UE, Scotland, UK

Abstract   The effect of variations in plastic deformation percentage on hydrogen embrittlement of super duplex stainless steel alloy was investigated. Samples were strained to 4%, 8%, 12%, and 16% of plastic strain prior to hydrogen charging. Sufficient hydrogen for embrittlement was achieved by cathodic charging in 0.1 M H_2SO_4 for 48 h at a current density of 30 mA/cm^2. Hydrogen embrittlement susceptibility was highly dependent on the amount of plastic deformation. Experimental results showed that prestraining of super duplex stainless steel and hydrogen charging affected the elongation and the values of the strain required to failure. The total elongation for the samples with no prestraining deformation and tested in air was 29%. This elongation reduced to 25% when the same sample condition (no prestraining) charged with hydrogen. Further reduction in elongation and strain to failure was observed when the prestraining samples were charged with hydrogen prior to tensile testing. Load–displacement results showed that as the percentage of the plastic deformation increased, the elongation and strain to failure decreased. Comparison between the prestrained samples, charged and uncharged with hydrogen, showed a noticeable difference in strain at failure in the hydrogen charged specimens.

Keywords: Super Duplex Stainless Steel, Plastic Deformation, Hydrogen Embrittlement.

1. Introduction

The oil and gas industry has been designing equipment and facilities made of carbon steels for decades. In recent years however, with the discovery of deep, sour-gas wells, the use of corrosion resistant alloys (CRAs) has increased [1]. These CRAs contain alloying elements, such as chromium, nickel, and molybdenum, to improve the materials resistance to corrosion and cracking. Some CRAs combine this high corrosion resistance with high strength. The increased mechanical properties are sometimes achieved through the application of cold work during the mill manufacturing process. The effect of cold-wok on the corrosion performance of specific alloys is often not well understood. Duplex and super duplex stainless steels are one of the groups of corrosion resistance alloys of interest. They are attractive materials for both surface and downhole applications due to their combination of high strength and high resistance to pitting corrosion and chloride stress corrosion cracking [2].

Despite their good resistance to stress corrosion cracking in chloride solution, under some circumstances environmentally assisted cracking in the duplex stainless steels by absorbed hydrogen atoms in the environments containing hydrogen should be considered [3].

One of the ways in which hydrogen can be absorbed in metals is either by atomic hydrogen generated on the metal surface during natural corrosion or during cathodic polarization when metals are connected galvanically with a more active metal and by cathodic charging in aqueous solutions. Protection in corrosive environments, via the use of sacrificial anodes, can result in in-service potentials in the order of −1000 to −1100 mV (SCE).

At more negative potentials, generation of atomic hydrogen at the steel surfaces may lead to significant hydrogen pick-up. The body centered cubic ferrite phase is generally susceptible to hydrogen embrittlement, whilst face centered cubic austenite is much less susceptible but not immune. Consequently, duplex and super duplex steels with mixed ferrite–austenite structure show susceptibility to hydrogen embrittlement [2–4].

One grade of particular interest for downhole applications is UNS 39274, 25Cr–07Ni–0.28N which is cold-worked as a seamless tube. While the effect of straining on the hydrogen embrittlement susceptibility of single phase stainless steels has been studied by a number of authors, see [5] for a list of references, there are a limited number of studies examining the behaviour of super-duplex grades [6]. Understanding of the material's behaviour following hydrogen absorption under conditions of cathodic charging is therefore of significance from a practical standpoint. The aim of this study was to quantify the effect of hydrogen absorption in super duplex stainless steel and the effect of cold-work on hydrogen embrittlement behaviour.

2. Experimental procedure

The material used in this study was UNS 39274 super duplex stainless steel with chemical composition shown in Table 1. This material was solution annealed at 1050°C for 1hour followed by water quench. Cylindrical samples 5 mm in diameter and 100 mm in length were machined into tensile specimens described in schematic view in Fig. 1a.

The region of the specimens to be exposed in the test were ground with emery paper up to 1200 grit, polished with alumina powder to 0.3 micron, then washed with distilled water and dried by hot air. The specimens were then strained in the axial direction beyond the elastic limit and into the plastic deformation range. Five different specimen types were created by applying different amounts of strain namely 0%, 4%, 8%, 12% and 16% elongation at a slow strain rate of 0.1 mm/mm. Following cold-work, one group of specimens was exposed to a hydrogen charging solution while a second reference group was not.

Hydrogen charging was carried out using a cathodic charging cell which consisted of a power supply controlling the applied current, platinum electrode connected to the positive lead in the power supply and the tested sample connected to the negative lead at the power supply was applied, Fig. 1b is a schematic for the cathodic charging cell.

The working electrode of super duplex stainless steel was cathodically charged at a constant current of 30 mA/cm^2 for 48hrs in solution containing 0.1 M H_2SO_4 with 10 mg/L of Arsenic oxide as a promoter element for the rate of hydrogen uptake in the duplex stainless steel during the cathodic charging process. Both charged and non-charged specimens were then strained to failure in air in a uniaxial tensile test at a strain rate of 1 mm/min. The elongation and strain to failure were measured after each tensile test and the results were recorded. After the tensile tests, all specimens were examined using optical and scanning electron microscopic techniques.

Table 1. SDSS chemical composition (wt%)

C%	Si%	Mn%	Cr%	Ni%	Mo%	W%	N%	Cu%	Fe%
0.02	0.34	0.45	24.84	6.54	3.10	2.07	0.280	0.46	Rest
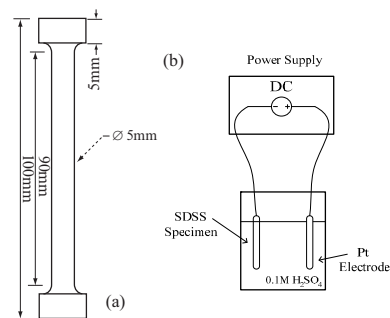
Fig. 1. Experimental apparatus, (**a**) straining test sample and (**b**) cathodic charging cell

3. Experimental results

3.1. Load–displacement results

The load versus displacement behavior of super duplex stainless steel alloy obtained in air for the hydrogen free specimens and specimens charged in 0.1 M H_2SO_4 solution are shown in Fig. 2.

Dealing with the hydrogen free specimens first, Fig. 2a shows that the yield load was increased with increasing cold work, 12.7 kN for 0% pre-strain and

17.15 kN for 16% pre-strain. A small increase in the ultimate load was also recorded for increasing cold-work. There was a decrease in strain to failure with increasing cold work, 0.29 at 0% pre-strain down to 0.086 at 16% pre-strain. The significant reduction in the displacement and an increase in the yield load were caused by the plastic strain hardening of the specimens during the pre-straining. All three results together demonstrate the effect of the cold-work on the material's constitutive relation. Turning to the specimens charged with hydrogen for 48 h in 0.1 M H_2SO_4. Figure 2b shows the load–displacement behaviour was affected by the hydrogen at all pre-straining levels. There was a small increase in the yield load of 0.55% across all specimens compared with the non-charged specimens. However, there was a sizable reduction in the extension to failure with exposure to hydrogen. The extension to failure for 0% pre-strain was reduced from 29.2 mm in the hydrogen free specimen to 24.28 mm in the hydrogen exposed specimen, a reduction of approximately 20%. Similar reductions were experienced at 4%, 8%, 12% and 16% specimens.
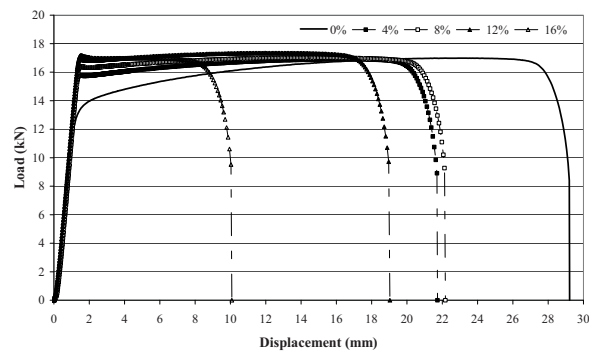
(a) No Hydrogen charging
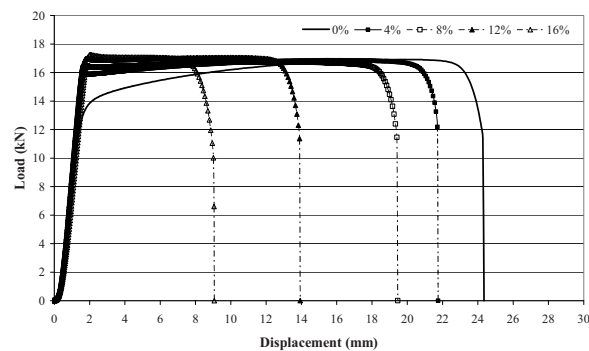
(b) Hydrogen charged specimens

Fig. 2. Displacement curves for SDSS specimens strained in air

A comparison of the elongation to failure of the hydrogen free and the hydrogen charged specimens is contained in Fig. 3. The results show that the largest difference between hydrogen free/hydrogen charged specimens occurred at the 12% pre-strain level. The figure confirms that the properties of SDSS are adversely affected by exposure to hydrogen environment, and that the materials resistance to hydrogen embrittlement reduces with increasing cold work from 0–12%. The 16% pre-strained specimens showed only a small reduction in strain to failure, consistent with the fact that the pre-straining level was well beyond yield and close to the ultimate strain of the material.
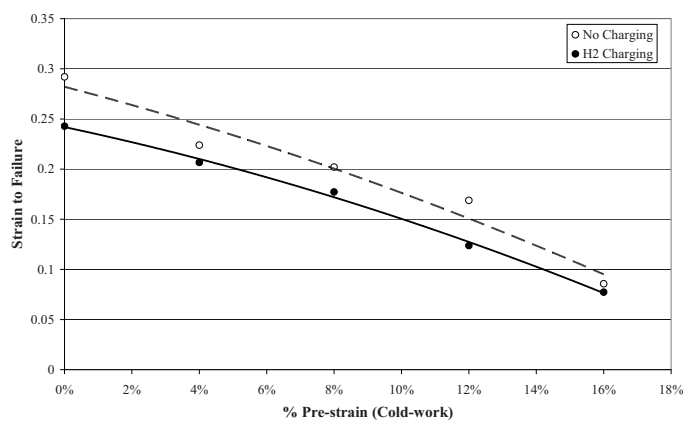
Fig. 3. The effect of hydrogen charging and cold-work on strain to failure of SDSS

3.2. Fracture morphology results

3.2.1. Low power magnification microscope

A fracture morphology investigation was carried out using low power optical micro-scope. The difference in behaviour between specimens which were not exposed to hydrogen and the hydrogen charged specimens is shown in Fig. 4a–d.

Figure 4a shows that the hydrogen free specimen exhibited typical ductile fracture behaviour with severe necking around the fracture. The charged specimen, shown in Fig. 4b, behaved in a different manner, with high numbers of secondary cracks running perpendicular to the direction of loading. Unlike the hydrogen free specimen, the charged specimens showed only minimal necking at the fracture indicating a loss of ductility. The effect of pre-straining deformation on the materials behaviour was investigated by comparing the external fracture surfaces of the specimens charged with hydrogen after 0%, 4%, 8%, 12%, and 16% pre-strain.
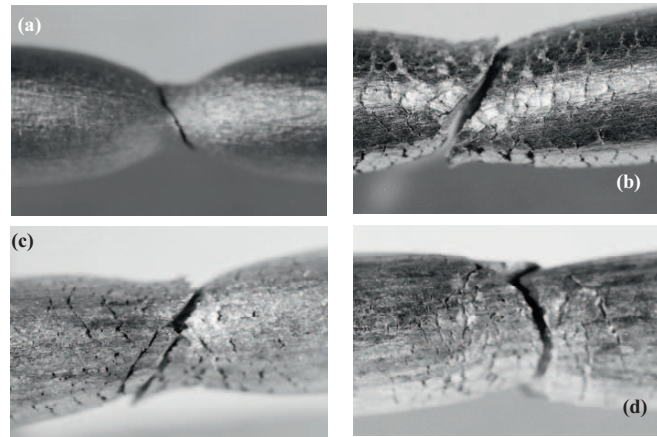
Fig. 4. Low magnification images of the strained to failure specimens
(**a**) X1.25 0% pre-strain, No-charging, (**b**) X1.25 0% pre-strain, H_2 charging, (**c**) X1.25 8% pre-strain, H_2 charging and (**d**) X1.25 12% pre-strain, H_2 charging

Results revealed that the area affected by secondary cracks decreased with increasing plastic deformation. However, the mass and the severity of these secondary cracks increased with increasing the amount of deformation. Examples of this behaviour are shown in Fig. 4c, d which show 8% and 12% pre-strained specimens charged with hydrogen.

3.2.2. High power magnification microscope SEM

A second fracture morphology investigation was carried out using a scanning electron microscope (SEM). Figure 5a shows the fracture surface for 0% pre-strain specimen with no hydrogen. Ductile fracture with extensive necking was observed as shown in the figure, and the fracture surface has a typical dimpled ductile fracture aspect. Contrary results were found for the same metallurgical condition specimen charged in 0.1 M H_2SO_4 solution and strained to failure in air.

Figure 5b image shows extensive brittle fracture around the edges of fracture surface where the material was exposed to hydrogen. The center of fracture surface of this specimen evidenced ductile fracture aspect. The effect of deformation associated with cold work on the material's resistance to hydrogen embrittlement is demonstrated in Fig. 5c, d which shows SEM fractographs of 8% pre-strain and 16% pre-strain.

The images show that the material was embrittled to a greater depth in the pre-strained specimen. Observing the fracture surface of the 4%, 8%, 12%, and 16% pre-strained specimens demonstrated that the greater the pre-strain percentage, the greater the depth of the embrittlement zone. Observing the embrittled zone at higher magnification revealed that a combination of the deformation caused by pre-straining and the hydrogen charging resulted in trans-granular hydrogen cracks and the appearance of severe cleavage fracture.

The SEM results provided evidence of the physical mechanisms involved in the reduction of elongation to failure recorded in the specimens charged with hydrogen, and that the greater the plastic deformation present in the specimen, the greater the embrittlement of the material.
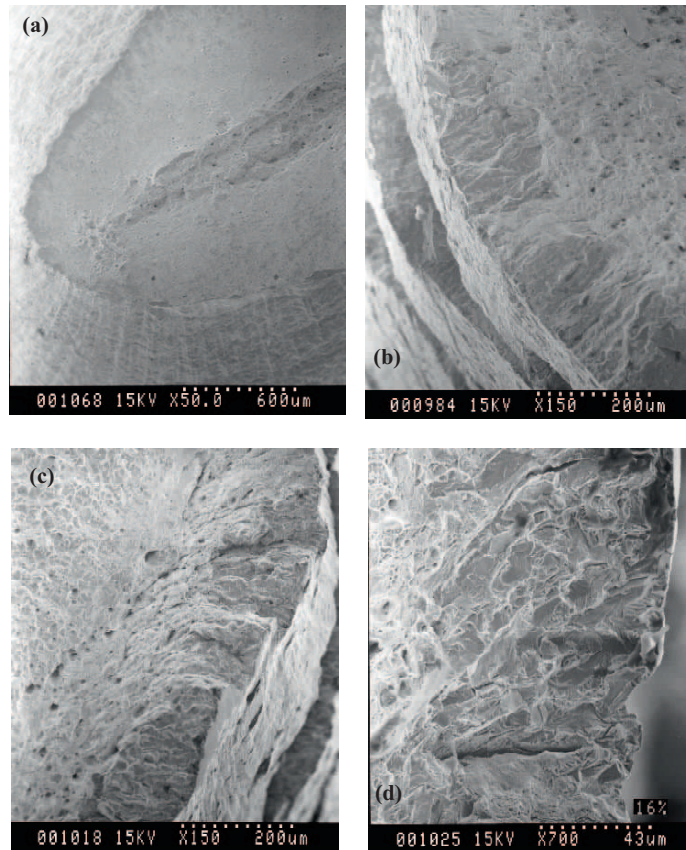
Fig. 5. SEM fracture morphology: (**a**) 0% pre-strain, No-charging, (**b**) 0% pre-strain, H_2 charging, (**c**) 8% pre-strain, H_2 charging and (**d**) 16% pre-strain, H_2 charging

4. Discussion

The experimental results confirmed that cold-work increases the strength of super-duplex in specimens not exposed to hydrogen.

This increase in strength is often the reason behind the selection of cold-worked materials for engineering applications. Cold work can result in an increase in both vacancy and dislocation densities, and one would therefore expect the hydrogen content of a steel to increase with cold work.

Hudson and Stragand [7] measured the hydrogen concentration in steels cold worked to different amounts, after different exposure times to an aqueous sulfuric acid solution. The results indicated that the concentration of hydrogen and the absorption rate are increased significantly with increasing cold work. This is caused by the creation of more hydrogen trapping sites, such as slip bands and dislocations during the plastic deformation process. These potential sites promote hydrogen adsorption on the metal surface and more absorption inside the metal thickness. This increases the hydrogen saturation phenomena for the material.

In this study, the effect of plastic deformation and cold work on hydrogen embrittlement of super duplex stainless steel was investigated by straining the alloy to a wide range of plastic deformation then pulled to failure after charging with hydrogen. The hydrogen charged specimens confirmed the mechanisms described above and the detrimental effect of cold-work on the hydrogen embrittlement susceptibility of the super duplex stainless steel alloy.

This was evidenced by the reduction of elongation and strain to failure as a function of increasing pre-strain 4%, 8%, 12%, and 16%, these finds are shown in detail in Fig. 2 and summerised in Fig. 3. This effect was noted at even comparatively small deformations such as those caused by low cold work up to 4% deformation in the super duplex stainless steel material studied. Failure and fracture morphology at all pre-straining levels confirmed that the SDSS was highly affected by cold work and hydrogen related embrittlement. Huang et al. [8] confirmed that cold work results in both an increase in permeability and decrease in diffusivity of hydrogen in steel.

This implies an increase in the solubility of hydrogen in the steel and the authors have suggested that cold work increases hydrogen uptake. This increase often has a detrimental affect on the material's mechanical properties, such as crack resistance and notch tensile strength [9, 10]. The high magnification images gained from the SEM investigation, shown in Fig. 5, revealed that hydrogen trapping had occurred around the external surface of the specimen.

The depth of material affected by hydrogen saturation phenomenon was clearly controlled by the amount of cold-work. Increasing the cold work also led to deeper secondary and transgrannular cracks. It can be concluded that plastic deformation associated with cold-work increases the solubility of hydrogen in super duplex stainless steel alloys causing hydrogen embrittlement by the interaction of dissolved hydrogen atoms with stress defects and dislocations.

This has a detrimental effect on SDSS's mechanical properties, with a reduction in strain to failure and likely reduction in crack resistance. New developments in the oil and gas industry are seeing greater reservoir depths, higher pressures and downhole temperatures, and an increase in corrosive species.

To keep up with these demands, further research is required to identify the role that cold-work has on the in-service performance of corrosion resistant alloys such as super-duplex stainless steel.

5. Conclusions

The conclusions of the study are as follows:

- Cathodic charging in 0.1 M H_2SO_4 at room temperature for 48 h, results in hydrogen embrittlement susceptibility of SDSS.
- Experimental results confirmed that pre-straining cold work of super-duplex stainless steel is detrimental to the material's resistance to hydrogen embrittlement. This susceptibility to hydrogen embrittlement increases as plastic deformation increase. The strain to failure of the super duplex stainless steel alloy reduced by a combination of hydrogen and cold-work.
- Fracture morphology revealed deformation controlled embrittled zones. The depth of these zones increased as the amount of deformation increased.
- End users should consider the detrimental effect of cold work on SDSS's susceptibility to hydrogen embrittlement during material selection. Practical engineering examples include cold-drawn and expandable production tubulars.

Future research will focus on the effect of charging temperature on embrittlement behaviour.

References

[1] S. E. Mahmoud and C. W. Petersen, Temperature and texture effect on properties of CRAS, P828, Corrosion 92. The NACE Annual Conference and Corrosion Show (1992).

[2] P. Woollin and W. Murphy, Hydrogen embrittlement stress corrosion cracking of super duplex stainless steel. Corrosion, paper 01018 (2001).

[3] T. Sourmail, A review of the effect of cold-work on resistance to sulphide stress cracking. Corrosion, paper 07104 (2006).

[4] Shyan-Liang Chou, Wen-Ta Tasi, Hydrogen embrittlement of duplex stainless steel in concentrated sodium chloride solution. Materials Chemistry and Physics 60, 137–142 (1999).

[5] A. M. Brass and J. Chene, Hydrogen uptake in 316L stainless steel, Consequences on the tensile properties. Corrosion Science 48, 3222–3242 (2006).

[6] T. Zakroczymski, A. Glowacka, W. Swiantnicki, Effect of hydrogen concentration on the embrittlement of a duplex stainless steel. Corrosion Science 47, 1404 (2005).

[7] R. M. Hudson and G. L. Stragand, Effect of cold drawing on hydrogen behavior in steel. Corrosion 16, 253–257 (1960).

[8] Y. Huang, A. Nakajim, A. Nishikata, and T. Tsuru, Effect of mechanical deformation on permeation of hydrogen in iron. ISIJ 43, 548–554 (2003).

[9] H. Asahi and M. Ueno, Effect of cold-working on sulfide stress cracking resistance of low alloy martensitic steels. ISIJ 33, 1275–1280 (1993).

[10] H. Fuchigami, H. Minami, and M. Nagumo, Effect of grain size on the susceptibility of martensitic steel to hydrogen related failure. Philosophical Magazine Letters 86, 21–29 (2006).

Hydrogen Effect on Local Fracture Emanating from Notches in Pipeline Steels

Julien Capelle[1], Igor Dmytrakh[2], Joseph Gilgert[1] and Guy Pluvinage[1]

[1]Laboratoire de Fiabilité Mécanique, École Nationale d'Ingénieurs de Metz et Université Paul Verlaine Metz, France

[2]Karpenko Physico-Mechanical Institute of National Academy of Sciences of Ukraine, (KPhMI), Ukraine

Abstract   The comparative assessment strength and fracture of three API grade pipeline steels: X52; X70 and X100 has been done for conditions of hydrogenating. The factors of cathodic hydrogen charging, time of exposition, hydrogen concentration in metal and applied load were taken into account. The relationship between hydrogen concentration and critical (failure) loading has been found. Also, the existence of some critical hydrogen concentration, which causes the significant loss of local fracture resistance of material, was shown.

1. Introduction

Nowadays, pipelines for gas and oil transportation are very significant component of national economic infrastructures as well as global. There are the huge plans for installation of new transcontinental pipelines that require of increased attention to their reliable and safe exploitation. In this frame, the hydrogen degradation of pipeline steels is the important problem among other structural integrity problems from the following reasons. Specific long term exploitation of pipelines promotes of steel hydrogenating process. First of all, pipeline steels encounter hydrogen during transport of sour crude oil and other petroleum products [1]. Moreover, external environmental conditions cause free corroding processes, where hydrogen can evaluate on metal surface as result of cathodic counterpart of the anodic dissolution reaction. This fact has been proved by several studies [2–4]. Also under in-service condition when a cathodic protection system is in place, hydrogen charging of pipeline steels is possible too [4, 5]. As result there is the problem of structural integrity of aging buried pipelines having cathodic protection [5]. Second reason, which increases of attention to the problem hydrogen degradation of pipeline steels, is fact that hydrogen will play a decisive role in a future energy system, when fossil fuels have become scarce and thus expensive and/or unsuitable

from ecological reasons. The number of aspects related to the technical feasibility and economics of developing a hydrogen energy infrastructure are presented and discussed in literature during last decades [6, 7]. The possible use of existing pipeline networks for mixtures of natural gas and hydrogen offers a unique and cost-effective opportunity to initiate the progressive introduction of hydrogen as part of the development of a full hydrogen energy system [6, 8]. In the present study the comparative assessment strength and fracture of three API grade pipeline steels: X52; X70 and X100 has been done for conditions of hydrogen charging. Here, the factors of cathodic hydrogen charging, time of exposition, hydrogen concentration in metal and applied load were taken into account. The relationship between hydrogen concentration and critical (failure) loading has been considered.

2. Object of study

The objects of study were three API grade pipeline steels, namely: X52; X70 and X100. The specimens for tests were machined from real pipes (Table 1).

Table 1. Pipes size and mechanical properties of steels in air

Steel grade	Outerdiameter (mm)	Thickness (t, mm)	σ_U (MPa)	σ_Y (MPa)	Elongation (%)
X52	610	11.0	528	410	30.2
X70[*]	710	12.7	702	578	45
X100[*]	950	15.0	833	858	17

[*]According to works [1, 11].

3. Experimental procedure

3.1. Specimens

For fracture toughness test the special "Roman tile" [9] specimens were used. As an example, this type specimen with X52 steel is presented in Fig. 1. The specimens were notched for modelling of the longitudinal external defects under operating internal pressure. The notch geometry is given in Fig. 2.
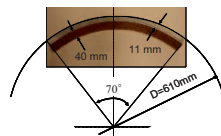
Fig. 1. "Roman tile" specimen with X52 steel
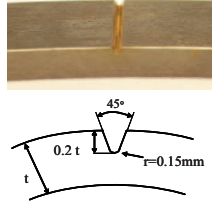
Fig. 2. Geometry of notch

3.2. Hydrogen evolution reaction on pipeline steel in near-neutral pH solution

The study was conducted in special soil solution NS4 with pH = 6.7 [10]. Chemical composition of this environment is given in Table 2.

Table 2. Chemical composition of NS4 solution (g/L) [10]

NaHCO$_3$	KCl	CaCl$_2$	MgCL$_2$.H$_2$O
0.483	0.120	0.137	0.131

In these conditions i.e., in deoxygenated, near-neutral pH solution, hydrogen atoms are generated on the steel surface by the electrochemical reduction of water molecules [2, 3]:

$$H_2O + e \rightarrow H_{ads} + OH^- \qquad (1)$$

The adsorbed hydrogen atoms can subsequently combined to H_2 molecules by the chemical reaction:

$$2H_{ads} \rightarrow H_2 \qquad (2)$$

Or the electrochemical reaction:

$$H_{ads} + H_2O + e \rightarrow H_2 + OH^- \qquad (3)$$

Or can be absorbed by the steel:

$$H_{ads} \rightarrow H_{abs} \qquad (4)$$

The absorbed hydrogen atom concentration under the cathodic polarisation depends on the hydrogen atom recombination mechanisms. When the chemical reaction (2) dominates the hydrogen atom recombination, the applied cathodic polarization enhances the generation of hydrogen atoms and thus the amount of

hydrogen atoms penetrating into the steel. The absorbed hydrogen atom concent-ration will increase continuously with the cathodic polarization potential. In the case of electrochemical reaction (3) dominating the hydrogen atom recombination, the cathodic polarization promotes the generation of hydrogen atoms through reaction (1), and simultaneously, enhances the hydrogen atom recombination through reaction (3). Thus, the role of cathodic polarisation is to generate hydrogen atoms and also to recombine hydrogen atoms.

3.3. Procedure of hydrogen charging of specimens

Here, should be noted that prevail number of reported studies [11–14] were conducted with using of cathodic charging of hydrogen under high density of polarisation current. Such charging is not truly representative of the hydrogen entry conditions in real operating pipelines, where there is the situation of freely corroding system [15]. This fact was pointed out in work [4]. Accounting the fact that a steady state condition of hydrogen charging cannot be imposed nor obtained in a freely corroding situation, in presented study the following procedure has been made. The specimens were hydrogen charged at some constant potential of polarisation $E_p = const$, which is slightly negative than free corrosion potential for given steel: $E_{cath} = -1000$ mV (SCE) and $E_{corr} = -800$ mV (SCE). For this experimental procedure the Potentiostat VMP [16] has been used. The specimens were immersed into the cell with special NS$_4$ solution and exposed under constant potential of polarisation $E_{cath} = const$. The surface of auxiliary electrode was parallel to notch plane with some constant distance h. The mutual location of working (specimen) and auxiliary electrodes is given in Fig. 3.

Fig. 3. Mutual location of working electrode (specimen) and auxiliary electrode

During the hydrogen-charging process, the specimens are loaded. The level of load was defined as gross hoop stress σ_{gross} which corresponds of the internal pressure in pipe under exploitation $p_{exp} = 70$ bar. The hydrogen-charging process was controlled by registration of the cathodic polarisation current $I_{cath}(\tau)$. The total quantity of evaluated hydrogen on metal surface can be assessed as:

$$Q_H^{ev} = \int_0^{\tau_{exp}} I_{cath}(\tau)\,d\tau \quad under\ E_{cath} = const. \tag{5}$$

3.4. Determination of hydrogen concentration in pipelines steels

Hydrogen concentration in metal has been determined on the base of hydrogen discharging process under anodic polarisation with using of hydrogen electro-chemical oxidation method proposed in work [17]. Hear, the standard three-electrode electrochemical cell has been used (Fig. 4). The hydrogen discharging of specimen were curried out in 0.2 M NaOH (pH = 12.4) solution under anodic polarisation E_{anodic} = +168 mV (SCE) during some defined time τ_{dis} (see Fig. 5). The total quantity of absorbed hydrogen by metal can be defined as

$$Q_H^{abs} = \int_0^{\tau_{dis}} \left[I_{cath}(\tau) - I_{ref}(\tau) \right] d\tau \quad under \ E_{anodic} = const. \tag{6}$$

where $I_H(\tau)$ is anodic polarisation current for hydrogen charged specimen and $I_{ref}(\tau)$ is anodic polarisation current for specimen without hydrogen (reference curve).
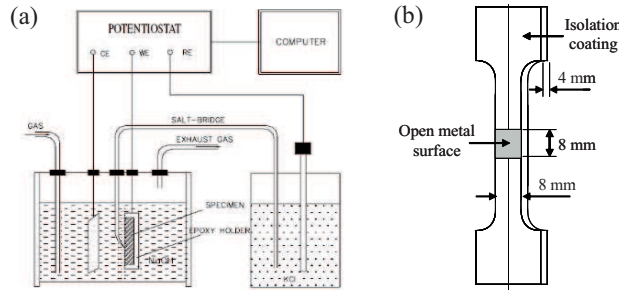
Fig. 4. View of the electrochemical cell (**a**) and specimen (**b**) for determining of hydrogen concentration
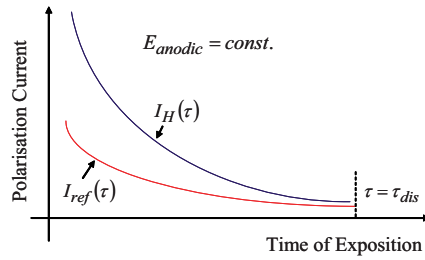
Fig. 5. Schematic view of hydrogen discharging process under anodic polarisation

Calculation of hydrogen concentration was done according to formula:

$$C_H = Q_H^{abs} / zF_v \tag{7}$$

where z is the number of electrons take in reaction; F is the Faraday constant; v is the effective volume of specimen: $C_H \left[\text{mol}/\text{cm}^3 \right]$; $Q_H^{abs} \left[A \cdot s \right]$; $z = 1$; $F = 9{,}65 \cdot 10^4 \ \text{C}/\text{mol}$.

3.5. Sequence of fracture toughness tests

After assigned exposition under hydrogenating conditions, all specimens were tested to failure under increasing static loading, according to three-point bending scheme. Testing machine INSTRON [18] was used under the constant rate of displacement of grips $d\Delta/d\tau = 0.02$ mm/s. The "load – displacement" diagram and acoustic emission (AE) signals (Fig. 6) were simultaneously registered by PC during the tests. The start of fracture process has been defined by acoustic emission method [19]. The general scheme of test is given in Fig. 6.
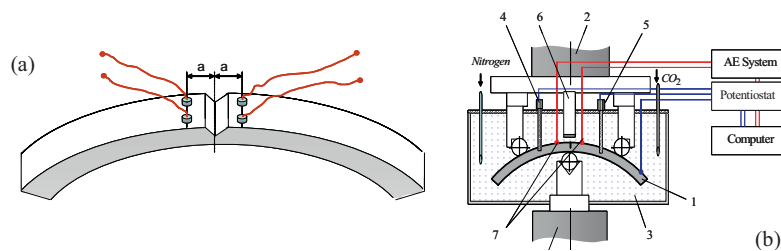
Fig. 6. (**a**) Location of AE sensors on specimen. (**b**) View of testing equipment for fracture toughness determining of hydrogen charged specimens: 1 – "Roman tile" specimen; 2 – loading device of machine; 3 – corrosion cell; 4 – pH electrode; 5 – reference calomel electrode; 6 – auxiliary electrode; 7 – acoustic sensors

4. Assessment of hydrogen concentration in pipeline steels under "SOFT" cathodic charging

Process of electrolytic hydrogen charging of pipeline steels was characterised by following parameters: hydrogen concentration in metal C_H; total quantity of evaluated Q_{ev} and absorbed Q_{abs} hydrogen; averaged meaning of cathodic current density i_C and coefficient of efficiency of hydrogen permeation in metal $k = Q_{abs}/Q_{ev}$. The values of these parameters are given in Tables 3 and 4. Comparative assessment of three steels showed that last possesses of highest resistance to hydrogen absorption.

The steel X70 is the most sensitive to hydrogen-charging in assigned testing conditions (Fig. 7). The hydrogen evaluation process is slightly intensive for X100 steel the for X52 and X70 steels (Fig. 8).

For all, the efficiency of hydrogen permeation in metal is quite low and depends on time of exposition. It can be stated that under $\tau \geq 20$ h there is the tendency of monotonic decreasing of parameter $k = Q_{abs}/Q_{ev}$ up to level $k = 0.0012 - 0.0024$ (Fig. 9). Applied stress (gross stress σ_{gross} which corresponds of the internal pressure in pipe under exploitation $p_{exp} = 70$ bar) can intensify the hydrogen charging process in several times at least (Figs. 10, 11 and 12). Under $\tau \geq 100$ h the difference between concentration in unloaded and stressed metal can exceed more than five times.

Table 3. Data for determining of hydrogen concentration in unloaded pipeline steels

| | τ, hours | Q_H^{ev}, mA·s | i_c, mA/cm² | $\tau_{dis} = 1$ hour | | $k = \dfrac{Q_H^{abs}}{Q_H^{ev}}$ |
				Q_H^{abs}, mA·s	C_H, 10^6 mol/cm³	
API X52	1	297.59	0.129	4.18	0.169	0.0140
	3	636.23	0.092	9.85	0.399	0.0155
	15	989.55	0.029	18.43	0.746	0.0186
	66	5148.3	0.038	22,11	0.895	0.0043
	148	5371.3	0.0157	15.51	0.628	0.0029
	168	12443.3	0.0364	16.75	0.678	0.0013
API X100	1	157.991	0.0281	2.830	0.115	0.0179
	3	458.481	0.0663	18.455	0.747	0.0403
	18	2251.34	0.0651	12.139	0.491	0.0054
	72	6890.18	0.0453	9.689	0.392	0.0014
	141	11726.7	0.0344	14.196	0.575	0.0012
API X70	1	322.725	0.0574	0.536	0.022	0.0017
	3	541.672	0.0784	5.652	0.229	0.0104
	17	2126.96	0.0543	16.193	0.655	0.0076
	64	3584.19	0.0243	14.499	0.397	0.0024

Table 4. Data for determining of hydrogen concentration in stressed pipeline steels

| | τ, hours | Q_H^{ev}, mA·s | i_c, mA/cm² | $\tau_{dis} = 1$ hour | | $k = \dfrac{Q_H^{abs}}{Q_H^{ev}}$ |
				Q_H^{abs} mA·s	C_H, 10^6 mol/cm³	
X52	46	57360	0.226	362.4	2.224	0.0063
	101	168798	0.240	1216.5	5.924	0.0072
	118	147522	0.524	458.6	2.814	0.0031
	167,3	178564	0.463	–	–	–
X70	24	55189	0.276	346.1	1.408	0.0063
	64	144032	0.246	576.4	2.133	0.0040
	115	300806	0.315	490.662	1.997	0.0016
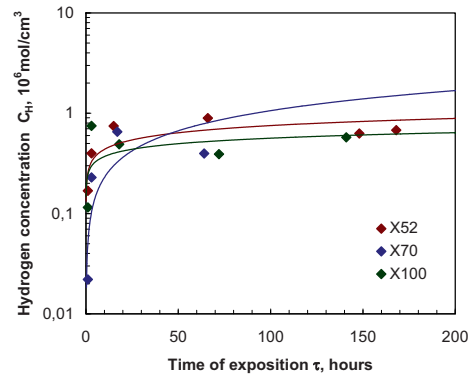
Fig. 7. Hydrogen concentration in metal versus time of exposition of unloaded specimens under cathodic polarisation of pipeline steels API X52, X70 and X100
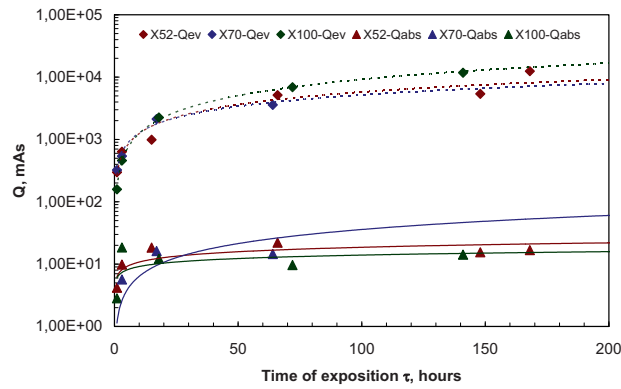
Fig. 8. Total quantity of evaluated and absorbed hydrogen versus time of exposition of unloaded specimens under cathodic polarisation of pipeline steels API X52, X70 and X100
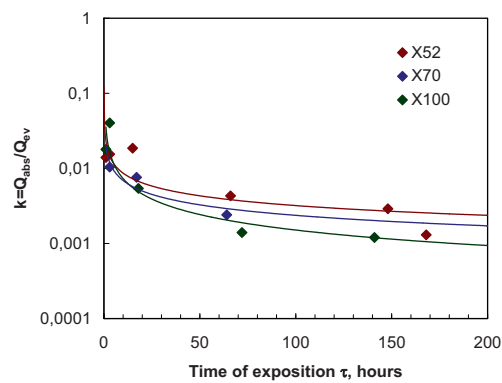
Fig. 9. Efficiency of hydrogen permeation in metal versus time of exposition of specimens under given cathodic polarisation of pipeline steels API X52, X70 and X100
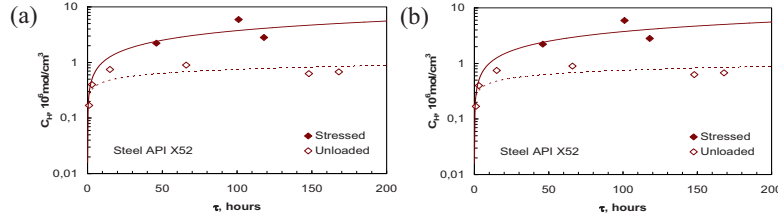
Fig. 10. Influence of applied stress on hydrogen concentration in steels X52 (**a**) and X70 (**b**)
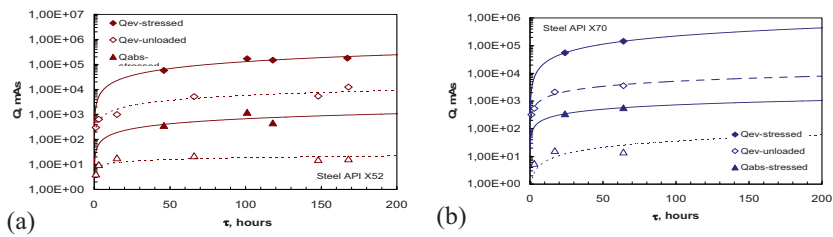
Fig. 11. Influence of applied stress on total quantity of evaluated and absorbed hydrogen in steels X52 (**a**) and X70 (**b**)
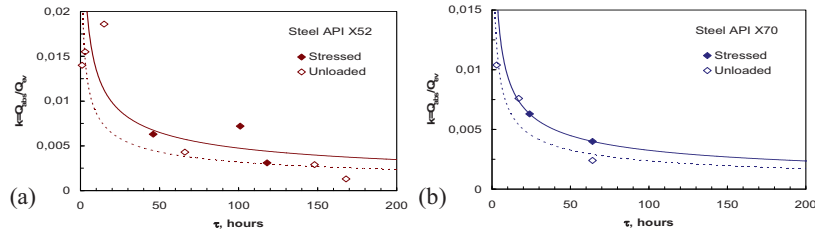
Fig. 12. Influence of applied stress on efficiency of hydrogen permeation in steels – X52 (**a**) and X70 (**b**)

Based on experimental results, the increasing of hydrogen concentration in metal versus time of exposition of specimens in the hydrogenating conditions can be described by power relation (8) and Table 5.

$$C_H = A \cdot 10^{-6} \cdot \tau^m \left[mol/cm^3 \right], \; A \text{ and } m \text{ are constants} \tag{8}$$

Table 5. Meanings of constants in formula (8)

Steel	Unloaded metal	Stressed metal
API X52	$C_H = 0.253 \; 10^{-6} \; \tau^{0.24}$	$C_H = 0.300 \; 10^{-6} \; \tau^{0.57}$
API X70	$C_H = 0.049 \; 10^{-6} \; \tau^{0.67}$	$C_H = 0.400 \; 10^{-6} \; \tau^{0.42}$
API X100	$C_H = 0.200 \; 10^{-6} \; \tau^{0.19}$	–

5. Local strength of pipelines steels at notches in presence of hydrogen

There are known studies [11–13, 20] of pipeline steels in with the aim of determining of their standard mechanical characteristics under the presence of hydrogen. These data reflect of hydrogen influence on the bulk of material properties. Below, the results of fracture toughness study of notched specimens are given, which reflect of local strength of pipeline steels in presence of hydrogen. The data were presented as dependencies of total work of local fracture $W_{f(total)}$ emanating from notch or its plastic component $W_{f(plastic)}$ versus time of exposition τ of specimens under hydrogenating conditions (Fig. 13).
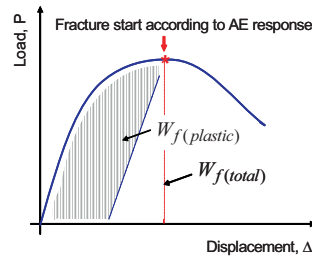
Fig. 13. Scheme of local fracture work determining

The dependencies of parameters $W_{f(total)}$ and $W_{f(plastic)}$ on the hydrogen concentration C_H in metal were also presented. It has been done with using of analytical relation (8). The received data are presented in diagrams (Figs. 14 and 16) and in Table 6. The main observation to be made from these results is existence of some critical time of exposition and as consequence – some critical hydrogen concentration $C_{H(critical)}$, when the essential decreasing of fracture toughness value is observed. Therefore, a concentration of hydrogen in metal defines its fracture resistance.

Table 6. Data of fracture toughness tests of notched Roman tile specimens

	τ, hours	$W_{f(total)}$ N·m	$W_{f(plastic)}$ N·m	$W_{f(elastic)}$ N·m	C_H, 10^6 mol/cm^3	C_H, 10^6 mol/cm^3
X52	46	32.12	19.22	12.91	2.224	2.660
	101	26.57	15.44	11.12	5.924	4.165
	118	15.53	4.68	10.85	2.814	4.551
	167.3	10.47	3.90	6.57	–	5.553
X700	Air	9.50	0	9.50	0	0
	24	5.28	0	5.28	1.408	1.520
	64	3.81	0	3.81	2.133	2.294
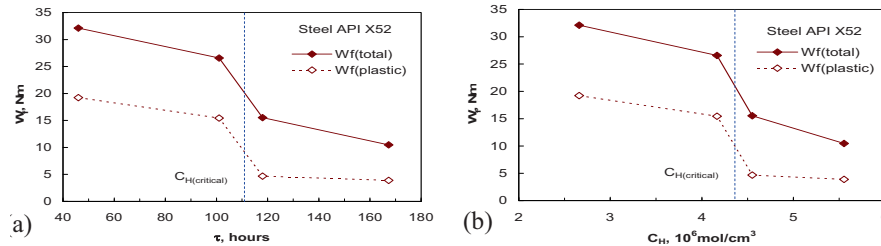
Fig. 14. Work of local fracture emanating from notch in steel API X52: as function of time of exposition of specimens in hydrogenating conditions (**a**), as function of hydrogen concentration in metal (**b**)
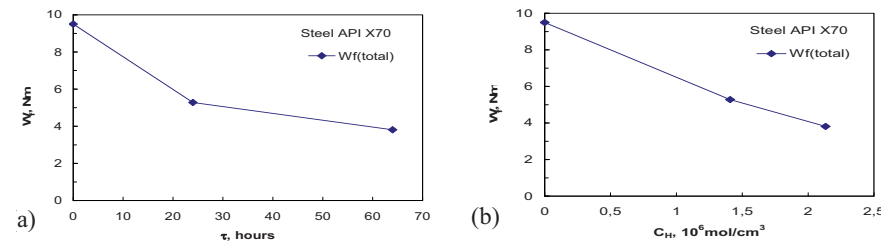
Fig. 15. Work of local fracture emanating from notch in steel API X70 as function of time of exposition of specimens in hydrogenating conditions (**a**) and hydrogen concentration in metal (**b**)

For steel X52 the value of critical hydrogen concentration is $C_H \geq 4.3 \cdot 10^{-6}$ mol/cm^3 (Fig. 14). The steel X70 is very sensitive to notch effect even in air and the presence of hydrogen strengthens this tendency. The hydrogen concentration about $C_H \geq 2.1 \cdot 10^{-6}$ mol/cm^3 can be considered as critical, because at this conditions the given steel losses in 2.5 times its local strength with comparison of test in air (Fig. 15). Therefore, for assigned testing conditions, steel X52 is preferable than steel X70 from the point of view of local strength at notches (Fig. 16).It should be stated that definition "critical concentration" is often used in studies of problems of hydrogen in metals and alloys [7, 21–23]. Although in different works this term has different physical sense. For example, according to work [21], hydrogen treatment below the "critical" content was found to cause the substantial rearrangement of dislocations and de-cohesion of grain boundaries and in overcritical condition, the formation of micro crevices at the grain and phase boundaries has been occurred. Others authors use this definition under developing of local fracture criteria [7, 22]. Here, in given study two characteristic value of hydrogen concentration in metal of pipe may be classified. First one is concentration $C_{H(0)}$, beginning from which hydrogen affects on local strength of material. Second one is critical concentration $C_{H(critical)}$, which causes the significant loss of local fracture resistance of material.
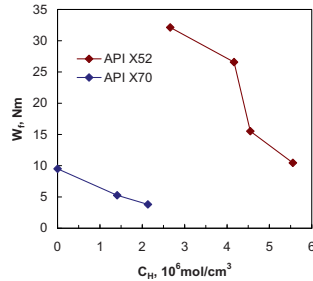
Fig. 16. Comparison of local fracture work emanating from notch in steel API X52 and X70 versus hydrogen concentration in metal

The general tendency of hydrogen effect on local strength of pipeline steels at notches is given in Fig. 17.
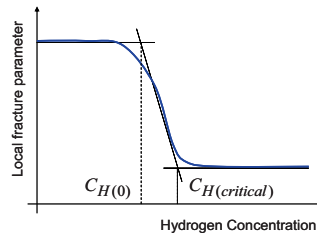
Fig. 17. General tendency of hydrogen effect on local strength of pipeline steels at notches

Presented study is limited by a case of fracture toughness of notched specimens that is modelling of the mechanical defects like to scratches or dents. It is evident that for deeper understanding of hydrogen contribution in durability of pipelines under real operating conditions, the corrosion and corrosion fatigue studies are required. The hydrogen may affect on early stages of fatigue damage accumulation on the surface [24], especially when there is a gradient of hydrogen concentration at near-surface layer and bulk of material [25]. The problem of fatigue crack propagation accelerated by hydrogen is also important, because sometimes the pipeline leak occurs as result of sub-critical crack growth [26].

6. Conclusions

The studies of hydrogen-charging process of three API grade pipeline steels: X52; X70 and X100 were conducted and their local strength at notches in presence of hydrogen was determined. The received results have led to the following conclusions. All steel demonstrate the sensitivity to hydrogenating in deoxygenated, near-neutral pH NS$_4$ solution under "soft" cathodic polarisation at $E_{cath} = -1000mV(SCE)$.

Comparative assessment of X52, X70 and X100 steels showed that last possesses of highest resistance to hydrogen absorption. The steel X70 is the most sensitive to hydrogen-charging in assigned testing conditions. For all steels, the efficiency of hydrogen permeation in metal is quite low and depends on time of exposition. It can be stated that under $\tau \geq 20\,\text{h}$ there is the tendency of monotonic decreasing of parameter $k = Q_{abs}/Q_{ev}$ up to level k=0.0012–0.0024. Applied stress, which equivalent to gross hoop stress in pipe wall under operating internal pressure 70 bars, significantly accelerates hydrogen-charging of steels. For example, for steel X52 the difference between hydrogen concentration in unloaded and stressed metal can exceed more than five times. Concentration of hydrogen in metal defines its local fracture resistance. For assessment of local strength at notches in presence of hydrogen the diagram "work of local fracture – hydrogen concentration" is effective and it can be considered as an invariant curve for a given system "material – environment". For steel X52 some critical hydrogen concentration exists ($C_H \geq 4.3 \cdot 10^{-6}\ \text{mol}/\text{cm}^3$), which causes the significant loss of local fracture resistance of material.

This value can be recommended as one of important engineering parameter for reliability assessment of exploited pipelines. Steel X70 is very sensitive to notch effect even in air and the presence of hydrogen strengthens this tendency. The hydrogen concentration about $C_H \geq 2.1 \cdot 10^{-6}\ \text{mol}/\text{cm}^3$ can be considered as critical, because at this conditions the given steel losses in 2.5 times its local strength with comparison of test in air.

References

[1] Azevedo C. Failure analysis of a crude oil pipeline. Engineering Failure Analysis 14 (2007) 978–994.

[2] Cheng Y.F., Niu L. Mechanism for hydrogen evolution reaction on pipeline steel in near-neutral pH solution. Electrochemistry Communications 9 (2007) 558–562.

[3] Cheng Y.F. Fundamentals of hydrogen evolution reaction and its implications on near-neutral pH stress corrosion cracking of pipelines. Electrochimica Acta 52 (2007) 2661–2667.

[4] Dey S., Mandhyan A.K., Sondhi S.K., Chattoraj I. Hydrogen entry into pipeline steel under freely corroding conditions in two corroding media. Corrosion Science 48 (2006) 2676–2688.

[5] Shipilov S.A., May I.L. Structural integrity of aging buried pipelines having cathodic protection. Engineering Failure Analysis 13 (2006) 1159–1176.

[6] Yurum C.R. (ed.) Hydrogen energy systems: production and utilisation of hydrogen and future aspects. Kluwer Academic Publisher, the Netherlands, (1995), 352p.

[7] Hanneken J.W. Hydrogen in metals and other materials: a comprehensive reference to books, bibliographies, workshops and conferences. International Journal of Hydrogen Energy 24, No. 10 (1999) 1005–1026.

[8] Ibeh B., Gardner C., Ternan M. Separation of hydrogen from a hydrogen/methane mixture using a PEM fuel cell. International Journal of Hydrogen Energy 32 (2007) 908–914.

[9]   Adib-Ramezani H., Jeong J., Pluvinage G. Structural integrity evaluation of X52 gas pipes subjected to external corrosion defects using the SINTAP procedure. International Journal of Pressure Vessels and Piping 83 (2006) 420–432.

[10] Mao S.X., Li M. Mechanics and thermodynamics on the stress and hydrogen interaction in crack tip stress corrosion: experiment and theory. Journal of the Mechanics and Physics of Solids 46 (1998) No. 6, 1125–1137.

[11] Hardie D., Charles E.A., Lopez A.H. Hydrogen embrittlement of high strength pipeline steels. Corrosion Science 48 (2006) 4378–4385.

[12] Torres-Islas A., Salinas-Bravo V.M., Albarran J.L., Gonzalez-Rodriguezd J.G. Effect of hydrogen on the mechanical properties of X-70 pipeline steel in diluted NaHCO3 solutions at different heat treatments. International Journal of Hydrogen Energy 30 (2005) 1317–1322.

[13] Zhang T., Chu W.Y., Gao K.W., Qiao L.J. Study of correlation between hydrogen-induced stress and hydrogen embrittlement. Materials Science and Engineering A347 (2003) 291–299.

[14] Cheng Y.F. Analysis of electrochemical hydrogen permeation through X-65 pipeline steel and its implications on pipeline stress corrosion cracking. International Journal of Hydrogen Energy 32 (2007) 1269–1276.

[15] Li M.C., Cheng Y.F. Mechanistic investigation of hydrogen-enhanced anodic dissolution of X-70 pipe steel and its implication on near-neutral pH SCC of pipelines. Electrochimica Acta 52 (2007) 8111–8117.

[16] Potentiostat V.M.P., Manual, Priceton Applied Research, Oak Ridge, TN, USA, 2004.

[17] Yan M., Weng Y. Study on hydrogen absorption of pipeline steel under cathodic charging. Corrosion Science 48 (2006) 432–444.

[18] INSTRON-8500 testing machine. Manual, USA, 1997.

[19] Vallen-Systeme acoustic emission. Manual, Vallen-Systeme GmbH, Germany, 2006.

[20] Contreras A., Albiter A., Salazar M., Perez R. Slow strain rate corrosion and fracture characteristics of X-52 and X-70 pipeline steels. Materials Science and Engineering A407 (2005) 45–52.

[21] Lunarska E., Ososkov Y., Jagodzinsky Y. Correlation between critical hydrogen concentration and hydrogen damage of pipeline steel. International Journal of Hydrogen Energy, 22 (1997) No. 2/3, 279–284.

[22] Lufrano J. and Sofronis P. Enhanced hydrogen concentrations ahead of rounded notches and cracks – competition between plastic strain and hydrostatic stress. Acta Metalurgica 46 (1998) No. 5, 1519–1526.

[23] Venegas V., Caleyo F., Gonzarlez J.L., Baudin T., Hallen J.M., Penelle R. EBSD study of hydrogen-induced cracking in API-5L-X46 pipeline steel. Scripta Materialia 52 (2005) 147–152.

[24] Akid R., Dmytrakh I.M. and Gonzalez-Sanchez J. Fatigue damage accumulation: the role of corrosion on the early stages of crack growth. Corrosion Engineering, Science and Technology 41 (2006) No. 4, 328–335.

[25] Olden V., Thaulow C., Johnsen R., Ostby E. Cohesive zone modelling of hydrogen-induced stress cracking in 25% Cr duplex stainless steel. Scripta Materialia 57 (2007) 615–618.

[26] Dmytrakh I. Corrosion fatigue cracking and failure risk assessment of pipelines. In: Safety, Reliability and Risks Assessments with Water, Oil and Gas Pipelines (edited by G. Pluvinage and M.H. Elwany), Springer Netherlands (2008).

Reliability Assessment of Underground Pipelines Under Active Corrosion Defects

A. Amirat[1], A. Benmoussat[2] and K. Chaoui[1]

[1]Research Laboratory LR3MI: mechanics of materials and plant maintenance University
 Badji Mokhtar, BP 12, Annaba 23000, Algeria

[2]Mechanical department, University Aboubaker Belkaid, Tlemcen, Algeria

Abstract Reliability assessment of underground pipeline steel structures for hydrocarbon transmission and distribution systems under active corrosion defects has been investigated. The aim of this work is to obtain a decision-making tool for risk-based inspection and maintenance program. The basic idea consists in statistical analysis of corrosion defect measurements in a buried pipeline as to sort out the corresponding depths and lengths after several years of service. As a result steady corrosion rate model is proposed to estimate the growth in the dimensions of corrosion defects. Then, a degradation model based on ASME modified B31G standard is used as a mechanical model in order to assess the failure probability or the reliability index through defect dimensions and associated uncertainties. Meanwhile, the main assumption of the probabilistic analyses for corroded pipelines is the randomness of load and resistance parameters determining the limit state functions. The statistical distribution of the uncertainties in the parameters involved in the limit state functions is modeled using normal and lognormal distributions. The reliability software PHIMECA is used to compute the reliability index β and the probability of failure *Pf*, when increasing dimensions of the defect within the respective measured values of depth and length during inspection and maintenance operations. The reliability calculation allows carrying out the sensitivity of the variables according to their importance, their mean value and their coefficient of variation. The probability of failure and reliability index are obtained assuming in one hand constant depth of defect with increasing length and in the other hand a relationship between the depth to length corrosion defect ratio is given as a function of reliability index β. The latter can be used as a parameter for risk-based inspection and maintenance operations.

Keywords: Reliability Analysis, Corrosion, Underground Pipelines.

1. Introduction

Corrosion is a major problem for steel hydrocarbon pipelines despite considerable effort and material expenditures spent in the last four decades on their failure prevention or on research [1, 2]. Coatings, cathodic protection, paints are usually used to protect the pipes. Unfortunately, corrosion protection failures do occur because of a variety of causes leading to localized corrosion [3, 4, 5]. As a consequence there have been several techniques such as those specified in B316

[6] or Z184 [7] as well as hydrostatic test to estimate the remaining strength of a localized corrosion defect in a pipeline.

Meanwhile, the most commonly used method for evaluating corroded pipe is the ANSI/AMSE Modified B31G Criterion [6]. The latter is usually based on deterministic approach wherein the nominal values are used for both load and resistance parameters neglecting the uncertainty of random variables rising from geometrical measurements, pipe manufacturing and operating conditions. Therefore probabilistic approach [8, 9] is the only way to give realistic answers for design and maintenance by handling the system uncertainties and fluctuations. There is much effort nowadays in reliability assessment in preventing pipeline failures [10, 11].

The aim of the present paper is to provide a reliability based inspection tool for corroded pipeline for better estimates of the remaining life of underground pipelines. The major results of this work are to sort out a relationship between lengths to depth ratio of a defect as a function of reliability index to make it a parameter risk based decision. In addition the sensitivity analyses have been carried out on random variables to identify the importance of the parameters involved in the reliability mechanical model.

2. Mechanical model

For pressurized pipelines, much attention is usually given to longitudinal surface corrosion defects existing in the wall. It is rarely that circumferential corrosion defects are concerned. This defect may be geometrically modeled as shown in Fig. 1.
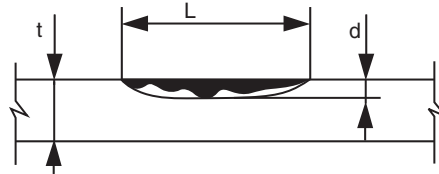
Fig. 1. Section through pipe wall showing an idealised defect

Where t is the pipe wall thickness, d is the defect depth and L is the defect length. The commonly used equation, and widely accepted in practice in based on the criterion safety for pipeline specified in B31G on which details are largely diffused in literature [6]. The summary of the B31G model is given in Eqs. (1) to (6).

$$
S = \overline{S} \cdot \left[\frac{\left(1 - \dfrac{A}{A_0} \right)}{\left[\left(1 - \dfrac{A}{A_0} \right) \cdot M^{-1} \right]} \right]
\tag{1}
$$

$$A = \left(\frac{2 \cdot L \cdot d}{3} \right) \qquad (2)$$

$$A = \left(\frac{2 \cdot L \cdot d}{3} \right) \quad A_0 = L \cdot t \qquad (3)$$

$$M = \left[1 + 0.6275 \frac{L^2}{Dt} - 0.003375 \frac{L^4}{D^2 t^2} \right] \text{ for } \frac{L^2}{D \cdot t} \qquad (4a)$$

Otherwise $\qquad M = 0.032 \frac{L^2}{Dt} + 3.3 \text{ for } \frac{L^2}{D \cdot t} > 50 \qquad (4b)$

$$\bar{S} = \sigma_e + 68.95 \ MPa \qquad (5)$$

$$Pu = \frac{2St}{D} = 2 \left[(\sigma_e + 68.95) \frac{1 - \frac{2}{3} dt}{1 - \frac{2}{3} dt M^{-1}} \right] \cdot \frac{t}{D} \qquad (6)$$

where, A – Area of the missing metal; A_0 Original cross sectional; D External tube diameter; d – defect depth; L Distance between defect supports; M Follias factor; Pu ultimate fluid pressure capacity of a corroded pipe; S Hoop stress at failure; $\bar{S}$ Material flow stress area; t pipe wall thickness; σ_e – Specific minimum yield strength of the material.

In site, the evaluator must determine the overall axial and circumferential extent of each separate area of metal loss. There are two main decisions [6] to take according to the depth of defect.

In one hand, if the deepest pit (d) is determined to be less than or equal to 20% of the specified nominal wall thickness and that the least remaining wall thickness (t − d) is at least 80% of the original wall thickness, the segment containing the area is acceptable for continued service.

In the other hand, if the deepest pit (d) is determined greater than 80% of the original wall thickness, than the segment containing the area of metal loss should be replaced or repaired.

3. Corrosion pipe inspection

Measurements of defect dimensions together with their orientation, and the measuring position have been achieved using ultra sound inspection probe through a 75 km pipeline portion on one of the main Algerian high pressure gas transportation that has been in service for three decades. The depth and length of corrosion pits have been reported in charts as illustrated in Figs. 2 and 3.

The evolution of depth of the pits along the pipeline portion allows determining the exact position of the defects. Basically, most of the defect depths were below 30% of the wall thickness. The longest pit was 3152 mm for d/t of 57% and the smallest pith length was 5 mm for d/t of 11%. The most important observation is that there has been is no correlation between the length of the pit and its depth. In fact for a given pit depth there has been a great number of corresponding pit lengths and vice versa.

4. Reliability model

In this section, the probabilistic model to be used in remaining life pipeline reliability analyses is presented. Each parameter has to be represented by random variable, described distribution type and parameters generally, mean and standard deviation. Specific algorithms are applied for searching the most probable failure configuration. In the present work, the software PHIMECA [12] has been used to perform the reliability analyses. This software offers several methods for reliability calculation such as Monte Carlo simulations and First/Second Order Reliability Methods (FORM/SORM) [13]. Investigating the effect of pit length will be of great interest in making a decision of repairing or replacing the damaged portion.
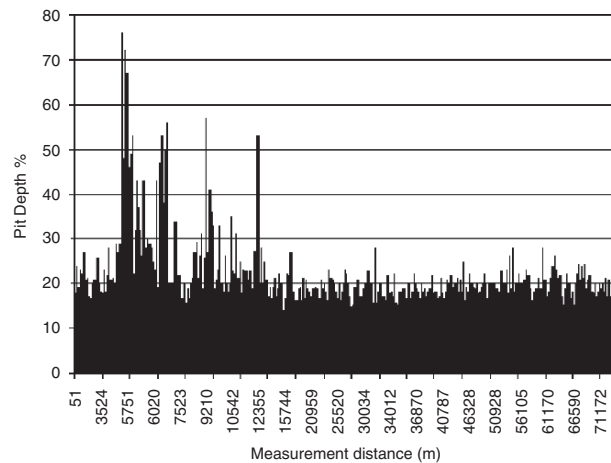
Fig. 2. Depths of corrosion defects along a 30-year-old pipeline
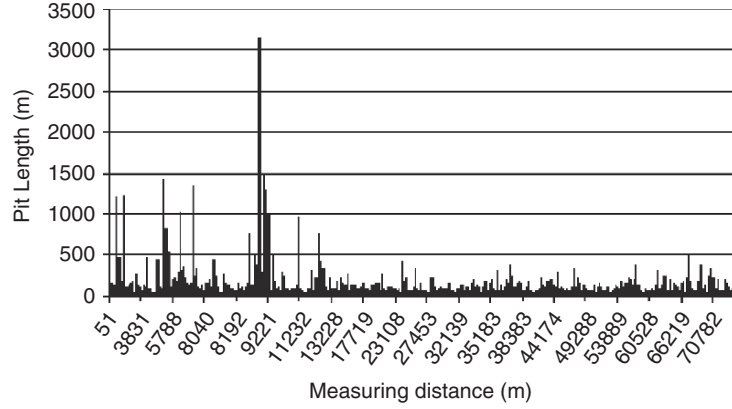
Fig. 3. Lengths of corrosion defects along a 30-year-old pipeline

The limit state function G(x) corresponds to a boundary between desired and undesired performance of a structure. In this case, a mode of pipeline failure could be when the pipeline operating service or loads exceeds the pipeline failure pressure or capacity. The limit state function or performance function can be then defined as the difference between the pipeline failure pressure P_{fp} and the pipeline operating pressure P_{op}.

$$G(x) = P_{f_0} - P_{op} \qquad (7)$$

This margin is defined such as $G(x) > 0$ indicates safety and $G(x) \leq 0$ corresponds to conventional failure: x_j are the random variables in the system. In this expression, the operating pressure is dependent on the pit dimensions. For the failure scenario, the reliability index β is defined as the minimum distance between the origin and the failure domain in the equivalent Gaussian space u_i. In first order reliability methods (FORM), the failure probability P_f is simply calculated by:

$$P_f = \Pr[G \leq 0] = \Phi(-\beta) \qquad (8)$$

where Pr is the probability operator and Φ is the cumulative Gaussian probability function. The uncertainties have been associated with the corrosion parameters, and many others result from geometry, loading, manufacturing and service conditions.

For instance, as our work is focussed on defect dimensions and the corrosion phenomena, the related probabilistic models are established using geometrical measurements and material testing.

Table 1 indicates the principal random variables involved and their statistical parameters.

5. Pipeline remaining life assessment

Corrosion measurements revealed that there is no correlation between the depth and the length of the corrosion defect. In fact for a given depth of the corrosion pit there is a range of associated lengths. For example, for a depth of 20% of the wall thickness, the length varied from 8 to 608 mm.

Therefore the reliability assessment is focussed on the effect of defect length on the remaining life of a corroded pipeline. How this range affects the lifespan of the pipeline is of great interest. For instance, the defect depth is taken as a random variable with a probabilistic distribution and the length as a deterministic parameter ranging from 8 to 608 mm. This allows running parametric reliability analyses. Figure 4 illustrates the effect of defect length on the reliability index β, for different defect depths.

Table 1. Random variables and corresponding parameters

Type of variables	Symbols	Description	Dimension	Distribution	Coefficient of variation
Material	σ_e	Yield strength	MPa	Lognormal	0.1
Geometry	D	External diameter	Mm	Normal	0.003
	D	Defect depth	Mm	Normal	0.1
	L	Defect length	Mm	Normal	0.05
	T	Wall thickness	Mm	Normal	0.1
Load	P_{op}	Operating pressure	MPa	Normal	0.1
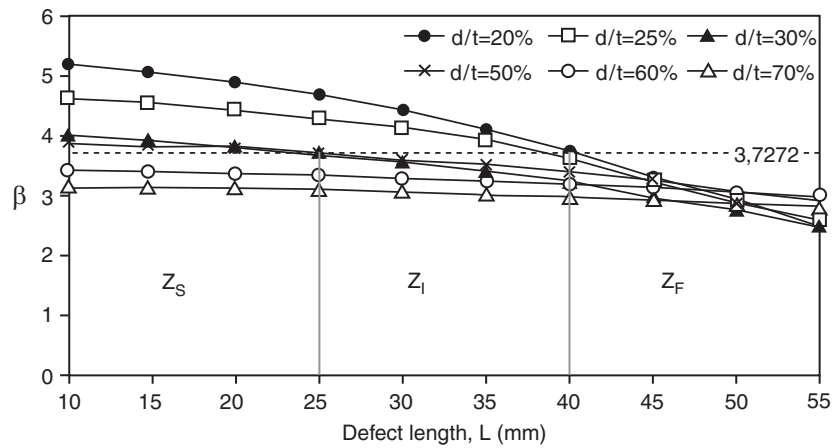
Fig. 4. Effect of defect length on the reliability index

Considering an acceptable value of β equals to 3.7272, which is used in industrial structures, one can make some discussion around this value. The discussion can be divided into two parts as a function of depth to thickness d/t ratios; when d/t is above 50%, the failure domain is reached, and when d/t is below 50%, the behaviour is dependent of the defect length. The present investigation stopped after only 55 mm pit length as β decreased drastically.

Therefore all the following discussions are made for a depth to thickness d/t ratio up to 50% within a range of lengths of 8 to 55 mm. The remaining life of the pipeline can be divided into three zones: safety zone Z_S, Transition zone Z_T and Failure zone Z_F. In the safety zone, up to a defect length of 25 mm, all the values of β were above the acceptable value, which means that the pipeline is within a safety domain, therefore there is no need to drop the pressure service. In the transition zone, 25 to 38 mm defect length, much care should be taken because the reliability index β falls below the acceptable value when d/t exceeds 25%.

The third zone is the failure zone when the length of the corrosion pit increases beyond 38 mm. In this case, in all cases of d/t ratios, the pressure service must reduced leading to a fall in gas production in to order to maintain the pipeline safer. A correlation can be obtained between the three main geometrical parameters d, L and t by considering the evolution of the reliability index β as a function of the depth to length d/L ratio. This is illustrated in Fig. 5 which shows that β is an important index to estimate the remaining life of the pipeline as a function of the two ratios: d/t and d/L.
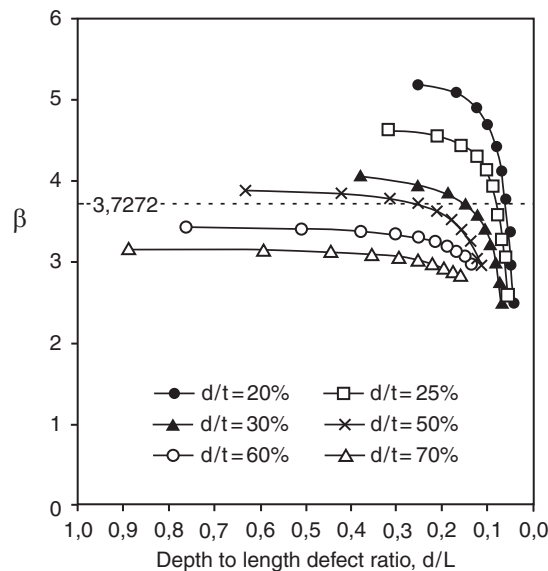
Fig. 5. Reliability index β as a function of d/t and d/L defect ratios

A risk based decision can be taken as summarised in Table 2 which gives the performance of the pipeline as the difference between the pipeline failure pressure P_{fp} and the pipeline operating pressure P_{op} with regard to d/t and d/L. The proposed reliability assessment based on acceptable reliability index β is very objective in preventing lost in production and failure that can lead to disaster if the good decision has not been taken at the right time. Three parameters are of great importance when a corrosion pit starts: the depth of defect d, the pipe wall thickness t and the yield strength of the material σ_e.

The reliability analysis permits also to find out what is the importance of the variables involved in the mechanical model. A good illustration is given in Fig. 6 which gives the part of each variable. The most dominant parameter for d/t ratio equals to 0.2 is the defect depth which is 70% importance against 22% for the thickness and 7% for the yield strength.

As the pit gets deeper, the depth d becomes more and more dominant until, neither the wall thickness nor the yield strength can withstand the stressing depth of the defect. It is evident that at the end the only rescue for the pipeline is to avoid the rupture of the last ligament of the remaining material.

Table 2. Pipeline performance as a function of d/t and d/L

N°	d/t	d/L	Performance	Dicision
1	<25%	<0.1	Safety	Ok
2	<50%	<0.2	Safety	Ok
3	>50%	= 1	Failure	Decrease P_{op}
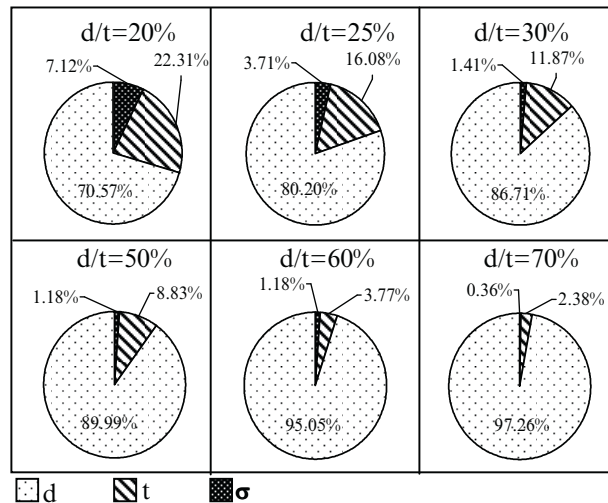
Fig. 6. Variable importance for the remaining pipeline safety

6. Conclusions

The remaining life of a three-decade service underground pipeline affected with corrosion pits has been investigated using reliability method. The mechanical model is based on the modified ANSE/ASME B31G criterion.

The main objective of this work consists in determining the effect of defect dimensions on the probability failure of the pipeline. The idea comes from statistical analyses of corrosion pits dimensions measured on a 74 km portion of a gas pipeline.

They revealed that for a given depth there has been a great range of defect lengths and vice versa and that there is no correlation between the depth of the pit and its length. Introducing the reliability index β is of great importance since it allows defining a correlation between the geometrical ratios of the defect d/t and d/L and hence helps to take a risk based decision in assessing the remaining life of a gas pipeline.

References

[1] Maes M.A, Dann M and Salama, M.M. Influence of grade on the reliability of corroding pipelines, Reliability Engineering and System Safety 93(3) (March 2008) 447–455.
[2] Teixeira, A.P, Guedes Soares C, Netto T.A and Estefen S.F. Reliability of pipelines with corrosion defects. International Journal of Pressure Vessels and Piping, 85(4) (April 2008) 228–237.
[3] 2000 pipeline investigation report. Report No. P00H0037. Transportation Safety Board of Canada, Hull, 2001.
[4] 1999 pipeline investigation report. Report No. P99H0021. Transportation Safety Board of Canada, Hull, 2002.
[5] Stress Corrosion Cracking (SCC) Workshop. Office of Pipeline Safety. US Department of transportation, December 2003. http://primis.rspa.dot.gov/gasimp/mtg_120203.htm.
[6] ASME-B31G. Manual for determining the remaining strength of corroded pipelines – a supplement to ASME B31G code for pressure piping. New York: American Society for Mechanical Engineer, 1991.
[7] CANICSA-ZKWM86. Gas Pipeline Systems. Canadian Standards Association, 1986.
[8] Ahammed M. Probabilistic estimation of remaining life of a pipeline in the presence of active corrosion defects. International Journal of Pressure Vessels and Piping 75 (1998) 321–329.
[9] Caleyo F, Gonzalez J.L. and Hallen J.M. A study on the reliability assessment methodology for pipelines with active corrosion defects. International Journal of Pressure Vessels and Piping 79 (2000) 77–86.
[10] Shipilov S.A, Iain Le May. Structural integrity of aging buried pipelines having cathodic protection. Engineering Failure Analysis 13 (2006) 1159–1176.

[11] Amirat A, Mohamed-Chateauneuf A, Chaoui K. A Reliability assessment of underground pipelines under the combined effect of active corrosion and residual stress. International Journal of Pressure Vessels and Piping 83 (2006) 107–117.
[12] PHIMECA Engineering. PHIMECA – reliability-based design and analysis. Users manual, version 1.6, Aubiere, France; 2002.
[13] Lemaire M. Evaluation des indices de fiabilité associés à des modèles de mécanique de structure. Revue Française de Mécanique 1992.

An Overview of the Applications of NDI/NDT in Engineering Design for Structural Integrity and Damage Tolerance in Aircraft Structures

A.M. Abdel-Latif

Adjunct Professor, Faculty of Engineering and Design, Carleton University, Ottawa, Ontario, Canada

Abstract   Most of the civilian commercial aircraft were designed in the past for at least 20–25 years and up to 90,000 flights. The aircraft design philosophy was based on safe life or fail-safe approaches. Many operators of commercial transport aircraft exceed these design service goals. Consequently, Non-destructive inspections (NDI) are mandatory for determining maintenance cycles, and as means for assessing damage and extent of the needed repair work. Presently, aircraft types are designed for the same service life, structural design according to fatigue and damage tolerance requirements. The ultimate purpose of the damage tolerance evaluation is the development of a recommended structural inspection program considering probable damage locations, crack initiation mechanisms, crack growth time histories and crack detectability, in the airframe structure and engine components to minimize the maintenance costs and to comply with the requirements of airworthiness regulations. The applications of damage tolerance requirements and the advances in light weight materials and composites lead to the need for defining structural integrity through NDI inspection program to ensure a high degree of reliability supported by evaluation tests for structural integrity. The damage tolerance principles, fatigue life assessment and new advances of NDI methodologies will be reviewed.

1. Introduction

The current generation of civil transport aircraft were designed for at least 20–25 years and up to 90,000 flights. Many operators of jets and turboprops have exceeded these design service goals. Future aircraft types are designed for at least the same goals, but structure with higher fatigue life (endurance); higher damage tolerance capability and higher corrosion resistance are required to minimize the maintenance costs and enhanced airworthiness regulations. Ageing aircraft fleets are required to remain in service well beyond their original life expectancy. Life management tools range from those that may be employed during the initial design phase of new aircraft to those required to make technology insertion, repair and retain or-retire decisions.

Traditionally, fatigue has been the limiting factor in the determination of the economic life of aircraft fleets.

Recent research has also identified interactions between corrosion and fatigue such that the presence of corrosion accelerates damage due to fatigue; thereby further reducing the total service life of an aircraft [1, 2].

The total economic service life of any aircraft fleet is determined by damage incurred as a result of fatigue and corrosion. The challenges to aircraft manufacturers, military and commercial users and technical community are: (a) identify and correct structural deterioration that could threaten aircraft safety; and (b) prevent or minimize structural deterioration that could become an excessive economic burden or affect the safety of the aircraft.

Non-destructive inspections (NDI) are significant means to monitor defects and assessment of repairs. The aim of this article is to review the aging of aircraft; current fatigue design approaches, and presents an overview of the role of non-destructive testing and evaluation within the application of damage tolerance and structural integrity approaches.

2. Fatigue damage in aging aircraft

One of the signs of aging in aircraft structures is the occurrence of multiple damages at adjacent locations, which influence each other. There are two types of damage that are likely to result from the interaction of dynamic loading conditions and environment. The first type is the multiple site fatigue damage (MSD in the same structural element. The second type is the multiple element damage (MED) in the form of fatigue cracking in similar adjacent structural elements. Widespread Fatigue Damage (WFD) is reached when the MSD or MED cracks are of sufficient size and density that the structure will no longer meets structural integrity and safety criteria. Recent research has also identified interactions between corrosion and fatigue at the fastener holes further reducing the total service life of an aging aircraft [3–5].

The USA Air Force has initiated the Aircraft Structural Integrity Program (ASIP) and durability studies and damage tolerance assessments of aging aircraft [6]. There is a requirement to develop new techniques and instrumentation to detect fatigue, corrosion-fatigue interactions, stress corrosion cracking, and nondestructive inspection of corrosion initiation at fastener holes, without prior removal of the fasteners [7, 8]. Proper application of NDE technology can offer significant improvements in diagnostic capabilities by monitoring fatigue cracking, and stress corrosion conditions that are, or could become, a flight-safety concern.

3. Fatigue design philosophies

Purely static loading is rarely observed in modern engineering components or structures. Fatigue, or metal fatigue, is the failure of a component as a result of cyclic stress.

Failure occurs in three phases: crack initiation, crack propagation, and catastrophic overload failure. The duration of each of these three phases depends on many factors including fundamental raw material characteristics, magnitude and orientation of applied stresses, processing history. Therefore, the design analysts must address the implications of repeated loads, fluctuating loads, and rapidly applied loads. As a result, fatigue analysis has become an early driver in the product development processes in the aerospace industry.

Fatigue failures are typically characterized as low-cycle or high cycle. Low cycle fatigue failures involve large cycles with significant localized plastic deformation and relatively short life. Most metals with a body centered cubic crystal structure have an endurance limit, a threshold stress limit below which fatigue cracks will not initiate within the first 2×10^6 cycles as shown in Fig. 1. Total lives are then reported as the sum of the initiation and propagation segments. Metals with a face center cubic crystal structure (e.g., aluminum, austenitic stainless steels, copper, etc.) do not typically have endurance limits. High-cycle fatigue failures occur where stresses and strains are largely confined to the elastic region. The Stress-Life (S-N) or Total Life (TL) method is widely used for high-cycle fatigue applications [9, 10].
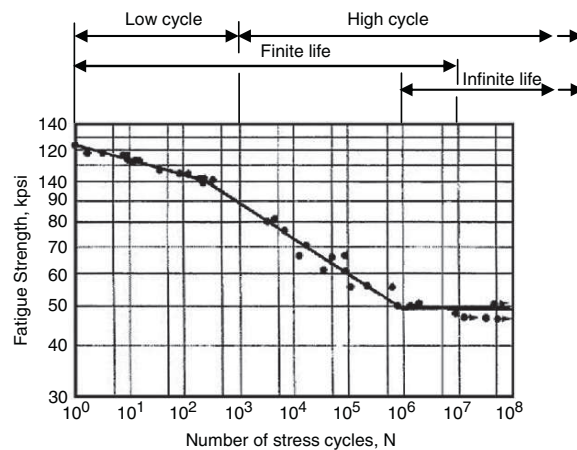
Fig. 1. An S-N diagram plotted from the results of completely reversed axial fatigue tests. Material: UNS G41300 steel normalized SMT = 1.16 kpsi, maximum SMT = 125 kpsi (data from NACA Technical Note 3866, December 1966)

4. Design principles

Two approaches are mainly used to design for establish the retirement life of parts considering the possibility of the presence of initial flaws or cracks of realistic size, and supplementing retirement lives by inspection plans based on testing and analysis.

4.1. Safe-Life

In aerospace, fatigue life evaluation has been specifically based on using a probabilistic approach for establishing the safety of their aircraft in the past on what is defined as safe-life design, whereby, the component/aircraft is virtually able to withstand its whole design-life without inspection. The "safe life" approach was introduced as the result of the Aircraft Structural Integrity Program (ASIP) to take into consideration the effects of cyclic loading on the airframe. The Safe- Life Design is based on Miner's rule of linear cumulative damage. Miner's Rule simply states that failure will occur when the summation of the damage caused by individual cycles exceeds unity [11]. Once a crack has occurred, or whenever the design life has expired, the component has to be removed. This highly conservative approach gives rise to very short inspection intervals that cannot be practically implemented by operators in an inspection program [10–12].

4.2. Damage tolerance

With the emergence of fracture mechanics, damage tolerance design principle was introduced to allow each individual component in an engineering structure to be used to the limit of its ability. Depending on the materials used in manufacture, many engineering components can tolerate the propagation of preexisting cracks, provided they do not exceed some critical size [13]. The critical size is the point at which the defect becomes unstable and very rapid crack growth to final failure may be expected [15, 16]. The point of instability is reached when the stress intensity at the crack tip (K) reaches the fracture toughness of the material (K_C), then the crack will run to failure at a catastrophic speed (Figs. 2 and 3). For values of (K) much lower than (K_C) slow and stable crack growth may be expected and the part may operate relatively safely [13–16]. Damage tolerance allows each individual part to be operated until a crack is detected by the best available NDT inspection method. If a crack is not detected then the part is returned to service. If no crack is found, then the same procedure is applied again, for the same inspection period.
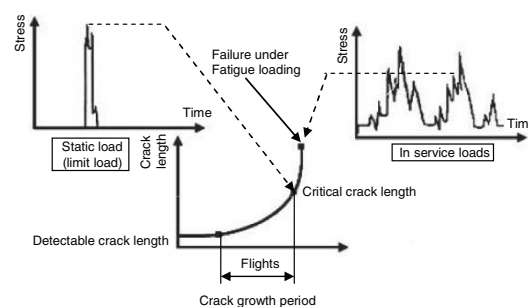
Fig. 2. Principle of damage tolerance investigation [3]
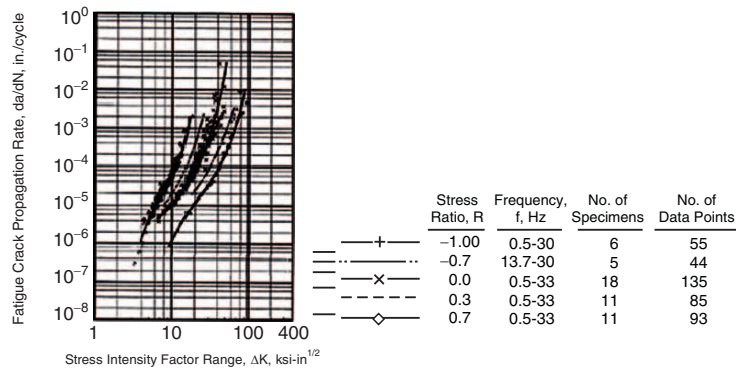
Fig. 3. A sample display of fatigue crack propagation rate [5]

Once a crack is determined, it has to be clearly quantified with respect to its dimensions. This approach requires knowledge of crack growth rate, and critical crack sizes to allow for a limited continuation of the aircraft's operation as long as the crack cannot reach the maximum allowable crack length. Thus, more flexible maintenance schedules (Fig. 4) could be implemented based on the development of NDT structural inspection program [11–14].
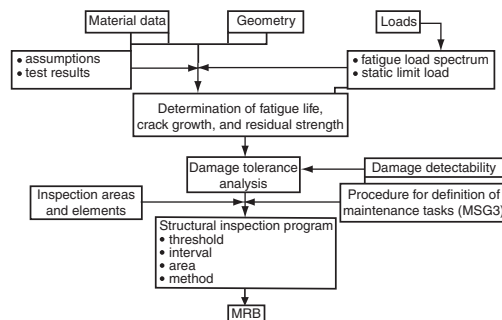
Fig. 4. Development of structure inspection program [3]

4.3. Holistic structural integrity program (HOLSIP)

The total economic service life of any aircraft fleet is determined by damage incurred as a result of fatigue and corrosion. Traditionally, fatigue has been the limiting factor in the determination of the economic life of aircraft fleets. Corrosion was not included in the current life prediction paradigms namely, safe-life and/or damage tolerance. Therefore, any corrosion damage that is discovered had to be repaired immediately, resulting in significant aircraft maintenance costs and reduced aircraft availability [15, 16].

ASSOCIATED CONCEPTUAL STEP	ASSUME ANY DSC BELOW A GIVEN DETECTION LIMIT IS PRESENT AT THE CRITICAL LOCATION	DSC PROPAGATES AS CRACK UNDER CYCLIC AND STATIC LOADING, RATE IS INFLUENCED BY ENVIRONMENT	CRACK PROPAGATES UNTIL CRITICAL LOAD/CRACK SIZE IS REACHED: FRACTURE OCCURS
INFORMATION REQUIRED	NDI INSPECTION LIMITS AND/OR PROOF CYCLE SCREENED LIMITS	ANTICIPATED SERVICE STRESSES AND ENVIRONMENTS	INFLUENCE OF LOAD HISTORY & ENVIRONMENT ON FINAL FRACTURE
REQUIRED DATA	PROBABILITY OF DSC DETECTION VS. DSC SIZE AND SHAPE	da/dN vs.ΔK, DETERMINE Kth, da/dt vs. Kmax IN SERVICE ENVIRONMENT	KIc, Kc, KIsec, KIb, KIIc, JIc, Stu OR STATIC FRACTURE CRITERIA
FRACTURE CONTROL STEPS	SET INITIAL INSPECTION REQUIREMENT SELECT MATERIALS & PROCESS CONTROL	DETERMINE EXPECTED SERVICE LIFE	SET INSPECTION INTERVALS TO AVOID FRACTURE OR DETECT CRACK WELL BEFORE INSTABILITY

Fig. 5. Conceptual diagram of the HOLSIP program

The Holistic Structural integrity program (HOLSIP) was proposed to address the synergistic effects of cyclic loading and environmental exposure to ensure structural integrity of aging aircraft and accurate determination of proactive planned maintenance cycles (Fig. 5). The success of this new program depends on the development of novel NDI/NDT methods and techniques for detecting wide spread fatigue (WFD) and Wide Spread Corrosion Damage wide spread damage (WSCD) in fasteners, as well as detecting delamination in composites.

5. Role of NDT in structural integrity and fatigue management

Non-destructive testing (NDT) are noninvasive techniques to determine the integrity of a material, component or structure or quantitatively measure some characteristic of an object. The reliability and sensitivity of an NDT method is an essential issue. By use of artificial flaws, the threshold of the sensitivity of a testing system has to be determined. If the sensitivity is to low defective test objects are not always recognized. If the sensitivity is too high parts with smaller flaws are rejected which would have been of no consequence to the serviceability of the component [16–18]. The Aircraft inspection involves multiple inspection solutions and diversification of inspection equipment to optimize the cost-effectiveness of the system. The most common NDT Methods are: Ultrasonic Testing (UT), Radiographic Testing (RT), and Eddy Current (EC). Other methods include guided wave inspection techniques (GW), Edge-Of-Light EOL, conventional ultrasonic pulse-echo (UT) and eddy current techniques (ET) for corrosion detection in aircraft structures [19, 20].

6. Evolving DNT methods

Computed Tomography is a radiographic NDT-method to locate and size planar volumetric details in three dimensions.

A CT-scanner generates X-ray attenuation measurements that are used to produce computed reconstructed images of defects in composite structure with their effects to the fatigue and the damage behavior of the test specimen [19–22]. Ultrasonic inspection using C-Scan (Fig. 6) is widely used in aircraft inspection for the detection of delimitations in composite structures, detection of crushed core, de-bonds in honeycomb structures, impact damage, and exfoliation corrosion. Ultrasonic inspection is usually performed with two techniques: (a) Reflection (Pulse echo) technique and (b) through transmission technique. Pulse echo' technique is most widely used in estimating location and size of the defect in testing metallic, nonmetallic, magnetic or nonmagnetic materials. Ultrasonic energy data (transmitted or reflected) are displayed or recorded and presented in two dimensional graphical presentations that could be digitized, stored for post processing [20–23].
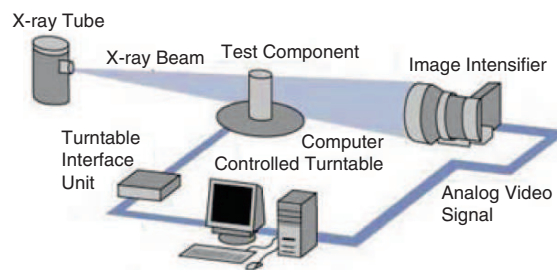
Fig. 6. A schematic sketch of a CT-scan

6. Conclusions

1. The "safe-life" approach was introduced as the result of the Aircraft Structural Integrity Program (ASIP). It involves rigorous fatigue testing of a representative of crack free airframe and certain components for 40,000 h "ensuring" a safe life of 10,000 h.
2. The damage tolerance design principle accommodates the presence of preexisting cracks in aerospace structures. Fracture mechanics provides the concepts to predict the propagation of these cracks based on a rigorous NDT inspection program.
3. The holistic approach was developed to incorporate corrosion and fretting into ASIP program.
4. New inspection techniques such as computer tomography and Acoustic emission, thermography are being developed to monitor structural integrity of engineering structures containing composites and newly developed lightweight materials.
5. There is a requirement to develop new techniques and instrumentation to detect corrosion initiation at fastener holes, without prior removal of the fastener, and to quantify the detectability of corrosion damage.

References

[1] Swift T (Sept. 1997), Aging aircraft from the viewpoint of FAA. Presentation at Daimler-Benz Aerospace Airbus GmbH, Hamburg, Germany.

[2] Research agenda for test methods and models to simulate the accelerated aging of infrastructure materials: Report of a Workshop. http://www.nap.edu/catalog/9622.html.

[3] Schmidt HJ, Tober G (June 1999), Design of modern aircraft structure and the role of NDT. NDT.net, vol 4, no 6.

[4] Hobbs C, Smith R, Beneath the surface. British Airways Technical Journal.

[5] Haviland GP (1973), The USAF aircraft structural integrity program (ASIP). USAF, Aeronautical Systems Div., Wright-Patterson AFB.

[6] Manual on low cycle fatigue testing (1969), American Society for Testing and Materials. ASTM STP 465, ASTM (Philadelphia).

[7] Bannantine J, Comer J, Handrock J (1990), Fundamentals of metal fatigue analysis. Prentice Hall, New Jersey.

[8] Miner MA (1945), Cumulative damage in fatigue. Journal of Applied Mechanics, vol 12, Trans. ASME, vol 67, pp. A159–A164.

[9] Dowling NE (1982), A discussion of methods for estimating fatigue life. Proceedings SAE Fatigue Conference. Society of Automotive Engineers, Warrendale, PA, p. 109.

[10] Broek D, Fail safe design procedures. Fracture Mechanics of Aircraft Structures, Chapter V, Liebowitz, Ed Agard, Document No 176.

[11] Nicholls LF, Jefferson A, Martin CIP, Application of fracture mechanics in the fail-safe

[12] Smith SH, Simpson FA, Damage tolerance analysis of an aircraft structural joint. AGARD-AG-257.

[13] Damage Tolerance Design Handbook (1973). Parts 1 and 2, MCIC-HB-01.

[14] Design of integrally stiffened structures, %–1. AGARD-AG-257.

[15] Bellinger NC, Liao M, Forsyth DS, Komorowski JP, Advances in risk assessment technologies – HOLSIP. NRC Presentation in Canada.

[16] Shinde S, Hoeppner DW (2007), Fretting fatigue case studies and failure analysis in holistic structural integrity closed loop design. Siemens Power Generation, Inc., Presented at ISFF5, Montreal, Quebec, Canada, April 21.

[17] Birt EA, Jones LD, Nelson LJ, Smith RA (March 2006), NDE corrosion metrics for life prediction of aircraft structures, insight vol 48, no 3.

[18] ASNT-Nondestructive Testing Handbook (1996), vol 9 and vol 10.

[19] Khan AU (1999), Non destructive application in commercial aircraft maintenance. NDT-net June 1999, vol 4, no 6.

[20] Forsyth DS, Komorowski JP, Marincak (February 2005), Correlation of enhanced visual inspection image features with corrosion loss measurements. III International Workshop on Advances in Signal Processing in NDE, Quebec City.

[21] Mustafa V, Chahbaz A, Hay DR, Brassard M, Dubois S (December 1996), Imaging of disbonds in adhesive joints with lamb waves. Nondestructive Evaluation of Materials and Composites, SPIE vol 2944.

[22] Chahbaz J, Gauthier M, Brassard and Hay R (September 20–23, 1999), Ultrasonic techniques for hidden corrosion detection in aircraft wing skin. Third Joint DoD/FAA/NASA conference on Aging Aircraft, Albuquerque, New Mexico.

[23] Oster R, Eurocopter, Munich D (March 15–17, 1999), Computed tomography as a non-destructive test method for fiber main rotor blades in development, series and maintenance. International Symposium on Computerized Tomography for Industrial Applications and Image Processing in Radiology, Berlin, Germany.

Improvement in the Design of Automobile Upper Suspension Control Arms Using Aluminum Alloys

M. Bouazara

Applied Sciences Department, University of Quebec at Chicoutimi, Saguenay, Quebec, G7H-2B1, Canada

Abstract   Suspension control arms are important parts in a vehicle. Conventionally, these parts were made of steel, a heavy metal. Their geometry was designed by means of traditional engineering methods. Today we try to use the much lighter metal aluminum, to manufacture these parts instead of steel. Fuel consumption and emission of polluting gases are strongly dependent on car weight. So the automotive industry is looking at innovative technological processes making use of light alloys and new design methodologies. Cutting weight by using aluminum parts can help cars and trucks brake quicker, handle better and accelerate faster. Hence, aluminum is the fastest growing material in the automobile industry today. In this work, we present a static, dynamic behavior and road profile study of automobile vs. aluminum mechanical parts (control arms) and stress analysis using advanced methods.

Keywords: Design of Automobile, Upper Suspension, Aluminum Alloys, Arms.

1. Introduction

The application of light alloys designed to reduce weight is becoming an urgent need in the transport industry due to environmental and social pressure. Fuel consumption and emission of polluting gases are strongly dependent on car weight and for this reason the automotive industry is looking at innovative process technologies which make use of light alloys and new design methodologies [1–4]. Aluminum helps build a better car because it delivers environmental, safety and driving performance advantages.

Environmental performance, Aluminum saves weight, which leads to fewer emissions and greater fuel economy. Safety performance, Aluminum can absorb more crash energy. Driving performance, Cutting weight by using aluminum parts can help cars and trucks brake quicker, handle better and accelerate faster. Figure 1 shows examples of current aluminum applications in vehicles produced in North America [3, 4]. The aluminum content of an average passenger car or light truck is 267 and 279 pounds per vehicle, respectively [3, 4]. Aluminum can offer a weight saving of up to 55 percent compared to an equivalent steel structure, while matching or exceeding crashworthiness standards of same-sized steel structures.

The lifetime fuel savings of these vehicles can amount to 500-700 gallons of gasoline. This equals about $600 in the U.S. today, and more than three times that amount in Europe and Japan. Many companies in the world now have aluminum-intensive test vehicles on the road, providing a weight reduction of 46 percent in the structure, with no loss in crash protection. We know that the design of aluminum parts is not easy in particular suspension arms.
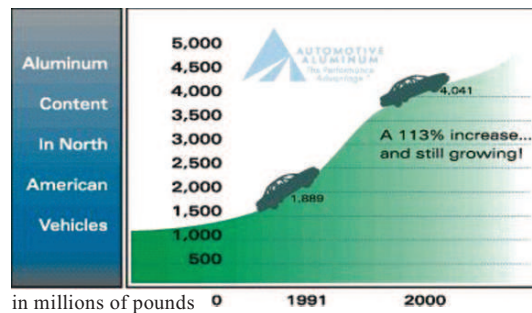
Fig. 1. Aluminum content in North American vehicles [2]

The problem is that the aluminum part must satisfy the same performance standards as the steel part. Fig. 2 shows an example of steel and aluminum control arms. Note that in the aluminum alloy, we need an evolved design as shown by Fig. 3. Suspension control arms are important parts in a vehicle as shown by Figure 4 [5, 6]. Conventionally, these parts were made of steel, which is a heavy metal. Their design geometry was created by means of traditional engineering methods. In this study, we use a modern engineering method to design and optimize the geometry of suspension arms, to reduce their weight and to improve their reliability and resistance. Static and dynamic analytical methods are used to cut weight, optimize shape, measure strength and natural frequency of dynamic behaviour.

The Evolutionary Structural Optimization (ESO) method is used in this study. ESO is based on the idea that by gradually removing inefficient material, the residual shape of structure evolves toward an optimum. This method has been successfully used for this work [7]. It is necessary to evaluate the dynamic behaviour of the suspension system and the roadway profile model.

Rahnejat studied the dynamics of the Macpherson suspension system in a quarter vehicle model [8]. The spring and the shock absorber are modeled as a single element with a constant stiffness. In the present study, a complete vehicle model is developed.

In this model, the partial stability of the vehicle is ensured by a suspension control system. The validity of this research is demonstrated through the use of aluminum alloys replacing steel in the suspension control arm. The upper control suspension arm is made of A357 materials.
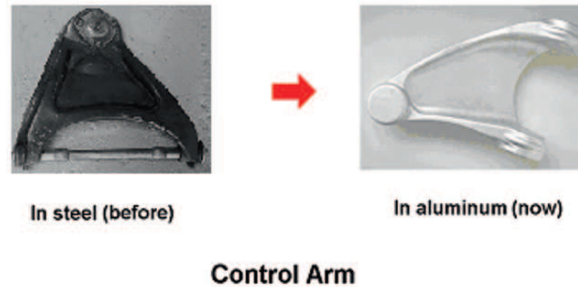
Control Arm

Fig. 2. Examples of two control arms in different materials

Aluminum control arm
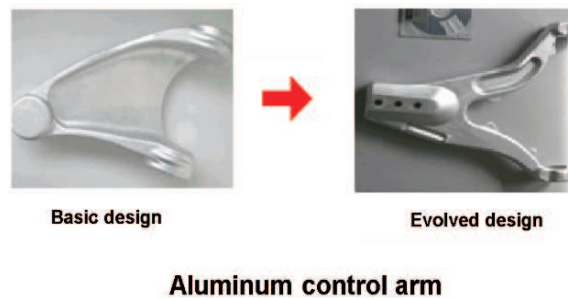
Fig. 3. Examples of two different designs of control arms

2. Vehicle model

In general, a vehicle is composed of the body (sprung mass), the suspension and the wheels (unsprung mass). On any vehicle, the primary job of the suspension is to isolate the body from shock loading and vibration. The suspension does all this by allowing the wheels to move vertically with respect to the chassis. Secondly, it prevents the car from shaking itself to pieces. The suspension must help and not impair the stability and handling of the entire car. This is accomplished with a damping system that also helps in the load distribution onto the wheels. The main materials for suspension arms were steel. Most suspensions in use today are of the independent type as shown by Fig. 4. As indicated by the name, an independent suspension works on its own and does not affect the suspension of the other wheels [8, 9].

When designing suspension parts, the vibration must be studied. Mechanical vibration is always associated with the fluctuation of mechanical loads; therefore, with fluctuation of mechanical stresses, there is fatigue failure of mechanical components such as the loosening of threaded connections, friction and wear, and damage of other delicate components.
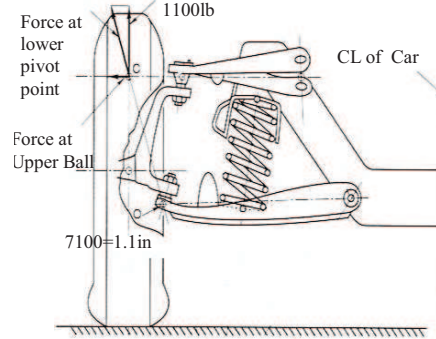
Fig. 4. Suspension system

Finally, vibration can affect comfort, performance and the health of people sub-jected to it, as in motion sickness due to ship, car or high-rise building oscillation. These facts make it imperative that engineers understand the vibration behaviour of every mechanical component, machine, structure, and system. To model a vi-bratory automotive system, there are many approaches described in literature. The following section presents the kinematics equations of a vehicle. The kinematics equations of a vehicle are based on three approaches: the three bar mechanism, four bar mechanism and a quarter vehicle models [6, 10]. The three-bar mecha-nism as shown by Fig. 5, represents the sum of the components at $Y=0$, where:

$$-L_7 \cos\theta_F - L_8 \sin\theta_D + L_9 = 0 \tag{1}$$

And the sum of the components at $Z=0$:

$$L_7 \sin\theta_F - L_8 \cos\theta_D + L_{10} = 0 \tag{2}$$

By solving these two equations with the Newtonian method for a non-linear systems, we can find the values of $\dot{\theta}_F, L_7$ as a function of θ_D. By finding the rate of change of L_7 as a function of time, we can find the force exerted by the mass system, spring and shock absorber.

$$\theta_H = \pi/2 - \theta_F \tag{3}$$

$$\theta_I = \pi/2 - \theta_D - \theta_H \tag{4}$$

$$L_7 = L_8 \dot{\theta}_D \cos\theta_i \tag{5}$$

We find that the force exerted by the mass system, spring and shock absorber is represented by the following equation:

$$F_7 = K(S + L_{10} - L_7) + C\dot{L}_7 \tag{6}$$

Where S represents the initial compression of the spring and C, the dynamic viscosity coefficient of the shock absorber.
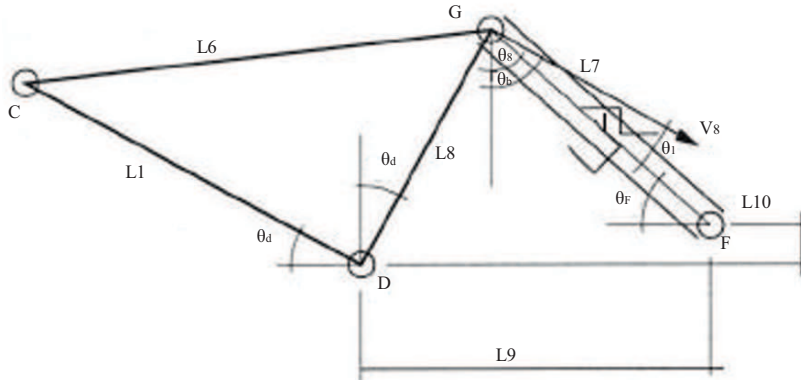
Fig. 5. Three bar mechanism

The four bar mechanism is shown in Fig. 6. The vehicle is composed of three main parts: the chassis, the suspension and the wheel. The four bars mechanism is defined by the points ABCD. Suppose the chassis rotates around the point P. The equations of the position constraint and the velocity of point E are obtained by [10]. Using the sum of the components at $Y=0$:

$$-L_2 \sin\theta - L_1 \cos(\theta_D - \theta) + L_3 \sin\theta_b + L_0 \cos(\theta_A - \theta) = 0 \tag{7}$$

The sum of the components at $Z=0$:

$$L_2 \cos\theta + L_1 \sin(\theta_D - \theta) - L_3 \cos\theta_b - L_0 \sin(\theta_A - \theta) = 0 \tag{8}$$

The sum of the components of the upper chord members at Z is equal to 0:

$$\frac{L_2}{2} \cos\theta - L_4 \sin\theta + L_1 \sin(\theta_D - \theta) - \frac{L_3}{2} \cos\theta_b - L_5 \sin\theta = 0 \tag{9}$$

By solving equations 7, 8 and 9 using the Newtonian method for non-linear systems, we can find the values of θ_D, θ_b and θ_A as a function of θ.

For the equations of speed constraint we use the speed at Z of point E expressed by the superior and inferior chord members is equal to 0:

$$-\frac{L_2}{2}\sin\theta\dot\theta - L_4\cos\theta\dot\theta + L_1\cos(\theta_D - \theta)(\dot\theta_D - \dot\theta) +$$
$$\frac{L_3}{2}\sin\theta_b\dot\theta_b - L_5\cos\theta\dot\theta = 0 \tag{10}$$

$$\frac{L_2}{2}\sin\theta\dot\theta - L_4\cos\theta\dot\theta + L_0\cos(\theta_A - \theta)(\dot\theta_A - \dot\theta) -$$
$$\frac{L_3}{2}\sin\theta_b\dot\theta_b - L_5\cos\theta\dot\theta = 0 \tag{11}$$

And finally, the sum of the speeds at Y of the two chord members is equal to:

$$-L_2\cos\theta\dot\theta + L_1\sin(\theta_D - \theta)(\dot\theta_D - \dot\theta) -$$
$$L_0\sin(\theta_A - \theta)(\dot\theta_A - \dot\theta) + L_3\cos\theta_b\dot\theta_b = 0 \tag{12}$$

By solving these three equations with the Newtonian method for non-linear systems, we can thus find the angular velocity values of $\dot\theta_D$, $\dot\theta_b$ and $\dot\theta_A$ as a function of $\dot\theta$.

An automotive suspension can also be represented by two-degrees of freedom system, where the suspension system is described by a quarter vehicle model as shown by Fig. 7 [6]. In this case, four springs and four dampers support a car weighing about 1600 kg; the chassis weight is about 1200 kg. (300 kg on each wheel) and the wheel unsprung weight is 40 kg /wheel. To avoid the kinematics complexities of the suspension system, many researchers use this simplified quarter vehicle model.

Fig. 6. Four bar mechanism

$$m_c \ddot{z}_c = -K_s(z_c - z_w) - C_c(\dot{z}_c - \dot{z}_w)$$
$$m_w \ddot{z}_w = K_s(z_c - z_w) + C_c(\dot{z}_c - \dot{z}_w) - K_w(z_w - z_t)$$

m_c : Mass of chassis;

m_w : Mass of wheel with suspension;

K_s : Coefficients of linear stiffness for spring;

C_c : Coefficients of damping for damper;

K_t : Coefficients of linear stiffness for tire;

$(z_c - z_w)$: Suspension deflection;

$\dot{z}_c$: Absolute velocity of the mass of chassis;

$(z_w - z_t)$: Tire deflection;

$\dot{z}_w$: Absolute velocity of the wheel mass;

$\ddot{z}_c$: Absolute acceleration of the chassis mass;

$\ddot{z}_w$: Absolute acceleration of the wheel mass

Fig. 7. quarter vehicle model

3. Optimization methods

Today, new and faster computer technology is increasing the use of software iteratively to apply finite element analysis to design, while varying dimensional characteristics of the design. This is called size and shape optimization. Most commonly, shape optimization is the process of changing the physical dimensions of a structural part to reduce weight while staying within design constraints, usually maximum stress or deflection. There are many optimization methods in the literature, such as the Simplex optimization method, Fuzzy sets for multicriteria optimization and Evolutionary Structural Optimization (ESO) [7, 11].

The ESO is a new technology that draws inspiration from nature to produce computer code that will always seek the optimum structure under any set of single or multiple conditions. This new development from Australia can treat size, shape and topology optimization.

The process of structural optimization has traditionally followed a parametric or design variable path where the shape or topology of an object is defined by a set of parameters. An optimization objective is set, such as minimum volume or maximum stiffness and the parameters are adjusted, allowing for constraints, using a mathematical search engine such as sequential quadratic programming (SQP). After more than forty years of intensive research this still proves to be difficult and of limited success. The ESO method developed in 1993 by Steven and Xie overcomes all of the difficulties associated with traditional methods and is able to

treat size, shape and topology optimization. It has also proved to be very general with its capabilities and can support: completely general and multiple load environments including thermal loads and inertial loads: completely general and multiple kinematics environments; completely general structural shapes in 2D and 3D; completely general and multiple material environments¸ static, dynamic and stability optimizations, and combinations of these and material and geometric nonlinearity. The process of ESO starts with a high density finite element mesh. Following multiple finite element analysis with all the load and kinematics environments treated, each element is assessed for its effect on the optimization objectives, be it stress, stiffness, natural frequency or whatever, and if the element is not important to these objectives then it is removed. Elements are removed in a steady, orderly way. After much analytical iteration, with tighter tolerances on the range of stress or strain, the final optimized structure evolves. Many practical situations have been examined and some have been modeled to demonstrate the efficacy of the ESO method. The ESO method has been chosen for this work, because it has been found to be the most suitable.

4. Design of suspension control system

We used the numerical method to formulate our design. The conventional upper arm is shown in Fig. 8. The weight is 1.19 kg and the size is 320mm x 260mm x 68mm [3]. We choose the thixoforming alloy A357 for upper arm. The advantages of thixoforming A357 are: dimensional precision; light weight; complex net shape; low porosity; high volume; thin wall capability; and competitive pricing. The properties of A357 are: Density = 2670.3 kg/m³; Heat treat T6; Tensile strength =330-358MPa; Yield strength = 275MPa; Elongation=9%; Elastic modulus= 70-80 GPa and Poisson's ratio= 0.33. These typical automobile suspension arms have been chosen for the static, dynamic and vibration analysis that will allow us to cut down weight and develop an optimal shape.
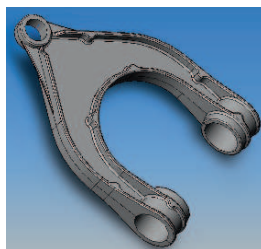
Fig. 8. Aluminum alloy suspension upper control arm

This takes advantage of the geometric modeling and automatic analyzing capabilities of the parametric associative CAD system. In our situation, we are doing shape development by Abaqus. This software cannot do shape optimization auto-

matically, but it can measure the strength for each element and give us necessarily information. Hence, we can develop parts by the ESO method. ESO, described below, is an evolutionary structural optimization [7].

First, we have a safety factor defined by $\sigma_y/\sigma_{max}=k$ (k=1.05-1.15), σ_y is yield strength and σ_{max} is maximum strength of the part under the force. So σ_{max} should be less than σ_y. Then we verify the rate σ_e/σ_{max} <75% ($\sigma_e<\sigma_y$), where σ_e is the stress on the element. So the objective function can be written as $f(\sigma) = \sigma_e/\sigma_{max} < value$ (the value<75%). In this area, we can cut the materials for reducing the weight. Depending on this function, we can reduce the weight and optimize the shape of the part.

Load Setting: Using the vehicle suspension system developed in the previous section, we set the boundary conditions at the two holds as shown by Fig. 9. We consider two kinds of conditions. First, all directions and rotations are fixed (axes: X=Y=Z=0; Rotation: URx=URy=URz=0). We define BC fixed. Second, axes X=Z=Free, Y=0; Rotation URz, URx=0, URy=0.52, we define BC UR2 [3]. In this study, we use a random amplitude curve that represents the real case of main road excitation. This amplitude is derived from the vehicle model described in the previous section. The Maximum Stress Misses contour of the upper arm is 203.6 MPa in BC fixed boundary condition and 109 MPa in BC UR2 boundary condition.
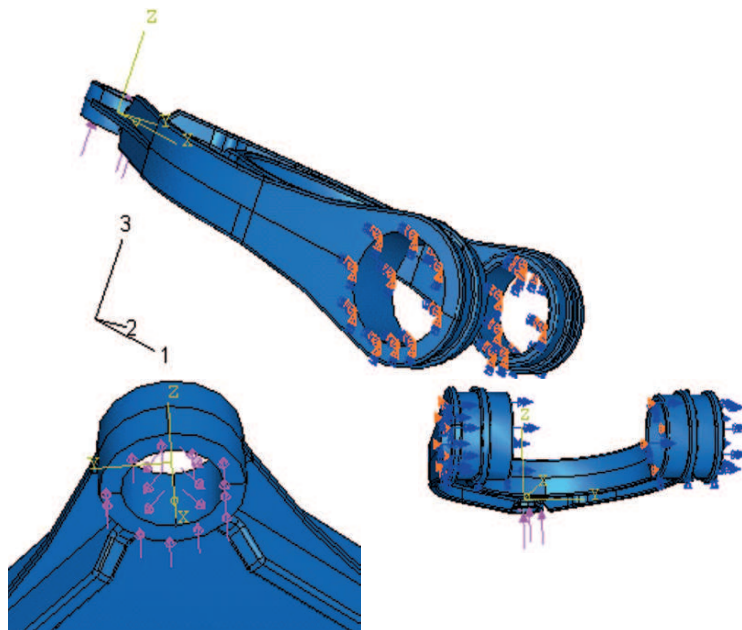
Fig. 9. Boundary conditions

Using the ESO method, we can continue to render the aluminum parts lighter. The final upper arm shape obtained depends on our objective function. The results in Figs. 10 and 11 shows that the maximum stresses are 156 MPa in BC fixed boundary condition and 103.9 MPa in BC UR2 boundary condition. It is less than the yield strength of 275 MPa of aluminum A357.

This demonstration proves that the design of aluminum upper suspension arm is successful in replacing the steel one. In the simulation above, we have loaded random forces under the fixed and rotation boundary conditions. Through the simulation of vibrations (not shown in this paper), we verified vibrations and improved the suspension arms.
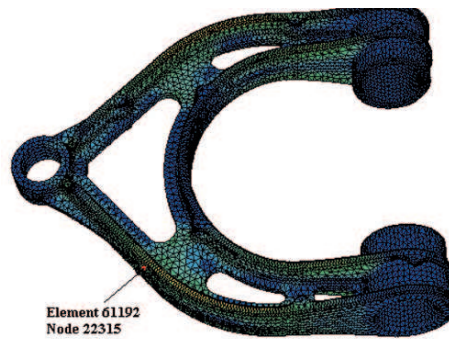
Fig. 10. Stress Misses contour of development upper arm with random force, BC fixed
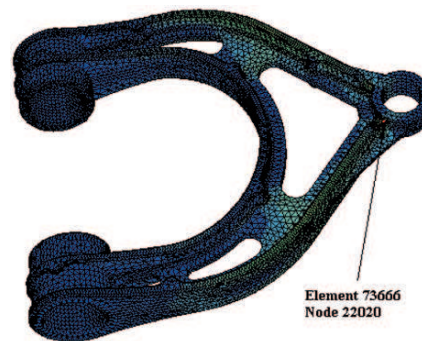
Fig. 11. Stress Misses contour of development upper arm with random force, BC-UR2

The final shape of the upper arm is obtained after analysing their natural frequency. To highlight this result, Fig. 12 illustrates the deformation mode associated with the natural frequency (mode 1 and mode 3).

The results of the vibration analysis are satisfactory. Finally, Table 1 highlights the comparison of weight and mechanical properties of an aluminum vs. steel suspension arm. The weight of the aluminum arm is 51.2% less than the steel one.
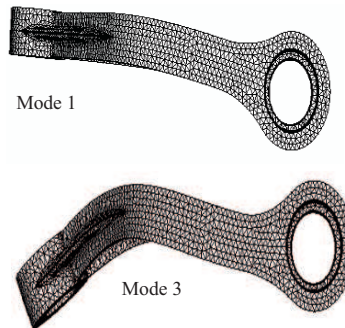
Fig. 12. Deformation mode

Table 1. Comparison of aluminum vs. steel suspension control arm.

Suspension upper control arm	Material	Yield strength (Pa)	Density (kg/m^3)	Mass (kg)	Weight save (%)
	Steel	2.9e+008	7800	2.04	N/A
	A357	2.75e+08	2670.3	0.996	51.2

5. Conclusions

Through this research, we have developed a flexible method for designing aluminum parts for automobile application. This method enables us to closely imitate real life conditions and make accurate predictions based on set boundaries. We have studied the kinematics of the mechanical systems, aluminum properties and application of aluminum parts in an automobile. We did complex part design using the CAD system and the knowledge of mechanical design. We have also studied the vibration movement of a dynamic system and the amount of stress it induces in a mechanical part.

It is important to analyze this in order to prevent part failures, which is crucial in ensuring the safety of the passengers. Through this research, the use of modelling

and simulation software in conjunction with the ESO method allowed us to compare the properties and advantages of aluminum alloy versus steel in the manufacturing of an automobile control arm.

The results demonstrate that the aluminum alloy under specific design conditions is able to efficiently sustain the stresses acting on the control arm with the advantage of a weight loss compared to steel parts.

This advantage is significant since it will not only allow considerable savings in the manufacturing process, but a lighter car also improves energy consumption and driving performance, leading to not only a reduction in cost for both the manufacturer and the consumer but also to a safer and better driving experience.

References

[1]   SAE world congress papers confirm, «Aluminum technologies offer SUVS safety and fuel economy», March 5, 2003.

[2]   The Aluminum Association Inc., «Automotive aluminum the performance advantage», Webpage http://www.autoaluminum.org, 2004.

[3]   Fanglin Cai, «Conception et analyse mécaniques des pièces en aluminium pour application automobile», Master thesis, University of Quebec at Chicoutimi, Quebec, Canada, 2006.

[4]   Sheng Mhau Industray Co., Ltd., «Specialist in steering & suspension system», 1998.

[5]   GILLESPIE, Thomas D., «Fundamentals of Vehicle Dynamics», Warrendale: Society of Automotive Engineers, 495p, 1992.

[6]   M. Bouazara, «Étude et analyse de la suspension active et semi-active des véhicules routiers» Ph.D. thesis, Laval University, Quebec, Canada, 197p, 1997.

[7]   O. M. Querin, «Evolutionary structural optimisation: stress based formulation and implementation». Ph.D thesis, Department of Aeronautical Engineering, University of Sydney, Australia, 1997.

[8]   H. Rahnejat, «Multi-Body-Dynamics: vehicles, machines and mechanisms», Society of Automotive Engineers, 355p, 1998.

[9]   M. Bouazara and M. J. Richard, «An optimisation method designed to improve 3-D vehicle comfort and road holding capabilities through he use of active and semi-active suspension» Eur. J. Mech., A/Solids 20, pp. 509-520. 2001.

[10] J. P. Trejo, «Simulation d'une suspension automobile», Master thesis, Laval University, Quebec, Canada, Page 41-46, 2005.

[11] T. Lindby and J. L. T. Santos, «Shape optimization of three-dimensional shell structures with the shape parameterisation of a CAD system», Page 6, 2, 1999.

Performances of Vehicles'Active Suspensions

Nadhira Kheznadji Messaoud-Nacer

Laboratoire de Mécanique Avancée, Département CMP, Faculté GM&GP,USTHB, BP32
BEZ, El Alia, 16111 Alger, Algeria

Abstract Most complex industrial systems are difficult to control automatically. Such difficulties are due to the non linearity and to the variation of these systems' parameters, as well as to the quality of measurable variables. In view of the efficiency and of the performances obtained by the introduction of active suspension systems in vehicles, researchers undertook more work on this field. Until now, in the modelling used for such systems, the least possible degrees of freedom are introduced in order to mitigate the difficulties of the study. Hence, many studies on models of a quarter of vehicles, with two degrees of freedom only, are available. This article deals in the first section with the performances that are obtained on this type of model by the method of fuzzy sliding mode which uses, in the present case, the fuzzy logic techniques to adjust the control gains that occur under the sliding mode. To put into evidence the efficiency and the performances of such a control system, we have compared the results obtained through the sliding mode technique solely, then through the combination of the fuzzy logic theory and the set up by the sliding mode, and the fuzzy sliding mode. The second section of the study aims at extending this kind of work to a half vehicle model with four degrees of freedom. The computation of the command force to apply to the system in order to control the suspension was based on the fuzzy logic theory for which three essential steps were developed: fuzzification, inferences, and defuzzification. The simulations made were validated, on the one hand, through a comparison to the same passive system and, on the other hand, to results available in literature.

Keywords: Vehicle Suspension, Active Control, Fuzzy Logic, Sliding Mode.

1. Introduction

Nowadays, for the purpose of providing more comfort conditions, more safety for passengers, and a better road holding by vehicles, it is essential to conceive optimized suspension systems. As passive suspensions are not always able to meet such requirements, researchers were rather interested in the conception of semi-active or active suspensions which could change their control parameters in function of the road conditions.

2. Active suspension system of a quarter vehicle model

Let us consider an active suspension system of a quarter vehicle model with two degrees of freedom (see Fig. 1). The matrix equation of the motion for the vehicle body is given by

$$\dot{X} = AX + BU + EW , \quad \text{where } X = [x_1, x_2, x_3, x_4]^T \tag{1}$$

X is the state vector with $x_1 = z_s - z_u$, $x_2 = \dot{z}_s$, $x_3 = z_u - z_r$, $x_4 = \dot{z}_u$
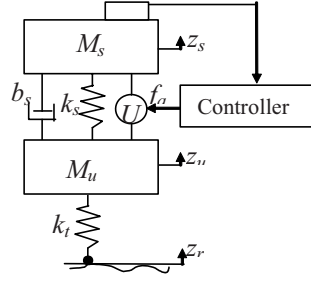
Fig. 1. Quarter vehicle model   **Fig. 2.** Control strategy by fuzzy sliding mode
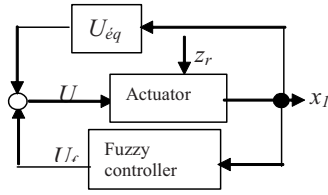
$$A = \begin{pmatrix} 0 & 1 & 0 & -1 \\ -k_s/M_s & -b_s/M_s & 0 & b_s/M_s \\ 0 & 0 & 0 & 1 \\ k_s/M_u & b_s/M_u & -k_t/M_u & -b_s/M_u \end{pmatrix}, \begin{array}{l} B = (0, 1/M_s, 0, -1/M_u)^T \\ E = (0, 0, -1, 0)^T \\ W = \dot{z}_r \\ U = f_a \end{array} \tag{2}$$

2.1. Optimal control theory applied on a quarter vehicle model

The criteria of comfort, road-holding, and suspension travel were selected to optimize the system studied. The performance index can hence be written as follows [4]:

$$J = E \left\{ \frac{1}{2} \int_0^\infty \left(q_1 (z_s - z_u)^2 + q_2 (z_u - z_r)^2 + q_3 \dot{z}_s^2 + q_4 \dot{z}_u^2 + \rho U^2 \right) dt \right\} \tag{3}$$

As the general form of the performance index is

$$J = E \left\{ \left(X^T Q X + 2 X^T N U + U^T R U \right) dt \right\} \tag{4}$$

Problem solving will therefore consist in determining control force U, while minimizing linear performance index J: $U = -G.X$. Where G is the control gain matrix: $G = B^{-1}(N^T + B^T P)$. P is a symmetric matrix defined as positive, given by the solution of Riccatti's equation:

$$A^T P + PA + Q - (PB + N) R^{-1} . (B^T P + N^T) = 0 \tag{5}$$

We consider that it is system disturbance, due to road surface velocity $\dot{z}_r$, and that this is a white noise: $E[\dot{z}_r(t)] = 0$ and $E[\dot{z}_r(t)\dot{z}_r(t+\tau)] = HV\delta(\tau)$. H is a parameter related to the roughness of the road; V is the speed of the vehicle and δ is Dirac's function. The spectrum density of the road profile reads then: $\Phi_{z_r}(\omega) = HV/\omega^2$.

2.2. Sliding mode control

It is a non linear control which consists in bringing the state trajectory of a system towards the sliding surface [1]. In the case of the suspension system studied, the sliding surface takes the following analytical form:

$$S(x_1, x_2) = x_2 + \lambda x_1, \ \lambda > 0 \tag{6}$$

Control law U, meeting the sliding condition, is constituted of two components: $U = U_{\acute{e}q} + U_g$; where $U_{\acute{e}q}$ is the equivalent control force, as defined by Utkin [7], and U_g is the singular one. In ideal sliding mode, the expression of surface and its derivative form are nulls, thus:

$$U_{\acute{e}q} = -B^{-1}[AX + EW] \text{ or } U_{\acute{e}q} = -\hat{b}^{-1}[a_1 x_1 + (a_2 + \lambda)x_2] \tag{7}$$

where a_1 and a_2 are respectively $-k_s/M_s$, and $-b_s/M_s$. $\hat{b}$ is a gain of the control related to M_s as: $\hat{b} = \sqrt{(b_{min} \cdot b_{max})}$. b_{min}, b_{max}: empty or loaded vehicle respectively. $\hat{b}$ can be also chosen among the values of a limited interval defined by: $\beta^{-1} < \hat{b}/b < \beta$ where $\beta = \sqrt{(b_{min}/b_{max})}$.

The singular control U_g is introduced to ensure convergence towards the sliding surface. It is defined by:

$$U_g = -\hat{b}^{-1}K \cdot \text{sgn}(S), \tag{8}$$

K satisfying the sliding condition [5, 6]

2.3. Fuzzy sliding mode control

The fuzzy sliding mode control appeared in order to ease the chattering pheno-menon which constitutes the main inconvenience of the sliding mode, as it can damage actuators and be prejudicial to the performances of the system.

The fuzzy sliding mode control requires the application of the principle of self-adaptation of the gains which occur at the force control. Figure 2 summarizes the control principle of the fuzzy sliding mode using a self-regulator [3]: $U = U_{\acute{e}q} + U_f$ where:

- $U_{\acute{e}q}$ is calculated in the same way as for the sliding mode solely.
- $U_f = GU \cdot u_{pf}$ (force control calculated by the fuzzy logic theory [2]). u_{pf} is calculated with the first controller (see Fig. 3).
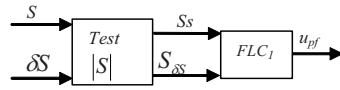
Fig. 3. Calculation steps of u_{pf} **Fig. 4.** Calculation of GU
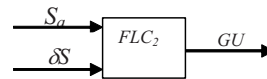
The variation δS is such as $\delta S(t) = S(t) - S(t - T)$ and the average $S_a(t)$:

$$S_a(t) = \frac{1}{N} \sum_{i=0}^{N-1} S(t - iT) \tag{9}$$

where T is a sampling period, and N is the number of samples: $N = t/T$. The first fuzzy controller has two inputs [3]:

$$\begin{cases} S_s = S \times GS \\ S_{\delta s} = \delta S \times CGS \end{cases} \tag{10}$$

GS and CGS are gains that are conditioned by the evolution of the sliding surface. The center of gravity method is used to defuzzify the inferred output u_{pf}. The gain GU is obtained from the output of a 2nd fuzzy controller (see Fig. 4). Defuzzification process allows the obtention of the value of gain GU.

2.4. Simulations and results

For comparison and validation purposes of our results with what is available in literature, we have deliberately taken an excitation of the road profile, under a sinusoidal form:

$$z_r(t) = CK \sin(\omega t) \Big/ \left(\frac{\omega}{2\pi V}\right)^{2.5} \tag{11}$$

where: $\omega = 7.7$ rad/s; CK is function of the quality of the road; $V = 30$ m/s $M_u = 30$ kg ; $M_s = 230$ kg ; $k_s = 15\,000$ N/m. $k_t = 150,000$ N/m; $b_s = 1000$ N/m s^{-1} ; $\lambda = 10$; $K = 70$; $\hat{b}^{-1} = 250$. The results obtained with these values, by optimal control, sliding mode, and fuzzy sliding mode are presented on Figs. 5 and 6. The suspension travel (see Fig. 5) is better respected by the sliding mode. Responses of the fuzzy sliding mode and of the optimal control are nearly similar, and equally satisfactory. As a whole, we can affirm that optimal control and fuzzy sliding mode yield very close results.
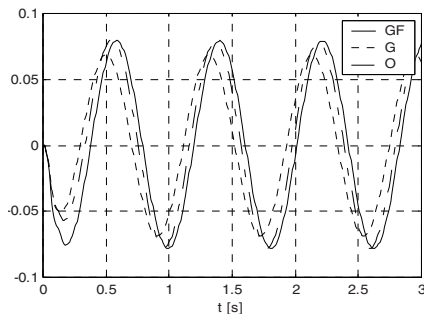
Fig. 5. Suspension travel (GF = Fuzzy Sliding, O = Optimal control)
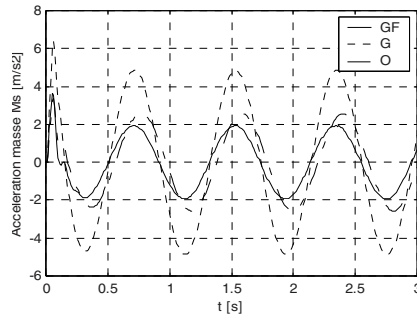
Fig. 6. Sprung mass acceleration G = Sliding,

For a slightly higher cost, the setting up by fuzzy sliding mode produces better performances in terms of comfort, whereas the sliding mode is more appropriate to the functioning space of suspension. Furthermore, let us notice, that by deteriorating some 30% of the intrinsic characteristics of the suspension studied, (by increasing the mass of the frame and decreasing by 30% the damping stiffness) we could also check the strong validity of these control methods.

3. Half vehicle model of the active suspension system

Figure 7 gives a representation of the half vehicle model of the active suspension system with four degrees of freedom. Calculations are based on the setting of the control forces by means of fuzzy controllers directly acting on the system (Figs. 8, 9 and 10). The matrix equation of the motion for the vehicle body reads therefore as follows:

$$M\ddot{X} + (C(t) - DF)\dot{X} + K(t)X + d(t) = Du + EW \qquad (12)$$

$W = (W_a, \dot{W}_a, W_b, \dot{W}_b)^T$ is the excitation that is due to the road profile at the front and rear wheels; $X = (x_{1a}, x_{2a}, x_{1b}, x_{2b})^T$ the state-vector.
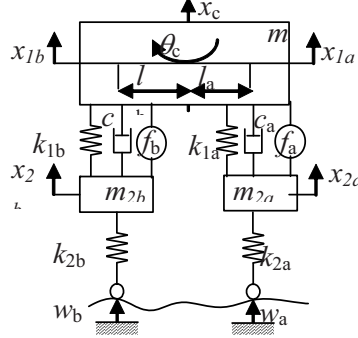
Fig. 7. Half vehicle model

To calculate the damping and stiffness forces of suspension, we took: $f_{ci} = c_i(\dot{x}_{1i} - \dot{x}_{2i}) + d_{ci}$ and $f_{ki} = k_{1i}(x_{1i} - x_{2i}) + d_{ki}$, $i = a, b$. f_{ci} and f_{Ki}: are respectively the damping and spring forces of suspension. $f = (f_a, f_b)^T$ is the force vector whose components f_a et f_b are given by the actuators of front and rear secondary suspensions. These are generated by pistons in the hydraulic cylinders of each one of the two actuators, (see Ref. [8]). We can therefore write that:

$$f_i = -A_{yi}(\dot{x}_{1i} - \dot{x}_{2i}) + u_i, \; i = a, b \tag{13}$$

With A_{yi} representing the surfaces of the pistons, and u_i corresponding to control forces that we will calculate later. Under the matrix form, we will then have: $f = F\dot{x} + u$ where F is the matrix of surfaces:

$$F = \begin{bmatrix} -A_{ya} & A_{ya} & 0 & 0 \\ 0 & 0 & -A_{yb} & A_{yb} \end{bmatrix} \text{ and } u = (u_a, u_b)^T \tag{14}$$

Two regulators intervene at the control by the fuzzy logic for the front wheel and the rear wheels with two inputs α_{1i}, α_{2i} and one output β_i. On this scheme:

$$\alpha_{1i} = \left[(x_{1i} + \lambda_{1i}\theta_c)/C_{1isf}\right] \text{ and } \alpha_{2i} = \left[(\dot{x}_{1i} + \lambda_{2i}\dot{\theta}_c)/C_{2isf}\right] \tag{15}$$

$\lambda_{1i}, \lambda_{2i}$ are due to rotation effect. C_{1isf} and C_{2isf} are scale factors. u_{Li} is a *linear* control function of the vertical acceleration of the frame. $u_{Li} = -g_{Li}$ and $u_{Ni} = g_{Ni}\gamma_i$ where u_{Ni} is a *non-linear* control obtained by the fuzzy regulators. g_{Li} et g_{Ni} are control gains, and γ_i is calculated at the output of the fuzzy controller. Membership functions are totally similar for the input and output variables of the two fuzzy regulators. They are of triangular and trapezoidal symmetrical shapes with an equidistant distribution, and a number of fuzzy subsets equal to seven in order to have a fine tuning. The basis for the rules is set under the form of a diagonal and

symmetrical inferences table. It aims at covering all possible situations of the system, assess the various values attributed to α_{1i}, α_{2i} and all corresponding values of γ_i. In our computations, we used the "Sum – Prod" inference method and proceeded with defuzzification through the gravity center method.

The various parameters that intervene in the model are: $m_c = 430$Kg; $I_c = 600$ Kgm^2; $m_{2a} = 30$ Kg; $m_{2b} = 25$ Kg; $l_a = 0.871$ m; $l_b = 1.469$ m; $k_{2a} = k_{2b} = 152$ KN/m; $v = 20$ m/s; $a = 0.05$ m^{-1}; $A = 10^{-6}$ m; $A_{ya} = A_{yb} = 15$ Ns/m; $C_{1asf} = C_{1bsf} = 0.02$; $C_{2asf} = C_{2bsf} = 0.03$; $\lambda_{1a} = 3.2$; $\lambda_{2a} = 0.5$; $\lambda_{1b} = -5.2$; $\lambda_{2b} = -0.8$.

We tested three typical excitations: sinusoidal, white noise and bump. For each case, it was necessary to adapt command gains to come up with a satisfactory control. In what follows, we nevertheless limited ourselves to some results only. In general, we note on all the responses that the amplitudes of the active system are very small as compared to those of the passive system (Figs. 11, 12 and 13).
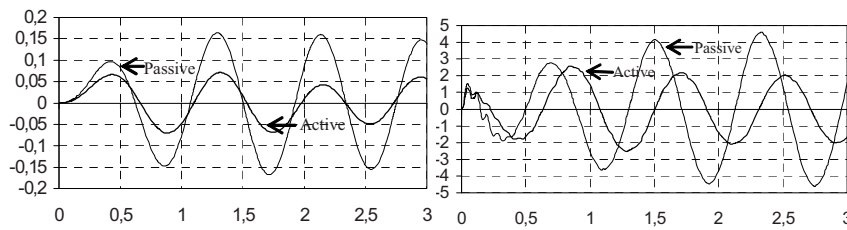
Fig. 8. Displacement of the vehicle body

Fig. 9. Pitching Acceleration
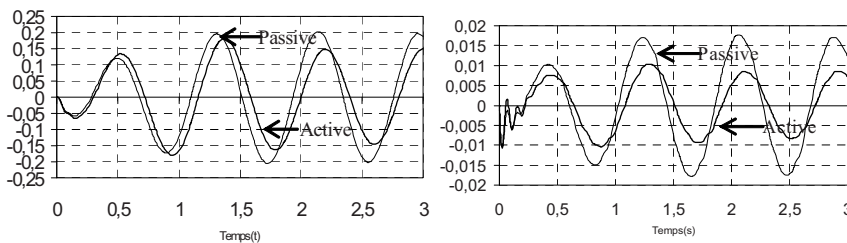
Fig. 10. Suspension deflexion of the front

Fig. 11. Tire deflexion of the front
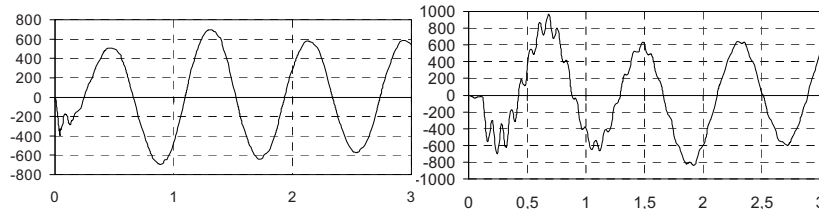
Fig. 12. Control force f_a

Fig. 13. Control force f_b

4. Conclusions

The application of the sliding mode solely to the suspension system of a quarter vehicles allows the obtention of good performances, but the introduction of the fuzzy logic in this same control mode does improve the results. Optimal control ends up with results that are very close to the fuzzy sliding mode. Among the inconveniences met in the application of these methods, we have noticed that:

- The selection of the sliding surface for the fuzzy mode and the fuzzy sliding mode is very complex when the order of the system to control is high.
- The determination of computation coefficients by sliding mode is subject to the rules of automatism, which are often very tedious.
- Chattering phenomenon leads to high frequency commutations of the actuator that can damage the controller.
- The fuzzy logic theory applied to the sliding mode enables to fix the chattering phenomenon.
- The sliding and fuzzy sliding methods are very stout as compared to the optimal control which yields good performances only for the system nominal values.

The fuzzy logic control done on an active suspension system of a half-vehicle model with four degrees of freedom led to the conclusion that fuzzy controllers provide a great improvement in terms of comfort and road-holding as compared to the passive suspension system, on the one hand, and to ensure that the results that are obtained by the fuzzy logic are globally of the same scale of sizes than those calculated by other control methods. But, in order to obtain the best results with the fuzzy logic, the control gains must be carefully adjusted. This research is still preceded by trial and error, which keeps it particularly tedious and time-consuming.

References

[1] Bühler (1986). Réglage par mode de glissement. Presses Polytechniques Romandes.
[2] Bühler (1994). Réglage par logique floue. Presses Polytechniques Romandes.
[3] Chen-Sheng Ting, Tzuu-Hseng S Li and Fan Chu Kung (1995). Design of fuzzy controller for active suspension control system. Mechatronics, Vol. 5(2), pp. 365–383.
[4] Hac A (1985). Suspension optimization of a 2 DOF vehicle model using a stochastic optimal control technique. J. Syst. Vehicle, Vol. 100(3), pp. 343–357.
[5] Slotine J.J. (1984). Sliding controller design for non linear systems. Int. J. Control, Vol. 40, pp. 421–434.
[6] Slotine J.J. (1986). Adaptative sliding controller synthesis for non linear systems. Int. J. Control, Vol. 43, pp. 1631–1651.
[7] Utkin V. (April 1986). Variable structure systems with sliding modes. IEEE Transactions on automatic control, Vol. AC-22, (2).
[8] Yoshimura T, Nakaminami K, Kurimoto M and Hino J (1999) Active suspension of passenger cars using linear and fuzzy-logic controls. Control Eng. Pract., Vol. 7, pp. 41–47.

Damaging Influence of Cutting Tools on the Manufactured Surfaces Quality

Idriss Amara, Embarek Ferkous and Fayçal Bentaleb

Mechanical Laboratory, Mentouri University of Constantine, Chaab Ersas, Campus, Ain El Bey Road, 25000 Constantine, Algeria.

Abstract   Since their apparition, machining techniques underwent multiple improvements. The put on shape material processes by abduction of material are constantly revised on order to satisfy the economic or ecological industrial requirements. Nowadays, the manufacture engineer must be able to answer multitude questions in order to achieve pieces quickly wile satisfying the required quality with least cost. The cutting tools have generally a complex geometry which results often from compulsory and purely empirical focusing within the workshop, sometimes from more analytical studies observing diverse criteria (damage resistance or generated surface quality), but rarely from a real optimization which would require a modelling of the drainage of one or several shavings. In the field of the metals cutting, the wear of the cutting tools leads to a degradation of the cutting zone and work. It is thus important to study the evolution of the cutting criteria allowing to follow the tool degradation during a manufacturing operations and thus to decide whether to replace he tool or not. An experimental device, particularly, a high resolution sensor, had been used and gave the real wear shape of the cutting face. In order to deduce this shape by using the B-Spline method, a mathematical model has been proposed.

Keywords: Cutting Tools, Machining, Surfacing Geometry, Roughness, Damage.

1. Introduction

The part design by machining requires an implementation of machining operations. These operations can provide a multiplicity of processes which must fulfil the part's specification requirements, whose dimensions and their surface qualities must be within an interval of tolerance, obtained by machining, and the constitutive material properties. The metal machining represents a significant part of the modern industrial activity. In this field, as in much of other, the increase demand in one hand, and, the competition laws in the other, incites the industrialists to implement and produce as the lowest possible cost [1]. The metals cut phenomenon showed when a tool penetrates in a metal part to form a chip, the material located close to surface is strongly sheared. The deformation is carried out at very high speeds. The temperatures and stresses at the interface level are considerably high and lead to complex physicochemical phenomena. Those taking place in a very small area around the tool point, the cut tribology related phenomena related are very difficult to study and model [2].

From that we can say that the cut of metals is a strongly coupled thermo-mechanical process in which plastic deformations, the heat and the friction phenomena play a critical role in term of wear [3].

2. Experimental study

The work undertaken within the framework of this study shows that the various cutting tools change the cutting conditions of materials, as well as, on the chip forming and on the level of the energy necessary to the cut (forces and power). The objective of this work is to apprehend, as much as possible, the dynamics of wear of the coatings. It is integrated in order a large industry concern, to set up a protocol of tests allowing the characterization of the coating wear. Actually, there are many coating characterization methods:

- Chemical compositions, structural and texture
- Mechanical properties: hardness, module, etc.
- Friction coefficient, etc.

But, these modes of characterization are static based tests. However the coating dynamic behaviour is very different from the static one. Consequently, we endeavoured to use techniques allowing recording the dynamic variations of the coatings behaviour and if possible to characterize its mode deterioration.

2.1. Determination of the entry parameters

The entry parameters to be defined are referred to

- The cutting tools and selected coatings
- The machined materials whose mechanical properties of workability will aim to differentiate the behaviour of the tungsten carbide coatings
- The cutting conditions adopted on a machine tool better adapted better to an experimental design

2.1.1. Tools and coatings

- To define a tool, a great number of geometrical data enter in account
- The choice of the substrate (mechanical cutting tool behaviour)
- The cut edge shape
- The cut angle: pressure angle on the part
- The shape breeze chip intended to attenuate the wear of the tool by limiting the chip friction surface on the tool
- It is thus essential to set operating conditions as reproducible and simple as possible. This is why, it was selected:

- The tool carrying plate shape fixed and adapted to the turning conditions (reference CTGPL 16 16 K16)
- A not comprising chip breakers plate shape, since it introduces an additional variability into the chip flow on the tool and must be adapted to the coating

2.1.2. Plates description

The selected plate (Fig. 1) selected is reversible, Sandvik type (reference TPMN 16 03 08) comprising three cut edges by plate.
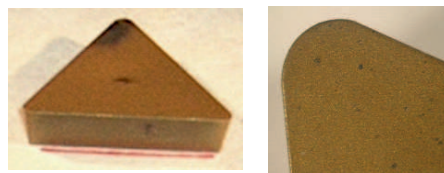
Fig. 1. Sandvik plate TPMN 16 03 08

2.2. Cutting geometry

The cutting geometry is influenced by several parameters

- The type of machining: here slide-lathing
- Orientation space plate compared to the machined matter

2.3. Machined matter

The behaviour of the coatings and their wear depend on the machined matter and its crystalline state, because the mechanical cut conditions depend on the matter characteristics. It is thus significant to take account of this effect. The used matter during the experimentation is steel a slightly allied soaked with fine grains, $F_k20MnCr5$, used in industry, initially, with a 50 mm on diameter of and 500 mm in length.

2.4. Cutting parameters

The general framework selected to test our coatings is slide-lathing. It results from it that we can schematize the configuration of the cut by the following drawing (Fig. 2). It is necessary to define the machining parameters, in order to avoid to be placed under cutting edge degradation conditions too fast. To define these parameters,

it is necessary to delimit first of all the entry field. This last was defined in order to limit wear phenomena [4, 5]. Once the field is fixed, it is appropriate to fix the cutting conditions.
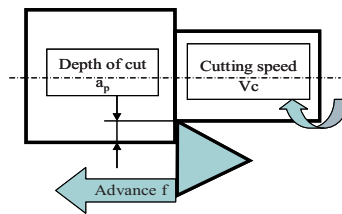
Fig. 2. Machining configuration

2.4.1. Cutting speed

For the determination of the cutting speeds we used the coatings under industrial tests conditions, i.e. under optimal but very likely, different machining conditions [6]. The objective is to study the deterioration of the coatings. That poses a certain number of additional questions because, like we noted in the preliminary tests, the deterioration determination is generally not accessible by direct controls means. Consequently, we can test the coatings under the same conditions and to compare the obtained results in

- Lifespans
- Minimum cutting forces
- Surface qualities of the machined part, etc.

But, this simple procedure presents a double disadvantage:

- It deliberately challenges the couple tool-matter concept, on which machining in the industrial world is founded.
- It does not satisfy a scientific step, if it leads to tests out of the using intrinsic optimal zones of the coatings in machining. Moreover, the conclusions of such tests would have only a little interest for industry.

According to [7] for an operation of light outline, to machine steel slightly allied with a coating carburizes metal (the case of material and the plate used) under industrial conditions, the cutting speeds are limited to 85 m/min. For the experimental case, the cutting speeds vary from 45 to 77 m/min.

2.4.2. Advance cutting tool

This study is situated within the framework of a light outline, which forces to limit advance tool speeds. We know that roughness R_a can be determined according to the geometry of the tool, the advance and the cutting depth, in accordance with

Fig. 3. In order to have an acceptable surface quality and to do not degrade the parameter R_a, it is necessary to have a minimal advance. However, it is also significant to take account of a minimum speed required in advance by the formation of a chip having a sufficient and no thickness. Indeed, below a lower limit, the machined matter is crushed by plasticization and slips under the tool, generating a significant wear by abrasion. In order to locate, as much as possible, these tests under industrial conditions, according to [7] the advance value is 0.1 mm/tr. For our case the advance value is 0.11 mm/tr.
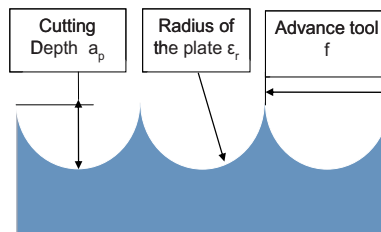
Fig. 3. Bond between surface quality, advance tool and depth of the cut

2.4.3. Cutting depth

In order to present the surface quality criterion industrially primordial, under the light outline machining conditions, we must also limit the cutting depth in an interval well determined; for that, and according to [7] cutting depths vary from 1.5 to 4 mm. For our case the cutting depth is 1.5 mm.

2.5. Machining and measurement procedures

Slide-lathing was selected like machining operation in this experiment (Fig. 4). The cutting conditions applied during this experiment are given in the Table 1.

Fig. 4. Test-tube in machining

Table 1. Values of the cut parameters and the tool geometry

$V_c = 47 - 71$ (m/min)	$\alpha = 6$
F = 0.11 mm/tr	$\gamma = 6°$
$a_p = 1.5$ mm	$r_\varepsilon = 0.8$ mm
Tool	P 40

Microscopy analyses with a microscope L2000-A indicate that for certain cutting conditions, wear by diffusion strongly prevails, the image acquisition was done by a numerical camera Canon Power Shot G5 type (Fig. 5). These analyses were undertaken at the Laboratoire Mécanique des Matériaux et Maintenance Industrielle Structure (LR3MI) Annaba University – Algéria.

The measurements were carried out on a three-dimensional measuring site without contact equipped with a High Resolution Sensor (HRS) (Fig. 6) at the Laboratoire de l'Equipe d'Analyse et de Modélisation des Systèmes Mécaniques et de leurs Signatures (EA(MS)²) de l'Institut Universitaire de Technologie d'Aix en Provence – France.
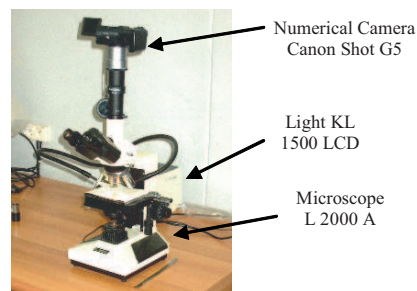
Fig. 5. Microscope L 2000-A
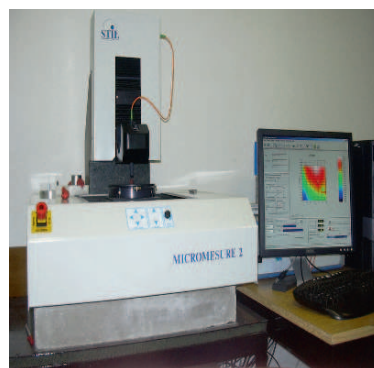
Fig. 6. Measuring site

3. Observations

During this experiment, a variation of the plate radius topology was noticed, as showed in Fig. 7. A brought back edge was formed on the ray of the plate. The brought back edge mechanism is of great practical importance, it is due to a wear by adhesion, since the rupture occurs within the chip mass and from the fragments of chips come to adhere on the tool by diffusion (Fig. 8), which modifies the machined part dimensions and its surface quality.

Fig. 7. Variation of the plate radius topology

From the undertaken test investigation, it will be necessary then to develop a methodology making characterization possible, and to define the influence of the cutting parameters (modes of wear) but especially to understand the influence of the evolution of the coatings wear on the surface quality and the integrity of the finished part [8, 9].
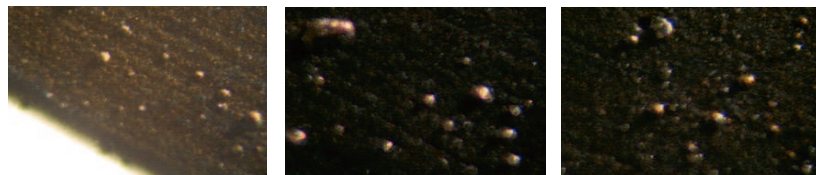
Fig. 8. Diffusion of the matter in plate (enlargement 400 times)

4. Results and interpretations

The use of the HRS equipped 3-D measuring without contact station has permitted to trace the various wear shapes, the number of points obtained through various measurements, as well as the real tracing of the nozzle ray variation of the used plate, and the cutting face (Fig. 9).

The number of points recorded by the sensor at each of its displacements is of 1,000 points, and the number of passes is 65, which gives a number of 65,000 points for each measurement [10]. But for the following calculations, 64 points will be taken into account, which represents the real pace of the nozzle ray variation.

For that, the edge topography was divided into regular steps having variation $\Delta x = 50$ µm and $\Delta y = 100$ µm. The goal is to define the wear equation for a uniform curve passing by the 64 points of control which represents the real pace of the nozzle radius variation (Fig. 10).
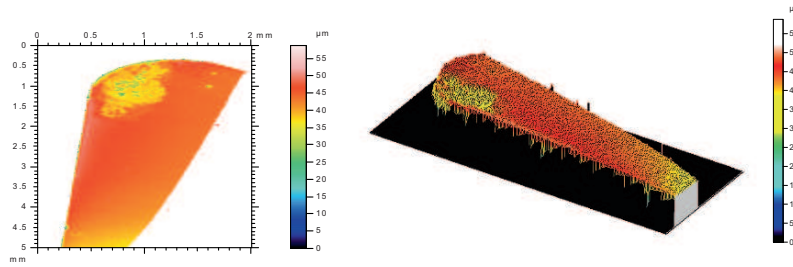
Fig. 9. Surface of cut in 2D and 3D
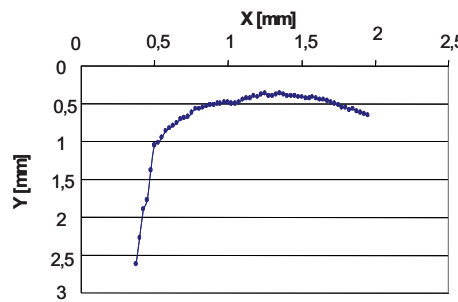
Fig. 10. Real pace of the nozzle ray variation
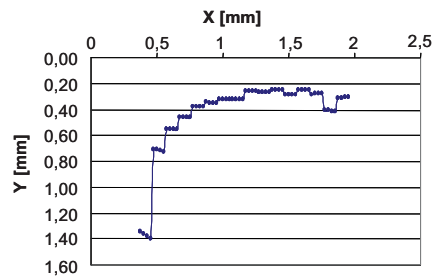
Fig. 11. Pace obtained by B Spline méthod

To define the equation of this wear, we used the B Spline method expressed by the following relation:

$$P_i(t) = \left(t^3 \; t^2 \; t \; 1 \right) . M_{BSpline} \left(M_{i-1} \; M_i \; M_{i+1} \; M_{i+2} \right)^t \tag{1}$$

With:

- M_i: co-ordinates of the control points
- $M_{B\text{-}Spline}$: The B Spline matrix given by

$$M_{B\,Spline} = \frac{1}{6}\begin{bmatrix} -1 & 3 & -3 & 1 \\ 3 & -6 & 3 & 0 \\ -3 & 3 & 0 & 0 \\ 1 & 0 & 0 & 0 \end{bmatrix} \qquad (2)$$

We found 16 equations, each one of them is the interpolation of 4 points with the B Spline method. The obtained results are

$$P_1(x) = -0.0133x^3 + 0.01x^2 - 0.04x + 0.4402 \qquad (3)$$

$$P_2(x) = 0.04x^3 - 0.03x^2 + 0.01x + 0.3835 \qquad (4)$$

Hence the last equation:

$$P_{16}(x) = -0.1868x^3 + 0.5003x^2 + 0.2501x + 1.1839 \qquad (5)$$

Figure 11 gives a representative form of the real pace of the nozzle ray variation after interpolation with the B-Spline method.

5. Conclusions

The cutting operation consists in transforming a material into a part by the action of tools animated by a machine tool. It is carried out by efforts, couples and heating, which generally moves and fluctuates during the operation and which are likely to compromise the respect of the dimensional tolerances.

In the zones of strong pressure on the edge of cut, deterioration is manifest since the first passes. The coatings which have a very low thickness of deposit, about a few microns, are thus eliminated from the initial edge of the tool from the first seconds of machining. We deduce that this presence is enough to modify the cutting conditions. On the other hand, we identified deterioration modes of the tungsten carbide coatings: abrasion, diffusion, surface heating, plastic deformation, cracking, etc, as well as the formation of a brought back edge.

The experimental device used made it possible to better see the real wear pace of the cutting face. The mathematical model suggested facilitated the deduction of this pace by the interpolation of this result by using the method of B-Splines method.

Finally, the surface elaboration process of or the cutting process can be considered as creation of a surface with a prescribed precision and roughness on the machined part, by the mean of the relative movement tool-part, carried out by the machine tool.

References

[1] A. Benamar, G. Inglebert, M. Boumahrat. Durée de vie d'un carbure P20 pour le chariotage d'un acier C38 à rugosité contrôlée. Mécanique et Industries, 2006 (6), p 635–640.

[2] L. Gautier (2004). Etude des mécanismes d'endommagement des outils carbure WC-CO par la caractérisation de l'interface outil copeau application à l'usinage à sec de l'alliage d'aluminium aéronautique AA2024 T351. Thèse de doctorat soutenu en décembre 2004 à l'Ecole Nationale Supérieure d'Arts et Métiers Centre de Bordeaux – France.

[3] H. Gökkaya, M. Nalbant (2005). The effects of cutting tool geometry and processing parameters on the surface roughness of AISI 1030 steel. Materials and Design Vol. 28, p 717–721.

[4] B. Roumesy. C. Bedrin. Mise en œuvre de plans d'expériences pour la détermination de la loi d'usure des outils de coupe. Technologies et Formations, 1994, N°52, p23–34.

[5] B. Roumesy. Détermination des lois d'usure des outils de coupe. Machines outils, Mai 1975, N°301, pp. 34–36.

[6] Radu Pavel et al, (2005). Effect of tool wear on surface finish for a case of continuous and interrupted hard turning. Journal of Materials Processing Technology 170, 341–349.

[7] Outils de tournage. Sandvik Cormant, (2000), p A 248–249.

[8] J. Wang, C.Z. Huang, W.G. Song. The effect of tool flank wear on the orthogonal cutting process and its practical implications. Journal of Materials Processing Technology Vol. 142 (2003), 338–346.

[9] C. Pagés. Comportement de revêtements céramiques sur outil en tournage à sec de finition, thèse de doctorat, soutenue en novembre 2003 à l'Ecole Centrale de Lyon – France.

[10] Bentaleb Fayçal (2007) Impact du phénomène de coupe sur la géométrie des outils de coupe. Thèse de magister soutenu en juillet 2007 au Département de Génie Mécanique, Faculté des Sciences de l'Ingénieur, Université Mentouri Constantine Algérie.

Design and Test of a Sandwich T-Joint for Naval Ships

Lotfi Hamitouche[1], Mostapha Tarfaoui[1] and Alain Vautrin[2]

[1]ENSIETA, LBMS-Mechanics of Naval Structures Laboratory, 2 rue François Verny 29806 Brest Cedex 9, France.

[2]Ecole des Mines de Saint-Etienne, France.

Abstract   Within the EUCLID project, 'Survivability, Durability and Performance of Naval Composite Structures', one task is to develop improved fiber composite joints for naval ship super structures. One type of joint in such a super structure is a T-joint between sandwich panels. An existing design consists of panels joined by filler and over-laminates of the same thickness as the skin laminates. In a superstructure a T joint may be loaded in tension if an internal blast occurs in two adjacent compartments or by an underwater explosion if two adjacent rooms have no support underneath the separating wall. Improved T-joints have been designed and investigated with focus on improved strength (survivability) and limiting delamination progress in over-laminates. This paper describes the design and test of a sandwich T-joint with reduced weight but with the same or higher strength than the existing design. The lightweight T-joint is designed for sandwich panels with 38 mm thick balsa foam core and 4 mm thick glass fiber/vinylester skin laminates. The panels are joined by filler forming a smooth transition (radius 35 mm) from the T-panel to the base panel, and over-laminated with laminates of 6mm thickness. Tensile (pull-out) tests are performed to load the structures in tension and the strength and failure mode are compared with results from tests on the existing T-joint base design. For the geometries in the present study, an increase of the over-laminate plies resulted in a 13% increase in the failure load.

Keywords: Plane-Strain Compression Test, Yield Stress, Plastic Flow, Amorphous Polymers.

1. Introduction

Structures manufactured from advanced composite materials are used extensively in many applications, including aerospace, ground transport, civil infrastructure and maritime. Composites are commonly used because of their high strength and stiffness, low mass, excellent durability and ability to be formed into complex shapes. For maritime applications, composites also offer improved corrosion resistance, improved fuel efficiency and reduced magnetic signature. However the joining of large structural panels always provides complications and inevitable compromises in performance. In military applications, composite structures [1] also help to minimize electromagnetic radar signature for stealth operation. The

mode of failure [2] of GFRP under static or dynamic loadings could be mainly due to matrix cracking or delaminations.

Delamination, being the more severe of the two, causes stiffness reduction and often leads to the catastrophic failure of the structure. Even invisible delaminations can severely degrade the mechanical properties and the load carrying capability of the structure.

Recently, a European collaborative project (EUCLID), "Survivability, Durability and Performance of Naval Composite Structures", has been carried out to experimentally investigate static and dynamic response of composite T-joints [3]. The objective of the project is to strengthen the technological basis for the large-scale application of fiber reinforced composite materials for naval vessels and structures, so that such vessels (or major parts thereof, e.g. superstructures) can be designed with confidence on the basis of modeling and failure predictions [4, 5]. One task is to develop improved joints for naval ship super structures manufactured from fiber composites. Among the joints in such a super structure we consider a T-joint between sandwich panels.

In the first phase of the project an existing design, called Base Design (BD), of a T-joint has been tested and characterized [6]. The Base Design T-joint consists of balsa core sandwich panels joined by filler forming a smooth transition (radius 35 mm) from the T-panel to the base panel, and over-laminated with laminates of the same thickness as the skin laminates. In the next phase of the project Candidate New Designs (CND) of T-joints were proposed, and some of them were selected for further investigation by testing. One of these CND T-joints, proposed by the Danish consortium, is inspired by Karlskronavarvet in Sweden [7], and it is based on sandwich panels with PVC foam core, which are joined by filler by the aid of two triangular PVC foam fillets. Investigations performed on a T-joint with triangular fillets and over-laminates loaded in compression state that the efficiency of the joint is not so good as for T-joints with over-laminates and filler fillet or a foam pad fillet [8]. In the other hand, a number of papers have paid attention to the analysis and improvement of single composite skin T-joints [9–15].

Hawkins and Shenoi [16] investigated geometry effects, including fillet radius and over-laminate thickness, for T-joints under 45° pull-off loading, which simulates the worst case scenario of flooding inside one compartment of the ship [9]. Phillips and Shenoi [9] found that the curved parts of the T-joint over-laminate, where the delamination first occurred, were the critical component under 45° pull-off loading as well as three point-bending. Similar results have also been reported by Rispler et al. [12] and Kumari and Sinha [13]. Read and Shenoi [17] also investigated the behavior and failure mechanisms of T-joints under fatigue loading. Dharmawan et al. [14] investigated the effect of geometry and disbond between the fillet and the over-laminate on the T-joint with a triangular fillet. It was found that the presence of an initial disbond altered the distribution of axial strain through the thickness of the over-laminate; this caused outward bending of the over-laminate when the T-joint is subjected to tension load. This effect

indicated that the fillet functioned as an important medium of load transfer in the T-joint.

In contrast to the use of a single composite skin, composite sandwich panel T-joints has been investigated [18–21].

Two kinetic models of fracture were identified: (1) the delamination between the leg and base panel, and (2) core shear failure in the base panel. Turaga and Sun [21] developed a few designs to improve the strength of T-joints. It was shown that using bolts in a circular fillet joint could cause early failure in the core and would not increase the ultimate join strength. Theotokoglou and Moan [18] stated that there were no significant differences in the ultimate strength of the two failure modes; the ultimate failure mode for a specific T-joint depends on the fabrication defects, e.g. voids in the fillet area. It is also found that the strength of T-joints is slightly influenced by the geometry of the over-laminate.

Toftegaard and Lystrup [22] proposed a new design of sandwich T-joint with reduced weight by use of two triangular PVC foam fillets, rather than the traditional circular fillet. It was found that the new T-joint configuration has 20% higher strength than that of the existing design and the weight reduced by 60%. To ensure the T-joint reliability, the behavior and performance under various loading conditions must be known. This paper outlines a study on the fracture behavior of a glass fiber reinforced polymer T-joint commonly used in composite marine vessels.

Experimental analysis was conducted to investigate the fracture behavior of the structure for the present design. In this paper we present a new T-joint, witch is over-laminated as a Base Design T-joint, but with a few ply laminates of base panel. This paper focuses on the design and test of the static tensile strength of the new T-joint, as one of the tests performed to characterize the Base Design T-joint. Also, the observed modes of damage during the tests will be reported here and discussed. This paper focuses on the design and test of the static tensile strength of the DCNS New Design T-joint, as one of the tests performed to characterize the T-joint.

2. Design of lightweight T-joint named DCNS_1, DCNS_2 and DCNS_3

The selected design based on the outcome of the EUCLID RTP3.21 study of the BD is called DCNS_X (X = 1, 2, 3). The specification for the design, materials and the over-all dimensions of the test specimens for the DCNS_T are summarized in Table 1, and the T-joint is illustrated in Fig. 1.

Table 1. Materials and basic dimensions of the composite T-joint, DCNS_T

Item description	Materials	Item symbol	Value (mm)
T-joint		Overall Width	250
		Overall Length, L	800
		Height of T-section, H	300
		Rounding radius, R	35
Over-laminate	E glass fiber: taffetas 500 g/m^2	Length, L_1 & L_2	150
	Matrix: vinylester dion	Thickness, T_{01}	6
		Thickness, T_{02}	4
Skin laminate	E glass fiber: taffetas 500 g/m^2	Thickness, T_{s1}	4
	Matrix: vinylester dion	Thickness, T_{s2}	2
Core	Baltek SB100	Thickness, C_1 & C_2	38
		R	28.5
Fillet	Crestomer 1152 PA	Thickness, T_g	5
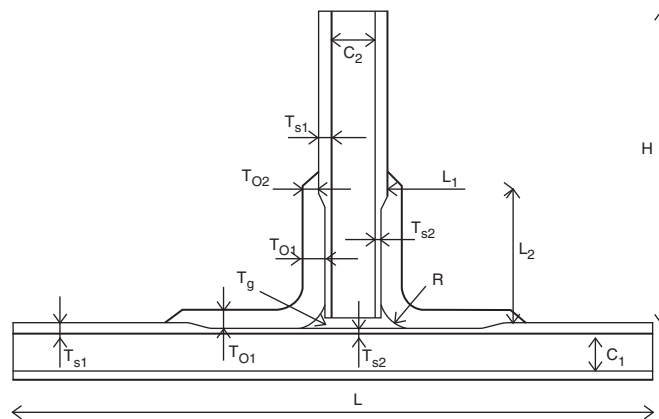
Fig. 1. Sketch of a new T-joint

3. Inspection of T-joint

The T-joints are manufactured by DCNS. The T-joint specimens are used for the tensile tests. An incoming quality inspection of the dimension, geometry and weight of the T-joint is performed, and shown in the quality inspection sheets, Table 2. Holes in the filler material are observed at both sides on both specimens. The thickness of the filler and the dimensions of the over-laminates deviate from the specifications.

The following is measured:

Table 2. Inspection of T-joint

Thickness of filler	T_g = 5–6 mm
Length of over-laminates	L_1 & L_2 = 150–155 mm
Thickness of over-laminate	T_{01} = 6.1 mm, T_{02} = 4.1 mm
Rounding radius	R = 28–29 mm

4. Manufacturing of test specimens

The sandwich panels for the T-joints are manufactured by a resin infusion technique. All the glass fiber fabrics and the balsa core are laid up on a flat table, vacuum bagged, evacuated and vacuum resin infused in one shot. The base panel is infused in a size of 1,000 × 1,750 mm, and the T-panel in a size of 420 ×1,750 mm. The vacuum infusion is done at room temperature under a vacuum pressure of about 100 mbar. At the end of the infusion the pressure is raised to about 900 mbar, and the panel is allowed to cure at room temperature before it is demoulded and post cured at 60°C for 24 h. The edges of the infused and cured panels are trimmed to the desired geometry. Small grooves are used as spacers to ensure correct gaps for the filler. The T-joints are manufactured and completed in widths of approximately 1.75 m and subsequently sectioned into the 250 mm wide test specimens, Fig. 2.

Fig. 2. Manufacturing of T-joint

5. Test specification

5.1. Test set-up and test rig

In the static tensile test of the T-joint, the sample is mounted to the load cell at the top of the T-panel, and the load is applied at both ends of the base panel, with a

distance of 640 mm. The test rig with a sample mounted in the testing machine is shown in Fig. 3.

The test sample is loaded through pairs of square steel tubes $400 \times 80 \times 25$ mm, which are connected by two 20 mm diameter threaded steel rods. The steel rods are mounted in spherical bearings to allow for free rotation of the test sample at the ends.

The top of the T-panel is connected to the testing machine through two 10-mm thick steel plates of 400×140 mm (H $\times$ W). The steel plates are bolted to the test sample by five M20 bolts positioned at the end of the T-panel, symmetrically around the mid-plane and with a distance of 76 mm between each bolt. The top-end of the steel plates is connected to the load c ell though a spherical bearing, Fig. 3.
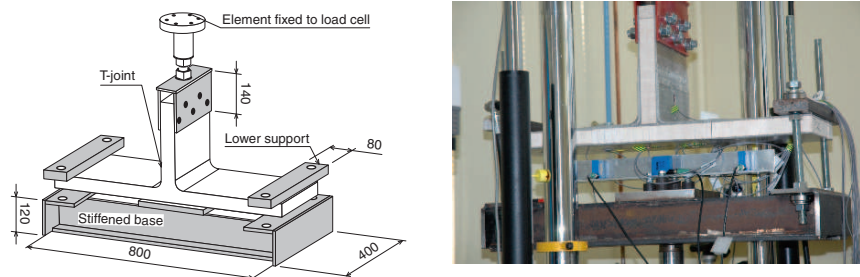
Fig. 3. Sketch of the principal test set-up for quasi-static testing

5.2. Instrumentation and test procedure

Strain gauge data was performed with a SPIDER device. The gauges were mounted on specimens at the middle of the width of the sample and at the nine locations as shown in Fig. 3. Gauge n° 2 to 8 are 2 mm long with a resistance of 120 Ω (KYOWA KFG-2-120-C1-11).

Gauges 1 and 9 are a 0°/90° couple (KYOWA KFG-2-120-D16-11), where each single gauge is 2 mm long with a resistance of 120 Ω. Gauge 2, 3, 4, 5, 8 and the 0° gauge of couple 1 and 9 are oriented parallel to *x*-axis (G1X, G2X, G3X, G4X, G5X, G8X and G9X), gauge 6 and 7 parallel to the *y*-axis (G6Y and G7Y) and the 90° gauge of couple 1 and 9 parallel to the *z*-axis (G1Z, G9Z). Load, displacement and strain gauges are computer sampled at a rate of one per second, Fig. 4a. The load is recorded by a certified 250 kN load cell. The displacement is both recorded as the movement of piston (cross-head) on the tensile machine, and by three calibrated LVDT (Linear Variable Differential Transformer, DINEL P 925 L1 AN S) devices, which detect the displacement of the bottom plate of the base panel. One LVDT, with a working range of 40–60 mm, is positioned at the centre, and the other two are positioned symmetrically 188 and 198mm away from

the centre, respectively. The tests are also recorded on video and still-photos with the cameras in a fixed position during the test, showing a side view of the T-joint. The tensile test is performed on a 250 kN servo hydraulic testing machine (Instron 1342), at a constant cross-head speed of 1 mm/min. Load, displacement, strain gauges and LVDT gauges are computer sampled at a rate of one data set per second, Fig. 4b.
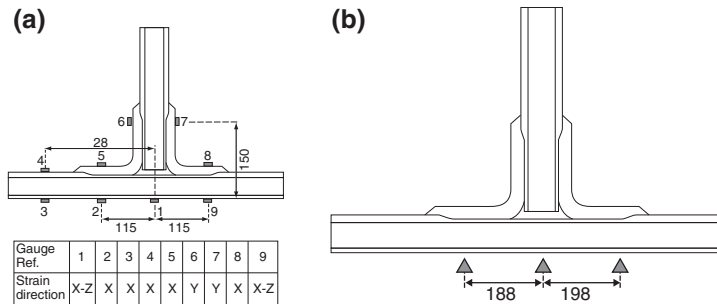
Fig. 4. Position numbering of strain gauges and the three LVDT devices

6. Results

6.1. Load, displacement and strain

Plots of load versus cross-head displacement and load versus LVDT displacement are shown for one of the three specimens in Fig. 5. The initial value of the load is around 0.2 kN due to pre-stressing and the weight of the four square steel tubes and the four threaded steel rods. The measured cross-head position and measured position from each of the three LVDT devices are used to determine the cross-head displacement and the LVDT displacements. The LVDT's away from the centre show a symmetric deformation, indicating a symmetric load of the sample. The load–displacement curve at the centre (for $x = 0$) is almost linear up to a load
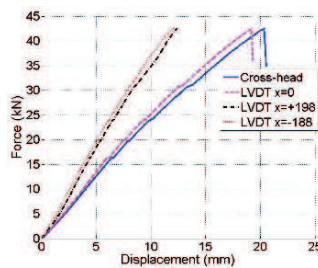
Fig. 5. Load versus displacement of specimen

of 25 kN (displacement 10mm). Thereafter, the curve becomes slightly non-linear until a load of 32 kN (displacement 13 mm). From there on, the test sample undergoes heavy deformation for only a slight increase in load until final failure at a load and displacement of 42 kN and 20 mm, respectively.

In Fig. 6 the strain values were arbitrarily set to zero at the start of the test. Negative strains were multiplied by "–1" and a minus sign was added in front of the strain gauge name (–G1X, –G2X, –G3X and –G9X). A plus sign was added in front of the positive strain (+G4X, +G5X, +G6Y, +G7Y, +G8X and +G9Z).
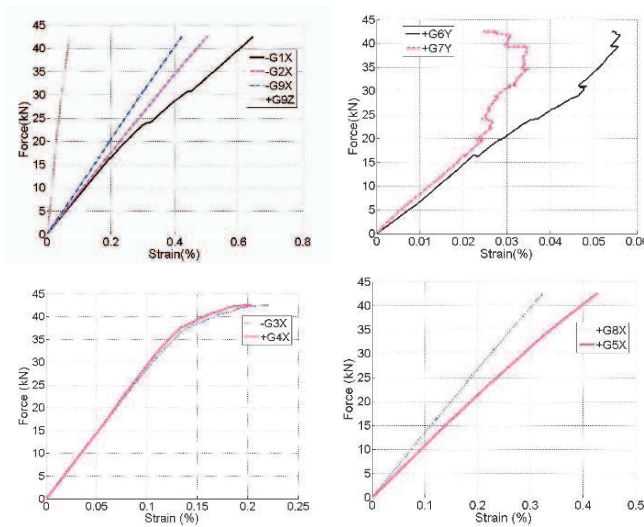
Fig. 6. Load versus strain

6.2. Failure load and damage kinetic

The ultimate tensile failure load, corrected for weight of fixtures, for the three specimens is 42.8, 42.0, and 41.8 kN, respectively. With a specimen width of approximately 250 mm it corresponds to a failure load per width (in the z-direction - see Fig. 4) of 171.2, 168, and 167.2 kN/m, respectively. This is an increase in failure

Table 3. Failure load of static tensile tested T-joints

Sample #	Elastic strength (kN/mm)	Failure load (kN)	Failure load per unit length (kN/m)
New	DCNS_1	2.8	42.8	171.2
	DCNS_2	2.6	42.0	168.0
	DCNS_3	2.7	41.8	167.2
	Average	2.6	42.2	168.8
EUCLID	–	2.5	36.0	141.4

load of about 20% compared to the reference Base Design T-joint, which has a failure load per width of 141kN/m, Table 3. Audible cracking started early during the tests, and continued to failure.
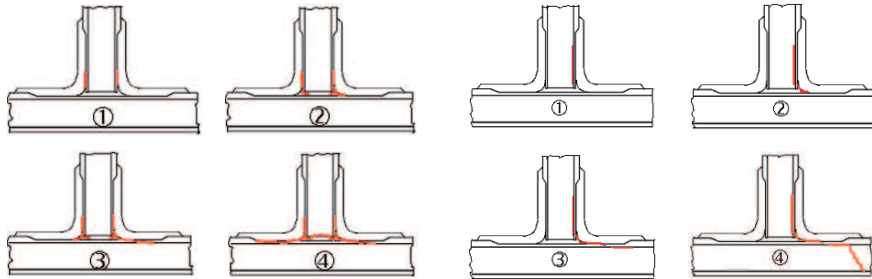
Fig. 7. T-joint, specimen DCNS_1 and DCNS_2   **Fig. 8.** T-joint, specimen DCNS_3

The relation between cross-head displacement and load (Fig. 5) is seen to be linear. The actual fracture appearance was quite different for the three specimens. Specimen DCNS_1 and DCNS_2 showed both a shear failure at the base panel, a de-bonding between the over-laminates and the skin laminate of the base panel, and fracture in the filler material.

Whereas specimen DCNS_3 showed a shear failure in the base panel, the interface failure between the skin and the core of T-panel, and a minor de-bonding between the over-laminate and the skin laminate at middle of the over-laminate on one side only. Figs. 7 and 8 show a damage history of the T-joint specimens.

7. Conclusions

In this paper we present a new T-joint, witch is over-laminated as a Base Design T-joint, but with a little geometrical modification of the skins and the over-laminates. This simple technique provides a higher strength in tension, 169 kN/m. This is an increase in failure load of about 20% compared to the reference Base Design T-joint, which has a failure load per width of 141 kN/m.

In a super structure a T-joint may be loaded in tension if an internal blast occurs in two adjacent compartments, or by an underwater explosion, where the whole ship is moving upward (out of the water), and acceleration forces act on heavy equipment placed in two adjacent rooms with no support underneath the separating wall. In this study one can introduce these conclusions:

- Three sandwich T-joints have been tested in static tensile in a special designed fixture
- The average tensile failure load per unit length is 169 kN/m

- Two type of damage kinetic for the three specimens
- A majority of the load/strain signals in the joint region are linear until failure

References

[1] http://research.dnv.com/euclid_rtp3.21.

[2] B. Haymana, A.T. Echtermeyer, D. McGeorge. Use of composites in naval ships. Warship 2001 – future surface warships. 20–21. London: Royal Inst. of Naval Architects, 2001.

[3] A. Groves, A. Lystrup, D. McGeorge, and H.V. Aanhold. Dynamic and static performance of composite T-joints. Presented at Symposium on Combat Survivability of Air, Space, Sea and Land Vehicles, NATO/RTO, Aalborg, Denmark, 2002.

[4] B.D. Agarwal, L.J. Broutman. Analysis and performance of fiber composites. New York: Wiley-Interscience, 1990.

[5] G.H. Sih, A.M. Skudra. Failure mechanics of composites. New York: Elsevier Science, 1985.

[6] J.E. Van Aanhold, A. Groves, A. Lystrup, D. McGeorge. Dynamic and static performance of composite T-joint. Symposium on combat survivability of air, space, sea and land vehicles. Denmark: NATO/RTO Aalborg, 2002.

[7] S.E. Hellbratt. Use of lightweight sandwich joints in a 72m high speed vessel entirely built of carbon fibres. In: Bäcklund J et al., editors. Composites and sandwich structures. Second north European conference (NESCO II), Stockholm, 22–23 October 1997. EMAS Publishing, pp. 151–155, 1997.

[8] R.A. Shenoi, F.L.M. Violette. A study of structural composite Tee joints in small boats. Journal of Composite Mater, vol. 24, pp. 644–666, 1990.

[9] H.J. Phillips, R.A. Shenoi. Damage tolerance of laminated tee joints in FRP structures. Composites Part A: Applied Science and Manufacturing, vol. 29, pp. 465–478, 1998.

[10] R.A. Shenoi, G.L. Hawkins. Influence of material and geometry variations on the behaviour of bonded tee connections in FRP ships. Composites, vol. 23, pp. 335–345, 1992.

[11] A.R. Dodkins, R.A. Shenoi, G.L. Hawkins. Design of joints and attachments in FRP ships' structures. Marine Structures, vol. 7, pp. 365–398, 1994.

[12] A.R. Rispler, G.P. Steven, L. Tong. Failure analysis of composite T-joints including inserts. Journal of Reinforced Plastics and Composites, vol. 16, pp. 1642–1658, 1997.

[13] S. Kumari, P.K. Sinha. Finite element analysis of composite wing T-joints. Journal of Reinforced Plastics and Composites, vol. 21, pp. 1561–1585, 2002.

[14] F. Dharmawan, R.S. Thomson, H. Li, I. Herszberg, E. Gellert. Geometry and damage effects in a composite marine T-joint. Composite Structures, vol. 66, pp. 181–187, 2004.

[15] H.C.H. Li, F. Dharmawan, I. Herszberg, S. John. Fracture behaviour of composite maritime T-joints. Composite Structures, vol. 75, pp. 339–350, 2006.

[16] G.L. Hawkins, R.A. Shenoi. A parametric study to determine the influence of geometric variations on the performance of a bulkhead to shell plating joint. In: Proceedings of the 9th International Conference on Composite Materials, ICCM/9, 12–16 July 1993, Madrid: Woodhead Publishing Ltd., vol. 4, pp. 97–104.

[17] P.J.C.L. Read, R.A. Shenoi. Fatigue behaviour of single skin FRP tee joints. International Journal of Fatigue, vol. 21, pp. 281–296, 1999.

[18] E.E. Theotokoglou. Study of the numerical fracture mechanics analysis of composite T-joints. Journal of Reinforced Plastics and Composites, vol. 18, pp. 215–223, 1999.

[19] E.E. Theotokoglou, T. Moan. Experimental and numerical study of composite T-joints. Journal of Composite Materials, vol. 30, pp. 190–209, 1996.

[20] E.E. Theotokoglou. Strength of composite T-joints under pull-out loads. Journal of Reinforced Plastics and Composites, vol. 16, pp. 503–518, 1997.
[21] U.V.R.S. Turaga, C.T. Sun. Failure modes and load transfer in sandwich Tjoints. Journal of Sandwich Structures and Materials, vol. 2, pp. 225–245, 2000.
[22] H. Toftegaard, A. Lystrup. Design and test of lightweight sandwich T-joint for naval ships. Composites Part A: Applied Sci. and Manufacturing, vol. 36, pp. 1055–1065, 2005.

Vibroacoustic Sources Identification of Gear Mechanism Transmission

Abbassia Derouiche[1], Nacer Hamzaoui[2] and Taoufik Boukharouba[1]

[1]Laboratoire de Mécanique Avancée (LMA), Faculté de Génie Mécanique et Génie des Procédés, BP 32 El Alia 16111 Bab Ezzouar, Alger, Algérie

[2]Laboratoire Vibrations Acoustique, Institut National des Sciences Appliquées de Lyon Domaine Scientifique de la Doua, Bt Antoine de Saint Exupéry, 25 bis, avenue Jean Capelle 69621 Villeurbanne Cedex, France

Abstract The prediction and the identification of the vibroacoustic sources of the toothed gearings remain rather complex in spite of various carried out work. Often, they are experimental statements on a significant number of transmissions which finish by councils given to the designers in order to limit or to reduce the radiated noise. Our work consists in contributing to treat on a hierarchical basis the vibroacoustic sources on a transmission system defined well, and this, while being based on the method of principal components analysis (PCA). PCA method is based on the statistical analysis, thus partial virtual coherence and multiple virtual coherence are used to quantify the coherent shares with the acquired signals autospectres.

Keywords: Gears, Vibration, Noise, Signal Processing, PCA, Coherence.

1. Introduction

The vibratory and acoustic behaviour of gear transmission result from several sources and numerous works have been done [1, 2]. It is allowed generally that the radiated noise is due mainly to the vibrations of the casing, itself excited by internal and external sources which are transmitted to it. We seek to implement a methodology who would allow us to make a hierarchisation of the vibroacoustic sources. Tests were carried out on a transmission system by gears transmission mechanism at the acoustics and vibration laboratory of the INSA of Lyon. We used sensors which are accelerometers and microphones in order to raise measurements of acceleration and acoustic pressure for various operation configurations. We calculate the interspectral matrix for the 32 ways simultaneously acquired that we will be able to define for any engine speed and various positions of the accelerometers as well as a sweeping of the antenna comprising the microphones around the vibrating mechanism. The principal components analysis method is one of the techniques which can contribute to the hierarchisation of the vibroacoustic sources of our gears transmission mechanism, by estimating the partial virtual

coherences and multiples shares between the virtual sources and the acquired signals [3].

2. Principal Components Analysis (PCA)

The spectral analysis in principal components has the autospectres and the interspectres as data. The principle consists in numerically separating the various signals considered in "virtual" incoherent sources. The decomposition in principal components formulation results from the autospectres and interspectres matrice expression of all the signals acquired simultaneously [5, 6].

2.1. Interspectral matrix formulation

The interspectral matrix of all the signals acquired simultaneously is built as follows:

$$[S_{XX}] = \begin{bmatrix} S_{11} & S_{12} & ... & S_{1m} \\ S_{21} & S_{22} & ... & S_{2m} \\ ... & ... & ... & ... \\ S_{m1} & S_{m2} & & S_{mm} \end{bmatrix} \tag{1}$$

With S_{ii} autospectre of i way and S_{ij} interspectre of i and j ways.

2.2. Interspectral matrix decomposition

The matrix square shape $[S_{XX}]$ enables us to write the following relation based on its decomposition in eigenvalues and eigen vectors:

$$[S_{XX}]_{mm} = [\Phi]_{mp}[\Sigma]_{pp}[\Phi]^*_{mp} \quad (p \le m) \tag{2}$$

With $[\Sigma]_{pp}$ diagonal matrix of the p nonzero eigenvalues and p corresponding eigen vectors matrix $[\Phi]_{mp}$ arranged in columns.

While posing $[\sigma^2]_{pp} = [\Sigma]_{pp}$, we can rewrite:

$$[S_{XX}]_{mm} = [\chi]_{mp}[\chi]^*_{mp} \text{ with } [\chi]_{mp} = [\Phi]_{mp}[\sigma]_{pp} \tag{3}$$

The interspectral matrix $[S_{XX}]$ can be expressed by the superposition of the interspectral matrices:

$$[S_{XX}] = [S_{XX}^{sv1}] + ... + [S_{XX}^{svi}] + ... + [S_{XX}^{svp}],$$
$$\text{with } [S_{XX}^{svi}] = \{\chi^{svi}\}\{\chi^{svi}\}^* \quad , \{\chi^{svi}\} i^e \text{ column of } [\chi]_{mp} \tag{4}$$

Such a summation of interspectral matrices is characteristic of the superposition of uncorrelated vibratory phenomena. Each virtual source contribution in fact is characterized by the answer vector $\{\chi^{svi}\}$, being able to be interpreted like the structure deformation induced by the single virtual source n°i.

2.3. Virtual coherence and multiple virtual coherences

Coherence is a tool which quantifies the share of the coherent signal autospectre with another signal. Virtual coherence will quantify the share of the signal coherent autospectre with a virtual source. The autospectre decomposition in <contributions> of the virtual sources is simple and robust, being given the virtual sources incoherence. Partial virtual coherence of a signal $X_j(t)$ compared to the virtual source i is:

$$\gamma_{j,svi}^2 = \frac{S_{jj}^{svi}}{S_{jj}} \tag{5}$$

Virtual coherence is a tool possibly making it possible to locate the physical sources related to the principal components, by admitting that the strongly coherent signals with a particular virtual source are physically close to the real source. But it is an expertise tool to be used with precautions. The principal interest of virtual coherence is that it easily makes it possible to determine the number of uncorrelated phenomena observed on a particular signal. For that, we introduce the multiple virtual coherence of a signal $X_j(t)$:

$$\gamma_{j:sv1,sv2,...,svi}^2 = \frac{S_{jj}^{sv1} + S_{jj}^{sv2} + ... + S_{jj}^{svi}}{S_{jj}} \tag{6}$$

When the virtual sources number i make it possible to obtain a multiple virtual coherence near to 1, which means that the maximum number of uncorrelated phenomena observed on signal $X_j(t)$ is i. The PCA is a tool for pre-processing of multi-source results of measurement in environment.

The spectral analysis technique in principal components (PCA) was used since the article of Price and Bernhard [4].

3. Experimental set up

The experiments were made in acoustics and vibration laboratory (LVA) of the INSA of Lyon. The measurements were made in a semi-anechoic room, the ground being out of concrete and the covered glass wool walls (Fig. 1). At the beginning of each accelerations and acoustic pressures acquisition, the background noise of the room is measured.
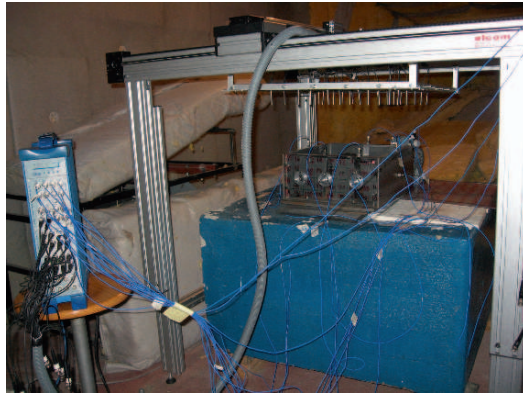
Fig. 1. Test rig in semi-anechoic room (LVA INSA Lyon)

3.1. Description of the gear transmission mechanism

The mechanism to study consists of a cylindrical gear including a couple 45/65 teeth. The principal characteristics of this gear are given in Table 1. The wheels of steel are full and assembled on diameter shaft equal to 0.020 m. The entry shaft is connected to the engine by a flexible coupling.

Table 1. Test gear main parameters (LVA, INSA Lyon)

	Pinion	Driven wheel
Number of teeth	45	65
Normal module (m)	0.002	0.002
Face width (m)	0.020	0.020
Base radius (m)	45	65
Normal pression angle (deg)	20	20
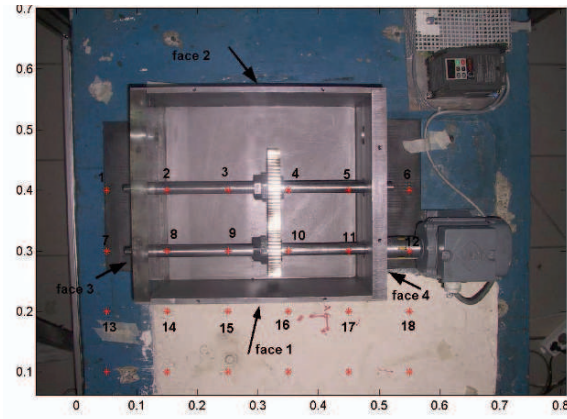
Fig. 2. Gear mechanism transmission

The shafts are guided in rotation by bearings. The simple casing form is a parallelepiped of dimensions ($0.40 \times 0.35 \times 0.16$ m) and the thickness is 0.025 m except for face 5 of the top casing, it is of 0.005 m. The casing consists of two materials, steel and Perspex. They have as a density of 7,800 kg/m^3 and 1,300 kg/m^3, a Young modulus $E = 2.10^{11}$ N/m^2 and $3.3. \ 10^9$ N/m^2 and for Poisson's ratio 0.3 and 0.37, respectively. Faces 3 and 5 (cover) are of Perspex, all others are of steel. The mechanism was coupled with an engine at variable speed.

3.2. Data acquisition

The measurement accelerometers number is 14 distributed as follows with their respective direction:

- Three accelerometers on the engine (19(y), 20(x), 26(z))
- Two accelerometers on face 1 (25(y), 29(z))
- Two accelerometers on face 2 (21(y), 30(z))
- Three accelerometers on face 3 (22(z), 23(z), 32(x))
- Four accelerometers on face 4 (24(x), 27(z), 28(z), 31(z))

An antenna microphones placed at the top of the mechanism can move on a parallel level (Z constant). It makes it possible to measure in a number of desired points the acoustic pressures; the antenna comprises 30 microphones. Several configurations were considered for measurements.

We will treat two cases for our mechanism sources radiation; the first corresponds to the case where the mechanism is open (without cover) and the second to the case of the closed mechanism (with cover). The position of the 18 microphones carried by the antenna and the face number of the carter are shown on the gear mechanism transmission (Fig. 2). Measurements were recorded on OROS 32 ways.

The recorder is connected to a portable computer, and we used the software NVGate for the recordings, the time being 10 s for each acquisition. Once the various ways gauged with the autorange, we carry out measurements.

The data recorded by OROS are downloaded on NVGate from frontal OROS towards the PC, and then exported in mat format of MATLAB in order to be to exploit.

For any operation configuration, the 32 ways are recorded over a time of 10 s, sampled at the frequency of 32,768 Hz. We chose a frequential resolution of 1 Hz. To find the virtual sources, it is necessary to make a spectral decomposition in principal components of the interspectral matrix on the 32 ways. We visualize the energy contributions of the 32 virtual sources representing these ways.

The virtual sources can be classified by order of preponderance, i.e. in the order descending of the associated eigenvalues.

We realize that the first virtual source is rather dominating and that the first two virtual sources are enough alone to represent the vibroacoustic mechanism. Their sum in energy contribution exceeds the 85%.

The curves (Figs. 3 and 4) represent the contribution of the 32 virtual sources obtained by respectively considering the mechanism closed and open and operating at the speed of the engine equal to 2,500 rpm. We notice a similarity between them to the surroundings of 10,000 Hz, beyond there is a change in the percentage of the first virtual source and it is more significant for the closed mechanism. On the other hand, for the second and the third virtual sources, they are more significant in high frequencies for the open mechanism.
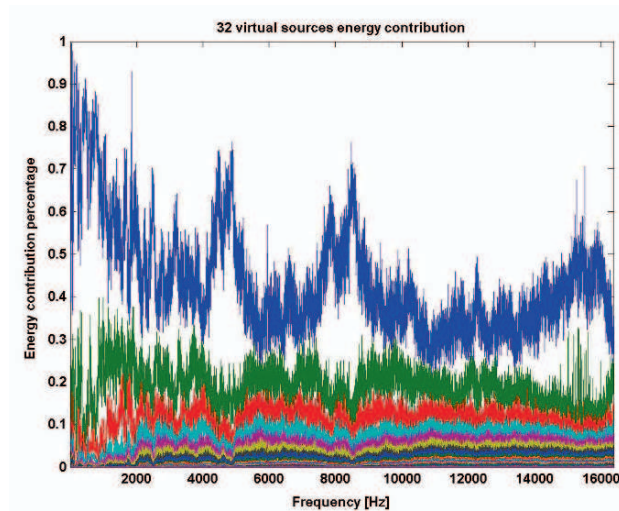
Fig. 3. Energy contribution of the 32 virtual sources (closed mechanism)
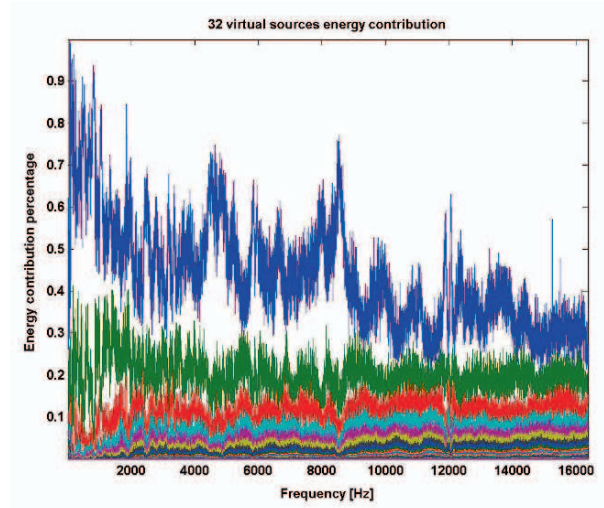
Fig. 4. Energy contribution of the 32 virtual sources (open mechanism)

The averages of multiple virtual coherences are traced on the curves (Figs. 5 and 6), by taking as reference one, two, three and four dominating sources. The average virtual coherences carried out (Figs. 5 and 6) on the first virtual source expressed as a percentage shows an energy contribution of about 53% on all the ways put besides those of the engine i.e. numbers 19, 20 and 26. For the second virtual source, the virtual coherence average is about 20%. The third and fourth virtual sources are more marked on the engine ways; their sum reaches the 30% of energy contribution.

The average of virtual coherences on the virtual source 1 (SV1) for the closed mechanism (Fig. 5), shows the effect in staircase on the 18 ways measuring the acoustic pressures, this is explained by the position of the microphones (Fig. 2). The virtual coherences contribute for 55% to ways 1, 7 and 13, decrease slightly on ways 2, 8 and 14 and so on for ways 3, 9 and 15 etc. For the other ways (21, 22, 23, 24, 25, 27, 28, 29, 30, 31 and 32), their virtual coherences resemble each other and are about 52%. The SV1 can be assigned to the way of the bearing located on face 3 (with Perspex). Concerning the SV2, its average shows a contribution of about 20% and it seems homogeneous for the ways. For the SV3 and SV4, their contributions in virtual coherence are more significant on the levels in the engine ways (19, 20 and 26).

When the mechanism is open (Fig. 6), the virtual coherence of the SV1 is of the same order of magnitude 50% on the 18 ways of the antenna, on the other hand it decreases to reach the 40% on the ways of the casing, and it is about 20% on the level of the engine ways. Concerning the SV2, its virtual coherence is about 20% on the microphones, 26% on the casing ways and 13% on the engine ways. The average of virtual coherences for SV3 and SV4 are almost parallel with a percentage

variation from 10% to 13% for the SV3 and below 8% for the SV4. Their level in the engine ways is about 15% for the SV3 and 16% for the SV4. This curve (Fig. 7) shows the average of multiple virtual coherences with one, two and three virtual sources most dominating in the frequency band 0–2,000 Hz. With three virtual sources the average of coherence tends towards 1 in interval 0 to 1,300 Hz and decreases slightly afterwards.
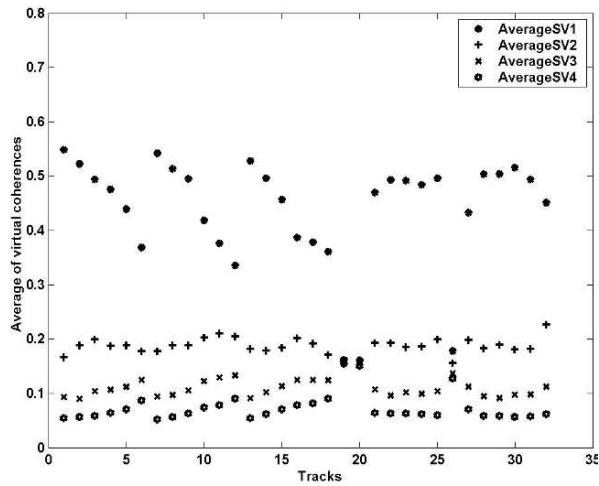
Fig. 5. Average of virtual coherences for the 32 tracks (closed mechanism)
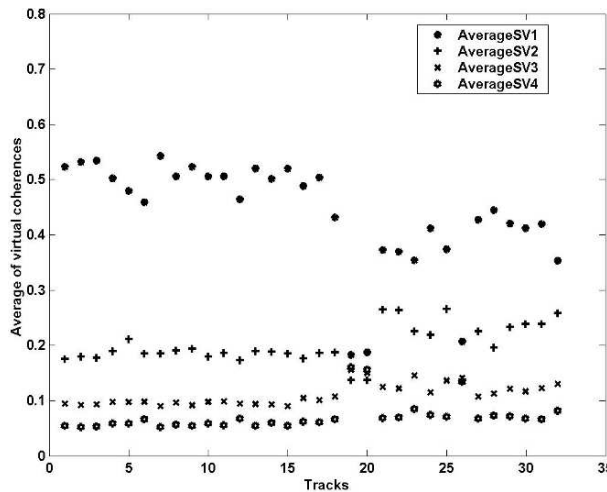
Fig. 6. Average of virtual coherences for the 32 tracks (open mechanism)
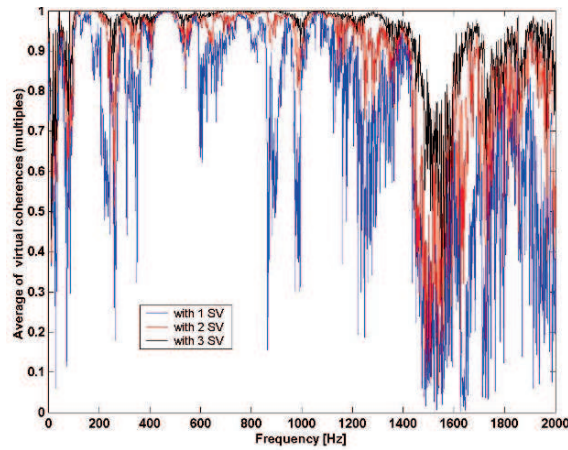
Fig. 7. Average of virtual coherences (multiples) with 1(2, 3) dominating virtual source(s)

4. Conclusions

The PCA method was applied in order to treat on a hierarchical basis the vibro-acoustic sources of a transmission system by gears. The decomposition of the interspectral matrix enables us to estimate the contribution expressed as percentage energy of each virtual source.

The multiple virtual coherences which represent the share of an autospectre of answer caused by all the virtual sources, was also used. This method effectively quantifies the number of uncorrelated vibratory phenomena of the vibrating mechanism. The total uncorrelation of the phenomena makes it possible to provide robust virtual indicators (virtual coherence, virtual transfer function). The relation between real physical sources and virtual sources is not obvious, because a principal component can characterize several different sources physical according to the frequency observed.

The PCA method was used as a tool for pre-processing of multi-source results of measurement in environment. We tried to bind these virtual sources to the reference signals where the sensors are situated and to look for a way given to the strongest virtual source.

References

[1] H. Opitz. Noise of gears. Phil. Trans. of Royal Society, vol. 263, pp. 369–380, 1969.
[2] D. Welbourn. Fundamental knowledge of gear noise-a survey. Conference on Noise and Vibrations of Engines and Transmissions, Cranfield Institute of Technology. C177/79, 9–29, 1979.

[3] J.S. Bendat et A.G. Piersol Engineering applications of correlation and spectral analysis. New York: Wiley-Interscience, 1980, 302 p.

[4] S.M. Price. et R.J. Bernhard, Virtual coherence: A digital signal processing technique for incoherent source identification. In: Proceedings of IMAC 4, Schenectady, NY, USA, 1986.

[5] Q. Leclère, Support technique de la toolbox matlab d'analyse spectrale ACP, 2003, p. 1–10.

[6] Q. Leclère, Etude et Développement de la mesure indirecte d'efforts, Application à l'identification des sources internes d'un moteur Diesel, thèse: Insa, Lyon, 2003.

Prediction of Structural and Dynamic Behaviors of Impacted Plates

Abdelhamid Miloudi and Mahmoud Neder

Advanced Mechanical Laboratory, University of Science and Technology Houari Boumediene USTHB, BP 32, Al Alia 16112, Algiers, Algeria

Abstract   A numerical model for the flexural vibrations of rectangular isotropic and orthotropic plates is developed, in order to investigate transient response of impacted plate. The established model, referred to a modified Hertzian contact law, has been validated and used to study the influence of different impact parameters. The obtained results are in good agreement with those given with the finite element simulations. The validated model has been used to study the distribution of the stress field and its evolution under the effect of the different impact parameters.

1. Introduction

There are many practical situations where plate structures are subjected to transient impact loading of high intensity. Despite their importance, however, impact effects are usually ignored or oversimplified in the dynamic analysis of plate structures.

One reason is the complexity involved as contact-impact problems. Understanding of the impact phenomenon and damage mechanisms is essential for developing improved materials and design methods accounting for impact. Many experimental works carried out on materials subjected to dynamic loads allowed a satisfactory characterisation of these materials and the identification of the damages induced. However, such works remain expensive and require very sophisticated equipment. This is why, any analytical or numerical study which permit a suitably approach of the behaviour of structures subjected dynamic loads would be a great help to the scientific and industrial community.

Mathematical models used for the prediction of the contact force and the structural response must adequately represent the global motion of the structure, the dynamics of the impactor, and the local deformation in the contact region. In order to predict the structures vibration, analytical models are used for simple cases, usually using the modal analysis approach. In this case, using the modal analysis method, a large number of modes need to be included to determine the response, and the wave propagation approach may be more practical. For more complex situations, the finite element method is also used.

2. Elastic modelling of impact

Several modelling of the impact have been adopted, we can note those consist in representing the impact by an energy balance. The main advantage of this present-ation type, reside in the fact that parameters of entry are directly the characteristic parameters of the impact: incidental speed, geometric and mechanical properties of the plate and the impactor. In his works, Greszuk [1] has modelled the impact while adding the contact energy to the one of bending. Shivakumar et al. [2] improved the previous model while coupling to bending a rigidity of K_s shearing and while introducing a rigidity of membrane K_m in the case of the thin plates. The balance of energy is constituted of the contact energy and the one of bending. While using this model, Benmedakhène [3], made predictions of displacements values of and the maximal loads according to energies of impact. In this survey it showed that values of the model remain near of the experience in the low energies where the weak damages don't change the global behaviour of the plate.

2.1. Mass-springs model

The model based on the balance of energy presented permits to calculate the ultimate values of displacements and strengths previously, but it doesn't permit to predict the history of the loading, the speed or the displacement. On the other hand, the use of the model mass-spring will permit to retrace all the history of the different parameters of the impact. Different types of models mass-springs have been developed for modelling the impact at low speed. The main characteristic of this model type consists in the fact that they don't take in account any localization of the distortion. So the projectile incidental energy is absorbed on all the volume of the plate. Among the most important models presented in the literature, the one of Caprino et al. [4] are mentioned. These authors present the impact by only one degree of freedom. The rigidity of the spring corresponds to the static rigidity of the plate.

A good agreement, between calculated and measured strength, is noted until 2.5 m/s speed. In this model bending effects, the plate inertia is not taken in consideration, from where limits of use for the more important speeds. Sjoblom et al. [5] suggested a model of two dof that permits to integrate the non linearity at the contact level. With this model it's possible to uncouple contact and the plate rigidity. Nevertheless, the shearing effect is localized around the impact point, important for the thick plates or is not taken in account for the very elevated speeds. It is why Lal [6] developed a model to three springs K_{cs}, K_{bs} and K_s representing rigidities of stamping, bending and shearing respectively. This model is valid for small displacements, diverges for the big ones. Shivakumar et al. [2] took them in consideration membranes effects while using mass-spring models of one and two degrees of freedom (Fig. 1) with four springs of rigidity K_m, K_{bs}, K_s and K_{cs}. The indications m, s, b and c represent the membrane, shearing, bending and the plate contact respectively with impactor.
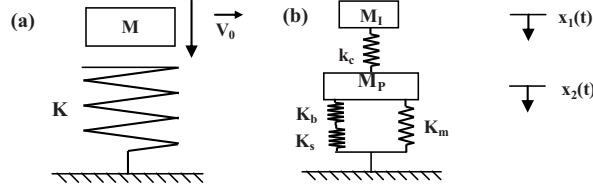
Fig. 1. Mass-springs models: (**a**) one degree of freedom, Caprino et al. [4], (**b**) two degrees of freedom model, Shivakumar et al. [2]

In this model the two masses M_I and M_P are connected by a spring Hertzian representing the law of load-deformation of contact. Properties of transverse strength-deformation are represented by the combination of bending, shearing and membrane springs. Displacements $x_1(t)$ and $x_2(t)$ represent the displacement response of the two masses at every instant t.

The corresponding speeds are represented by $\dot{x}_1(t)$ and $\dot{x}_2(t)$. The transverse displacement of the plate is represented by $x_2(t)$, and the contact deformation is represented by: $\alpha = x_1(t) - x_2(t)$. The balance of the projectile and the plate can be written:

$$M_I \ddot{x}_1(t) + \lambda\, n\left[x_1(t) - x_2(t)\right]^{3/2} = 0$$
$$M_P \ddot{x}_2(t) + k_{bs}\, x_2(t) + k_m\left[x_2(t)\right]^3 - \lambda\, n\left[x_1(t) - x_2(t)\right]^{3/2} = 0 \tag{1}$$

where:

$$\lambda = 1 \qquad pour\ x_1 > x_2$$
$$\lambda = -1 \qquad pour\ x_1 < x_2 \tag{2}$$

The initial conditions are:

$$x_1(0) = 0\ ,\ \dot{x}_1(0) = V_I\ ,\ x_2(0) = 0\ ,\ \dot{x}_2(0) = 0 \tag{3}$$

These two coupled equations are non linear differential equations which can be solved by a numeric integration method [7] until $x_2(t) \le 0$.

2.2. The numerical model

The numerical model that we propose is simple, efficient and gives very satisfactory results. This model takes into account the higher modes in the impact force and the dynamic plate response calculations. It refers also to the Hertz contact law and the plate classical theory.

At the beginning of the contact, the spherical impactor is animate by an incidental speed Vi, knock a thin plate and apply on this one, the force P which represents the impact force (Fig. 2). By the action and reaction principle, the plate applies on the sphere an equal force to P but in opposite sense. The dynamic balance of the spherical striker and the plate is given respectively by

$$\begin{cases} M_I \ddot{z}_I + P = 0 \\ z_I(0) = \ddot{z}_I(0) = 0 \qquad et \qquad \dot{z}_I(0) = V_I \end{cases} \tag{4}$$

And:

$$\begin{cases} \rho h \ddot{w} + D\nabla^4 w = P\delta(x - x_o)\delta(y - y_o) \\ w(x, y, 0) = \dot{w}(x, y, 0) = 0 \end{cases} \tag{5}$$

The expression for the contact force P developed during elastic impact of a spherical impactor or radius R with a rigid plane surface of a semi-infinite solid was given by Hunter [8] as a function of the relative advance between impactor and the impacted plane surface:

$$P = n\alpha^{3/2} \tag{6}$$

where α: is the relative advance between impactor and the impacted plane surface:

$$\alpha = z_I(t) - w(x_o, y_o, t) \tag{7}$$

And k_c is the contact stiffness, which depends on the geometrical and rheological characteristics, of the two bodies in contact, given by

$$k_c = \frac{4}{3}\sqrt{R}\left(\frac{(1 - \upsilon_1^2)}{E_1} + \frac{(1 - \upsilon_2^2)}{E_2}\right) \tag{8}$$

υ_1, υ_2 and E_1, E_2 are Poisson's ratios and elasticity modulus of the sphere and the impacted object, respectively. x_o and y_o are the impact point coordinates.

The contact force given in Eq. (3) is an extension of the well-known Hertz contact theory developed for the static contact of curved bodies.

Thereafter, we solve the motion equations simultaneously by an iterative numerical method using the modal decomposition for the transverse deflexion of the plate and a Newmark integration scheme for the contact force [9].
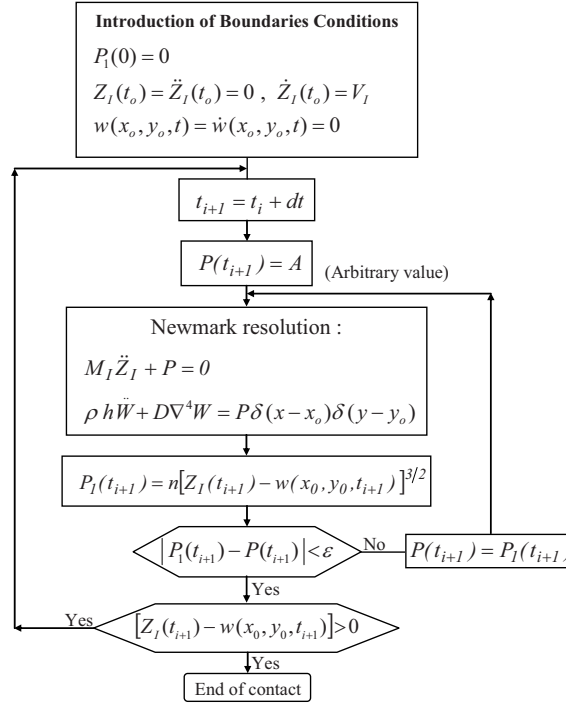
Fig. 2. Scheme of the impact force calculus

Once, the impact force temporal evolution obtained, we can calculate any vibratory characteristics at any plates point, by using the modes superposition. To validate the model of excitation by impact, we make simulations of impact between a spherical ended impactor and a plate [10]. In one of our articles [11], we noted that the influence of the modes number taken into account during the calculation of the vibratory response to the point of impact is rather significant, contrary to what was advanced by Shivakumar et al. [2]. This is due to the fact that in our case, the mass of the plate is not low with that of the impactor as it was the case of Shivakumar et al. [2] where the impactor mass is more than four times larger than that of the plate (Table 1).

Table 1. Mechanical characteristic of the plate and impactor

Plate parameters		Impactor parameters	
Dimensions (m^2)	0.2×0.2	Mass (kg)	0.0328
Thickness (m)	0.008	Radius (m)	0.01
Young's modulus (N/m^2)	$2.06 \ 10^{11}$	Young's modulus (N/m^2)	$2.1 \ 10^{11}$
Shear's modulus (N/m^2)	$0.7985 \ 10^{11}$	Impact velocity (m/s)	1
Poisson's coefficient	0.28		
Density (kg/m^3)	7833		

To this end, we compare our results with those obtained in the bibliography (Lu Chun [12]) where we took the first 49 modes contributions of a simply supported plate. We propose to compare the forces of interaction calculated by the numerical approach suggested and those obtained by Lu Chun [12], in the case of an impact applied to the centre of the plate. The results of simulations are represented in Fig. 3, with the contribution of 49 modes. The analysis of the results obtained by our approach shows that they are almost identical to those obtained by the references (Wu et al. [13] and Karas [14]) mentioned on the Fig. 3a. Let us note that the results obtained by Wu et al. [13] resulted from finite element method calculations.

(a) Reference (Lu Chun [12])   (b) Our approach
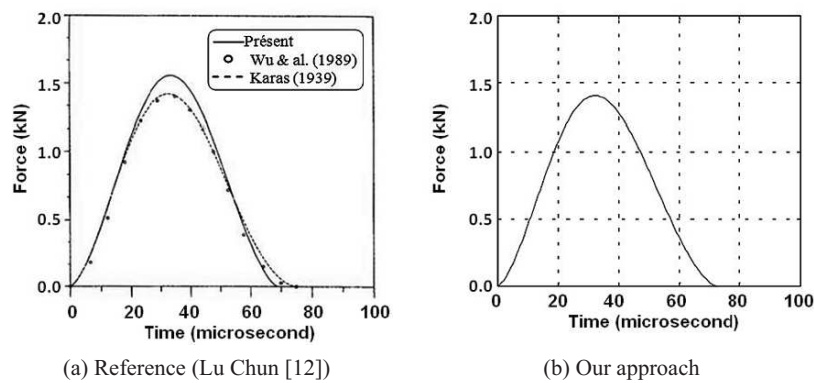
Fig. 3. Impact force comparison

3. Numerical example and discussion

In what follows, we study the effect of different parameters affecting the impacted plate's behaviour. The studied parameters will be: the impact point position, impact velocity and the impact energy. For this, two plates of the same surfaces and boundary conditions will be an application subject. To treat the most factors which influence the impact force, we made some simulations to show their effects on the magnitude and the impact duration.

3.1. Effect of the boundaries conditions on the impact force

We are now studying the influence of the plate's boundaries conditions on the impact force. To this end, we conduct numerical simulations on the same plate that previously with the impact characteristics as follows (Table 2):

Table 2. Characteristic of the impact

Impact parameters			
Impactor mass (kg)	1	Impactor Radius (m)	0.0125
Density (kg/m^3)	7800	Incident velocity	2
Young's modulus (N/m^2)	2.1 10^{11}		

As shown in Table 3, the obtained results prove that the plate's boundaries conditions have a significant influence on the impact force.

Table 3. Effect of the boundaries conditions on the magnitude and the impact duration

Boundaries conditions	Impact point (0.5a, 0.5a)		Impact point (0.12a, 0.38a)	
	Maximum magnitude (N)	Impact duration (ms)	Maximum magnitude (N)	Impact duration (ms)
SFSF	7096	8.20×10^{-2}	6901	8.05×10^{-2}
SSSF	6503	7.75×10^{-2}	6309	6.60×10^{-2}
SCSF	6404	7.70×10^{-2}	6185	7.50×10^{-2}
SSSS	6610	7.85×10^{-2}	6096	7.45×10^{-2}
SSSC	6482	7.75×10^{-2}	6003	7.35×10^{-2}
SCSC	6396	7.70×10^{-2}	5913	7.30×10^{-2}

3.2. Influence of some parameters on the stress temporal evolution

For this part, two plates of same surfaces and boundaries conditions will be studied. The geometrical and mechanical characteristics of the two plates are summarised in Table 4.

Table 4. Geometrical and mechanical characteristics of the plates

Characteristics	Isotropic plate	Orthotropic plate
Length (m)	a = 0.5	a = 0.5
Width (m)	b = 0.5	b = 0.5
Thickness (m)	h = 0.002	h = 0.00609
Mass density (kg/m^3)	ρ = 7800	ρ = 2094
Young modulus (N/m^2)	E = 2.1 10^{11}	E_x = 23.514 10^9; E_y = 23.514 10^9; E_z = 7.46 10^9
Shear modulus (GPa)	G = 8.4 10^{10}	G_{xy} = 8.4 10^{10}; G_{xz} = 8.4 10^{10}; G_{yz} = 8.4 10^{10}
Poisson's coefficient	υ = 0.3	υ_{xy} = 0.1; υ_{xz} = 0.29; υ_{yz} = 0.29

In order to validate the used method, it will be preceded to a comparison between the evolution of the stress deduced from the proposed analytic method and that determined by finite element software (Cosmos [15]).

This comparison is illustrated on Fig. 4. The results obtained show a perfect agreement between the two methods.
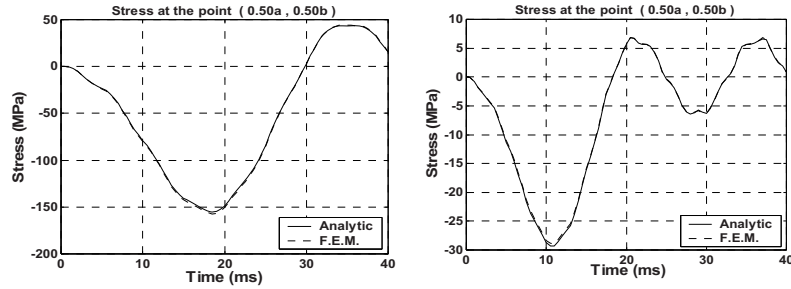
Fig. 4. Comparatives studies of σ_x at the impact position (**a**) isotropic plate and (**b**) orthotropic plate

3.2.1. Influence of the impact point position

The temporal evolution of the stress σ_x according to the impact point is illustrated on the Fig. 5. It is necessary to note the good similarity of the different impact positions behaviors. However the central position (0.5a, 0.5b) remains most unfavourable.
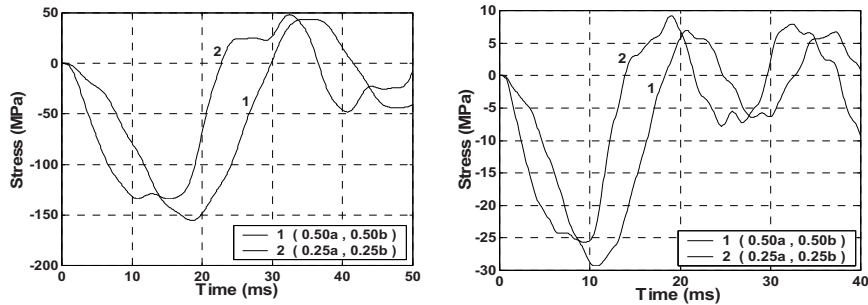
Fig. 5. Influence of the impact point position on the stress σ_y evolution at the impact point position, (**a**) isotropic plate and (**b**) Orthotropic plate

The distribution of the stress field on the plate surface solicited by impact, is illustrated by the equal-contours (Fig. 6). These last was traced for the instant t corresponding to the maximum stress affecting the plate. They have already been drawn for the three impact positions of already selected. It should be noticed that the equal-contours of circular shape around the impact point position tend to be deformed far from the impact point position.

a) Stress σ_x, plate impacted at (0.5a, 0.5b)

b) Stress σ_y, plate impacted at (0.5a, 0.5b)

c) Stress σ_x, plate impacted at (0.25a, 0.25b)

d) Stress σ_y, plate impacted at (0.25a, 0.25b)

e) Stress σ_x, plate impacted at (0.50a, 0.25b)

f) Stress σ_y, plate impacted at (0.50a, 0.25b)
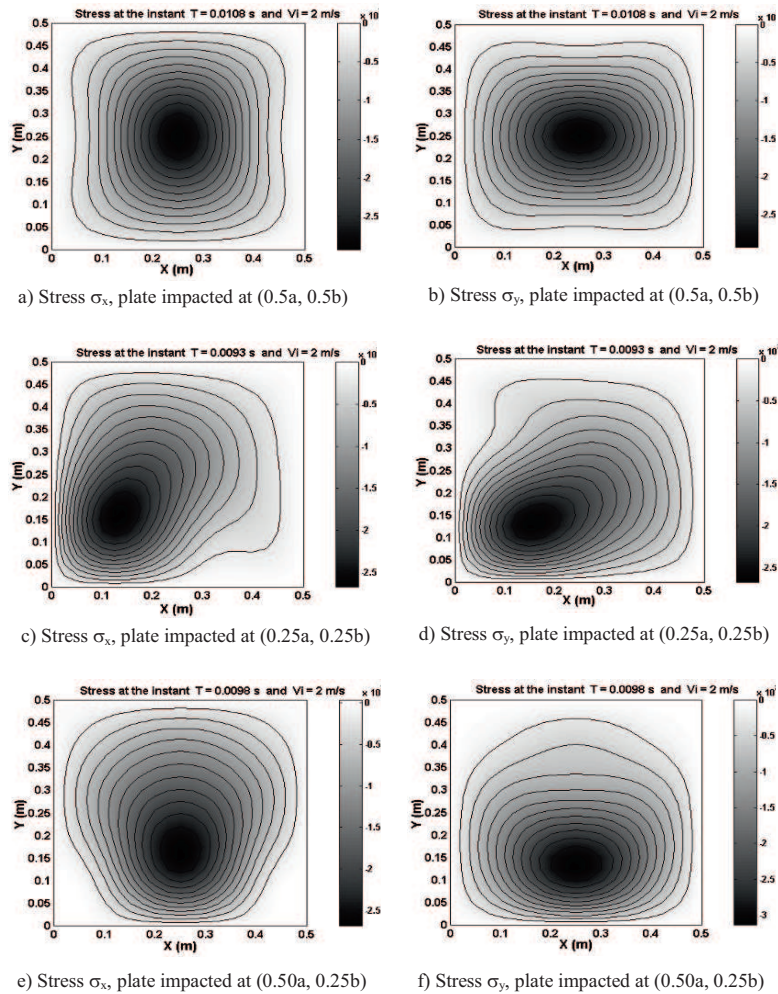
Fig. 6. Stress field for an orthotropic plate

4. Conclusions

In this study, we developed a numerical approach to determine the impact force and dynamic response of a rectangular plate impacted by a spherical projectile. The plate's response is determined by modal decomposition using a Newmark integration scheme. The obtained results were validated by those given by the literature. Finally, a study of the influence of some parameters on the impact force, the plate dynamic response and the stress distribution was made. From this study we can highlight the following:

- When calculating the impact force, the modes of higher order are not negligible, when the mass of the plate is important in front of the impactor.
- The plate boundaries conditions have a significant influence on the impact force.
- The shock is not perfectly elastic, but we can see that the shock is less elastic when the impactor mass becomes important.
- The equal-contours of circular shape around the impact point position tend to be deformed far from the impact point position.

References

[1] L.P. Greszuk. Damage in Composite Materials due to Low Velocity Impact. Impact Dynamics, Z.A Zukas et al., Wiley editions, New York, pp 55–94, 1982.

[2] K.N. Shivakumar, W. Elber and W. Illg. Prediction of Impact Force and Duration due to Low Velocity Impact on Circular Composite Laminates. J. Appl. Mech., 52, pp 674–680, 1985.

[3] S. Benmedakhène, Etude phénoménologique du comportement à l'impact des matériaux composites, Thèse de Doctorat de l'Université de Technologie de Compiègne, France, 1996.

[4] G. Caprino, I. Crivelli-Visconti and A. Di Ilio. Elastic Behaviour of Composite Structures under Low Velocity Impact. Composites, 15, 3, pp 213–234, 1984.

[5] P. Sjoblom. Simple Design Approach Against Low Velocity Impact Damage. Proc. 32nd SAMPE Symp., Anaheim, CA, pp 30–52, 1987.

[6] K.M. Lal. Residual Strength Assessment of Low Velocity Impact Damage of Graphite-Epoxy Laminates, Jour. Reinf. Plast. Comp, 2, pp 226–238.

[7] K.J. Bathe and E.L. Wilson. Numerical Methods in Finite Element Analysis, Prentice-Hill, inc. Englewwood Cliffs, New Jersey, 1976.

[8] S.C. Hunter. Energy Absorbed by Elastic Waves During Impact. J. Mech. Phys. Solids 5, pp 162–171, 1957.

[9] M. Neder et A. Miloudi, Approche Numérique pour la Prédiction du Comportement Dynamique de Plaques Impactées, Actes de la 4ème Conférence Internationale sur les Mathématiques Appliquées et des Sciences de l'Ingénieur, Casablanca, Maroc, 2002.

[10] B. Hachemane , M. Neder, A. Ahmed Benyahia A. Miloudi and T. Boukharouba. Study of the Dynamic Behaviour of Plates Subjected to Impact – A Numerical Approach. The 7th International Conference on Production Engineering, Design and Control, Vol. II, pp 661–669, Alexandria, Egypt, 2001.

[11] M. Neder et A. Miloudi, Etude paramétrique du Comportement Dynamique de Plaques Impactées ", Actes du 16ème Congrès Français de Mécanique, Nice, France, 2003.

[12] Lu Chun, K.Y. Lam. Dynamic Response of Fully-Clamped Laminated Composite Plates Subjected to Low-Velocity Impact of a Mass. Int. J. Solids Struct., Vol. 35, No. 11, Elsevier, pp 963–979, 1998.

[13] T. Wu, His-Yung and Fu-Kuo Chang. Transient Dynamic Analysis of Laminated Composite Plates Subjected to Transverse Impact. Comput. Struct., 31(3), pp 453–466, 1989.

[14] K. Karas. Platten Unter Seitlichem Stoss, Ing. Archiv 10, pp 237–250, 1939.

[15] Cosmos/M2.0 for Windows A Complete Finite Element Analysis System, Structural Research and Analysis Corporation (SRAC), May 1998.

Application of Structural INTegrity Assessment Procedure to Nuclear Power Plant Component

Nenad Gubeljak and Jozef Predan

University of Maribor, Faculty of Mechanical Engineering, Maribor, Slovenia with Smetanova 17, SI-2000 Maribor, Slovenia.

Abstract   Quite few analytical flow assessments methods as specific standard and guidelines there have been developed in recent years. Today, as one of a most comprehensive assessment procedure is SINTAP- Structural INTegrity Assessment Procedure. The SINTAP introduced the basic principles of R6 (rev. 3) and ETM. SINTAP procedure is possible to performed assessment for inhomogeneous configurations such as strength mis-matched weldments and an effect of residual stresses. Nevertheless, the SINTAP procedure take into account temperature transition region from ductile-to-brittle behavior of material. In the contribution the SINTAP procedure was applied to the failure analysis of cracked component. Structure integrity assessment is issued to failure prediction of cracked structural component regarding to increasing applied load or crack size. In order to ensure safe use of cracked structural component the many standards and procedures are available (e.g. SINTAP). The results obtained by using of these procedures consist always certain portion of conservatism, what leads to underestimation of the real carrying capacity of engineering component. In this paper a T-joint of 8 in. RHR nozzle on 29 in. RC hot leg as the part of a high pressured pipeline of the nuclear power plant has been considered as engineering component subjected to thermal shock.

Keywords: Integrity Assessment, Steam Pipeline, T-Joint, Finite Element Analysis.

1. Introduction

Structure integrity assessment is issued to failure prediction of cracked structural component regarding to increasing applied load or crack size. In order to ensure safe use of cracked structural component the many standards and procedures are available (e.g. BS7910, API 579, SINTAP, R6), cited as Refs. [1–4]. The results obtained by using of these procedures consist always certain portion of conservatism, what leads to underestimation of the real carrying capacity of engineering component. The calculation based on analytical solutions given in such procedures defines in the rule a lower value of critical crack size, which causes the failure of structure. In the other hand the solutions for component carrying capacity or critical crack size determined by numerical model corresponds specific geometry of component and crack's parameters. The main disadvantage of this approach is that numerical model demands long term and exhausting modelling, especially in the case when the engineering component geometry or crack geometry is complex, e.g. semi-elliptical and spherical crack located out of the model symmetry.

In this paper a T-joint of 8 in. RHR nozzle on 29 in. RC hot leg as the part of a high pressured pipeline of the nuclear power plant has been considered as engineering component. The critical part of a T-joint is the transition between two pipes of different diameters, because the difference in the pipes' shell thicknesses causes higher stress intensity. Some experiences of operators show that a semi-elliptical surface crack can occur at this place during exploitation of steam pipelines.

T-joint of pipes as the part of primary pipeline of the power plant (Fig. 1) is subjected to the operating pressure of 17.13 MPa and temperature of +290°C up to +350°C according to the technical specification. Weld joint has been made from the material with higher strength than base material, what could be the reason for crack appearing in the base metal at the vicinity of the joint. Material properties are obtained by testing at service temperature +350°C (yield strength $R_{p0,2} = 270$ MPa, ultimate tensile strength $R_m = 575$ MPa, elastic modulus $E = 185$ GPa, Poisson's number $\nu = 0,3$ and fracture toughness $CTOD_{mat} = 0,75$ mm) [5]. This crack due to dynamic loading during the service could extend from the outer side toward inner surface. The possible location of the surface crack is presented in Fig. 1 (in the heat affected zone parallel to the axis of symmetry of the pipe with greater diameter). Based on the project documentation a solid model of the T-joint of pipes with no crack has been modelled by using of SolidWorks [6] and it is presented on Fig. 2. From the theoretical point of view, the highest stresses could be expected on the outer side of the pipe with larger diameter. The first step by finite element analysis (ANSYS 10.0 [7]) was to prove this assumption defining the critical place of the surface crack (position and orientation). In that sense, 3D finite element model (Fig. 3) has been performed increasing the internal pressure incrementally to the value, which causes the stresses over the yield strength of corresponding base material in the region of highest stress concentration. This region could be recognised from Fig. 4, where the principal stresses are presented as the stress vector. The aim of the structural integrity calculation is to estimate the loading conditions of cracked component, where the existed crack or flaw could propagate either stable (leak before break – LBB or plastic collapse effect) or unstable, what has brittle fracture for the consequence. From the safety side, toughness of component material should be high enough, in order to ensure leak-before-break or plastic collapse. It makes possible stopping of the system operation without any extraordinary measures.

$R_1 = 370,2$mm
$t_1 = 59,18$mm
$R_2 = 88,875$mm
$t_2 = 79,45$mm
$a = 19$mm
$2c = 100$mm
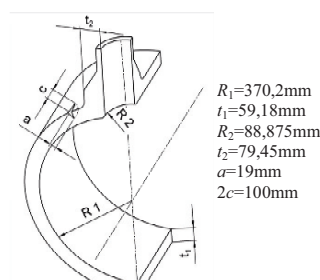
Fig. 1. Geometry of the T-joint
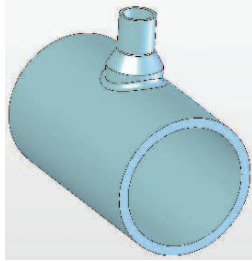
Fig. 2. Solid model of the T-joint
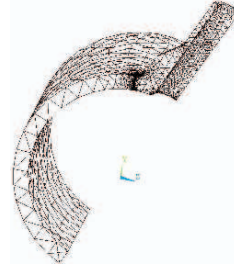
Fig. 3. Finite element model of T-joint
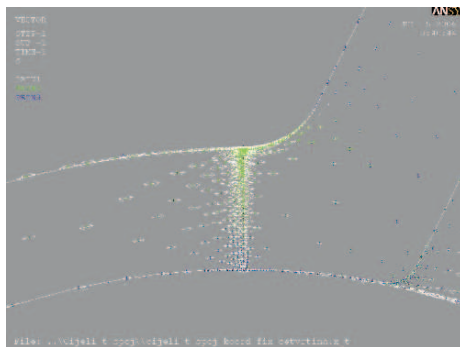
Fig. 4. Vector of principal stresses

2. SINTAP procedure

The SINTAP (Structural Integrity Assessment Procedure) is structured in a hierarchic manner consisting of various analysis levels constituted by the quality and completeness of the required input information.
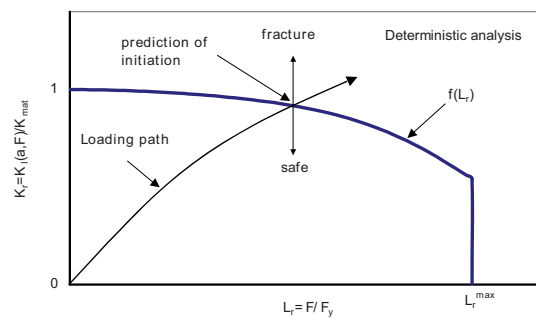
Fig. 5. Schematic illustration of fracture initiation at Failure Assessment Diagram (FAD)

Higher levels are more advanced than lower levels: they need more complex input information but the user is "rewarded" by less conservative results. An important feature of the procedure is that the analyses can alternatively be based on a Failure Assessment Diagram (FAD) philosophy (Fig. 5). Applying the FAD philosophy a failure line is constructed by normalising the crack tip loading by the material's fracture resistance. The assessment of the component is then based on the relative location of a geometry dependent assessment point with respect to this failure line. In the simplest application the component is regarded as safe as long as the assessment point lies within the area enclosed by the failure line. It is potentially unsafe if it is located on or above the failure line. The normalising crack tip loading parameter L_r is defined as ratio of the applied load (i.e. service pressure $p = 17,133$ MPa) and the limit load (i.e. pressure p_Y), or respectively as the ratio of an applied net section stress σ_{ref} and the yield strength of the material, σ_Y:

$$L_r = \frac{F}{F_Y} = \frac{p}{p_Y} = \frac{\sigma_{ref}}{\sigma_Y} \tag{1}$$

The latter being given as $\sigma_Y = P_{eL}$ for materials with and $\sigma_Y = P_{P0.2}$ for materials without the Lüders plateau. The reference stress of the plate geometry considered within this paper can easily be determined as hoop stress σ_{hoop} or by profile of stress distribution through thickness of cylinder. At the basic level only the toughness and both the yield strength and the ultimate tensile strength of the material have to be known. Different sets of equations are offered for materials with and without Lüders plateau. At basic level failure acceptance curve $f(L_r)$ without the Lüders plateau is defined as

$$f(L_r) = \left[1 + \frac{1}{2} L_r^2\right]^{-1/2} \text{x} \left[0,3 + 0,7 \exp\left(- \mu L_r^6\right)\right] \text{ for } 0 \le L_r \le 1 \tag{2}$$

With:

$$\mu = \min \begin{bmatrix} 0,001 \, E / R_{p0,2} \\ 0,6 \end{bmatrix} \tag{3}$$

And

$$f(L_r) = f(L_r = 1) \text{ x } L_r^{(N-1)/2N} \quad \text{for} \quad 1 \le L_r \le L_r^{max} \tag{4}$$

$$N = 0{,}3 \left[1 - \frac{R_{p0,2}}{R_{m}} \right] \tag{5}$$

$$L_r^{max} = \frac{1}{2} \left[\frac{R_{p0,2} + R_{m}}{R_{p0,2}} \right] \tag{6}$$

With L_r^{max} being the limit against plastic collapse.

3. Determination of the carrying capacity of the T-joint of pipes

It is necessary to perform structural integrity assessment of T-joint of pipes regarding the loading level. The crack geometry is usually determined by non-destructive inspection of component (e.g. ultrasonic testing). In our paper the semi-elliptical surface crack has been considered. The assumed size of crack ($a = 19$ mm, $2c = 100$ mm) can be reliably determined by ordinary testing equipments. Integrity assessment generally is based on analytical expressions for fracture mechanics parameters (stress intensity factor, limit load).

The solutions are given in literature (e.g. [8]) or in software packages, but solutions are constrained to a very small range of pipe thicknesses and diameter ratios. Such expressions for stress intensity factors given in literature are used for the structural integrity assessment of structures with present cracks. They can later significantly differ from real solutions for observed components. Thus the confidence level of the obtained result stays unknown.

Opposite to this, numerical modelling of the joint geometry and moreover of the crack geometry requires the time and experience. Numerical solutions for stresses obtained by FEM are closest to the real stresses in the joint. This is because it takes into account all the geometric details of the joint and shows a realistic model of the material behaviour. However, the FEM results are usually limited to only one-crack geometry, as for every crack length a new model has to be created or algorithms for crack propagation have to be used.

Alternatively, analytical expressions for the stress intensity factor calculation could be based on the stresses distribution obtained by FEA with no crack. Therefore, the aim of this paper was to compare these three different approaches defining the carrying capacity of one cracked T-joint in steam pipes:

   (a) Engineering approach based on the stress intensity factor (SIF) calculation by using equations given in literature and an expression for the *hoop stress*
   (b) Combined approach based on the analytical SIF calculation by using *arbitrary stress distribution* through the thickness obtained from the finite element analysis for the structure with no crack and

(c) *Numerical calculation* of SIF from the finite element model of the joint with real crack geometry.

3.1. Engineering approach

Expression for the SIF for the semi-elliptical axial surface crack in tube [8]:

$$K = \sigma \cdot \sqrt{\pi \cdot a} \cdot Y\left(\frac{a}{c}, \frac{c}{t}\right) \text{ where } \sigma \text{ is hoop stress} \tag{7}$$

$$\sigma = \frac{R_o + R_1}{2 \cdot t} \cdot p \tag{8}$$

R_o is outer radius, R_1 is inner radius of pipe, t is the wall-thickness and p is internal pressure, a is crack depth and Y is the geometry shape function and for the interval $3 < 2c/a < 12$ is valid as

$$Y\left(\frac{a}{c}, \frac{c}{t}\right) = \frac{1}{\sqrt{Q}} \cdot \left\{ \begin{array}{l} 1{,}12 + 0{,}053\left(\frac{2c}{t}\right) + 0{,}0055\left(\frac{2c}{t}\right)^2 + \\[2mm] + \left[1 + 0{,}02\left(\frac{2c}{t}\right) + 0{,}0191\left(\frac{2c}{t}\right)^2\right] \cdot \frac{\left[2 - \frac{0{,}05}{t}(R_o + R_i)\right]^2}{14} \end{array} \right\} \tag{9}$$

$$Q = 1 + 1{,}464\left(\frac{a}{c}\right)^{1{,}65} \tag{10}$$

For earlier defined piping tees geometry and crack parameters ($a = 19$mm, $2c/a = 5.263$) the value of SIF at the surface of pipe by using Eqs. (7–10) for $p = 17.133$ MPa was calculated as: $K = 1779.43$ Nmm$^{-3/2}$. Yield pressure could be calculated either by using formulae for semi-elliptical axial surface crack in tube [11]:

$$p_Y = \frac{\eta}{1 - \dfrac{1-\eta}{M}} \cdot \frac{t}{R_i} \cdot \sigma_Y \tag{11}$$

$$\eta = \frac{t-a}{t} \text{ and } M = \sqrt{1 + 1{,}61 \cdot \frac{c^2}{R_i \cdot t}} \tag{12}$$

Or by using of equation defined by Zahoor [12] for surface crack at crotch in piping tees:

$$p_Y = p_o \text{x} \frac{1 + 1,1 \cdot \left(\dfrac{a}{t}\right)^{0,8} \text{x} \left(1 - 0,4 \cdot \dfrac{a}{t}\right)}{1 - \dfrac{1,2}{M} \cdot \left(\dfrac{a}{t}\right)^{1,4}} \tag{13}$$

where:

$$p_o = \frac{t}{R_o} \text{x} \sigma_Y \text{ and}$$

$$M = \left[1 + 1,2987\lambda^2 - 0,026905\lambda^4 + 5,3549\text{x}10^{-4}\lambda^6\right]^{0,5} \text{ and } \lambda = \sqrt{\frac{c^2}{R_o \cdot t}} \tag{14}$$

Yield pressure calculated by using of Eqs. (13) and (14) is much closer to real solutions and is equal to $p_Y = 30$ MPa. In that case the normalised crack tip loading parameter amounts to $L_r = 0.57$.

3.2. Combined approach

In this approach the stress distribution through the thickness of T joints is calculated by using of FEM. This distribution is used for calculation both Stress Intensity Factor-SIF and limit load for surface crack, as is described in the Ref. [9]. It is known that the tension and bending stresses are usually required as input data to calculate the limit load of the component with a crack.
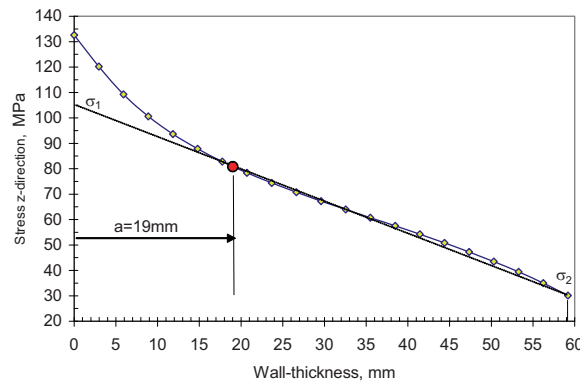
Fig. 6. Opening stress distributions over the wall-thickness of the larger pipe at $p = 17.133$ MPa

The SIF-solutions based on the method of weight functions can be used for an arbitrary stress distribution over the wall-thickness. Figure 6 shows the stress distribution and principles for determination σ_1 and σ_2 as edges stress values over the wall-thickness of the no-cracked pipe with larger diameter.

By linearization of stress distribution at crack tip position (crack opening stress σ_z in our case at $p = 17.133$ MPa), the membrane and bending stress can be calculated as:

$$\sigma_\mathrm{m} = \frac{\sigma_1 + \sigma_2}{2} = \frac{105 + 30}{2} = 67.5 \,\mathrm{MPa}$$

and :   (15)

$$\sigma_\mathrm{b} = \frac{\sigma_1 - \sigma_2}{2} = \frac{105 - 30}{2} = 37.5 \,\mathrm{MPa}$$

Now it is possible to calculate the parameter L_r for FAD diagram from the values of the membrane stress σ_m and bending stress σ_b by using simplified expressions for the semi-elliptical surface crack in the plate under variable stress:

$$L_r = \frac{g(\xi) \cdot \dfrac{\sigma_\mathrm{b}}{3}}{(1 - \xi^2) \cdot R_\mathrm{e}} + \frac{\sqrt{\left(g(\xi) \cdot \dfrac{\sigma_\mathrm{b}}{3}\right)^2 + (1 - \xi)^2 \cdot \sigma_\mathrm{m}^2}}{(1 - \xi)^2 \cdot R_\mathrm{e}}$$ (16)

where:

$$g(\xi) = 1 - 20\xi^3 \left(\frac{a}{2c}\right)^{0,75} \quad \text{and} \quad \xi = \frac{a \cdot c}{t \cdot (t + c)}$$ (17)

Considering the yield strength for the corresponding material as $R_\mathrm{e} = 270$ MPa, and using Eqs. (16) and (17), the parameter L_r is calculated as $L_\mathrm{r} = 0.36$.

3.3. Numerical determination of the SIF

The value of SIF determined by finite element analysis presents most accurate solution, but it consumes the time and requires good experience of operator. Its main disadvantage is that obtained SIF solution is valid for only specific crack-geometry.

Semi-elliptical surface crack has been modelled by ABAQUS [10] combining tetrahedral and hexagonal elements in the vicinity of the crack front. Equivalent stress distribution in the T-joint at $p = 17.133$ MPa is presented in the Fig. 7a and more detailed in Fig. 7b.

SIF solution for the considered surface crack with 2c/a = 5.263 and a = 19 mm was determined numerically. Figure 8 shows comparison between numerically determined loading paths against failure assessment curve. The crack size is constant, only internal pressure was increased up to $p = 60$ MPa.

Figure 8 shows that increase of loading causes crack propagation at inside point of semi-elliptical crack. Solution based on the hoop stress provides linear loading path and higher loading ration. Since, linear hoop-solution cross the failure curve at lower internal pressure value than FEM solution, it is possible to recognize that hoop solution is most conservative compare to arbitrary stress solution and finite element solutions, e.g. critical pressure by hoop stress is $p^*crit = 45$ MPa, arbitrary stress solution $p^{**}crit = 48$ MPa while by FEM analysis, the critical stress is $pcrit = 53.6$ MPa for surface point.
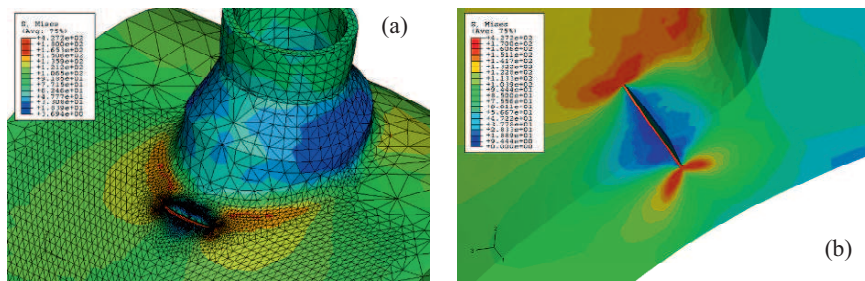
Fig. 7. Mises stress distributions in the T-joint of pipes at $p = 17.133$ MPa
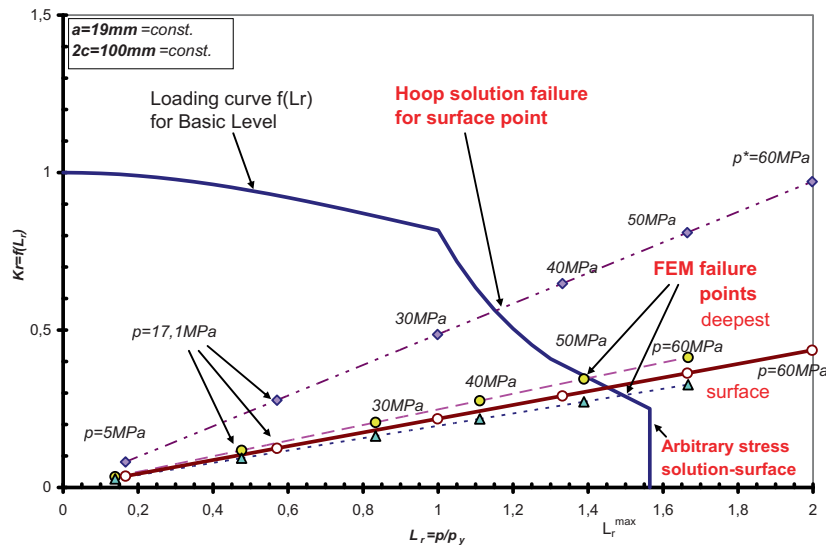
Fig. 8. Comparison between hoop stress solution, arbitrary stress solution and FEM solution during increasing internal pressure

4. Conclusions

The structural integrity assessment is performed on one cracked T-joint in steam pipes, using two different approaches based on fracture mechanics. The obtained results show significant differences depending on the expressions used in the calculations. The largest deviation from the results obtained by FEM is noted in those solutions, where the stress intensity factor was calculated by using the expression for hoop stress. It is possible to assume that the solution obtained by FEM is closest to the real stress in the joint. This is because it takes into account all the geometric details of the joint and shows a realistic model of the material behaviour, indicating that for such a solution greater effort is needed, as well as time and knowledge. The FEM results are also limited to only one-crack geometry, as for every crack length a new model has to be created or algorithms for crack propagation have to be used. In a single case an alternative approach can be used, where analytical expressions for stress intensity factor calculation are combined with the crack geometry and stress state. Thus, geometry of the joint is partially or completely simplified, because the crack geometry is almost neglected when calculating the stress intensity factor. The analytically or numerically obtained distributions of the stress crack opening through the thickness serves as the basis for determination of membrane stress and bending stress independent of the crack length. The results obtained in such a way can be of acceptable accuracy, they are obtained over a shorter time, and enable partially change of crack length and depth as opposed to the FEM solutions.

References

[1]   BS 7910. Specification Formulation. Journal of Engineering, Vol. 2, No. 2, 1999, pp 223–228.
[2]   API 579. API Recommended Practice 579. Fitness for Service, First Edition, March 2000.
[3]   SINTAP: Structural INTegrity Assessment Procedures for European Industry. Final Revision, EU Project BE 95-1462, Brite Euram Programme, 1999.
[4]   R6: Assessment of the integrity of structures containing defects. Nuclear Electric Procedure R/H/R6, Revision 3, 1998.
[5]   Gubeljak, N., Kozak, D., Vojvodič-Tuma, J., Predan, J., Aplikacija mehanike loma pri revitalizaciji energijskih komponent, Končno poročilo, Elaborat za nuklearno elektrarno Krško
[6]   SolidWorks, 2005.
[7]   ANSYS Release 10.0, 2005.
[8]   Schwalbe, K.-H., Zerbst, U., Kim, Y.-J., Brocks, W., Cornec, A., Heerens, J., Amstutz, H., "EFAM ETM 97- the ETM method for assessing the significance of crack-like defects in engineering structures, comprising the versions ETM 97/1 and ETM 97/2", GKSS-Forschungszentrum Geesthacht GmbH, Geesthacht, 1998.
[9]   Berger, Ch., et al. Fracture mechanics proof of strength for engineering components. FKM Guideline, Forschungskuratorium Maschinenbau (FKM), 2004.
[10] ABAQUS Release 6.5, 2006.
[11] Kiefner, J.F., Maxey, W.A., Eiber, R.J., Duffy, A.R., (1973) Failure Stress Loads of Flaws in Pressurised Cylinders, ASTM STP 536: 461–481.
[12] Zahoor, A., Closed Form Expressions for Fracture Mechanics Analysis of Cracked Pipes. ASME J. Pressure Vessel Technology, 107: 203–205.

Failure Assessment Diagrams in Structural Integrity Analysis

Yu. G. Matvienko

Mechanical Engineering Research Institute of the Russian Academy of Sciences, 4 M. Kharitonievsky Per., 101990 Moscow, Russia

Abstract   The methodology of the criterion of average stress in the cohesive zone ahead of the crack/notch was employed to develop failure assessment diagrams for a solid with a finite crack/U-notch under mode I loading. The cohesive stress is treated according to Von Mises yield criterion as a property of both the yield stress and the T-stress which was introduced into the criterion to quantify constraint in different geometries and type of loading. A brief survey of the basic principles of a failure assessment diagram for a body with a crack- or notch-like defect and its application in the structural integrity analysis has been presented. To determine an acceptable (safe) region of the damaged component, safety factors against fracture and plastic collapse were introduced in the fracture criterion and the failure assessment diagram. Basic equations have been presented to calculate the safety factor against fracture and to estimate an acceptable (safe) region for an engineering component with a crack- or notch-like defect of the acceptable size. It was shown that the safety factor against fracture for a notch-like defect is a function of the yield stress as well as the elastic stress concentration factor and the safety factor against plastic collapse. The methodology of the failure assessment diagram has been employed for the structural integrity analysis and assessment of acceptable sizes of surface longitudinal notch-like defects in a pressure vessel. The load separation method is recommended to measure the notch fracture toughness in terms of the J-integral for non-standard specimens with a notch.

Keywords: Failure, Integrity, Crack/Notch, Von Mises Yield Criterion, Diagram FAD.

1. Introduction

The basic failure curve of the failure assessment diagram (FAD) is written as $K_r = f(L_r)$, where $K_r = K / K_{1C}$ is the ratio of the applied stress intensity factor K to the material's fracture toughness K_{1C} and L_r is equal to the ratio of applied load P to plastic collapse load P_Y. If the assessment point (K_r, L_r) is situated within the non-critical region enclosed by the line of the FAD, failure of the cracked structure does not occur. Details of the FAD approach are given in the SINTAP procedure. In engineering, most assessment of component reliability are made deterministically so that failure is avoided by including safety factors on each of the different equation inputs. In this case, safety factors against fracture and plastic collapse have been considered [1, 5]. The safety factors are set to unity for the evaluation of critical conditions.

The aim of this paper is to give a brief survey of the basic principles of a failure assessment diagram for a component with a crack- or notch-like defect and its application in the structural integrity analysis. The FAD has been based on the criterion of the average stress ahead of the crack/notch tip and considered in terms of K_{1notch}/K_{1C} and σ_C/σ_Y. Acceptable state of the damaged component with a crack- or notch-like defect will be determined by introducing safety factors against fracture and plastic collapse in the fracture criterion describing the failure assessment diagram.

2. Failure assessment diagram for a solid with a crack

2.1. Failure criterion

The local failure criterion in the form of the average stress limitation in the fracture process zone ahead of the sharp crack tip can be given in the following form [3].

$$\frac{1}{d}\int_0^d \sigma_y(r)dr = \sigma_o \tag{1}$$

To describe a critical state of a solid with a crack. Here, d is the fracture process zone length, $\sigma_y(r)$ is the normal elastic stress distribution ahead of the crack/notch tip. The critical stress σ_0 is the material strength which depends on the material model and can be assumed to be the yield strength, ultimate strength or some effective strength taking into account the constraint effect. An infinite plate with a crack length $2a$ is assumed to be subject to remote uniaxial stress σ. The stresses $\sigma_y(r)$ on the crack extension line are the principal normal stresses described by the exact elastic solution according to Westergaard's theory.

$$\sigma_y(x) = \frac{\sigma x}{\sqrt{x^2 - a^2}} \tag{2}$$

Averaging the local stress (see Eq. 2) over the fracture process (cohesive) zone, the failure criterion (Eq. 1) leads to the following equation [3].

$$K_1 = K_{1C}\sqrt{1 - \left(\frac{\sigma_C}{\sigma_{coh}}\right)^2} \tag{3}$$

Which describes the failure assessment diagram. Here, K_I is the stress intensity factor at the crack tip, σ_C is the applied (critical) stress at failure.

2.2. The cohesive strength

To estimate the cohesive strength, the following approach has been suggested. The general form of the linear elastic stress fields ahead of the crack tip can be given by Williams's solution.

$$\sigma_{ij} = \frac{K}{\sqrt{2\pi r}} f_{ij}(\theta) + T\delta_{1i}\delta_{1j} \qquad (4)$$

where δ_{ij} is Kronecker's delta, functions $f_{ij}(\theta)$ define the angular variations of in-plane stress components. The T-stress can be used as a constraint parameter which has an influence on the cohesive strength ahead of the crack tip.

The T-stress scales linearly with applied load in infinite geometries, most computational studies report T-stress values for various crack configurations as follows.

$$T = \beta(a/W)\sigma \qquad (5)$$

where $\beta(a/W)$ is a dimensionless parameter (so-called biaxiality ratio) which depends on geometry and loading mode, σ is an applied stress, a and W are the crack length and width of a body, respectively. Values of $\beta(a/W)$ can be considered as a normalized measure of the crack tip constraint and have been tabulated for various geometries in the literature.

In the present work, the cohesive strength σ_{coh} ahead of the crack tip is determined by von Mises yielding criterion within the fracture process zone according to flow law.

$$\Phi(\sigma_1, \sigma_2, \sigma_3, \sigma_Y) = (\sigma_1 - \sigma_2)^2 + (\sigma_2 - \sigma_3)^2 + (\sigma_1 - \sigma_3)^2 - 2\sigma_Y^2 = 0 \qquad (6)$$

where σ_Y is the yield strength.

Moreover, the cohesive strength is treated as the stress which is independent on the separation distance because the effect of the shape of the traction-separation curves in the fracture process zone can be relatively weak. The stresses σ_1, σ_2 and σ_3 are the principal normal stresses and assumed to be constant in the fracture process zone ahead of the crack tip for certain crack geometries and loading conditions.

Analogously to Williams's solution, the stress σ_2 parallel to the crack plane is suggested to be given by equation $\sigma_2 = \sigma_1 + T$. The stress σ_3 is equal to $\nu(\sigma_1 + \sigma_2)$ and 0 for plane strain and plane stress, respectively. The cohesive strength σ_{coh} is supposed to be σ_1 and can be expressed from von Mises yield condition (Eq. 6) taking into account Eq. (5) as follows.

$$\frac{\sigma_{coh}}{\sigma_Y} = -\frac{\beta}{2}\left(\frac{\sigma_C}{\sigma_Y}\right) + \sqrt{\frac{1}{4}\left(\frac{\beta\sigma_C}{\sigma_Y}\right)^2 - \frac{\left(1+\nu^2-\nu\right)\left(\beta\sigma_C/\sigma_Y\right)^2 - 1}{\left(1-2\nu\right)^2}} \text{ , plane strain} \quad (7)$$

$$\frac{\sigma_{coh}}{\sigma_Y} = -\frac{\beta}{2}\left(\frac{\sigma_C}{\sigma_Y}\right) + \sqrt{1 - \frac{3}{4}\left(\frac{\beta\sigma_C}{\sigma_Y}\right)^2} \text{ , plane stress} \quad (8)$$

Thus, the cohesive strength for finite geometries can be rewritten as a function of the applied failure stress $\sigma = \sigma_C$ and the crack tip constraint.

3. Notch failure assessment diagram

The criterion of the average stress (Eq. 1) has been adopted for a solid with a notch as well as a crack. The stress distribution is simplified considerably on the continuation of the U-notch [2].

$$\sigma_y(r) = \frac{K_{1notch}}{\sqrt{2\pi r}}\left(1 + \frac{\rho}{2r}\right) \quad (9)$$

where ρ is the notch tip radius. The stress intensity factor at the notch tip is denoted as K_{1notch}. It should be pointed out that such stress distribution was suggested for blunt cracks when the distance ahead of the crack tip is much smaller than the crack length and greater than the crack tip radius. Averaging the local stress (Eq. 9) over the fracture process zone ahead of the notch tip, the failure criterion (Eq. 1) leads to the notch failure assessment diagram [3, 4].

$$K_{1notch} = K_{1C}\sqrt{1 - \left(\frac{\sigma_C}{\sigma_{coh}}\right)^2}\left[1 - \left(\frac{\sigma_{coh}}{\sigma_C}\right)^2 \frac{1}{K_t^2}\right]^{-1/2} \quad (10)$$

Here, K_t is the elastic stress concentration factor. The cohesive strength σ_{coh} ahead of the notch tip in Eq. (10) is given by Eqs. (7) and (8).

The failure criterion (Eq. 10), describing the notch failure assessment diagram, suggests that the loss of constraint due to a notch is independent on the loss of constraint due to the *T*-stress which was introduced into the cohesive strength to quantify constraint in different geometries and type of loading. It should be also noted that, in contrast to the SINTAP procedure and the FITNET assessment, this simple methodology does not require finite element analysis to obtain the effective distance for calculating the notch failure assessment diagram.

4. Structural integrity assessment of a notch-like defect

The notch failure assessment diagram (Eq. 10) can be adopted for a component with a notch-like defect (or blunt crack with a finite tip radius). To determine an acceptable (safe) region, it should be reasonable to introduce safety factors (e.g. [1, 5]) in the failure criterion. The following condition should be fulfilled if detected or assumed notch-like defect of a certain size should be assessed as acceptable.

$$K_{1notch} \leq \frac{K_{1C}}{SF_K} \sqrt{1 - \left(\frac{\sigma_C}{\sigma_{coh}}\right)^2} \left[1 - \left(\frac{\sigma_{coh}}{\sigma_C}\right)^2 \frac{1}{K_t^2}\right]^{-1/2} \tag{11}$$

where SF_K is safety factor against fracture. The acceptable applied stress σ_C is suggested to be not more than: σ_Y / SF_Y, i.e.

$$\sigma_C \leq \frac{\sigma_Y}{SF_Y} \tag{12}$$

where SF_Y is safety factor against plastic collapse.

For the evaluation of critical conditions for the acceptable stress, the safety factor SF_K in Eq. (11) is set to unity. Any reliable method to calculate the stress intensity factor K_{1notch} can be employed if these methods are validated. The safety factor SF_K can be calculated by making an assumption that the applied acceptable stress should be not less than the yield stress (Eq. 12) of material for an engineering component with a notch-like defect of the acceptable size [5]. In this case, the failure criterion for a notch-like defect of the acceptable size on the boundary of fracture and plastic collapse can be given by

$$\frac{1}{2}\sqrt{\pi\rho}\sigma_T K_t = K_{1C} \sqrt{1 - \left(\frac{\sigma_Y}{\sigma_{coh}}\right)^2} \left[1 - \left(\frac{\sigma_{coh}}{\sigma_Y}\right)^2 \frac{1}{K_t^2}\right]^{-1/2} \tag{13}$$

Here, the stress intensity factor at the notch-like defect tip is assumed to be as given by the relationship.

$$K_{1notch} = \frac{1}{2}\sqrt{\pi\rho}\,\sigma K_t \tag{14}$$

The safety factor SF_Y against plastic collapse corresponding to Eq. (12) is introduced in the failure criterion (Eq. 11) to determine the acceptable defect as:

$$\frac{1}{2}\sqrt{\pi\rho}\,\frac{\sigma_Y}{SF_Y}K_t = \frac{K_{1C}}{SF_K}\sqrt{1-\left(\frac{\sigma_Y/SF_Y}{\sigma_{coh}}\right)^2}\left[1-\left(\frac{\sigma_{coh}}{\sigma_Y/SF_Y}\right)^2\frac{1}{K_t^2}\right]^{-1/2} \tag{15}$$

Combining Eqs. (13) and (15), the safety factor SF_K against fracture can be presented as:

$$SF_K = SF_Y\frac{\sqrt{1-\left(\dfrac{\sigma_Y/SF_Y}{\sigma_{coh}}\right)^2}\sqrt{1-\left(\dfrac{\sigma_{coh}}{\sigma_Y}\right)^2\dfrac{1}{K_t^2}}}{\sqrt{1-\left(\dfrac{\sigma_Y}{\sigma_{coh}}\right)^2}\sqrt{1-\left(\dfrac{\sigma_{coh}}{\sigma_Y/SF_Y}\right)^2\dfrac{1}{K_t^2}}} \tag{16}$$

Here, the cohesive strength (Eqs. 7 and 8) can be defined taking into account Eq. (12).

$$\frac{\sigma_{coh}}{\sigma_Y} = -\frac{\beta}{2SF_Y}+\sqrt{\frac{1}{4}\left(\frac{\beta}{SF_Y}\right)^2-\frac{\left(1+\nu^2-\nu\right)\left(\beta/SF_Y\right)^2-1}{\left(1-2\nu\right)^2}}\ , \text{ plane strain} \tag{17}$$

$$\frac{\sigma_{coh}}{\sigma_Y} = -\frac{\beta}{2SF_Y}+\sqrt{1-\frac{3}{4}\left(\frac{\beta}{SF_Y}\right)^2}\ , \text{ plane stress} \tag{18}$$

Thus, the right-hand side of Eq. (11) defines the acceptable region in the notch failure assessment diagram. If the assessment point falls within this region, the component with a notch-like defect is acceptable, i.e. it fulfils the required safety demands. For the special case of a crack ($K_t \to \infty$) the failure assessment diagrams (Eqs. 10 and 11) are transferred to the failure assessment diagram for component with a sharp crack, and the safety factor (Eq. 16) becomes the safety factor against fracture of cracked component.

It can be seen from Eq. (16) that the safety factor against fracture is a function of the yield stress as well as the elastic stress concentration factor and the safety factor against plastic collapse. Calculation of the safety factor against fracture as a function of the elastic stress concentration factor leads to the following dependence for plane strain and plane stress (Fig. 1). The value σ_{coh}/σ_Y was accepted in the form given by Eqs. (17) and (18). A crack-like defect is transferred in a sharp crack at $K_t \to \infty$. In this case, the safety factor against fracture tends to its minimum value, i.e. typical value for a sharp crack.
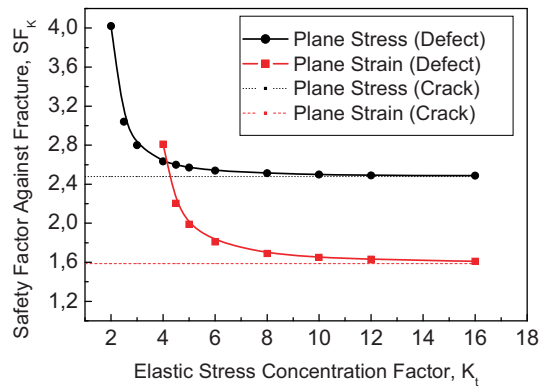
Fig. 1. The effect of the elastic stress concentration factor on the safety factor against fracture ($\beta = 1$, $\nu = 0.3$, $SF_Y = 1.5$)

To demonstrate the structural integrity assessment procedure, an infinite plate with a notch-like defect under uniform remote tensile stress has been considered. Equation (15) gives the approximate relation for a notch-like defect of the acceptable size $[a]$ as follows:

$$[a] = \frac{1}{\pi} \frac{K_{1C}^2}{SF_K^2} \frac{SF_Y^2}{\sigma_Y^2} \left[1 - \left(\frac{\sigma_Y}{\sigma_{coh} SF_Y} \right)^2 \right] + \frac{\rho}{4} \left(\frac{\sigma_{coh} SF_Y}{\sigma_Y} \right)^2 \tag{19}$$

The elastic stress concentration factor is assumed to be equal to the acceptable factor $[K_t]$, i.e. $K_t = [K_t] \approx 2\sqrt{[a]/\rho}$. The following mechanical properties of the material and the safety factor against plastic collapse for plane strain were used: $K_{1C} = 102\,\text{MPa}\sqrt{\text{m}}$, $\sigma_Y = 340\,\text{MPa}$, $\beta = -1$, $\nu = 0.3$, $SF_Y = 1.5$. Calculation of the safety factor against fracture from Eq. (16) at $K_t \to \infty$ gives $SF_K = 1.59$. It is seen that the acceptable size of a notch-like defect decreases with the increase of the elastic stress concentration factor tending to its limiting value, i.e. the acceptable size of a sharp crack (Fig. 2).

An acceptable (safe) region for an engineering component with a notch-like defect of the acceptable size can be represented from Eq. (11).
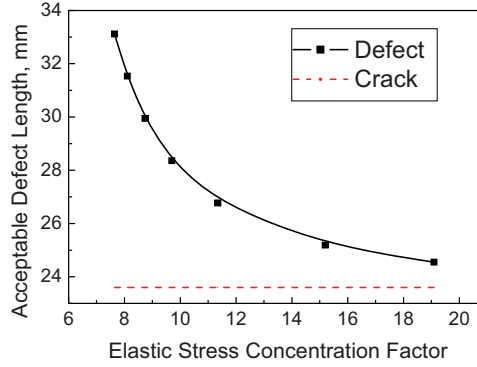
Fig. 2. Acceptable defect length in an infinite plate as a function of the elastic stress concentration factor

5. Acceptable surface longitudinal notch-like defects in a pressure vessel

An assessment of the acceptable surface longitudinal notch-like defects in a pressure vessel is based on the notch failure assessment diagram described by Eq. (15). Substituting Eq. (16) into Eq. (15), the acceptable elastic stress concentration factor $[K_t]$ can be written as follows:

$$[K_t] = \sqrt{\frac{4}{\pi\rho}\frac{K_{IC}^2}{\sigma_T^2}\left[1-\left(\frac{\sigma_T}{\sigma_{coh}}\right)^2\right]+\left(\frac{\sigma_{coh}}{\sigma_T}\right)^2} \qquad (20)$$

Thus, acceptable state of the damaged pressure vessel has been presented by the following criterion $K_t \leq [K_t]$, where K_t is the elastic stress concentration factor for the surface notch-like defect under consideration.

The pressure vessel/defect geometry is described by the wall thickness t, vessel outer diameter D, defect depth l and defect tip radius ρ. In the analysis presented below a wall thickness of 30 mm and a diameter of 1,200 mm are applied. The notch-like defect length is assumed to be an infinite value.

$$K_t = 2\sqrt{\frac{l}{\rho}}Y\left(\frac{l}{t}\right) \qquad (21)$$

where $Y(l/t)$ is a geometrical correction factor for the stress intensity factor in the case of the SENT specimen.
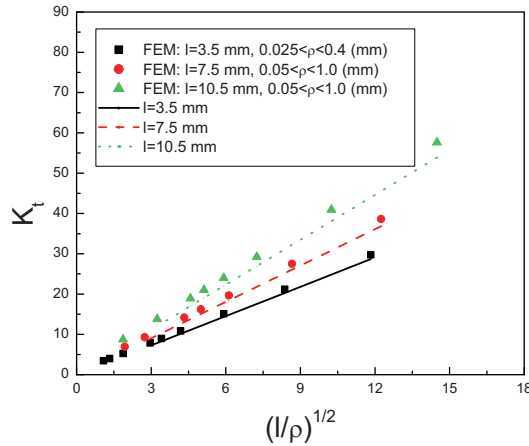
Fig. 3. The results of calculation of the elastic stress concentration factor for surface longitudinal notch-like defects by the FEM and Eq. (21)

To determine the elastic stress concentration factor for the surface external defect, the 2D finite element simulations of steel pressure vessels were carried out using the ANSYS code. It was shown that the elastic stress concentration factor can be given by the following equation (Fig. 3).

The following mechanical properties of the steel and the safety factor against plastic collapse for plane strain were used: $K_{1C} = 100\,\text{MPa}\sqrt{\text{m}}$, $\sigma_Y = 285\,\text{MPa}$, $\nu = 0.3$, $SF_Y = 1.5$. In this case, the acceptable depth of a surface notch-like defect in the pressure vessel amounts to 10.23 mm.

6. Conclusions

Structural integrity assessment of the engineering components damaged by crack- or notch-like defects is discussed from point view of the failure assessment diagram. The methodology of the criterion of average stress in the fracture process zone ahead of the crack/notch was employed to develop failure assessment diagrams for a solid with a finite crack/U-notch under mode I loading.

The cohesive strength is treated according to von Mises yield criterion as a property of both the yield stress and the *T*-stress which was introduced into the criterion to quantify constraint in different geometries and type of loading.

Acceptable state of the damaged component with a crack- or notch-like defect was determined by introducing safety factors against fracture and plastic collapse in the fracture criterion describing the failure assessment diagram. It was shown that the safety factor against fracture is a function of the yield stress as well as the elastic stress concentration factor and the safety factor against plastic collapse. The methodology of the notch failure assessment diagram has been employed for the structural integrity analysis and assessment of acceptable sizes of surface longitudinal notch-like defects in a pressure vessel.

References

[1] Brickstad B, Bergman M, Andersson P, Dahlberg L, Sattari-Far I, Nilsson F (2000) Procedures used in Sweden for safety assessment of components with cracks. Int J Pres Ves Piping 77: 877–881.
[2] Creager M, Paris PC (1967) Elastic field equations for blunt cracks with reference to stress corrosion cracking. Int J Fract 3: 247–252.
[3] Matvienko YuG (2003) Local fracture criterion to describe failure assessment diagrams for a body with a crack/notch. Int J Fract 124: 107–112.
[4] Matvienko YuG (2005) Erratum: Local fracture criterion to describe failure assessment diagrams for a body with a crack/notch. Int J Fract 131: 309.
[5] Matvienko YuG, Makhutov NA (1999) Strength and survivability analysis in engineering safety for structures damaged by cracks. Int J Pres Ves Piping 76: 441–444.

Degradation and Failure of Some Polymers (Polyethylene and Polyamide) for Industrial Applications

Boubaker Bounamous and Kamel Chaoui

LR3MI, Mechanical Engineering Deptartment, Badji Mokhtar University, BP 12, Annaba, 23000, Algeria

Abstract   The use of polymeric material such as polyethylene (PE) and polyamides (PA) made it possible to achieve significant profits in design construction times and installation costs. The objective of this study is to highlight the various mechanisms of rupture of polyethylene pipes in service and in laboratory conditions under fatigue and creep loadings. It is known is some cases that at least two mechanisms control PE pipe failures based on results cumulated in operating conditions. They are nominally ductile and brittle mechanisms respectively characterizing short and long-term failures. Several laboratory tests are used to extract design data for long-term failure-type prediction based on stress and time-to-failure relationship. It remains difficult to assess the relation between creep and fatigue loadings on one side. On the other side, the manufacturing process of the test specimens influences considerably the obtained performance for viscoelastic materials subjected to working conditions and environmental effects. Brittle-to-ductile transition is studied under fatigue crack propagation mode using an energy criterion. The brittle fracture damage zone is characterized by a single craze made up by locally drawn fibers and dispersed voids whereas ductile rupture is rather dominated by highly yielded material and significantly transformed matter as observed under polarized-light microscopy. The assessment of polyethylene pipe and polyamide parts failure mechanisms is to contribute to a better understanding of effects of other external chemical agents such as solvents in degrading the pipe overall resistance. Recent results from environmental stress cracking of PE pipe and exposed polyamide PA66 to detergent will be presented and correlated to mechanical properties degradation.

Keywords: Polyethylene, Polyamide, Failure, Fatigue, Creep; Damage, Wear.

1. Introduction

Despite the large acceptance of polymers as an economic alternative, safety and reliability remain basic issues, especially for long-term brittle-like failure and accelerated stress corrosion cracking for many industrial applications. Many studies have been carried out to highlight various behavioral aspects of usual polymers in terms of service lifetime, mechanical characterization, failure mechanisms and environmental effects [1, 2]. To a certain extent, it is possible to control the mechanical properties of semicrystalline polymers by morphology management during processing operations. Substantially improved Young's moduli and tensile

strengths have been obtained in shear-controlled orientation in injection-molded and high-pressure injection-molded HDPE because of the appearance of highly oriented structures. The search for homogeneous geometrical dimensions imposes rapid cooling and as a result, residual stresses in the extrusion or injection molding processes are generated on external layers, whereas internal layers develop positive stresses. The resistance to crack propagation is influenced by the state and magnitude of these residual stresses.

This work is aimed to investigate mechanisms of failure in polyethylene pipes and those of wear in polyamide gears under service and laboratory conditions. The understanding of those mechanisms needs to study some associated phenomena such as damage evolution and the various changes in mechanical properties caused the extrusion or injection processes. Also, it is necessary to understand the effects of environment on the long-term behavior.

2. Polyethylene pipe interactions

In real conditions, plastic pipe is in constant interaction with the other underground networks (sewers, drinking water, cables, etc.), which are not necessary made out of polymers. So its vulnerability increases as the risks of being deteriorated might become significant. The protection measures are re-examined by including different means of protections and suitable pipe backfills. It should be emphasized that most significant applications of PE pipes remain related to fluid conveyance. HDPE is the reference material used for gas transport under pressure. Stress is related to the allowable pipe pressure through the following equation shown in French Standard NF EN 921 for pressurized plastic pipe:

$$\sigma_{hoop} = P \cdot \frac{OD - h}{2h} \qquad (1)$$

where, σ is hoop stress, P is gas pressure, OD is average outside diameter and h is minimum wall thickness. ASTM D-2837 defines the pressure rating of the pipe as the estimated maximum pressure that the medium in the pipe can exert continuously with a high degree of certainty that failure of the pipe will not occur. Safety factors impose a working pressure in the pipe lower than this upper limit. When exposed to hot water, long-term HDPE pipe failure occurs by precipitation and diffusion-controlled migration of antioxidants combined to thermal oxidation of the polymer.

For drainage pipes, most gravity water flow systems are constructed using corrugated HDPE pipes. They basically comprise mostly sewers, drains, under-drains and sanitary sewers. In drainage systems, underground pipe diameters may be as large as 1,524 mm and they are calculated to support both soil and live loads. HDPE pipe flexibility is used to transfer a portion of the overload onto the surrounding soil. The risk of pipe buckling exists as a result of excessive deformation.

Corrugation is incorporated into the pipe profile to increase the structural stiffness of the structure and according to AASHTO M294 standard; three types of HDPE pipe profiles are used. They are: (1) *Type C:* Full circular cross-section with an annular corrugated surface both inside and outside, (2) *Type S:* Full circular dual-wall cross-section with an outer corrugated pipe and (3) *Type D:* Circular cross section consisting with smooth inner wall joined to an outer wall.

Observed field problems [3] included: (i) deflection resulting from the lack of control of construction procedures and the use of poor backfill materials, (ii) erosion at outlet ends which often resulted in significant loss of material and longitudinal bending and cracking of the corrugated HDPE pipe and (iii) erosion as a result of joint leakage. In this case protection ducts, HDPE pipes are used as external shields to isolate cables or pipes from external aggressive environments. Usually, the protection is aimed to reduce significantly the presence of both moisture and oxygen.

In the gas industry, HDPE ducts are commonly used to protect steel pipelines crossing swampy and marine environments.

3. Polyethylene pipe testing

The Plastic Pipe Institute selected stress rupture testing as the most suitable test method for rating plastic piping materials. The design of is achieved through the "Rate Process Method for Projecting Performance of Polyethylene Piping Components" which is standardized in ASTM D-2837, ISO 9080 and D-2513. It well established that PE creep rupture curve may be divided into three regions as illustrated in Fig. 1 and the same testing procedure allows differentiating between various PE resins and manufacturing processes.
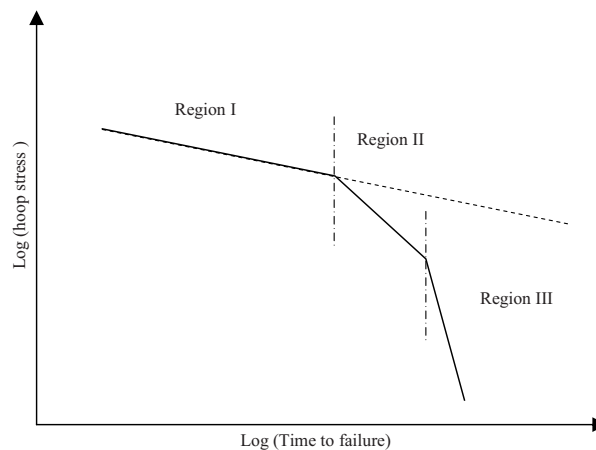
Fig. 1. Schematic of a creep rupture curve for PE pipes at high temperature and long-term

The calculation is based on three coefficients equations [4], which relates lifetime, t or the time-to-failure (in hours), hoop stress, σ (in Pa) and testing temperature, T (in K) in the following form:

$$Log\, t = A + \frac{B}{T} + \frac{B \cdot Log\,\sigma}{T} \qquad (2)$$

where A, B, C are constants. Either ASTM D-2837 based on hydrostatic design basis (HDB) or ISO 9080 based on minimum required strength (MRS) use data from sustained hydrostatic pressure tests of pipe specimens, but the extrapolation protocols are different.

It is understood that the actual long-term performance under internal pressure and temperature will be the same regardless of the method. Normally, HDB and MRS are used to obtain allowable pressure ratings considering pipe diameter, thickness and a safety factor. Under conditions of constant low stress and room temperature, it is established that PE resins fracture by slow crack growth. This mode of failure limits pipe lifetime but constant tensile load (CTL) test was devised to extract long-term information from accelerated testing [5]. Available data from such a test is able to differentiate between similar products coming from different manufacturers or using different copolymers in the extrusion process. CTL is a good quality assurance test to evaluate new pipe lots and to set a minimum required resistance.
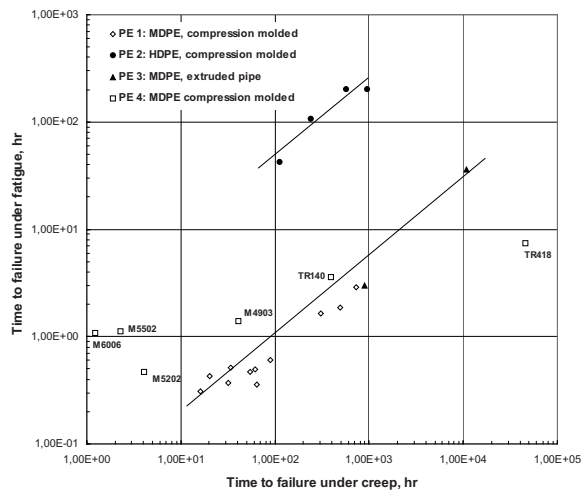
Fig. 2. Relationship between failure times under creeps and fatigue modes for different resins

Generally, fatigue can be defined as a phenomenon that takes place in components and structures subjected to time-varying external loading and that manifests itself in the deterioration of the material ability to carry an applied load that is well

below the elastic limit. Testing under fatigue has been used in different studies as an accelerating agent to deduce PE lifetime under specific conditions. The correlation between creep and fatigue strengths, undertaken by Parsons et al. [6], showed that MDPE was much more creep resistant than HDPE, but MDPE pipes was much more sensitive to strain rate in fatigue In the same approach, Zhou and Brown [7] concluded that a higher resistance to fatigue does not necessarily correlate with a higher resistance to failure under creep. Since ASTM tests are based on creep data, it is interesting to compare it with fatigue data. Figure 2 illustrates such relation between failure times from both creep and fatigue modes.
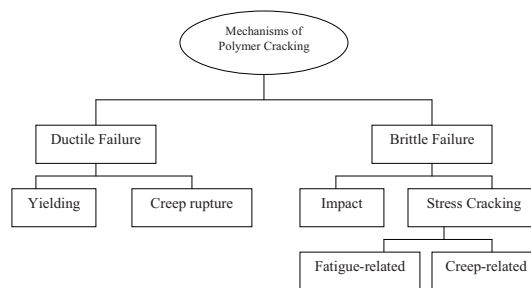
Fig. 3. Failure mechanisms occurring during polymer cracking under different loadings

The data were gathered from literature and a proportional relation is found to characterize both modes. This is an important result which states that fatigue tests can also be used to draw conclusion on pipe life under acting pressure. Figure 3 shows the various mechanisms of cracking in polymers. Usually, ductile and brittle cracking are in competition and which are aggravated with environmental factors such as temperature and stress cracking chemical agents.

4. Wear measurements in polyamide gears

In the following example, the wear resistance of gear teeth is measured on commercial PA66 polyamide wheel produced by mould injection process. In order to assess the effect of water on wears in each flank of wheel teeth, an industrial polyethylene-washing machine is used. The testing machine consists in PA66 spur gears composed of a 19-teeth pinion and a 132-teeth driven wheel. The pinion under investigation is enclosed in an upper box and rotates at a speed of 140 rpm. The driven wheel is a crown wheel supporting a 3 kg capacity cylindrical clothes drum that is placed in a lower box shaped basin (520 mm high, 460 mm wide and 570 mm deep).

The upper box is linked to the lower box through pins that allows closing and opening when loading or unloading the lower box. The machine for wear test is shown in Fig. 4.
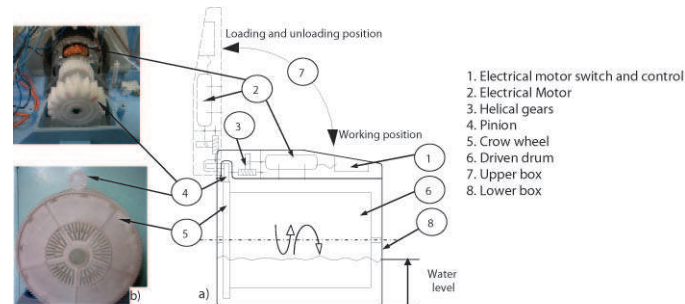
Fig. 4. (**a**) Kinematics diagram of the testing rig, (**b**) back view of the gears

Wear measurement of the pinion is carried out every 250,000 wheel revolutions in the clockwise direction. Before each measure, the test piece is cleaned in order to remove small sticking particles that have been generating from the wear process and dried to squeeze out humidity. Three testing conditions have been applied: in water, in detergent water solution and under dry driving. The water detergent solution has the following composition:

- Less than 5% of nonionic tension credits soap
- From 5% to less than 15%: tension anion credits, bleaching agents
- From 15% to less than 30%: phosphates

It also contains: enzymes, perfume, activator, carbonate, silicate, optical bluing. It is interesting to note that throughout the testing period, all the teeth have been subjected to wear resistance only in the addendum zone, between the pitch diameter and the outside diameter. This is due to two main reasons. First, when gearing, the normal force due to the applied pressure on the contact point at the pitch diameter with a pressure angle of 20° generates axial force that is fairly high enough to push out the gears as to create a small displacement. Secondly, the material is water absorber, since polyamides have a water absorption rate of 1.5% at 23°C after 24 h. Regarding the flanks, there is a slight difference between the right and left flanks wear. In fact, when operating the testing rig follows a washing machine cycle. The distribution of wear around the wheel can be obtained when observing its morphology throughout the 19 teeth. In this case, wear measurements on the surface (XY-plane) at a distance of 0.5 mm from the external diameter have been reported in histogram plots for the three testing conditions.

5. Failure mechanisms of polyethylene pipes

Ductile failures are characterized by large-scale material yielding adjacent to the failure location. For instance, a flow phenomenon takes place represented by cold drawing during in typical tensile tests of semicristalline polymer samples. Ductility is more expressed as applied stresses are higher and usually rupture occurs in a relatively short time.

This mechanism is related to the viscoelastic behaviour of PE materials and specifically refers to the creep rupture. Typical brittle and ductile failures in HDPE pipes are exhibited in Fig. 5. Less deformation characterizes the fracture process, which is a long-term mechanism.

Temperature [8] is known to accelerate brittleness from sustained pressure tests. Brittle failure in semicrystalline polymers has been claimed to originate from chain disentanglement in fibrils, and recently other studies have also concluded that chain breaking due to applied stress during crack propagation involves fibrillation within the damage zone [9].

A level of complexity lies in the intramolecular heterogeneity of co-unit distribution that should be as efficient as intermolecular heterogeneity for producing tie molecules and random chain folding at the expense of regular chain folding. Crystalline domains within semicrystalline polymers strongly influence such low-strain-rate properties as the elastic modulus, yield stress, SCG, and environmental stress cracking, whereas high-strain-rate properties such as impact, tear, and rapid crack propagation are basically controlled by amorphous regions. In many cases, complementary techniques have been adopted to assess from physical property measurements molecular information.
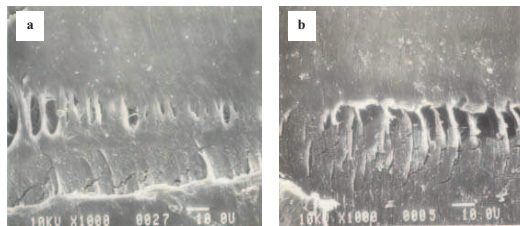
Fig. 5. SEM observation of the inner part of the craze zone at higher magnification; (**a**) brittle crack and (**b**) ductile crack

For instance, brittle fracture toughness, crazing, and SCG measurements have been used to determine the tie-molecule concentration and to infer valuable structural information. In simpler cases, tie-molecule concentrations have been evaluated from the modulus of a mechanically oriented material. Post yield experiments assume that tie molecules and entangled chains behave like rubbery networks in the drawing and strain-hardening regions; these molecules are steadily pulled out from fragmented lamellae to become part of an oriented amorphous domain.

6. Brittle to ductile transition

In the brittle regime, the plastic zone is very small and is associated with a main craze. The latter is made of yielded material and structural voids. Under polarized light, the extent of damaged material is confined to a narrow zone next to the

crack plane. For the ductile regime, the damaged zone is much important and the craze are longer compared the brittle stage. The SEM examination illustrates the multiple crazes and the highly deformed material at the crack-tip. Around the damage zone, another part of the transformed material is highly affected plastically as its limits extend many folds until the specimen edge. At higher magnifications, the hierarchical events inside the craze zone appear to be constituted of highly yield local matter and important voids. In order to study the FBDT, it is interesting to use an energetic approach proposed by Klingbeil [10] for ductile solids failed under fatigue. This study is concerned with a new theory of fatigue crack growth (FCG) in ductile solids based on the total plastic energy dissipation per cycle ahead of the crack tip. The FCG is explicitly given in terms of the total plastic dissipation par cycle and the plane strain fracture toughness of the material from the equation:

$$\frac{1}{t_0} \frac{da}{dN} = \frac{1}{G_C} \frac{dW}{dN} \tag{3}$$

where G_c is the critical energy release rate. In this instance, typical plots of the rate of irreversible plastic work as a function the crack propagation rate are constructed. These plots for 20%, 25%, 30% and 35% of yield stress are shown in Fig. 6. It is observed that both damage mechanisms are well separated and each slope would represent an independent resistance to fatigue crack propagation. It is found that the brittle regime critical energy release rate so calculated lays between 97.7 J/m^2 and 264 J/m^2 and these values are quite small compared to the measured energy rates from potential energy evolution.
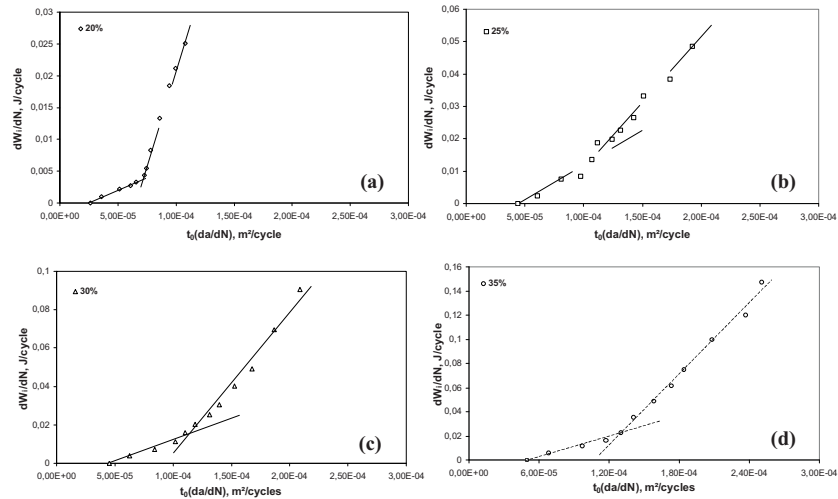
Fig. 6. Rate of irreversible work spend on deformations as a function of fatigue crack growth rate at (**a**) 20%, (**b**) 25%, (**c**) 30% and (**d**) 35% of applied stress

The ductile regime energy is important as it considers a lot of energy spent on damage and high deformation. There is a consistent evolution of calculated G_c as this value is much higher when ductility becomes important. This approach is interesting as it allows separating brittle from ductile contributions in a given FCP test. The use of microscopy enables to confirm the extents of each mechanism from fracture surface analysis and damage dissemination within PE. Compared to long-term hydrostatic strength (LTHS), FCP may be considered as a more efficient approach since it helps produce BDT in much shorter times.

7. Wear evolution on polyamide 66

Figure 7 is a view of new and used polyamide gears. It is observed that wear changes teeth shapes and such result allows measuring wear evolution. In Figs. 8 and 9, the evolution of wear as a function of number of cycles for the 19 teeth, in dry condition, detergent water solution and water is illustrated. It can be clearly seen that wear behavior on the right flanks is not the same for all wheel teeth. In all conditions, it appears that the most sensitive tooth to wear is the flaw molding injection tooth and the less sensitive is the opposite tooth. As far as the teeth are away from the injection tooth, as they are more resistant to wear. A conventional trend is obtained throughout the three testing conditions for both flanks. The first feature to sort out is that wear is faster in wet condition then in dry conditions. This is obviously as explained above, due to water absorption that gives more volume to the tooth. When adding detergent in water solution, wear drops down. In fact, the presence of soap helps the gears to slide easily rather than in water, therefore wear phenomenon is reduced. In dry conditions, wear occurs because of dry friction but the temperature generated is soon dissipated as the next meshing tooth occurs. Three phases characterized by a running in, a youth and a final phase are observed. Regarding trends on the right flank, the running in phase for the three conditions is reached within the 250,000 cycles where 17.22 mm^3 in water, 13.08 mm^3 in detergent and 11.27 mm^3 in dry conditions. The youth phase longs up to 1,250,000 cycles in water, 1,500,000 cycles in detergent and 1,750,000 cycles in dry conditions; the corresponding values in volume reduction are 25.23, 20.22 and 16.86 mm^3.
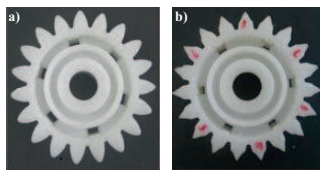
Fig. 7. Polyamide pinion (PA66): (**a**) initial shape, new gear; (**b**) final shape, worn gear

When the youth phase ends the final phase starts with rapid increase in volume lost until the gears stops after 3×10^6 cycles when significant wear occurs to run out the gears; the corresponding values are 46.88, 36.3 and 29.7 mm^3. As wear is

concerned in polyamide gears, and in order to increase lifetime and reduce energy consumption, it is evident to consider the right flank trend for wear assessment. The wear trend shows a regular evolution from the beginning of the youth phase to the end of the final phase leading to a fitting curve that can be expressed by an equation for each testing condition.
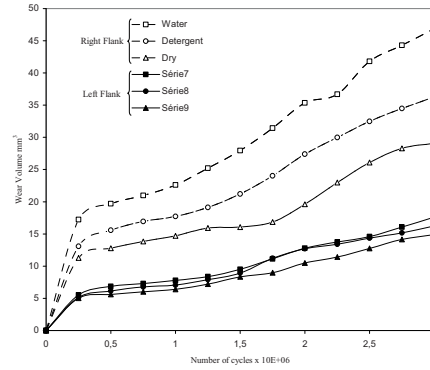
Fig. 8. Evolution of wear volume in flanks of a polyamide pinion tooth
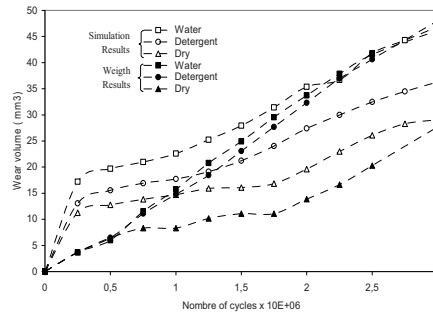
Fig. 9. Comparative wears volume removal between acquisition system simulation (dimensional measurements) and weight results

In water solution:
$$W_{wat} = 15.97 \cdot e^{3.7\,10^7\,N} \tag{4}$$

In detergent solution:
$$W_{det} = 12.43 \cdot e^{3.7\,10^7\,N} \tag{5}$$

Dry conditions:
$$W_{dry} = 10.26 \cdot e^{3.4\,10^6\,N} \tag{6}$$

8. Environmental stress cracking

Perhaps this topic is the most complicated when considering mechanisms of failure in PE pipes. It is a mixture of aspects in connection with material integrity, environment parameters and the stress-strain relationship (Fig. 10). Environmental stress cracking (ESC) occurs when PE or PA is subjected to a combination of a stress field and an environmental agent (chemical). Although, fundamental molecular mechanism of ESC in both PE and PA is still discussed; nevertheless, both ESC and SCG share many similarities, such as load and temperature dependence of failure time, and brittle-like failure surface. Therefore, it is thought that they probably have a common microscopic deformation mechanism that governs failure. If so, it would be valuable to use ESC as a tool to evaluate the long-term behavior of polyethylene and polyamide materials, since the ESC testing times are much shorter compared to other tests [11]. The acceleration process is supposed to be due to the pressure of aggressive agents and to diffusion and/or absorption within crystallites.
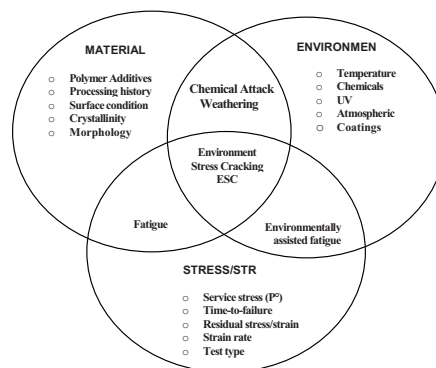
Fig. 10. Interaction between material, environmental parameters and the stress–strain relationship in ESC in polymers

It is concluded that both solvents (mixture of toluene-benzene and dichloro-methane solution) are very aggressive to PE pipe materials. On the other hand, detergents are also aggressive to polyamide materials [12, 13]. The problem is that those solvents could be present in natural gas streams and might degrade irreversibly the polymer parts. The evolution of cristallinity should also be studied and how it is redistributed after, injection moulding, welding; cutting and machining at high speeds [14]. Our studies conclude towards a specific evaluation of ESC of polymers that should be governed by reliability approaches. In a recent work, we have shown that such an approach is desirable as it answers many questions to the uncertainty and probabilistic variable controlling lifetime in polymeric and metallic materials [15]. Therefore, many aspects have to be considered such as the knowledge of thermal history, the degree of molecular interpenetration from both melts and the role of pigments and some additives.

9. Conclusions

Polymers are finding various technical applications in industry due to important advantages. Technical developments of PE and PA are found in long-term performance evaluation and how research is trying to bridge between different approaches such as fatigue and creep. Mechanisms of failure of PE pipes are basically driven towards the understanding of brittleness, as it is the most dangerous for the integrity of a PE underground structure. The study of brittle-to-ductile transition is a potential way to establish PE toughness from short-term fatigue tests. Wear analysis of PA is possible to approach experimentally and integrating the effect of stress cracking environments.

References

[1]   W. G. Perkins. Polymer toughness and impact resistance. *Polym. Eng. Sci.* 39 (12) (1999) 2445–2460.

[2]   R. Seguela. Critical review of the molecular topology of semicrystalline polymers: The origin and assessment of intercristalline tie molecules and chain entanglements. *J. Polym. Sci. Part B: Polym. Phys.* 43 (2004) 1729–1748.

[3]   Y. G. Hsuan and T. J. McGrath. HDPE pipe: Recommended material specifications and design requirements, Report 429, NCHRP (1999).

[4]   T. Trankner, M. Hedenqvist and U. W. Gedde. Structure and crack growth in gas pipes of medium and high density PE. *Polym. Eng. Sci.* 36(16) (1996) 2069–2076.

[5]   H. B. H. Hamouda, M. Somoes-betbeder, F. Grillon, P. Blouet, N. Billon and R. Piques. Creep damage mechanisms in polyethylene gas pipes. *Polymer* 42 (2001) 5425–5437.

[6]   M. Parsons, E. V. Stepanov, A. Hiltner, E. Baer. Correlation of fatigue and creep SCG in MDPE pipe material. *J. Mater. Sci.* 35 (2000) 2659–2674.

[7]   Y. Zhou and N. Brown. Anomalous fracture behaviour in polyethylenes under fatigue and constant load. *J. Mater. Sci.* 30 (1995) 6065–6069.

[8]   A. L. Ward, X. Lu, N. Brown. Accelerated test for evaluating slow crack growth of polyethylene copolymers in Igepal and air. *Polym. Eng. Sci.* 30(18) (1996) 1175–1179.

[9]   R. Khelif, A. Chateauneuf and K. Chaoui. Statistical Analysis of HDPE Fatigue Lifetime. Meccanica, published on line 3 April 2008, DOI: 10.1007/s11012-008-9133-7.

[10] N. W. Klingbeil. A total dissipated energy theory of fatigue crack growth in ductile solids. *Int. J. Fatigue* 25 (2003) 117–128.

[11] N. Kiass, R. Khelif, B. Bounamous, A. Amirat and K. Chaoui. Etude expérimentale des propriétés mécaniques et morphologiques dans un tube de gaz en HDPE-80. *Mécanique & Industries,* N° 7 (2006) 423–432.

[12] K. Mao. Gear tooth contact analysis and its application in the reduction of fatigue wear. Wear 262 (2007) 1281–1288.

[13] C.H. Kim. Durability improvement method for plastic spur gears. Tribology International 39 (2006) 1454–1461.

[14] Brauer, S. Andersson. Simulation of wear in gears with flank interference – a mixed FE and analytical approach. Wear 254 (2003) 1216–1232.

[15] A. Amirat, B. Bounamous, R. Khelif, A. Chateauneuf, K. Chaoui. Reliability Assessment of Pipelines Using Phimeca Software. Proceedings of the NATO Advanced Research Workshop on Safety, Reliability and Risks Associated with Water, Oil and Gas Pipelines. Alexandria, Egypt, 4–8 February 2007, pp. 233–259.

On the Structural Integrity of the Nano-PVD Coatings Applied on Cutting Tools

Miroslav Piska, Ales Polzer, Petra Cihlarova and Dagmar Stankova

Institute of Manufacturing Engineering, BUT FME Brno, Technicka 2, 616 69 Brno, Czech Republic

Abstract   Many modern trends in metal cutting, high speed/feed machining, dry cutting, hard cutting and ecological impacts set more demanding characteristics for cutting tool materials. The exposed parts of the cutting edges must be protected against the severe mechanical and chemical loading conditions resulting in wear of tools and quality of products. The paper deals with three modifications of the hard (Ti1-xAlx)N/a nano-crystallites embedded in an x-ray nearly amorphous Si_3N_4 matrix, analyses of the WC carbide-coating interface, its integrity and cohesion to the substrate. Advanced cutting tests and wear morphology in the operation of longitudinal turning of carbon steel C45 were done. Some technological and economical impacts for an application of the coatings are also highlighted that confirms their a very good cutting performance, characterized by the very good of chip formation, mean standard deviation of the machined surface from Ra = 1.00–1.50 μm to Ra = 6.30–12.50 μm (start and end of testing), convenient cutting force composition, tool life 52–56 min (compared to the expected 15–20 min) for cutting speed 130 m/min, depth of cut 1.5 mm and feed per revolution 0.18 mm. Two mechanism of wear have been watched – sub-layers delaminating and abrasion.

Keywords: Nano-Composite, Coating, Integrity, Interface, Cutting, Wear.

1. Introduction

Hard coatings for cutting tools can be divided by production methods and physical properties. The coating protects the tool against abrasion, adhesion, diffusion, formation of comb cracks and other wear due to the high strength of their covalent inter-atomic bond, small bond distance, high coordination number and its Vickers hardness HV of 40–60 and >70 GPa [1, 2, 5–9]. The widely used PVD hard coatings are TiN (the long-term standard from the late 1970s), Ti(C,N), (Ti,Al)N, (Al,Ti)N, (Ti,Al,Si)N, (Al,Cr)N and CrN are applicable not only to the carbides, but also on HSS tools. In many cases the deposition of the cutting tool with a hard coating increases cutting performance and tool life in the range of 100–1,200%.

The reasons for the outstanding features of the (Ti, Al)-based coatings [9] can be seen in a very high hardness (25–38 GPa), with relatively low residual compression stresses 3–5 GPa), high hot hardness, resulting in low hardness lost

(30–40%) up to temperatures of 800°C, high oxidation resistance (the same rate for Ti(C,N) at 800°C as for TiN at 400°C) and low heat conductivity (up to 30% lower relative heat indention coefficient than for TiN).

The research of the substrates or the highly protective coating in specific machining operations can have serious impact on machining productivity and economy. The coating industry is enormously innovative today. There is a lot of research and solutions even to improve these outstanding features of coatings, especially the (Ti, Al)N for a suitable combination of ARC and sputtering, an effective filtering of ARC-droplets, an optimization of process parameters like ARC-current, BIAS-voltage, N2-pressure, etc.

Some research works have been focused on a optimization of the crystalline structure to avoid the columnar structure and corrosion, a deposition of the multilayers to increase coating toughness and thickness, convenient addition of other alloying components, such as chromium and yttrium (to increase oxidation resistance), zirconium, vanadium, boron and hafnium (to improve wear resistance) or silicon to increase hardness and resistance against chemical reactions coatings [9].

Nevertheless, the three most important nano-structures are deposited today:

- Nanogradients (with continuous changing of the composition from the substrate to the top of a cutting tool)
- Nanolayers (with typical sublayer's thicknesses of 3–10 nm) and non-linear relation of hardness depending on precisely specified periods of coating)
- Nanocomposites – nanocrystalline grains nc-AlTiN are embedded into an amorphous matrix a-Si3N4 due to the spinodal segregation (silicon is not in the metallic phase); the strong interface hinders grain boundary sliding at crystallite size less than 10 nm

Generally, the coatings can be divided into two main categories:

1. Superhard nanocomposites – ceramic based coatings, e.g. nc-MenN/a-Si_3N_4 (Me = Ti, V), nc-TiN/a-BN/a-TiB2, nc-(Ti1-xAlx)N/a-Si_3N_4. The coatings offer superhardness (H $\geq$ 50 GPa), high resistance to brittle fracture, high thermal stability and oxidation resistance.
2. multi-functional nanostructured coatings – these coatings offer high hardness (20–35 GPa) and excellent wear resistance combined with other important properties, such as high toughness, impact resistance, dry lubrication or biocidal, antibacterial and antifungal properties.

Nevertheless, some typical problems can arise from the application of the hard coatings and structural integrity between coatings and substrate – Figs. 1 and 2, stemming from the technological processes or due to the physical and chemical bonds and imperfections.
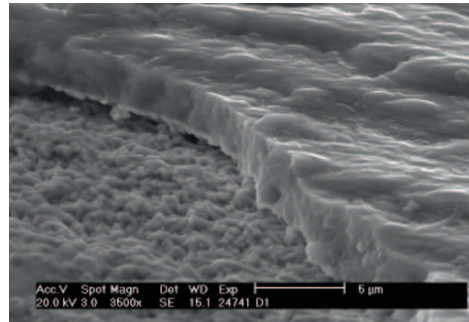
Fig. 1. A decohesion on the tool-coating interface (REM)
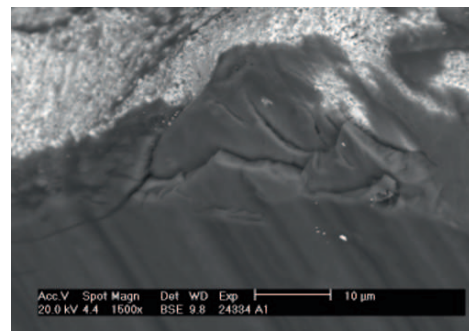
Fig. 2. Flank wear of the multilayered tool (BSE)

2. Theory of the cutting tests

There are many techniques how measure the performance of hard coatings – laboratory techniques, case studies in companies, etc. Machining technologies seem be very effective methods of the coating resistance testing due to complexity of stresses and other impacts on the active surfaces [3, 10]. A precise measurement of cutting forces can directly reflect changes in the geometry of chip–tool contact without any interruption of testing and a manipulation with cutting tool – see Figs. 3, 4 and 5 and Eqs. (1, 2 and 3), based on modern method of metrology [4]. The time development of feed force F_f is linked to flank and the flank wear land, measured normally by the VB parameters [3].

Figure 5 shows differences at the wear land for coated tools and distinguishes the area of pure wear of coating {ABC} and the period of composed wear following (behind the point D) with a substrate share (according to ISO the land between points B–D is known as VB parameter) A similar situation is on the general face between points {EFG}, where the upper surface is compressed and sheared by the chip flow and the point G limits the coating-substrate interface.
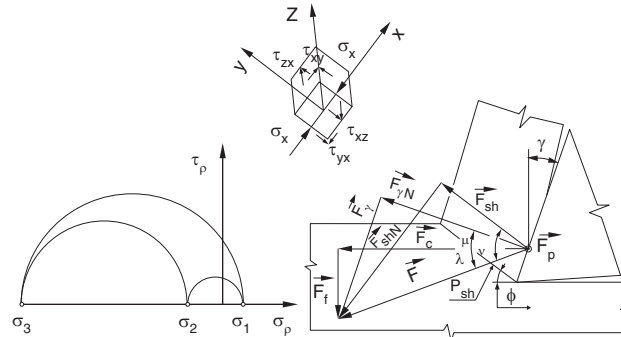
Fig. 3. A principle of tool force composition when orthogonal cutting [11], force and stress composition (in the shear plane)
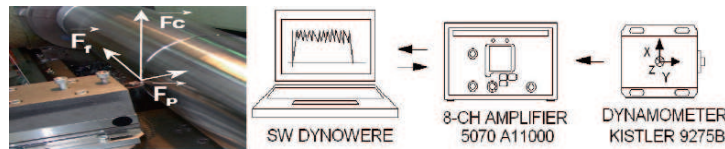
Fig. 4. The system of force measurement with dynamometer Kistler 9257B

Similar calculations can be derived for the rake wear and other force components (cutting force F_c, passive force F_p, coefficient of friction μ cutting force F_c and the other variables (1–3). However, a lot of variables can affect the final cutting result such as technological preparation of the substrate [6, 7], its chemical composition, grain size, phase distribution, thermal stability, hardness/toughness, etc. A special care should be put in the technology of grinding, lapping, polishing, cutting edge chamfering, rounding and pre-preparation of the interface for a coating procedure to avoid such typical problems of decohesion and extensive delamination of the coatings on the rake of cutting tools.

$$dF = \sqrt{\left(\frac{\partial F_{x1M}}{\partial t} dt\right)^2 + \left(\frac{\partial F_{y1M}}{\partial t} dt\right)^2 + \left(\frac{\partial F_{z1M}}{\partial t} dt\right)^2} =$$
$$\sqrt{\left(\frac{\partial F_{c1}}{\partial t} dt\right)^2 + \left(\frac{\partial F_{f1}}{\partial t} dt\right)^2 + \left(\frac{\partial F_{\gamma 1}}{\partial t} dt\right)^2} \tag{1}$$

$$dF_{cl} = \frac{\partial F_{cl}}{\partial t} dt = \frac{\partial F_{cl}}{\partial \gamma_0} d\gamma_0 + \frac{\partial F_{cl}}{\partial r_n} dr_n + \mu \cdot dF_{f1} \tag{2}$$

$$dF_{f1} = \frac{\partial F_{f1}}{\partial t} dt = \frac{\partial F_{f1}}{\partial VB} dVB + \frac{\partial F_{f1}}{\partial r_n} dr_n \tag{3}$$

3. Experimental work, results

Three chemically the same hard nanocomposite coatings (Ti,Al)N in amorphous $Si_{1-x}N_x$ matrix (thickness 2.5–3.0 µm) were tested. Different coating technologies (with purity covering the range from >1000 ppa up to <100 ppa) were used on six multi-carbide indexable turning inserts – ISO P20, code CNMA 120408/ 029 96001527, producer Pramet Tools Ltd. (Seco). A standard series (A) and two R&D PVD technologies (B, C) – from TUM, Germany were tested. To guarantee safe clamping conditions a new turning holder SCLCR2525H09 KT241 was used.

The constructional carbon steel CSN 41 2050.1 (DIN C45), in a blank ϕ200/ 1100 mm, chemical composition according to the Table 1, with pearlitic–ferritic structure was used as workpiece material. The blank was turned to the starting diameter ϕ189/1070 mm. Standardized centres were drilled in each face and a new life centre was used. A universal lathe SU 50A 1500/11kW equipped with a continuous regulation of cutting speed and number of rotations was used. No releasing, chattering or a failure of the apparatus has been watched during all machining tests.

Table 1. Chemical composition of the machined material

Steel DIN C45	Weight content of elements						
	C (%)	Mn (%)	Si (%)	P (%)	S (%)	Cr (%)	Ni (%)	Fe (%)
ČSN 41 2050.1	0.42–0.5	0.5–0.8	0.17–0.37	0.004	0.004	0.25	0.30	rest
Hardness 270–272 HB (minimal tensile strength Rm = 530 MPa)							

Table 2. Cutting data

Cutting condition	unit	Set values
Cutting speed (v_c)	(m/min)	130
Rotations (n)	(1/min)	According to the real workpiece diameter
Feed per revolution (f)	(mm)	0,18
Axial depth of cut (a_p)	(mm)	1.5
Cooling	–	Dry longitudinal turning
Wear criterion (phenomena)	–	Steep rise of cutting forces (~25 N/min), VB ≈ 0.5–0.7 mm, deterioration of machined surface, burrs

All data were worked out with Statgpraphics v.5 software (ANOVA of the time series). Analytical electron microscopy (AEM) was done with REM PHILIPS

XL30. Cutting conditions were set according to the machine, workpiece, machined material and safety regulations – Table 2.

4. Results

All coated tools confirmed a very good cutting performance; a safe chip formation was watched. Analysis of the cutting forces confirmed a gradual rise of all components, so good stability of cutting edge (geometry, substrate, coating) measured and checked by means of specific cutting variables was confirmed. Some differences in cutting forces were watched at the beginning of cutting, but a continuous rise in all force components was watched for all tested tools – Figs. 5 and 6 (selected results).
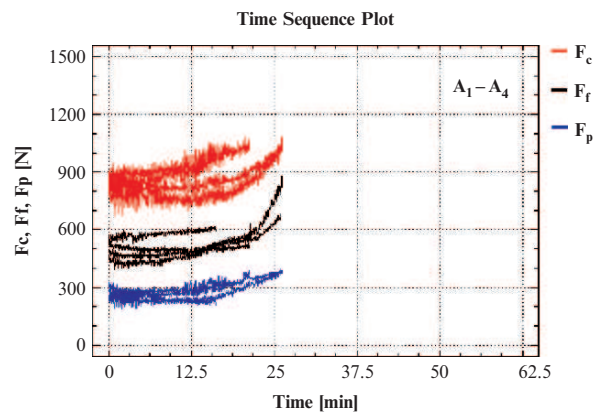
Fig. 5. Cutting performance of the A-tools
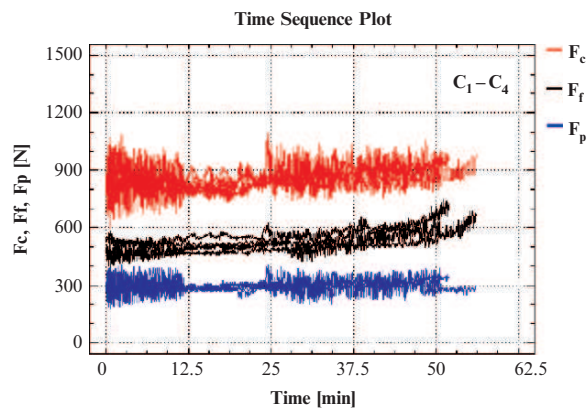
Fig. 6. Cutting performance of the C-tools

Multiple regression analyses of mean cutting forces for all tested series ($\mu \pm 2.\sigma$, reliability 95%) confirmed the following relations (4–6) for the cutting forces (time series with t in minutes):

$$\text{Coatings A: } F_c = 895.012 - 3.080 \cdot t + 0.314 \cdot t^2 \tag{4}$$

$$\text{Coatings B: } F_c = 841.232 - 0.095 \cdot t + 0.026 \cdot t^2 \tag{5}$$

$$\text{Coatings C: } F_c = 844.081 - 0.700 \cdot t + 0.037 \cdot t^2 \tag{6}$$

The mode of loading on the rake consisted mainly from thrust normal stresses (more then 90%). The samples with standard coatings in the end of testing exhibited sharp rise in the feed force reflecting bigger wear land.
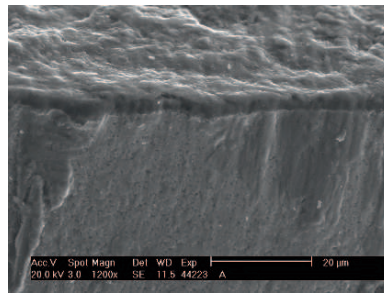
Fig. 7a. Wear of a tool from the series A (BSE)
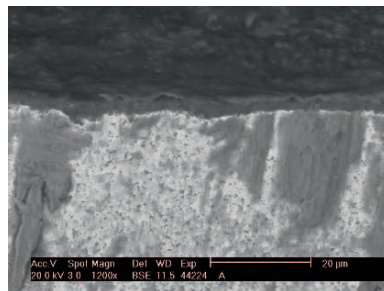
Fig. 7b. Wear of the tool A – (BSE)

The wear morphology of the cutting tool (Fig. 7a, b) showed prevailing abrasive mechanism. No cobalt bleaching on the WC-coating interface has been found. A different integrity of the substrate-coating interface can be recognized from Fig. 8a, b.

On the photos a thin sub-layer between the coating and substrate was observed (containing some impurities and mainly oxides). It was not possibly to quantify the properties of the interphase reliably (by the AEM). However, the tool life increased dramatically (more then 100%) when a production of the interphase layer has been suppressed compared to the standard coating conditions (this phenomena is a subject of a new project).
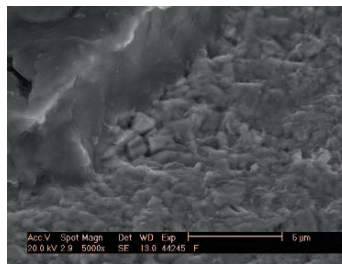
Fig. 8a. Wear of the tool C – SEM
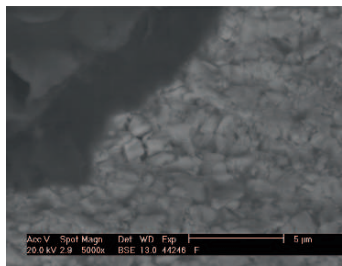
Fig. 8b. Wear of the tool C – BSE

The values for achieved tool lives can be seen in the Table 3, box and whiskers plots (Sheffé 95%) for tested series in the Fig. 9. This analyses denoted a statistically significant differences of the group A against B and C, not B against C. Surface roughness measured with hand device Talysurf Intra showed a rise of mean standard deviation from Ra = 1.00–1.50 μm at the beginning of tests compared to Ra = 6.30–12.50 μm in the end of testing (some local deteriorations of the machined surface by burrs and unsuitable chip was also observed).

Table 3. Tool lives for all tested samples

Samples	A1–A4	Average	B1–B4	Average	C1–C4
Tool lives (min)	16.25	22.34	41.30	48.69	46.80
	21.25		44.10		50.40
	25.60		53.10		51.60
	26.25		56.25		56.25
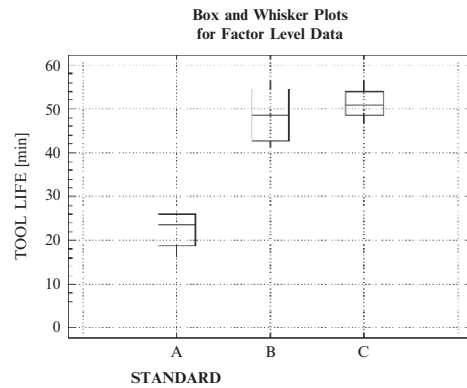
Fig. 9. Tool life box and whiskers plots (95%) for the tested series

5. Discussion

According to Veprek [2], quasi-binary superhard nanocomposites – such as nc-TiN/a-Si$_3$N$_4$ – show oxidation resistance significantly better than (Ti-xAlx)N coatings. Moreover, a Si$_3$N$_4$ barrier in the superhard nc-(Ti1-xAlx)N/a-Si$_3$N$_4$ coatings stabilizes them up to a temperature of 1,200°C and preserve this decomposition to a level typical for cemented carbide substrates. Very similar results and research conclusions for superhard nanocomposites based on spinodal phase segregations suitable for machining purposes were published [11] and wide range of research results were published recently.

6. Conclusions

All tested coated tools protected with hard (Ti1-xAlx)N in Si$_3$N$_4$ matrix confirmed a very good cutting performance in the turning test, overcoming standard nano-coating and tool life by more than 100%. A very smooth, acceptable machined surface was observed. A very slow mean of cutting force rise and good chip formation was achieved in the dry cutting conditions for the series C.

Nevertheless, it has been analysed that the coating-substrate interface (Ti1-xAlx)N/Si$_3$N$_4$ matrix to the carbides/Co-binder influences the mechanical properties and cutting performance of the extremely loaded cutting edges. The purity of coating and interfacial bonding of the nano-crystallites (coherent, semi-coherent bond to crystalline/amorphous matrix and other phases) belong to the most important factors for coatings protecting cutting tools. Ultra-pure target, pre-cleaning of the deposition chamber and fast pumping of residuals can influence the interfacial strength and interphase integrity. Interphase de-cohesion and different size of phases can result in a weakening of the structural integrity, rapid wear of coating and low tool life.

Anyway, nano-structured multifunctional coatings prevail in a strong protective capability of the cutting edges in general, combined with a very good wear resistance. These important functional properties of cutting tools make remarkable technological and economical benefits in such specific applications like high speed cutting, high feed cutting, hard machining, dry machining, etc.

References

[1] Veprek S. et al. (2003). Limits to the strength of super and ultrahard nanocomposite coatings. J. Vac. Sci. Technol. A, Vol. 21, No. 3, pp. 532–545.

[2] Veprek S., Männling H.-D., Jilek M., Holubar P. (2004) Avoiding the high-temperature decomposition and softening of (Al1−xTix)N coatings by the formation of stable superhard nc-(Al1−xTix)N/a-Si3N4 nanocomposite. Materials Science and Engineering A, Vol. 366, Issue 1, pp. 202–205.

[3] Shaw M.C. (2005) Metal Cutting Principles. Oxford University Press, 2nd ed., Oxford (2005), pp. 651, ISBN 0-19-514206-3.

[4] Mrkvica, I. a Moravec, V. Funktionsvergleich von VHM-Bohrergeometrie. In. Science Report Project PL-007 Modern Metrology in Quality Management Systems. Kielce: Kielce University of Technology (2006), p. 181–188. ISBN 978-83-8906-66-4. Bunshah, R.F. (2001) Handbook of hard coatings. Noyes Publications/William Andrew Publishing, New York, p. 550. ISBN 0-8155-1437-7.

[5] Prochazka J., Karvankova, P. Veprek-Heijman M.G.J., Veprek S. (2004). Conditions required for achieving superhardness of ≥45 GPa in nc-TiN/a-Si3N4 nanocomposites. Mater. Sci. Eng., A 384, pp. 102–116.

[6] Rosén J., Larsson K., Schneider J.M. (2005). J. Phys.-Condens. Mat. 17, L137.

[7] Rosén J., Widenkvist E., Larsson K., Kreissig U., Mráz S., Martinez C., Music D., Schneider J.M. (2006). Appl. Phys. Lett. 88, 191905-1.

[8] Baranek, I. (2004) Cutting materials for HSC, hard and dry machining. TnUAD, Trenčín (2004), pp. 112, 1sted., ISBN 80-8075-013-0.

[9] Cselle T., Holubar P. (2003) Driving forces of today´s manufacturing technology. p. Milling III. pp. 33–60, Brno (2003), ISBN 80-214-2436-2.

[10] Marinescu, I.D. et al. (2004) Tribology of abrasive machining processes. 1st ed. William Andrew, Norwich, pp. 724, ISBN 0-8155-1490-5.

[11] Humar, A., Piska, M. (2004) Modern cutting tools and cutting materials. MM Prumyslove spektrum, Vol. 2004, No. Special IX, pp. 112. ISSN 1212-2572.

Investigation of Energy Balance in Nanocrystalline Titanium Under Cyclic Loading

O. Plekhov[1], O. Naimark[1], R. Valiev[2] and I. Semenova[2]

[1]Institute of continuous media mechanics of Russian Academy of Sciences, 614013 Perm, Koroleva 1

[2]Institute of physics of perspective materials УГАТУ, 450000, Ufa, Charles Marksa 12

Abstract   The paper investigates thermodynamics of the cyclic deformation of the bulk nanostructural titanium Grade 2 prepared by the method of intensive plastic deformation. The peculiarities of energy balance in nanocrystalline titanium were investigated using IR techniques for fast determination of the fatigue limit. The polycrystalline titanium exhibits an ordinary behavior. After passing the fatigue limit the temperature rises abruptly due to a sharp change of the damage accumulation kinetics. The dependence of temperature kinetics on the stress amplitude in the nanocrystalline titanium is linear up to a failure of the specimen. This fact allows us to conclude that nanocrystalline titanium, characterized by a specific state of the ensemble of grain-boundary defects, has a unique structural mechanism for energy absorption and dissipation and can use this mechanism both at small and high stress amplitudes. Based on these experimental results and our previous theoretical investigation on collective properties of mesodefect ensemble we propose to investigate a poly-nanostructural transition in metals by analogy with phase transitions.

Keywords: Nanocrystalline Titanium, Cyclic Loading, Energy Absorption Mechanisms.

1. Introduction

Recent discoveries of the unique properties of bulk submicrocrystalline materials (BNM) (unusual mechanisms of deformation, anomalies of conductivity, magnetic and optical properties) have given an impetus to a new scientific direction – nanotechnology. Physical and mechanical properties of solid nano- and mesostructural media offer unique possibilities for electronics, medicine, various technical applications, for instance in the field of aero-space technologies.

At present time, two general approaches to the development of BNM are considered. The first approach, the so-called "bottom-up approach", involves compaction of the nano-size powders (ultra disperse powders can be obtained by gas condensation in the inertial atmosphere or by plasma-chemical method, aerosol and chemical synthesis, and also by grinding of powders in a spherical mill, etc.). Some of these methods have been successfully used for creation of BNM and serve as a basis for studying the structure and properties in the nanocrystalline state.

At the same time, development of these methods represent considerable problems related to residual porosity formed at compacting of bulk material, pollution of samples during powder preparation or their consolidation.

The second approach, originally proposed by V.M. Segal and developed by R.Z. Valiev [1], is widely known as the "top-down approach". According to this technique, the formation of BNM is by grinding of the initial microstructure up to a nano-size scale under intensive plastic deformation (IPD). The IPD methods provide refinement of the grain structure in various metallic materials, however, the character of grain structure (size and shape of grains, types of grain size, phase structure, etc.) depends on the processing conditions, phase structure and initial microstructure of materials. IPD processing leads to the formation of ultra fine grains separated by nonequilibrium grain boundaries. This state is characterized by generation of high density lattice defects and grain boundary defects with long-range correlation properties.

The BNM prepared by the methods of intensive plastic deformation are characterized by specific state of the ensemble of grain-boundary defects with long-range spatial correlation that provides a unique mechanical behavior of the material. Physical properties of BNM are defined by the length and intensity of the grain boundaries, which for the grain sizes of about 10–100 nm contain 10–50% of atoms of the material. Hence, the transition to bulk nanocrystalline state is characterized by pronounced scaling effects and a change of the material properties caused by a decrease of the grain size and increasingly growing role of the grain boundary defects. One of the most important questions in studying the BNM physics is the existence of a sharp boundary between the bulk polycrystalline and nanocrystalline state, i.e. the existence of an area below some characteristic grain size, where the properties are characteristic of a nanocrystalline solid. There is also a thermodynamic statement of the problem, which considers the analogy of the transition from polycrystalline to nanocrystalline state with the first kind phase transition. An effective method for studying material properties under transition to nanocrystalline state is the analysis of energy absorption mechanisms, which by analogy with phase transitions can lead to qualitative changes in materials with fine-grain structure related to the specific interaction between the grain boundary defects. This paper is concerned with investigation of the energy absorption process in coarse grain and fine grain titanium under cyclic loading. It has been found that BNM exhibit energy dissipation anomaly, which can be treated as a result of specific structural evolution in this material.

2. Material and experimental conditions

The samples of titanium Grade 2 in submicrocrystalline state were manufactured by the method of intensive plastic deformation [2] and had the grain size of about 150 nm. The mechanical properties of titanium Grade 2 in polycrystalline and submicrocrystalline state are presented in Table 1.

The geometry of samples is represented in Fig. 1. The cyclic loading was carried out using a resonant electrodynamic testing machine Vibrophore Amsler providing uniaxial loading with the prescribed boundary conditions for stress. The resonance frequency of the sample was 76 Hz. The temperature field was recorded with the infra-red camera CEDIP Jade III. Sensitivity of the camera is higher than 25 mK at 300°K, a spectral range is 3–5 μm, and the maximal size of the frame is 320×240 points. The experimental procedure corresponded to the express IR techniques for determination of the fatigue limit [3]. This technique was based on the hypothesis about correlation of the value of the fatigue limit with the stress threshold of structural evolution. After passing the fatigue limit (loading with stress amplitude higher than the fatigue limit) an intensive structural evolution and, as a result, an intensive temperature rise was observed in the specimens. The fatigue history of each sample including "cyclic" blocks contained 30,000 cycles, with the asymmetry factor of a cycle equaling 0.1.

Table 1. Mechanical properties of titanium Grade 2 at coarse and fine grain states

Type of treatment	Tensile strength, σ_B (MPA)	Yield stress, $\sigma_{0.2}$ (MPa)	Ultimate elongation (δ %)
Initial coarse grain state (grain size 25 μm)	440	370	38
IPD + hot rolling (grain size 0.3 μm)	1090 ± 20	980 ± 20	13 ± 1
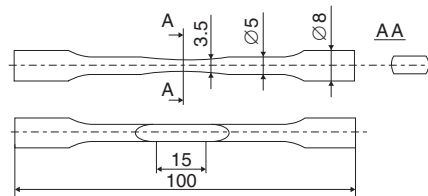
Fig. 1. Geometry of samples used for cyclic tests. The sizes of a gage part of a sample $15 \times 5 \times 3.5$ mm

For each subsequent block the average stress was increased by 10 MPa. At each step of loading a temperature rise in the sample was measured. Between cycles the samples were unloaded and relaxed until they reached thermal equilibrium with the environment.

3. Experimental results

Figure 2 presents the results of experiments. The polycrystalline titanium shows nonlinear two-step growth of heat dissipation.

According to the used technique the point of crossing of straight lines in Fig. 2 determines the value of the fatigue limit for the coarse-grained titanium (the average stress is 80 MPa, the maximal stress is 145 MPa).
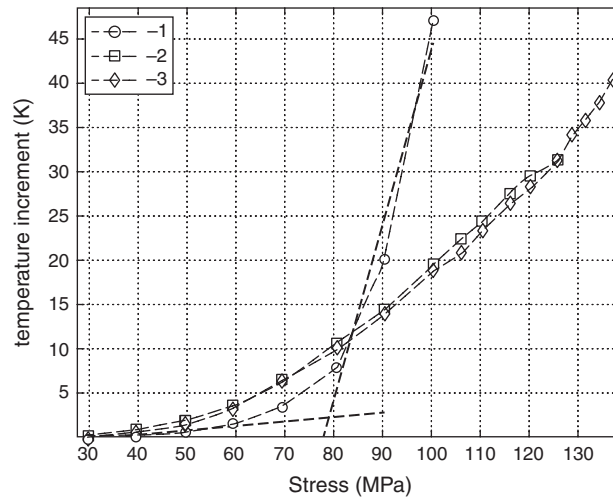
Fig. 2. Mean temperature increment of titanium samples in coarse-grained (curve 1) and nano-crystalline states (curves 2, 3) versus mean stress; dashed lines determine approximately the value of fatigue limit (the stress corresponding to the knee point)

Experiment with the coarse-grained titanium was stopped before failure in the case when the sample temperature overran a working range of the camera with exposition 1100 μs (75°C).

The results of infra-red scanning show that cyclic loading of nanocrystaline titanium is accompanied by a qualitative change in the mechanisms of dissipation. At small stress amplitudes the average temperature of the sample with a fine grain structure insignificantly exceeds the temperature of the coarse-grained titanium sample. At the stress of about the fatigue limit the picture qualitatively changes. For the stress higher than the fatigue limit of the coarse-grained titanium the increment of temperature in the nanocrystalline sample is much less than in the samples in a polycrystalline state. A linear dependence of the temperature growth rate on the average stress was observed for all fatigue histories of nanocrystalline samples.

The temperature of samples is stabilized approximately after 20,000 cycles which reflects the ability of the samples with submicrocrystalline structure to form an equilibrium defect system (probably grain boundary defects) and qualitatively confirms the theoretical result about the formation of defect "lattice", whose characteristic size (density of dislocation) homogeneously increases with increase in the average stress.

   Submicrocrystalline samples during cyclic loading experienced brittle failure, which occurred at the stress amplitude 35–40% higher than in titanium samples in an ordinary polycrystalline state.
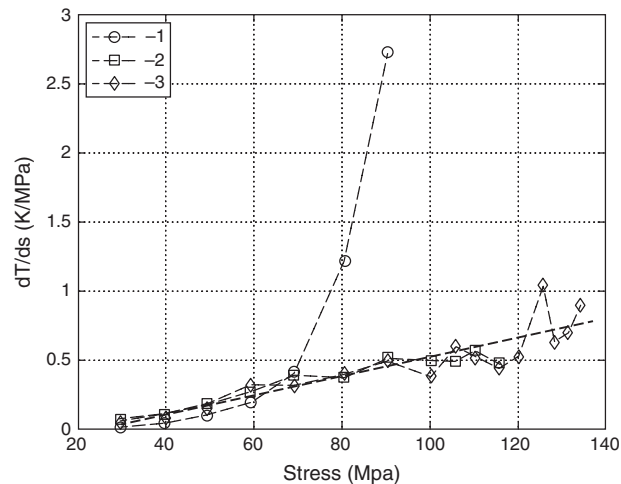
Fig. 3. The plot of mean temperature growth rate versus mean stress for coarse-grained (curve 1) and nanocrystalline titanium (curves 2, 3); dashed line denotes linear approximation of curves 2, 3

4. Discussion

Intensive plastic deformation of titanium leads to the formation of ultrafine-grained nonequilibrium structures containing high density lattice and grain boundary defects with long range elastic stress fields. This circumstance allows us to consider nanostructural state of materials as metastable. As a result the plastic and/or cyclic deformation of these materials is accompanied by anomalies of energy dissipation and absorption. The earlier developed statistical-thermodynamic theory of solids with mesodefects allowed us to define a new class of the critical phenomena caused by collective behavior of the ensembles of dislocation defects - structural-scaling transitions, and to suggest an explanation of the laws governing the transitions from polycrystalline to bulk nanostructural conditions [4].

   The main feature of this new class of the critical phenomena, which is characteristic of nonequilibrium systems with defects, is the existence of additional order para-meter – the parameter of structural scaling depending on the scale characteristics of materials and the interaction between the defects. The thermodynamics and phenomenology developed on the basis of the statistical description is the generaliz-ation of the Ginsburg-Landau approach. It allowed us to establish qualitatively different dynamics of structural-scaling transitions in the corresponding areas of structural scaling parameters. These dynamics were defined by the types of collective modes of the defect ensembles typical for quasi-brittle, plastic and bulk

nanocrystalline conditions. Kinetics of the specified order parameters defines a relaxation ability of a material during formation of plastic shifts; the characteristic features of transitions from disperse to macroscopical destruction, the law of absorption and dissipation of the energy during deformation.

Qualitative distinctions in the behavior of materials in poly- and nanocrystalline states are caused by various types of collective modes in the dislocation substructures (ensembles of grain boundary defects) formed under conditions of structural-scaling transitions. These features are demonstrated most clearly at cyclic loading, in particular, at high cyclic loading – the wide-spread type of deformation characterized by repeated (more than 10^6 cycles) periodic changes in the stress amplitude.

The change in the kinetics of the structural-scaling transitions is determined by the type of collective modes related to a change of deformation mechanisms and, as a consequence, to a change of the system symmetry. It is shown in [4] that a transition from polycrystalline to bulk nanocrystalline state is accompanied by a replacement of the collective modes described by the solution-like solution by spatially located motionless structures formed at some characteristic spatial scales. A qualitative change of the collective modes reflects the change of the deformation mechanisms defined by the threshold stress (it is characteristic of solution-like modes describing localization of plastic deformation) in the case of polycrystalline materials and the formation of "lattices" of the grain boundary defects ("dislocation crystals") in the submicrocrystalline state.

It is well known, that the energy balance at plastic deformation is characterized by dissipation and configuration contributions. The former leads to a temperature rise in the sample, the latter, configuration, is determined by the quantity of energy stored in the elastic stress fields of the structural defect at various scale levels. For polycrystalline materials plastic deformation is realized as a consecutive scale transition to dislocation substructures of greater and greater scales until it reaches the last scale characterized by exhausting shift mobility and formation of the failure centers. For materials with nanocrystalline structure the scale transitions are implicit and deformation is accompanied by formation of the "lattice" of the grain boundary defects and their rather homogeneous growth. A transition to failure in this case is accompanied by formation of a cluster of grain boundary defects and leads to the development of quasi-brittle fracture scenario. This difference in evolution of dislocation substructures for poly- and nanocrystalline materials has qualitative analogy to phase transitions.

The analysis of the data presented in Figs. 2 and 3 confirms the conclusion about the qualitative difference in the energy dissipation and failure mechanisms of polycrystalline and nanocrystalline titanium. In Fig. 3 the dependence of "intensity" of the energy dissipation on the average stress is well approximated by the line for different samples of nanocrystalline titanium. This qualitatively differs from a behavior of the material in coarse-grained polycrystalline state. In the material with a fine grain the fatigue limit cannot be treated as stress value the achievement

of which leads to a qualitative change in the mechanisms of structural relaxation characterized by multi-scale character of the final stage of deformation.

The growth of the average temperature of the nanocrystalline sample, and, hence, the integrated capacity of heat sources caused by material structure evolution is directly proportional to the quantity of energy (a square of the stress amplitude), spent on deformation of a sample for all investigated values of the applied stress. This fact characterizes the ability of a submicrocrystalline material to use effectively the structural (configuration) channel of energy absorption, involving in this process all nanocrystalline volume. Our observation revealed much less difference in the mechanical properties of coarse-grain and fine grain material under cyclic loading than under quasi-static tensile loading.

This difference can be explained by the difference in the defect kinetics under cyclic loading. Actually, the structural relaxation of materials with fine-grained structure is less pronounced than in the coarse-grained (plastic) materials owing to the effects of localization of deformation. This explains a quasi-brittle character of failure of nanostructural materials, which is mainly due to formation of coherent clusters of grain boundary defects. It should be noted that in nanostructural materials (in contrast to coarse-grained) this transition is typically not accompanied by localization of deformation and corresponding structural relaxation.

References

[1] R.Z. Valiev, T.G. Langdon. Principles of equal-channel angular pressing as a processing tool for grain refinement. Progress in Materials Science, Vol. 51 (2006), pp. 881–981.

[2] V. Latysh, I. Semenova, G. Salimgareeva, I. Kandarov, Y. Zhu, T. Lowe, R. Valiev. Microstructure and Properties of Ti Rods Produced by Multi-Step SPD. Materials Science Forum, Vol. 503–504 (2006), pp. 763–768.

[3] M.P. Luong. Infrared thermographics scanning of fatigue in metals. Nuclear Engineering and Design, 158 (1995), pp. 363–376.

[4] O.B.Naimark. On topological transitions in ensembles of grain boundary defects and physics of nanocrystalline state. The Physics of Metals and Metallography, Vol. 84, No. 4 (1997), pp. 327–337.

Behavior of Stainless Steel 316L Under Impact Test

M. Benachour, A. Hadjoui and F.Z. Seriari

Automatic Laboratory of Tlemcen, Department of Mechanical Engineering, University of Tlemcen, BP 230, 13000, 13000, Algeria

Abstract   The stainless steels remain not easily replaceable taking into consideration their high mechanical characteristic (capacity resistance, hardness and impact resistance) what their offer to be used in significant fields such as the nuclear power, the storage of the chemical products. This work presents an experimental study of the behavior of austenitic stainless steel 316L under the impact. The various tests with the impact were led to various temperatures. The increase in the temperatures shows their effects on energy of fracture and tenacity. The Charpy test specimen are used where the influence of the angle and the depth of the notch were studied. The results thus presented show the effect of the temperature on the ductile behavior of material.

1. Introduction

Stainless steels are primarily of steel, i.e. metal alloys Fe–C. The addition of chromium, the essential element to the corrosion of steel, led to the development of various grades of steel, and then stainless qualified. For the phenomenon of passivity of a steel can establish and sustain, it is necessary that the alloy has a minimum chromium content in the range of 10–11%, chromium is in solution [1]. Beyond this concentration, steel form spontaneously in the surface layer and protective continues chromite Cr_2O_3. Austenitic stainless steels at ordinary temperature retain CFC austenitic.

These steels are the group most stainless steels used in practice. Outside of chromium which ensures the inoxydabilité, nickel is the largest of the alloying materials mainly because of its genre. Austenitic stainless steels are commonly called 18–8 or 18–10 of after their respective levels chromium and nickel [2]. Different parameters affect the formation of precipitates of stainless steel such as: temperature, chemical composition, time of precipitation [3, 4]. This precipitation affects the fracture behavior.

Much empirical evidence had been accumulated by the 1920/1930s which showed that high strain rates applied at temperatures close to or somewhat below room temperature in the presence of notches were more likely to result in brittle or sudden failure [5].

This issue was highlighted in a number of catastrophic failures in steel structures and whilst the science of fracture mechanics increasingly allows a rigorous approach to designing against brittle fracture in steel structures, the Charpy test remains as a well recognized method of specifying steel quality. After the mid 1950s, Charpy testing became an essential part of steel specification.

Empirical correlations have been shown between Charpy value and service performance. Temperature is the one parameters effect used and presented in the. The temperature effect between 20°C and 600°C was made for an austenitic stainless steel 316L under a specified environment [6]. The aim of this work is to shown the effect of temperature, dimension of notch of the stainless steel 316L under impact test (Charpy test).

2. Material and impact tests

The Charpy test provides a measure of the energy required to break a material under impact loading. It was first standardized some 60 years ago to allow comparison between different types of steel made from a variety of manufacturing processes. The test consists essentially of a hammer with a given amount of energy striking a notched test piece of fixed dimensions and recording the energy required to fracture test piece at a specific temperature and recording whether the fracture mode was ductile or brittle.

Test specimens of stainless steel 316L were obtained from 12 mm thickness plate, which were produced by rolling. Chemical composition of the studied material is shown in Table 1 and mechanical properties are shown is Table 2 obtained by tensile tests [7].

Table 1. Chemical compositions of 316L in wt%

Fe	Cr	Ni	Mo	Mn	N	S	C	Si	P
$62 \div 72$	$16 \div 18$	$10 \div 14$	$10 \div 14$	$2 \div 3$	$0 \div 1$	$0 \div 0.3$	$0 \div 0.3$	0.75	$0 \div 0.45$

Table 2. Mechanical properties

σ_e (MPa)	$\sigma_{0.2}$ (MPa)	σ_r (MPa)	E (GPa)	A%	Z%
378	390.54	710	186.75	51.5	50

Impact test (Charpy test) was performed on pendulum motion "Charpy 300J" shown in Fig. 1. Charpy specimens with U and V notch are obtained in two orientations L-T and T-L. The variation of temperature test is obtained by using an electric furnace (Fig. 2). The Charpy specimens are heated to 500°C and maintained at one hour before the test. Temperatures are measured before each test once the specimen deposited at the sheep pendulum through an electronic thermometer.
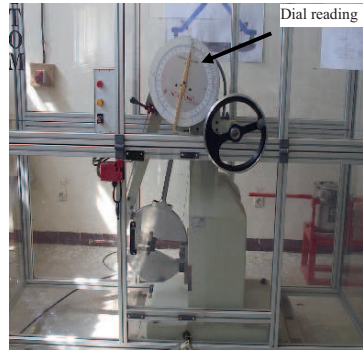
Fig. 1. Charpy pendulum

Fig. 2. Electrical furnace

3. Experimental results and discussions

Once the testing, the absorbed energy is determined on the dial reading (see Fig. 1). The absorbed energy is used to determine the toughness of the material by the relationship:

$$K = \frac{W}{S} \tag{1}$$

W is absorbed energy and *S* the section of the specimen.

3.1. L-T specimen orientation

Figure 3 shows the variation of the tenacity as a function of temperature in U-notch specimen. The increase in temperature from 25°C to 200°C permits to increase the tenacity of the material. Between 25°C and 80°C is the constant tenacity, this present the ductile stage.

The tests on the V-notch specimen (V60°) (Fig. 4) also show the ability to resistance shock by increasing the temperature up to 200°C. Between 100°C and 150°C, tenacity is almost constant which is reflected the same micro structural resistance.
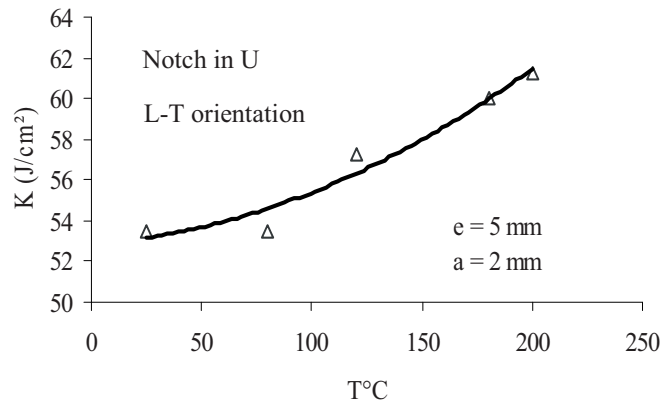
Fig. 3. Tenacity vs. Temperature
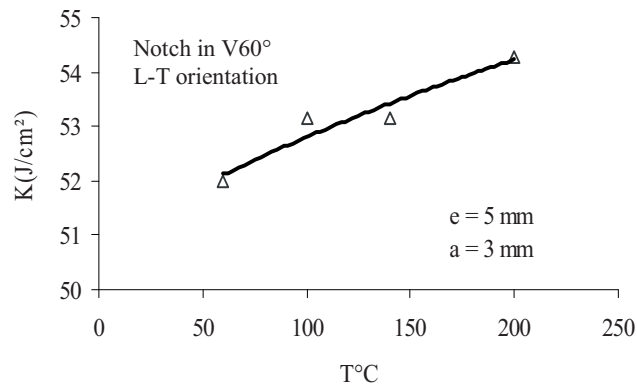
Fig. 4. Tenacity vs. Temperature

3.2. T-L specimen orientation

The impact test performed on specimens machined in T-L orientation (Figs. 5, 6 and 7) shows the same variation of change of tenacity. A slight augmentation of the tenacity is noticed between tests at room temperature and tests at temperatures above nearby. This increase is due to micro structural changes. The resilience has been increased and the material is more ductile.
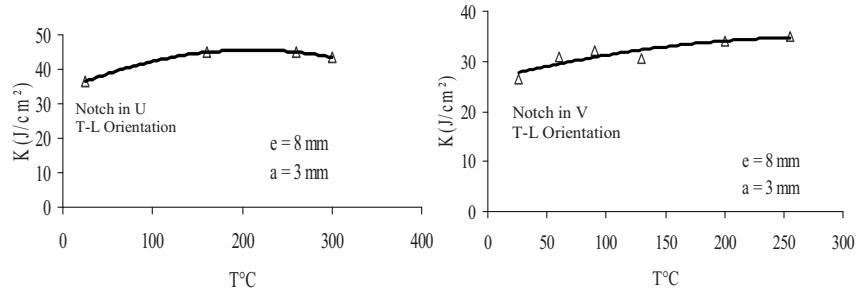
Fig. 5. Tenacity vs. Temperature

Fig. 6. Tenacity vs. Temperature (V45°)
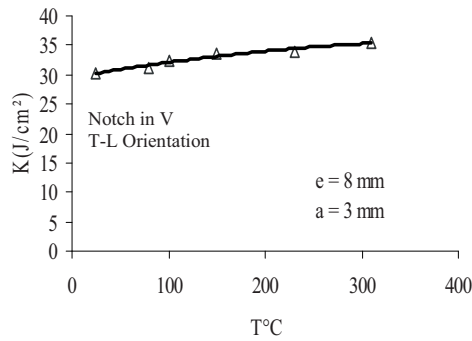
Fig. 7. Tenacity vs. Temperature (V60°)

3.3. Notch effect

Experimental results show the variation in the shape of the notch impact on the capacity of resistance to shock. Figure 8 shows a higher variation of the tenacity for U-notch and V-notch specimen (V60°) with 5 mm of thickness. At high temperatures, a difference on the tenacity is important. The increase in the thickness affects the variation of tenacity (Fig. 9).
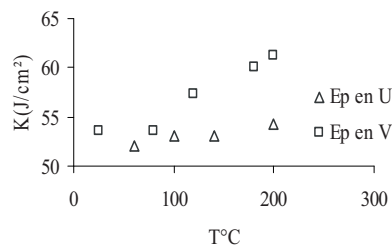
Fig. 8. Notch effect (thickness 5 mm)
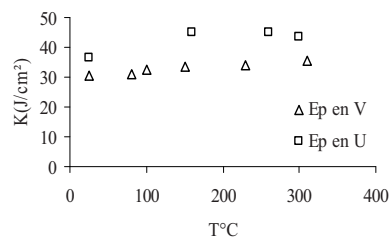
Fig. 9. Notch effect (thickness 8 mm)

The variation of the depth of the notch showed the lower variation of the tenacity (Fig. 10). Figure 11 shows the influence of the angle of notch on the variation of tenacity where it is noticed that for an angle of 60°, the specimen is more resistant to the shock especially at ambient temperature.
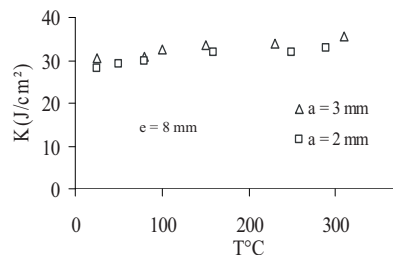
Fig. 10. Effect of depth in V notch   **Fig. 11.** Effect of angle notch
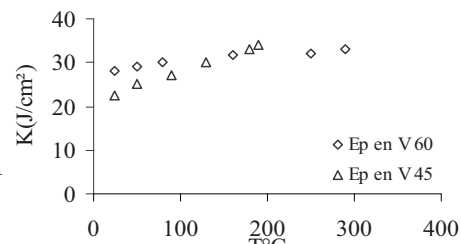
4. Conclusions

The influence of temperature on impact resistance of stainless steel 316L was investigated by performing Charpy tests experiments in the temperature range 20–300°C. The increase in the latter makes the material 316L ductile. The influence of different geometric parameters were highlighted namely the shape of the notch (U or V), the angle notches. For the same temperature and thickness, the U-notch specimen presents greater resistance comparatively to the V-notch specimen. For the same V-notch specimen, the increase of the angle provides superior toughness (tenacity).

References

[1] Bernstein, I.M. and Peckner, D. (1977) Handbook of stainless steels. McGraw Hill, New York.

[2] Bucher, L. (2004) Etude de l'endommagement en fatigue thermique des aciers inoxydables F17TNB et R20-12 pour application automobile. Doctorat thesis, Ecole des Mines de Paris-France.

[3] Weiss, B. and Stickler, R. (1972) Phase instabilities during high temperature exposure of 316 austenitic stainless steel. Metallurgical Transactions, 3: 851–866.

[4] Sourmail, T. (2001) Precipitation in creep resistant austenitic stainless steels. Materials Science and Technology, 17: 1–14.

[5] History of Brittle Fractures (2007). http://www.steeluniversity.org. June 2007.

[6] Mendez, J. (1999) On effect of temperature and environment on fatigue damage processes in Ti alloys and in stainless steel. Materials Science and Engineering A, 263: 187–192.

[7] Seriari F.Z., Benachour M. and Hadjoui A. (2007) Mechanical properties of 316L. First report of mechanical tests, mechanical engineering dept., University of Tlemcen, Algeria.

Spall Fracture in ARMCO Iron: Structure Evolution and Spall Strength

Oleg Naimark, Sergey Uvarov and Vladimir Oborin

Institute of Continuous Media Mechanics of Russian Academy of Sciences, 1 Koroleva str., 614013 Perm, Russia.

Abstract   The experimental study of material responses in a wide range of loading rate reveals some insight into dynamic failure and shows the linkage of solid behavior with the evolution of mesoscopic defects such as microcracks and microshears. This situation is strongly connected to dynamic and shock wave loading, when the time for mesodefect evolution, across different length-scales approaches the characteristic loading times. Taking into account the nature of plastic deformation and failure the key problems are related to the statistics and thermodynamics of the mesoscopic defects. This is revealed in the features of non-equilibrium systems with "slow dynamics". "Slow dynamics" is the consequence of collective interactions between mesodefect modes with slow spatial-temporal response in comparison to the acoustic properties of the material (elastic wave propagation). The existence of these slow modes dominates the failure in dynamically loaded and shocked materials. The original study was conducted to support theoretical results and constitutive relations, which describe a different scenario of damage-failure transition with a self-organized criticality in mesodefect behavior – the structural-scaling transition.

Keywords: Dynamic Fracture, Plate Impact, Spalling, Mesodefect, Self-Similarity.

1. Collective modes in mesodefect ensembles

Statistical theory of the collective behavior of mesodefect ensemble [1] allowed us to describe the phenomenology of solids with mesodefects and the interpretation of failure kinetics as non-equilibrium structural-scaling transition in mesodefect ensembles. The non-equilibrium free energy F represents generalization of the Ginzburg-Landau expansion in terms of order parameters - defect density tensor (defect induced deformation $p = p_{zz}$ in uni-axial case) and structural scaling parameter δ, that depends on characteristic length-scales of mesodefects and plays a role similar to the "effective temperature" in non-equilibrium mesoscopic systems.

$$F = \frac{1}{2} A(\delta, \delta_*) p^2 - \frac{1}{4} B p^4 - \frac{1}{6} C(\delta, \delta_c) p^6 - D\sigma \cdot p + \chi(\nabla_l p)^2 \qquad (1)$$

where $\sigma = \sigma_{zz}$ is the stress, χ is the non-locality parameter, A, B, C, D are the material parameters, δ_* and δ_c are characteristic values of structural-scaling parameter (bifurcation points) that link the range of nonlinear material response to the defect growth. These ranges correspond to the characteristics of the collective modes generated in different ranges of δ, (Fig. 1).
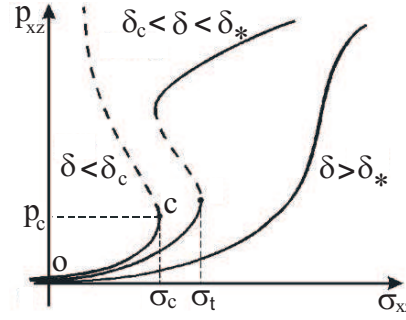
Fig. 1. Characteristic responses on the defect growth

These are responsible for plastic relaxation and the damage-failure transition. These collective modes are the self-similar solutions $p(x,t)_S$ of the growth equations [1]:

$$\dot{p} = -\Gamma_p (\partial F / \partial p - \partial / \partial x_l (\chi \, \partial p / \partial x_l)),$$
$$\dot{\delta} = -\Gamma_\delta \, \partial F / \partial \delta \tag{2}$$

where Γ_ς, Γ_δ are the kinetic coefficients, χ is the non-locality parameter. These solutions have the form of the quasi-periodic solution for the fine-grain state S_1, the auto-solitary waves for plastic strain localization area S_2 and blow-up dissipative structures S_3 for damage localization "hotspots", Fig. 2. The blow-up solution reads.

$$p = g(t) f(\xi)$$
$$g(t) = G(1 - t / \tau_c)^{-m}, \ \xi = x / L_C \tag{3}$$

where τ_c is the so-called "peak time" ($p \to \infty$ at $t \to \tau_c$), L_C is the scale of damage localisation, $G > 0$, $m > 0$ are the parameters describing the non-linearity, which characterise the free energy release rate for $\delta < \delta_c$.

The function $f(\xi)$ determines the distribution of defect density in the damage zone. The characteristic stages of damage-failure transition are similar to the

kinetics of heat localisation in the theory of combustion [2, 3] and include an induction, or nucleation, time and the "peak-time" or growth-rate parameter.
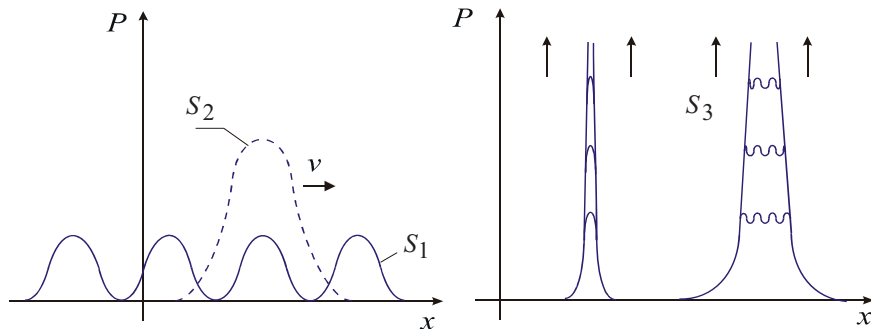
Fig. 2. Dissipative structures

Solution (3) describes the nucleation of simple structure–failure hotspot (localized on the scale L_C) and the generation of complex dissipative structures on the scales $L_D \sim kL_{\tilde{N}}, k = 1, 2...$, due to the interaction on the spatial scales related to the current blow-up localization scales. Depending on the load history (stress amplitude, pulse duration) different scenario of damage-failure transitions can be realized: generation of simple dissipative structure that is characteristic for high amplitude impact load and complex dissipative structures that can be excited by low amplitude but temporally long pulse. The failure wave phenomenon in glasses was linked in [3, 4] with subsequent excitation of simple blow-up dissipative structures with a minimum delay time τ_C of failure front after the back stress front. Similar phenomena were observed in [5] for spall failure as the asymptotic limit of spall failure time, the so-called "dynamic branch under the spall".

2. Experiment

Spalling is a specific kind of fracture which is loading history dependent. The multiscale nature of failure hotspot nucleation was studied in the recovery plate impact test for Armco-iron specimens subject to low amplitude shock. A setup for plate impact experiment has been developed at ICMM UB RAS to study dynamic fracture at strain rates up to 10^6 s^{-1}. Setup consists of 125 mm gas gun and measurement equipment (VISAR).

Soft recovery of a specimen allowed us to investigate structure changes caused by plate impact. Specimen (target) was 10 mm thick and polished with 1 μm diamond powder in order to make sharp wave front. Impactor was made from the same material and was 5 mm thick. So spall should be at 5 mm from the rear (free) surface of the specimen.

Experiments were carried out at a different impactor velocity in order to investigate dependency on loading conditions. Pure (so-called "ARMCO") iron specimens were tested (Table 1).

Table 1. Chemical composition of material under investigation (rest of material – Fe)

C%	Mn%	Si%	S%	P%	Cu%	Cr%	Ni%	Mo%	W%	Al%	N%
0.004	0.04	0.05	0.005	0.005	0.051	0.038	0.057	0.01	0.015	0.07	0.006

All specimens was annealed at 800°C for 4 h. Optical microscopy and 3D profilometer observations was used for investigation of the mechanisms of spall fracture at different scales. Cross-section of the specimen was analyzed. Etching reveals the residual stresses because different rate of etching caused by residual stress leads to formation of corresponding 3D profile (Fig. 3 *left image*). On Fig. 3 one can find slip bands inside grains. These slip bands (pointed by arrows) corresponds to damage accumulation on the "thermodynamic" brunch (stresses from zero to σ_c on Fig. 1). In the material closer to the spall surface (Fig. 4) one
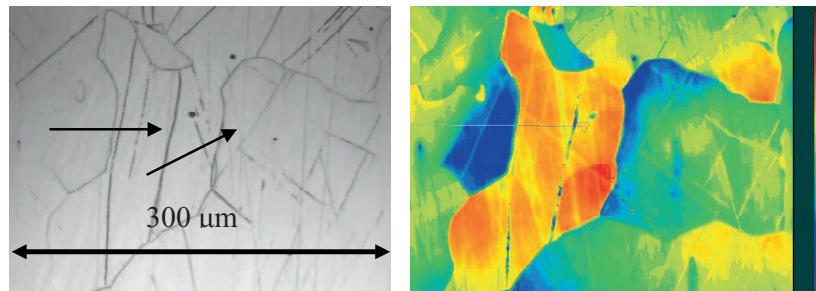
Fig. 3. 2 mm from the free surface. Impact velocity is 375 m/s. *Left image* – optical, *right* – 3D profile
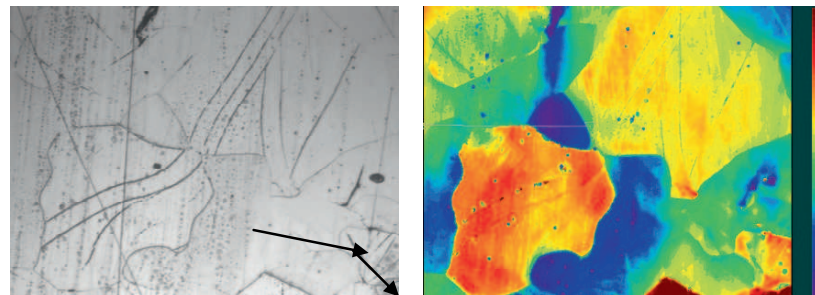
Fig. 4. 3.5 mm from the free surface Impact velocity is 375 m/s. *Left image* – optical, *right* – 3D profile (scale is the same as in previous figure)

can find small cracks. The concentration of these cracks increases with approaching to the spall surface (Fig. 5). This shows that stress level and defect density is approaching to the critical value. On Fig. 6 one can point high level of fragmentation of the grains in the layer close to the spall surface (*left side* of the image) and comparative lower residual stress level.
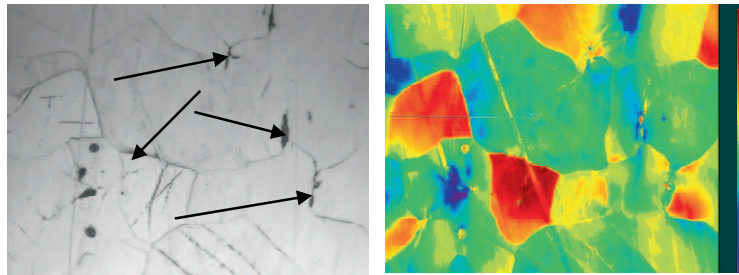
Fig. 5. 4 mm from free surface Impact velocity is 375 m/s. *Left image* – optical, *right* – 3D profile (scale is the same as in previous figure)
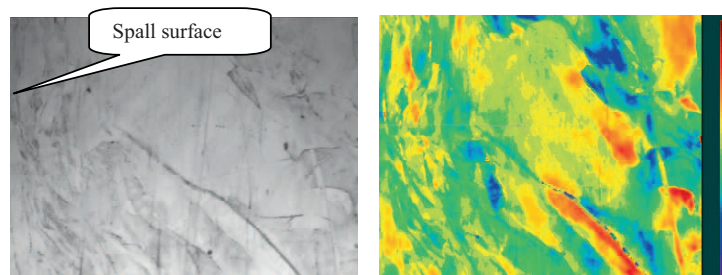
Fig. 6. 4.9 mm from the free surface. Spall surface is on the left impact velocity is 375 m/s. *Left image* – optical, *right* – 3D profile (scale is the same as in previous figure)
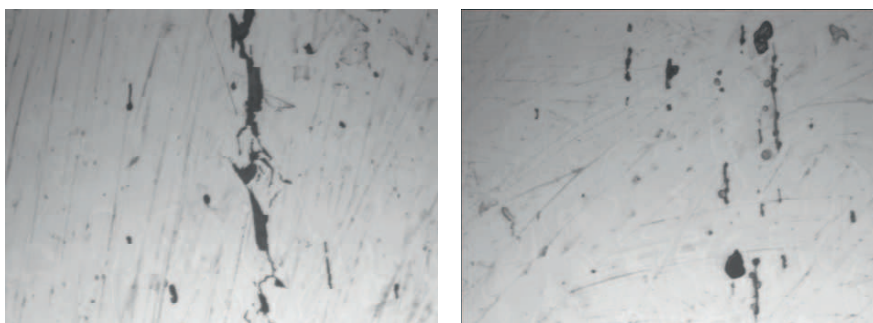
Fig. 7. Microcracks in the bulk of the specimen 3.5 (*left*) and 1.5 (*right image*) mm from free surface (1.5 and 3.5 mm from the spall surface respectively), impact velocity is 250 m/s
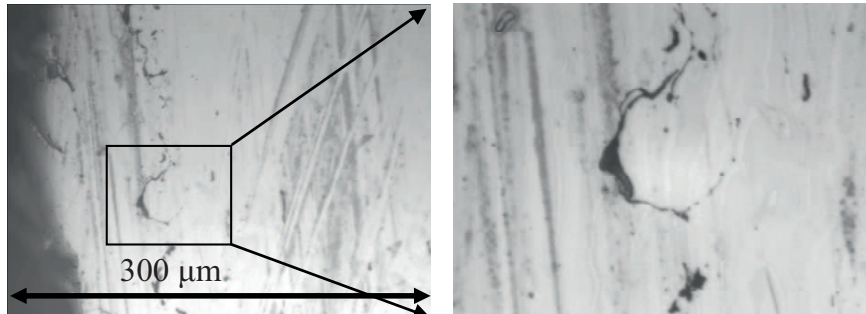
Fig. 8. Microcracks close to the spall surface (on the *right*), impact velocity is 250 m/s

At lower impact velocities type of the failure is different. One can see sets of cracks parallel to the main spall situated quite far (comparing to previous case). This can be explained as follows: as stress level is low there is not enough initial defects generated by the compression pulse. And rate of defect growth prior to reach of critical value is low. So spall failure takes longer time (because induction time is bigger) and area where stress level is enough to create damage is wider (Figs. 7 and 8).

3. Conclusions

Damage-failure transition is described as a specific form of self-organized criticality in the ensemble of mesoscopic defects – structural-scaling transition. Characteristic features of this transition are the generation of collective modes in mesodefect ensemble that are responsible for damage localization and transition to failure. Collective modes have the nature of self-similar solution and describe the blow-up damage localization kinetics with characteristic time (peak-up time) on the set of spatial scales. Mechanism of spall failure can be linked with resonance excitation of blow-up collective modes and has the nature of delayed failure with the delay time corresponding to the peak-time of the self-similar solution.

References

[1] O.B. Naimark. Defect induced transitions as mechanisms of plasticity and failure in multifield continua (review paper). In Advances in Multifield Theories of Continua with Substructure, Birkhauser Boston, Inc., Eds: G. Capriz, P. Mariano, 2003, pp. 75–114.
[2] O.B. Naimark. Collective properties of mesodefect ensembles and some nonlinear problems of plasticity and failure. Physical Mesomechanics, 2003, v. 6, pp. 45–72.
[3] O.B. Naimark, S.V. Uvarov. Nonlinear crack dynamics and scaling aspects of fracture (experimental and theoretical study). International Journal of Fracture, 2004, v. 128, n. 1, pp. 285–292.

[4] O.B. Naimark, S.V. Uvarov, D.D. Radford et al. The failure front in silica glasses, In Fifth International Symposium on Behaviour of Dense Media Under High Dynamic Pressures, Proceedings of the International Conference, Saint Malo, France, 2003, v. 2, pp. 65–74.

[5] O.A. Plekhov, D.N. Eremeev and O.B. Naimark. Failure wave as resonance excitation of collective burst modes of defects in shocked brittle materials. Journal of Physique IV Colloq C., 2000, v. 10, pp. 811–816.

Damage Modelling of Impacted Tubular Structures by Using Material Property Degradation Approach

Mostapha Tarfaoui[1], Papa Birame Gning[1] and Francis Collombet[2]

[1]ENSIETA, LBMS-Mechanics of Naval Structures Laboratory, 2 rue François Verny 29806 Brest Cedex 9, France

[2]Ecole des Mines de Saint-Etienne, France

Abstract   This paper presents a finite element analysis of dynamic tests on thick filament wound glass/epoxy tubes. The overall objective of the current research is to develop progressive failure analysis methodology for laminated composite structures under impact loading conditions. The first part deals with the identification of damage initiation and its development in dynamic tests. Under impact the dynamic responses without damage are well simulated just like the loading in biaxial stress of the tubes. The FEA results of the dynamic tests resulting in no damage appeared satisfactory. The second part of the paper is concerned with an impact model used for damage prediction. Most of the well established failure criteria are included in the damage model. A simple post-failure property degradation scheme is proposed for carrying out the progressive failure analysis. Simulated damage is compared with that obtained experimentally. The sizes of projected and cumulated surfaces are of the same order of magnitude as experimental measurements.

Keywords: Tubular Structures, Damage, Material Property Degradation.

1. Introduction

During their use, it is noted that certain impacted composite cylinders do not sustain operating pressures which correspond to the dimensioning values. However, the damage introduced by accidental impact can jeopardize the capacity to fulfill the designated function. Indeed, taking into account the low speed of the immersed objects, it is a question of studying the impact behavior at the time of a low-energy impact. The lack of understanding of the tolerance to impact for the tubular structures is one of the aspects which prevent greater use.

In order to improve the safety of the composite structures in marine environment, it is important to evaluate and predict the damage resulting from an impact with a low incidental speed and to assess the incidence of the damage compared with a stress in external hydrostatic pressure.

Krishnamurthy et al. [1] made a vast finite element analysis (FEA) study, similar to that of Kim et al. [2], on the dynamic response of thin carbon/epoxy composite cylinders in, subjected to impact by a falling weight. Tubes, 200 mm in diameter, 2.54 mm thick and 420 mm long with 0°, 45° and 90° lay-up are studied. The results are compared with those obtained on models of cylindrical panels of the same thicknesses, with variable curvature. The projectile is 12 mm in diameter with an incident speed of a few meters per second. The Fourier series analysis used to determine the shell deflection during impact as proposed by Christoforou and Swanson [3] and the Choi and Chang criterion [4] is adopted.

They produced results of a parametric FEA study whose variables are the mass of the projectile, incidental speed, panel curve, layers orientations and boundary conditions. They showed that speed had more influence on the contact force than the mass of the projectile, both for elastic and plastic impact. From this point of view the cylindrical shells behavior is similar to that of the plates at the time of impact. As Kim et al. [2] noted, the contact force increases with the curve while the deflection of the target and the contact time decrease.

The damage form and size tend to stabilize towards a peanut shape when the curves are low. However, for large curves, the effects on the damage cannot be correctly studied due to the fact that this curve significantly changes the size of the studied panel and influences its response to the impact.

After carrying out the static, dynamic and implosion tests on the composite cylinders [5–7], the aim of this study is their modeling by using finite element method. Initially, certain models are used for validating material characteristics and predicting their elastic behavior for static and dynamic loadings. Then, the prediction of the damage after impact is studied. For that, analytical models and finite element analysis are presented.

2. Materials, geometry and reference mark

The materials examined in the study were all manufactured using the filament winding process. E-glass fibres were impregnated with a low viscosity epoxy resin. These cylinders were cured at 125°C for 7 h and measured fiber volume fraction Vf was 62%. Porosity was about 10%. The cylinders used have an internal diameter of 55 mm and a wall thickness of 6.5 mm. Samples for impact and pressure testing are 110 mm long. Micrographic observations show a [±55]10 stacking sequence lay-up. Material properties are shown in Table 1. Figure 1 shows the principal notations and coordinates adopted in this study.

Table 1. Material properties used for modeling

Material	E_{11} (GPa)	E_{22} (GPa)	G_{12} (GPa)	ν_{12}
Glass/epoxy ply 0°	49.5	15.9	5.6	0.255

(a) Sample   (b) Tube coordinates and notations
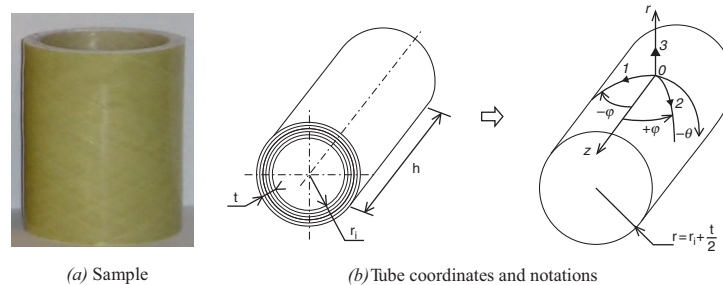
Fig. 1. Materials, geometry and reference mark

3. Finite element analysis (FEA)

The studied cylinders are thick ($d_i/t > 10$) because of dimensioning to the buckling which confers a strong thickness. Furthermore, they are modeled by two types of finite elements, solid and shell elements. The models presented were studied using ABAQUS version 6.2 [8]. Shell elements with reduced integration S4R with Mindlin formulation and hexahedral solid elements, C3D8R, in impact cases available in the library were used with geometric nonlinearity. Based on microscopic observations, the tube's thickness was modeled as shell and solid laminated cylindrical elements with transversely isotropic plies. The impactor, of great stiffness (quenched steel) compared to the composite cylinder, was modeled as rigid body. Modeling as deformable body requires 3D elements which demands considerable computing time. Plate and cradle, were considered also as rigid bodies and were taken as the "master surface". The contact algorithm used is based on the penalty method. Also, a specific contact law is implemented to reproduce local Hertzian contact effects during the quasi-static indentation phase. Meshes consist of isometric elements. For these two types of elements, five integration points are considered in the thickness of each layer. The integration method uses the Simpson rule. The selected elements have linear interpolation. They give better results for modeling contact and impact with the possibility of severe distortions of the elements.

4. Impact without damage

A series of impact tests was performed on 40 cylinders. A new cylinder was impacted for each test, using a 1.6 kg, 50 mm diameter hemispherical quenched steel impactor. Increasing drop height varied the impact energy. In this part, an examination of the prediction of the dynamic responses of the cylinders under impact by finite element analysis is proposed. In order to model the dynamic phenomena under ABAQUS, it is possible to solve the problems with an Explicit or Implicit algorithm.

Our choice being carried on a modeling with shell elements, the simulation of the elastic impact uses the same geometries as those of Fig. 2a. The impact speed is imposed as an initial condition on the projectile at reference point 1.6 kg weight. An example of the recorded force and displacement versus time plot for one of non-damaging tests is shown in Fig. 2, together with a model prediction. Comparatively, the results give a satisfactory prediction to the filtered experimental signals. Moreover, the models in implicit dynamics predict the experimental results well and are invaluable in order to have short computing times compared with those of explicit modeling. Also, regarding the continuation of the numerical study, modeling with Abaqus/Standard would seem more judicious. The other reason for this choice is of a technical nature. Indeed, the subroutine used in Section 5, in order to take into account the damage of the tubes after impact, is available only in the implicit dynamics algorithm in this version of ABAQUS.
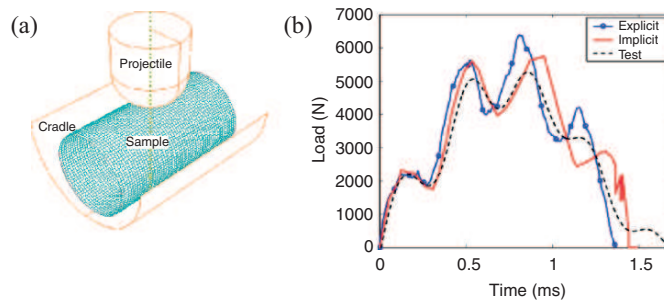
Fig. 2. Model (a) and elastic responses with explicit and implicit algorithms (b), 2J impact (1.55 m/s)
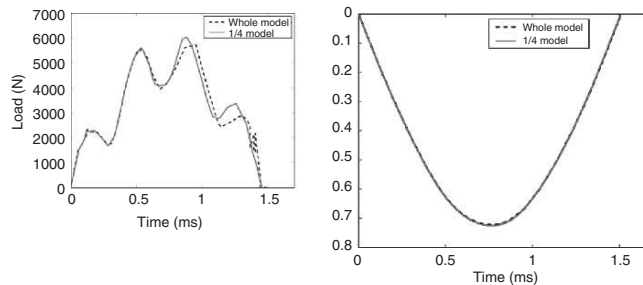
Fig. 3. FEA of a quarter and a whole tube, 2J impact (1.55 m/s)

In order to reduce computing times by the reduction in the element number of the models without harming the quality of simulation results, one strategy consists in exploiting the geometrical symmetries. Knowing that there are terms of membrane/twist coupling related to the $[\pm 55]_n$ lay-up, it should be checked that their effects do not deteriorate the modeling of a quarter cylinder. The results are compared in Fig. 3. The two models give the same responses for the contact load and the displacement of the projectile versus time. This satisfactory result led us to work on a quarter of cylinder with shell elements.

5. Numerical study of the damage

All preceding simulations related to tube behavior are compared and validated by experimental measurements. The tests showed that beyond 4J incidental energy, damage occurs in the wall of the tubes tested. This damage corresponds to through-the-thickness delamination, which propagates as the incident energy increases. The damage mechanism in static punching and impact tests is the same [7, 8]. Firstly, a small local indentation at the contact point is noted for low incident speeds or energies. At that level only the superficial resin coat layer of about 0.3mm thickness is damaged and after the threshold energy level is reached, delamination occurs through the thickness as noted by Alderson and Evans [9]. For energies up to 7 J, transverse intra-layer cracks appear, weakening the already delaminated plies. Delamination propagates through the tube thickness in conical shape of damaged volume for lower energies.

5.1. Damage modeling: material property degrdation

To simulate the evolution of the damage, modeling must take into account the various forms of damage occurring at the impact tests. It is not necessary that the numerical model take account all the physical phenomena observed if their presence does not affect in a relevant way the tubes behavior. It was decided to restore only the damage of the matrix and fiber/matrix shear. For that, the Hashin criteria [10] were used.

The expressions (1) and (2) predict the matrix cracking, respectively in traction and compression, when e_m reaches unity. Equation (3) predicts fiber/matrix shear for a value of e_f equal to 1. These criteria are calculated in all the integration points of all the layers of the cylinder.

$$\left(\frac{\sigma_2}{Y_c}\right)^2 + \left(\frac{\sigma_{12}}{S}\right)^2 = e_m^2 \tag{1}$$

$$\left(\frac{\sigma_2}{Y_t}\right)^2 + \left(\frac{\sigma_{12}}{S}\right)^2 = e_m^2 \tag{2}$$

$$\left(\frac{\sigma_1}{X_c}\right)^2 + \left(\frac{\sigma_{12}}{S}\right)^2 = e_f^2 \tag{3}$$

Table 2. Dependence of the elastic properties on the field's variables FV1 and FV2

State of material	Elastic properties		FV1	FV2			
Undamaged	E_1	E_2	ν_{12}	G_{12}	0	0	
Matrix cracks	E_1	0	0	G_{12}	1	0	
Fiber-matrix de-bonding	E_1	E_2	0	0	0	1	

In progressive failure analysis, once failures are detected in a ply, the corresponding material properties are degraded (the corresponding mechanical characteristic becomes nil). Since damage initiation was observed along all the edges of specimen, a uniform mesh size was used. A standard user subroutine USDFLD in ABAQUS was written, which allows the user to define material properties as a function of the field variables (FV1, FV2) at a material point. The material properties of the laminated tube were defined in order to be dependent upon two field variables. The states of material taken into account are the healthy case, the damage of the matrix and the decohesion fiber/matrix presented in Table 2.

5.2. Damage evolution

The progressive failure analysis methodology uses the C0 four-node shell element S4R of the ABAQUS element library based on the first order shear deformation theory, due to its better performance in large deformation analysis. Loads and displacement versus time are coherent with experimental measurements. The damage is initiated and progresses as much as the tube becomes deformed until maximum deformation has been reached. When the impactor rebounds, the damage does not evolve any more. To validate this modeling method, we measure the evolution of the projected and cumulated delamination area as a function of incident energy. Figure 4 compares the evolutions of the surfaces predicted by the model with experimental measurements [5–6].
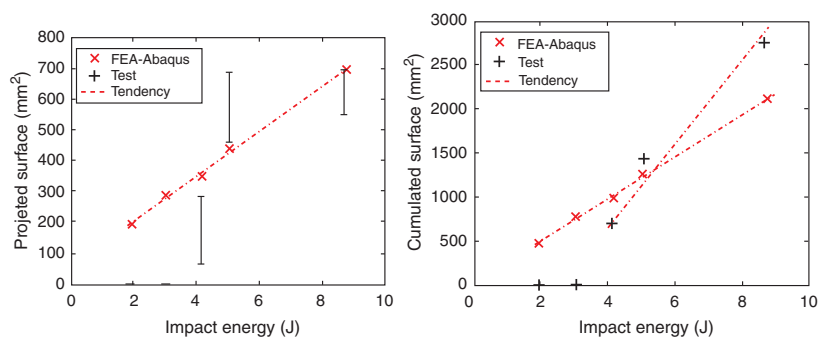
Fig. 4. Comparison of the measured and calculated surfaces damaged

One notices a reasonable coherence between the numerical results obtained and those noted in experiments. The model predicts damage for impact energy of 2-3J, which is not observed on the tested samples. This can be related to the sensitivity of the experimental methods of control for such low amounts of damage.

6. Influence of damage on residual strength

This part aims to simulate on ABAQUS/Standard the composite tubes behavior subjected to external pressure. The implosion tests are presented by Gning et al. in [7]. They are useful for validating the results of modeling for operational tubes. Furthermore, this study makes it possible to appreciate finite element prediction of the numerical analysis of damage influence on the residual behavior in external pressure. The implosion stress is restored in the form of a Pressure-Strain relation.

6.1. Buckling

In order to exploit the symmetries in the numerical analysis of the implosion tests, it is necessary to make sure that the first buckling mode excited is symmetrical. The cylinders buckling calculation reveals the configuration of samples as in Fig. 5, presenting the first mode for a tube embedded at its ends and subjected to circumferential pressure field.

The corresponding critical pressures are indicated. The cylinder is modeled with shell elements. The caps are not taken into account in this analysis. The modes observed do not predict axial buckling because the cylinder is short (low height as compared with the diameter).

The critical pressure of instability of the finite element model is identified to be 110 MPa. The experimental study showed that the implosion pressure of the operational tubes lies between 105–120 MPa. These results validate the buckling calculation of the tubes under external pressure.
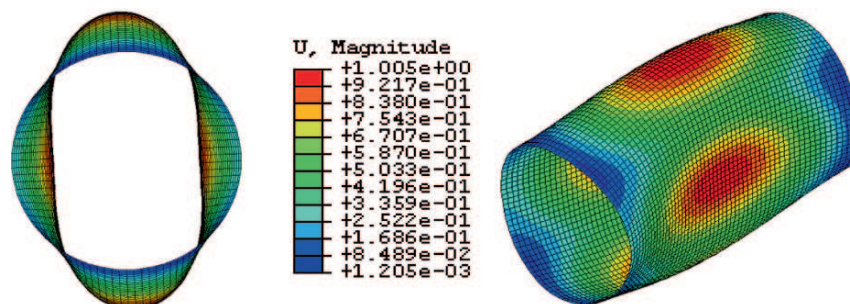
Fig. 5. Strain and critical pressure of the first buckling mode

6.2. Influence of damage on residual strength

The tube behavior under external hydrostatic pressure loading is well predicted numerically. The damage is introduced into the modeling of the impact tests. The purpose of this section is to check the damage influence in the simulation of implosion tests. The steps consist in modeling the impact on a tube then recovering the geometry of the damaged tube for a calculation of loading under external pressure. There are two different simulations. In the first case, the modeled tube interacts with a rigid cradle and projectile, while in the second it is necessary to have the deformable closing caps at the ends of the tube.

To pass from one to the other, it is necessary to safeguard the state of damage (FV1 and FV2) of all the integration points of the tube at the end of the impact calculation, then to reallocate this state at the same points of integration of the tube at the beginning of the implosion simulation. In this second calculation, the initial damage resulting from the impact can evolve with the pressure.

The material characteristics degradation is included when the criteria (3), (4) and (5) are reached. Table 3 shows the external collapse pressure as a function of the impact energy. Up to 5 J the impact residual pressure is retained at the same level as that of undamaged tubes. Beyond this value the loss of pressure resistance is very significant, up to 40% between 5 J and 9 J impacts. Further increase in impact energy leads to a small additional loss and for a 9 J impacted tube the loss of pressure is about 50%. This indicates a significant loss of pressure resistance for quite low impact energies. Simulations of external pressurization are made for tubes impacted between 2 and 9J.

Table 3. Numerical and experimental critical pressures for various energies of impact

Impact energy (J)	FE pressure (MPa)	Tests pressure (MPa)
0	110	113
2	39	110
4	39	–
5	39	111
9	36	72

7. Conclusions

The FEA results of the quasi-static and dynamic tests without damage appear satisfactory. The simulation of implosion of the tubes gives results in coherence with the experimental values. The impact model, including material property degradeation, predicts a truncated form of the damaged volume. The sizes of projected and cumulated surfaces are of the same order of magnitude as experimental measurements.

The simulation of implosion of previously impacted FE models is complex. The study showed an effect of the damage on the residual pressures of implosion with a fall more severe than what is observed in experiments. The validity of the model depends on the choice of the failure criteria and precision on the materials parameters. In our case, Hashin criterion was selected. The identification of the data materials to failure is facilitated by the assumption of brittle elastic behavior. The study showed that there is a strong coupling between the structure and material and it is then important to control the influence of the conditions of development on the limiting values of material. Once validated, the modeling allows for parametric studies.

References

[1] Krishnamurthy K.S., Mahajan P., and Mittal R.K. Impact response and damage in laminated composite cylindrical shells. Composites Structures, 59: 15–36, 2003.

[2] Kim S.J., Goo N.S., and Kim T.W. The effects of curvature on the dynamic response and impact-induced damage in composite laminates. Composites Science and Technology, 57: 763–773, 1997.

[3] Christoforou A.P. and Swanson S.R. Analysis of simply supported orthotropic cylindrical shells subjected to lateral impact loads. Journal of Applied Mechanics, 27: 376–382, 1990.

[4] Choi H.Y. and Chang F.K. A model for predicting damage in graphite/epoxy laminated composites resulting from low velocity point impact. Journal of Composite Materials, 26(14): 2134–2169, 1992.

[5] Gning P.B., Tarfaoui M., Davies P. and Collombet F. Damage development in thick composite tubes under impact loading and influence on implosion pressure: Experimental observations. Composites Part B: Engineering, 36(4): 306–318, June 2005.

[6] Gning P.B., Tarfaoui M., Davies P. and Collombet F. Prediction of damage in composite cylinders after impact. Journal of Composite Materials, 39(10): 917–928, 2005.

[7] Tarfaoui M., Gning P.B. and Collombet F. Residual strength of damaged glass/epoxy tubular structures. Journal of Composite Materials, 41(18): 2165–2182, 2007.

[8] Hibitt, Karlsson, and Sorensen, Inc. ABAQUS 6.3 Example problems Manual. 2003.

[9] Alderson K.L. and Evans K.E. Failure mechanisms during the transverse loading of filament-wound pipes under static and low velocity impact conditions. Composites, 23(3): 167–173, 1992.

[10] Hashin Z. Failure criteria for unidirectional fiber composites. Journal of Applied Mechanics, 47: 329–334, 1980.

Fracture Control for Northern Pipelines

W.R. Tyson

CANMET Materials Technology Laboratory
Natural Resources Canada 568 Booth St. Ottawa, Ontario, K1A 0G1, Canada

Abstract   Natural gas has been discovered in Canada's north, and a pipeline is being designed to bring it to markets in the south. The line will cross regions of unstable terrain, and may be required to withstand substantial deformation from ground movement. Prevention of fracture under these conditions is an engineering challenge. The main features of the fracture control plan being developed will be discussed, in particular the prevention of girth weld rupture and the arrest of running fractures.

Keywords: Pipeline, Steel, Fracture, Toughness, CTOA.

1. Introduction

Canada's conventional reserves of gas and oil have passed peak production, and increasing reliance is being placed on "frontier" resources in the tar sands of Alberta, the east coast offshore, and the north. Major reserves of gas have been identified in the Mackenzie Delta, and a gas pipeline down the Mackenzie Valley is in an advanced stage of planning (line through the Northwest Territories, Fig. 1).

Fig. 1. Planned gas pipelines in Canada's north

237

These pipelines will pass through environmentally sensitive terrain, and the consequences of a leak or rupture would be severe. Also, the unstable terrain can cause deformation of the pipe through ground movement in the form of landslides or frost heave. These conditions place heavy responsibility on an adequate fracture control plan.

2. Fracture Control

There are two main approaches to fracture control at the design stage: prevention of initiation, and assurance of arrest. In the longer term, environmental degradation can lead to corrosion and stress-corrosion cracking, which is outside the scope of this paper and will be dealt with elsewhere.

Fig. 2. Incomplete fracture of Charpy sample of high-strength steel

Regarding crack arrest, the problem is to choose a material that is tough enough to stop a crack within a short distance. This has traditionally been done using a model developed by Battelle in the 1970s, relying on Charpy absorbed energy to characterize toughness and calibrated using steels then available. However, with the introduction of clean steelmaking and advanced rolling practices, steel is now much tougher and may not be completely fractured in a traditional test (Fig. 2). This has led to a need for alternative approaches to characterize the toughness. A leading candidate is the crack-tip opening angle (CTOA) (Fig. 3), which can be measured [1] by analysis of the load-time trace in a drop-weight tear test (DWTT). Methods to measure CTOA are now well advanced, and there is a draft ASTM standard for measurement of CTOA in sheet materials. However, consensus on the best approach for assuring crack arrest in pipelines using CTOA has not yet been established, and it is likely that full-scale burst-test validation of arrest capabilities of candidate steels will be required for some time to come.

Regarding crack initiation, this generally occurs from pre-existing defects. In the case of northern pipelines, the concern is about small imperfections in the girth welds that may escape detection. If the pipe is subjected to bending deformation or tensile loading, and if the toughness is inadequate, these imperfections may grow into through-wall cracks and cause leaks or ruptures. There is a well-developed technology to estimate the material toughness required to prevent crack growth beyond an acceptable amount that began with the introduction of the "COD design curve" in the 1960s.
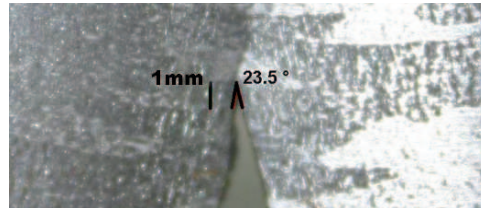
Fig. 3. Crack opening profile of a propagating crack; CTOA = 23.5

This methodology has evolved into the "Failure Acceptance Diagram" approach exemplified by the British standard BS 7910 [2]. The toughness measure used in the FAD is the crack-tip opening displacement (CTOD) or, equivalently, the J-integral. The amount of crack growth corresponding to a given CTOD is measured to generate the "resistance curve", or R-curve. This is then related to the crack driving force in service which can be calculated using finite element methods, and the toughness at an acceptable amount of crack growth or at instability can then be deduced. Traditionally, the R-curve has been measured using a pre-cracked bar subjected to a bending load (Fig. 4). This gives a conservative measure of the resistance and, if the specimen is above a certain minimum size, the R-curve will be a material property, i.e., independent of specimen size.
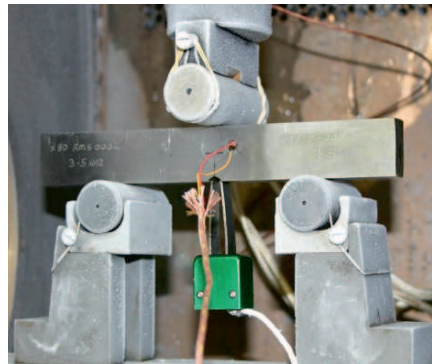
Fig. 4. Test set-up for CTOD measurement

The FAD approach to defect assessment has served engineering practice well. Applied to pipelines, the method enables the selection of materials and welding procedures to guard against brittle fracture and excessive ductile crack growth. The vast majority of applications have been in a "stress-based design" context, in which the applied loads are designed to be below the yield stress of the material. In some circumstances the design stress can be as high as 80% of the yield stress, but even so the total strains are small, i.e. less than 0.5%. However, for pipelines passing through unstable terrain such as Canada's north, it is necessary to design against large-scale ground movement in which the pipe can be subjected to deformations large enough to cause plastic strain in the pipe.

In particular, the girth welds can be subjected to tensile strains significantly larger than 0.5%, and it is necessary to ensure that even in this case any weld imperfections do not cause fracture. To achieve this, the approach of "strain-based design" has been introduced.

2.1. Strain-based design (SBD)

The basic approach to fracture control using SBD is the same as in stress-based design, that is, the crack driving force (J or CTOD) is calculated using finite element methods for a given material (i.e. stress–strain properties) as a function of load and geometry. The results (i.e., critical strain as a function of critical CTOD, yield-to-tensile ratio Y/T, and crack geometry 2c/t and a/t) are usually approximated with an analytical expression for convenience in use. It is then straightforward to deduce the required toughness properties for a given applied strain. The difficulty, however, is that the toughness requirements can be quite severe – so severe, in fact, that the R-curve measured using the conventional bend test may give unacceptably low values. Fortunately, however, it is well known that the R-curve for steels of thickness typical of line pipe is geometry dependent, i.e. that the results depend on specimen size and, more importantly, on mode of loading. The toughness in tension is significantly higher than in bending, typically by a factor of two or so.

A typical result, calculated using the Gurson model for ductile fracture, is shown in Fig. 5. It is important to take this effect into account in order to design against fracture in SBD using high-strength steels. For steels of X80 or X100 grade, the yield-to-tensile ratio Y/T can be high (0.9 or so) and the uniform strain small (10% or so), and it can be a challenge to guarantee adequate toughness, particularly in the heat-affected zone (HAZ) of circumferential girth welds. To take advantage of the full tensile toughness of the material, it is necessary to have an established method for performing the test – in other words, a standardized test. Unfortunately however, such a test has not been standardized in North America, although there is a DNV recommended practice for installation methods involving cyclic strain that includes a fracture test in tension.
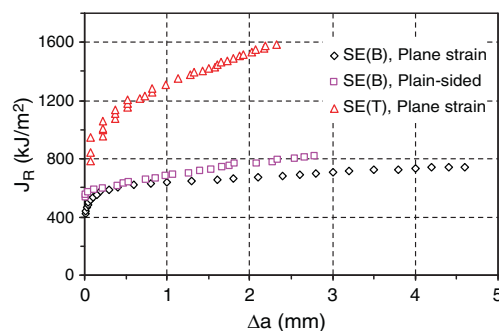
Fig. 5. J-resistance curves evaluated by FEA (Gurson model) for 3D SE(B) and SE(T) samples
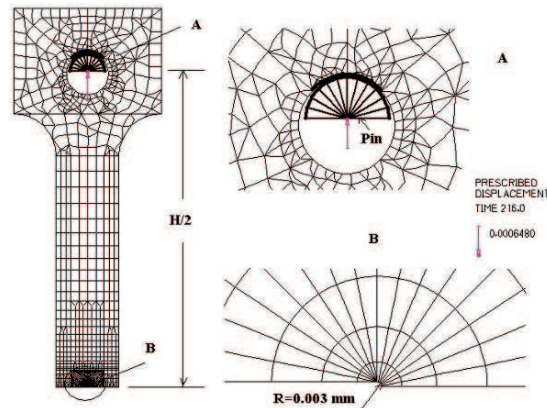
Fig. 6. FEA mesh for SE(T) pin-loaded sample

A pin-loaded sample is shown in Fig. 6. In addition to the crack depth and cross-section width and thickness, the significant variables are the distance between the points of load application H and the mode of loading (pin-loaded as in the figure, or fixed-grip, i.e. clamped). The reason for the relevance of the loading mode is that pin loading allows the specimen to rotate which introduces bending into the specimen, while a fixed-grip condition minimizes the amount of rotation. As the specimen becomes longer (i.e., as H increases), the difference between pin-loaded and fixed-grip conditions diminishes.

2.2. Constraint

The basic reason for the difference in R-curves in tension and in bending is the difference in constraint between the two loading modes. Figure 7 shows a side view of a notched sample loaded in tension in the y direction. The contraction in the through-thickness direction is evident. This contraction gives rise to a strain gradient in the through-thickness direction that generates stresses and causes the central region of the crack front to be in a state of near plane strain. This is the so-called "out-of-plane" constraint, in contrast to the "in-plane" constraint that corresponds to stress and strain gradients in the x–y plane. It has been shown clearly by Wallin [4] that the fracture toughness is controlled by the in-plane dimensions, and especially by the size of the ligament (the distance in the x direction between the crack front and the specimen back plane). The reason for this is that the majority of the crack front is in a state of nearly plane strain even for specimens much thinner than is normally assumed, and it is the constraint resulting from the degree of confinement of the plastic deformation in the x–y plane that dominates the R-curve. In particular, the much more highly contained plasticity in the bend specimen compared to the tensile specimen leads to much higher stresses at the crack tip in bending than in tension. This drives the cracking processes – in ductile fracture, these are microvoid initiation, growth and

coalescence – to completion in the so-called "process zone" at the crack tip more rapidly in bending than in tension and lead to more crack growth in bending.
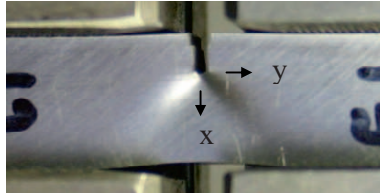
Fig. 7. Cracked sample loaded in tension

Figure 8 shows the stress distribution at the crack tip of a part-circumferential crack in a pipe calculated using 3-D finite element analysis; the HRR curve gives the asymptotic Hutchinson–Rice–Rosengren stress. The crack-tip opening stress $\sigma_{\theta\theta}$ has been normalized by the yield stress σ_0, and the distance r from the crack tip has been normalized by J/σ_0. It is helpful to recall that the CTOD = (1/m) (J/σ_0) where m (= 1 to 4) is a parameter dependent on material and mode of loading. Hence, at a distance of one CTOD from the crack tip we have $r/(J/\sigma_0) = 1/m$. That is, the peak stress in the finite element solution occurs at a distance from the crack tip of the order of one CTOD. The finite element calculations shown in Fig. 8 have been carried out for increasing J. Normalization of J by $b\sigma_0$ (where b is the ligament length) enables comparison of the ligament length with the CTOD. Since $J/(b\sigma_0) = m(CTOD/b)$, this parameter is of the order of the inverse of the ligament divided by the CTOD. In other words, for the range of $J/(b\sigma_0) = 0.0047$ to 0.0645, the CTOD increases from approximately 0.005 to 0.06 of the ligament (for m = 1), i.e. from 1/200th to 1/15th of the ligament. The crack-tip stresses are significantly below the HRR limit even for small J values, i.e. there is significant loss of constraint for this geometry. Note in Fig. 8 that the finite element stresses at a given J value lie at approximately a constant amount below the HRR stress within the region of $r/(J/\sigma_0) = 1$ to 5, i.e. within approximately one to five CTODs of the crack tip. This region is the fracture "process zone" referred to above, within which the micromechanical fracture processes of void growth and coalescence take place. It has also been shown that the loss of constraint in the process zone can be represented by the superposition of a hydrostatic stress on the HRR field. The magnitude of this stress (normalized by the yield stress) has been represented by the Q parameter defined as $Q = (\sigma_{\theta\theta} - \sigma_{HRR})/\sigma_0$, usually evaluated at $r/(J/\sigma_0) = 2$. The value of Q gives a good measure of the extent of constraint loss; constraint loss increases as Q becomes more negative. Since void growth and coalescence are very sensitive to hydrostatic stress, it is expected that at a given value of the crack driving force (i.e., J) the amount of crack growth would depend on the value of Q. That is, Q = 0 represents a highly constrained condition, equivalent to small-scale yielding which is modelled by the HRR field and approximated by the high-constraint bend test. For the toughness test to give a good simulation of service conditions, it is required that the constraint in the test be matched to that in service, i.e. that the J–Q relations be similar.
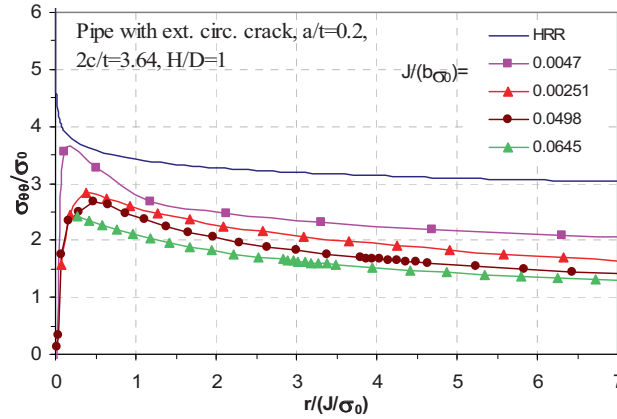
Fig. 8. Crack-tip opening stress for an external part-circumferential crack (3D) in a pipe

Figure 9 compares the J–Q relations for cracks in single-edge-notched tension SE(T) specimens with those for circumferential cracks in pipe (i.e., girth weld defects). In these calculations, the loading arrangements for the SE(T) tests are either fixed-grip (clamped) or pin-loaded, and the spacing H between the load points is given by H/W = 10 where W is the specimen width. This value of H/W has been chosen by DNV [3] for tension testpiece geometry to match surface circumferential cracks in a pipe. Results for crack depths of a/W = 0.2 and 0.5 are shown in the figure. As expected, the J-Q curve for the shallow crack lies below that of the deep crack, i.e., Q is more negative for the shallow crack, corresponding to more constraint loss, at a given value of J. Note also that the mode of loading, i.e. clamped or pin-loaded, has negligible effect on the J–Q relation for this condition of a rather large "daylight" between the loading points.
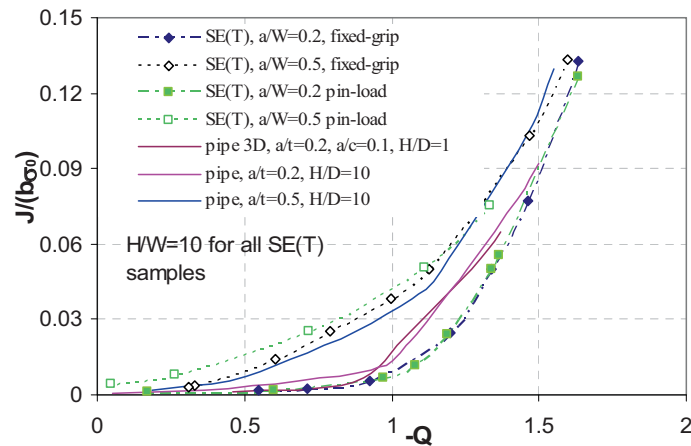
Fig. 9. J–Q relations for pipe and SE(T) samples [5]

It may be concluded from Fig. 9 that a tensile specimen with H/W = 10 loaded in either fixed-grip or pin-loaded mode provides reasonable constraint matching to long surface circumferential cracks in pipes subjected to large-scale bending or tension.

3. Summary

Fracture control is critical for pipelines that traverse environmentally sensitive and unstable terrain such as that found in Canada's north. Adequate fracture control relies on two components: resistance to initiation, and arrest of running fracture. Crack arrest is assured by specifying the impact toughness, traditionally the Charpy absorbed energy CVN. However, it has been found for modern high-strength steels that the CVN may be questioned as a reliable measure of arrest capability, and increasing attention is being paid to characterization of toughness using full-thickness specimens and drop-weight tear testing, with the toughness parameter being the crack-tip opening angle CTOA. Initiation resistance is achieved by assuring that girth weld defects are below a critical size that is calculated using the toughness of the weld. It is argued here that the toughness should be characterized by the CTOD in a tensile test of a pre-cracked sample with the geometry chosen to provide constraint matching to girth weld defects in pipe subjected to bending or tension load.

References

[1] Xu SR, Bouchard R, Tyson WR (2007). Simplified single-specimen method for evaluating CTOA. Eng. Fract. Mech 74: 2459–2464.
[2] Guide on methods for assessing the acceptability of flaws in metallic structures, BS 7910, British Standards Institution, UK.
[3] Fracture control for pipeline installation methods introducing cyclic plastic strain (2006). Recommended Practice DNV-RP-F108, Det Norske Veritas, Norway.
[4] Wallin, KRW (2005). ASTM STP 1461. American Society for Testing and Materials, West Conshohocken, PA, pp 433–453.
[5] Shen G, Bouchard R, Gianetto JA, Tyson WR (2008). Fracture toughness evaluation of high strength steel pipe, submitted to PVP2008. ASME Pressure Vessel and Piping Division Conference, July 27–31, 2008, Chicago, Illinois, USA.

The Influence of the Interface on Fracture Parameters

L. Marsavina[1, 2] and T. Sadowski[1]

[1]Lublin University of Technology, Faculty of Civil and Sanitary Engineering, 20-618 Lublin, Nadbystrzycka 40 street, Poland

[2]POLITEHNICA University of Timisoara, Department Strength of Materials, Blvd. M. Viteazu, Nr.1, Timisoara 300222, Romania

Abstract   The presence of cracks has a major impact on the reliability of advanced materials, like fiber or particle reinforced ceramic composites, and laminated ceramics. The understanding of the failure mechanisms is very important, as much as the estimation of fracture parameters at the tip of the crack approaching an interface. This paper presents the numerical results for singularity order, asymptotic stress field and fracture parameters for a crack ending on a bi-material ceramic interface. The effect of bi-axial loading on asymptotic stress field and stress intensity factors was investigated.

Keywords: Crack, Bi-Material Interface, Singularity Order, Stress Intensity Factor.

1. Introduction

The presence of cracks has a major impact on the reliability of advanced materials, like fiber or particle reinforced ceramic composites, and laminated ceramics. The understanding of the failure mechanisms is very important, as much as the estimation of fracture parameters at a tip of the crack approaching an interface and crack propagation path.

Four major classes of interface crack problems could be identified:

- Crack approaching a bi-material interface, Fig. 1a
- Crack reaching the interface, Fig. 1b
- Crack deflection on interface, Fig. 1c
- Crack penetration the interface, Fig. 1d

Different researchers have investigated the interaction between an interface and a perpendicular or inclined crack. Zak and Williams [1] showed that the stress field singularity at the tip of a crack perpendicular to an interface or terminating at the interface is of order $r^{-\lambda}$, where λ is the real part of the eigenvalue and depends on the elastic properties of the bi-material. Cook and Erdogan [2] used the Mellin transform method to derive the governing equation of a finite crack perpendicular to the interface and obtained the stress intensity factors. Erdogan and Biricikoglu

[3] solved the problem of two bounded half planes with a crack going through the interface.

Bogy [4] investigated the stress singularity of an infinite crack terminated at the interface with an arbitrary angle. Wang and Chen [5] used photoelasticity to determine the stress distribution and the stress intensity factors of a crack perpendicular to the interface. Lin and Mar [6], Ahmad [7] and Tan and Meguid [8] used finite element to analyze cracks perpendicular to bi-material in finite elastic body. Chen [9] used the body force method to determine the stress intensity factors for a normal crack terminated at a bi-material interface. Chen et al. [10] used the dislocation simulation approach in order to investigate the crack tip parameters for a crack perpendicular to an interface of a finite solid. He and Hutchinson [11] also considered cracks approaching the interface at oblique angles. Chang and Xu [12] presented the singular stress field and the stress intensity factors solution for an inclined crack terminating at a bi-material interface. A theoretically description of the stress singularity of an inclined crack terminating at an anisotropic bi-material interface was proposed by Lin and Sung [13]. Wang and Stahle [14] using a dislocation approach presented the complete solution of the stress field ahead of a crack approaching a bimaterial interface. They also calculate the stress intensity factor solutions and the T-stress. Liu et al. [15] determined the mixed mode stress intensity factors for a bi-material interface crack in the infinite strip configuration and in the case where both phases are fully anisotropic. Kaddouri et al. [16] and Madani et al. [17] used the finite element analysis to investigate the interaction between a crack and an interface in a ceramic/metal bi-material.

They investigated the effects of the elastic properties of the two bonded materials and the crack deflection – penetration at the interface using the energy release rate. Marsavina and Sadowski [18] highlighted the effect of shielding and anti-shielding at a tip of a crack approaching a bi-material interface. A biaxial specimen subjected to mixed mode load was studied using finite element analysis. The competition between deflection and penetration of a crack ended on a bi-material interface was investigated by He et al. [19], Zhang and Suo [20], Marsavina and Sadowski [21] among others. This paper presents the asymptotic stress field and the fracture parameters at the tip of cracks ended inclined to a bi-material interface. The numerical results were obtained by considering the two materials as combinations of Al_2O_3 and ZrO_2, often used in ceramic composite materials.
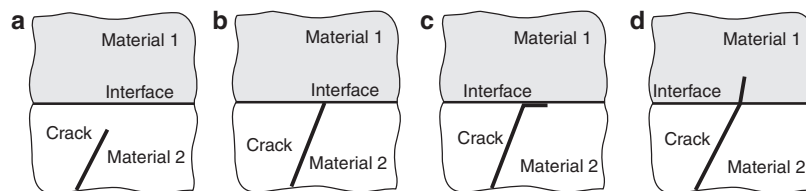
Fig. 1. Classes of cracks and interfaces

2. Singular stress field for an inclined crack terminating at a bi-material interface

Considering the general case of an inclined crack terminating at the interface with angle θ_0 (Fig. 2) the stress and displacement fields could be described by [12]:

$$
\sigma_{\theta\theta,j} + i\sigma_{r\theta,j} = r^{\lambda-1}\left[A_j\lambda^2 e^{i(\lambda-1)\theta} + \overline{B_j}\lambda e^{-i(\lambda-1)\theta} + C_j\lambda e^{i(\lambda+1)\theta}\right] +
$$
$$
+ r^{\overline{\lambda}-1}\left[B_j\overline{\lambda}^2 e^{i(\overline{\lambda}-1)\theta} + \overline{A_j}\overline{\lambda} e^{-i(\overline{\lambda}-1)\theta} + D_j\overline{\lambda} e^{i(\overline{\lambda}+1)\theta}\right] \tag{1}
$$

$$
2\mu_j\left(u_{r,j} + iu_{\theta,j}\right) = r^{\lambda}\left[A_j\kappa_j e^{i(\lambda-1)\theta} - \overline{B_j}\lambda e^{-i(\lambda-1)\theta} - \overline{D_j} e^{-i(\lambda+1)\theta}\right] +
$$
$$
+ r^{\overline{\lambda}}\left[B_j\kappa_j e^{i(\overline{\lambda}-1)\theta} - \overline{A_j}\overline{\lambda} e^{-i(\overline{\lambda}-1)\theta} - \overline{C_j} e^{-i(\overline{\lambda}+1)\theta}\right] \tag{2}
$$

where (r,θ) represents the polar coordinates, λ is the stress singularity (the eigenvalue), $\overline{\lambda}$ the complex conjugate of λ, A_j, B_j, C_j and D_j and their conjugates are undetermined complex coefficients, $j = 1, 2, 3$ corresponding with region "j", and $i = \sqrt{-1}$. The boundary conditions near the crack tip are:

$$
u_{r,1}(r,\theta_0) = u_{r,2}(r,\theta_0) \tag{3a}
$$

$$
u_{\theta,1}(r,\theta_0) = u_{\theta,2}(r,\theta_0) \tag{3b}
$$

$$
u_{r,1}(r,-\pi+\theta_0) = u_{r,3}(r,-\pi+\theta_0) \tag{3c}
$$

$$
u_{\theta,1}(r,-\pi+\theta_0) = u_{\theta,3}(r,-\pi+\theta_0) \tag{3d}
$$

$$
\sigma_{\theta\theta,1}(r,\theta_0) = \sigma_{\theta\theta,2}(r,\theta_0) \tag{3e}
$$

$$
\sigma_{r\theta,1}(r,\theta_0) = \sigma_{r\theta,2}(r,\theta_0) \tag{3f}
$$

$$
\sigma_{\theta\theta,1}(r,-\pi+\theta_0) = \sigma_{\theta\theta,3}(r,-\pi+\theta_0) \tag{3g}
$$

$$\sigma_{r\theta,1}(r,-\pi+\theta_0)=\sigma_{r\theta,3}(r,-\pi+\theta_0) \tag{3h}$$

$$\sigma_{\theta\theta,2}(r,\pi)=0 \tag{3i}$$

$$\sigma_{r\theta,2}(r,\pi)=0 \tag{3j}$$

$$\sigma_{\theta\theta,3}(r,-\pi)=0 \tag{3k}$$

$$\sigma_{r\theta,3}(r,-\pi)=0 \tag{3m}$$

Substituting Eqs. (1) and (2) into Eq. (3) leads to a linear equation system with twelve undetermined coefficients: A_j, B_j, C_j, D_j and their conjugates. From its nontrivial condition it can be obtained the following eigenequation which allows the determination of the singularity order:

$$\left[\alpha+\beta^2-(1-\beta)(\alpha-\beta)\lambda^2(1-\cos2\theta_0)+(1-\beta^2)\cos\pi\lambda\cos(\pi-2\theta_0)\right]^2+ \\ (1-\beta^2)\sin^2\lambda(\pi-2\theta_0)\left[(1-\beta^2)\cos^2\pi\lambda+\beta^2-\alpha^2\right]=0 \tag{4}$$

With α and β the Dundur's bi-material parameters [22]:

$$\alpha=\frac{\mu_1(\kappa_2+1)-\mu_2(\kappa_1+1)}{\mu_1(\kappa_2+1)+\mu_2(\kappa_1+1)} \quad \text{and} \quad \beta=\frac{\mu_1(\kappa_2-1)-\mu_2(\kappa_1-1)}{\mu_1(\kappa_2+1)+\mu_2(\kappa_1+1)} \tag{5}$$

where μ_i and ν_i are the shear modulus and Poisson's ratio of material i ($i = 1, 2$), $\kappa_i=3-4\nu_i$ for plane strain and $\kappa_i=(3-\nu_i)/(1+\nu_i)$ for plane stress. Equation (4) has basically two solutions in the interval 0 to 1 named λ_1 and λ_2. It can be observed that the stress singularity depends on the material parameters and crack inclination angle. For $\theta_0 = 0$ or $\pm\pi$ the considered model from Fig. 1 becomes an interface crack model, and Eq. (4) simplifies to:

$$\beta^2\sin^2\pi\lambda+\cos^2\pi\lambda=0 \Rightarrow \lambda_{1,2}=\frac{1}{2}\pm i\varepsilon \tag{6}$$

Known the oscillatory singularity solution for the interface crack, where the oscillatory index ε:

$$\varepsilon = \frac{1}{2\pi} \ln \frac{1-\beta}{1+\beta} \tag{7}$$

Here if $\alpha = \beta = \varepsilon = 0$ we obtain the well known singularity for a crack in homogenous material $\lambda_1 = \lambda_2 = 0.5$.

For $\theta_0 = \pm \pi / 2$ the case of normal crack to interface Eq. (4) reduces to:

$$\alpha + \beta^2 - 2\lambda^2(\alpha - \beta)(1 - \beta) + (1 - \beta^2)\cos \pi \lambda = 0 \tag{8}$$

According with [3] and shows two equal real eigenvalues $\lambda_1 = \lambda_2$.

An extrapolation method could be applied for the determination of the stress intensity factors. For example if the singularity orders $\lambda_1 \neq \lambda_2$) are real values the stress field could be expresses as:

$$\sigma_{\theta\theta 1} + i\sigma_{r\theta 1} = K_1 r^{\lambda_1 - 1} + iK_2 r^{\lambda_2 - 1} \text{ for } \theta = 0 \tag{9}$$

And the stress intensity factors could be found:

$$K_1 = \lim_{r \to 0}(r^{1-\lambda_1} \sigma_{\theta\theta 1}|_{\theta=0}), \quad K_2 = \lim_{r \to 0}(r^{1-\lambda_2} \sigma_{r\theta 1}|_{\theta=0}) \tag{10}$$

In order to investigate the stress singularity, combinations between two ceramic materials were considered: Al_2O_3 and ZrO_2 and angles between crack and interface from 0^0 to 90^0 with 5^0 increments. The results of Eq. (4) are presented in Fig. 3 for plane strain. Only the stress singularities λ_1 and λ_2 values between 0 and 1 were considered.

Table 1. Material properties and Dundur's parameters

Properties/material	Al_2O_3	ZrO_2
Modulus of elasticity (MPa)	400000	200000
Poisson's ratio	0.22	0.25
Fracture toughness (MPa m$^{0.5}$)	4.5	12
Combinations:	ZrO_2/Al_2O_3	Al_2O_3/ZrO_2
Material 1/Material 2		
Dundur's parameters		
E_1/E_2 (−)	0.5	2.0
α (−)	−0.333	0.333
β (−)	−0.120	0.120

For both material combinations at small angles θ_0 we obtained complex oscillatory solutions for λ_1 and λ_2, than multiple singularities $\lambda_1 \neq \lambda_2$ and double root singularity $\lambda_1 = \lambda_2$ for $\theta_0 = 90^0$. It can be observed in Fig. 3 that higher singularities than 0.5 were obtained when the crack is in the ZrO_2 ($E_1/E_2 = 0.5$), and lower values when the crack was in the stiffer material for $E_1/E_2 = 2$.
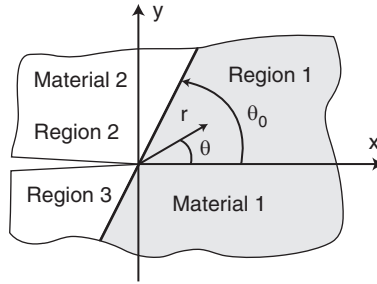
Fig. 2. Crack terminating at a bi-material interface
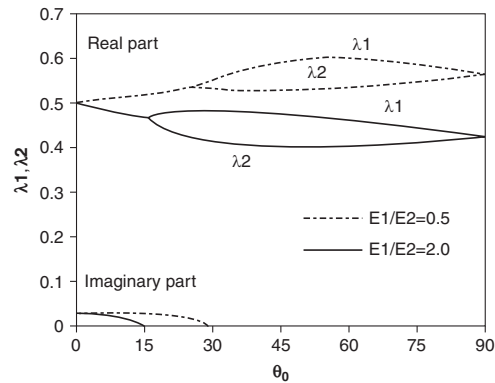
Fig. 3. Singularity orders λ_1 and λ_2 as function of crack angle θ_0

3. The influence of bi-axial loading on the asymptotic stress field

In order to study the effect of the biaxial load on the asymptotic stress field a quarter of a biaxial specimen with an interface was numerically investigated with FRANC2DL code [23]. Plane strain conditions were considered and the model dimension was w = 50 mm. The materials for the analysis were combinations between Al_2O_3 and ZrO_2, Table 1. Quadrilateral isoparametric elements were used for the model with a refined mesh near to crack tip. The mesh consists on 11754 elements connected in 34353 nodes, Fig. 4a. Eight singular elements were placed around the crack tip as a common technique to model the stress singularity, Fig. 4b.

a. Mesh and boundary conditions   b. Crack detail
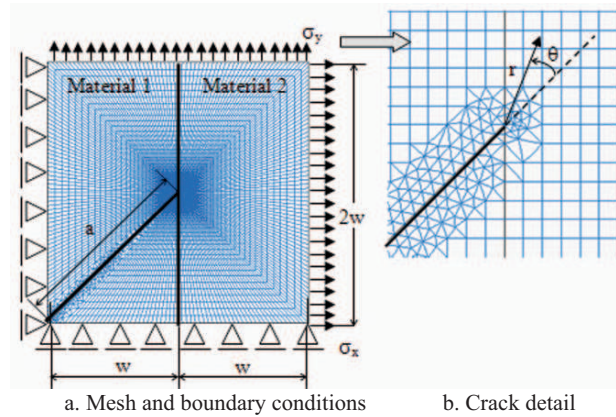
Fig. 4. Mesh, boundary conditions and crack detail for the FEM model

The model was loaded with different combinations of the applied stresses σ_x and σ_y ($k = \sigma_x/\sigma_y$) in order to produce mixed modes from pure Mode I ($k = 1$) to pure Mode II ($k = -1$). The symmetric boundary conditions were imposed. The polar coordinate system (r, θ) was considered with the origin at the crack tip, Fig. 4b.

The singularity orders λ_1 and λ_2 were determined numerically from the asymptotic stress field on a direction $\theta = -15^0$ as the slope ($1 - \lambda_{1,2}$) of the log ($\sigma_{\theta\theta}/\sigma_y$) versus log (r/a), respectively log ($\sigma_{r\theta}\tilde{\sigma}_y$). The results of singularity orders are presented in Table 2.

Table 2. Singularity orders for different combinations of mixed mode loading

Material combination	k	1.0	0.50	0.0	−0.5	−1.0
E1/E2 = 0.5	λ_1	0.5475	0.5566	0.5730	0.5995	0.6501
	λ_2	0.8342	0.8321	0.6342	0.6457	0.5942
E1/E2 = 2.0	λ_1	0.4587	0.4475	0.4296	0.4086	0.3756
	λ_2	0.1955	0.2250	0.371	0.4039	0.4186

The results from Table 2 show that the singularity orders vary significantly with applied load combination and material properties. Figure 5 presents the radial variation of the stresses $\sigma_{\theta\theta}$ and $\sigma_{r\theta}$ for the case when material 1 is ZrO_2 on a radial direction with $\theta = -15^0$ and for $0 < r/a < 0.028$.

For both material combinations it can be observed that the singularity order is changing with the load parameter k. In Table 2 and Fig. 5.a it can be observed that the singularity order λ_1 increase with the increasing of mode II load (decreasing k). The singularity order λ_2 which characterize the singularity of $\sigma_{r\theta}$ decreases with decreasing k. In contrary for the material combination with $E_1/E_2 = 2.0$ the singularity order λ_1 decrease and λ_2 increase with decreasing k.

The circumferential stress distributions are plotted at a distance $r/a = 0.01$ from the crack tip, in order to be in the singularity zone. For the materials combination with $E_1/E_2 = 0.5$ in Fig. 6 are plotted the circumferential variations of the normalized stresses to the applied stress in y direction.
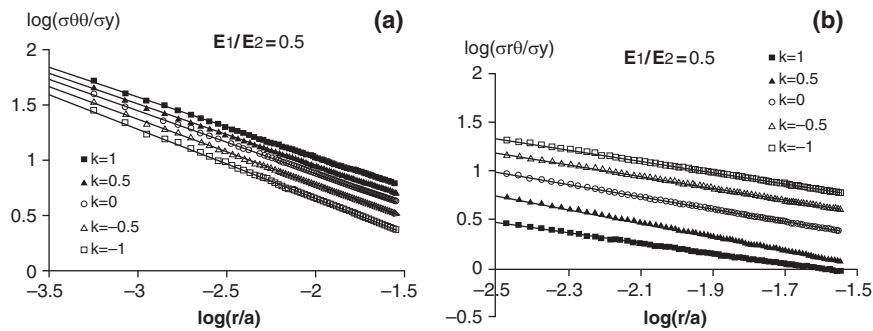
Fig. 5. Logarithmic distribution of stresses on a radial direction ($\theta = -15^0$, $E_1/E_2 = 0.5$)

It can be observed that the distribution of $\sigma_{\theta\theta}$ is changing from symmetric for $k = 1$ to skew-symmetric for $k = -1$, and vice versa for $\sigma_{r\theta}$ distribution. The maximum values for the normal stress $\sigma_{\theta\theta}$ on the crack direction ($\theta = 0^0$) were obtained for $k = 1$ (mode I) and the minimum for $k = -1$ (mode II) Fig. 6.a as we expect. Figure 6b shows that the maximum circumferential stress $\sigma_{r\theta}$ on the crack line ($\theta = 0^0$) was obtained for $k = -1$ (load in pure mode II) and is 0 for $k = 1$ (load in pure Mode I). The maximum values of the circumferential stress $\sigma_{r\theta}$ moves from $\theta = 0^0$ for $k = -1$ to $\theta = 74.5^0$ for k = 1. The stress results from Fig. 6 confirm the stress free boundary conditions on the crack faces ($\theta = \pm 180^0$).
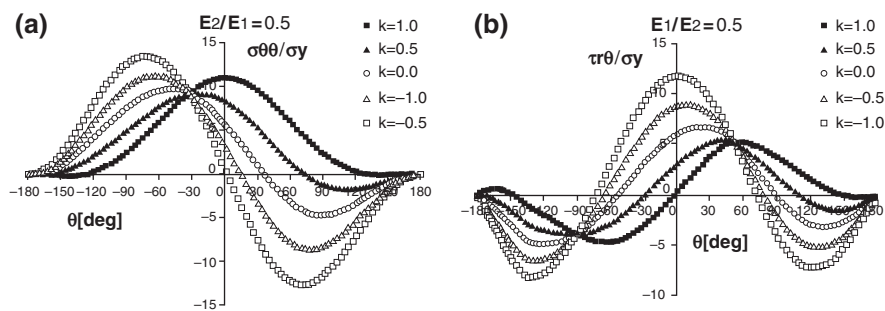
Fig. 6. Circumferential distribution of normal stresses at distance r/a = 0.01 from the crack tip for, $E_1/E_2 = 0.5$

The determination of the stress intensity factors was performed using Eq. (10), by extrapolating at the crack tip the asymptotic results of $\sigma_{\theta\theta}$ and $\sigma_{r\theta}$ for $\theta = 0^0$. Taking into account the dimensions for the SIF's (MPa m$^{1-\lambda}$) it is hard to make comparisons between other published results. The results were normalized:

$$f_{1,2} = K_{1,2} / (\sigma a^{1-\lambda_{1,2}}) \tag{11}$$

And are shown in Fig. 7. The computed values of the non-dimensional SIF's cover entire domain from pure mode I ($k = 1$) to pure mode II ($k = -1$). Higher values for non-dimensional SIF's were obtained for the case when the crack is in the compliant material for all load combinations.
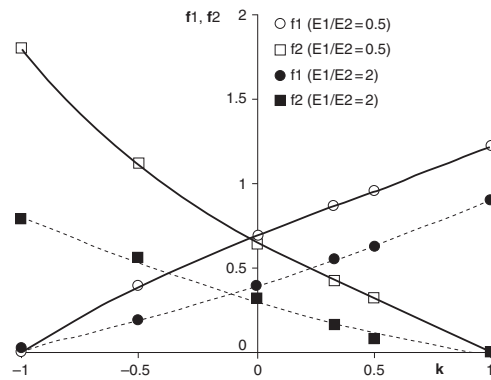
Fig. 7. Non-dimensional stress intensity factors f_1, f_2

4. Conclusions

For the two material combinations by solving the eigenequation different types of singularities were obtained: complex, multiple or double depending on crack angle θ_0 and on material combinations. The singularity orders $0 < \lambda_{1,2} < 0.5$ when the crack is in the stiffer material and meets the compliant ones, and $0.5 < \lambda_{1,2} < 1$ when vice versa. Two material combinations for an inclined crack terminating on a bi-material interface were numerically investigated.

The eigenequation has multiple solutions and the numerical results confirmed this. The stress intensity factors are estimated by extrapolation technique, based on the numerical results for the asymptotic stress field. The effect of the bi-axial load on the asymptotic stress field and on the stress intensity factors for an inclined crack terminated on the interface was highlighted for five applied mixed modes and for two material combinations.

References

[1] Zak AR, Williams ML (1963) Crack point stress singularities at a bi-material interface. J. Appl. Mech 30:142–143.

[2] Cook TS, Erdogan F (1972) Stress in bonded materials with a crack perpendicular to the interface. Int. J. Eng. Sci. 10:677–697.

[3] Erdogan F, Biricikoglu V (1973) Two bonded half planes with a crack going through the interface. Int. J. Eng. Sci. 11:745–766.

[4] Bogy DB (1971) On the plane elastic problem of a loaded crack terminating a material interface. J. Int. Fract. 38:911–918.

[5] Wang WC, Chen JT (1993) Theoretical and experimental re-examination of a crack at a bimaterial interface. J. Strain Anal. 28:53–61.

[6] Lin KY, Mar JW (1976) Finite element analysis of stress intensity factors for crack at a bimaterial interface. Int. J. Fract. 12:451–531.

[7] Ahmad J (1991) A micromechanics analysis of cracks in unidirectional fibre composite. J. Appl. Mech. 58:964–972.

[8] Tan M, Meguid SA (1996) Dynamic analysis of cracks perpendicular to bimaterial interfaces using new singular finite element. Finite Elements in Analysis and Design, 22:69–83.

[9] Chen DH (1994) A crack normal to and terminating at a bimaterial interface. Eng. Fract. Mech. 19:517–532.

[10] Chen SH, Wang TC, Kao–Walter S (2003) A crack perpendicular to the bi-material interface in finite solid. Int. J. Solids Struct. 40:2731–2755.

[11] He MY, Hutchinson JW (1993) Crack deflection at an interface between dissimilar elastic materials. Int. J. Solids Struct. 25:1053–1067.

[12] Chang J, Xu J-Q (2007) The singular stress field and stress intensity factors of a crack terminating at a bimaterial interface. Int. J. Mechanical Sciences, 49: 88–897.

[13] Lin YY, Sung JC (1997) Singularities of an inclined crack terminating at an anisotropic biomaterial interface. Int. J. Solids Struct. 38:3727–3754.

[14] Wang TC, Stahle P (1998) Stress state in front of a crack perpendicular to bi-material interface. Eng.. Fract. Mech. 4:471–485.

[15] Liu L, Kardomateas GA, Holmes JW (2004) Mixed – mode stress intensity factors for a crack in an anisotropic bi-material strip. Int. J. Solids Struct. 41:3095–3017.

[16] Kaddouri K, et al. (2006) Finite element analysis of crack perpendicular to bi-material interface: Case of couple ceramic–metal. Comput. Mater. Sci. 35:53–60.

[17] Madani K, et al. (2007) Crack deflection at an interface of alumina/metal joint: a numerical analysis. Comput. Mater. Sci. 35:625–630.

[18] Marsavina L, Sadowski T (2008) Fracture parameters at bi-material ceramic interfaces under bi-axial state of stress. Comput. Mater. Sci. doi:10.1016/j.commatsci.2008.06.005.

[19] He MY, Hsueh CH, Becher PF (2000) Deflection versus penetration of a wedge-load crack: effects of branch-crack length and penetrated-layer width. Composites: Part B 31:299–308.

[20] Zhang Z, Suo Z (2007) Split singularities and the competition between crack penetration and debond at a biomaterial interface. Int. J. Solids Struct. 44:4559–4573.

[21] Marsavina L, Sadowski T (2007) Effect of biaxial load on crack deflection/penetration at bi-material ceramic interface. Int. J. Fracture 148:79–84.

[22] Dundurs J (1969) Effect of elastic constants on stress in a composite under plane deformation. J. Compos. Mater. 1:310–322.

[23] Iesulauro E (2002) FRANC2D/L a Crack Propagation simulator for plane layered materials. Cornell University, Ithaca.

Crack Propagation in the Vicinity of the Interface Between Two Elastic Materials

Luboš Náhlík, Lucie Šestáková and Pavel Hutař

Institute of Physics of Materials ASCR, Žižkova 22, 616 62 Brno, Czech Republic and
Institute of Solid Mechanics, Mechatronics and Biomechanics, Faculty of Mechanical
Engineering BUT, Technická 2, 616 69 Brno, Czech Republic

Abstract The objective of the paper is to investigate the direction of a further crack propagation from the interface between two elastic materials. The angle of crack propagation changes when the crack passes the interface. The suggested procedure based on a generalized form of Sih's strain energy density factor makes it possible to estimate an angle of propagation under which the crack will propagate into the second material. The assumptions of linear elastic fracture mechanics and the elastic behavior of the body with interfaces are considered. The finite element method was used for numerical 2D and 3D calculations. The results obtained might contribute to a better understanding of the failure of materials with interfaces (e.g. layered composites, materials with protective coatings, etc.).

Keywords: Bimaterial Interface, Crack Propagation Direction, Layered Composites.

1. Introduction

Real structures often contain regions with different material characteristics, which are mutually divided by an interface. The presence of the interface, where the material characteristics are changed in step, has an important influence on stress distribution in the structure as well as on fracture failure resistance. The influence of the interface between two materials on crack propagation has been studied in many works from various points of view. The existence of a material interface changes the local stress distribution in the vicinity of a crack tip. In contrast to a crack in a homogeneous body where the stress singularity around the crack tip is of type $r^{-0.5}$, the stress singularity of a crack touching the interface is of type r^{-p}, where r is a radial distance from the crack tip and p is a stress singularity exponent that can be complex and its real part resides within the interval $0 < \mathrm{Re}(p) < 1$ (e.g. [4, 7]). This fact complicates the use of classical linear elastic fracture mechanics (LEFM) approaches and the establishing of criteria for estimating the behaviour of cracks of this type. Due to the different properties of each material(s), the crack changes its propagation direction at the interface. Crack behaviour of this kind has been described e.g. in experimental work [5].

In the paper presented we report the results of a theoretical study concerning the behaviour of a crack with its tip at the interface, see Fig. 1. The aim of the paper is to answer the following question**:** In which direction in the second material will the crack propagate after its passing through the interface? The problem is studied under the assumptions of linear elastic fracture mechanics, small scale yielding conditions and the interface is considered as being of a welded type (perfect adhesion).
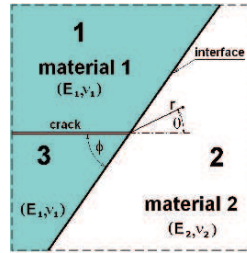
Fig. 1. Crack terminating at the interface between two materials

2. Stress field around the crack tip

The stress distribution around a crack touching the interface (Fig. 1) can be found e.g. in [4]. Stress-free crack faces require the following boundary conditions:

$$\sigma_{1\theta\theta}(r,\pi) = \sigma_{3\theta\theta}(r,-\pi) = \sigma_{1r\theta}(r,\pi) = \sigma_{3r\theta}(r,-\pi) = 0 \tag{1a}$$

where the subscript 1, 3 indicates region 1 and 3, in Fig. 1. Continuity conditions at the interface lead to the following eight equations for displacements and stress components:

$$
\begin{aligned}
u_{1r}(r,\phi) &= u_{2r}(r,\phi) & u_{3r}(r,\phi-\pi) &= u_{2r}(r,\phi-r) \\
u_{1\theta}(r,\phi) &= u_{2\theta}(r,\phi) & u_{3\theta}(r,\phi-\pi) &= u_{2\theta}(r,\phi-\pi) \\
\sigma_{1\theta\theta}(r,\phi) &= \sigma_{2\theta\theta}(r,\phi) & \sigma_{3\theta\theta}(r,\phi-\pi) &= \sigma_{2\theta\theta}(r,\phi-\pi) \\
\sigma_{1r\theta}(r,\phi) &= \sigma_{2r\theta}(r,\phi) & \sigma_{3r\theta}(r,\phi-r) &= \sigma_{2r\theta}(r,\phi-r)
\end{aligned}
\tag{1b}
$$

Twelve conditions Eqs. (1a,b) lead to the system of 12 linear equations $[B(\lambda)]_{12x12}\{x\} = \{0\}$, where $[B(\lambda)]$ is the matrix of the system and $\{x\}$ is the vector of 12 unknown coefficients. The system contains 13 unknowns in total. The thirteenth unknown is the eigenvalue λ which can be obtained from the condition of the existence of a nontrivial solution of the system, i.e. $\det[B(\lambda)] = 0$. The solution of the system (1) has generally two complex roots λ_1 and λ_2.

For most of the crack orientations considered the eigenvalues λ_1 and λ_2 have only real part that furthermore resides within the interval $(0;1)$, see [2, 4] for details. The corresponding stress singularity exponents can be determined from eigenvalues as:

$$p_1 = 1 - \lambda_1 \text{ and } p_1 = 1 - \lambda_2 \tag{2}$$

The general expression describing the stress field around the crack tip touching the interface between two materials (see Fig. 1) is given by the following equations (generally, two stress singularity exponents p_1 and p_2 exist):

$$\sigma_{ij} = \frac{H_1}{\sqrt{2\pi}} \cdot r^{-p_1} f_{1ij}(p_1, \theta, \alpha, \beta, \phi) + \frac{H_2}{\sqrt{2\pi}} r^{-p_2} f_{2ij}(p_2, \theta, \alpha, \beta, \phi) \tag{3}$$

where $H_1\ [MPa \cdot m^{P_1}]$ and $H_2\ [MPa \cdot m^{P_2}]$ are generalized stress intensity factors, $f_{1ij}(p_1, \theta, \alpha, \beta, \phi)$ and $f_{2ij}(p_2, \theta, \alpha, \beta, \phi)$ are known functions, (r, θ) are polar coordinates with their beginning at the crack tip and p_1 and p_2 are stress singularity exponents. α, β are Dundurs parameters [3] and represent elastic constants of a bimaterial body:

$$\alpha = \frac{-\mu_1(\kappa_2 + 1) + \mu_2(\kappa_1 + 1)}{-\mu_1(\kappa_2 + 1) + \mu_2(\kappa_1 + 1)} \qquad \beta = \frac{-\mu_1(\kappa_2 - 1) + \mu_2(\kappa_1 - 1)}{-\mu_1(\kappa_2 + 1) + \mu_2(\kappa_1 + 1)} \tag{4}$$

where the shear modulus $\mu = E_m / 2(1 + \upsilon_m)$ (E_m is Young's modulus) and parameters $\kappa_m = \dfrac{3 - \upsilon_m}{1 + \upsilon_m}$ for the case of plane stress or $\kappa_m = 3 - 4\upsilon_m$ for plane strain (m = 1, 2 corresponds to the number of the material).

Note that values H_1 and H_2 do not mark the appurtenance to the normal or the shear mode of loading, but the values include both modes of loading. For a crack touching the interface the general form of the stress components is given by Eqs. (5).

$$\sigma_{rr}^{(j)} = -\sum_{i=1}^{2} \frac{H_i}{\sqrt{2\pi}} \cdot r^{\lambda_i - 1} \lambda_i \begin{bmatrix} a_i^{(j)}(\lambda_i + 1)\sin(\lambda_i + 1)\theta + b_i^{(j)}(\lambda_i + 1)\cos(\lambda_i + 1)\theta + \\ c_i^{(j)}(\lambda_i - 3)\sin(\lambda_i - 1)\theta + d_i^{(j)}(\lambda_i - 3)\cos(\lambda_i - 1)\theta \end{bmatrix} \tag{5a}$$

$$\sigma_{\theta\theta}^{(j)} = -\sum_{i=1}^{2} \frac{H_i}{\sqrt{2\pi}} \cdot r^{\lambda_i - 1} \lambda_i \cdot (\lambda_i + 1) \begin{bmatrix} a_i^{(j)} \sin(\lambda_i + 1)\theta + b_i^{(j)} \cos(\lambda_i + 1)\theta + \\ c_i^{(j)} \sin(\lambda_i - 1)\theta + d_i^{(j)} \cos(\lambda_i - 1)\theta \end{bmatrix} \tag{5b}$$

$$\sigma_{r\theta}^{(j)} = -\sum_{i=1}^{2}\frac{H_i}{\sqrt{2\pi}}\cdot r^{\lambda_i-1}\lambda_i\begin{bmatrix} a_i^{(j)}(\lambda_i+1)\cos(\lambda_i+1)\theta - b_i^{(j)}(\lambda_i+1)\sin(\lambda_i+1)\theta + \\ c_i^{(j)}(\lambda_i-1)\cos(\lambda_i-1)\theta + d_i^{(j)}(\lambda_i-1)\sin(\lambda_i-1)\theta \end{bmatrix} \tag{5c}$$

The subscript $i = 1, 2$ means the number of singularity within the interval (0;1). The superscript $j = 1, 2, 3$ marks the number of region in Fig. 1. The constants $a_i^{(j)}, b_i^{(j)}, c_i^{(j)}, d_i^{(j)}$ represent the known eigenvector $\{x\}$, see e.g. [2, 4] for details.

3. Estimation of crack propagation direction

In this section the procedure for an estimation of crack propagation direction is formulated for a crack terminating at the interface at an angle ϕ, see Fig. 2. Note that the crack generally propagates under mixed mode loading conditions. The strain energy density factor S was originally introduced by Sih (e.g. [12, 13]) for cracks in homogeneous materials. In the following the generalized strain energy density factor Σ for a crack terminating at the interface is presented. Note that the generalized strain energy density factor in the case of the stress singularity exponent is different from the ½ used by Sih and Ho [14] or Seweryn [11] for cracks growing from sharp V-notches. In the case of a crack touching the interface between two materials Σ was used in the author's works [8, 9].
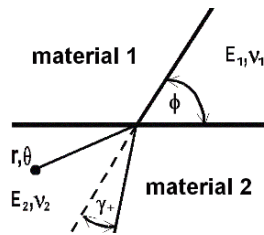
Fig. 2. A crack terminating at the interface at the angle ϕ. The direction of the crack growth in the material 2 is given by the angle γ

3.1. Strain energy density factor

The strain energy density for plane problems can be written as follows:

$$\frac{dW}{dV} = \frac{1}{8\mu}\cdot\left(k(\sigma_{rr}+\sigma_{\theta\theta})^2 + (\sigma_{rr}-\sigma_{\theta\theta})^2 + 4\sigma_{r\theta}^2\right) \tag{6}$$

where μ is a shear modulus, σ_{rr}, $\sigma_{\theta\theta}$ and $\sigma_{r\theta}$ are polar stress components and the constant $k = (1-v)/(1+v)$ for plane stress and $k = (1-2v)$ for plane strain conditions. In the vicinity of the crack tip Eq. (6) can be written as:

$$\frac{dW}{dV} = \frac{1}{r} \cdot \left(a_{11} K_I^2 + 2a_{12} K_I K_{II} + a_{22} K_{II}^2 \right) \qquad (7)$$

where r is a radial distance from the crack tip, K_I and K_{II} are stress intensity factors for mode I and II of loading respectively, a_{11}, a_{12} and a_{22} are known functions of polar angle θ (e.g. [12]). Sih introduced the strain energy density factor S which is independent on the radial distance r ahead of the crack tip:

$$S = w \cdot r = a_{11} K_I^2 + 2a_{12} K_I K_{II} + a_{22} K_{II}^2 \qquad (8)$$

It is assumed that the crack starts to grow in the direction γ where S possesses the minimum, i.e.:

$$\left(\frac{\partial S}{\partial \theta} \right)_{\gamma} = 0 \quad \left(\frac{\partial^2 S}{\partial \theta^2} \right)_{\gamma} > 0 \qquad (9)$$

By substituting the stress components Eq. (5) into the Eq. (6) and after some arrangement, we can obtain a generalized form of the strain energy density factor $\Sigma(r,\theta)$ for bimaterial body, which contrary to S depends on the radial distance from the crack tip, $\Sigma = \Sigma(r,\theta)$:

$$\Sigma(r,\theta) = r^{1-2-p_1} A_{11} H_1^2 + r^{1-p_1-p_2} 2A_{12} H_1 H_2 + r^{1-2p_2} A_{22} H_2^2 \qquad (10)$$

where H_1, H_2 are generalized stress intensity factors. Constants A_{11}, A_{12} a A_{22} are described in details in [10].

The function $\Sigma(r,\theta)$ generalizes the strain energy density factor for cracks terminating at the interface, i.e. for the case of stress singularity different from ½.

3.2. Choice of radial distance ahead of crack tip

Due to the dependence of $\Sigma(r,\theta)$ on radial distance from the crack tip, the distance r must be appropriately chosen. The distance r is related to the crack propagation mechanism. For a brittle type of fracture, the distance r can be related to the 'fracture ligament', i.e. the distance ahead of the crack tip, where the opening stress $\sigma_{\theta\theta}$ reaches the value of the failure stress of the material, see e.g. [14] for details. A suitable value of distance r is different for a different ratio of Young's modulus (E_1/E_2), but its dependence on the ratio E_1/E_2 is not strong and does not have a significant effect on the estimated crack propagation direction. It is necessary to determine only the order of the distance r.

4. Numerical example

As a numerical example of the procedure suggested, the influence of the interface between two dissimilar elastic materials was studied on a bimaterial body loaded by a tensile load. The dimensions of the bimaterial body were chosen as $100 \times 20 \times 30$mm (length $\times$ width $\times$ thickness), see Fig. 3. The thickness of both materials considered (1 and 2) was the same, i.e. $t_1 = t_2 = 15$ mm.

The elastic properties of the bimaterial were: Poisson's ratio $\upsilon_1 = \upsilon_2 = 0.3$ and ratio of Young´s moduli of materials 0.5, 1 and 2. For necessary finite element calculations the commercial system Ansys was used. The calculations were made under different conditions: for a 2D body under plane stress and plane strain conditions and for a 3D body.

The change of crack propagation direction at the interface was studied under both the conditions referred to in the plane models. In the case of the 3D model further crack propagation direction was estimated in the center of the body (i.e. for $w/2$) and on the surface. The crack front was touching the interface along all its length. The bimaterial body was subjected to the remote tensile load $\sigma_{appl} = 100$ MPa.
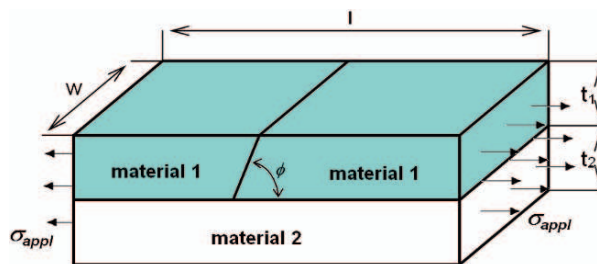
Fig. 3. Scheme of considered bimaterial specimen
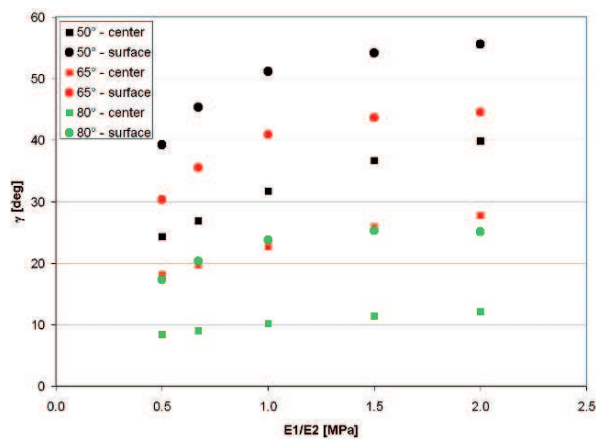
Fig. 4. Comparison of estimated crack propagation direction for surface and center of 3D specimen for different ratio of Young's modulus of materials and angle of initiation ϕ

The radial distance r ahead of the crack tip, where the criterion for the estimation of crack propagation direction was applied, had been chosen as 0.01 mm. Results obtained from 2D and 3D numerical calculations are shown in Figs. 4 and 5.
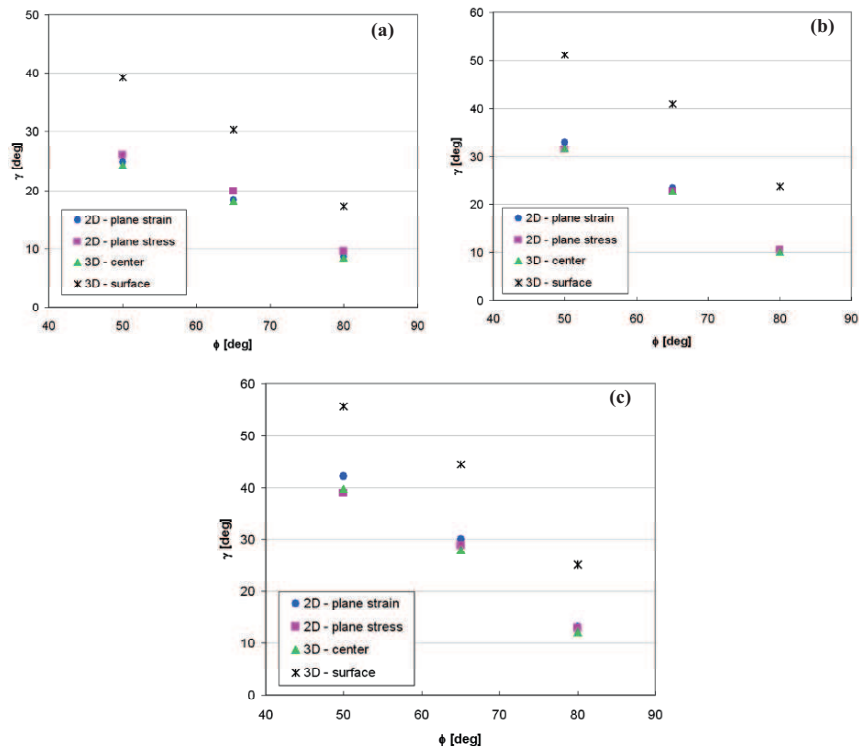
Fig. 5. Estimation of crack propagation direction for different Young's moduli ratio: a) $E_1/E_2 = 0.5$; b) $E_1/E_2 = 1$ (homogeneous case); $E_1/E_2 = 2$

5. Discussion

The influence of the interface between two different materials on further crack propagation direction in material 2 can be seen in Fig. 5. For ratio $E_1/E_2 < 1$ (crack propagates from softer material to the stiffer one) the deviation angle γ is smaller than in the homogeneous case (i.e. for $E_1/E_2 = 1$). In the opposite case (for $E_1/E_2 > 1$) the deviation γ is bigger than in the homogeneous case. This means that the crack will incline in its further propagation to the direction perpendicular to the remote load more rapidly.

This conclusion is valid for all the cases and conditions studied. The results are similar for 2D simulations (plane strain and plane stress conditions) as well as for

deviation angles obtained from 3D simulations in the center of a bimaterial body (conditions in the center of the body are comparable with a 2D solution under plane strain condition). The results obtained for an estimation of crack propagation direction on the surface of a bimaterial body are different from 2D solution under plane stress condition. This difference can be explained by corner (vertex) singularity which influences the stress distribution close to the free surface (see e.g. [1, 6] for details). Due to the existence of corner stress singularity it is not possible to use accurately the procedure suggested for an estimation of crack propagation direction in thin bimaterial bodies (the influence of the free surface is significant in this case). Figure 4 provides a comparison of results obtained for the center and for the surface of a bimaterial body for all the Young's moduli ratios considered. The difference is evident. For a more precise estimation of crack propagation direction in the case of thin bodies, corner singularity should be taken into account.

6. Conclusions

A tentative procedure for an estimation of crack propagation direction was introduced for a crack touching the interface between two dissimilar elastic materials. Sih's strain energy density factor S was generalized for a crack with its tip at the bimaterial interface and used for the estimation of the crack propagation direction for different angles between crack and interface and different material properties of a bimaterial body.

The procedure is based on the extension of linear elastic fracture mechanics to general singular stress concentrators. The numerical simulations were performed on 2D and 3D models and the results mutually compared. The results show that for the ratio of Young's moduli $E_1/E_2 > 1$ the angle γ of further crack propagation in material 2 is bigger than for a homogeneous material (i.e. $E_1 = E_2$). In the opposite case (for $E_1/E_2 < 1$) the deviation angle γ is smaller than in the homogeneous case. The different crack propagation direction estimated for the center and surface of 3D specimen was discussed. To prove the validity of the procedure, comparison with suitable experimental data is being prepared.

The results obtained contribute to a better understanding of the failure of materials with interfaces (e.g. composites, materials with protective coatings) and to a more reliable estimation of the service life of such structures.

References

[1] Bažant Z P, Estenssoro L F (1979) Surface singularity and crack propagation. International Journal of Solids and Structures 15:405–426.

[2] Bogy D B (1971) On the plane elastostatic problem of a loaded crack terminating at a material interface. Journal of Applied Mechanics 38(4):911–918.

[3] Dundurs J (1967) Effect of elastic constants on stress. In: A Composite Under Plane Deformation. Journal of Composite Materials 1:310–322.

[4] Fenner D N (1976) Stress singularities in composite materials with an arbitrarily oriented crack meeting an interface. International Journal of Fracture 12(5):705–721.

[5] Hadraba H, Klimes J, Maca K (2007) Crack propagation in layered Al2O3/ZrO2 composites prepared by electrophoretic deposition. Journal of Materials Science 42:6404–6411.

[6] Heyder M, Kuhn G (2006) 3D fatigue crack propagation: experimental studies. International Journal of Fatigue 28:627–634.

[7] Meguid S A, Tan M, Zhu Z H (1995) Analysis of cracks perpendicular to bimaterial interfaces using a novel finite element. International Journal of Fracture 73:1–23.

[8] Náhlík L, Knésl Z (2001) Estimation of the critical stress for failure of protective coating. In: Proceedings of International conference on Materials structure & micromechanics of fracture 3, Brno University of Technology, Brno.

[9] Náhlík L, Šestáková L, Hutař P (2008a) Estimation of the crack propagation direction of a crack touching the interface between two elastic materials. Materials Science Forum 567–568:225–228.

[10] Náhlík L, Knésl Z, Klusák J (2008b) Crack initiation criteria for singular stress concentrators. Part III: an application to a crack touching a bimaterial interface. Engineering Mechanics 15(2):99–114.

[11] Seweryn A, Lukaszewicz A (2002) Verification of brittle fracture criteria for elements with V-shaped notches. Engineering Fracture Mechanics 69:1487–1510.

[12] Sih G C (1974) Strain energy density factor applied to mixed mode crack problems. International Journal of Fracture 10(3):305–321.

[13] Sih G C (1977) A special theory of crack propagation. In: Sih G C (ed) Mechanics of Fracture, Noordhoff International Publishing, Leyden.

[14] Sih G C, Ho J W (1991) Sharp notch fracture strength characterized by critical energy density. Theoretical and Applied Fracture Mechanics 16(3):179–214.

Fracture Behaviour of TiAl Intermetalics

Ivo Dlouhý, Zdeněk Chlup, Hynek Hadraba and Vladislav Kozák

Institute of Physics of Materials, Academy of Sciences of the Czech Republic, Zizkova 22, 61662 Brno, Czech Republic

Abstract   The role of microstructural parameters in fracture behaviour of TiAl intermetalics at room and increased temperatures will be in focus of interest. Based on experimental findings sampled in this field and arising from literature knowledge an overview of typical fracture micromechanisms acting in different microstructures of TiAl intermetalics will be presented. Where possible semi-quantitative evaluation of toughening effects will be presented. Tensile properties, flexural strength and fracture toughness have been evaluated mainly for Ti-40Al-2Cr-2Nb-1B and Ti-46Al-0.7Cr-0.1Si-7Nb-0.2Ni alloys. For fracture toughness determination chevron-notch specimen technique have been applied except for standard pre-cracked samples. Positive effect of Nb on fracture resistance has been found; fracture toughness of the high Nb alloy increased at contemporary increase of flexural strength. Fracture surfaces have been evaluated using scanning electron microscopy showing the key role of mechanical twinning in deformation of both alloys followed. As a governing mechanism of crack nucleation microcrack formation at boundaries between mechanical twins and γ grains has been confirmed.

Keywords: TiAl Intermetalics, Crack Nucleation, Behaviour.

1. Introduction

TiAl based intermetalics represent structural material with high application potential. They are being considered as structural materials in a number of aerospace and automotive applications as turbocharger wheels, turbine blades etc. [1, 8, 13].

They experienced intensive development during last decade, in particular in field of refinements of grain and lamellar microstructure [2, 13], alloying modification and microalloying [10, 12], fabrication technologies development [2, 16], including synergy of these factors and their relationship to high temperature properties. Much less effort has been paid to the TiAl intermetalics performance and fracture resistance at room and slightly increased temperatures. Just this behaviour represents an obstacle for more extensive applications [15, 16].

The exceptional properties of TiAl intermetalics are predetermined by strong partly covalent bonding between atoms. The alloys containing γ-TiAl and less volume fraction of α_2-Ti$_3$Al are mostly interesting [18]. The first phase is formed by face centered slightly tetragonal lattice, not too much different from the cubic

one, the later by hexagonal closed packed structure. From the point of view of microcrack nucleation three typical microstructures can be distinguished:

- Microstructures formed by equiaxed γ-TiAl grains, typical for alloys containing higher Al content (about 52 at%) [11].
- Duplex microstructures (46 to 50 at% Al) that are formed by heat treatment into two-phase $\alpha + \gamma$ region or by passing through this region during cooling [2].
- Lamellar microstructures (less than 48 at%) that are formed by γ-TiAl and α_2-Ti$_3$Al created by α-phase decomposition below 1125°C [4].

Low ductility and fracture toughness at room temperature is caused by strong interatomic bonds causing crystal ordering and therefore by limited number of slip systems.

Intrinsic and extrinsic mechanisms can be used for the toughness enhancement [3]. In the first case, the suitable alloying and heat treatment represent the only way. General trend consists of Al content decrease and, at the same time, increase of elements affecting the creep resistance (Cr, W, Si) and/or oxidation resistance (Nb) [14, 16, 17]. For room temperature plastic properties the Nb content and small amounts of Cr, Si and B were found as the most effective [10]. In case of extrinsic mechanisms, crack tip shielding effects can lead to toughness increase, e.g. crack bridging and/or crack trajectory change, the last reflected by increase of crack path tortuosity. Fully lamellar structures are more resistant to fracture than those having near γ and/or duplex microstructures [4, 5].

Specification of conditions for microcrack nucleation and fracture initiation explaining the role of microstructure in failure micromechanism at the same time is important for further optimisation of TiAl intermetalics. Aim of the paper was to analyse the acting fracture micromechanisms in investigated TiAl alloys based on mechanical characteristics evaluation and fracture surfaces investigation.

2. Material and experimental methods

Two experimental alloys, labelled as I and F, were used for investigation. (Table 1). The alloys were produced by Flowserve Corporation Dayton and were supplied in form of round rods (ingots) with diameter of 60 mm.

The average grain sizes determined using optical micrographs by line intercept method were 105 and 182 μm for alloy I and F, respectively [9]. Samples for mechanical tests were fabricated in longitudinal direction by electric discharge machining and finished by electrochemical polishing.

Table 1. Alloys used for investigations (in at %)

Alloy I	Ti-40Al-2Cr-2Nb-1B
Alloy F	Ti-46Al-0.7Cr-0.1Si-7Nb-0.2Ni

   Flat samples with rectangular cross-section of 3×4 mm in gauge length with wedge heads were applied for tensile properties determination. Tests were carried out at constant cross-head speed of 100 μm/min, specimen elongation was measured by means of extensometer with 12 mm initial gauge length. Tensile strength (rupture stress) has been determined as the maximum force divided by cross-sectional area measured after the test. For fracture toughness determination rectangular bars of cross-section 3×4 mm were applied. Chevron notch in direction of higher dimension was produced by two cuts of thin diamond wheel. The tests were carried out in three-point bending using 20 mm distance of rollers and loading rate of 100 μm/min. Fracture toughness K_{IC} was determined from maximum force and chevron notch depth [6]. For the alloy F also flexural specimens with cross-section of 6x9 mm were used for fracture toughness determination. Specimens were pre-cracked and tested at room temperature according to corresponding standards [7].

3. Results

3.1. Basic mechanical properties of alloys

Tensile stress-strain curves are shown in Fig. 1. They reflect main differences in deformation behaviour. Very limited plastic deformation in tension leads to earlier fracture initiation and premature fracture for alloy I. The fracture load is thus affected by the limited deformation ability.
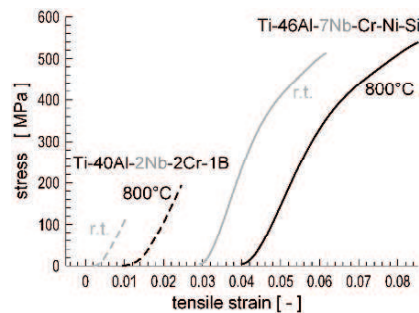
Fig. 1. Tensile stress–strain curves obtained at room temperature and 800°C

   Fracture surface macromorphology in Fig. 2 confirms this higher susceptibility of the alloy I to premature fracture. The fracture was triggered from the specimen surface (left side of the Fig. 2a). Contrary to this behaviour the alloy F initiated from location lying on some distance from the specimen surface (Fig. 2b). Its higher plasticity inhibits the susceptibility of the alloy to surface defects and premature fracture.
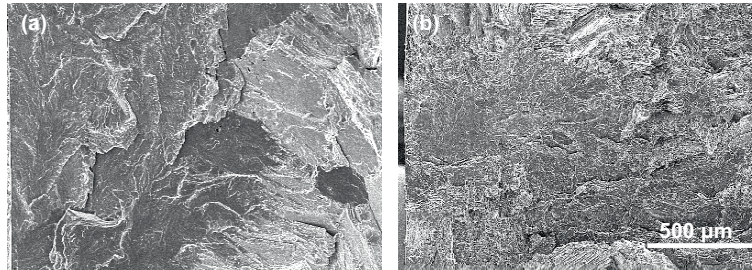
Fig. 2. Fracture surfaces of the tensile samples broken at room temperature for alloy I (**a**) and alloy F (**b**); specimen surface left

For both alloys Fig. 3 shows a comparison of tensile strength values obtained at room temperature and at 600°C. The stresses are represented here in normalised values as a ratio of measured values of rupture stress to supposed lowest limit value predetermined by potential applications. Not only the strength but also plastic properties are comparably higher for the high Nb alloy. A part of the strength enhancement observed in alloy F comparing to alloy I is due to higher plasticity lowering the alloy susceptibility to surface flaws effect and to premature fracture.
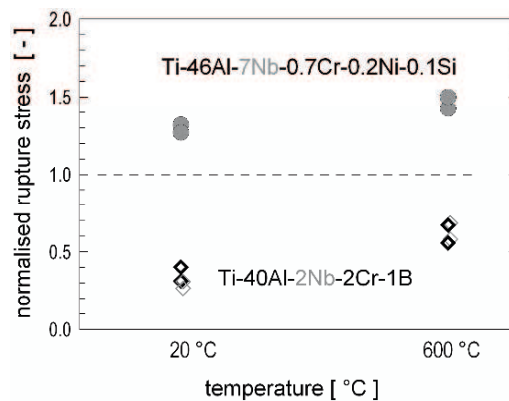
Fig. 3. Normalised tensile rupture stress (ratio of measured rupture stress to optimum design stress) for both alloys investigated

3.2. Fracture behaviour

Temperature dependence of fracture toughness of alloy I is shown in Fig. 4. This alloy possesses very brittle behaviour. Even at 800°C the alloy displayed fracture without extensive plastic deformation work. The temperature increase was probably not sufficient to activate additional slip systems and dislocation mobility both necessary for the alloy plasticity increase.
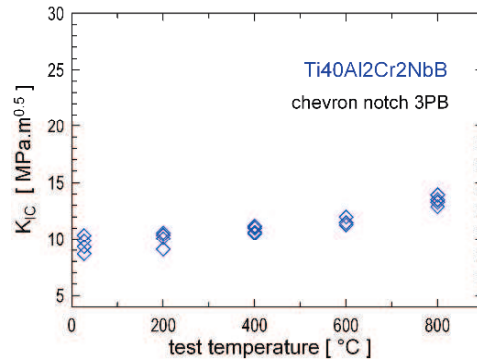
Fig. 4. Temperature dependence of fracture toughness for alloy I
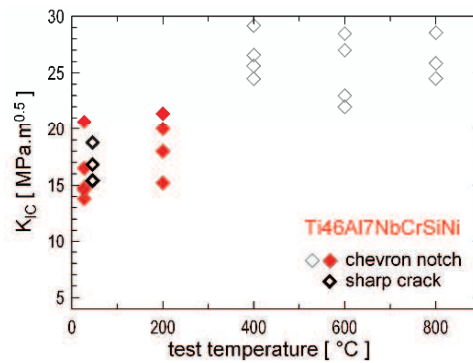
Fig. 5. Temperature dependence of fracture toughness for alloy F

This is not the case of the alloy F. At room temperature the alloy shows evidently higher fracture toughness values comparing to alloy I, as follows from Fig. 5. In addition, higher scatter of data is possible to observe.

By measurement on larger samples with fatigue pre-cracking, tested according to standard procedures, validity of the chevron notch values obtained at room temperature has been proved. The data are lying in the scatter band of data obtained with chevron notch specimens (Fig. 5).

Nearly twofold increase of fracture toughness level is possible to observe with increasing test temperature for alloy F. Change in dislocation mobility can be only responsible for such marked toughness increase. Although still valid, the tests at 400°C and higher temperatures were on the limit of chevron notch functionality. These fracture toughness values are shown as informative values only in Fig. 5 and must be verified. Experiments at higher temperatures are in progress. The fracture surfaces investigation revealed dependence of fracture behaviour on orientation of lamellar structure in relation to main fracture plane, the last being controlled by chevron notch plane. Fracture surface morphology observed for the minimum and maximum toughness value of the scatter band is in Fig. 6.

When cleavage planes of γ-phase or lamellar phase were parallel to the chevron notch plane easier sharp crack initiation occurred (Fig. 6a) and the toughness values were lower. However, once the direction of longitudinal axis of lamellar colonies was deflected from the chevron notch plane the change of the crack trajectory was significant (Fig. 6b).
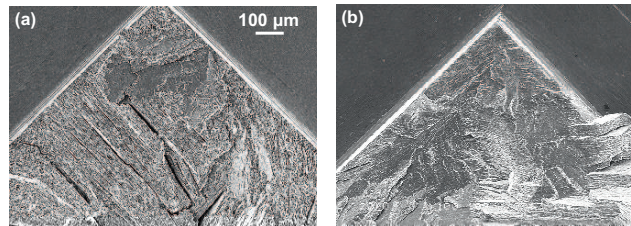
Fig. 6. Fracture surface morphology of chevron notched samples tested at room temperature; alloy F

The fracture toughness data proved good properties of the alloy F. With increasing test temperature marked increase of alloy plasticity and fracture toughness enhancement was possible to observe. It is important that the toughness enhancement was obtained by intrinsic toughening mechanisms.

4. Discussion

4.1. Microcrack nucleation

Detailed fractographic analysis of fracture surfaces and metallographic sections perpendicularly to fracture surfaces carried out in both alloys have shown that microcrack nucleation occurred in a number of locations in front of the crack tip. The microcrack nucleation micromechanism was about the same in both alloys. There are typical configurations in Fig. 7.
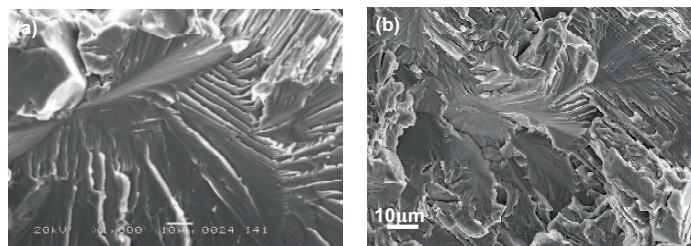
Fig. 7. Examples of microcrack nucleation in fracture surfaces of the alloy I (**a**) and alloy F (**b**)

Usually, it is possible to observe several damage sites on certain distances from the crack tip showing the fracture initiation occurred by joining the main crack tip with the nearest microcrack/damage site. The separate microcracks are often nucleated at boundaries of two lamellas or on boundary of lamellar colony with equiaxed γ-TiAl grain. Local influence of deformation twin and/or intensive slip band onto this boundary and microcrack nucleation in neighbouring grain in local tensile stress field appears to be the most probable mechanism of the microcrack formation. For the alloy I, there is a facet formed by fracture of equiaxed grain, a step morphology formed by fine lamellar microstructure and river like traces typical for fracture of nonlamellar microstructure component (see Fig. 7a). The occurrence of facets created by equiaxed grains cleavage is comparably lower in alloy F, one of such locations is shown in Fig. 7b. In almost all facets of alloy F some curvature due to plastic deformation typical for quasicleavage was possible to observe, Fig. 7b. The fracture mechanism of both alloys is nearly the same differing only by the extent of plastic deformation proceeding to cleavage facets nucleation. Configuration of fracture facets shown in Fig. 7a is the most frequently observed phenomena in fracture surfaces once the equiaxed γ-TiAl grains are present in microstructure. The presence of the equiaxed γ-TiAl grains is detrimental for crack resistance; it affects strongly both the crack initiation toughness and crack resistance curve. The equiaxed γ-phase is supposed to degrade the crack growth resistance by inhibiting action of shear ligament toughening.

4.2. Fracture initiation

For pre-cracked test specimens of both alloys tested at room temperature crack tip stress-strain distributions preceding and corresponding to fracture initiation have been calculated by finite element modelling. Development of maximum principal stress at forces below and at the fracture force has shown that there is no plastic deformation nearly up to fracture load. Certain amount of effective plastic deformation was developed just before the reaching the critical load (700–770 N). This is because of singularity on the stress distribution still at loads corresponding to yield stress and zero value of effective plastic deformation at 600 N loads. Only after this point a peak on maximum stress distribution is formed and shifted to higher distances from the crack tip. Presumably, critical stress for crack nucleation and plastic deformations for the joining the microcrack nuclei with the crack tip are the necessary condition for the crack initiation. The plastic deformation itself is more or less apparent value, because the joining of microcrack nuclei with the main crack tip is carried out mainly by microdamage processes rather than deformation, in particular in alloy I. In the last the effective plastic deformation was comparably lower and no evidences of plastic deformation could be found in fracture surfaces. For the alloy F the stress-strain conditions at the moment of crack initiation are obvious from Fig. 8. From the micromechanical point of view additional analyses will be needed (e.g. determination of critical values of stress and of strain), nevertheless coincidence of the peak position on maximum principal stress distribution and triaxiality distribution could reflect unfavourable

conditions for the crack tip blunting. Inhibiting this blunting process and local stress relaxation at the crack tip a stage ready for crack initiation followed by immediate crack propagation is reached.
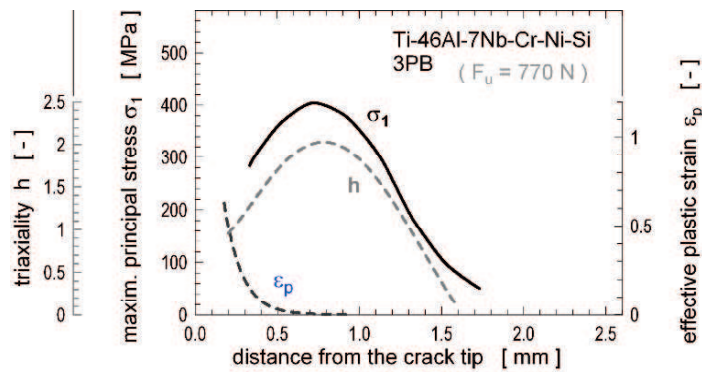
Fig. 8. Distributions of maximum principal stress, stress triaxiality and effective plastic strain below the crack tip, alloy F
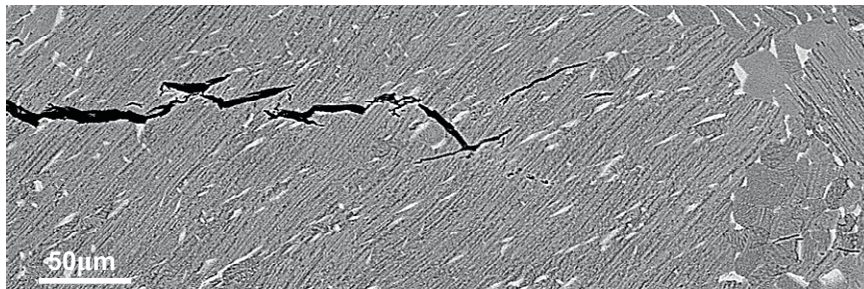
Fig. 9. Section perpendicularly to main crack plane in vicinity of the crack tip in unbroken test specimen (SEM-BSE)

The possible source for intrinsic toughening thus can be seen in such changes in alloy chemistry and microstructural state that produce different positions of the peak on maximum tensile stress distribution and the peak on stress triaxiality distribution below the crack tip.

This can be obtained by increase of plasticity of the alloy, excluding the detrimental effect of the γ-TiAl grains in lamellar microstructure and/or by forming microstructure with more plastic constituent, e.g. β-γ alloys are the best hope for this. When comparing the room temperature fracture properties and fracture micromechanism the niobium appears to be one of elements increasing effectively the plasticity and toughness of the alloy. It has been already mentioned that this is the most effective way of toughness enhancement if titanium aluminides when the intrinsic mechanisms are exploited.

5. Conclusions

Mechanical properties and fracture performance of two TiAl alloys with different Nb content have been followed in the work. Positive effect of Nb on tensile strength and, at the same time, on deformation properties has been shown. Enhancement of fracture toughness was observed at the same time. Significant dependence of the scatter in fracture characteristics on orientation of lamellas in location of fracture initiation origin has been proven. In both alloys, effective toughening mechanism, shear ligament toughening, i.e. combination of multiple microcrack nucleations in lamellar microstructure and shear bridges between these microcracks has been observed.

Defectiveness of the microstructure paradoxically contributes to significant toughening; the higher the interlamellar distance is the higher defectiveness and thus toughness increase is possible to detect. Thanks to intrinsic toughening exploited in alloy F this alloy possesses very high toughness level and increasing crack resistance curve.

References

[1]   Bieler TR, Pourboghrat, Mason DE, et al. (2005). Fracture initiation/propagation parameters for duplex TiAl grain boundaries based on twinning. Intermetallics 13:979–984.

[2]   Campbel JP, Venkateswara Rao KT, Ritchie RO (1999). The effect of microstructure on fracture toughness and. Metall and Mat Trans 30A(3):563–577.

[3]   Cao R, Yao HJ, Chen JH, Zhang J (2006). On the mechanism of crack propagation resistance of fully lamellar TiAl alloy. Mat Sci Eng A420:122–134.

[4]   Chan KS, Kim YW (1995). Effects of lamellae spacing and colony size on the fracture resistance of a fully lamellar TiAl. Acta Metall Mater 43(2):439–451.

[5]   Chan KS, Wang P, Bhate N, Kumar KS (2004). Intrinsic and extrinsic fracture resistance in lamellar TiAl alloys. Acta Mater 52:4601–4614.

[6]   ČSN P CENT/TS 14425-3 (2003). III: Method of flexural test with chevron notch specimen.

[7]   ISO 12135 (2002). Metallic materials – Unified method of test for determination of quasistatic fracture toughness.

[8]   Kim YW (1992). Microstructural evolution and mechanical properties of a forged gamma titanium aluminide alloy. Acta Met et Mat 40(6):1121–1134.

[9]   Krahula K, Dlouhý I (2005). Microstructure and mechanical properties of TiAl based intermetalics (in Czech). In Multilevel Design of Advanced Materials, 95–102.

[10] Mercer C, Soboyejo WO (1997). Effects of alloying on crack tip definition and shielding in gamma-based titanium aluminides. Acta Mater 45(3):961–971.

[11] Ng BC, Simkin BA, Crimp MA, Bieler TR (2004). The role of mechanical twinning on microcrack nucleation and crack propagation. Intermetallics 12:1317–1323.

[12] Quast JP, Boehlert CJ (2007). Comp. of the microstructure tensile and creep behaviour for Ti24Al17NbxMo alloys. Met and Mat Trans 38A(3):529–536.

[13] Schaden T, Clemens H, Fischer FD, Ebner R (2005). Intermetallics in Technology: Needs and Application, KMM-NoE Integr. Summer School, Udine.

[14] Simkin BA, Crimp MA, Bieler TR (2003). A factor to predict microcrack nucleation at γ-γ grain boundaries in TiAl. Scripta Mater 49(2):149–154.

[15] Werwer M, Kabir R, Cornec A, Schwalbe KH (2007). Fracture in lamellar TiAl simulated with the cohesive model. Eng Fract Mech 74:2615–2638.

[16] Xu XJ, Xu LH, Lin JP, Wang YP, Lin Z, Chen GL (2005). Pilot processing and microstructure control of Nb containing TiAl alloy. Intermetallics 13:337–341.

[17] Yang CT, Li YC, Koo CH (2002), The high temperature tensile properties and microstructural analysis of Ti–40Al–15Nb alloys. Intermetalics 10:161–169.

[18] Zheng RT, Cheng GA, Li XK, Cao GX, Fu LF, Zhang YG, Chen CQ (2007). The relationship between fracture toughness and. J Mater Sci 42:1251–1260.

Numerical and Experimental Investigations of Mixed Mode Fracture in Granite Using Four-Point-Bend Specimen

M.R.M. Aliha, M.R. Ayatollahi and B. Kharazi

Fatigue and Fracture Lab., Department of Mechanical Engineering, Iran University of Science and Technology, Narmak, Tehran, 16846, Iran

Abstract   Asymmetric four-point-bend (FPB) specimen is an appropriate test configuration for investigating mixed mode fracture behaviour in engineering materials like ceramics, rocks, polymers and metals. In this paper, a combined numerical, experimental and theoretical study of mixed mode I/II fracture behaviour using this specimen is presented. For calculating the stress intensity factors, K_I and K_{II}, the specimen is analyzed using finite element software, ANSYS. Then mixed mode fracture is investigated experimentally for a type of granite by means of the FPB specimen for different combinations of mode I and mode II. The obtained test data are then compared with some well known two fracture theories. It is shown that the test data are in agreement with the theoretical predictions of well known fracture criteria the maximum tangential stress theory and the maximum energy release rate theory.

Keywords: Mixed Mode Fracture, Asymmetric Four-Point-Bend Specimen, Finite Element, Granite, Experiment.

1. Introduction

It is well established that the crack growth is one of the main reasons for the overall failure and brittle fracture in various engineering materials. Cracks and inherent discontinuities are frequently found in rock materials and concrete structures. In many practical applications, such as concrete dams, tunnelling, mining, excavation process and analyses of rock slope stability, the evaluation of crack growth is an important task for rock and concrete structures designers. Most of previous rock and concrete fracture studies have concentrated only on crack opening mode (or mode I loading) which is induced from the tensile stresses. However, in practice, the cracked rock structures are usually subjected to complex loading and hence the fracture of rock masses may occur under a combination of tension-shear (mixed mode I/II) loading. Therefore, it is important to investigate the mode I, the mode II and mixed mode fracture in rock structures and geo-materials. There are some theoretical and experimental methods for evaluating the fracture behaviour under mixed mode I/II loading conditions. Fracture toughness of cracked materials is generally investigated by means of suitable test samples. The cracked rectangular bar subjected to asymmetric four-point-bend loading is

one of the favourite test configurations frequently used by researchers investigating mixed mode fracture in rocks and concretes (e.g. [1–4]) and also in other brittle materials [5–9]. The simple geometry and loading set up, the convenient pre-cracking of specimen and the ability of introducing full mode mixities (from pure mode I to pure mode II) are among the advantages of FPB specimen. Additionally the specimen is loaded by a compressive type of load which is more suitable for testing brittle materials like rocks. For studying mixed mode fracture in each test specimen, the mode I and mode II stress intensity factors (K_I and K_{II}) should be known. In this paper, a combined numerical and experimental study using the FPB specimen is presented for mixed mode loading. In the forthcoming sections, first the stress intensity factors of the four-point-bend specimen are determined by means of the finite element analysis. Then mixed mode fracture is investigated experimentally for a granite sample using the FPB specimen.

2. Four-point-bend specimen

Fig. 1 shows a schematic drawing of asymmetric four point bend (FPB) specimen. The ratio of mode I and mode II stress intensity factors can be easily changed in this specimen by moving the locations of top and bottom supports. This is because the shearing force and the bending moment along the crack plane and hence the crack opening and the crack sliding are dependent on the locations of loading points. Therefore, the FPB specimen can be used for providing pure mode I (crack opening), pure mode II (in-plane sliding) and various mode mixities for fracture experiments. When the loading points are symmetric with respect to the crack plane ($L_1 = L_2$ and $L_3 = L_4 < L_2$), the specimen is subjected to pure mode I loading. Pure mode II is also provided by anti-symmetric loading of specimen (i.e. $L_1 = L_4$ and $L_2 = L_3$). In this situation unlike the symmetric condition, the crack line in the FPB specimen is subjected to a pure shear force. For any other options for the locations of top and bottom supports (L_1, L_2, L_3 and L_4) the specimen experiences mixed mode loading conditions.
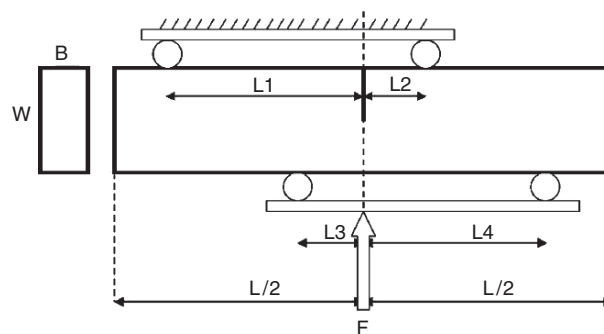
Fig. 1. Cracked rectangular plate subjected to asymmetric four point bending

Some analytical [7, 8] and numerical [10] methods are available for obtaining the stress intensity factors in the FPB specimen. The finite element method is a suitable and powerful technique for calculating K_I and K_{II} in cracked specimens. In the next section, the finite element method is employed for analyzing the FPB specimen under various loading conditions.

3. Finite element modeling

Fig. 2 shows a typical mesh pattern generated for simulating the FPB specimen in the finite element code ANSYS. In the created model, the following dimensions have been considered: crack length $a = 20$ mm, specimen thickness $B = 19$ mm, width $W = 40$ mm and length $L = 220$ mm. Thus the crack length ratio, a/W, was equal to 0.5. A total number of 568 plane stress and eight-nodded elements were used for simulating the model. The crack tip stress singularity was generated by using the singular elements in the first ring of elements surrounding the crack tip. The stress intensity factors, K_I and K_{II}, for the FPB specimen can be written as:

$$K_i = \frac{Y_i\, F\, (\pi a)^{0.5}}{BW}\left(1 - \frac{L_3}{L_1}\right), \quad i = I, II \tag{1}$$

where Y_I and Y_{II} are the mode I and mode II geometry factors, respectively. In the analyzed models, pure mode I (symmetric loading), pure mode II (anti-symmetric loading) and different mixed mode conditions were considered. All models were solved by considering a constant value of F = 5,000 N and fixed values for L_1, L_2 and L_4 as $L_1 = 70$ mm, $L_2 = 30$ mm, $L_4 = 70$ mm. In order to change mode mixity, different values were taken for L3. The Material properties of a typical granite (E = 45 GPa and $\nu = 0.28$) were used for the finite element analysis of FPB specimen. The mode I and mode II stress intensity factors were directly extracted from the ANSYS code. Variations of Y_I and Y_{II} versus L_3/L_1 for the analyzed FPB specimens are presented in Fig. 3. It is seen from this figure that by moving from the symmetric loading conditions (pure mode I) toward anti-symmetric loading conditions (pure mode II), Y_I decreases and Y_{II} increases.
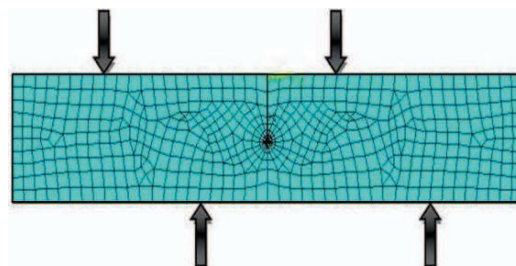
Fig. 2. Finite element model created for asymmetric four-point-bend specimen

4. Fracture experiments

A series of mixed mode fracture experiments were conducted on a type of granite using the four-point-bend specimen. Several test specimens with dimensions of $220 \times 40 \times 19$ mm were cut from a sheet of Takkab (a region in the north western of Iran) granite.

Then an edge crack having a length of 20 mm was created in the centre line of each test specimen using a thin rotary diamond blade. For each desired mode mixity, the specimen was placed in a suitable location inside the loading fixture and then was loaded until the final fracture. Figure 4 shows the loading set up for one of the tests. The servo hydraulic Amsler/Zwick test machine was used for fracture tests.

The loading rate for all tests was 0.25 mm/min. the load–displacement history for each test was recorded during the test using a computerized data logger. The critical stress intensity factors for each loading condition were calculated using Eq. (1) and the fracture load obtained from the tests.
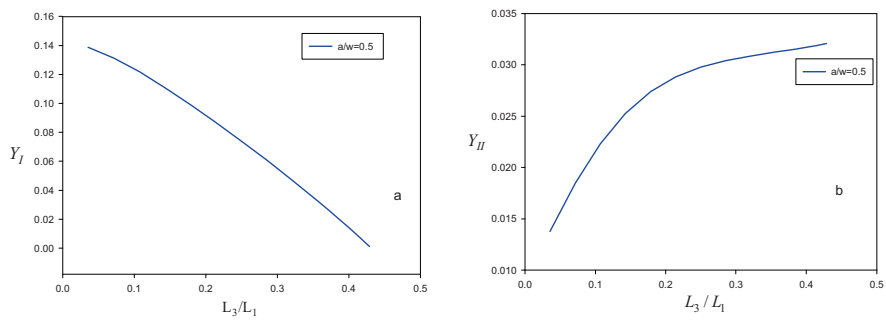
Fig. 3. Variations of (**a**) mode I geometry factor Y_I and (**b**) mode II geometry factor Y_{II} with L_3/L_1 in the FPB specimen
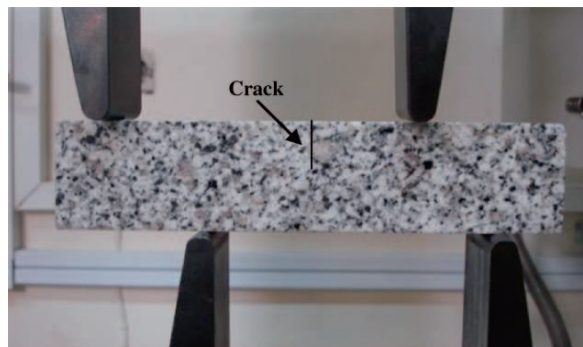
Fig. 4. Loading set up for FPB specimen made of Takkab granite

5. Results and discussion

The maximum tangential stress (MTS) criterion [17], the minimum strain energy density criterion [18] and the maximum energy release rate criterion [19] are three well-known theories for mixed mode fracture. Based on these criteria, fracture in a cracked body under mixed mode I/II loading will occur in a specific direction when the stress or energy quantities in this direction reaches its critical value. For example, the onset of fracture for a cracked body subjected to mixed mode loading takes place according to the maximum tangential stress criterion [17] when:

$$K_{Ic} \leq \cos\frac{\theta_0}{2}\left[K_I \cos^2\frac{\theta_0}{2} - \frac{3}{2}K_{II}\sin\theta_0\right] \qquad (2)$$

And based on the maximum energy release rate or G criterion [19] when:

$$K_{Ic} \leq \left(\frac{2}{3+\cos^2\theta_0}\right) \cdot \left(\frac{1+\frac{\theta_0}{\pi}}{1-\frac{\theta_0}{\pi}}\right)^{\frac{-\theta_0}{2\pi}} \cdot$$

$$\left[\left(1+3\cos^2\theta_0\right)K_I^2 - 8\sin\theta_0\cos\theta_0 \cdot K_I K_{II} + \left(9+5\cos^2\theta_0\right)K_{II}^2\right]^{\frac{1}{2}} \qquad (3)$$

where θ_0 is the angle of fracture initiation with respect to the original crack line. The angle θ_0, is predicted by the MTS criterion from:

$$\theta_0 = 2\tan^{-1}\left(0.25 \cdot \left[\left(\frac{K_I}{K_{II}}\right)^2 + \sqrt{\left(\frac{K_I}{K_{II}}\right)^2 + 8}\right]\right) \qquad (4)$$

Similar relation can be found in [19] for θ_0 when using the G criterion. By increasing the load, the stress intensity factors, K_I and K_{II} in the right hand side of Eqs. (2) and (3) also increase. Mixed mode fracture occurs when the right hand side of Eqs. (2) or (3) reaches or exceeds the mode I fracture toughness K_{Ic}. The theoretical predictions of fracture by these criteria can be presented in a K_{II}/K_{IC} versus K_I/K_{IC} diagram as shown in Fig. 5. Also shown in this figure is the test data obtained from mixed mode fracture experiments conducted on Takkab granite. Despite a natural scatter that exists in the experimental results, Fig. 5 shows that the obtained test data are generally in agreement with the theoretical predictions of the maximum tangential stress and the maximum energy release rate criteria. In fact, the mixed mode data lie between the curves related to these two fracture criteria. The scatter observed in the test data can be attributed to parameters like natural inhomogeneity and anisotropy of tested granite and possible inaccuracies

in manufacturing, pre-cracking and loading set up of FPB test samples. The mixed mode fracture toughness of engineering materials can be displayed by effective stress intensity factor, K_{eff}:

$$K_{eff} = \frac{\sqrt{K_I^2 + K_{II}^2}}{K_{Ic}} \tag{5}$$

where K_I and K_{II} in Eq. (5) are the stress intensity factors corresponding to the fracture load. Figure 6 shows the variations of mixed mode fracture toughness versus the mode mixity parameter (M^e) for Takkab granite. The parameter M^e is defined by:

$$M^e = \frac{2}{\pi} \arctan\left(K_I \middle/ K_{II} \right) \tag{6}$$
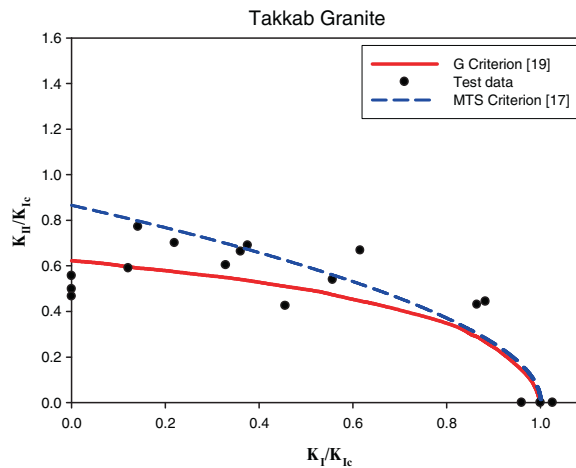
Fig. 5. Mixed mode fracture toughness data obtained for tested granite using FPB specimens

A curve fitted to the test results is also shown in Fig. 6. A comparison between the results of pure mode I and pure mode II indicates that the mode II fracture toughness (K_{IIc}) for the tested granite is less than its mode I fracture toughness (K_{Ic}). However, previous investigations [20–23] suggest that unlike K_{Ic} the value of measured K_{IIc} is not merely a material constant and depends also on the geometry of test specimen and its loading configuration. For example, the ratio of K_{II}/K_{IC} for cracked materials tested with various test samples varies in a wide range from 0.45 to 2.3 [7, 20–23]. The experimental results show that Takkab granite is weaker against shear loads compared to the tensile loads since K_{II}/K_{IC} is about 0.51.

The curve presented in Fig. 6 can be used as a design curve for estimating the optimum condition for practical applications like rock cutting process to determine the minimum required cutting energy and in hydraulic fracturing to calculate the fluid pumping power.

The compressive loading set up used for the cracked beams subjected to bending makes the FPB specimens more suitable for fracture testing on brittle materials like rocks and concretes which are weak against tensile loads. In comparison with the asymmetric three-point-bend loading configuration (which is another well known test specimen being used for mixed mode loading [11–13]), the FPB configuration requires a more complicated fixture and also more care in the experimental set up. However, the three-point-bend test configuration can be used only for limited combinations of mode I and mode II.

In particular, pure mode II cannot be introduced by this specimen. But as mentioned earlier, the full combinations of modes I and II can be easily introduced in the four-point-bend specimen by changing the locations of loading rollers. The mode I fracture toughness obtained for the tested granite is about 1.4 MPa m$^{0.5}$ which is in good agreement with the reported values for other types of granite materials [14–16]. As shown in Fig. 7, for mode I condition where the applied loads are symmetric relative to the crack line, fracture occurs in a self-similar manner and along the initial crack line.

However, for mixed mode conditions where both shear force and bending moment are present along the crack line, the path of crack growth deviates from the initial crack line. Such deviations can be seen in Fig. 7 that shows the crack growth trajectory in some of the granite specimens tested under different mode mixities. In all of the experiments it was observed that the crack growth started from the crack tip, extended along a curvilinear path, and finally terminated at the nearest loading roller.
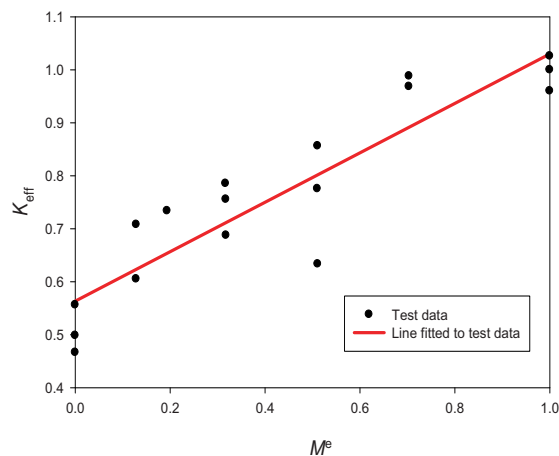
Fig. 6. Variations of mixed mode fracture toughness (K_{eff}) with M^e in the tested granite samples

6. Conclusions

Mixed mode I/II fracture toughness of Takkab granite was investigated numerically and experimentally by means of the asymmetric four-point-bend (FPB) specimen in the full range of mixed mode loading from pure mode I to pure mode II.

The experimental results obtained for the tested granite falls between the theoretical curves predicted by the maximum tangential stress criterion and the maximum energy release rate criterion.

According to the FPB test results, Takkab granite is weaker in mode II fracture than in mode I fracture.

Mode I   Mode II

$K_I/K_{II} = 1.988$ $K_I/K_{II} = 1.035$

$K_I/K_{II} = 0.545$ $K_I/K_{II} = 0.204$
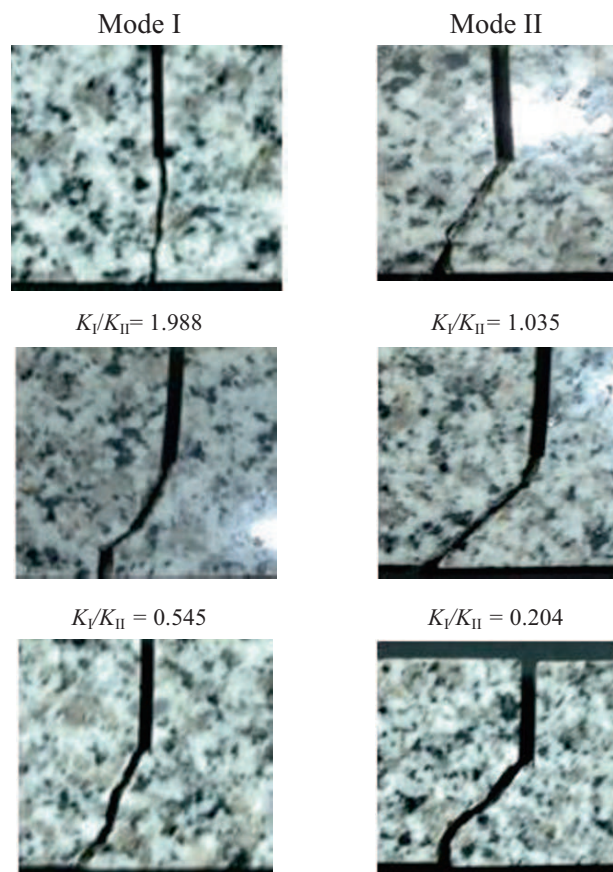
Fig. 7. Crack growth trajectory in some of the FPB specimens broken different mode mixities

References

[1] Ingraffea R (1981) Mixed mode fracture initiation in Indiana limestone and Westerly granite. Proc. 22nd US Symp. On Rock Mechanics, Cambridge MA, pp 186–191.

[2] Huang J., Wang S (1985) An experimental investigation concerning the comprehensive fracture toughness of some brittle rocks. Int J Rock Mech. Min. Sci Geomech Abstr, 22(2):99–104.

[3] Li S, Huang SM, Yang SC (2004) Experimental investigation on criterion of three-dimensional mixed-mode fracture for concrete. Cem Conc Res 34:913–916.

[4] Mario MA, Francis TL (2005) Numerical simulation of quasibrittle fracture in concrete. Eng Fract Mech 72(3):387–411.

[5] He MY, Cao HC, Evans AG (1990) Mixed mode fracture: the four-point shear specimen. J Metallurg Mat 38:839–846.

[6] Suresh S, Shih CF, Morrone A, O_Dowd NP (1990) Mixed-mode fracture toughness of ceramic materials. J Am Ceram Soc 73(5):1257–1267.

[7] Li M, Sakai M (1996) Mixed-mode fracture of ceramics in asymmetric four-point bending. J Am Ceram Soc 79(10):2718–2726.

[8] Tikare V, Choi SR (1997) Combined mode I–mode II fracture of 12-mol%-ceria-doped tetragonal zirconia polycrystalline ceramics. J Am Cer Soc 80:1624–1626.

[9] HE MY, Hutchinson JW (2000) Asymmetric four-point crack specimen. J Appl Mech 67:207–209.

[10] Shahani AR, Tabatabaei SA (2008) Computation of mixed mode stress intensity factors in a four-point bend specimen. Appl Math Model 32(7):1281–1288.

[11] Fett T, Gerteisen G, Hahnenberger S, Martin G, Munz D (1995) Fracture tests for ceramics under mode-I, mode-II and mixed-mode loading. J Eur Cer Soc 15:307–312.

[12] Xeidakis GS, Samaras IS, Zacharpoulos DA, Papakaliatakis GE (1996) Crack growth in a mixed-mode loading on marble beams under three point bending. Int J Fract 79:197–208.

[13] Jenq TS, Shah SP (1987) Mixed mode fracture parameters of concrete. SEM/RILEM Int Conf on fracture of concrete and rock, Texas, Shah SP, Swartz SE, (EDS), pp 359–369.

[14] Olofsson T (1978) Evaluation of fracture parameters and elastic properties of rock materials. Report 195E, university of Lulea, Sweden.

[15] Singh RN, Sun GX (1989) Relationships between fracture toughness, hardness indices and mechanical properties of rocks. Department of Mining engineering university of Nottingham, England, Magazine XLI, pp 49–62.

[16] Chang SH, Lee CI, Jeon S (2002) Measurement of rock fracture toughness under modes I and II and mixed-mode conditions by using disc-type specimen. J Eng Geol 66:79–97.

[17] Erdogan F, Sih GC (1963) On the crack extension in plates under plane loading and transverse shear. J Basic Eng Trans ASME 85: 519–525.

[18] Sih GC (1974) Strain-energy-density factor applied to mixed mode crack problems. Int J of Fract 10:305–321.

[19] Hussain MA, Pu SL, Underwood J (1974) Strain energy release rate for a crack under combined mode I and Mode II Fracture Analysis. ASTM STP 560. American Society for Testing and Materials, Philadelphia, pp 2–28.

[20] Awaji H, Kato T (1999) Criterion for combined mode I–II brittle fracture. Mat Trans JIM (Japan Institute of Metals), 40(9):972–979.

[21] Ayatollahi MR, Aliha MRM (2007) Fracture toughness study for a brittle rock subjected to mixed mode I/II loading. Int J Rock Mech Min Sci 44(4):617–624.

[22] Aliha MRM, Ashtari R, Ayatollahi MR (2006) Mode I and mode II fracture toughness testing for marble. J Appl Mech Mater 5-6:181–188.

[23] Singh D, Shetty DK (1989) Fracture toughness of polycrystalline ceramics in combined mode I and mode II loading. J Am Cer Soc 72 (1):78–84.

Experimental and Numerical Determination of Stress Intensity Factors of Crack in Plate with a Multiple Holes

S. Belamri[1], T. Tamine[2] and A. Nemdili[3]

[1]ARCELOR MITTAL, Direction Régionale Ouest, 02 rue Mekki Khalifa 31000 Oran, Algeria

[2]Laboratoire LCGE, Faculté de Génie Mécanique, Université des Sciences et de la Technologie d'Oran Algérie, BP 1505 EL M'NAUER 31000 Oran, Algérie

[3]Laboratoire LRTTFC Faculté de Génie Civil & d'Architecture

Abstract   The optical method of photoelasticity was used to measure stress field and stress intensity factors of crack with the presence of holes in a polycarbonate PSM-1 birefringeant plates under tension. Tests were used for variable numbers and dimensions of holes. The present study takes into account the several positions of holes and crack in plates. Stress intensity factor has been determined from the crack tip fringe pattern by multiple points' technic. Experimental results have been confirmed with a good agreement numerical estimation of stress intensity factors obtained with the finite element method (FRANC 2D).

Keywords: Photoelasticity, Fringe, Crack, Stress Field, Stress Intensity Factor, FRANC 2D.

1. Introduction

The lifetime of engineering materials may be associated with the size, the shape and the location of flaws or cracks in components. In mechanic applications it is often used a perfored or drilled holes. They can be a large number with a regular or random distribution. Then, it is important to estimate the stress concentration around theses holes and their influence on the mechanic behaviour. The problem of calculating the displacement and stress field in an elastic body containing holes interested many authors. For infinite plane with multiple circular holes under uniaxial tension [4, 6, 7, 9] resolved stress problems on multiply connected domains with the boundary integral equation. The application of this theory showed an extreme stability of this approach for a higher number of holes and cracks in loaded infinite plate. The circumferential stress is determined for different configuration and location of circular holes. Knowing the role of stress field near the crack tip in fracture mechanics analysis, authors in [12] used for isotropic and orthotropic material an optimization analysis in order to decrease the stress intensity factor. It is shown that the stress field at the crack boundary can be significantly improved by noncircular shapes.

Furthermore to adhesive patching, it is well known that drilled stop holes can reduce stress intensity factor. In this context, Junping Pu [8] used sub region BEM (Boundary Element Method) to study the effect of defective holes on crack. Results show that if the location of these drilled holes are chosen unsuitably, they can not only decrease the stress intensity factor, but also increase the crack expanding even more. It showed that for elliptic defective holes, the effect for the stress intensity factor on Mode-I loading is less than those of circular holes of which the radii are equal to the elliptic length axis. Also, Murdani et al. [2, 3] studied the effectiveness of the arrangement of a stop-drilled hole and additional holes on retarding crack growth and developed an analysis on the stress concentration. In the present study, a finite element method and the experimental technique of photoelasticity is used to determine the stress field around circular holes in finite plate under uniaxial tension. Effect of the number of holes and distance on the magnitude of the stress concentration is also analysed. The presence of crack emanating from central hole and the location of lateral holes complete our study through their interaction and their influence on the stress intensity factors.

2. Experimental method

Tension load testing is applied to a drilled holes and crack hole specimens. A photoelasticity method (Fig. 1) is applied to measure stress around holes. By rotating the circular polariscope, it can be obtained a monochromatic or a white light from which an isochromatic or isocline fringe patterns can be recorded. The photos are taken with a numerical camera and are treated by image digitalisation software.
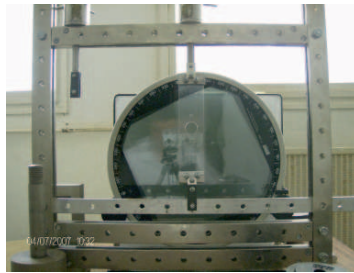
Fig. 1. Photo of photoelasticimetry installation

2.1. Material

Photoelastic specimens are machined from a polycarbonate sheet with a dimension of 254 × 254 mm and a thickness of $t = 5$ mm.

According to the manufacturer, the Young's modulus and Poisson's ratio of the sheet material are $E = 2390$ MPa and 0.38, and the material fringe value f is 7.1 KPa (fringe/m).

2.2. Test specimens

Specimens are cut from a polycarbonate sheet, material having height sensitivity to the stress. Specimen E-1 (Fig. 2) is a plate with two holes aligned with the x-axis and separated by a distance $\delta = 4$ a (a is the small hole radius). The geometric plate ratio is W/H = 0.25 and the radius ratio is equal to b/a = 5. Figure 3 shows a plate with the ratio W/H = 0.2, containing a colineair holes with the same radius a and a distance $\delta = 4a$.
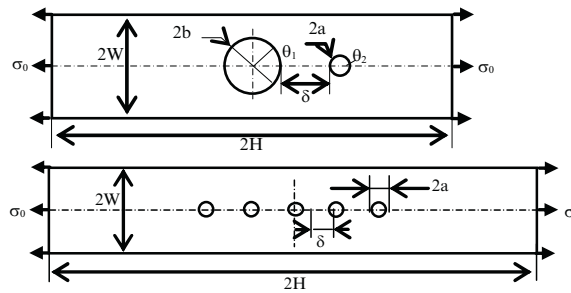
Fig. 2 and 3. Specimen E-1 and E-1

For the stress intensity factor study, the specimens F-1, F-2 and F-3 are used (Figs. 4, 5 and 6). In addition to the holes, a symmetrical crack with a depth l is machined from the central hole. The radius ratio is equal to b/a = 2 and the distance between holes is $\delta = 4a$ in the load direction (X axis) and $\eta = 2a$ in the Y axis (for the specimen F-2 and F-3).
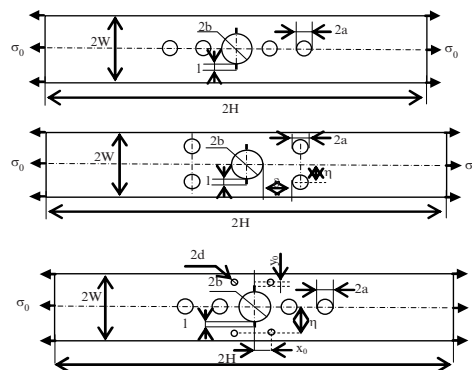
Fig. 4, 5 and 6. Specimen F-1, F-2 and F-3

3. Method of resolution

During tests, photoelasticity method is applied and the isochromatic fringes have been recorded with a numerical camera. The data measures are obtained from the fringe by using the image digitalisation software. From the separation of principal stresses technique [1, 5, 10, 11], local stress can be determined. For any point of the model, the maximum shear can be written as:

$$\tau_{\max} = \frac{\sigma_1 - \sigma_2}{2} = \frac{N.f}{2h} \tag{1}$$

σ_1 and σ_2 are respectively the principal stress in the first and the second direction, N is the fringe pattern order, f is the sensitivity of the material, h is the specimen thickness.

The shear stress τ_{xy} can be found from Mohr circle and its formulation is:

$$\tau_{xy} = -\frac{\sigma_1 - \sigma_2}{2}.\sin 2\alpha = -\frac{N.f}{2.h}\sin 2\alpha \tag{2}$$

α is the angle between σ_x (or σ_y) and σ_1 (or σ_2).

In plane stress, [8] used the following equilibrium equations:

$$\frac{\partial \sigma_x}{\partial x} + \frac{\partial \tau_{xy}}{\partial y} = 0 \quad \text{and} \quad \frac{\partial \tau_{xy}}{\partial x} + \frac{\partial \sigma_y}{\partial y} + = 0 \tag{3}$$

Integrating on the X direction, stress can be written as:

$$\sigma_x(x_1) = \sigma_x(x) - \int_{x_0}^{x_1} \frac{\partial \tau_{xy}}{\partial y} dx = \sigma_x(x_0) - \Delta\tau_{xy}((x_0 + x_1)/2) \tag{4}$$

x_0 and x_1 are the corresponding points boundary of meshing line where the stress should be determined.

Applying Matlab 6.5 software, it can be possible to resolve the system of equations and to calculate the local stress. For F-1 and F-2 specimens, experimental results are obtained from digitalisation of fringe patterns in the vinicity of crack and by applying the multipoints method [5, 11]. Therefore, stress intensity factor is related to fringe parameters by the relationship:

$$K_I = \frac{\sqrt{2\pi r}}{h} \cdot N \cdot f \tag{5}$$

4. Results

The application of separation of principal stress technique and the mutipoints method with a MATLAB program allowed the determination of local stress and the stress intensity factors. In the other hand, finite element method with Franc 2D software is used for all specimens. As most of specimens are symmetrical, just a quarter of them are meshed with T6 and Q8 elements. A plane stress resolution is applied.

As example, Fig. 7 shows a superposition of an experimental fringes and numerical shear stress for collinear holes. The same concentration of shear stress is observed on the experimental and the numerical resolution.
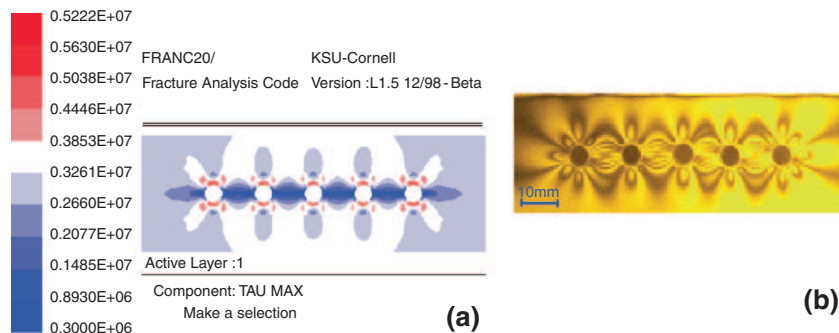
Fig. 7. Example of experimental and Numerical Shear stress distribution in Specimen E2; (**a**) Experimental results and (**b**) Numerical results

4.1. Specimen with two holes (E-1)

Experimental and numerical results have allowed plotting the normalized stress acting on the boundary of the first (central) and the second hole respectively versus the angle θ_1 and θ_2 (Fig. 8). For the central hole, the numerical resolution gives the maximum stress concentration at a location $\theta_1 = 89.2°$. The same value is found by the photoelasticimetry method for the radius ratio b/a = 5.

The stress concentration decrease when the ratio (b/a) is equal to 3. This observation is noted by Jianlin Wang et al. [6] for the same radius ratio and distance δ for infinite plate with two holes. We have studied the effect of the ratio (δ/a) the stress in the first hole and the second (Fig. 9). We notice that δ/a, has a very little influence on the variation of local stress for the central hole whereas it is important for the second hole.
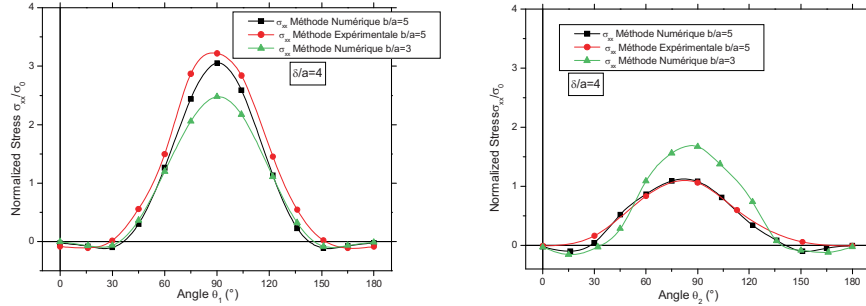
Fig. 8. Stress distribution in the first (central hole) and second holes of specimen E-1
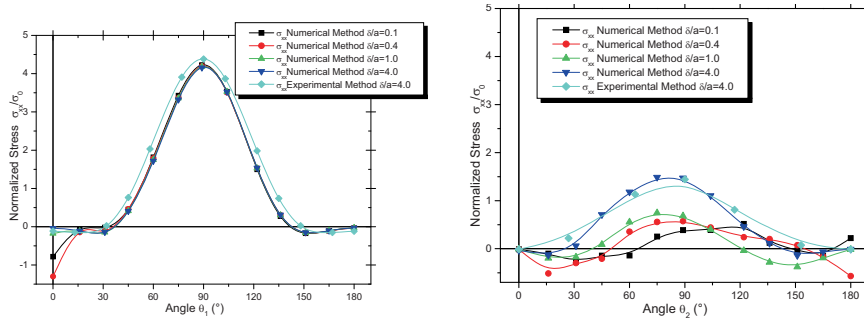
Fig. 9. Stress distribution in the first hole (central hole) and second hole for various ratio δ/a

4.2. Specimen with collinear holes

Loaded Plate with equally spacing collinear circular holes along x axis (specimen E-2) is considered. A variable number of holes has been studied (1, 3,…15 holes) with $\delta/a = 1$, $\delta/a = 2$ and $\delta/a = 4$. Normalized stress for $\delta/a = 4$ and $\delta/a = 1$ are plotted in Fig. 10.

For $\delta/a = 1$ and $\delta/a = 4$ the maximum stress in central hole is located at the angle $\theta_1 = 89.2$ some either the number of holes in specimen. For a number of holes $N \geq 3$ and $\delta/a = 4$, the maximum stress values are higher than those obtained for $\delta/a = 4$.Taking into account the maximum values from the above graphs, we have plotted the stress concentration factor (σ_{max}/σ_0) for a number N of colineair holes in the specimen E-2 (Fig. 11). Stress concentration curve for $\delta/a = 4$ is more important than for $\delta/a = 2$ and $\delta/a = 1$. For $\delta/a = 4$, results approach the asymptotic value of 2.80 for N = 3 holes. When this ratio is equal to 2, the asymptotic begins from N = 5 holes with a value of 2.55.This value decreases to 2.35 from N = 7 holes when $\delta/a = 1$.

Upon comparing the results obtained for $\delta/a = 2$ by the present method with those of [4] we found the same distribution of the stress concentration with an asymptotic tendency. Our values are slightly overhead compared to results of these authors. It would seem that the finite geometrical size of plate has an effect on the concentration values.
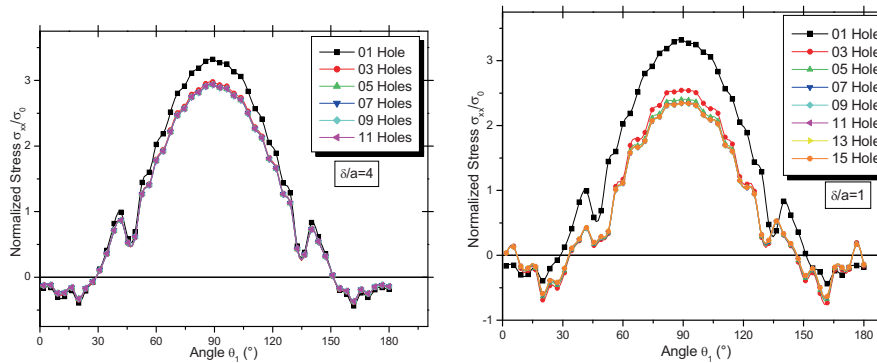
Fig. 10. Evolution of normalized stress in central hole for $\delta/a = 1$ and $\delta/a = 4$
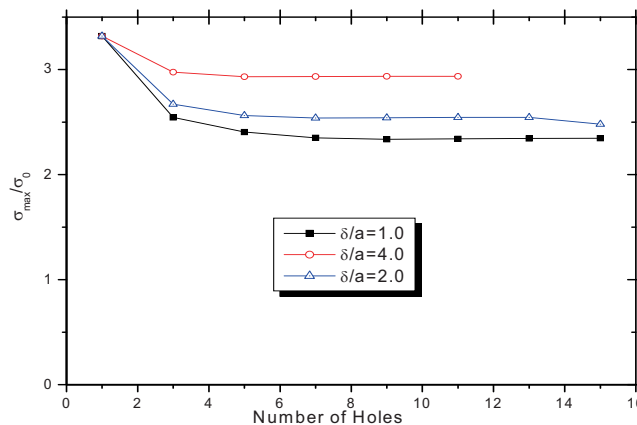
Fig. 11. Stress concentration factor for N holes

4.3. Specimen with collinear holes and a symmetrical crack

From the previous case it has been found that the maximum stress is located in the central hole for the angle $\theta_1 = 90°$. Then, a symmetrical crack emanating from central hole has been machined at this position. After loading the F-1 specimen, we obtained the fringes from experimental method and shear stress distribution by

finite element method. It is noticed in Fig. 12 that the fringes concentration is around the crack tip. This is confirmed by the numerical results.

(a) (b)

| 0.2198E+02 |
| 0.1979E+02 |
| 0.1760E+02 |
| 0.1540E+02 |
| 0.1321E+02 |
| 0.1102E+02 |
| 0.8828E+01 |
| 0.6635E+01 |
| 0.4443E+01 |
| 0.2251E+01 |
| 0.5926E - 01 |
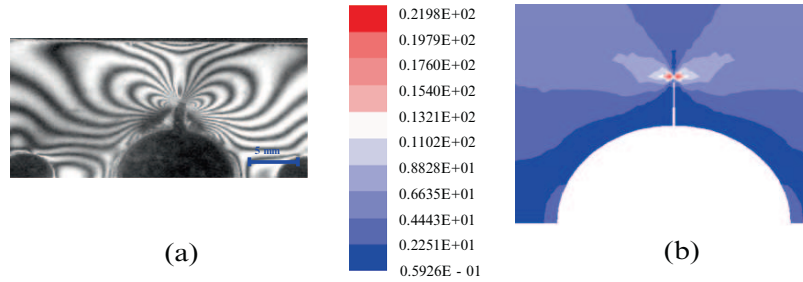
Fig. 12. Shear stress distribution in collinear holes with symmetrical crack specimen (**a**) Experimental shear stress and (**b**) Numerical shear stress distribution
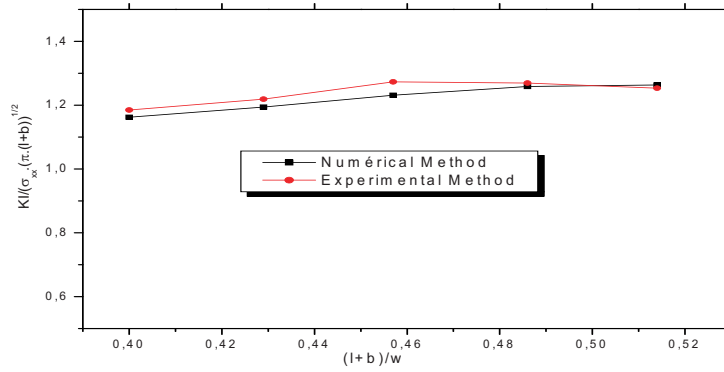
Fig. 13. Evolution of normalized stress intensity factor
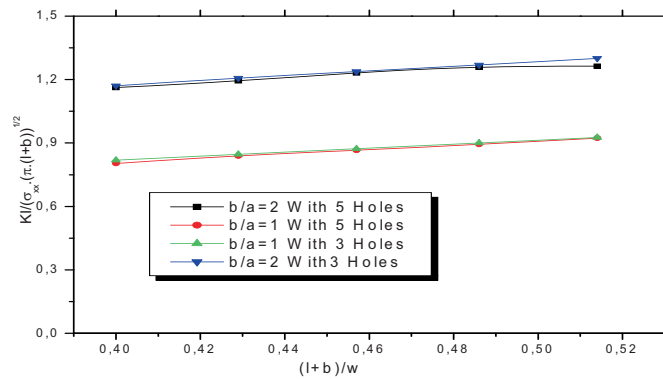
Fig. 14. Evolution of normalized stress intensity factor with number of holes

The stress intensity factor is evaluated by Eq. (5) and numerically with the FEM using the fracture post-processor available on Franc 2D software. Results are

plotted in Fig. 13. Analyse of experimental and numerical values showed that the divergence between them is low, estimated to 3%. The influence of the presence of a high number of holes in X direction (collinear) and the radius ratio b/a on the stress intensity factors are represented in Fig. 14. For the same distance between holes $\delta/a = 4$, either the number of holes, the normalized stress intensity factor values decreases appreciably (30%) when b/a = 1.

4.4. Central hole with symmetrical crack and lateral holes

Specimen F2 is loaded in tension. Experimental and numerical methods are applied. Figure 15 represents the experimental fringes and the numerical shear stress distribution around the crack tip. The normalized stress intensity factor is plotted for different value of normalized crack depth (Fig. 16). A good agreement is observed between the numerical and the experimental results if we take into account the effect of fringe interference between lateral holes and crack tip.
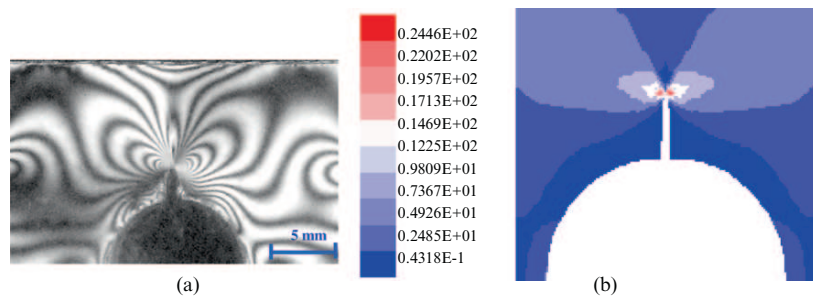
Fig. 15. Shear stress distribution for specimen F-2: (**a**) experimental shear stress and (**b**) numerical shear stress distribution
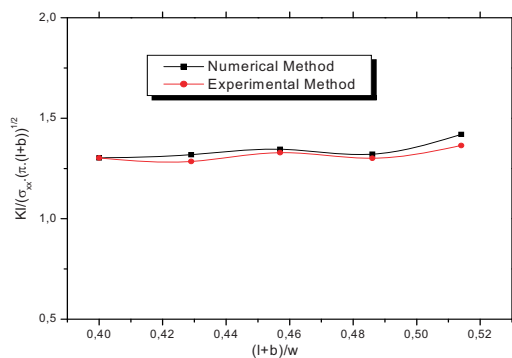
Fig. 16. Evolution of normalized stress intensity factor for specimen F-2

4.5. Collinear holes with symmetrical crack and lateral holes

It is interesting to study if the effect of drilling holes near the crack can decrease the stress intensity factor. We consider a plate with the same geometrical ratio as the specimen F-1 but having in more four holes (two on all sides of crack tip) with the radius ratio $d/b = 0.2$ for the first analysis and $d/b = 0.4$ for the second. The lateral hole is located from the crack tip by the coordinate (X_0, Y_0).

For the resolution, we used the normalized crack depth $(l + b)/W = 0.514$ as the above case (Fig. 17) and a constant position $X_0/l = 1$. By varying the lateral holes position Y_0, we found the stress intensity factor for symmetrical crack. Figure 17 present the twin case resolution corresponding to $d/b = 2.5$ and $d/b = 5.0$.
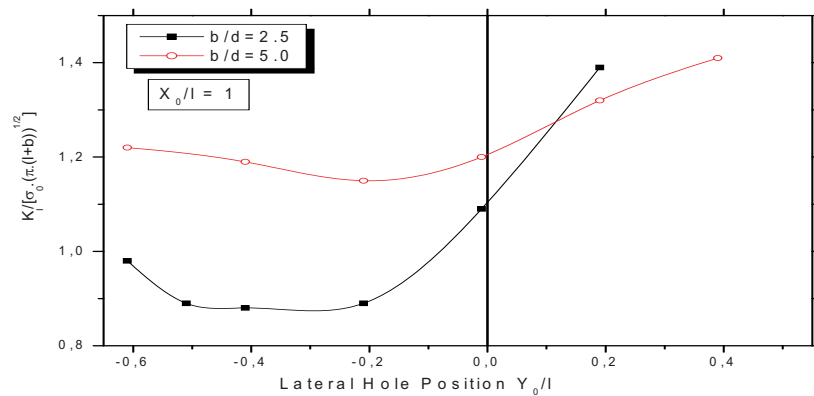
Fig. 17. Evolution of normalized stress intensity factor for various lateral hole location

The presence of lateral holes decreases the stress intensity factor. It is confirmed if we compare the results with the above case for the specimen without lateral holes. The fall in the value of this parameter is as much more important when the lateral holes radius increases.

The minimum value of the stress intensity factor is noted for the position of lateral holes Y_0/l included between -0.3 and -0.2. For this position the stress intensity factor decreases of about 29% in comparison with the results of the specimen F-1. The same constitution have been found by [6] who study the effect of circular or elliptic hole position on the stress intensity factor for a plate with a central crack.

5. Conclusions

For all specimens tested, stress concentration and stress intensity factors determined by the finite element method are in good agreement with results obtained by experimental photoelasticimetry technique. For a plate with two holes, the maximum stress is observed in the central hole at the angle position $\theta = 89.2°$.

The effect of the ratio (b/a) is important since the maximum stress decrease when this ratio change from the value 5 to 3. On the other hand the maximum stress in the second hole increase when b/a decrease.

The ratio (δ/a) has a very little influence on the stress for central hole whereas it is important for the second hole. These results are noted for the infinite plate study by [6]. Results on specimens E-2 with collinear holes showed that for the same number of holes, the stress concentration factor increase with the ratio δ/a.

The evolution of the stress concentration factor (σ_{max}/σ_0) has an asymptotic tendency. For the crack specimens, a small divergence of results in term of stress intensity factors (3%) between numerical and experimental method are obtained in spite of the fringe interference in the crack tip. The hole number don't affect the value of stress intensity factors. On the other hand, this parameter is influenced by the radius ratio of holes b/a.

In our study, we have incorporated lateral holes near the crack tip by using the specimen F-3. It showed that for the same crack depth, the stress intensity factor decreases of about 29% with the lateral holes location in comparison with the result of specimen F-1 (without lateral holes). The size of lateral hole and the position by report to crack tip has high influence on the stress intensity factor (Fig. 17). This is noticed by [8] in their works on the effect of defective holes on a central crack in plate.

References

[1] A Ajovalasit, G Pitarresi, B Zuccarello (2006). Limitation of carrier fringe methods in digital photoelasticity. Optics and Lasers in Engineering 45(5): 631–636.

[2] A Murdani, C Makabe, A Saimoto, R Kondou (2008). A crack growth arresting technique in aluminium alloy. Engineering Failure Analysis 15: 302–310.

[3] A Murdani, C Makabe, A Saimoto, Y Irei, T Miyazaki (2007). Stress concentration at stop drilled holes and additional holes. Engineering Failure Analysis 15(7): 810–819.

[4] B Wang, K T Chau (2001). New boundary element method for mixed boundary value problems involving cracks and holes: Interactions between rigid inclusions and cracks. International Journal of Fracture 110: 387–406.

[5] H Mahfuz, T L Wong, R O Case (1990). Separation of principal stresses by SOR technique over arbitrary boundaries. Experimental Mechanics 30(4): 319–327.

[6] Jianlin Wang, Steven L Crouch, Sofia G Mogilevskaya (2003). A complex boundary integral method for multiple circular holes in an infinite plane. Engineering Analysis with Boundary Elements 27: 789–802.

[7] Johan Helsing, Anders Jonsson (2002). Stress calculations on multiply connected domains. Journal of Computational Physics 176: 456–482.

[8] Junping Pu (2006). Effect of defective holes on crack using the boundary element method. Engineering Analysis with Boundary Elements 30: 577–581.

[9] K T Chen, K Ting, W S Yang (2000). Stress analysis of two dimensional perforated plates using boundary element alternating method. Computers and Structures 75: 515–527.

[10] M R Ayatollahi, H Safari (2003). Evaluation of crack tip constraint using photoelasticity. International Journal of Pressure Vessels and Piping 80: 665–670.

[11] W Dally, W F Riley (1978). Experimental Stress Analysis, second edition, Mc Graw Hill, Kogakushi.

[12] P Pederson (2004) Design study of hole positions and hole shapes for crack tip stress releasing. Structural and Multidisciplinary optimization, 28(4): 243–251.

Dynamic Response of Cracked Plate Subjected to Impact Loading Using the Extended Finite Element Method (X-FEM)

R. Tiberkak[1], M. Bachene[2], B.K. Hachi[3], S. Rechak[4] and M. Haboussi[5]

[1]Département de Mécanique, Université Saad Dahleb, BP 270 Soumaa, Blida 09000, Algérie

[2]Département de Mécanique, Université de Médéa 26000, Algérie

[3]Département Electromécanique, Centre Universitaire de Djelfa, BP 3117 Ain-Cheih 17000, Djelfa, Algérie

[4]Laboratoire de Génie Mécanique et développement, Ecole Nationale Polytechnique, BP 182 El-Harrach 16200, Alger, Algérie

[5]Laboratoire d'Energétique et de Mécanique Théorique et Appliquée (LEMTA), ENSEM-INPL, BP 160 F-54504 Vandœuvre-Lès-Nancy, France

Abstract   Yet and according to our knowledge, the extended finite element method X-FEM has not been used in the dynamic response of cracked plates subjected to impact loading, subject of this study. From prior knowledge of the impact properties (contact force and central deflection) of a virgin plate, one can quantitatively through the present study predicts the eventual presence of discontinuities in plates by comparison of impact properties of cracked plate to the virgin ones. In the numerical implementation, conventional finite element without any discontinuity is first carried out, then enriched functions are added to nodal displacement field for element nodes containing cracks. Therefore no remeshing of the domain is required, leading to a great gain in time computing. The mathematical model includes both transverse shear deformation and rotatory inertia effects. Based on the above, a self contained computer code named "REDYPLAF", written in FORTRAN is hence developed. The effects of Crack length and crack position on contact force and on plate deflection are analyzed. The obtained results show that the contact force is divided into three zones. The same fact is also observed for the maximum plate deflection. Another observed fact is related to crack dissymmetry which has a direct effect on the maximum plate deflection.

Keywords: Dynamic Response, Cracked Plate, Extended FEM, Impact Loading.

1. Introduction

The presence of cracks, at least at a microscopically level, always exists in mechanical components. After certain hours of services, these micro cracks initiate and propagate to become effectively dangerous by decreasing the dynamic-mechanical properties of components.

The existence of discontinuities in structures generally induces difficulties during their numerical implementation. The extended finite element method (X-FEM) applied to divers fracture mechanic problem has proved its efficiency where all numerical difficulties and all shortcomings associated with meshing of the crack surfaces encountered with the classical finite element are alleviated. However, the finite element method is used as the building block in the extended finite element method, and hence much of the theoretical and numerical developments in finite elements can be readily extended and applied. For crack modeling, a discontinuous function and the two-dimensional asymptotic crack-tip displacement yields are added to the displacement-based finite element approximation. Partition of unity enrichment methods for discontinuities and near-tip crack yields were introduced by Belytschko and Black [1]. Moes et al. [2] proposed the generalized Heaviside function as a means to model the crack away from the crack tip, and developed simple rules for the introduction of the enrichment function at the crack-tip.

In the present study, enriched finite element method (X-FEM) is developed for the dynamic analysis of cracked plates subjected to impact loading. Plates containing through edge crack and central crack are considered. In addition, different configurations in which we vary crack parameters, i.e.; crack length and crack position are included. The hypothesis made in the study is to consider the crack parallel to one edge of the plate and to stop at the end of each element. Contact force and maximum deflection of the plate are therefore computed. The paper is structured as follow. In the next section, the extended finite element method is presented. We first present the mathematical model used followed by the X-FEM formulation and ending up with the establishment of mass and stiffness matrices. In Section 3, we describe the development in the computation of the contact force and central deflection. Numerical applications are presented and discussed in Section 4. We finalize the paper by drawing some conclusions.

2. Mathematical model and X-FEM formulation

2.1. Displacement field

The mathematical model is based on Mindlin plates. Let us consider a Cartesian co-ordinate system in such a way that the xy plane coincides with the midplane of the plate of sides a, b and thickness h (Fig. 1). The displacement field can be expressed as [3, 4]:

$$
\begin{aligned}
u(x, y, z) &= z\theta_x(x, y) \\
v(x, y, z) &= z\theta_y(x, y) \\
w(x, y, z) &= zw_0(x, y)
\end{aligned}
\tag{1}
$$

where u, v, w are the displacements in the x, y, z directions, respectively, w_0 denotes the transverse displacements of the mid surface, θ_x and θ_y are the normal rotations of the mid surface normal in the xz and yz planes, respectively.
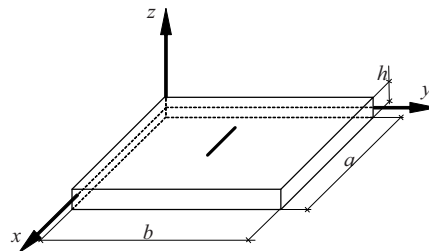
Fig. 1. Geometry of cracked rectangular plate

2.2. X-FEM formulation

The X-FEM analysis consists first in the discretization of the plate by conventional finite element method without crack consideration [5, 6]. The effects of the discontinuity of the nodal displacement of cracked elements are enriched by the enrichment functions. Details of the enrichment can be found in [1, 2]. Since in the dynamic analysis, we consider that the crack path is parallel to one side of the plate and supposed to stop at the end of each element, the X-FEM approximation can be written as follows:

$$u = \sum_{i \in I} N_I u_i + \sum_{j \in J} N_j H(x) u'_j \tag{2}$$

As represented by Eq. (2), the X-FEM can be regarded as the superposition of the classical FEM represented by the first right hand side term and a discontinuous enrichment represented by the second right hand side term. In Eq. (2), N_i and u_i are the classical shape function, and the classical nodal displacement at node i, respectively. I is the set of all nodal points of the plate, while J represents the set of nodes of the elements located on the discontinuity. $u'_j (j \in j)$ are the nodal degrees of freedom to be enriched, and $H(x)$ is a discontinuous function defined as the Heavyside function:

$$H(x) = \begin{cases} +1 \; on \; the \; \text{top surface of the crack} \\ -1 \; on \; the \; \text{top surface of the crack} \end{cases} \tag{3}$$

In the following, elements of stiffness matrix and mass matrix will be derived from the expression of the potential energy and the kinetic energy. The FEM formulation based on the Mindlin–Reissner plate theory tacking into account the effects of shear deformation and rotatory inertia is used. Each node possesses three degrees of freedom w_i, θ_{xi} and θ_{yi}. In conjunction with Eq. (2), the displacement field in the X-FEM formulation can be written as:

$$\begin{Bmatrix} w_0 \\ \theta_x \\ \theta_y \end{Bmatrix} = \sum_I N_i \delta_i + \sum_J N_j H \delta_j' \tag{4}$$

The strain fields in curvature and transverse shear derived from Eq. (4) are as:

$$\begin{Bmatrix} \kappa_{x0} \\ \kappa_{y0} \\ \kappa_{xy0} \\ \gamma_{xz} \\ \gamma_{yz} \end{Bmatrix} = \sum_I \begin{bmatrix} 0 & \dfrac{\partial N_i}{\partial x} & 0 \\ 0 & 0 & \dfrac{\partial N_i}{\partial y} \\ 0 & \dfrac{\partial N_i}{\partial y} & \dfrac{\partial N_i}{\partial x} \\ \dfrac{\partial N_i}{\partial x} & N_i & 0 \\ \dfrac{\partial N_i}{\partial y} & 0 & N_i \end{bmatrix} \begin{Bmatrix} w_{0i} \\ \theta_{x0i} \\ \theta_{y0i} \end{Bmatrix} + \sum_J \begin{bmatrix} 0 & \dfrac{\partial N_j}{\partial x}H & 0 \\ 0 & 0 & \dfrac{\partial N_j}{\partial y}H \\ 0 & \dfrac{\partial N_j}{\partial y}H & \dfrac{\partial N_j}{\partial x}H \\ \dfrac{\partial N_j}{\partial x}H & N_j H & 0 \\ \dfrac{\partial N_j}{\partial y}H & 0 & N_j H \end{bmatrix} \begin{Bmatrix} w_{0j}' \\ \theta_{x0j}' \\ \theta_{y0j}' \end{Bmatrix} \tag{5}$$

The above equations can be written in a compact form:

$$\varepsilon = B_i u + B_j' u' \qquad B_j' = H B_j \tag{6}$$

The stress field in term of moments and transverse shear force is:

$$\sigma = C B_i \delta_i + C B_j' \delta_j' \tag{7}$$

where C is the matrix of elastic rigidities, and σ are the generalized stresses. When the plate is discretized with the usual finite element method, the potential energy of an element e of the plate can be written as follows:

$$U^e = \frac{1}{2} \begin{Bmatrix} u^T & u'^T \end{Bmatrix} K^e \begin{Bmatrix} u \\ u' \end{Bmatrix} \tag{8}$$

where K^e is the element stiffness matrix, expressed as follows:

$$K^e = \begin{bmatrix} K^e_{ii} & K^e_{ij} \\ K^e_{ji} & K^e_{jj} \end{bmatrix} = \begin{bmatrix} \int\limits_{A_e} B_i^T C B_i\, dA & \int\limits_{A_e} B_i^T C B'_j\, dA \\ \int\limits_{A_e} B'^T_j C B_i\, dA & \int\limits_{A_e} B'^T_j C B'_j\, dA \end{bmatrix} \tag{9}$$

The kinetic energy of an element e of the plate is:

$$T^e = \frac{1}{2} \left\{ \dot{u}^T \quad \dot{u}'^T \right\} M^e \left\{ \begin{matrix} \dot{u} \\ \dot{u}' \end{matrix} \right\} \tag{10}$$

where the dot point indicates the first derivative of the displacement field with respect to time and ρ is the material density of the plate. Where M^e is the element mass matrix:

$$M^e = \begin{bmatrix} M^e_{ii} & M^e_{ij} \\ M^e_{ji} & M^e_{jj} \end{bmatrix} = \begin{bmatrix} \int\limits_{A_e} N_i \rho\, N_i h\, dA & \int\limits_{A_e} N_i \rho\, N_j h\, dA \\ \int\limits_{A_e} N_j \rho\, N_i h\, dA & \int\limits_{A_e} N_j \rho\, N_j h\, dA \end{bmatrix} \tag{11}$$

3. Contact force

In the following section, we present the mathematical development for the computation of contact force and central deflection. The dynamic equation of plate is given by the following [7, 8]:

$$[M]\{\ddot{u}\} + [K]\{u\} = \{F\} \tag{12}$$

where $[M]$ *and* $[K]$ are the plate mass matrix and stiffness matrix, respectively. $\{u\}$ and $\{\ddot{u}\}$ are respectively the displacement and acceleration vector. $\{F\}$ is the equivalent of external load, which include the impact force. The dynamic equation of a rigid ball is given by the use of the Newton's second law:

$$m_i \ddot{w}_i = -F_c \tag{13}$$

where m_i is the mass of the ball (impactor) and F_c is the contact force. Consider the contact between a spherical ball made of an isotropic material and a target laminated composite plate containing N transversely thin layers. The contact is located at the center of the plate. Figure 2 describes the impact procedure of the two structures (rigid body and the composite plate).
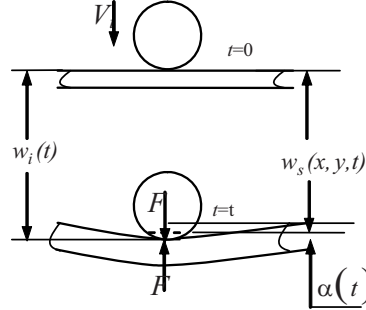
Fig. 2. Description of impact procedure

The contact force between the impactor and the plate is calculated using a modified non-linear Hertzian indentation law proposed by Yang and Sun [9].

$$F = \begin{cases} k\alpha^{3/2} & \textit{For loading} \\ F_m\left(\dfrac{\alpha - \alpha_0}{\alpha_m - \alpha_0}\right)^q & \textit{For unloading} \end{cases} \tag{14}$$

where q, β are experimental constants, k is a contact stiffness coefficient, the various analytical and experimental techniques for determination of k have been proposed in the literature. Coefficient F_m and α_m means, respectively, maximum impact force reached before unloading, and corresponding maximum indentation depth, corresponding to F_m, before the unloading phase. α_0 is the permanent indentation depth in the target (plate). The contact deformation α, defined as the difference between the displacement of the impactor and that of the composite laminates (Fig. 2), is given by the following:

$$\alpha(t) = w_i(t) - w_s(t) \tag{15}$$

$w_i(t)$ and $w_s(t)$ are the displacement of the impactor and the impacted point on the mid surface of the plate. The displacement of impactor at the time step $(n+1)$ is determined by applying Newmark's integration scheme for the differential equation:

$$(w_i)_{n+1} = (w_i)_n + \Delta t(\dot{w}_i) + \left(\frac{\Delta t^2}{4}\right)(\ddot{w}_i)_n - \left(\frac{\Delta t^2}{4m_i}\right)(F_c)_{n+1} \tag{16}$$

Substituting the above expression for w_i in the contact laws defined in Eqs. (14) and (15) we obtained the following equations for the loading and unloading phase:

$$(F_c)_{n+1} = K\left[(w_i)_n + \Delta t(\dot{w}_i)_n + \left(\frac{\Delta t}{4}\right)(\ddot{w}_i)_n - (w_s)_{n+1} - \frac{\Delta t^2}{4m_i}(F_c)_{n+1}\right]^{1.5} \quad (17)$$

$$(F_c)_{n+1} = K_1\left[(w_i)_n + \Delta t(\dot{w}_i)_n + \left(\frac{\Delta t}{4}\right)(\ddot{w}_i)_n - (w_s)_{n+1} - \alpha_0 - \frac{\Delta t^2}{4m_i}(F_c)_{n+1}\right]^q \quad (18)$$

4. Numerical applications

In this section, the one through crack model (Fig. 3) parallel to x axis is present before the contact force is applied. The crack is of length a and extends along the x axis. Non-dimensionalized parameters used in the text are given: $\bar{a} = a/l, \quad \bar{b} = b/L,$ and $\bar{c} = c/l$.
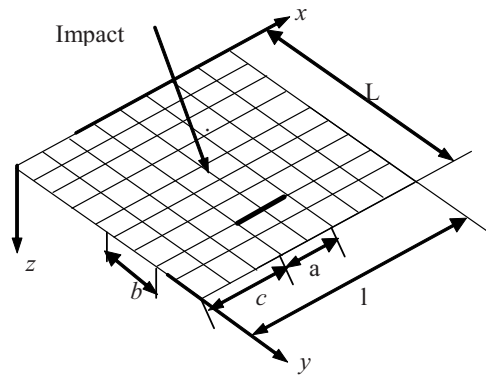
Fig. 3. Geometry and sign convention

A parametric study by varying various parameters such as: crack length, position of the crack in x and y directions, is performed. Contact force and central deflection are thus computed using REDYPLAF computer code.

- $\bar{a} = a/l$ (Ratio of crack length along x-axis to the plate length)
- $\bar{b} = b/l$ (Ratio of crack position along y-axis to the plate length)
- $\bar{c} = c/l$ (Ratio of crack position along x-axis to the plate length)

The properties of the target plate and of the impactor used in the numerical applications are: plate proprieties: $E = 67$ GPa, $v_{12} = 0.33$, $\rho = 2,800$ Kgm^{-3}.

Impactor proprieties: $E = 200$ GPa, $v_{12} = 0.3$, $\rho = 7,800$ Kgm^{-3}, $r = 12.5$ mm.

4.1. Effect of the crack length

An isotropic square plate 20 cm long, 20 cm wide, 8 mm thick, and clamped on its four edges is considered. The plate is impacted at its center by a steel ball of 12.7 mm diameter with an impact velocity equal to 5 m/s. Figures 4 and 5 show the maximum contact force and maximum central deflection for various parameters of the crack, from which general observations are made.

One can effectively observe that the maximum contact force decreases with the increase of crack length, while the maximum central deflection increases with the increase of the crack length.

From Fig. 4 it can be observed that the variation of the maximum contact force versus the ratio $\bar{a}$, and for different values of ratio $\bar{b}$ passes generally by three different zones: Zone 1, Zone 2, and zone 3. Zone 1 is characterized by a constant variation of the maximum contact force F_c, meaning that the presence of crack does not influence the maximum contact force.
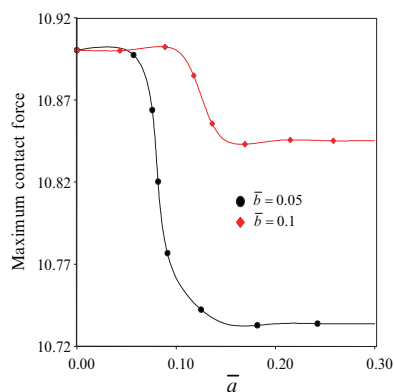
Fig. 4. Maximum contact force for two different position of crack
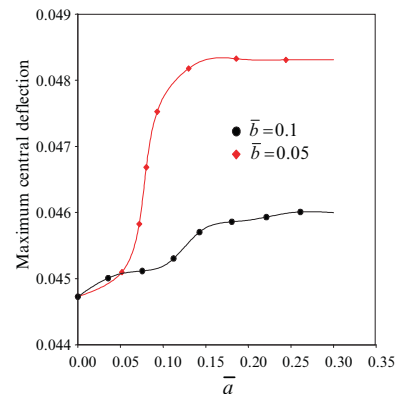
Fig. 5. Maximum central deflection for two different position of crack

The maximum contact force remains constant in the interval of the crack ratio $0 \leq \bar{a} \leq 0.1$. Zone 2, is characterized by a brusque variation of the maximum contact force F_c. The maximum contact force decreases rapidly when the crack ratio $\bar{a}$ varies between 0.1 and 0.15.

The plate in this region looses rapidly its strength. Zone 3, is characterized by a slow variation of the maximum contact force F_c for values of crack ratios $\bar{a}$ greater than 0.15. Almost, similar physical fact is observed for the case of the maximal central deflection.

4.2. Effect of the crack position

The variation of contact force and central deflection versus time is illustrated for different values of position of the crack ratio along y-axis $\bar{b}$. According to Fig. 6, the presence of symmetric crack affects slowly the contact force for crack ratios $\bar{b}$ less than 0.1. When $\bar{b}$ is greater than 0.1 there is no significant effect on the contact force. However, for crack ratios less than 0.3 a significant effect on the central deflection is observed (Fig. 7).
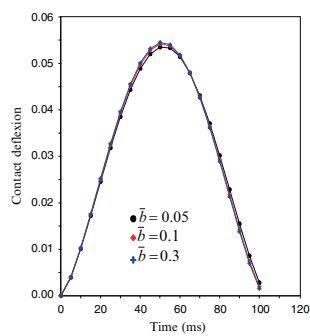
Fig. 6. Contact force history: $\bar{a} = 0.2$, $\bar{c} = 0.4$
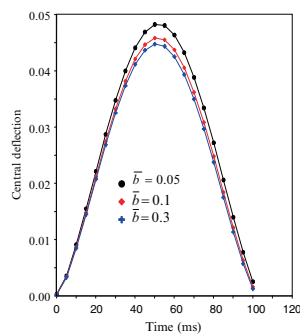
Fig. 7. Central deflection history for: $\bar{a} = 0.2$, $\bar{c} = 0.4$

Figure 8 show central deflection with respect to the crack position ratio in the x-axis $\bar{c}$. It can be seen from this figure that central deflection increases with the increase of the crack position ratio $\bar{c}$. This can be explained by the fact that the central deflection increases when the crack position is close to the impact surface.
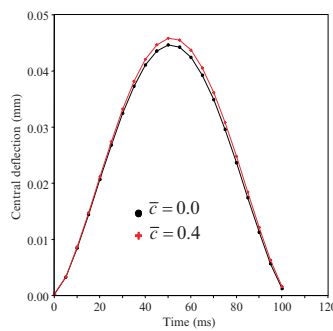
Fig. 8. Central deflection history for $\bar{a} = 0.2$, $\bar{c} = 0.1$

5. Conclusions

The effects of crack on the dynamic response of impacted crack are studied. A model including both transverse shear deformation and rotatory inertia has been numerically implemented using the extended finite element method (X-FEM). A FORTRAN computer code REDYPLAF has been developed. A parametric study in which the effects of crack length and position has been studied. The tendency of results show that the contact force decreases with the increase of the crack length, while but the central deflection increases with the increase of crack length. It is observed that the path of the maximum contact force and central deflection pass by three different zones. This study can be extended to the cases of composite plates.

References

[1] Belytschko T and Black T (1999). Elastic crack growth in finite elements with minimal remeshing. Journal for Numerical Methods in Engineering 45(5): 601–620.
[2] Moes N, Dolbow J and Belytschko T (1999). A finite element method for crack growth without remeshing. J Numerical Methods in Engineering 46(1): 131–150.
[3] Tiberkak R, Bachene M, and Rechak S (2007). The effect of cracks on impact of isotropic plates using the extended finite element method (X-FEM). First National Conference on Mechanics and Engineering Systems NCMES'07. Boumerdes, May 26–27.
[4] Bachene M, Tiberkak R, and Rechak S (2007). Analyse modale des plaques fissurées par la méthode des éléments finis étendus X-FEM.18e Congrès Français de Mécanique CFM'07, du 27 au 31 Août. Domaine Universitaire De Grenoble. France.
[5] Zienkiewicz O C and Taylor R L (2000) The Finite Element Method. Fifth edition: The basis. Vols 1 & 2. Butterworth-Heinemann.
[6] Bathe K J and Wilson E L (1976) Numerical methods in finite element analysis. Prentice Hall Engle-wood Cliffs, N.J.
[7] Tam T M and Sun C T (1982) Wave propagation in graphite/epoxy laminates due to impact. NASA CR 168057.
[8] Tiberkak R et al. (2008) Damage prediction in composite plates subjected to low velocity impact. Journal of Composite Structures 83: 73–82.
[9] Yang S H and Sun C T (1981) Indentation law for composite laminates. Amercian Society for Testing And Materials, ASTM STP 787: 425–449.

On Heterogeneity of Welded Joint by Modelling of Diffusion

L. Řeháčková, J. Kalousek and J. Dobrovská

Faculty of Metallurgy and Materials Engineering, VŠB-Technical University Ostrava, 17. listopadu 15, 708 33 Ostrava, Czech Republic

Abstract   The paper deals with estimation of chemical heterogeneity by modelling of diffusion of selected substitutive elements across the weld interface of two steels. The work presents proprietary approach in obtaining and evaluation of data set. Heat-resistant low-alloyed CrNiMoV and silicon steel, both of ferrite structure, form welded joint. The welded pairs were isothermally annealed in electric furnace from 500°C to 1,000°C. Concentration profiles in the plane perpendicular to the weld were investigated by energy dispersion X-rays microanalysis (EDX), along three abscissas. Theoretical fundament for evaluation of data was the solution of 2nd Fick's law. Parameters of the diffusion equation were calculated by non-linear regression. The new adaptation of Levenberg-Marquart's algorithm was developed, accompanied by statistic quantities. Differences in position of concentration profiles in three segments can be considered as a measure of heterogeneity. They prove that the parameters of diffusion equation depend on local conditions. The detailed description follows below in the paper.

Keywords: Diffusion, Mathematical Modelling, Welded Joint of Steels, Distribution of Substitution Elements.

1. Introduction

Welded joints of steel with increased contents of alloying elements are almost always accompanied by higher chemical and structural heterogeneity that is characteristic particularly for transition zone of the welded joint. The accompanying redistribution of interstitial carbon strengthens the tendency of heterogeneity. Chemical and structural heterogeneity in transition zone caused by redistribution of elements can also considerably determine strength and other mechanical properties of contacting metals. In technical practice adverse effects of chemical and structural heterogeneity manifest themselves in welded joints of heat-resistant steels that are subjected to long-time loads by increased temperatures statically during operation and dynamically during interruption of operation. The margin of safety – or vice versa danger – depends certainly on time and temperature of annealing. Cases of catastrophic failures of steam piping due to instability of transition zones of welded joints exposed to high temperatures were registered in steam piping of both conventional and nuclear power plants.

References [1, 2] introduced various models of diffusion with application on interstitial elements, particularly carbon. This work follows the above mentioned publications as far as the substitution elements are concerned. The aim is to show primarily a possibility of assessment of chemical heterogeneity of the weld on the basis of difference of positions of calculated concentration profiles of three lines. Modelling comprises also determination of diffusivities of investigated elements. The paper deals with diffusion of silicon as an example of many other investigated elements.

2. Experimental part

2.1. Welded joint of steels, its chemical composition and temperatures of diffusion annealing

Measurement of redistribution of silicon was made in the welded joint formed by heat-resistant low-alloy CrNiMoV steel (steel marked as P2) and low-alloy silicon steel (steel marked as V) in the temperature range 500–1,000°C. Table 1 gives chemical composition of the steels.

Table 1. Chemical composition of steels of welded joint (wt%)

Steel	C	Mn	Si	P	S	Cr	Ni	Cu	Mo	V	Al	Fe
P2	0.16	0.48	0.28	0.009	0.010	2.20	1.29	0.06	0.59	0.100	0.01	rest
V	0.80	0.66	2.34	0.026	0.033	0.09	0.05	0.09	0.004	0.007	0.15	rest

2.2. Preparation of samples

Samples in the form of small flat cylinders with diameter of 12 mm and height 4mm were prepared from the steels of the specified chemical composition. Polished metallographic section was prepared on frontal surface of each cylinder. Samples were welded on ground and polished surfaces in diffusion pairs by electric shock under protective argon stream. Welded diffusion pairs were afterwards sealed into quartz tubes with titanium splinters and they were isothermally annealed in electric resistance furnace in the temperature range from 500°C to 1,000 C with grading of 50 C. The samples were after annealing removed from quartz tubes, cut in half perpendicularly to the welded interface. Then as the further processing by microanalysis requires planparalel, not incurvate, surface opposite to the metallographic section – the halfcylinder has been cut by electric spark to the height of approximately 4 mm. Finally, the surface of metallographic section has been cleaned and polished again.

2.3. Analysis of selected elements diffusing through the weld interface

Distribution of selected elements perpendicularly on both sides of the weld interface were investigated by energy dispersion X-ray micro-analysis with use of the instrument JEOL – JXA 8600/KEVEX. This analysis was made in selected points, along three straight lines, perpendicularly to the weld interface, long approx. 180 μm, with step of 3 μm. Concentration set containing 61 values of concentrations of silicon and other measured elements – aluminium, nickel, titanium, chromium, manganese, iron and molybdenum were obtained from one measured segment. Three such sets were obtained from each sample (see Fig. 1). The aim of Fig. 1 is to present the mutual position of the three lines, which is the same for all samples.
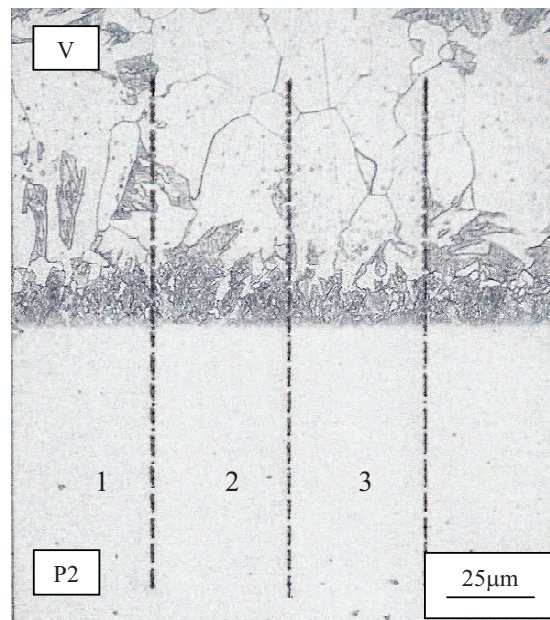
Fig. 1. Structure of welded joint P2/V with marked lines for microanalysis, sample (650°C/80 h)

2.3.1. Theoretical basis

Calculation of concentration profiles is based on solution of one-dimensional diffusion according to the 2nd Fick's law. Basic equations are given in the work [3], possibly with respect to analogy between diffusion and conduction of heat also in the work [4], then for $x > 0$:

$$N_1(x,t) = A_1 + B_1 \operatorname{erf} \frac{x}{2\sqrt{D_1 t}} \qquad (1)$$

For $x < 0$:

$$N_2(x,t) = A_2 + B_2 \operatorname{erf} \frac{|x|}{2\sqrt{D_2 t}} \qquad (2)$$

The values N, D correspond to concentrations and diffusivities in relevant areas, the constants A, B are determined from initial and boundary conditions. Initial conditions assume concentrations N_1, N_2 identical with chemical composition in both areas. Boundary conditions are based on the presumption of equality of concentrations and densities of diffusion flux at the co-ordinate $x = 0$ in time $t > 0$. Concentration profile is continuous at $x = 0$, if diffusivities of the given component in both areas are identical. Solution results in this relation:

$$N_i(x,t) = N_1 + 0.5(N_2 - N_1) \operatorname{erfc}\left(\frac{x - x_0}{2\sqrt{D_i t}} \right) \qquad (3)$$

Here $N_i(x,t)$ corresponds to the measured concentrations at the distance x from the welded joint in the time t, indexed values N_1, N_2 correspond to initial concentrations in both areas of the welded joint, x_0 is correction of the coordinate eliminating inaccuracy of measurement of the interface between metals of the welded joint. More detailed information about this deduction can be found in the works [5, 6].

2.3.2. Evaluation of experimental data

The objective of data evaluation consists in calculation of concentration profiles and diffusivities. The tool for achieving this objective is the calculation optimisation program, which determines free optimisation parameters for solution of the diffusion equation (3) that is D, x_0, N_1, N_2. The values N_1 (corresponding to the initial concentration in the steel P2), N_2 (corresponding to the steel V) were included into this group because local chemical microanalysis can differ from the average chemical analysis of the whole due to chemical and structural heterogeneity of the given area of the sample. Substance of solution lies in non-linear regression. A proprietary original method was developed, which uses adaptation of the basic Levenberg-Marquardt's algorithm [7].

Calculation with data encumbered with scatter showed that merit function – in fact residual sum of squares – is not uni-modal and can contain many minima in dependence on starting values. For this reason heuristic adaptation of the mentioned

algorithm was chosen, which is based on the following steps: exclusion of physically inadmissible negative values of parameters D, N_1, N_2 and limitation of deviation of parameters N_1, N_2 from the average chemical analysis of the sample. Afterwards the most advantageous relative minimum was searched by successive variations. Three sets of measured concentrations from all lines enable variant access of optimisation processing:

(A) Complex of all measured concentrations uses all available data from three lines as input into computation program
(B) Optimisation of the mean experimental concentrations from three data sets.
(C) Optimisation of each set separately.
(D) Determination of an arithmetic mean of parameters N_1, N_2, D and of their errors from method C.
(E) Optimisation of a median of all experimental concentrations. This procedure is a certain form of robust regression; that is it does not exclude boundary points, but gives lesser weight to them.

The following Tables 2, 3 and 4 present the results of evaluation of diffusion coefficients according to above mentioned methods.

Table 2. Comparison of diffusion coefficients values for sample (550°C, 529 h) according to different methods

Method	$10^{15}D_{Si}$ (cm^{2}s^{-1})	Coefficient of determination	Adj. coefficient of determination
A	4.4 ± 1.6	0.987	0.987
B	4.4 ± 1.9	0.995	0.995
C – line 1	3.8 ± 2.7	0.989	0.989
C – line 2	2.4 ± 1.8	0.988	0.988
C – line 3	7.9 ± 3.1	0.992	0.992
D	4.7 ± 2.6	0.990	0.990
E	4.2 ± 2.1	0.995	0.995

Table 3. Comparison of diffusion coefficients values for sample (600°C, 383 h) according to different methods

Method	$10^{15}D_{Si}$ (cm^{2}s^{-1})	Coefficient of determination	Adj. coefficient of determination
A	10.1 ± 5.8	0.948	0.947
B	10.1 ± 2.6	0.996	0.996
C – line 1	8.5 ± 4.3	0.990	0.990
C – line 2	14.7 ± 5.1	0.991	0.990
C – line 3	9.3 ± 2.8	0.994	0.994
D	10.8 ± 4.1	0.992	0.991
E	10.4 ± 2.8	0.996	0.996

Table 4. Comparison of diffusion coefficients values for sample (750°C, 7 h) according to different methods

Method	$10^{13}D_{Si}$ (cm^{2}s^{-1})	Coefficient of determination	Adj. coefficient of determination
A	5.8 ± 0.8	0.990	0.990
B	5.8 ± 0.7	0.997	0.997
C – line 1	8.7 ± 1.6	0.993	0.993
C – line 2	4.9 ± 1.2	0.990	0.990
C – line 3	3.2 ± 0.8	0.992	0.992
D	5.6 ± 1.2	0.992	0.992
E	6.1 ± 0.8	0.997	0.997

   Figure 2 shows distinctly distinguishable three lines at higher concentration of silicon, which can manifest heterogeneity of chemical composition. The curves correspond to initial and boundary conditions according to Eq. (3). The term "calculated concentrations – all dates" is not the mean value of dates, related to lines 1, 2, 3, but the result of computation taking into account all measured points. Similar situation is given in Fig. 3 in this case the individual curves representing the silicon redistribution in 1st, 2nd, 3rd line practically coincide. Figures 2 and 3 represent two extreme examples of degree of heterogeneity, considered from the differences in mutual positions of calculated concentration profiles.
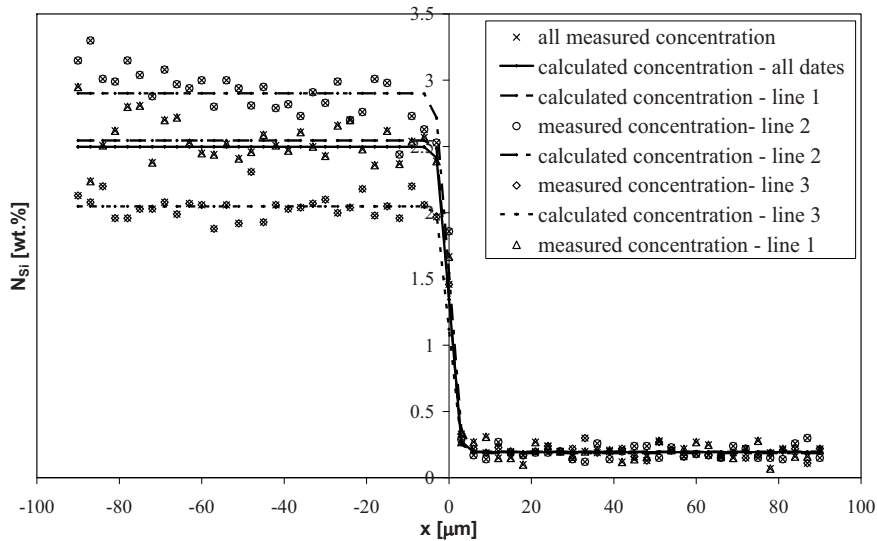
Fig. 2. Redistribution of silicon, sample (600°C, 383 h)
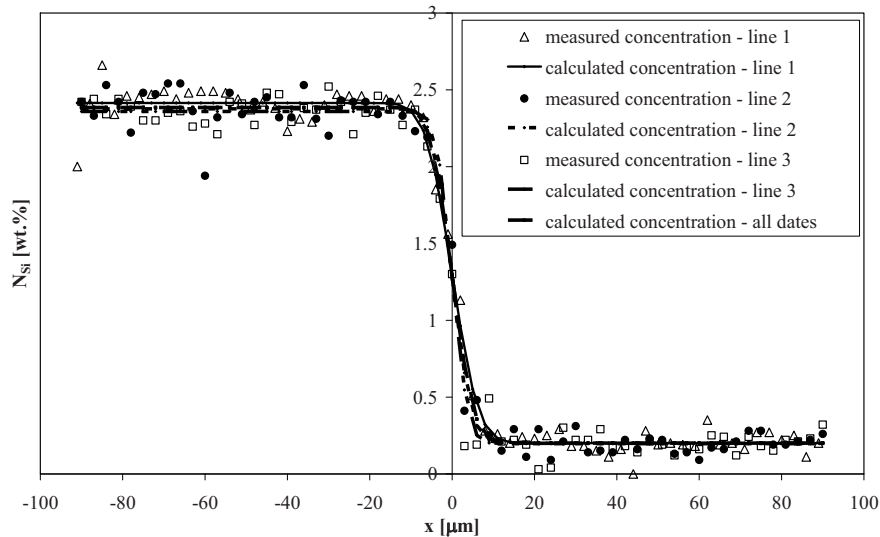
Fig. 3. Redistribution of silicon sample (750 C, 7 h)

3. Discussion

Dozens of calculations of parameters of concentration profiles for the elements Cr [5], Si, Mo and Ni were made by methodological approaches described above and they were successful even in case of large scatter of experimental data. Less favourable side of large scatters are magnitudes of parameters' errors.

The model used assumes diffusion in homogenous environment. This condition need not be always sufficiently fulfilled. There can occur various rates of diffusion in the mass of crystal and along grain boundaries [8] forming of inter-metallic compounds [9, 10], segregation in poly-component system, influencing of diffusion by phase transformations, by changing activities of diffusing components and by other situation of thermo-dynamic disequilibrium.

These phenomena need not be of random character and may not have Gaussian distribution. Until they are sufficiently quantified and implemented by the system of physical–chemical laws into calculation program, the statistic assessment of scatters remains as indirect quantitative indicator of heterogeneity of the area of welded joint.

The submitted model is based on use of the 2nd Fick's law individually for each element, it neglects influence of inter-diffusion coefficients, considered particularly in ternary systems, see e.g. [11]. Systematic error of simplified method reflects also in errors of parameters.

4. Conclusions

The paper presents original results of methodology for evaluation of experimental concentration data and heterogeneity of structure at redistribution of elements in the welded joint. This used methodology is illustrated by examples from re-distribution of silicon in two types of steels, which are poly-component system of elements.

Adaptation of the Levenberg-Marquardt's algorithm for solution of optimisation of parameters of diffusion equation is also original, as well as its use for evaluation of heterogeneity of transition area of the welded joint.

The obtained results can be potentially used for obtaining of practical information about redistribution and heterogeneity of silicon in the given or similar type of the welded joint as it is implied in discussion. They serve also as an incentive for next theoretical and experimental investigation of this topic.

References

[1]   Stránský K (1977). Thermodynamics of quasistationary diffusion of carbon in steels and its application (in Czech). Academia Praha.
[2]   Pilous V, Stránský K (1989). Structure stability of weld deposits and welded joints in energetic engineering (in Czech). Academia Praha.
[3]   Crank J (1975) The Mathematic of Diffusion, second ed. Oxford University Press, London, 38–39.
[4]   Carlslaw HS, Jaeger JC (1959). Conduction of Heat in Solids, second ed. Oxford Clarendon , London.
[5]   Řeháčková L, et al. (2006). On methodology of concentration data processing at mathematical modelling of substitution element diffusion in the zone of welded point of steels. Acta Metallurgica Slovaca 12: 388–398.
[6]   Kučera J, et al. (1996). Redistribuce substitučních a intersticiálních prvků ve svarových spojích ocelí (ČSN 412013+0,0755N)/(ČSN 417241). Kovove Mater. 34:336–348.
[7]   Press WH, Teukolsky SA, Vetterling WT, Flandery RB (1992). Numerical Recipes in C, second ed. Cambridge University Press, 609–689.
[8]   Zhu J, Chen LQ, Shen J, Tikare V (2001). Microstructure dependence of diffusional transport. Comp. Mater. Sci. 20:37–47.
[9]   Dimmler G, et al. (2003). Quantification of the Laves phase in advanced 9–12% Cr steels using a standard SEM. Mater. Charact. 512:341–352.
[10] Schaffernak C, Cerjak H (2001). Design of improved heat resistant materials by use of computational thermodynamics. Calphad 25:241–251.
[11] Zhang D, Morral JE, Brody HD (2006). Measurements for Cu and Si diffusivities in Al-Cu-Si alloys by diffusion couples. Mater. Sci. Eng. A 447:217.

Correlation of Microstructure and Toughness of the Welded Joint of Pipeline Steel X65

Rrahim Maksuti[1], Hamit Mehmeti[1], Hartmut Baum[2], Mursel Rama[1] and Nexhat Çerkini[3]

[1]Faculty of Mining and Metallurgy, Mitrovica-University of Prishtina, Kosova

[2]TU, Bergakademie, Freiberg, Germany

[3]IMK, Factory for welded steel pipes, Ferizaj, Kosova

Abstract   The integrity and the performance of the welded joint of pipelines depend on the microstructure and associated properties. The welded joint of steel pipes produced by two-pass double sided submerged arc welding (SAW) consisted of the weld metal (WM), heat affected zone (HAZ) and base metal (BM) and as a result the welded joint is characterized by a wide range of different microstructures. This microstructural heterogeneity of the welded joint cause substantial differences on the toughness behaviour of the welded joint. The object of this research work was to investigate these differences in toughness using Charpy V-notch impact testing in conjunction with microscopic observations of fractured surfaces of selected Charpy V-notch specimens. The obtained results using LOM (Light Optical Microscopy), SEM (Scanning Electron Microscopy) and Charpy V-notch (CVN) impact testing are presented in this study and this is an attempt to clarify a correlation between microstructure and impact toughness of two-pass double sided submerged-arc welded joint of pipeline steel API 5L grade X65.

Keywords: As-Deposited Microstructure, As-Reheated Microstructure, Pipeline, Impact Toughness, Weld Metal.

1. Introduction

The relationship between microstructure and mechanical properties of high strength low alloy steels (HSLA) has been the subject of considerable research. Line pipe steels fall into the category of HSLA steels and are widely used for oil and natural gas transport in the petroleum industry. These steels require combinations of various properties such as strength, toughness and weldability. API 5L (American Petroleum Institute) grade steels offer the appropriate ranges of desirable properties only by careful control of microstructure. It is well known that a steel can have a wide range of microstructures depending upon the chemical composition and manufacturing conditions (i.e. cast or wrought, any heat treatments, etc.) and that these microstructures can have very different mechanical properties. Research on the weld metal microstructures has evolved somewhat separately from the mainstream of steel research, and there are considerable problem in identifying microstructural constituents which differ in transformation mechanism [1, 2]. The interrelation of

microstructure and properties is an important factor in any investigation of the behavior of metals. Weld metal properties are mainly controlled by the microstructure in the low alloy steel welds [4–6]. The relationship between microstructures and toughness of weld metals is very complex since a number of factors are involved and thus several researchers have attempted to investigate this correlation.

Knowledge about weld pool solidification is very limited. It is mainly comprised of an extrapolation of the knowledge of the solidification of castings and related processes. However, in such cases the thermal gradient is much higher than in casting, and weld pool normally cooled very quickly so that it does not strictly obey the Fe-Fe$_3$C equilibrium diagram [1, 3].

The microstructure obtained as the weld cools from the liquid phase to ambient temperature is called the as-deposited or primary microstructure [7–9]. During two-pass or multi-pass welding some of the regions of the primary microstructure are reheated to temperatures high enough to cause reverse transformation into austenite, which during the cooling part of the thermal cycle retransforms into a variety of different microstructures. The microstructure of the reheated regions is called the reheated or secondary microstructure [7–9].

During two-pass welding of line pipes, underlying weld metal or previous (first-W_1) pass is often reheated to high enough temperatures to cause either partial or complete transformation to austenite. The weld metal of first pass adjacent to the fusion zone of the second pass (W_2) experiences complex thermal and stress alterations, giving heat affected zone (HAZ-WM) similar to those found in the base metal (HAZ-BM), Fig. 1. Toughness is a very important factor for welded joint of pipelines, in particular when they operate under low temperature conditions and taking account the microstructural heterogeneity of the welded joint (BM, HAZ, W), the object of this study was to investigate toughness properties of these distinct regions.
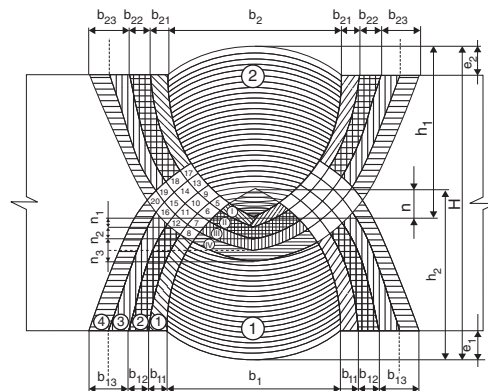
Fig. 1. Sketch of the welded joint of double sided SAW

2. Experimental procedure

Spiral line pipes Ø 813 × 12 mm were fabricated using high strength steel coils X65 according to API 5L (American Petroleum Institute) standard, which chemical composition and mechanical properties are given in Tables 1 and 2, according to the Certificate of Quality.

Table 1. Chemical composition of microalloyed steel X65

Steel coils	Chemical composition wt%					
	C	Mn	Si	P	S	V
API grade X65	0.09	1.31	0.43	0.020	0.005	0.048

Table 2. Mechanical properties of microalloyed steel X65

Steel coils	Mechanical properties						
	Re, MPa	Rm, MPa	A, %	Kv_1, J	Kv_2, J	Kv_3, J	Kv, J
				ISO-V-0°C			
API grade X65	549	649	23,6	132	102	143	126

Spiral line pipes Ø 813 × 12 mm were welded in two-stage process by double sided SAW through an "X" groove configuration, according to the BLOHM+ VOSS, with welding parameters given in Table 3.

Table 3. Welding parameters

Line pipe	Welding parameters							
	Welding flux: LWF780							
	Welding Wire: S_2Mo							
	First pass (inside weld): W_1				Second pass (outside weld): W_2			
	I	U	v	E	I	U	V	E
	A	V	m/min	kJ/cm	A	V	m/min	kJ/cm

The Charpy V-notch (CVN) testing is used to measure the impact energy. The Charpy V-notch specimens were cut out from the double sided welded joint, perpendicular to the welding direction and from base metal, perpendicular to the axis of line pipe Ø 813 × 12 mm, as shown in Fig. 2.

Impact test of standard Charpy V-notch specimens (10 × 10 × 55 mm), with 2 mm notch depth and 0.25 mm root radius, Fig. 3, were carried out with the instrumented impact machine MOHR-FEDERHAFF-LOSENHAUSEN, at 25°C, 0°C and −20°C.
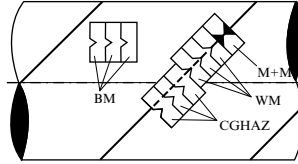
Fig. 2. Sketch illustrating the orientations of the Charpy V-notch test specimens used

Fig. 3. Shape and dimensions of the standard Charpy V-notch specimen

V-notch were located in the base metal (BM), in the center line, i.e. in the centre of the solidification front in the weld metal (WM) and in the coarse grained heat affected zone (CG HAZ), immediately adjacent to the fusion line, Fig. 4. The location of the V-notch positions were determined by light wet metallographic grinding and etching in 3% nital solution.
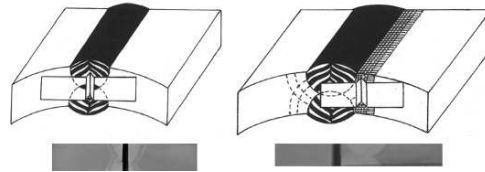
Fig. 4. Details of extraction of Charpy V-notch specimens from welded joint

For the observation of macro and microstructure of welded joint, metallographic specimen was extracted from the same region (specimen M + M). Metallographic specimen was wet ground and polished using standard metallographic techniques and etched in 2% nital solution, to develop the macro and microstructure for analysis with LOM (Light Optical Microscopy). In order to directly correlate the toughness to microstructural features, including the as deposited weld metal and reheated weld metal, Charpy V-notch testing were made on the base metal (BM), coarse grained heat affected zone (CG HAZ) and weld metal (WM).

3. Results and discussion

Macrostructure in Fig. 5 shows a typical cross section of double sided welded joint of line pipes at low magnification.
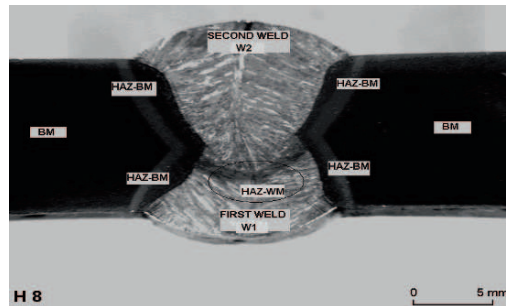
Fig. 5. Macrostructure of double sided welded joint of line pipes

The macrostructure of a double sided line pipe weld is generally non-uniform, being composed of areas of as-deposited metal with columnar grains and areas that have been reheated by subsequent pass. Light Optical Microscopy (LOM) is one of the most commonly used techniques for micro-structural characterization in the development of weld metals.

Figure 6 shows the microstructures of the welded joint. The following characteristic are indicated: BM-the as received microstructure of base metal (API grade X65) consisted of banded ferrite and pearlite elongated grains as a result of rolling. CGHAZ- coarse grained heat affected zone shows the presence of sideplate or lath ferrite with significant grain growth occurred as a result of the high peak temperature experienced during welding. In the inside weld (W_1), the microstructure was composed predominantly of acicular ferrite with small proportion of grain boundary ferrite and polygonal ferrite, whereas in the outside weld (W_2), the microstructure also consisted of acicular ferrite delineated by grain boundary ferrite and a small amount of polygonal ferrite.
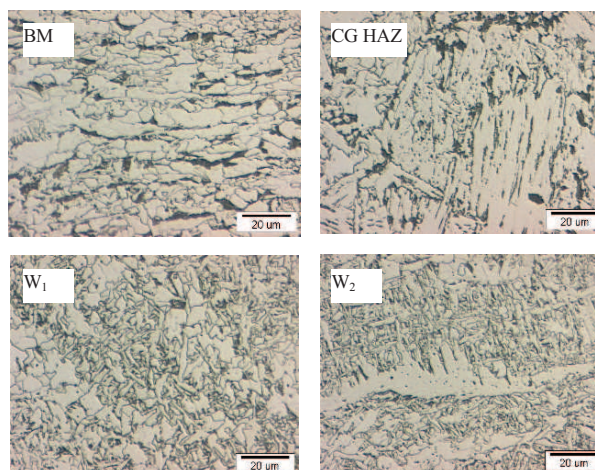
Fig. 6. Microstructures of the two pass welds

Visual inspection of the Charpy V-notch fracture surfaces shows that exist fracture morphology differences between BM, CGHAZ and WM. The fracture surfaces of the Charpy V-notch specimens of BM, CGHAZ and WM, with lowest impact energy tested at −20°C are illustrated in Fig. 7. The fracture surface of BM is fibrous and its color is dull, whereas the fracture surfaces of WM and CGHAZ are also fibrous with e little presence of shiny color. There are notable sliplines and other evidence of plastic deformation in the fractured surface. The width of the end opposite the notch shows large plastic deformation in all Charpy V-notch tested specimens. Fracture surface of BM shows some cracks like separations perpendicular to the axis of the V-notch.
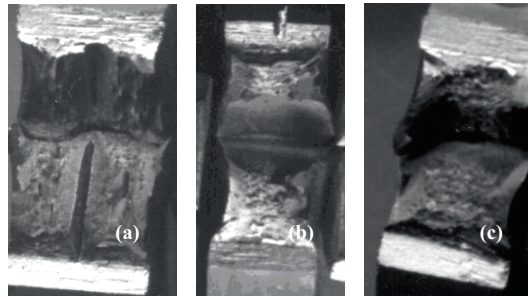
Fig. 7. Typical fracture surfaces of Charpy V-notch specimens

The SEM (Scanning Electron Microscopy) examinations of the fractured surfaces of Charpy V-notch specimens were carried out on SEM Leo 1530, and obtained results are shown in Figure 8. The scanning electron microfractographs show the fracture morphologies from the centre region of the fracture surfaces for BM and CGHAZ with lowest Charpy V-notch values at −20°C.

The fracture appearance of BM specimen (a) reveals numerous coarse and fine deep dimples, characteristic of a ductile fracture with high V-notch toughness. For the specimen of CGHAZ (b), the fracture occurs with mixed mode of ductile and brittle appearance.
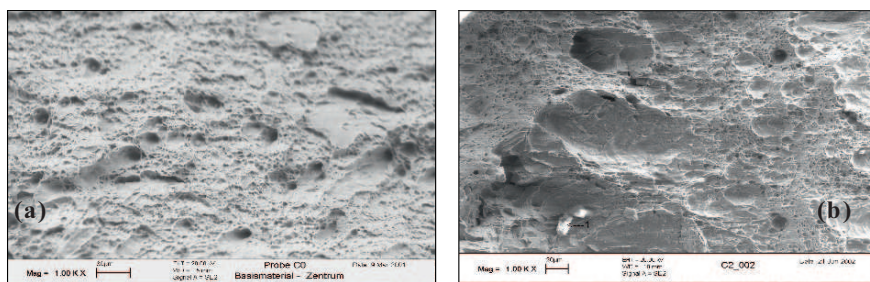
Fig. 8. SEM microfractographs of Charpy V-notch specimens

The toughness data obtained using the Charpy V-notch specimens are illustrated in Fig. 9. It can see from the figure that the BM has the highest absorbed energy, followed by the WM and CG HAZ. Each data point represents the average values of three samples and the test results revealed general decreasing tendency with decreasing of the temperature. The lowest toughness of the welded joint was measured in the CG HAZ (45.0 J), at −20°C whereas the highest toughness was measured in the BM (139 J), at 20°C CG HAZ. The lowest toughness of the CG HAZ (45.0 J), at −20°C fulfil the minimum average requirement of 27.0 J according to API 5L (American Petroleume Institute) standard.
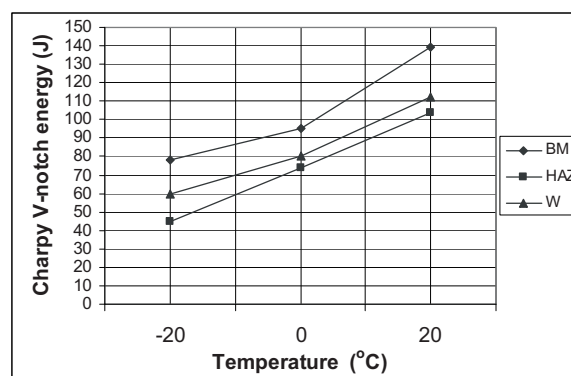
Fig. 9. Charpy V-notch toughness of the welded joint

4. Conclusions

From the results presented in this work, it is possible to draw the following conclusions:

The macrostructure of a two pass double sided submerged arc weld of line pipes is generally non-uniform, comprised of as-deposited region with columnar grains and reheated region with some characteristic sub-regions depending on the gradient temperature. Each regions of a two pass weld is characterized by unique microstructure and this necessarily lead to variations in mechanical properties, a feature which is most obviously reflected in the toughness properties of such welds.

Toughness properties of the double sided submerged arc welded joint depends to the location of the V-notch in the constitutive parts of the welded joint, due to the microstructural constituents existing within these parts. Weld metal (WM) with acicular ferrite microstructure has high notch toughness.

The presence of vanadium (V) from base plate dilution effects has contributed significantly to the formation of acicular ferrite in the as deposited weld metal, which is the most desirable microstructural constituents with high strength and good impact toughness. Coarse grained heat affected zone (CGHAZ) has lowest

toughness, due to the microstructural changes during submerged arc welding cycles. In this zone, presence of vanadium (V) also has contributed to produce some modification on the microstructural transformation behaviour.

The toughness of welded joint of line pipes is mainly determined by that of the weakest zone, i.e., coarse grained heat affected zone (CGHAZ).

Correlation between microstructure and toughness of the welded joint is very complex since a number of factors are involved; there is a need for further research to obtain more quantitative results between microstructure and toughness properties of the welded joint.

References

[1] L. G. Taylor and R. A. Farrar. Metallurgical Aspects of the Mechanical Properties of Submerged-Arc Weld Metal. Welding and Metal Fabrication, May 1975, pp. 305–310.
[2] R. E. Dolby. Advances in Welding Metallurgy of Steels. Metals Technology, September, 1983, Vol. 10, pp. 349–361.
[3] L. E. Svensson. Control of Microstructures and Properties in Steel Arc Welds, CRC Press, Boca Raton-Ann Arbor-London-Tokyo, 1994.
[4] Sh. Ohkita and Y. Hori. Recent Development in Controlling the Microstructure and Properties of Low Alloy Steel Weld Metals. ISIJ Int., Vol. 35, 1995, No. 10, pp. 1170–1185.
[5] H. K. D. H. Bhadeshia, L. E. Svensson and B. Gretoft. A Model for the Development of Microstructure in Low-Alloy Steel Weld Deposits. Acta Met. Vol. 33, No. 7, 1985, pp. 1271–1283.
[6] A. A. B. Sugden and H. K. D. H. Bhadeshia. A Model for the Strength of the As-Deposited Regions of Steel Weld Metals. Metallurgical Transactions A, 19A, 1988, pp. 1597–1602.
[7] J. F. Lancaster. Metallurgy of Welding. Abington Publishing, Cambridge, 1999.
[8] K. Easterling. Introduction to the Physical Metallurgy of Welding. Butterworth Heinemann Ltd, Oxford, 1992.
[9] R. Honeycombe and H. K. D. H. Bhadeshia. Steels – Microstructure and Properties, Second Edition. Edward Arnold, London, New York, Sydney, Auckland, 1995.

Effect of the Residual Fatigue Damage on the Static and Toughness Properties

P. Cadenas[1], A. Amrouche[1], G. Mesmacque[1] and K. Jozwiak[2]

[1]Laboratoire de Mécanique de Lille, UMR CNRS 8107, IUT A GMP Le recueil. Rue de la recherche BP 179, 59653 Villeneuve d'Ascq, France

[2]Poznan University of Technology, Institute of Materials Science, Poznan, Sklodowskiej-Curie 5, Poland

Abstract   This investigation has been carried out in order to study the influence of the residual fatigue damage on the tensile and fracture toughness properties of a 6082-T6 aluminum alloy during high cycle fatigue. The results obtained show that the tensile mechanical properties do not change with the amount of residual fatigue damage. The mechanical properties remained unchanged because in high cycle fatigue, the magnitude of plastic strain was smaller than for low cycle fatigue. However, the fracture toughness results have shown that the critical crack opening displacement CODc decreases in the range of 10–40% and the critical energetic parameter J1C decreases in the range of 20–25% with fractional lifetime n/Nf for the maximum stresses applied of 200 and 275 MPa respectively. This decrease of the toughness parameters could be attributed to microcracks evolution during high cycle fatigue.

Keywords: 6082-T6 Aluminum Alloy, Fatigue Damage, Toughness Parameters, Lifetime.

1. Introduction

Fatigue damage increases with the application of load cycles in a cumulative manner. Cumulative fatigue damage takes a large place in life prediction of components and structures. Since the introduction of fatigue damage accumulation concept [1], many damage models have enlarged the Miner's approach by integrating non linear rules [2] and by taking into account the loading histories. In another work [3], some propositions of these approaches were summarized. Lemaitre, for low cycle fatigue (LCF), has proposed a cumulative damage based on the variation of the Young's modulus [4]. Fatigue damage is a process of continuous deterioration of material properties under cyclic loading [2]. The damage variable is dependent on the number of cycles and the magnitude of the stress and strain applied. It is well known, that the static mechanical properties of a material, such as yield strength (Sy), ultimate strength (Su), as well as toughness properties, are the most important parameters in structural design, particularly in stress calculation and analysis of structural components and machine elements in service. For most engineering structures and components operating under cyclic loading conditions, a common noticeable feature is that their service properties, especially mechanical properties

deteriorate progressively with increasing lifetime [5]. This degradation in material mechanical properties due to cyclic loading, also called residual fatigue damage, seriously affects the in service safety of structures and/or machines elements and thus is an important consideration in safe design against fatigue failure. On the other hand, remaining lifetime studies of engineering structures and/or machines elements in service generally requires the evaluation of the damage degree of fatigued materials [6]. Therefore, the investigation of the change in the static mechanical properties of engineering materials subjected to cyclic loading and the correlation of such a change with fatigue damage evolution is of practical interest. The fatigue behavior of engineering alloys, including cyclic hardening/softening properties, cyclic stress–strain, S-N and ε-N curves, etc., have been widely investigated. However, only relatively few studies have been focused on the behavior and changes in the static mechanical properties of such materials during cyclic loading and the vast majority of such studies [7, 9] have been conducted under LCF conditions. Lehéricy and Mendez [9], on AISI 304L austenitic stainless steel, have observed on the specimen surface, after 15% of the fatigue lifetime (damage), very few slip traces and some more intense marks, which can be located at slip bands or at grain boundaries. In contrast, surface cracks were clearly identified in SEM examinations performed after 30% of the lifetime. Cracks were mainly initiated in some intense slip bands but they have also been observed at grain or twin boundaries. In the case of 50% damage, SEM examinations indicated that the number of slip traces remained very limited and but fatigue cracks were more numerous and longer. Thus, this present investigation has been carried out in order to study the change in static mechanical properties and fracture toughness parameters (critical value of the energetic parameter J (J_{1c}), critical value of critical crack opening displacement (COD_c) and tearing modulus (T(J)) of 6082-T6 aluminum alloy subjected to high cycle fatigue (HCF) and to obtain a better understanding of its mechanical behavior, such that it could be used in remnant life analysis. This aluminum alloy constitutes a very important engineering material widely employed in land transportation applications, for the manufacture of different parts and components, due to its high strength-to-density ratio. The variation in both the static mechanical properties and in the fracture toughness parameters of this alloy, as well as the correlation between such changes and the evolution of fatigue damage during HCF, are then discussed on the basis of the experimental results.

2. Experimental procedures

2.1. Fatigue test

The present investigation was carried out with samples of a 6082-T6 aluminum alloy of the following chemical composition (wt%): 0.6 Zn, 0.6 Mg, 0.06 Cu, 0.24 Fe, 0.70 Si, 0.90 Mn, 0.02 Cr and Al, bal. The material was supplied as sheets of $1 \times 1000 \times 1500$ mm, from which a number of tensile and fatigue specimens were

machined in longitudinal orientation relative to the rolling direction following the ASTM standard E466-96. A number of specimens were subjected to HCF for constant stress ratio R = 0.1 up to failure, at different level of maximum alternating stresses, which allowed the determination of the S-N curve applying a number of cycles to failure, N_f. The frequency used was 25 Hz while all tests were conducted at room temperature. The Eq. (1) represents the S-N curve of 6082-T6 aluminum alloy that was obtained for such experimental conditions. This relationship is based on a Basquin's fitting of the experimental results of the S-N curve.

$$\sigma = 710 \left(N_f \right)^{-0.0854} \tag{1}$$

In order to induce fatigue damage the specimens were subjected to cyclic loading applying a specified percentage of number of cycles, n, equivalent to a given lifetime at each maximum stresses applied. The selected maximal stresses were of 200, 225, 250 and 275 MPa. The corresponding total number of cycles to failure was of 2.9×10^6, 5.9×10^5, 2×10^5 and 70×10^3, respectively. The pre-fatigue tests were performed until the specimen has reached a predetermined fatigue damage degree n/N_f, namely between 20% and 70%. The tensile, fatigue and tearing tests were all conducted on a 100 kN conventional INSTRON servo-hydraulic machine. In every case, for the evaluation of the static and toughness properties three samples were tested. Optical Microscopy (OM) and Scanning Electron Microscopy (SEM) examinations were performed using a Nikon Epiphot and a JEOL JSM6480 LV, respectively.

2.2. Tensile test

Tensile tests using virgin specimens following the ASTM standard E8-04 were carried out in order to determine the initial mechanical properties (elastic modulus E_o, yield strength S_{yo}, ultimate strength S_{uo}, K_o, and hardening exponent, n_o). Specimens were previously subjected to cyclic loading at specified fractional lifetime at each different maximum stresses applied.

The specimens were tested by tension in order to evaluate their residual mechanical properties (E, S_y, S_u, K, and n).

2.3. Fracture toughness test

In order to determine the fracture toughness properties, not standardized specimen geometry were used (Fig. 1a). The machining of the fracture toughness samples involved a notch of 9 mm in length and 0.3 mm thick.

The notch was realized using a diamond disc (300 μm in thick) at low speed saw to avoid residual stresses. This notch was normal to the tensile axis, located in the middle section of specimens. The specimens were loaded by the two holes (10 mm in diameter) where the axis of load was located at the beginning of the notch. The samples were not precracked. During fracture toughness test, a video camera with scale of 0.05 mm was used to determine the crack opening displacement and the crack propagation. Figure 1b, gives an example of the registration to measure the COD and the crack propagation. The energetic parameter J was calculated by [10] equation:

$$J = \frac{\eta U}{B(W - a)} \tag{2}$$

where: elastic–plastic coefficient $\eta = 2$; B: thickness ($B = 1$ mm), W: width of minimal section ($W = 20$ mm), $a = (a_o + da)$, (a_o) is the the notch size ($a_o = 9$ mm), (da) is the crack propagation size and the relation a_o/W is equal to 0.45, U: potential energy that is equal to the area under load vs load displacement curve.
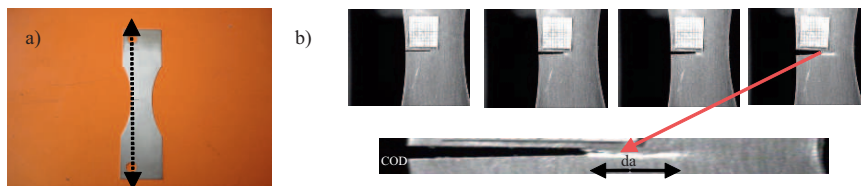
Fig. 1. (**a**) Specimen geometry for fracture toughness test, (**b**) COD and crack propagation measurement, da

3. Experimental results

3.1. Static mechanical properties after fatigue damage

The static mechanical properties for each fractional lifetime n/N$_f$, and maximum stress applied are given in Table 1.

It can be observed that after fatigue damage the static mechanical properties remain almost unchanged. Such results can be interpreted in terms of the small plastic strain amplitude achieved in HCF, in comparison with those achieved in LCF. Previous investigations [5, 7, 9] have shown that under the latter conditions, the static mechanical properties of the material vary with the number of cycles applied.

Table 1. Elastic modulus, E; Yield Strength, Sy; Ultimate Strength, Su; K and hardening exponent, n; after fatigue damage for each maximal stresses applied

σ_{max} (MPa)	n/N_f (%)	E (GPa)	Sy (MPa)	Su (MPa)	K (MPa)	n
	0	74	305	340	460	0.090
200	25	73.5	305	337	458	0.089
	50	72.1	303	339	459	0.089
	75	71.2	302	338	456	0.088
225	25	73.1	304	337	461	0.092
	50	72.6	303	339	458	0.085
	75	72	303	340	456	0.089
250	25	73	304	341	454	0.088
	50	72	302	342	456	0.088
	75	71	303	338	455	0.087
275	25	71	298	339	453	0.090
	50	70.3	300	336	460	0.089
	75	69.9	302	338	458	0.889

3.2. Toughness properties after fatigue damage

Figure 2 shows the evolution of the load versus load displacement obtained for each fractional lifetime at the corresponding maximum stress applied of 200 MPa. It can be observed in Fig. 2 that the position of load displacement at the maximal load (A, B, C, D) decreases with fractional lifetime. It seems that ductility of material decreases with fatigue damage, it means that the energy absorbed for the material with fatigue damage is less than the energy absorbed for the virgin material. Therefore, the ductility of alloy decreases with fatigue damage and this is in agreement with the literature concerning LCF [7, 8].
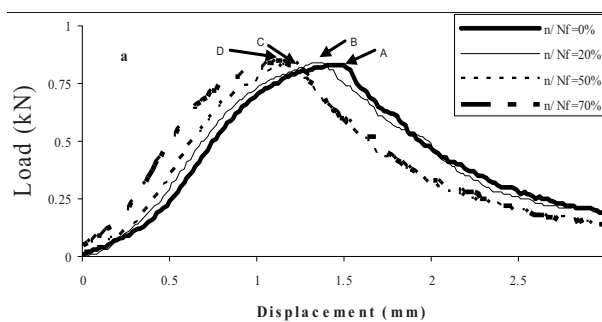
Fig. 2. Load versus load displacement at each fractional lifetime for maximum stresses applied of 200 MPa

Figure 3a shows the evolution of the crack opening displacement (COD) with the crack propagation (da) at each fractional lifetime for 200 MPa. The critical crack opening displacement (CODc) and the critical energetic parameter (J_{1c}) which describes the static toughness at initiation parameters were determined from Fig. 3a, b, respectively. The tearing modulus T(J) which describes the static tearing toughness parameter was determined from Fig. 3b. These results are given in Table 2. Figure 4a shows that CODc decreases in 10% and 40% with fractional lifetime for two maximum applied stresses (275 and 200 MPa). Figure 4b on the other hand, shows that the critical energetic parameter J_1c also decreases in 20% and 25% with fatigue damage for the same loading conditions. These results show that fatigue damage has an influence on the toughness properties.
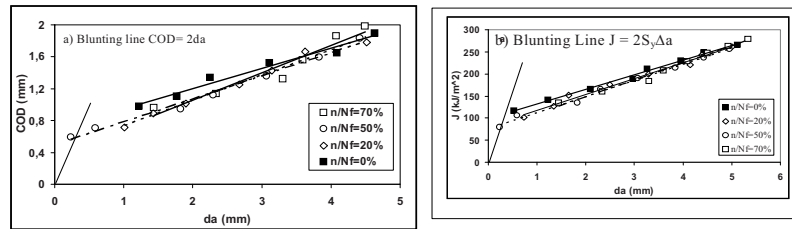
Fig. 3. (**a**) Crack opening displacement and (**b**) energetic parameter versus crack propagation at each fractional lifetime for maximum stresses applied of 200 MPa

Table 2. Critical crack opening displacement, CODc; Critical energetic parameter, J_{1c} and tearing modulus, T(J) after fatigue damage

σmax (MPa)	n/N_f %	COD_C (mm)	J_{1c} (kJ/m^2)	T(J)
-	0	0.82	104	33
200	20	0.75	88	36
	50	0.63	81	36
	70	0.48	78	38
275	30	0.69	104	32
	45	0.80	90	31
	70	0.75	93	29
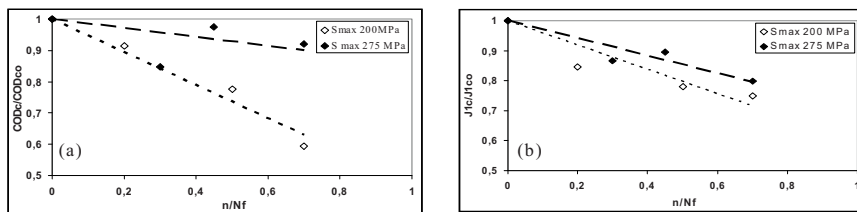
Fig. 4. (**a**) Critical crack opening displacement, (**b**) critical energetic parameter J_{1c}

3.3. Micrographic observations

Figure 5a shows the smooth surface of the virgin material, where only precipitations and/or inclusions (not analyzed) are present. Figure 5b, c show the surface of the pre-fatigued specimens at 70% of fractional lifetime for 275 and 200 MPa, respectively. Intergranular microcracks with an average size of 18 µm due to fatigue damage at higher stress applied were observed (Fig. 5b). The microcracks observed for lower stress were shorter with an average size of 10 µm (Fig. 5c). It is worth to notice that they have initiated on precipitates and propagated rather transgranulary and perpendicular to load direction. Figure 6 shows the fracture surface after tearing test at the initiation of the tearing crack propagation zone. Effect of coalescence of microcavities during tearing of virgin alloy typical for ductile fracture is shown in Fig. 6a, b and c show the fracture surface after tearing test for the specimens. With 70% fractional lifetime and for maximum stresses applied of 275 and 200 MPa, respectively. Mixed brittle – ductile fractures were observed for both cases with microcracks perpendicular to load direction which are generally longer (100 µm) than fatigue microcracks observed in OM (Fig. 5b, c).
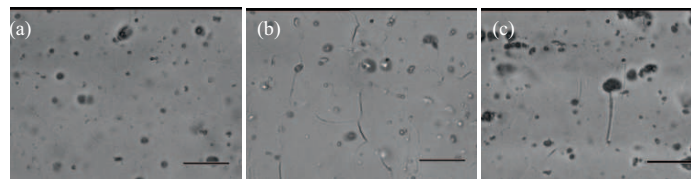
Fig. 5. Surface observation of specimens pre-fatigued: (**a**) virgin; $n/N_f = 0$; (**b**) $n/N_f = 70\%$; Smax = 275 MPa; (**c**) $n/N_f = 70\%$; Smax = 200 MPa (scale = 20 µm)
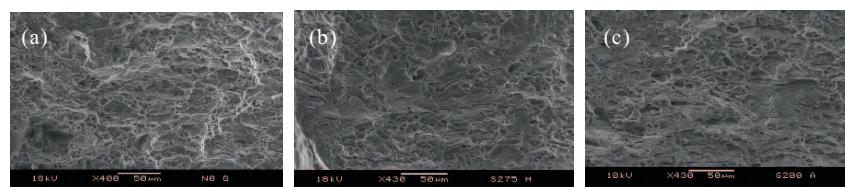
Fig. 6. Fracture surfaces of specimens at the initiation of crack propagation zone: (**a**) virgin; $n/N_f = 0$; (**b**) and (**c**) $n/N_f = 70\%$; Smax = 275 MPa and Smax = 200 MPa

4. Discussions

The results obtained show that, under the present experimental conditions, the tensile mechanical properties almost do not change with the amount of residual fatigue damage.

It seems that mechanical properties remain unchanged because in high cycle fatigue the magnitude of plastic strain is lower than during low cycle fatigue. Some works [7, 8] have proved that static mechanical properties decreased with increasing number of cycles during LCF. It seems that the microcracks observed in our study were long not enough to influence the tensile properties.

CODc which is the local parameter and J_{1c} which is a global parameter for crack initiation in static loading decreased with the fatigue damage and appeared sensitive to maximum applied stress in fatigue loading. We attribute the decrease of the two parameters to the damage induced by microcracks during fatigue (Figs. 5 and 6). On the other hand, the tearing modulus T(J), which describe the crack propagation by static loading is not sensitive to the damage accumulated and to the maximum applied stresses in fatigue loading (Table 2). This decrease of toughness properties is in agreement with data reported in the literature, and it is attributed to the decrease of the material abilities to absorb energy with the number of applied cycles [7]. Moreover, it is possible that the critical energetic parameter J_{1C} has decreased due to a loss of ductility because the predominant fracture mechanism in tearing test was the brittle (cleavage) one (Fig. 6b, c).

5. Conclusions

The static mechanical properties evaluated by means of tensile tests conducted after fatigue damage (E, Sy, Su, K and n) were weakly affected by the fractional lifetime n/N_f, whereas the global (J_{1c}) and local (CODc) parameters were quite sensitive to the residual damage induced by HCF. On the other hand the tearing modulus T(J) was not affected by fatigue damage in the HCF.

References

[1] Miner M (1945). Cumulative damage in fatigue. J. Appl. Mech., 67: A159–A164.
[2] Marco SM, Starky WL (1954). Transactions of the ASME, 76: 627–632.
[3] Fatemi A, Yang L (1998). Cumulative fatigue damage and life's prediction theories: A survey of the state of the art for homogenous materials. Int. J. Fatigue, 20 (1): 9–34.
[4] Lemaitre J (1992). A course on damage mechanics, 1st edn. Springer-Verlag, Berlin, Heidelberg New York.
[5] Lemaitre J, Dufailly J (1987). Damage measurement. Eng. Fract. Mech. 28: 643–661.
[6] Chaboche JL (1981). Continuous damage mechanics: A tool to describe phenomena before crack initiation. Nucl. Eng. Des. 64: 233–238.
[7] Duyi Y, Zhenlin W (2001). Change characteristic of static mechanical property parameters and dislocations structure of 45 medium carbon structural steel during fatigue failure process, Elsevier. Mat. Science Eng. A 297: 54–61.
[8] Murakami Y, Miller KJ (2005). What is fatigue damage. A view point from the observation of low cycle fatigue process. Int. J. Fatigue 27: 991–1005.
[9] Lehéricy Y, Mendez J (2006). Effect of low cycle fatigue damage on the residual fatigue strength of a 304l austenitic stainless steel. Int. fatigue Congress. Atlanta USA, F 335.
[10] Rice J, Paris P, Merkle JG (1973). Progress in flaw growth and fracture toughness testing ASTM STP 536: 231–245.

Influence of Fatigue Damage in Dynamic Tensile Properties of AISI 4140T Steel

U. Sánchez-Santana[1], C. Rubio-González[1], G. Mesmacque[2] and A. Amrouche[2]

[1]Centro de Ingeniería y Desarrollo Industrial. CEDESI, Pie de la Cuesta 702, Desarrollo San Pablo, 76130 Querétaro, Qro., México

[2]Laboratoire de Mécanique de Lille, Université de Lille 1, UMR CNRS 8107 Villeneuve d'Ascq 59650, France

Abstract   Usually material properties are determined from damage free materials, but is unknown if these properties can vary with respect to previous fatigue damage. In different engineering applications such as automobile and train crashes, the high speed impact of debris as well as the high speed manufacturing processes, makes it necessary to have deep understanding of the dynamic behavior of materials and components. In this work experimental results are presented in the static and dynamic behavior of steel with fatigue damage and subject to impact loading. Samples subjected to previous high and low cycle fatigue are considered. The material used is AISI 4140T steel, this material is used in several engineering applications and they present different mechanical behavior. Fatigue damage was introduced on the specimens at levels of 25%, 50% and 75% of the fatigue life. Once the fatigue damage was generated, the specimens were tested on a Hopkinson bar test apparatus modified to tension loading condition. The results show how the previous fatigue damage can modify the mechanical properties of the material tested, as the yield stress, ultimate stress, elongation percentage and reduction of area percentage.

Keywords: Fatigue, Damage, Dynamic, AISI 4140T Steel.

1. Introduction

The demand for increased vehicle safety has become a matter of considerable concern of users. Fatigue is the principal cause of premature failure of engineering components. Sometimes these failures can be quite catastrophic. It is well known that the mechanical behavior, such as yield stress, ductility and strength of materials, change under different strain-rate loadings and temperatures [1]. The consideration of rate dependence on material behavior is very important in the design of structures. An understanding of the deformation of metals over a wide range of temperatures and strain rates is important in metal forming, high speed machining, high velocity impact, penetration mechanics, explosive-metal interaction, and other similar dynamic conditions. Impact problems have been studied for long time. A complete material description involves not only stress–strain response as a function of large strains, high strain-rates, high temperatures, stress state and loading history variations, but also the damage accumulation and failure mode [2].

2. Experimental procedure

2.1. Test material and specimen preparation

The structural material tested was AISI 4140T steel, this chromium molybdenum alloy steel is oil hardening steel of relatively high hardening ability and is among the most widely used versatile machinery steels, the T condition consists a hardening and tempering heat treatment. The specimen geometries are shown in Fig. 1, one for the stress control tests (a) and the other by strain control tests (b).
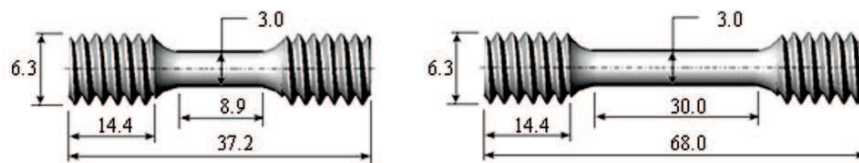
Fig. 1. Specimens used in the quasi-static and dynamic tests (dimensions in mm)

Table 1 gives the chemical composition, it was determined using a spark emission spectrometer. Quasi-static mechanical properties material was obtained on a MTS810 machine applying monotonic load at constant speed of 1 mm/min. The yield strength reported in Table 2 was obtained employing the 0.2% offset method, for both configurations. Additionally, a 25.4 mm MTS-634.11F-25 extensometer was used to measure the strain in the specimens.

In addition, SEM micrographs shown in Fig. 2 demonstrate the micrographic of steel, bands of martensite are observed in the samples, the steel sample was oxidized heating it at 850°C during 1 h. On that figure it is observed no grain deformation. Grain size is approximately ASTM 9.

Table 1. Chemical composition of AISI 4140 steel (wt.%)

Material	C	Mn	Si	Cr	Mo	P	S
AISI 4140T steel	0.38	0.75	0.20	0.80	0.15	0.40	0.04

Table 2. Quasi-static mechanical properties at different damage levels

	Stress control				Strain control			
	D	0.25	0.50	0.75	D	0.25	0.50	0.75
E (GPa)	185.7	185.5	185.5	185.5	185.7	178.6	169.9	163.8
Re	1026	778	789	748	1014.4	944.6	911.6	890.6
Rm	1265	1037	1014	1005	1265.2	1085.2	1023.8	984.7

D = Damage Free, Re = Yield Stress (MPa) and Rm = Ultimate Stress (MPa).
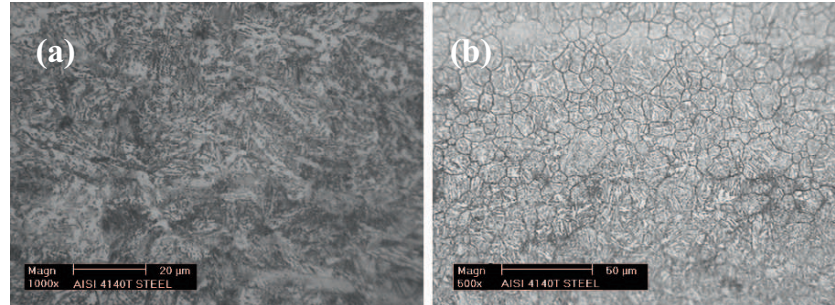
Fig. 2. Micrographs of the specimen cross-section

2.2. Stress control fatigue tests

Fatigue tests with stress and strain control were conducted in an MTS810 testing system using senoidal waveform at room temperature. Stress-life curves applying uniaxial cyclic loading with stress ratio $R = \sigma_{min}/\sigma_{max} = 0.2$, and 35 Hz were obtained. Strain-life curves were obtained as well with strain ratio $R = \varepsilon_{min}/\varepsilon_{max} = 0.75$ and 1 Hz. Knowing the fatigue life, it was possible to induce fatigue damage on the tensile specimens at damage levels of $D = 0.25$, 0.50 and 0.75, according with Palmgren-Miner model [3].

2.3. Impact test apparatus and dynamic tests

Hopkinson bar test has been widely accepted to produce strain rates in the order of 10^2 to 10^4 s^{-1}. The apparatus consists mainly of an air gun, a projectile, two Hopkinson pressure bars (one incident and one transmitter), a velocity measuring device and recording equipment [4]. Three fatigue damage levels were considered: $D = 0.25$, 0.50 and 0.75; and three projectile speeds were used on the Hopkinson bar tests $v = 18$, 25 and 30 m/s.

3. Results and Discussion

3.1. Quasi-static tension tests

To determine the influence of previous fatigue damage, quasi-static tension tests were performed on specimens with fatigue damage $D = 0.25$, 0.50, and 0.75. Quasi-static stress–strain curves material were determined and are shown in Fig. 3 with stress–strain curves of damage-free materials included for comparison. Table 2 gives the mechanical properties at room temperature of damage free material.

Quasi-static mechanical properties were obtained on a MTS810 machine applying monotonic load.
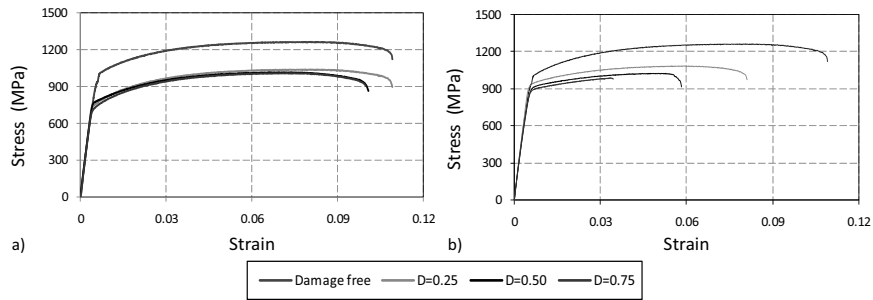
Fig. 3. Quasi-static stress–strain curves on (**a**) stress control and (**b**) strain control for different damage levels

Figure 4 shows micro-hardness profiles over the specimen cross-section, distance is measured from the edge.

The mechanical behavior material was investigated using Vickers microhardness. The values of Vickers microhardness on the specimens cross-section are measured with $D = 0$ (damage free) and $D = 0.75$ during the process of stress and strain controlled fatigue. In stress and strain controlled fatigue was observed an increase of 8.5% in the microhardness with a parallel trend line also with microhardness value in damage free material.
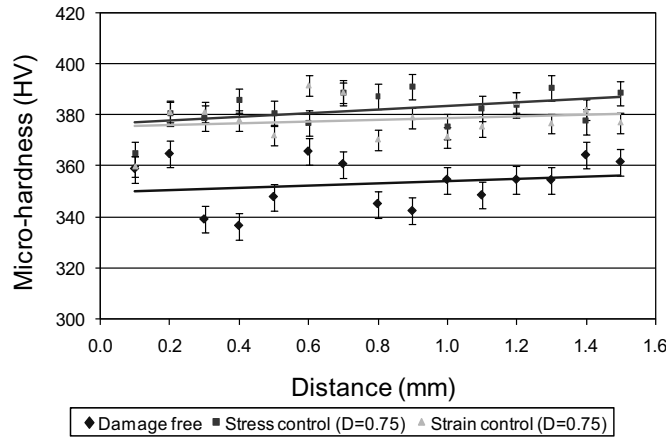
Fig. 4. Micro-hardness profiles on the specimen cross-section

3.2. Dynamic tension tests

Dynamic stress–strain curves obtained by using the Hopkinson bar apparatus for AISI 4140T steel are shown in Fig. 5. Quasi-static stress-strain curves for damage-free materials are included for comparison. Different damage levels and projectile velocities (strain rates) were considered. Note that in all cases the yield stress decreases as the damage level increases. Different damage levels and projectile velocities (strain rates) were considered. Note that in all cases the yield stress decreases as the damage level increases. This effect is better appreciated on Fig. 6 where the influence of strain rate is presented as well [5, 6]. Observe in Fig. 6a, stress control case, that σ_y decreases about 27% and σ_u about 20% increasing the damage level, that decrease is more important at low damage levels, there is a big change on the mechanical properties from $D = 0$ to $D = 0.25$. After $D = 0.25$ σ_y and σ_u remain almost stable.
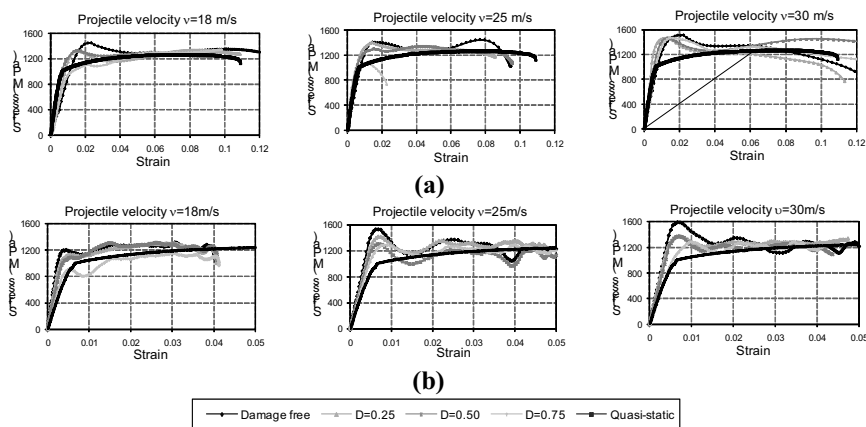
Fig. 5. Dynamic stress–strain curves for (**a**) stress control and (**b**) strain control for different damage levels
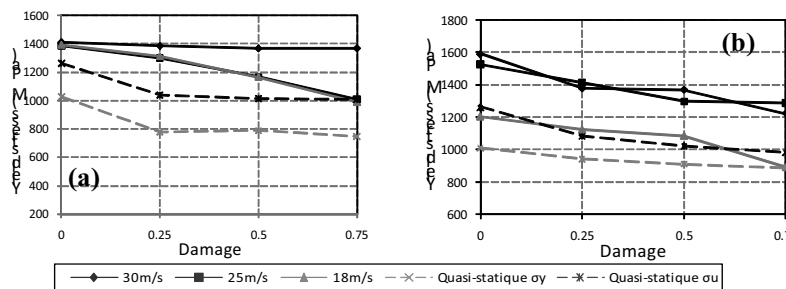
Fig. 6. Effect of fatigue damage on quasi-static and dynamic mechanical properties of AISI 4140T steel, (**a**) stress control and (**b**) strain control

Looking at Fig. 6a, it is observed that the yield stress is not affected by the damage level at high strain rates (projectile velocity $v = 30$ m/s), σ_y is almost constant at different values of D. However, at low strain rates ($v = 18$ m/s) the influence of D on σ_y is important; there is a reduction of about 29% on σ_y when increasing the damage level. Observe in Fig. 6b, strain control case, that σ_y decreases about 12% and σ_u about 22% increasing the damage level. There is a reduction on σ_y of about 23% increasing D. That reduction occurs at an approximately constant rate when increasing D.

3.3. Effect on ductility

To assess the effect of previous fatigue damage and strain rate on ductility of steel samples, two ductility related parameters were evaluated: the percent elongation, $\%\varepsilon_f$, and the percent reduction in area, $\%RA$, given by:

$$\%\varepsilon_f = 100\frac{L_f - L_i}{L_i} \quad \%R_A = 100\frac{A_i - A_f}{A_i} \tag{1}$$

These parameters compare the gage section final length, L_f, with the initial L_i; and the cross-sectional area after fracture, A_f, with the original area A_i. The percent elongation and the percent reduction in area of steel specimens for stress control are shown in Fig. 7a and strain control test in Fig. 7b. Note in Fig. 7a that $\%\varepsilon_f$ decreases considerably on the dynamic tests as D increases. This loss of ductility is more important after D = 0.5. There is a decrease of about 32% when increasing damage from D = 0 to 0.75. Also, there is a small effect of the projectile speed on this parameter. From the results of the quasi-static tests, $\%\varepsilon_f$ does not change when increasing D. A similar behavior is observed for %RA shown in Fig. 7b. On the dynamic response there is a loss of about 18% when increasing damage from D=0.75 to 0 and the projectile speed shows only slight effects. For the quasi static tests %RA changes from 8% to 3% increasing D. Hence, previous fatigue damage has a detrimental effect on ductility of 4140T steel, mainly on the dynamic tests.

Note in Fig. 8a, a decrease of about 15% to 9% when increasing damage from $D = 0$ to 0.75. Also, there is a small effect of the projectile speed on this parameter. From the results of the quasi-static tests, $\%\varepsilon_f$ with damage is included as well and it changes from 7% to 4% when D goes from 0 to 0.75. A similar behavior is observed for $\%RA$ shown in Fig. 8b. On the dynamic response there is a loss of about 20% to 10% when increasing damage from $D = 0.75$ to 0 and the projectile speed shows only slight effects. For the quasi static tests $\%RA$ changes from 16% to 8% increasing D. Hence, previous fatigue damage has a detrimental effect on ductility of AISI 4140T steel, mainly on the dynamic tests. This result in steel is a consequence mainly of strain hardening due to cyclic plasticity. In addition, SEM micrographs shown in Fig. 2 demonstrate bands of martensite in steel samples.
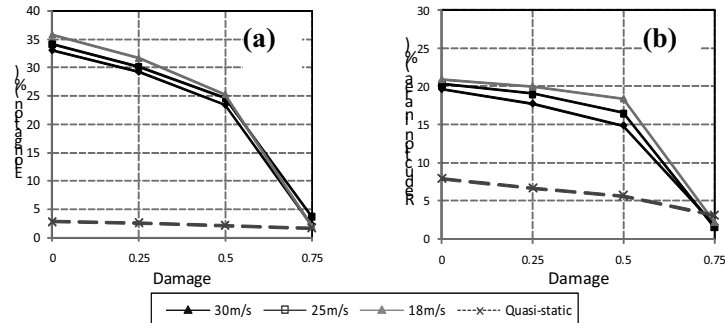
Fig. 7. Effect of fatigue damage on ductility parameters of AISI 4140T steel in stress control tests
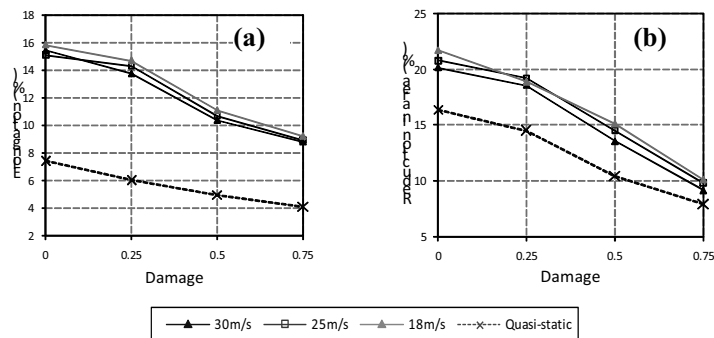
Fig. 8. Effect of fatigue damage on ductility parameters of AISI 4140T steel in strain control tests

3.4. Failure modes

Figure 9 shows the effect of fatigue damage and strain rate on the failure modes of steel samples on the dynamic experiments. The fracture surface plane is oriented about 45° with respect to the specimen axis when $v = 18$ m/s and approximately 60° when $v = 25$ m/s for damage free materials, while that angle is near 90° when $D = 0.75$ for both projectile speeds. In other words, yielding occurs on specimens with small values of D presenting fracture surfaces at inclined planes, while fracture surfaces become normal at high values of D. This suggests a transition on the steel behavior increasing D; a ductile response is observed at small values of D while a brittle behavior is exhibited by the material at high damage levels. Figure 10 presents the specimen surface after the quasi-static tension test. Note that specimens without damage exhibit a clean surface after the tension test, while specimens with previous fatigue damage present slip steps and surface cracks (mainly Fig. 10b).
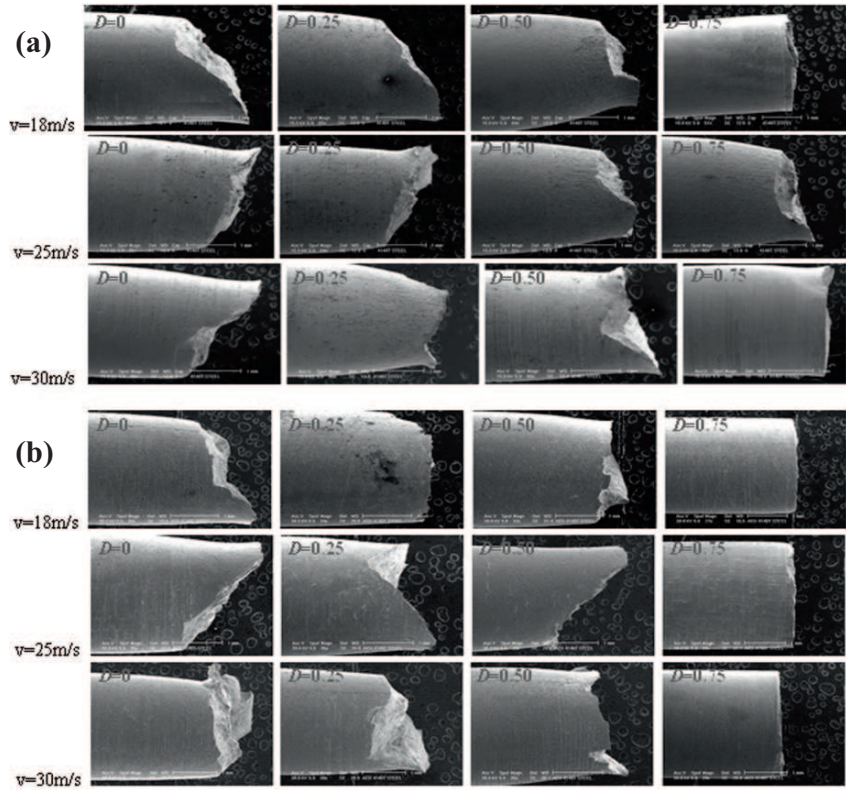
Fig. 9. Fracture modes of (**a**) stress control tests and (**b**) strain control tests at different strain rates and fatigue damages
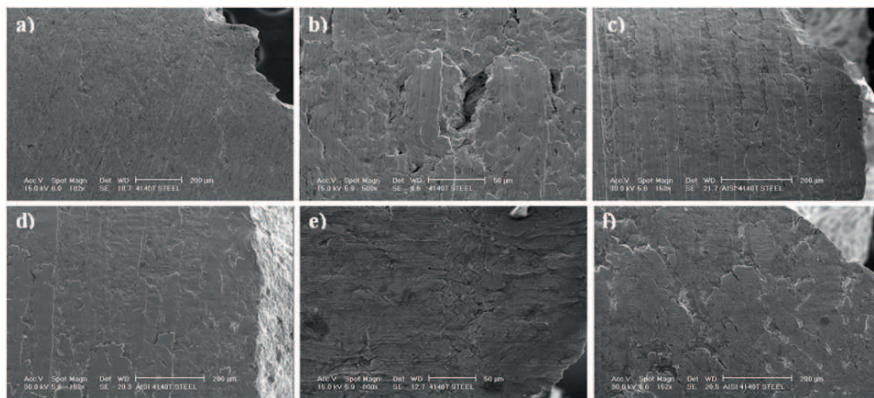
Fig. 10. Micro-photographs of the specimen surface without and with previous fatigue damage after the quasi-static (**a**) damage free, (**b**) $D = 0.75$ stress control damage, (**c**) $D = 0.75$ strain control damage, and dynamic tension test, in dynamics cases the projectile speed was v = 25 m/s, (**d**) damage free, (**e**) $D = 0.75$ stress control damage, (**f**) $D = 0.75$ strain control damage

Similarly, shows the specimen surface close to the fracture zone after the dynamic tension tests. Note that the steel specimen without damage (Fig. 11a) exhibits a typical ductile fracture mechanism, while the specimen with damage, $D = 0.75$ (Fig. 11b) presents a brittle fracture surface with evident cleavage and little plastic deformation [7]. This transition from ductile to brittle fracture increasing the damage level on steel specimens is in agreement with the loss of ductility observed previously.
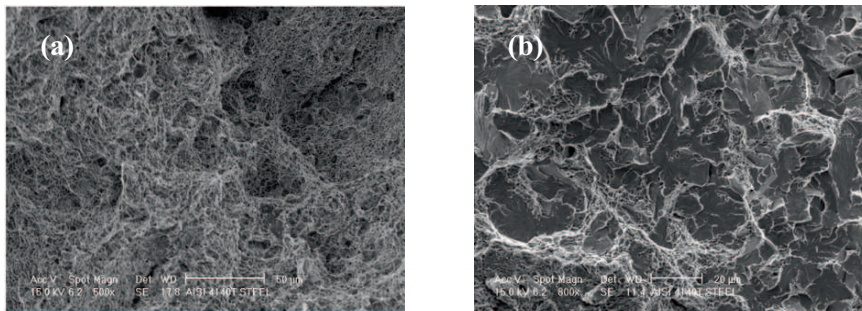
Fig. 11. SEM micrographs of specimens fracture surface, (**a**) no damage, $v = 30$ m/s, (**b**) $D = 0.75$, $v = 30$ m/s

4. Conclusions

The influence of previous fatigue damage on the quasi-static and dynamic tensile behavior of AISI 4140T steel has been evaluated. Dynamic tension tests were performed on a Hopkinson bar apparatus.

The yield and ultimate stresses are significantly higher for the damage-free material and do not change significantly with the damage level, they remain almost constant after $D = 0.25$. The yield stress is not affected by the damage level at high strain rates; however, at low strain rates the influence of damage on the yield stress is important, it decreases about 40% when increasing the damage level.

The behavior fracture surface plane was oriented about 45° with respect to the specimen axis for damage free specimens, while that angle was near 90° when $D = 0.75$ for all projectile speeds. In other words, yielding occurs on specimens with small values of D presenting fracture surfaces at inclined planes, while fracture surfaces become normal at high values of D.

This suggests a transition on the steel behavior increasing D; a ductile response is observed at small values of D while a brittle behavior is exhibited by the material at high damage levels. This is in agreement with the decrease in %ε_f and %RA when the damage level is increased.

References

[1] Meyers MA (1994). Dynamic Behavior of Materials. Wiley International Publication, New York, NY.

[2] Zucas JA (1990). Impact Dynamics, Wiley International Publication, New York, NY.

[3] Dowling NE (2007). Mechanical behavior of materials. Prentice Hall, ISBN-10: 0131863126.

[4] Kolsky H (1963). Stress waves in solid media. Dover Publications, New York, NY.

[5] Sánchez-Santana U, Rubio-Gonzalez C, Mesmacque G, Amrouche A and Decoopman X, (2008). Dynamic tensile behavior of materials with previous fatigue damage. Materials Science and Engineering: A, 497, 51–60.

[6] Sánchez-Santana U, Rubio-Gonzalez C, Mesmacque G, Amrouche A and Decoopman X, (2008). Effect of fatigue damage induced by cyclic plasticity on the dynamic tensile behavior of materials. International Journal of Fatigue, 30, 1708–1719.

[7] Rubio-González C, Gallardo-González JA, Mesmacque G, Sánchez-Santana U (2008). Dynamic fracture toughness of pre-fatigued materials. International Journal of Fatigue, 30(6), 1056–1064.

Low-Cycle Fatigue of Al–Mg Alloys

M. Bournane, M. Bouazara and L. St-Georges

Applied Sciences Department, University of Quebec at Chicoutimi, Saguenay, Quebec, G7H-2B1, Canada

Abstract   The effect of low-cyclic fatigue on the elastic and microplastic behaviours of concentrated solid solutions of Al–Mg alloys was studied using the internal friction method. For the porous alloy, it was established that the low-cyclic fatigue doesn't influence the elasticity (Young modulus) but changes the microplasticity (internal friction level). The microplastic behaviour doesn't vary but a variation of the modulus of elasticity for the nonporous solid solutions was observed. These behaviours can be associated to the different interactions of dislocations with the Mg solute elements in the oversaturated solid solutions of Al–Mg alloys.

Keywords: Fatigue, Al–Mg, Internal Friction, Microplastic, Elastic, Ageing.

1. Introduction

The study of the elastic and microplastic behaviours of materials under cyclic loading (fatigue) is of fundamental and practical importance.

A new revolution in the deformation mechanisms is to understand the basic nature of the fatigue at the microstrain level. This revolution is supported by the development of new materials and the need to understand the behaviour of conventional materials under various environments.

The internal friction (IF) method is widely used to study the elasticity and the microplasticity of solid materials, since the damping capacity (value of IF) caused by the microstrain is intimately related to the density and the mobility of dislocations [1–4]. The elasticity and the microplasticity of the diluted and concentrated solid solutions (SS) of Al–Mg alloys [5–8] were the subject of many studies.

It is very important to notice that when we measure each value of IF, the specimen is always maintained under constant cyclic strain amplitude (forced oscillations) before its free decay. These unwanted forced oscillations can cause the low-cyclic fatigue. This last phenomenon can affect the elastic and the microplastic properties of various solid materials. But unfortunately, it is often neglected if not completely ignored. The aim of this work is to study, by means of IF method, the elastic and microplastic behaviours characterised respectively by the resonance frequency of oscillations and the IF level of the concentrated SS of Al–Mg alloys taking into account the fatigue phenomenon.

2. Experimental procedure

For our study, the following Al–Mg alloys were used: Al-8 wt% Mg porous solid solution (Fig. 1a); Al-(3.8) wt% Mg non porous solid solution (Fig. 1b). The porous and non porous alloys were obtained by sand casting and die-casting respectively. The average size of the crystalline grains is 150 μm [9]. The metallographic observation shows that the pores are localised along the grains boundaries (Fig. 1a). The dimension of pores varies from 30 to 70 μm and the porosity level is 2%.
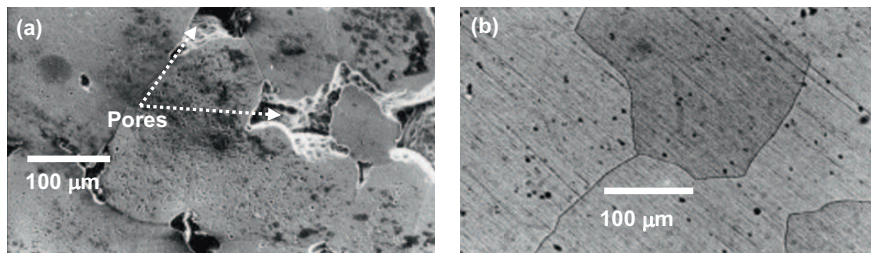
Fig. 1. Microstructure of Al-8 wt% Mg quenched supersaturated solid solutions: (**a**) – porous, (**b**) – non porous [9]

The samples for IF measurements have a cylindrical form with a diameter of 3.5 mm and useful length of 25 mm. They were cut out from the same ingot. The obtained specimens were homogenised at 430°C ± 5°C during 17, then quenched in heated water at 80°C. The oversaturated solid solutions (OSS) were obtained after this operation.

2.1. Internal friction method

In this study, the IF measurements were carried out at ambient atmosphere and strain amplitude varied within the range from 33×10^{-6} to 3311×10^{-6} while using a direct torsion pendulum. The measured data were obtained at ambient temperature and resonance frequency around 64 Hz.

During the measurement, a portion of the applied mechanical energy is transferred into heat (dissipation energy) when a sample is submitted to mechanical vibrations with small strain amplitude. The IF is not only an intrinsic property of the material; it can also be used to study the evolution of physical, elastic and microplastic properties of materials. Each domain of resonance frequency corresponds to a specific technique of IF measurement. For low frequencies, the direct torsion pendulum is the most proper technique. In this method, an individual IF value is obtained for each maximal strain deformation γ_{max} when sample is subjected to free damped vibrations. The strain amplitude γ_t, as a function of time, is given by:

$$\gamma_t = \gamma_{\max} \cdot e^{-\beta t} \sin \omega t \qquad (1)$$

where ω and β are the vibration pulsation and damping coefficient respectively.

Herein, the logarithmic decrement δ of free damped vibrations was used to measure the IF value Q^{-1} by means of the technique of the direct torsion pendulum (Fig. 2). For small strain amplitudes, the following relations are obtained:

$$\delta = \pi \cdot Q^{-1} \qquad (2a)$$

$$= \frac{1}{2\pi} \frac{\Delta E}{E} \qquad (2b)$$

$$= In \frac{\gamma_t}{\gamma_{t+T}} \qquad (2c)$$

where $\Delta E = E_t - E_{t+T}$ is the energy damped during one oscillation, T-oscillation period.

Considering n cycles of free damped vibration, we obtain:

$$\delta = \frac{1}{n} In \frac{\gamma_{t_i}}{\gamma_{t_n}} \qquad (3)$$

where $\dfrac{\gamma_{t_i}}{\gamma_{t_n}}$ – ratio of the initial strain amplitude γ_{t_i} divided by the stain amplitude after n cycles of vibration γ_{t_n}.

In our experiment, $\dfrac{\gamma_{t_i}}{\gamma_{t_n}} = 1$ was used. Consequently:

$$\delta = \frac{In\,2}{n} = \frac{0.693}{n} \qquad (4)$$

To measure n, the extremity of the specimen (1) is rigidly mounted on a clamped rod (2) made of a non-conducting material. The other end of the sample is fixed to a light T-shaped pendulum. A magnet (4) connected to a generator (5) is installed at the end of the horizontal rod of the pendulum (3).

The maximal strain amplitude is selected by means of an amplitude discriminator (7). When the start button of the generator is rapidly released, the specimen begins its free damped oscillations. The number of these oscillations n is given by the meter (6). The experimental setup can be operated in large ranges of temperatures (20–1,000°C) and maximum strain amplitudes (33–3311 × 10^{-6}). Measurements can be carried out at ambient atmosphere or in vacuum (up to 10^{-4} torr).

1. Sample	11. Power supply
2. Support rod	12. Chronometer
3. Titanium horizontal rod	13. Printer
4. Electromagnet	14. Commutation switch
5. Oscillation meter	15. Micro-voltmeter
6. Amplitude discriminator	16. Copper piece
7. Recording sensor	17. Solenoid
8. Furnace	18. AC source
9. Data recording system	19. DC source
10. Electronic key	
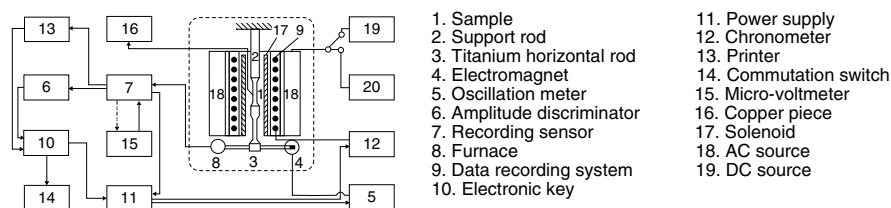
Fig. 2. Experimental setup used to measure internal friction

3. Results and discussion

In our former works [10, 11], the microplastic behaviour of the Al–Mg alloys in the field of the microstrain was studied. We showed that:

- The ascending and descending curves of strain amplitude-dependent internal friction (SADIF) of the Al–Mg nonporous OSS coincide almost perfectly.
- For the Al–Mg porous OSS, this superposition phenomenon was only observed in the high strain amplitudes field, whereas the ascending curve is always located below that of the descending one at low and average strain amplitudes.
- The presence of the pores in the material leads to an important damping capacity (value of IF).
- The rise of Mg concentration in the nonporous OSS involves an increase of the IF level.
- The mechanisms of deformation were associated to the reversible and the irreversible movements of dislocations in the nonporous and porous Al–Mg OSS respectively.

In [12], the ageing effect at 250°C of the Al–Mg porous OSS on the resonance frequency (elastic characteristic) and on the SADIF parameters was investigated. It was showed that the ageing leads to the no monotonous variation of the IF level: during the ageing, it raises first then decreases. It was established that the mechanism of deformation occurs by multiplication of dislocations. In our previous works, we never considered the fatigue effect which could occur during IF measurements before the beginning of the free decay. It is known that when the IF value is measured, the specimen involuntarily undergoes the forced oscillations under each

fixed strain amplitude during a short time before its free decay. Thus, it's probable that this holding at fixed amplitude could affect the elastic and/or the microplastic behaviours of the tested material. To our knowledge this effect was never studied.

Figure 3 shows that the IF level of the Al–Mg nonporous OSS remains constant for different holding times at fixed strain amplitude under forced oscillations of the specimen. This constancy indicates that the mechanism of deformation can be linked to the reversible movement of dislocations for these OSS [3, 13]. In another hand, the IF level of the porous OSS increases at the beginning then remains constant. This variation can be associated to the multiplication of dislocations [3]. It is known that the Young modulus and the modulus of rigidity of solid materials are proportional to the square frequency f^2: f is the resonance frequency of material subjected the cyclic oscillations [2, 15]. Considering the proportionality between the elastic modulus and the f^2, it is enough to follow the evolution of f^2 to study the elastic behaviour of a material. The value of f is easily determined by IF measurements. Figure 4 shows that, with the increase of the holding time at fixed stain amplitude under forced oscillations, the square of resonance frequency doesn't practically vary for the porous OSS and it deceases for nonporous OSS. In [14], Liu et al. studied the damping phenomenon of the pure aluminum with various densities of porosity. It was highlighted that the value of IF increases considerably with the increase of the density of porosity.
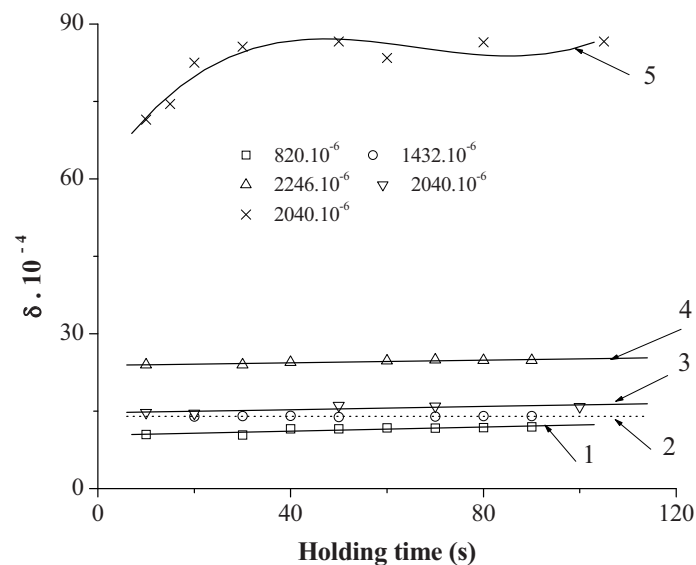
Fig. 3. Variation of logarithmic decrement (internal friction) of the Al–Mg oversaturated solid solutions as function as the holding time under forced oscillations (low-cyclic fatigue) for various strain amplitudes. Curves (1, 2, 3) – 3 wt% Mg nonporous alloy, 4–8 wt% Mg nonporous alloy, 5–8 wt% Mg porous alloy
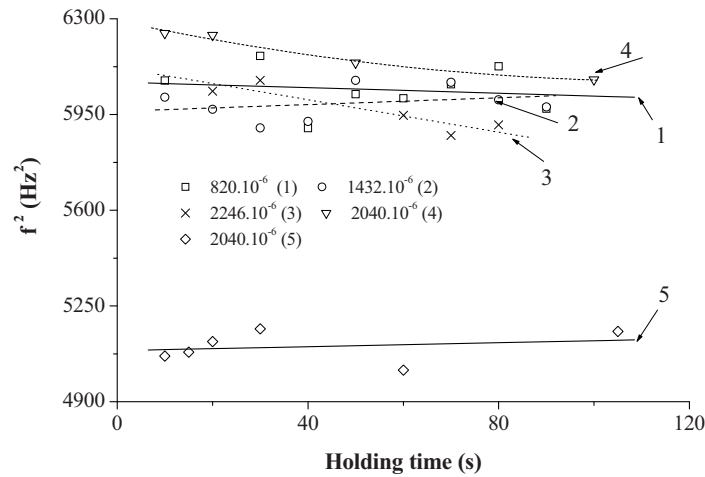
Fig. 4. Variation of the square frequency of Al–Mg oversaturated solid solutions as function of the holding time during at forced oscillations for various strain amplitudes: (1,2,3) – 3 wt% Mg nonporous, 4–8 wt% Mg nonporous, 5–8 wt% porous

This rise was associated to the irreversible movement of dislocations located on the surfaces of the pores. Theses surfaces constitute regions with high stresses concentrations. For the studied Al–Mg porous OSS, the variation and the non-variation of the IF level can respectively be attributed to the displacements of the mobile dislocations located on the surfaces of the pores and to the pinning of these dislocations by the diffused Mg solute elements. In the considered Al–Mg nonporous OSS, the mobile dislocations are strongly anchored by the Mg solute elements which are numerous in the mother matrix. This can lead to the non-variation of the IF level. The small variation of f^2 can be related to the movements of the Mg elements in the cores of dislocations.

4. Conclusions

The study of the effect of the low cyclic fatigue on the elastic and microplastic behaviours of the Al–Mg oversaturated solid solutions showed that the mechanism of deformation occurs differently for porous and nonporous alloys.

In the case of the nonporous OSS of Al–Mg alloys, this mechanism doesn't occur because the mobile dislocations are anchored solidly by the Mg solute elements; but the displacements of the mobiles dislocations present on the pores surfaces lead to the microplasticity of the oversaturated solid solution of Al–Mg porous alloy.

For this alloy, the pinning of the mobile dislocations by the diffusion of the Mg solute elements causes the non-variation of the IF level from a certain value of holding time under forced oscillations.

References

[1] Blanter MS, Golovin IS, Neuhäuser H, Sinning HR (2007). Internal Friction in Metallic Materials: A Handbook. Springer, Berlin Heidelberg.

[2] Kustov S, Gremaud G, Benoît W (1999). Strain amplitude-dependent anelasticity in Cu-Ni solid solution due to thermally activated and athermal dislocation-point obstacle interactions. J. Appl. Phys. 85: 1444–1459.

[3] PuskarA (2001). Internal Friction of Materials. CISP, Cambridge.

[4] Asano S, Amaki Y (2002). Change in damping capacity of aluminum as a result of work hardening, solid-solution hardening and precipitation hardening. J. Japan Inst. Metals 66: 109–116.

[5] Tan Q, Kê TS (1991). Development of the double amplitude internal friction peaks in cold-worded aluminum-magnesium solid solutions. Phys. Stat. Sol. (a) 126: 345–354.

[6] Kê TS, Fang QF (1990). Evolution of the anomalously amplitude dependent internal friction peaks in Al-Mg solid solutions and the discovery of a new peak. Phys. Stat. Sol. (a) 121: 139–148.

[7] Bournane M, Lahlouh M, Nedjar M (2003). Etude du mécanisme de microdéformation dans la solution solide Al-Mg. In: Proceeding of 6ème Congrès de Mécanique "Mécanique des Solides" Tome I. Tanger-Maroc, pp 215–216.

[8] Bournane M, Nedjar M, Sadaoui Y, Sirenko AF (1999). Elasticité et Microplasticité de l'Alliage Poreux Al-Mg. In: Proceeding of 4ème Congrès Marocain de Mécanique "Mécanique des Solides" Tome I. Mohammadia-Maroc, pp 99–100.

[9] Bournane M, Nedjar M, Sirenko A F (1999). Precipitation in solid solutions of Al-Mg. Scripta Materialia 40: 375–382.

[10] Bournane F, Bournane M, Sadaoui Y, Nedjar M (2001). Détermination des caractéristiques microplastiques de l'alliage poreux Al-Mg au cours de son vieillissement après déformation. In: Proceeding of 5ème Congrès Marocain de Mécanique "Mécanique des Solides" Tome I. Meknès-Maroc, pp 96–97.

[11] Bournane M, Nedjar M, Roebben G (2002). Amplitude-dependent internal friction in concentrated Al–Mg solid solutions. In: Abstracts Book of 13th International Conference on Internal Friction and Ultrasonic Attenuation in Solids. Bilbao.

[12] Bournane M, Nedjar M, Hakem A, Sirenko AF (2002). Amplitude-dependent internal friction in aged Al–Mg porous Alloy. In: Abstracts Book of XXX Summer School in Advanced Problems in Mechanics APM'2002. St-Petersburg.

[13] Asano S (1970). Theory of nonlinear damping due to dislocation hysteresis. J. Phys. Soc. Jap. 29: 952–963.

[14] Liu CS, Zhu ZG, Han FS (1998). Internal friction of foamed aluminium in the range of acoustic frequencies. J. Materials Science 33: 1769–1775.

[15] Krichtal MA, Piguzov YV, Golovin S A (1964). Internal Friction in Metals and Alloys (in russian). Metallurguya, Moscow.

Damage of Glulam Beams Under Cyclic Torsion: Experiments and Modelling

Myriam Chaplain[1], Zahreddine Nafa[2] and Mohamed Guenfoud[2]

[1]US2B, Université Bordeaux 1, 69 route d'Arcachon, 33612 Cestas Cedex, France

[2]LGCH, Université 08 mai 45, BP. 401, 24000 Guelma, Algérie

Abstract   The aim of this paper is to study the behaviour and the lifetime of glued-laminated small scale beams (GL) submitted to cyclic torsion. Experimental programmes have been carried out: periodic triangular alternate torques with varying amplitude is applied to GL samples with rectangular cross section. Experimental lifetime is presented by semi logarithmic SL-N curves (SL is the maximum torque stress level and N is the number of cycles to failure). From angular distortion records, we propose a method to obtain the damage evolution versus time. The prediction of load duration of GL specimens under cyclic torque is approached by a damage theory. The usual wood damage model proposed by Barrett and Foschi has been chosen. This model does not take into account the influence neither of the frequency nor of the middle moment. Also, to perform the model, we introduce a rheological model in the damage formula and the threshold moment is supposed to depend on the middle moment.

Keywords: Torsion, Damage, Modelling, Glued-Laminated.

1. Introduction

In timber constructions, structural elements are subjected to complex state stress due to combination of simple loads and also due to structure geometry. Thus, torsion stress can appear under the effect of simple torque or under the effect of a geometrical instability like lateral-torsion buckling. In addition, loading can be constant or varying (for example, loads due to wind or earthquakes). The aim of this paper is to study and to model the behaviour and the lifetime of glulam beams (GL) under cyclic torsion. Despite the importance of wood production, studies on the behaviour under cyclic loading of wood are limited. We can cite the work of Okuyama [9, 12]: the authors studied the behaviour of solid wood (spruce) under tension or compression cyclic loading. The influence of various parameters has been studied: for the same stress level, the number of cycles to failure is greater in compression than in tension; lifetime also increases with the frequency of the loading (Fig. 1). Regarding the effect of the signal shape, the authors found that the square loading is more severe and provides shorter time to failure than triangular loading. For a given number of cycles to failure, triangular loading produces smaller loss of energy.

Fatigue of wood has mainly been studied under bending loadings; thus, Bonfield [5, 8, 13] exposed results of tests putting in evidence simultaneous effects of slow cyclic fatigue and creep on chipboards. Four points bending test was carried out on several types of chipboards. Under the same peak stress, authors concluded that deformation rate of samples is greater than under cyclic load.

The recent application of glued-laminated in the manufacture of wind turbine blades has led researchers in the investigation of the fatigue properties of glulam. Bond and Ansell [3, 4] have carried out series of fatigue tests on glulam made of three different wood species. Tests have been essentially realised under alternating loading tension–compression (R = 1) but other R ratios were also explored; R is the ratio of minimum load to maximum load. Results suggests that for a given peak stress, the number of cycles to failure increases with the absolute value of R. There are few papers concerning the behaviour of wood or wood-based products in torsion: Ayina [1] presents results of short-term and long-term (creep) tests on glulam of Movingui and Bilinga species under torsion. The proposed models are linear and parabolic for short-term tests, while they proposed a power law and exponential models for creep tests. In another paper, Chen, Gabbitas and Hunt [7] study the effect of grain orientation on the torsional fatigue properties of hardwoods and softwoods. In both static and cyclic loading tests, failure mode of hardwoods is slow and incomplete, whereas, softwoods fail suddenly and completely. The crack growth is along the tangential direction in the hardwood cross-section and along the radial direction in the cross-section.
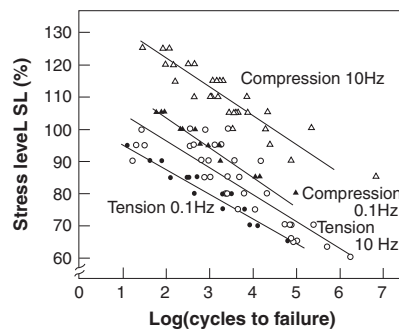
Fig. 1. Influence of the stress level and of frequency on number of cycles to failure (triangular loading) [9]

Through our study, we want to provide answers on the cyclic torsion behaviour of GL structural beams. In particular, we seek to understand the effects of the amplitude and maximum moment on the lifetime of these elements. Starting from cyclical results of tests on specimens, we develop a damage model applicable to structural elements subject to various repeated loadings. Although the effects of moisture are non-negligible on viscous behaviour of wood, they are not studied hereafter.

2. Experimental procedures and results

2.1. Experimental programme

The specimens were small models of beams used for construction. They were 900 mm long and were obtained by gluing six spruce lamellas of 40 mm wide and 10 mm thick (Fig. 2) [10, 11]. The used adhesive was Enocol RLF 185; it is a mixture of resorcine, phenol, and formalin. All tests were performed in a room where temperature and humidity were constant or varying weekly. The moisture content of specimens is about 11%.
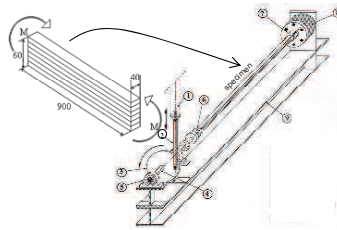
Fig. 2. Dimensions of specimen and experimental device

Short term (monotonous) tests were carried out to measure the "static" torsion strength moment. Tests were led under controlled displacement with a constant gradient of 2°/s. Long term tests were led under controlled moment with a constant speed of 110 N.m/s and different frequencies for each amplitude. The signal was triangular [10]. To emphasize the effects of the amplitude and of the maximum moment (Mmax), three fatigue programs were carried out. For the first set, the middle moment was equal to zero with various maximum moment ($R = M_{max}/M_{min} = -1$). For the second set, the amplitude was constant and the maximum moment changed. For the third set, the maximum moment was fixed while the amplitude changed. Because of the large number of specimens and in order to limit the total time of test execution, a conventional limit of 2,000 cycles was fixed. In this study, stress level (SL) is defined as the ratio of maximum moment applied to estimated static strength moment Ms of the specimen. Ms is the average monotonous failure torque (torsion strength) of the considered beam series.

2.2. Results and discussion

For different values of amplitude, the evolution of the torsion angle versus torque shows stabilization (accommodation) for SL lowers than 0.5 (Fig. 3a). Above this value, damage appears; it results in a progressive increase of torsion angle that leads to failure (Fig. 3b).
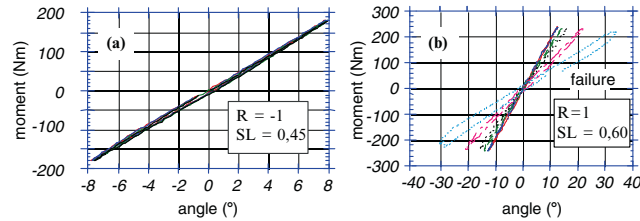
Fig. 3. Torsion angle-moment curves: (**a**) for low stress level SL-accommodation (**b**) for high stress level SL-failure

The alternating tests (R = −1) showed the existence of a limit value of the stress level around 50% above which failures appear. Above this limit, the number of cycles to failure decreases exponentially with the increase of amplitude. Under a constant maximum moment, the general observation is that maxi-mal distortion increases with middle moment. For a given maximum moment, the ruptures do not occur first for the highest but for the lowest middle moments. This can be explained by the fact that in torsion, there is neither positive nor negative stress as in tension-compression. One alternating loading cycle (R = −1) is equivalent to two wavy loading cycles (R = 0); alternating loading causes more damages than wavy loading (Fig. 8) (more dissipated energy). These results are in agreement with other experimental observations [3].

2.3. Damage measurement

The damage or the no-damage can be observed looking at the curve number of cycles – angular deformation. For tests at low amplitude (Fig. 4a), specimens are not damaged: after a first flow, the angular evolution versus number of cycles becomes quite linear (second flow). For higher amplitudes, as soon as a crack appears in the beam, the angle-cycles curves become exponential (third flow) and failure occurs after a little number of cycles (Fig. 4b). The determination of the damage evolution is obtained by considering the flow angular deformation (Fig. 5). The difference between the tertiary flow and the secondary flow is selected as damage index (Fig. 5a). The obtained flow p is normalized to 1 to obtain a damage parameter noted D (Fig. 5b).
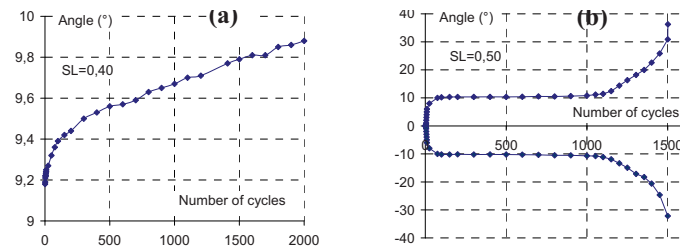
Fig. 4. Evolution of the torsion angle according to number of cycles
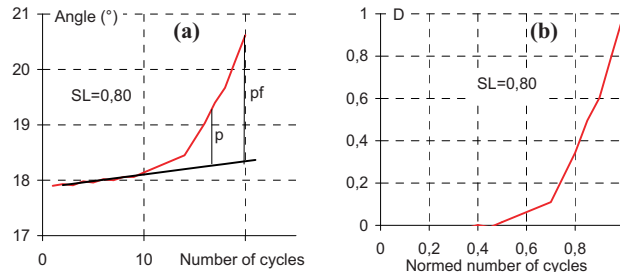
Fig. 5. Determination of the damage parameter D: (**a**) maximum angular deformation against number of cycles: determination of a damage index p (p = p_f at the failure) – (**b**) damage evolution D = p/p_f

3. Modelling

The prediction of number of cycles to failure is studied using a damage theory. The damage is characterized by a parameter D which varies between 0 when the material is not damaged and D_c when failure appears. Because of a lack of results, we take $D_c = 1$.

3.1. Damage model expression

The experimental results show the influences of stress level, frequency and loading amplitude on the time duration. Only non-linear damage evolution and non-linear cumulative damage have been held. The usual dam-age models do not take into account the influence of frequency, i.e. they do not integrate the viscoelastic behaviour of the material. To bridge this gap, Chaplain [6] has proposed to couple a rheological model (Fig. 6) with the damage model of Barrett and Foschi [2].
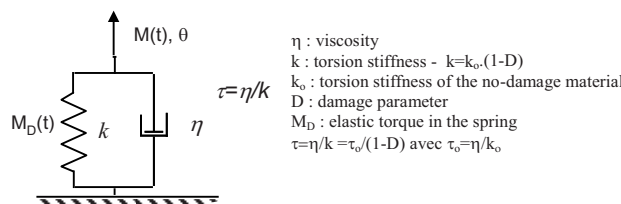
Fig. 6. Kelvin–Voigt model M: applied torsion torque, θ: angular deformation

The viscous behaviour of wood is represented by the basic rheological model of Kelvin–Voigt. We believe that only the elastic part of the material is damaged; thus, stiffness k depends on damage; k follows the law presented in Fig. 6.

In the damage model formula, we integrate the elastic torque (M_D) and not the applied torque Eq. (1). This moment M_D depends on the parameter τ and on the

state of damage D (hence its name). The expression of the new model obtained is as follows in Eq. (1):

$$\begin{cases} \dfrac{dD}{dt} = a \cdot \left(\dfrac{|M_D(t)| - M_o}{M_s} \right)^b + \lambda D(t) & \text{if} \quad |M_D(t)| > M_o \\ \dfrac{dD}{dt} = 0 & \text{if} \quad |M_D(t)| < M_o \end{cases} \qquad (1)$$

where M_D is the part of the moment in the spring. M_s is the static torsion strength and M_o is the threshold moment. a, b and λ are parameters. |.| means absolute value. As the applied moment can be negative, stresses must be expressed as absolute values. The model has not given good predictions for results of tests with varying middle moment yet. The model does not take into account the effect of middle moment or the effect of R on the failure. A new model is developed from the old one; it has the same expression except that the threshold moment is not constant anymore but it depends on the middle moment as shown in Eq. (2).

$$M_o = \overline{M} + M_{lo}(1 + \alpha \cdot \frac{\overline{M}}{M_s}) \qquad (2)$$

With: M_o threshold moment, $\overline{M}$ middle moment, M_{lo} threshold moment at R=-1, M_s static torsion strength, α fitting parameter. For a given stress level SL, when the amplitude decreases, i.e. when R in-creases, the threshold moment increases, which produces an increase of the lifetime predicted by the model.

3.2. Model predictions

The model parameters are determined from the results in alternating cyclic loading. In this case, the middle torque is equal to zero and the threshold moment M_o is equal to M_{lo}. Looking at the experimental results, the threshold (moment) level (M_{lo}/M_s) is taken equal to 0.47. It corresponds to values of damage threshold level found in literature. At the tested frequency (around 0.1 Hz), the viscosity of material is quite not solicited; the hysteresis loop observed is not very large (Fig. 3a). Viscosity η could not be measured. The value $\tau = 0.03$ s, found by Chaplain [6], has been chosen. The numerical values of a, b and λ are determined to obtain the best accuracy between predictions of time to failure and predictions of damage evolution for alternating loading ($R = -1$). Their values are obtained by successive simulations: simulations are performed for various set of parameters. The predicttions are visually compared with experimental results.

The "best" values of a, b, and λ obtained are: $a = 1$, $E14$ s^{-1}, b = 30, $\lambda = 0.05$ s^{-1}. The value of $\alpha = 1.26$ is also obtained after several simulations to obtained the best times to failure for different R values.
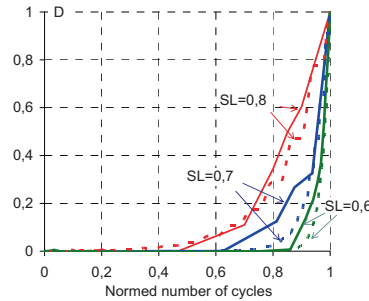
Fig. 7. Damage evolution under alternating torque (R = −1). *Full line*: experimental results – *dotted line*: theoretical evolutions
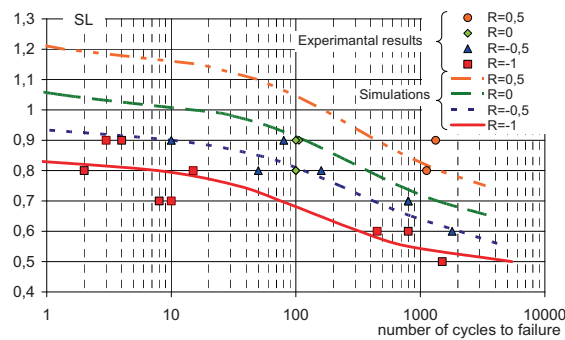
Fig. 8. Comparisons of model predictions and experimental results

Figure 7 shows the theoretical and experimental damage evolution under alternating cyclic loading $(R = -1)$. Figure 8 presents experimental and theoretical evolutions of the number of cycles to failure against the stress level for four values of R. Considering the uncertainties on the values of the stress level (estimation of M_s of the beam tested under cyclic loading) and despite the dispersion of results and the lack of experimental points, the model predictions are acceptable.

4. Conclusions

Cyclic alternating torsion tests show the influence of the stress level SL on behaviour and lifetime of glue-laminated beams. Obviously, a higher stress level leads to smaller time to failure. Failures appear before 2,000 cycles (test limit) only for SL above 50%.

Wavy cyclic tests with varying amplitude emphasize the effect of the shape of loading on duration of load. For a given stress level SL, alternating loading (amplitude level moment = 2SL) leads to smaller lifetime compared to wavy cycles load with amplitude level lower than 2SL. The developed damage model is

based on the second model of Barrett and Foschi. This model is coupled with the rheological model of Kelvin–Voigt to integrate viscoelastic behaviour of wood. The influence of the average moment on lifetime is taken into account through a threshold damage moment: this moment is not constant but it is function of the middle moment. The model has been applied to predict damage evolution and lifetime of beams under cyclic triangular torque at different R values. Despite the incertitude on determination of stress level, the predictions are in good agreement with experimental results. To improve the model, other tests must be realized in order to increase the number of fitted points and mitigate the effect of dispersion.

References

[1] Ayina O, Morlier P. Comportement en torsion du matériau bois. Materials and Structures, Vol 33, 1998, pp. 405–410.

[2] Barrett J D, Foschi R O. Duration of load and probability of failure in wood. Part I. Modelling creep rupture. Canadian Journal of Civil Engineering, Vol 5, 1978, pp. 505–514.

[3] Bond I P, Ansell M P. Fatigue properties of jointed wood composites. Part I. Statistical analysis, fatigue master curves and constant life diagrams. Journal of Materials Science, Vol 33, 1998, pp. 2751–2762.

[4] Bond I P, Ansell M P. Fatigue properties of jointed wood composites. Part II. Life prediction analysis for variable amplitude loading. Journal of Material Science, Vol 33, 1998, pp. 4121–4129.

[5] Bonfield P W, Dinwoodie J M, Ansell M P, Hacker C L. Fatigue and creep of chipboard. Part 1. Fatigue at R = 0.01. Wood Science and Technology, Vol 28, 1994, pp. 423–436.

[6] Chaplain M. Comportement sous sollicitations sévères des assemblages de structures en bois: modélisation de l'endommagement. Thèse de Doctorat, Université Blaise Pascal, Clermont Ferrand II, 1996.

[7] Chen Z, Gabbitas B, Hunt D. The fracture of wood under torsional loading. Journal of Material Science, Vol 41, 2006, pp. 7247–7259.

[8] Dinwoodie J M, Paxton B H, Bonfield P W, Mundy J S. Fatigue and creep of chipboard. Part II. The influence of slow cyclic fatigue on the creep behaviour of chipboard at a range of stress levels and moisture contents. Wood Science and Technology, Vol 29, 1995, pp. 64–76.

[9] Marsoem SN, Bourdonné P-A, Okuyama T. Mechanical responses of wood to repeated loading. II. Effect of wave form on tensile fatigue. Mokuzai Gakkaishi, Vol 33(5), 1987, pp. 354–360.

[10] Nafa Z. Etude du comportement de poutres en bois lamellé-collé sous torsion cyclique, doctorat d'état en Génie Civil, Universite Badji Mokhtar, Annaba, Algérie, 2007.

[11] Nafa Z, Araar M. Applied data for modeling the behavior in cyclic torsion of beams in glued-laminated wood: influence of amplitude. Journal of Wood Science, Vol 49, 2003, pp. 36–41.

[12] Kohara M, Okuyama T. Mechanical responses of wood to repeated loading. V. Effect of duration time and number of repetitions on the time of failure in bending. Mokuzai Gakkaishi, Vol 38(8), 1992, pp. 753–758.

[13] Thompson R J H, Bonfield P W, Dinwoodie J M, Ansell M P. Fatigue and creep of chipboard. Part 3. The effect of frequency. Wood Science and Technology, Vol 30, 1996, pp. 293–305.

Statistical Study of Temperature Effect
on Fatigue Life of Thin Welded Plates

Abdelmadjid Merabtine[1], Kamel Chaoui[1] and Zitouni Azari[2]

[1] LR3MI, Badji Mokhtar University, BP12, Annaba, 23000 Algeria.

[2] LFM, Ecole Nationale des Ingénieurs de Metz (ENIM) – Ile du Saulcy, 57045 France.

Abstract   Martensitic stainless steel sheets with 12% Cr are used as protective envelopes for hot and vibrating structures such as aircraft engines and gas turbines. Since the envelope shape may be complex, butt welding is chosen to assemble the parts which can undergo fatigue failure especially in the heat-affected zone (HAZ). The aim of this study is to present experimental fatigue life results showing the effect of temperature and to present a reliable statistical approach in order to correctly describe a given loading level, in relation to its fatigue life, which has not yet been tested using the only available experimental data. This situation is dictated by optimizing the costly and lengthy fatigue experiments for modeling. Normal and Weibull statistical models are used to predict fatigue lifetime based on S-N curves in welded and seamless plates. Both models provide comparable results with experimental data at 293 K and 690 K for failure probability limits of 5% and 95%. Based on Weibull model, untested levels are assessed using a cumulative fatigue life function. Two new dimensionless parameters (X: square stress ratio and H: thermal life ratio) are used to calculate, for a given stress level, the corresponding fatigue life in accordance to the sought lower and upper confidence limits. The proposed modified Weibull approach delivers results within less than 5% error.

Keywords: AISI 410, Welding, Fatigue, Temperature Effect, Weibul.

1. Introduction

Material damage and subsequent fatigue failure are usually led by progressive strength deterioration as a result of fluctuating applied stresses and eventually hostile service conditions. Several well-known steel structures, such as ferrite/pearlite, bainite, martensite and austenite are considered to manufacture industrial components. Each of these structures exhibits considerably different mechanical properties that may be up-rated using appropriate tempering and quenching treatments according to a given application [1].

Martensitic stainless steels obtained for 12% chromium and above are used as heat and corrosion resisting parts in the chemical industry, as heat-protecting metallic envelopes for aircraft engines, turbo-machinery equipment, propulsion motors and as gas turbines casing in the petroleum industry. These steels present many advantages; i.e., easily welded by most current procedures, stress corrosion resistant and usually harden by precipitation.

Commonly, heat treatments improve most of the mechanical characteristics, ameliorate corrosion résistance on polished surfaces, and lead to an improved fatigue life behaviour for welded joints [2].

Practically structural elements, assembled by welding techniques and which undergo cyclic loadings for long periods of time are subject of important reduction in intrinsic resistance. Some precautions are observed in order to improve both quality and resistance of welded joints in terms of surface preparation, welding parameters and operation skills which minimize the probability of defects occurrence. Common defects range from lack of fusion, incomplete melt penetration, irregularities of molten beat radius to geometrical misalignment [3]. The latter defects usually generate maximum local stresses at the joint and intensely influence the welded zone behaviour under alternating loading. Because of adverse effects of stress concentration produced by the geometrical discontinuities and temperature gradients in the welded zone, it is necessary to assess design procedures in a more conservative approach to ensure safety and to allow obtaining statistical strength and fatigue life time [4].

Many industrial structures such as gas turbine exhaust components used in jet planes, low pressure piping elements and rotating parts made out of stainless steels are butt welded and are operated at temperatures reaching 700 K [5]. Applied working stresses, added to welding residual stresses, act within the material and perpendicularly to the butt-welded joints. At this step, to raise hardness level in the heat affected zone (HAZ) and to lower residual stress intensity, it is mandatory to specify the heat treatment type which guarantees the highest fatigue life and the most improved weld reliability [6].

Fatigue analysis of welded structures is studied using the S-N curve approach (Wöhler curve) which presents the applied mean stress level as a function of elapsed number of cycles. Such reference curve once established informs about the endurance limit which is a design criterion for structures subjected to alternating loads. The statistical investigation concerning cyclic stress amplitude indicated that many distributions are fitting correctly the experimental data, meanwhile normal and minimum value models were most appropriate for correlations [7]. Because of the greatly randomized aspect of the fatigue behaviour in stainless steels, statistical characterization of component lifetime becomes an important matter when searching for correlations with damage extents, failure rates, reliability indexes and environmental parameters such as aggressiveness and temperature.

The objective of this work is to present experimental fatigue life results dealing with the effect of temperature in thin stainless steel sheets. Subsequently, make use of the generated results to propose a statistical approach in order to correctly describe a given loading level, in relation to its fatigue life for interpolation purposes. That means the studied condition has not yet been tested while reliable extracted data are needed to construct the complete evolution using the only available experimental ones. This situation is imposed from cost optimization of fatigue experiments used for design goals and reliability analyses.

2. Experimental approach

2.1. Material

The material used in this study is martensitic steel known as AISI 410 (also referred to as X15Cr13 for DIN, and CA15 for ASTM) and which was received in the form of rolled sheets 1 mm ± 0.1 thick. Basically, it is corrosion resistant stainless steel as its chromium content is above 12%. Table 1 summarizes the material chemical composition.

Table 1. Chemical composition of AISI 410 Stainless Steel (wt%)

C	Cr	Ni	Mo	Mn	P	Cu	S	Si
0.15	12.25	0.5	0.5	1.0	0.04	0.5	0.008	1.0

The tested steel is employed to wrap plane engines which have low horsepower as shown in Fig. 1. Usually an important heat flux is delivered from combustion chambers making overall temperature to reach approximately 690 K. For this reason, the latter temperature is chosen to be the maximum value at which tensile and fatigue testing will be carried out. Its fusion temperature T_f is 1758 K.

Fig. 1. Sectional view of a typical plane engine illustrating external envelope, compressor, combustion chambers and propulsion turbine [9]

2.2. Testing conditions

The tensile static tests are carried out using a servo-hydraulic MTS machine having a maximum loading capacity of 250 kN. A set of specially conceived grips is employed to maintain the test specimen aligned within the furnace. The specimen geometry for a welded case is shown in Fig. 2 with the various dimensions as expected from standard testing conditions.

The welded zone width did not exceed 3.5 mm and was obtained using TIG procedure to control uniformity in all the welds. Load displacement curves are obtained at 293 and 690 K. A constant speed of 2.5 mm/min is adopted for tensile tests. For high temperature tests, a furnace with an electrical resistance allows to obtain the controlled environment of 690 K. Three electrodes are placed along the central line of the sample in order to have a homogenous radiating heat flux within the confined volume of the furnace and bi-metallic thermocouples are used to monitor the temperature while testing.
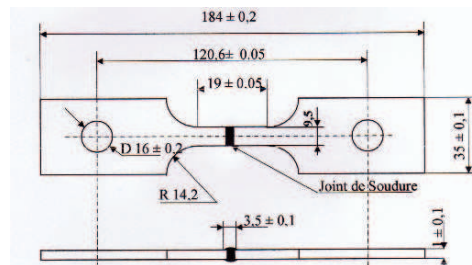
Fig. 2. Geometry of the test-specimen

For fatigue testing, a sinusoidal function with constant amplitude is chosen under controlled load mode. A frequency of 10 Hz and a ratio of load R = 0 are used to represent the practical working conditions of the envelope. Because of the low rigidity of the specimen and it's relatively low thickness. A reference preload is used to avoid the relaxation phenomenon which may occur especially at high temperature. Such preload did not exceed 5% of the mean applied load in all tested cases. Longitudinal strain is followed through a blade extensometer mounted on the central gauge length of the specimen. Each fatigue conditions is tested using six specimens for statistical purposes.

3. Results and discussion

3.1. Tensile strength

Tensile tests results for seamless and welded specimens at 293 and 690 K are summarized in Fig. 3. Globally, both type of specimens (seamless and welded) show the same behaviour for stainless steel testing for true stress strain curves. For seamless sheets, it is noted that temperature effect leads to an important reduction of the elastic limit and the elasticity modulus by 21.7% and 15.6% respectively. The effect is more pronounced for the stress at failure as it drops by 45.6%. Meanwhile, the total deformation is relatively high at room temperature but it is cut by half as the high limit temperature is reached.

This indicates the material hardening takes place with temperature. For the welded specimens, the same trend is also observed as there is a decrease in all mechanical properties. Elastic limit, Young's modulus and stress at failure show reduction by 19.4, 15.8 and 28.7% respectively; thus, indicating that material microstructure changes are occurring at elevated temperature [4].
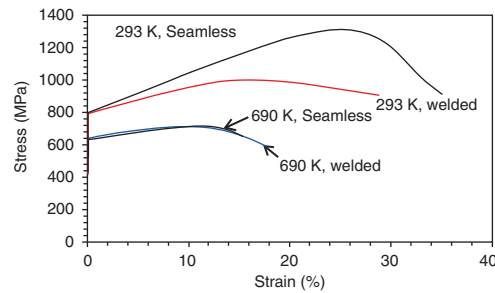
Fig. 3. Stress–strain curve for the samples with and without welding with 293 and 690 K

3.2. Fatigue

Fatigue experimental results are obtained at both temperatures for various mean loads. Three load levels are considered for each temperature. From S-N curves, it is shown that at 293 K. welding effect is negligible on strength at high load levels; however as the testing load level is decreased. The welded plates exhibit much lower fatigue lifetime. This change may be as low as 50% at 600 MPa. At high temperature, welded specimens show lower lifetimes ranging between 30% and 95% as compared to seamless ones. Consequently, the endurance limit of welded specimens falls to much lower values as stress concentration effects usually accompany welded areas tied to a redistribution of residual stresses within the weld which has not been heat treated.

4. Statistical analysis

In order to predict the fatigue lifetime of a material, a statistical analysis is carried out according to common distribution models which are the normal and the Weibull distributions. The application of these models is limited to estimating lifetime with a probability of failure for a given stress level where the experimental data are available [8]. As stated earlier, the gaol is to develop correlations between the parameters implied in such models and those specified by the testing conditions which are presented in S-N diagram.

The diagrams, thus suggested through such analysis, make it possible to evaluate the various parameters associated on an arbitrary stress level and then, to predict

the lifetime for this arbitrary condition. The majority of the existing methods for fatigue lifetime analysis in the literature are based on deterministic criteria which, by nature, cannot provide real failure estimates, for a given loading since total life is basically statistical. More, the searched goal is to determine basically a safety coefficient and as the number of external factors increases, it becomes delicate to use experimental data from tested specimens for design purposes. These factors could be temperature gradient effects, size or scale effects, weld joint nature, surface quality, heat treatments and environment factors.

4.1. Weibull distribution function

The density function of N lifetime in cycles is given by the following equation [9]:

$$F(N) = \frac{b}{N_a - N_0} \left[\frac{N - N_0}{N_a - N_0} \right]^{b-1} \exp \left[- \left[\frac{N - N_0}{N_a - N_0} \right]^b \right] \tag{1}$$

where b Shape parameter and often identified as the slope of Weibull plot; N_0 Scale parameter corresponding to a minimum life ($N_0 \geq 0$); N_a Characteristic of the fatigue lifetime associated with a failure probability of 63.2%. On the other hand, the cumulative Weibull function noted $F(N)$ is obtained by the integration of the density function:

$$F(N) = \int_{N_0}^{N} f(N) \, dN \tag{2}$$

Such calculation leads to the following result:

$$F(N) = 1 - \exp \left[- \left[\frac{N - N_0}{N_a - N_0} \right]^b \right] \tag{3}$$

Consequently, the cumulative function might be put in a linear form, by making use of a double logarithm of the previous equation:

$$\ln \left[\ln \frac{1}{1 - F(N)} \right] = b \ln(N - N_0) - b \ln (N_a - N_0) - 0.3662 \tag{4}$$

According to the cumulative equation, linear regression between $\left[\ln \left(\frac{1}{1 - F(N - N_0)} \right) \right]$ and $(N - N_0)$ coordinates is made. As a result, the N_0

parameter representing the minimum life is found from the linearity of the right-hand side using the method of least squares. Subsequently, the slope of the right-hand side b and N_a are calculated.

The experimental fatigue results at both temperatures for seamless and welded specimens were analysed with Weibull and normal statistical models. In both cases, failure probabilities of 5% and 95% were used as requested in fatigue analysis.

The results are shown in Fig. 4, for seamless specimens and in Fig. 5 for the welded ones. It is noted that for a 50% probability of failure, both models give the same difference, In addition, the normal distribution analysis gives up to 8% more conservative lifetime forecasts compared to the Weibull distribution for the lower probability limit as indicated in Figs. 4 and 5, whereas for seamless material, the prediction is less conservative at 690 K (Fig. 4).
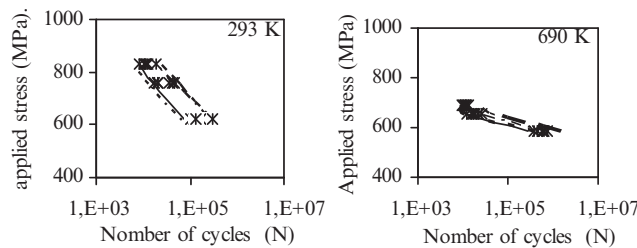
Fig. 4. S-N curve seamless specimen at 293 and 690 K with lifetime prediction at 5% and 95% levels
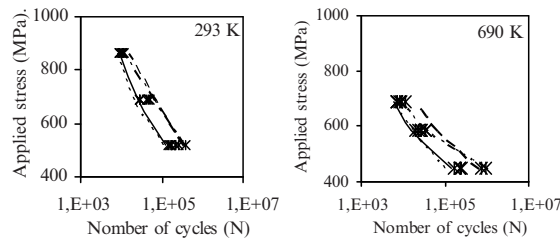
Fig. 5. S-N curve for welded specimen at 293 and 690 K with lifetime prediction at 5% and 95% levels

4.2. Correlation of the Weibull parameters

It is accepted that parameters b and N_0 for Weibull distribution can only be given at stress levels for which experimental data were obtained. In fact, experiments are needed for each of these two parameters as they condition the applicability of the Weibull model. For statistical reasons, it is needed to create intermediary positions for calculations as experimental data are costly and time consuming to obtain. The

idea is to develop correlations between these parameters and the static properties of material, including temperature changes. When examining the parameter b as a process variable. It is revealed that, for a given temperature, this parameter depends mainly on the level of the imposed stress.

Consequently, a new variable is introduced and defined according to the applied stress σ and the corresponding state of the static properties σ_u and σ_y. The proposed form of the squared stress ratio, X. is as follows:

$$X = \left[\frac{\sigma^2}{\sigma_u \cdot \sigma_y} \right]^2 \tag{5}$$

When plotting the parameter b as a function of the X. Which is a dimensionless quantity, it is seen that all data follow a regular curve as indicated in Fig. 6. The obtained correlation has a high determination coefficient (0.98) and represents at the same time welded and seamless specimens at low and high temperatures. The correlation of b is:

$$b = -0.3925 \ln X + 0.7172 \tag{6}$$

Alternatively, the scale parameter, N_0, is normalized by N_m (which is the experimental median) and associating a temperature ratio limited by fusion temperature T_f. The so-called thermal life ratio is defined as follows:

$$H = \left(\frac{N_0}{N_m} \right) \left(\frac{T}{T_f} \right)^{0.1} \tag{7}$$

The evolution of standardized H parameter according to the dimensionless stress ratio is shown in Fig. 6. A logarithmic relation is found describe very well the correlation between H and X as illustrated from determination coefficient (0.98). Again, all cases studied are (welded and seamless for low and high temperatures). The obtained relationship is:

$$H = 0.1765 \ln X + 0.5557 \tag{8}$$

In contrast to what is observed in Fig. 6 for the parameter b. the standardized parameter H is increasing with X for the fatigue data considered. Finally it can be concluded that by introducing the squared stress ratio X. it is possible to represent the Weibull shape parameter (or the slope. b) and the thermal ratio H using a linear logarithmic relationship in the forms:

$$b = -\alpha_1 \ln X + \alpha_2 \tag{9}$$

$$H = \beta_1 \ln X + \beta_2 \tag{10}$$

where α_1, α_2, β_1 and β_2 are constants depending on the material nature and the testing conditions.
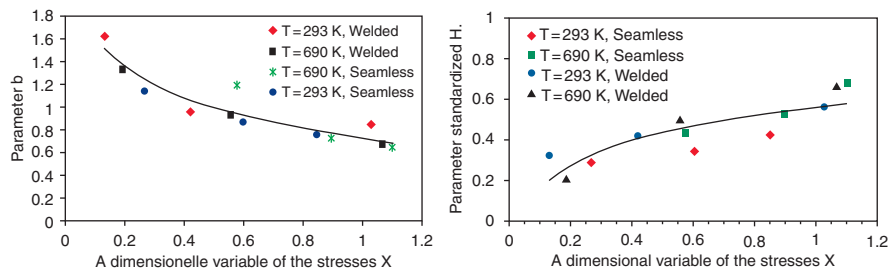
Fig. 6. Correlation of the parameter b and N_0 of Weibull with X

5. Conclusions

It is shown that welded specimens exhibit much lower resistance at high temperature while the global trend of the stress strain behaviour is very similar to seamless ones.

- In terms of fatigue lifetime. At 690 K. the reduction is 20% and 70% for welded and seamless cases respectively. Such differences may be caused by the heating effect within the welded zone (HAZ) and the subsequent microstructure changes accompanying applied alternating loads at high temperatures.
- Both Weibull and normal statistical models show the same difference at 50% of failure probability when comparing behaviours of both types of specimens at both temperatures. It should be noted that the normal model is more conservative than the Weibull model for the lower probability limit.
- Making use of fatigue life data. a modified Weibull model is presented to correlate stress level, temperature and fatigue lifetime for interpolation purposes. It makes use of the squared stress parameter parameters X and thermal fife ratio H.
- Both the Weibull shape factor b and H are found to be correctly described as a function of X with logarithmic equations of the form $b = -\alpha_1 \ln X + \alpha_2$ and $H = \beta_1 \ln X + \beta_2$ where $\alpha_1, \alpha_2, \beta_1$ and β_2 are constants which depend on the material nature and the corresponding testing conditions.

References

[1] W.-S. Lee, T.-T. Su. Mechanical properties and microstructure features of AISI 4340 high-strength alloy steel under quenched and tempered conditions. Journal of Materials Processing Technology, Vol. 87, pp. 198–206, 1999.

[2] K. Dang Van, A. Bignonnet. J.L, Fayard. Assessment of Welded Structures by a Structural Multiaxial Fatigue Approach. Biaxial Multiaxial Fatigue and Fracture. Editors: Andrea Carpinteri. Manuel de Freitas. Andrea Spagnoli. pp. 3–19. Elsevier Publication, 2003.

[3] L. Allais, Q. Auzoux, M. Reytier, A. Pineau. Fissuration en relaxation des jonctions soudées en aciers inoxydables austénitiques. Mécanique & Industries, Vol. 6, pp. 45–54, 2005.

[4] V. Le Corre, "Etude de la Compétition Déchirure Ductile/ Rupture Fragile: Application à la Tenue Mécanique des Tubes en Acier C-Mn et de leurs Joints soudés". PhD Thesis. Ecole Centrale de Lille. USTL France, 2006.

[5] T. K. Ha, H. T. Jeong, H. J. Sung. High temperature fatigue behaviour of stainless steels for automotive exhaust. Journal of Materials Processing Technology, Vol. 187, pp. 555–558, 2007.

[6] H. M. Shalaby, W.T. Riad. Failure investigation of gas inlet chamber. Failure Engineering Analysis, Vol. 15, pp. 38–42, 2008.

[7] F. Labesse-Jied, B. Lebr, E. Petitpay, J.L. Robert. Multiaxial Fatigue Assessment of Welded Structures by Local Approach. Editors: Andrea Carpinteri. Manuel de Freitas. Andrea Spagnoli. pp. 43–60. Elsevier Publication, 2003.

[8] G. Crupi, V. Crupi, E. Guglielmino, D. Taylor. Fatigue assessment of welded joints using critical distance and other methods. Engineering Failure Analysis, Vol. 12, pp. 129–142, 2005.

[9] L.F Zhang. M. Xie. L. C. Tang. A study of two estimation approaches for parameters of Weibull distribution based on WPP. Reliability Engineering and System Safety, Vol. 92, pp. 360–368, 2007.

Residual Stress Effect on Fatigue Crack Growth of SENT Specimen

M. Benachour[1, 2], M. Benguediab[2] and A. Hadjoui[1]

[1]Automatic Laboratory of Tlemcen, University of Tlemcen, BP 230, 13000 – Algeria

[2]Department of Mechanical Engineering, Sidi Bel Abbes University, 22000 – Algeria

Abstract   The safety of the structures in various fields with knowing aeronautics, the car and pipes rests on the study of the fatigue behaviour and the prevention of various scenarios. This study relates to the fatigue behaviour of aluminum alloy 2024 T351 SENT specimen with semi-circular notch where various scenarios are studied. The effect of the load ratio is highlighted, where one notices a shift of the curves of crack growth. The presence of the compressive residual stresses in structure is the significant scenario of crack growth retardation. The fatigue behavior with the presence of residual stresses is studied using the AFGROW code when NASGRO model is used. The comparative study between the fatigue behavior without and with residual stress shows the variation on the fatigue life.

Keywords: Fatigue, Crack, Aluminum Alloy, Compressive Residual Stress, Load Ratio.

1. Introduction

The behavior of crack propagation is a significant issue in the establishment of inspection and maintenance procedures in variety industries such as aerospace, automotive, oil industries, rail wheel...etc. In any analysis of crack propagation, crack must be based on the calculation and the use of the parameters of the breaking process. Such parameters describe the local effect of cracking on a structure. The primary parameters of fracture mechanics which can have interest for the crack propagation are the stress intensity factors K with and without residual stress. The determination of the crack growth rate curves of the materials subjected to the cyclic loading presents a major interest.

The major problem is to take into account the various parameters that affect the propagation of fatigue cracks in both the intrinsic and extrinsic parameters as well as the estimation of the fatigue life. In this context, we are studying the effect of compressive residual stress and the effect of load ratio on fatigue crack growth of aluminum alloy 2024 T351 for SENT specimen with semi circular notch. The important material used in aerospace applications is aluminum alloy 2024 T351. Many author's are studied the fatigue behavior of this material [1–6] when different effects are examined such as effect of load ratio, overload, corrosion, environment, residual stress, heat treatment, etc.

2. Generation of residual stress field and origin

The residual stresses are divided into three levels, residual first-order called residual macroscopic residual stresses of the second order, called microscopic residual stresses homogeneous and residual third-order called microscopic residual heterogeneous. The field of residual stress appears to be the superposition of residual stress of the three orders. The residual stresses present diver's origin and several shapes [7–16] namely shot-penning, expansion of hole, overloads, under-load, static load without cyclic load, welding. The stress field is beneficial if the stress is in compressive state [17, 18]. Contrary to this, the fatigue crack is accelerated. On one hand, the stress may be introduced in structures before putting into service [19]. On the other hand, they can be induced during the service with overload or under-load [20, 21].

For residual stresses induced by cold expansion [22], the fatigue life and the fatigue crack growth rate for aluminum alloy 2024 T351 are affected by a decline in the progress of expansion ratio. O'Dowd et al. [23] have introduced residual stress in CT specimen by mechanical compression. The level of compression load was determined by the finite element method. Mahmoudi and al. presented various methods of generation of residual stress on laboratory specimens [24] namely, the mechanical, thermal methods and welding process. To study the effect of residual stress on fatigue crack growth, a residual stress fields are adopted at the semi-circular notch. This field has been generated in a similar manner by cold expansion [22] before finishing specimen by machining. Three different levels of residual stress field are considered; low, medium and high level (Fig. 1).
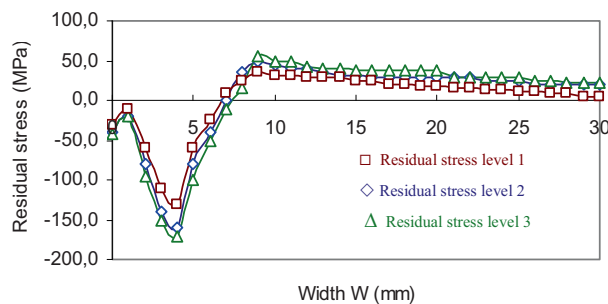
Fig. 1. Residual stress distribution a long the fatigue crack length

3. Fatigue crack growth of SENT specimen

The material used in this study is the aluminium alloy 2024-T351 heated and treated. L-T orientation is subjected to numerical fatigue tests. The basic mechanical properties for Aluminum alloys 2024-T351 are given in Table 1.

Numerical fatigue crack growth in mode I used SENT specimen with through crack located at the center of semicircular edge notch (Fig. 2).
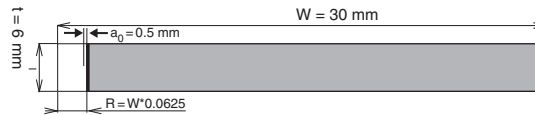
Fig. 2. SENT specimen with semicircular edge notch

Table 1. Mechanical properties of 2024 T351 (database of AFGROW code)

$\sigma_{0.2}$ (MPa)	K_{IC} (MPa. m$^{0.5}$)	K_C (MPa. m$^{0.5}$)	E (GPa)	ν
358.53	36.26	72.53	73.10	0.33

The stress intensity factor for the studied specimen "SENT specimen with semi circular edge notch" is developed by Newman [25] and implemented in AFGROW code. The equation of this factor depends on several parameters and is written bellow:

$$K = \sigma\sqrt{\pi a / Q} \cdot \beta_{ij} \tag{1}$$

When β is the boundary correction factor and Q is the shape factor.

AFGROW code developed by NASA [26] is used for simulation of fatigue crack growth with and without residual stress. Many models for fatigue crack growth are implemented. The interest model is NASGRO model when totality of fatigue crack growth curves is considered. Skorupa et al. [27] applied the strip-yield model from the NASGRO commercial computer software to predict fatigue crack growth in two different aircraft aluminium alloys under constant amplitude loading and programmed and random variable amplitude load histories.

The interaction between models such as Elber, NASGRO and Wheeler model is presented by Meggiolaro [28] when the modifications to the Wheeler model showed an excellent agreement with the experimental data and NASGRO model. NASGRO model are expressed bellow:

$$\frac{da}{dN} = C\left[\left(\frac{1-f}{1-R}\right)\Delta K\right]^n \frac{\left(1 - \frac{\Delta K_{th}}{\Delta K}\right)^p}{\left(1 - \frac{K_{max}}{K_{crit}}\right)^q} \tag{2}$$

f present the contribution of crack closure and the parameters *C*, *n*, *p*, *q* were determined experimentally and ΔK_{th} is the crack propagation threshold value of the stress–intensity factor range. For constant amplitude loading, the function f determined by Newman [29] can be written as:

$$f = \frac{K_{op}}{K_{max}} = \begin{cases} \max\left(R, A_0 + A_1R + A_2R^2 + A_3R^3\right) & R \geq 0 \\ A_0 + A_1R & -2 \leq R < 0 \\ A_0 - 2A_1 & R < -2 \end{cases} \qquad (3)$$

where the polynomial coefficients are given by:

$$A_0 = \left(0.825 - 0.34\alpha + 0.05\alpha^2\right)\left[\cos\left(\frac{\pi}{2}\sigma_{max}/\sigma_0\right)\right]^{\frac{1}{\alpha}},$$

$$A_1 = \left(0.415 - 0.071\alpha\right)\sigma_{max}/\sigma_0, \quad A_2 = 1 - A_0 - A_1 - A_3, \quad A_3 = 2A_0 + A_1 - 1 \qquad (4)$$

α is plane stress/strain constraint factor ($\alpha = 1$ for plane stress and $\alpha = 3$ for plane strain).

4. Results and discussions

4.1. Effect of load ratio

SENT specimens in L-T orientation are subjected to a constant loading with various load ratios. The Kmax fracture criteria are adopted for the limit of crack growth. Figure 3 showed the effect of load ratio on fatigue crack growth rate and illustrates a general increase in da/dN with R for a given ΔK. An important effect of R has been observed clearly for this material at high ΔK. Theses results are in agreement with the results of Srivastava and Garg [30].

4.2. Effect of compressive residual stress at notch

The residual stress fields presented in Fig. 2 are applied for fatigue crack growth simulation. Figure 4 show the variation and comparison of fatigue life with and without different residual stress fields for load ratio $R = 0.24$. The fatigue life increase when the level of compressive residual stress at notch increases. Retardation in fatigue crack is caused by the variation of compressive residual stress levels near the notch.

The effect of residual stress on fatigue crack growth rates da/dN is shown in Fig. 5. An influence of this residual stress has been observed at lower stress intensity factor for the variation of level compressive residual stress. In stable fatigue crack growth (Paris domain), we notice clearly the increase in crack growth rate in absence of the compressive residual stress. At high stress intensity factor, an

increasing of crack growth rates is shown for the curves with residual stress. This increasing is due for the presence of tensile residual stress at the end of specimen.
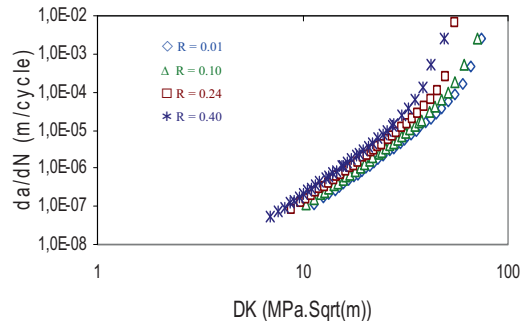
Fig. 3. Effect of load ratio R on fatigue crack growth rate for 2024 T351
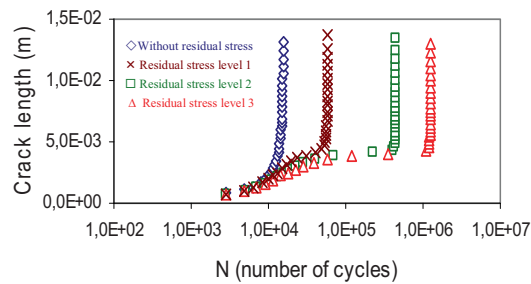
Fig. 4. Effect of residual stress on fatigue life for $R = 0.24$
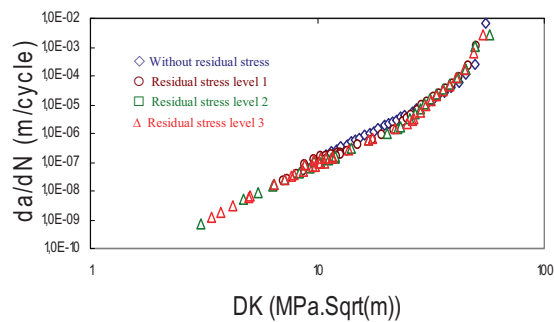
Fig. 5. Crack growth rates versus ΔK for $R = 0.24$

5. Conclusions

Paper presents the results of simulation of fatigue crack growth using AFGROW code. The effect of loading ratio and residual stress field are investigated. The

results showed that the presence of compressive residual stress affected the fatigue crack behavior by delaing crack propagation.

References

[1]   Mayon, G (2005). A unified a $(\Delta K + .K_{max})^{1/2}$ crack growth models for aluminum 2024 T351. International Journal of Fatigue, 27: 629–638.

[2]   Rodopoulos, C.A., Choi, J. H., De Los Rios, E.R., Yates, J.R (2004). Stress ratio and the fatigue damage map – Part II: The 2024 T351 aluminum alloy. International Journal of Fatigue, 26: 747–752.

[3]   Srivastava, Y.A. and Garg, S.B.L (2004). Influence of R on effective stress range ratio and crack growth. Engineering Fracture Mechanics, 22(6): 915–926.

[4]   Mahmoud, S., Lease, K (2004). Influence of R on effective stress range ratio and crack growth. Engineering Fracture Mechanics, 22(6) 915–926.

[5]   Imad, A., Wilsius, J., Naït Abdelaziz M. and Mesmacque, G (2003). Experiments and numerical approaches to ductile tearing in an 2024-T351 aluminum alloy. International Journal of Mechanical Sciences, 45: 1849–1861.

[6]   Benguediab, M. (1980). A fatigue crack propagation study under flight simulation loading based on a reduced spectrum. J. Petit and Col. Eds, Elsevier Applied Science, London, p. 309.

[7]   Pavier, M.J., et al. (1999). Effect of residual stress around cold worked holes on fracture under superimposed mechanical load. Engineering Fracture Mechanics, 63: 751–773.

[8]   Makabe, C., et al. (2004). Effect of surface deformation and crack closure on fatigue crack propagation after overloading and under-loading. International Journal of fatigue, 26: 1341–1348.

[9]   John, R., Jata K.V. and Sadananda, K (2003). Residual stress effects on near-threshold fatigue crack growth in friction stir welds in aerospace alloy. International Journal of fatigue, 25: 939–948.

[10] Wang, H., et al. (1999). Numerical and experimental analysis of residual stress for fatigue crack growth. Computational Materials Science, 16: 104–112.

[11] Barralis, J., Castex, L. and Maeder, G (2004). Précontraintes et traitements superficiels. Technique de l'Ingénieur, traité matériaux métalliques M1 180.

[12] Withers P.J., and Bhadeshia, H.K.D.H (2001). Residual stress – Part 2: Nature and Origins. Materials Sciences and Technology, 17.

[13] Lim Won-Kyum, Jeong-hoon Song, Sankar, B.V (1981). Effect of ring indentation on fatigue crack growth in an aluminum alloy plate. International Journal of Fatigue, 51: 61–69.

[14] Benedetti, M., Bortolamedi, T., Fontanriand, V. and Frendo, F (2004). Bending fatigue behavior of differently shot penned Al 6082 T5 alloy. International Journal of Fatigue, 26: 889–897.

[15] Fett, T. (1997). Residual crack profiles under weak phase transformation conditions. Engineering Fracture Mechanics, 56: 275–284.

[16] Silberschmidt, V.V. and Werner, E (1999). Analysis of thermal residual stresses in duplex-type materials. Computational Material Science, 16: 39–52.

[17] Lam, Y.C., and Lian, K.S (1989). The effect of residual stress and its redistribution on fatigue crack growth. Theoretical and Applied Fracture Mechanics, 12: 59–66.

[18] Beghini, M. and Bertini, L (1990). Fatigue crack propagation through residual stress fields with closure phenomena. Engineering Fracture Mechanics, 36: 379–387.

[19] Wagner, L., Lütjering, G. and Sedlàcek, V (1988). Fatigue crack growth retardation in an Al alloy 2024 in a residual compressive stress field. International Conference on Residual Stresses: ICRS2, 23–25 November, 803–808.

[20] Wahab, M.A., et al. (2004). Experimental study on the influence of overload induced residual stress field on fatigue crack growth in aluminum alloy. Journal of Materials Processing Technology, 153–154: 945–951.

[21] Suresh, S., and Ritchie, R.O (1981). On the influence of fatigue underload on cyclic crack growth at low stress intensities. Materials Sciences and Engineering, 51: 61–69.

[22] De Matos, P.F.P., et al. (2007). Analysis of the effect of cold-working of rivet holes on the fatigue life of an aluminum alloy. International Journal of Fatigue, 29 (3), 575–586.

[23] O'Dowd, N.P., Nikbin, K.M., Wimpory, R.C., Biglari, F.R. and O'Donnell, M.P (2006). Computational and experimental studies of high temperature crack growth in the presence of residual stress. PVP2006-ICPVT-11. ASME Pressure Vessels and Piping Division Conference, July 23–27, Vancouver, BC, Canada.

[24] Mahmoudi, A.H., Aird, C., Truman, C.E., Mirzaee-Sisan, A., and Smith, D.J (2006). Generating well defined residual stress in laboratory specimens. PVP2006-ICPVT-11, 2006 ASME Pressure Vessels and Piping Division Conference, July 23–27. Vancouver, Canada.

[25] Newman JC Jr (1992). Fracture parameters for small fatigue cracks. ASTM STP 1149, J. Larson and J.E. Allison, Eds. American Society for Testing and Materials, Philadelphia, 6–33.

[26] Harter, J.A (2006). AFGROW users guide and technical manual: AFGROW for Windows 2K/XP. Version 4.0011.14, Air Force Research Laboratory.

[27] Skorupa, M., Machniewicz, T., Schijve, J., and Skorupa, A (2007). Application of the strip-yield model from the NASGRO software to predict fatigue crack growth in aluminium alloys under constant and variable amplitude loading. Engineering Fracture Mechanics, 74: 291–313.

[28] Meggiolaro, M.A., and Pinho de Castro, J.T (2001). Comparison of load interaction models in fatigue crack propagation. 16th Brazilian Congress of Mec. Engineering Fracture Mechanics, 12: 247–256.

[29] Newman, J.C (1984). A crack opening stress equation for fatigue crack growth. International Journal of Fracture, 24(3): R131–135.

[30] Srivastava, Y.P. and Garg, B.L (1985). Influence of R on effective stress range ratio and crack growth. Engineering Fracture Mechanics, 22(6): 915–926.

Analysis of Elliptical Cracks in Static and in Fatigue by Hybridization of Green's Functions

B.K. Hachi[1], S. Rechak[2], M. Haboussi[3], M. Taghite[3], Y. Belkacemi[2] and G. Maurice[3]

[1]Department of Mechanical Engineering, Djelfa University, BP 3117 Ain-Cheih, 17000 Djelfa, Algeria

[2]LGMD, Department of Mechanical Engineering, E.N.P., BP 182 Harrach 16200, Algiers, Algeria

[3]LEMTA, Nancy University, CNRS, 2 avenue de la Forêt de Haye BP 160 F-54504, Vandoeuvre Cedex, France

Abstract   A hybrid weight function technique is presented. It consists of dividing an elliptical crack into two zones, then using the appropriate weight function in the area where it is more efficient. The proportion between zones is determined by optimizing two crack parameters (axis ratio and curvature radius). Stress intensity factors are hence computed by a self developed computer code. Static and fatigue loadings are considered. The results found by the present approach are in good correlation with the analytical and experimental solutions (when available) as well as with those obtained numerically by other researchers.

Keywords: Hybridization, Weight Function, SIF, Elliptical Crack, Fatigue-Crack-Growth.

1. Introduction

The principle of the weight function (called the Green's function) technique consists of employing one or more known solutions (known as reference solutions) of a particular case in order to find the solution for the general case. The reference solution generally comes from the analytical results (exact). But in some cases, the absence of such results obliges researchers to use approximate solutions which could be already existing weight functions. In this paper, a method improving the calculation of SIF in mode I for elliptical and semi-elliptical cracks is developed by means of hybridization of two weight functions and coupling to the Point Weight Function Method (PWFM). In the fatigue problems, two crack propagation laws have been incorporated. Crack propagation life and crack profile are investigated for various applications. The development of weight functions in fracture mechanics started with the work of Bueckner [2], based on the formulation by the Green's function, for a semi-infinite crack in an infinite medium. The investigation of the weight functions on the one hand and the evaluation of the energy balance formula of Rice [14] on the other hand, allowed the extension of the use of the weight functions by several authors such as Oore and Burns [10] and Bortmann

and Banks-Sills [1]. In 1986, Gao and Rice [4] introduced the study of the stability of the rectilinear form of a semi-infinite crack front during its coplanar propagation from which result the values of stress intensity factor (SIF) along the crack front. Recently, Sun and Wang [16] gave in-depth interpretations of the energy release rate of the crack front. Other investigations followed related especially to the crack shape (ellipse, half of ellipse, quarter of ellipse, rectangle, …) as well as to the fracture mode (I, II, III or mixed) and to the application domain (elastoplastic, elastodynamic, …). This paper is structured as follow. Detailed presentation of the hybridization approach is presented in Section 2. Fatigue crack propagation models are then implemented into the hybridization technique, subject of Section 3. In the next section, two industrial applications are discussed, one of them is in static and the other one is in fatigue loading. We end this paper by drawing some conclusions. This work is an extension of already published studies of crack modeling by the hybridization technique [5, 6, 8].

2. Presentation of the hybridization technique

The solution of the SIF in mode I using the weight function technique is given by the general form [10]:

$$K_{IQ'} = \int_S W_{QQ'} q(Q).dS \tag{1}$$

where $K_{IQ'}$ is the stress intensity factor in mode I at the Q' point of the crack front. $W_{QQ'}$ is the weight function related to the problem and $q(Q)$ symmetrical loading applied to the arbitrary Q point of the crack area S.

This study is based on the hybridization of two weight functions deduced from a Green's function formulation.

The first one is developed by Oore and Burns [10] to model any closed shape of a crack in an infinite body, including elliptical cracks. Its expression is as follows:

$$W_{QQ'} = \sqrt{2} \left/ \left(\pi l_{QQ'}^2 \sqrt{\int_\Gamma \frac{d\Gamma}{\rho_Q^2}} \right) \right. \tag{2}$$

The second one is developed by Krasowsky et al. [9] to model elliptical cracks in an infinite body. Its expression is as follows:

$$W_{QQ'} = 2\Pi^{1/4}(\theta) \left/ \sqrt{\pi a \left(1 - \frac{r^2(\varphi)}{R^2(\varphi)} \right)} l_{QQ'}^2 \int_\Gamma \frac{d\Gamma}{\rho_Q^2} \right. \tag{3}$$

In expressions (2) and (3), r and φ are the polar coordinates of an arbitrary point Q. $l_{QQ'}$ is the distance between the Q' point and the arbitrary Q point. Γ is the curve of the ellipse (the crack front), and ρ_Q is the distance between the Q point and the elementary segment $d\Gamma$, $\prod$ is a function such as $\prod(\theta) = (\sin^2\theta + \alpha^4\cos^2\theta)/(\sin^2\theta + \alpha^2\cos^2\theta)$ and $\alpha = a/b$.
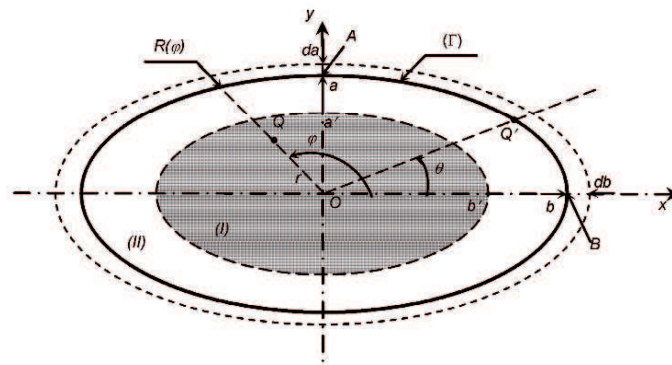
Fig. 1. Subdivision of the elliptical crack in two zones and its geometrical parameters

The principle of hybridization is to divide, as shown in Fig. 1, the elliptical crack into two zones, an internal zone I (ellipse in grey) and an external zone II (in white), then to use each of the two weight functions in the area where it is more efficient. The two zones are defined by the following relations:

$$\begin{cases} zone\ I : (x/b')^2 + (y/a')^2 \le 1 \\ zone\ II : (x/b')^2 + (y/a')^2 > 1 \end{cases} \tag{4}$$

where a' and b' are such as $a'/a = b'/b = \beta$ and $\beta \in [0,1]$, β being the proportion between the two zones and a, b are the axes of ellipse (e.g. Fig. 1).

The weight function of Eq. (3) is intended exclusively for cracks of elliptical form. Nevertheless, it presents an additional singularity $(1 - r/R)^{-1/2}$ compared to Eq. (2). This makes Eq. (3) less efficient in the vicinity of the crack front $(r \to R)$. This argument leads us to make the following choice:

$$\left. \begin{array}{l} W_{QQ'} = W_{QQ'}\ of\ Eq.\,(3)\ if\ Q \in Zone\ I \\ W_{QQ'} = W_{QQ'}\ of\ Eq.\,(2)\ if\ Q \in Zone\ II \end{array} \right\} \tag{5}$$

It remains to determine the appropriate proportion β between two zones I and II. By construction of each weight function (see details in [6, 8]), the function (2) is preferable to the function (3) in the two following cases:

- ○ When the crack front is close to a circle ($\alpha \to 1$)
- ○ When the crack front is close to a straight line (low values of α with value of θ far from zero)

In fact, these two cases correspond to situations where the variation of the curvature radius R_c of the crack front is weak, excluding a very narrow zone corresponding of the smallest values of R_c (θ close to zero with low values of α). In this case and for a relatively high variation of the curvature radius of ellipse, the weight function (3) of Krasowsky et al. is more adapted. This is confirmed by the presence via the function $\Pi(\theta)$ of curvature radius $R_c = (a/\alpha)\Pi^{3/2}(\theta)$ in the expression of the function (3).

Consequently, more the radius of curvature is relatively weak or its derivative (spatial gradient of the radius of curvature) is high, more the zone I should increase with respect to the zone II and vice versa.

Taking into account all these considerations, we propose the relative parameter expressed by:

$$\beta_1 = \left(b - \min(R_c, b)\right)/b \tag{6}$$

For the representation of the influence of the curvature radius compared to the large axis of the ellipse b, and the following one:

$$\beta_2 = \left[\left(\frac{\partial R_c}{\partial \theta}\right) - \left(\frac{\partial R_c}{\partial \theta}\right)_{\min}\right] \bigg/ \left[\left(\frac{\partial R_c}{\partial \theta}\right)_{\max} - \left(\frac{\partial R_c}{\partial \theta}\right)_{\min}\right] \tag{7}$$

To represent the influence of the gradient of the curvature radius for a given α. In this relation $\partial R_c / \partial \theta$ is the partial derivative with respect to the angular position of the point Q', its maximum and minimum values are calculated by "sweeping" completely the contour of the ellipse for a given α. The computation of the partial derivative is achieved numerically.

The proportion parameter β takes the value:

$$\beta = \max(\beta_1, \beta_2) \tag{8}$$

Details of the method regarding its numerical implementation, treatment of singularities, meshing can be found in references [5, 6, 8].

To extend the use of this hybrid approach for the semi-elliptical crack modelling, it's coupling with the point weight function method [11] (PWFM) is considered in order to take into account the free edge effect. More details of the coupling between the present hybrid technique and the PWFM method can be found in [7].

3. The hybrid method in fatigue

The fatigue crack growth prediction is classically based on the SIF approach, known as the Paris law [12]. This last one is given as follows:

$$da/dN_c = C(\Delta K_I)^m \tag{9}$$

C and *m* are material parameters related to Paris law usage.
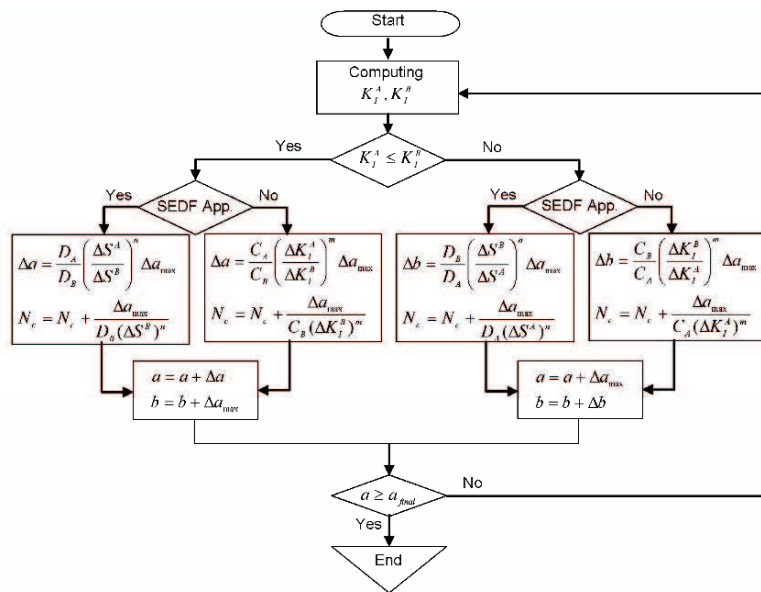
Fig. 2. Algorithmic schemes of the computing procedure

As previously mentioned, the fatigue crack growth prediction can also be based on the SEDF approach. Its expression has first been given in 1979 by Sih [15], in which the strain energy density factor range replaces the stress intensity factor range in classical laws (Paris law for example). The Sih's law (based on SEDF approach) has the following form:

$$da/dN_c = D(\Delta S_{min})^n \tag{10}$$

D and *n* are material parameters related to Sih's law usage.

In the above equation S_{min} is the necessary strain energy density factor for a crack to propagate, and satisfying the condition $dS = 0$. This factor may be obtained in mode I according to the SIF value [15].

Written for two points A ($\theta = 90°$) and B ($\theta = 0°$) of the ellipse contour (e.g. Fig. 1), one can obtain from Eqs. (9) and (10), respectively:

$$da/db = (C_A/C_B)\left(\Delta K_I^A / \Delta K_I^B\right)^m \qquad (11)$$

And:

$$da/db = (D_A/D_B)\left(\Delta S^A / \Delta S^B\right)^n \qquad (12)$$

From Eqs. (11) and (12), one can say that for two different values of SIF range ΔK^A and ΔK^B or SEDF range ΔS^A and ΔS^B, two different values of the crack growth segments da and db can be obtained. Consequently, a change in the crack profile is expected. On the algorithmic scheme presented in Fig. 2, are illustrated the different steps for the computation of the fatigue life and the evolution of the crack shape.

4. Numerical tests, results and discussions

In this section, practical applications are numerically treated using the computer operational software with graphic interface using the C++ object-oriented language named HWFun which we develop for this purpose.

4.1. Internal semi-elliptical surface crack in a pressurized tube

The theory of thick tubes (Lamé's theory) shows that longitudinal cracks located on an internal face of the tube are the most dangerous ones. For this kind of application, the efficiency of hybridization approach coupled with the PWFM [11] is evaluated. For values of $\alpha = 1.0$ and $\alpha = 0.4$, *n*umerical tests are carried out on tubes of $t/R_{int} = 0.1$, where t is the thickness of tube and R_{int} is its internal radius. The loading inside the crack has the form $p = (y/a)^i$ with $i \in \{1,2,3\}$.

In accordance with the PWFM method ad for the sake of comparison, we choose a reference solution in the form $p = \sigma_0$. The present results are for two characteristics angles $\theta = 0°$ and $\theta = 90°$, and for linear (i = 1), quadratic (i = 2) and cubic (i = 3) loadings. From Fig. 3, the present results are in good agreement with those found by Raju and Newman [13] using finite element method and those of Krasowsky et al. [9], Vainshtok [17] et Orynyak et al. [11] using weight function methods such as $\overline{K}_I = K_I E(k) / (\sigma_0 \sqrt{\pi a} \Pi^{1/4}(\theta))$, where $E(k)$ is the elliptic integral of second kind and $k = \sqrt{1 - \alpha^2}$. According to those graphs, loading mode has a significant effect on the stress intensity factor (SIF). In fact:

- The SIF values increase with the decrease of α
- The maximum value of SIF is for a uniform loading
- Only uniform loading induces a more important value of SIF at a surface point ($\theta = 0°$) than at a depth point of ($\theta = 90°$)
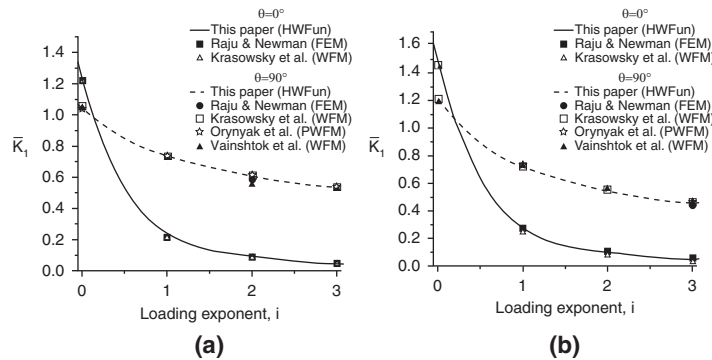
Fig. 3. Adimensional SIF of a semi elliptical crack at the internal surface of a tube

4.2. Out-of-plane gusset welded joint

To this mechanical component (see Fig. 4) a tensile cyclic load is applied. Due to stress concentration, a surface crack can initiate either at the junction between portions 2 and 1, or between portions 2 and 3. Two cases have been considered: $\rho = 0$ mm and $\rho = 30$ mm (ρ is the radius of curvature of the welded joint) as shown on Fig. 4. The numerical computations in [3] used a finite element code known as "LUSAS". The mechanical properties of the treated component are those of the steel called POSTEN 80. They are given in [3] as $\mu = 77 GPa$, and $\nu = 0.3$.

In the numerical computations, and in order to take into account of the stress concentration, the coefficient F_g was given in a format of curves [3]. It is introduced by modifying the value of the tensile stress by the term $F_g\sigma_t$ at both points A and B and at each crack growth da or db. To facilitate the numerical implementation, this coefficient F_g has been substituted by a fifth order polynomial obtained by fitting the above mentioned curves.

The values of the crack growth material parameters D, n, C, m are those used by [3]. It should be pointed out that the parameter D has been modified by multiplying it by a factor $(\pi)^n$. This difference comes from the fact that in the case of plane stress, the SEDF equals to $K_I^2(1-2\nu)/4\pi\mu$.
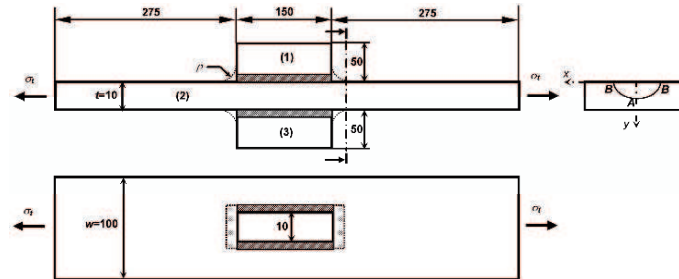
Fig. 4. Configurations and dimensions of the mechanical component

The first numerical tests deal with those treated in [3], and concern the following configurations:

(a) $\rho = 0$ mm, and $R = 0.1$

- $a_0 = 0.4\,\text{mm}$, $\quad \alpha_0 = 0.4$, $\quad \Delta a_{\max} = 0.2 a_0$, $\quad \Delta\sigma_t = 93\,\text{MPa}$
- $a_0 = 0.4\,\text{mm}$, $\quad \alpha_0 = 0.4$, $\quad \Delta a_{\max} = 0.2 a_0$, $\quad \Delta\sigma_t = 124\,\text{MPa}$
- $a_0 = 0.4\,\text{mm}$, $\quad \alpha_0 = 0.4$, $\quad \Delta a_{\max} = 0.2 a_0$, $\quad \Delta\sigma_t = 155\,\text{MPa}$

(b) $\rho = 30$ mm, and $R = 0.1$

- $a_0 = 0.3\,\text{mm}$, $\quad \alpha_0 = 0.1$, $\quad \Delta a_{\max} = 0.2 a_0$, $\quad \Delta\sigma_t = 124\,\text{MPa}$
- $a_0 = 0.3\,\text{mm}$, $\quad \alpha_0 = 0.1$, $\quad \Delta a_{\max} = 0.2 a_0$, $\quad \Delta\sigma_t = 155\,\text{MPa}$
- $a_0 = 0.3\,\text{mm}$, $\quad \alpha_0 = 0.1$, $\quad \Delta a_{\max} = 0.2 a_0$, $\quad \Delta\sigma_t = 207\,\text{MPa}$

Figure 5a, b shows the fatigue crack growth life numerically estimated via different approaches, and experimentally measured as well. At the first stage, one can make the following physical observations:

1. The fatigue life is much affected by the radius of curvature ρ. Indeed, as the radius of curvature decreases ($\rho = 0$), the fatigue life decreases.
2. The fatigue life is also affected by the stress range $\Delta\sigma$, i.e. as $\Delta\sigma$ increases, the fatigue life decreases.

The second observations deal with the numerical comparisons from which one can state the following:

1. The hybrid approach (HWFM) is in correlation with the experimental data, for both radius of curvature and for the various values of $\Delta\sigma$.
2. For the lower value of the radius curvature ($\rho = 0$), the SEDF approach gives better predictions than the SIF one.

In the following numerical computations, the influence of the physical stress ratio parameter R on the fatigue crack growth is discussed. Figure 6 shows in a

log-log scale, the number of cycles to failure N_c, versus the stress range $\Delta\sigma$ for the curvature radius $\rho = 0$ and $\rho = 30$, and for various values of the stress ratio R.

On the same figure, the experimental data given by [3], which are only available for R = 0.1 are inserted. One can observe that a good correlation exists between the previously mentioned data and the numerical results obtained by the HWFM when using the SEDF approach. However, the usage of the SIF approach gives less accuracy in the fatigue life prediction. From Fig. 6a, b, it is also observed that the fatigue life decreases as the stress ratio increases. Overall, it is noticed that the curve relative to the number of cycles versus stress range obtained by the usage of the SIF approach lies in between the curves $R = 0.1$ and $R = 0.3$, obtained when using the SEDF approach. This interval can be considered as the interval of validity of the SIF approach for such treated problem.
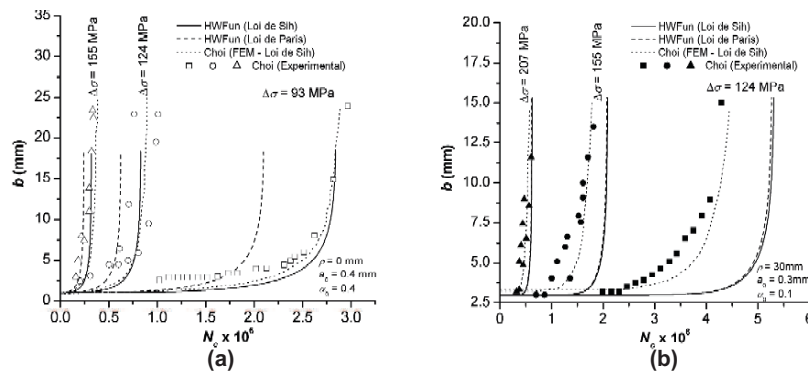
Fig. 5. Fatigue life prediction with different approaches: (**a**) ρ = 0, (**b**) ρ = 30 mm
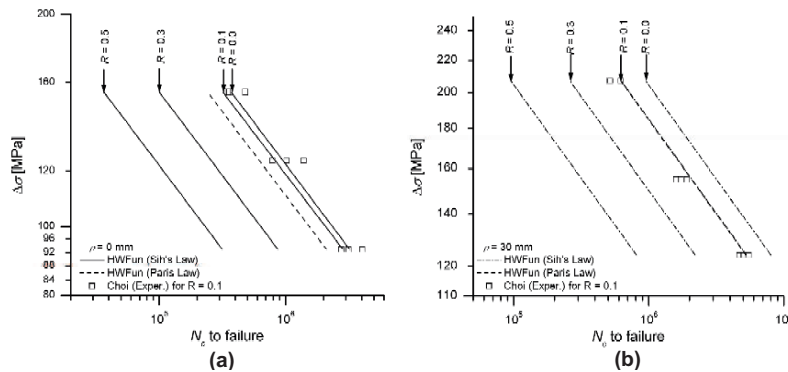
Fig. 6. Influence of the parameter R on the fatigue crack growth: (**a**) ρ = 0 mm, (**b**) ρ = 30 mm

5. Conclusions

In this work, a hybridization weight function approach based on Green's function formulation is developed. The method has been applied to static and fatigue loads. The idea of hybridization leads us to an optimization problem of two geometrical parameters (the ratio axes and curvature radius of ellipse). A computer code named *HWFun* has been developed and tested on various practical applications under static and fatigue loadings. In this modeling, a computation dealing with the stress intensity factors in mode I is first performed. The results obtained show a clear reduction in the error. The present approach was also tested on fatigue-crack-growth problems. The predicted crack shape evolution and the fatigue crack growth life are in perfect concordance with the results obtained by other researchers. The idea of hybridization undoubtedly opens horizons for the treatment of other complex problems in fracture mechanics such as mixed mode and interaction among cracks.

References

[1] Bortmann Y, Banks-Sills L (1983). An extended weight function method for 2D and 3D-problems. J. Appl. Mech. 50:907–909.
[2] Bueckner HF (1970). A novel principle for the computation of stress intensity factors. Z. Angew. Meth. 50:529–546.
[3] Choi DH, Choi HY (2005). Fatigue life prediction of out-of-plane gusset welded joints using strain energy density factor approach. Theor. Appl. Fract. Mech. 44:17–27.
[4] Gao H, Rice JR (1986). Shear stress intensity factors for planar crack with slightly curved front. J. Appl. Mech. 53:774–778.
[5] Hachi BK, et al. (2005). A Hybrid weight function approach for the computation of stress intensity factor in elliptical and semi-elliptical cracks. In: 11th International Conference of Fracture, Turin.
[6] Hachi BK, Rechak S, Belkacemi Y, Maurice G (2005). Modelling of elliptical cracks in infinite body and in pressurized cylinder by a hybrid weight function approach. Int. J. Press. Vess. Piping 82:917–924.
[7] Hachi BK, Rechak S, Ouadjaout M, Haboussi M (2005). Semi-elliptical cracks modelling by coupling of the hybrid weight function method with the point weight function method. In: CFM'2005, N° 887, U.T. Troyes.
[8] Hachi BK, Rechak S, Haboussi M, Taghite M (2006). Embedded elliptical cracks modeling with hybridization of weight functions (in French). C.R. Mecanique 334:83–90.
[9] Krasowsky AJ, Orynyak IV, Gienko AYu (1999). Approximate closed from weight function for an elliptical crack in an infinite body. Int. J. Fracture 99:117–130.
[10] Oore M, Burns DJ (1980). Estimation of stress intensity factors for embedded irregular cracks subjected to arbitrary normal stress fields. T-ASME J. Press. Vessel Technol. 102: 202–211.
[11] Orynyak IV, Borodii MV (1995). Point weight function method application for semi-elliptical mode I crack. Int. J. Fracture 70:117–124.
[12] Paris P, Erdogan F (1963) A critical analysis of crack propagation laws. T-ASME J. Basic Eng. 528–534.
[13] Raju IS, Newman JC Jr (1982). Stress-intensity factors for internal and external surface cracks in cylindrical vessels. T-ASME J. Press. Vess. Technol. 104:293–298.

[14] Rice JR (1972). Some remarks on elastic crack-tip stress fields. Int J Sol Struct 8:751–758.

[15] Sih GC (1979). An Introduction to Fracture Mechanics, Reference Material for the course on Adv. Fracture Mechanics. Lehigh Univ., Bethlehem-Pa, USA.

[16] Sun CT, Wang CY (2002). A new look at energy release rate in fracture mechanics. Int. J. Fracture 113:295–307.

[17] Vainshtok VA (1991). Application of the weight function method to solving multi-parametric three-dimensional fracture mechanics problems. Int. J. Fracture 47:201–212.

Influence of Coating on Friction and Wear of Combustion Engine Piston Rings

Abdelkader Guermat[1], Guy Monteil[2] and Mostefa Bouchetara[3]

[1]Institut des Sciences et de Technologie, Université de Mascara, BP 763, 29000, Algérie

[2]Laboratoire de Microanalyse des Surfaces LMS, ENSMM, 26 Chemin de l'épitaphe, 25030 Besançon cedex, France

[3]Laboratoire de Mécanique Appliquée, Faculté de Génie Mécanique, Université des Sciences et de la Technologie d'Oran USTO, BP 1505 El-Menouar, 31000, Algérie

Abstract   The top piston rings of the internal combustion engines are generally covered with a hard chromium coating ensuring a good longevity. However this type of coating is obtained by an electrolytic deposition process which uses CrVI, product classified as toxic. Consequently, it is necessary to identify other deposit processes or alternate materials of coating. In this work one tested a certain number of alternative solutions of coating likely to replace the current coating used on the piston rings of engine. One used a tribometer of the type PLINT TE 77 designed for the study of friction in lubricated mode and functioning with reciprocating motion. At the end of the tests and after the analysis of the results, a hierarchical list of these alternate materials will be drawn up, whose performances in friction and wear resistance will be higher or equal to the current solution.

Keywords: Friction, Combustion, Longevity, Performances.

1. Introduction

The protection of the environment and the safeguarding of the fossil resources constitute a major stake for the decades to come. Many efforts were already carried out in this field but it remains still much of possibilities to explore. Automobile transport constitutes a considerable source of gas emissions for greenhouse effect (CO_2). Indeed, the greenhouse effect of the gas emissions is due mainly to the incomplete fuel combustion. The most effective ways to reduce these emissions resides in the improvement of the effective output of the engine which can be obtained for example by the reduction of the friction losses in the piston ring–piston liner system which accounts for 40% of the friction losses and in the reduction of the consumption which involves a reduction of the emissions at the source [8].

One chose the reduction of frictions at the top piston ring /liner contact. The interest of this choice is double since one can implicitly contribute to improve the ecological and toxicological impact of the manufacture of these parts of engine.

The top piston rings of engine are very often covered with a hard chromium coating. However these coatings are obtained by an electrolytic process which requires the use of the hexavalent chromium at the time of its realization, product classified like toxic [10]. The identification of a solution of replacement to the electrolytic hard chromium which would make it possible reduce friction to the piston ring liner contact and improve the ecological and toxicological impact of manufacture constitutes the essential spot of this study.

2. Lubrication model

The control of the piston rings lubrication is based on the calculation of the oil film thickness, the oil flow and the friction of the piston rings. In several studies, one considers many identical assumptions.

The piston ring/cylinder liner assembly used for the study of tribological performances is generally assimilated, for the mathematical modelling, to a sample of cylinder liner in contact with a piston ring (Fig. 1) which has a parabolic profile and separated by an oil film [3].
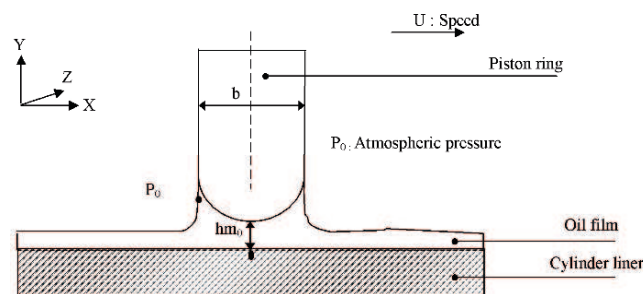
Fig. 1. Schematic model of the contact piston ring/liner

3. Importance of the selected parameters

The losses of power due to the segmentation are function of the oil viscosity and the piston ring/liner coefficient of friction. The control of lubrication of piston rings is very important for the reduction of power losses and oil consumption. The principal parameters of operation affecting the friction force are speed of engine and its load [4]. Many studies showed that unit piston ring/piston/liner has various modes of lubrication [7]. Increase in the engine speed involves an increase in hydrodynamic friction and reduction in mixed friction [4]. The impact of friction reductions, following the changes of the operating conditions, is important in fuel consumption at weak load, and is less important at full load [4].

4. Influence of coating

The surface treatments, in particular the unconventional processes developed recently, are the largest allies of metals since they contribute to mitigate their defects by deposit of a protective material. For many years it has been possible to deposit a wide range of hard wear-resistant coatings on to steel substrates using different PVD techniques and others [5]. Varieties of coatings were developed and employed such as coatings based on MoS2 or the carbon (graphite) [9] or nitriding which is extensively used in the automotive industry. However, only some special alloys steel showed the best characteristics after being nitrided. To mitigate that, the hardness of surface of some slightly allied steels was improved by surface alloying with Aluminium following by nitriding [2].

Coatings Diamond Like Carbon (DLC) are also used. They are hard and they produce a lower friction compared to the nitrided hard coatings. Me-C: H is a type of DLC coating which was tested on a great number of automobile parts during the 10 last years [6]. The coatings have proved to be very successful and are widely used in providing protection against wear for general components, such as gears and engine parts [5].

5. Experimental conditions

The tribological interactions met in a contact piston-ring-liner are difficult to reproduce in a system of laboratory (chemistries of the lubricants, temperature, pressure, combustion gas, etc.). For these reasons, one must use simpler means of laboratory which one easily controls the parameters most representative of the studied real contact. The tribometer Cameron Plint TE77 which kinematics is close to the operating conditions of a piston ring in an engine allows the use of samples taken in real parts. Using this machine one can vary the normal load (W) between 10 and 500 N, and the rotational frequency (f) of the engine between zero and 20 Hz (either the equivalent of 0 and 1 m/s). Also one can measure the displacement of the piston ring, the effort of friction (Ft) and the normal effort. Their values are posted and/or measured by the system of data acquisition. Thus, one can represent the efforts of friction according to the kinematics conditions of the contact.

5.1. Parts of test

The tests are carried out on samples of cast iron liners taken directly in parts of engine. The test-tubes of piston rings are also taken in compression piston rings of engine. Table 1 gives the list of the five coatings of piston rings to be tested in diesel engine architecture DW10 of PSA.

Table 1. Coatings of test for piston rings

Coatings	Specifications
A	cast iron + electrolytic chromium coating reinforced by alumina
B	cast iron + electrolytic chromium coating reinforced by diamond
C	cast iron + HVOF coating (WC-CrC)
D	lamellar cast iron without coating
E	spheroïdal cast iron + chromium nitride PVD coating
F	ion nitrided alloyed steel

The selected conditions of test are given with an aim of building the curve of Stribeck for each pair of piston ring and liner tested. Under these conditions, it is necessary to test a certain number of combinations of loads and speeds, in order to simulate the conditions met from the boundary regime to the hydrodynamic regime. The normal loads W used were fixed at 20, 40 and 80 N. For each one of these loads, the frequencies of oscillation f were 0.2; 1; 7 and 9 Hz. The race of sliding of the piston ring is 15 mm (±7.5 mm). The lubricant used is a pure mineral oil without additives of the type N175 (kinematics viscosity is 5 cST at 100°C). This lubricant is regarded as Newtonian. Measurements are taken for each condition of test on 10 cycles, with 400 points of measurement per cycle. All the couples tested undergo the same number of cycles. As regards the tests of wear, the applied load is about 90 N under a boundary functioning mode or regime with a frequency of oscillation equal to 0.4 Hz. Each couple is left in friction during 8 h where recordings were made at the beginning (just 2 min after the beginning of the tests, the process of wear not being started yet) and at the end of the tests (after 8 hof continuous friction).

6. Results

6.1. Lubrication modes of various coatings of piston rings

First one vary the load W (from 20 to 80 N) and/or speed f (from 0.2 to 9 Hz) according to displacement as that is illustrated by the figures (Figs. 2 and 3) for the case of the coating C. It clearly appears on these curves that one passes gradually from a mixed or boundary mode (Fig. 2) to a hydrodynamic mode (Fig. 3).

Tests with higher load and lower frequency would give a rectangular pace to the curve Ft = f (displacement) and give the same values of the maximum effort.

One can obtain for each type of coating a series of measurements of friction for various configurations (combinations of load W and frequency f) which make it possible to plot the corresponding curves of Stribeck (Fig. 4).
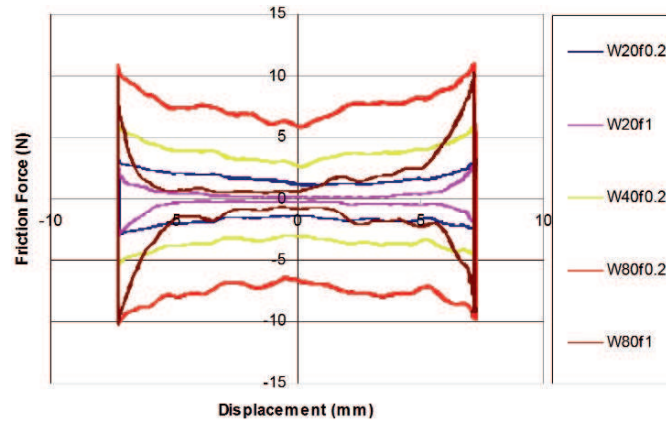
Fig. 2. Effort of friction according to displacement for boundary regime
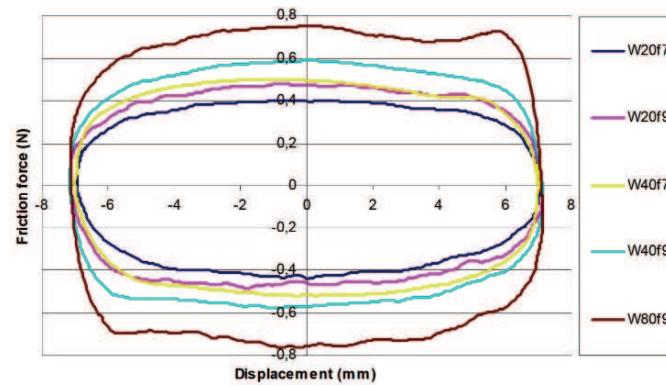
Fig. 3. Effort of friction according to displacement for the hydrodynamic regime
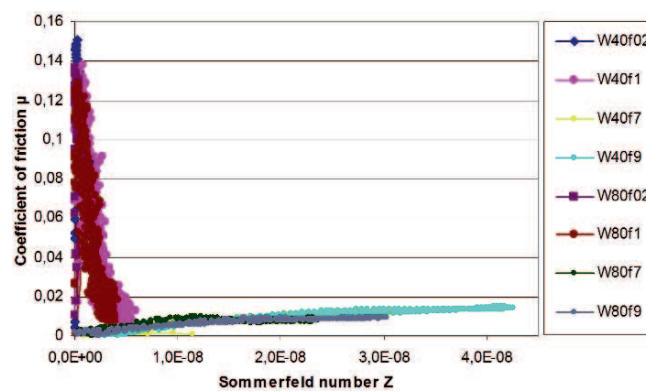
Fig. 4. Construction of the Stribeck curve

The maximum pressure of contact between the piston ring and the liner is calculated using the equation of Hertz (Eq. 1) [1]:

$$P_{max} = 0.798 \sqrt{\frac{\dfrac{W}{L} \cdot \dfrac{D_1 - D_2}{D_1 D_2}}{\dfrac{1 - \upsilon_1^2}{E_1} + \dfrac{1 - \upsilon_2^2}{E_2}}} \tag{1}$$

where W normal load, L length of the contact, ν_1 liner Poisson's ratio, ν_2 piston ring Poisson's ratio, E_1 liner Young modulus, E_2 piston ring Young modulus, D_1 diameter of the liner and D_2 diameter of the piston ring.

6.2. Comparative study of the coatings performances

6.2.1. Friction case

One can simplify the study of the various coatings by observing the levels of the efforts of friction translated into coefficients of friction in boundary regime. Under these conditions, one retains only the curves translating the tangential effort/ displacement relation where the friction efforts are maximum (the curves with frequencies of oscillations f equalize to 0.2 and 1 Hz) and then one trace a graph in the form of histogram to make the comparison (after the calculation of the friction coefficients). Such a graph is represented on figure (Fig. 5) where one notices a significant difference between the coefficients of boundary friction, and this in spite of uncertainties on the values of the friction coefficient of the various coatings tested. One notes that the piston rings with the coating C produces the lowest effort of friction in boundary mode. It is slightly lower than the piston ring of reference, covered with chromium-ceramics (coating A).
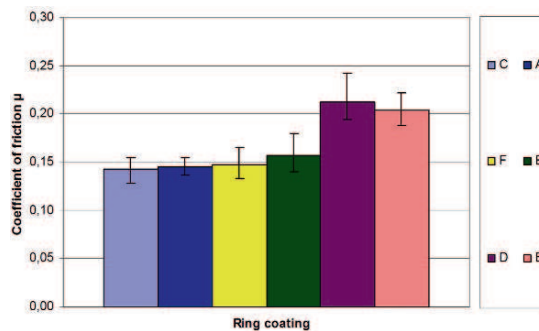
Fig. 5. Values of the friction coefficients in boundary regime for various coatings

One finds in fact two families of results, one whose level of the coefficient of friction is around 0.15 and the other whose value of the coefficient of friction is around 0.2. In the first family one find the coating C, the chromium of reference (A) and nitriding steel (F).

In the second family, one has the naked cast iron, chromium doped diamond (B) and the PVD deposit of CrN (E). After this comparison, the classification of the various coatings with respect to the coefficient of friction is as follows: C, A, F, E, B and naked cast iron D.

6.2.2. Wear case

In the study of wear one follows the same steps of analysis applied for the case of friction. In the tests of wear, the factor time plays a very significant part (8 h of continuous friction). Measurements of Ft were taken at the beginning (after 2 min from the beginning of the test for each couple) and at the end of the test. After 8h of continuous friction, under 90 N of load W and 0.4 Hz of frequency f for each couple, the changes of the friction curves shape were observed.

The comparison is carried, on this case, on the values of Ft in the middle of the race, which enabled to us to trace a histogram of each couple (Fig. 6). Figure 6 shows a difference in behaviour of the various coatings. As for the case of the friction tests, the coating C presents during the 8 h of tests the most stable behaviour compared to the other coatings, in spite of uncertainties.

For the naked Cast iron the situation is practically unchanged. For the other coatings, one has CrN PVD (E) which relatively changed. For the case of coatings A and F, they have about the same behaviour during 8 h of permanent contact. The couple which the form is much changed is the coating B.
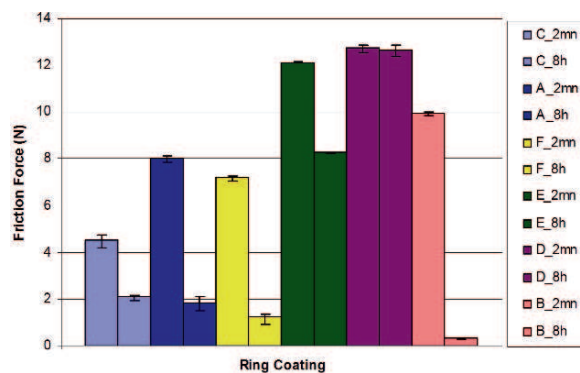
Fig. 6. Histogram of the friction efforts in the middle of the race

7. Conclusions

This study shows that it is possible using simple means of laboratory to simulate the contact piston ring/liner and to evaluate the performances in friction of a certain number of alternate coatings with hard chromium used currently. Interesting alternatives could be found by introducing new techniques of development such as thermal projection. Indeed, the coating HVOF chromium tungsten present the levels of friction much lower than the current reference coating, as well in a boundary mode, corresponding to the high and low dead points of a driving operation, as in quasi-hydrodynamic mode corresponding to the displacement of the piston in the middle of the race of an engine.

After a test of wear, it preserves its initial characteristics without generating wear on the liner. Nitriding steel proves to be also with an interesting level of friction but probably not rather low than the reference consisted by hard chromium reinforced ceramic (coating A).

The chromium nitride obtained by PVD deposit is close to the reference and presents the advantage of resorting to an alternative manufacturing process at the use of chromium VI. The reinforcement of hard chromium by diamond additions proves too abrasive a priori, especially during the launching phase of the engine.

References

[1] Aublin M, et al (1998). Systèmes mécaniques, théorie et dimensionnement. Dunod Ed., Paris.
[2] Bindumadhavan PN, et al (2000). Aluminizing and subsequent nitriding of plain carbon low alloy steels for piston ring applications. J Surface Coatings Technol 127:252–259.
[3] Dowson D, et al (1978). Piston ring lubrication. Part II. Theoretical analysis of a single ring and a complete ring pack. In: Energy conservation through fluid film lubrication technology, Frontiers in Research and Design. ASME Winter Annual Meeting, New York, pp 23–52.
[4] Feuga L, Bury C (1984). Piston and ring mechanical losses. J SAE 841296:173–179.
[5] Fox V, Jones A, Renevier NM, Teer DG (2000). Hard lubricating coatings for cutting and forming tools and mechanical components. J Surface Coatings Technol 125:347–353.
[6] Gåhlin R, et al (2001). ME-C: H coatings in motor vehicles. J Wear 249, 3-4:302–309.
[7] Monteil G, Lebeaud C (1998). Réduction des frottements dans le contact segment-piston-chemise d'un moteur thermique, Contribution à l'amélioration du rendement. J Ingénieurs de l'Automobile numéro de mars:45–49.
[8] Priest M, Taylor CM (2000). Automobile engine tribology, approaching the surface. J Wear 241, 2:193–203.
[9] Teer DG, Hampshire J, Fox V, Bellido V (1997). J Surface Coatings Technol 572:94–95.
[10] Théry D (2004). Le marché du chromage dur en Europe, présent et futur. In: Conférence Internationale sur le chromage, 4th edn. Saint-Étienne.

Optimization Constrained of the Lifetime of the CBN 7020 During the Machining of Steel 100 Cr6

Slimane Benchiheb and Lakhdar Boulanouar

Mechanical Research Laboratory of Materials and Industrial Maintenance (LR3MI), University Badji Mokhtar, BP12 Annaba 23000, Algeria

Abstract   The purpose of the study is to evaluate the performances of material of cut CBN 7020 produced during turning bearing steel 100 Cr6 soaked. The method adopted for the realization of these tests is that of the experimental designs. A mathematicals models validated by the criterion of Fisher, allowed to predict the lifetime T of the tested tool material, also the waited roughness Ra (surface integrity). They are necessary for optimization and the industrial exploitation. The experimental results has a better output in terms of lifetime (T = 68.64 min), and surfaces roughness (Ra = 0.38 to 1.04 μm) to Vc = 120 m/min (cutting speed) taken at the same moment as the comparable wear has for those the grinding (Ra = 0.2 to 1.1 μm). Non linear optimization of the life time material (CBN 7020) constrained inequality (surface roughness Ra) by the means of Matlab allowed to release an optimum (T = 68.33 min) to Vcop = 120 m/min near to the experimental value with 99%.

Keywords: Constrained optimization, Lifetime, Roughness, CBN 7020.

1. Introduction

The technological progress of machining steel is related to the behavior improvement of the cutting materials and the increases in their performances influence directly on the production. Manufacturers are in need of optimizing their production methods in order to increase the productivity, to reduce the wear of the cutting tools, to shape ecologically with a limited quantity of oil machinery, and to take the produced surface into consideration. In all of the time, the hard turning produces surfaces qualities, reduces the number of operations and the scrap components. The turning of steels hardened by soaks (the superior hardness to 50 HRC) needs the usage of constituent's materials which have better proprieties of hardness at high temperature, wear resistance (strength), and chemical stability. The advent of new tools such as micrograins coated carbides, ceramics, CBN and diamonds allows the industrial exploitation of this technology [1]. The latters show relatively a good performance when substituting turning for grinding finish operations [2]. In this case the choice of cutting material and the components of the mode of the cut is a delicate step. In fact it is difficult to cope with the choice of the complete factorial design method in order to investigate the effects of the tested variables on

the studied phenomenon. Different studies [3, 4] were done on the influence of the components that affect the tool's lifetime and the produced surface state. The results show that the components of the mode of cut have a considerable impact. Actually many studies are developed to optimize certain cutting parameters (cutting speed, feed rate and pass dept) with taking in consideration one or many criterions. Koenig et al. [5] presented the advantages of using hard turning over grinding and its potential to control surface integrity by optimizing tool geometry and machining parameters. Matsumoto et al. [6] addressed the issue of obtaining favorable surface integrity in hard turning processes. It is also evident from a large number of other experimental works that the tool geometry and selected machining parameters have complex relations with cutting forces, tool life, surface roughness and integrity of the finished surfaces. Chou et al. [7] showed the influence of using various cubic boron nitrite (CBN) contents in the cutting tools on tool wear and surface integrity. Thiele et al. [8] have shown that cutting edge geometry has a great influence on the residual stresses induced by hard turning. Özel et al. [9] have identified the factors influencing cutting forces and surface roughness. This complex nature of parameter relations makes it difficult to generate explicit analytical models for hard turning processes. On the other hand, according to a review by Dimla et al. [10], the relations between the machining parameters including tool geometry and the performance measure of interest can be obtained with non-linear models by training neural networks using experimental data as reported by many researchers. Özel and Nadgir [11] applied neural networks modeling to predict tool wear in different edge geometry tools in hard turning. It is also highly complicated to predict surface roughness generated by machining processes as claimed by Benardos and Vosniakos [12]. Özel and Karpat [13] have also shown that neural network modeling is a viable approach for predicting both surface roughness and tool wear for honed and chamfered cutting tools. In obtaining optimal solutions for these multi-objective problems, a number of heuristic algorithms including genetic algorithms (GA), evolutionary algorithms (EA) and simulated annealing (SA), as well as a recently developed optimization algorithm called particle swarm optimization (PSO) are used. These methods are summarized by Zitzler et al. [14]. The PSO is a population based research algorithm, which was inspired by the social behavior of bird flocks as originally developed by Eberhart and Kennedy [15]. The PSO operates on a population of potential solutions. Conventional optimization techniques, such as gradient-based methods, do not function effectively solving multiple objective functions without reducing the objectives into a single function and handling it accordingly. On the other hand, the PSO algorithms have some drawbacks such as exploration and exploitation while searching the solution space [16]. Many researchers such as Coello and Lechuga [17] find the PSO as an efficient alternative over other research algorithms especially when dealing with multi-objective optimization problems.

The chosen method used at the first time concerns the optimization of the function T of wear is based on the maximisation technic developed in Matlab software which uses a pre-programmed function (fmincon) [18].

In this case we seek to find a relative optimum of the cutting mode leading to better behavior of the tool's lifetime under a constrained surface state.

2. Experimental procedure

Tests have been conducted on a parallel lathe SN40 with a spindle power of 6.6 kW, a speed range of 45 to 2,000 RPM and feed rates from 0.08 to 6.4 mm/revolution. The workpieces have been quenched at 1,100°C in a 4.5 kW furnace. A 3°C precision digital thermometer probe has been used to check the homogeneity of the internal furnace temperature while heat treating is carried out. A 5 µm precision optical microscope having two cross travelling carriages has been employed to follow the wear propagation. The material used in this study is a quenched bearing 100 Cr6 (AISI 52100) with the following specifications [(1.41Cr, 0.96C, 0.22Si, 0.35Mn, 0.013S, 0.013P)%]. The material present a martensitic structure with large proportion of carbides M_7C_3 type of 1 µm size, and small proportion secondary carbides M_3C type. The heat treatment has followed quenching for 60 min at 850°C after 45 min temperature stabilization then tempering at 200°C for 60 min after 30 min stabilization time. This causes the hardness to increase from 28 to 60 HRC. The former steel is chosen on the basis that in machining applications, it presents 47% of the heat treated manufactured parts [19]. Turning tests have been conducted on cylindrical heat treated 100 Cr6 specimens of 57 mm diameter and 350 mm length. Because of its high wear resistance, it is largely employed for making bearing balls, rollers, rings and cages. It is also used in cold forming as in forming matrix, cylinders of rolling mill and wear coating. The tool insert material nuance CBN 7020 (57% CBN + 35% TiCN + 8% authors) are a mixture of CBN and TiCN with ceramic bind leading to combination of wear resistance, and chemical stability under high temperatures ideal for the turning of the hardness components. This kind of amovible tools inserts material of square shape is advised for continued cutting or weakly interrupted. The ISO standard for the tool insert material is given according to the following nuance: SNGA 12 04 08 S01020, and the tool bar insert holder is PSBNR2525M12 having a geometry as follows: Xr = 75°; α = 6°; γ = −6°; λ = −6°. The nozzle radius is $R\varepsilon$ = 0.8 mm.

3. Results and discussion

3.1. Flank wear (Vb)

The realised tests had allowed getting an experimental result shown in (Figs. 1 and 2). This forms expresses the effect time result on the cutting speed and the different combinations of complete factorial design of flank wear Vb of tested tool material (N = 2^3). Each combination has been reproduced twice. The acceptable wear recommended by ISO is Vb = 0.3 mm.

As a conclusion the effect of the cutting speed on the lifetime is more marqued for the spaces of high speeds. That means by the fact when we work with high cutting speeds, the shaping system becomes instable duo to high vibrations listed during machining, and the temperature in cutting zone increases (specially in interfaces "chip-rake face" and "component-principal flank surface"), which encourages the manifestations of different wear mechanisms of tool following the decrease of its hardness. The micrographies taken by mean of MEB (scanning electron microscopy) to the cutting speed Vc = 350 m/min (Fig. 3) with a different enlargements shows a flank wear Vb under the shape ladle caused by the friction of the principal flank surface with the cutting surface of the component.
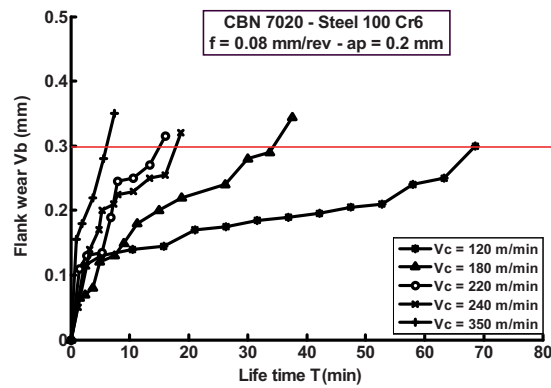
Fig. 1. Flank wear evolution (Vb) of CBN 7020 as a function of time with a different cutting speeds
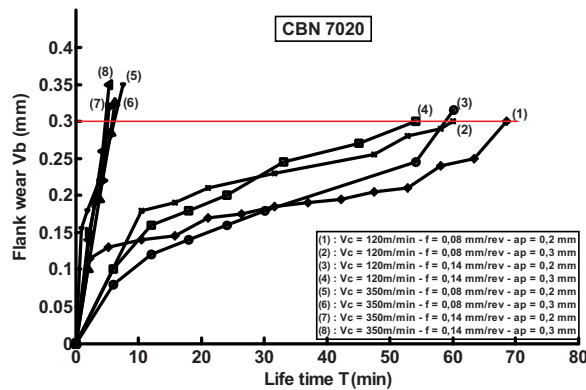
Fig. 2. Effect time on flank wear (Vb) of CBN 7020 for different combinations of complete factorial design
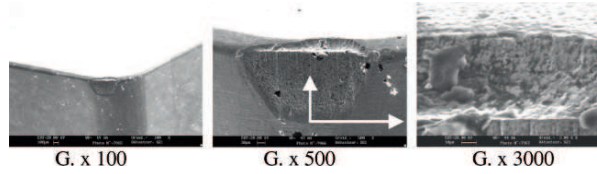
Fig. 3. Flank wear Vb of CBN 7020 to Vc = 350 m/min, f = 0.08 mm/rev, ap = 0.2 mm

3.2. Roughness (Ra)

The results show that the roughness decrease then it stabilize when the cutting speed increase (Fig. 4). This improvement of the surface state explains by the fact that the machining material is less ductile and the chosen cutting speeds are high, which is not in favour of the shaping built-up edge, (then the absence of surface degradation by sticking particles or chip fragments on the wear surface). This confirms that the tool works in agreeable conditions to very high cutting speeds. The CBN 7020 assure a good state of the surfaces (Ra = 0.38 to 1.04 μm) by grinding comparison (Ra = 0.2 to 1.1 µm) (Fig. 5) [20].
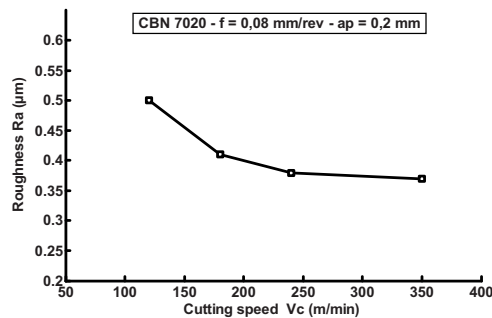
Fig. 4. The roughness (Ra) evolution of soaked steel 100 Cr6 through the cutting speed function obtained on a length of 10 mm
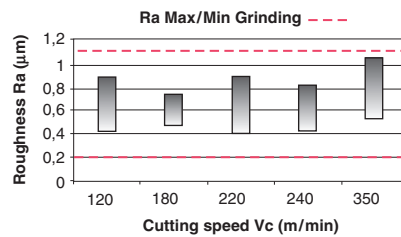
Fig. 5. Comparison of the getting surface quality with different cutting speed between hard turning and grinding for the CBN 7020 (f = 0.08 mm/rev, ap = 0.2mm)

3.3. Optimization

The optimization problem (P) of type Minimization or Maximization of n dimension can be written following the Eq (1):

$$Max\ f_{obj}$$
$$x\varepsilon\ r^n$$
$$(P)\quad G_I(X)\leq 0\quad I=1,2,\quad P$$
$$\qquad\quad H_J(X)=0\quad J=1,2,\quad Q \qquad\qquad (1)$$
$$\qquad\quad X\ Min\leq X\leq X\ Max$$

f_{obj} : It is a criterion to minimize or to maximize called also objective function;

X, X_{max} and X_{min} : They are respectively unknown vectors and the borders of the accessible field ; $h_j(x)$ et $g_i(x)$: present equalities and inequalities constraints. The problem's solution is given by a group of parameters X, for these the objective function presents a minimal value with respect to the equalities, inequalities and field constraints.

3.3.1. Mathematical models

In our case, these functions are polynomials calculated through the experiences design techniques (complete factorial design) [21]. The statistic handling of the behaviour T and the state surface Ra product through the coefficients trust interval. This handling permitted a deduction of mathematical models (Eqs. 2 and 3) that expresses a functional relation between cutting mode parameters and the studied one:

$$T = 32.942 - 0.239(x_1 - 235) - 74.16(x_2 - 0.11) - 35.04(x_3 - 0.25)$$
$$+ 0.4927(x_1 - 235)(x_2 - 0.11) + 0.2699(x_1 - 235)(x_3 - 0.25) \qquad (2)$$
$$+ 323.333(x_2 - 0.11)(x_3 - 0.25) - 2.8405(x_1 - 235)(x_2 - 0.11)(x_3 - 0.25)$$

$$Ra = 0.433 - 0.0005434(x_1 - 235) - 1.25(x_2 - 0.11) \qquad (3)$$

where x_1, x_2 and x_3 respectively represent the cutting speed Vc (m/min), the feed rate (mm/rev) and the pass depth (mm).

Statistical analyses have been carried out in order to determine the reliability of the results (Table 1) [22] according to Fisher criterion (Eq. 4).

$$F_{exp} = \frac{S^2 res}{S^2 rep} < F \text{ Theoretical} = 4.46 \tag{4}$$

For an adequate model, where S^2_{res} and S^2_{rep} representing respectively the residual variances and reproducibility.

Table 1. Models statistical exploitation

Studied parameters	$\Delta\beta i$ Coefficients trust interval	Experimental FISHER criterion
Lifetime T	0.418	$4.987.10^{-6}$
Roughness Ra	0.116	0.56

3.3.2. Optimum research

The problem is to maximize of the objective function T of the tool behavior under constraint inequality Ra (roughness) and it is written as follows (Eq. 5):

$$\begin{array}{l} T \\ 0.2 \le Ra \le 1.1 \\ Subject\,to \\ 120 \le x_1 \le 320 \\ 0.08 \le x_2 \le 0.14 \end{array} \tag{5}$$

The proposed system resolution leads us to call to the pre-programmed function fmincon. For this effect the following program (flow chart) was established.

```
FUNCTION F = OBJECTIF(X).
% PRINCIPAL PROGRAM:
% INITIAL SOLUTION BETWEEN LB AND UB:
X0 = [250 .1 .22];
% LOWER BOUNDS:
LB = [120 .08 .2];
% UPPER BOUNDS:
UB = [350 .14 .3];
% INEQUALITIES CONSTRAINTS (A*X < B):
A1 = [-.0003582 .956 0];
A2 = [.0003582 -.956 0];
A3 = [0 0 0];
A  = [A1; A2; A3];
B  = [0.06043; 0.2956; 0];
OPTIONS = OPTIMSET('LARGESCALE','OFF');
X = FMINCON(@MYFUN,X0,A,B,[],[],LB,UB,[], OPTIONS)
DISP(X)
THE OBTAINED SOLUTION IS:
```

X =
  120.0000
  0.0800
  0.2000

The optimal cutting parameter obtained is: Vc_{op} = 120 m/min, f_{op} = 0.08 mm/rev, ap_{op} = 0.2 mm.

4. Conclusions

The leading study on the behaviour of the cutting material (CBN 7020) and on the surface state produced during the steel 100 Cr6 machining allowed to get the following conclusions:

- The CBN 7020 allow to obtain surfaces states (Ra = 0.38 to 1.04 μm) include in the roughness boarders obtained by grinding (Ra = 0.2 to 1.1 μm).
- The non linear optimization of the lifetime material (CBN 7020) under the surface state taken as inequality constraint to Matlab mean allowed to release an optimum (T = 68.33 min) to Vc_{opt} = 120 m/min near to the experimental value with 99%.
- This technical optimization by maximization through Matlab mean had allows to obtain a satisfactory results (better lifetime in service of CBN 7020), which will lead us in the future works to broaden the issue to multi objective optimization by introducing other constraint functions, such as, the cutting force and the machining cost that are necessary for an industrial exploitation.

References

[1] Koenig W, Berktold A (1993) Comparison of surface integrity aspects and attainable accuracies. Annals of the CIRP 42/: 39–43.
[2] Schultz H (1997) State of the art of high speed machining. First French and German Conference of High Speed Machining, pp 1–7.
[3] Thiele JD, Melkote SN (2000) Effect of cutting-edge geometry and workpiece hardness on surface residual stresses in finish hard turning of AISI 52100 steel. ASME, Journal of Manufacturing Science and Engineering 122: 642–649.
[4] Barry J, Byrne G (2001) Cutting tool wear in the machining of hardened steels, Part II: CBN cutting tool wear. Wear 247: 152–160.
[5] König W, Komanduri R (1984) Machining of hard materials. Ann CIRP 33/2: 417–427.
[6] Matsumoto Y, Hashimoto F (1999) Surface integrity generated by precision hard turning. Annals of the CIRP 48/1: 59–62.
[7] Chou YK, Evans CJ (2002) Experimental investigation on CBN turning of hardened AISI 52100 steel. J. Mater Process Technol 124: 274–283.
[8] Thiele JD, Melkote SN (2000) Effect of cutting-edge geometry and workpiece hardness on surface residual stresses in finish hard turning of AISI 52100 steel. ASME J. Manuf Sci Eng 122: 642–649.

[9]   Özel T, Hsu TK (2005) Effects of cutting edge geometry, workpiece hardness, feed rate and cutting speed on surface roughness and forces in finish turning of hardened AISI H13 steel. Int J. Adv Manuf Technol 25: 262–269.

[10] Dimla DE, Lister PM (1997) Neural network solutions to the tool condition monitoring problem in metal cutting – a review critical review of methods. Int J. Mach Tools Manuf 39: 1219–1241.

[11] Özel T, Nadgir A (2002) A Prediction of flank wear by using back propagation neural network modeling when cutting hardened H-13 steel with chamfered and honed CBN tools. Int J. Mach Tools Manuf 42: 287–297.

[12] Benardos PG, Vosniakos GC (2003) Predicting surface roughness in machining: a review. Int J. Mach Tools Manuf 43: 833–844.

[13] Özel T, Karpat Y (2005) Predictive modeling of surface roughness and tool wear in hard turning using regression and neural networks. Int J. Mach Tools Manuf 45: 467–479.

[14] Zitzler E, Laumanns M A (2002) tutorial on evolutionary multiobjective optimization, Workshop on Multiple Objective Metaheuristics, MOMH, Springer, Berlin Heidelberg New York.

[15] Eberhart CR, Kennedy J (1995) Particle swarm optimization. Proc IEEE International Conference on Neural Networks, Piscataway, NJ, pp 1942–1948.

[16] Shi Y, Eberhart RC (1998) Parameter selection in particle swarm optimization. Proc 7th Annual Conference on Evolutionary Programming, San Diego.

[17] Coello CA, Lechuga MS (2002) Mopso: A proposal for multiple objective particle swarm optimization. Proc IEEE, World Congress on Computational Intelligence, pp 1051–1056.

[18] Coleman TF, Li Y. (1994) On the Convergence of Reflective Newton Methods for Large-Scale Nonlinear Minimization Subject to Bounds. Mathematical Programming 67/2: 189–224.

[19] Poulachon G (1999) Aspects phénoménologiques, mécaniques et métallurgiques en tournage des aciers durcis. Thèse de doctorat, Ecole Nationale Supérieure d'Arts et Métiers Centre de Cluny France, pp 38.

[20] Remadna M (2001) Le comportement du système usinant en tournage dur, Application au cas d'un acier trempé usiné avec des plaquettes CBN. Doctorat INSA-Lyon, pp 138–141.

[21] Clement B (2000) Design and analysis of experiments. Genistat Conseils Inc.

[22] Benchiheub S, Boulanouar L (2007) In Optimizing CBN 7050 lifetime during hard turning. International Review of Mechanical Engineering IREME 1/3: 250–256.

Comparison of Simulation Methods of Pulsed Ultrasonic Fields Radiated in Isotropic Solids

W. Djerir[1, 2], T. Boutkedjirt[2] and A. Badidi Bouda[1]

[1]Laboratory of Characterization and Instrumentation, Technical and Scientific Research
 Centre for Welding and control, BP64, Route de Dely Brahim, Chéraga, Alger, Algeria

[2]Faculty of Physics, USTHB, BP. 32, El-Alia, DZ-16111 Algiers, Algeria

Abstract   The modelling of pulsed ultrasonic fields radiated by transducers in materials of various types is of particular interest in industrial applications of non destructive testing. Knowledge of the ultrasonic field allows defining and optimizing the control conditions. For the calculation of harmonic and pulsed ultrasonic fields, various methods have been used such as exact, semi-analytical, asymptotic and purely numerical methods. In this work, these methods are reviewed for the case of a planar and circular ultrasonic source coupled to a semi-infinite isotropic solid. In the second part, the solution of a semi-analytical method, which uses particular approximations, is compared to that of an exact one. The numerical calculations achieved by using the exact method are very tedious but allow the interpretation of physical phenomena involved. In contrast to that, the semi-analytic one permits the calculations to be undertaken in a more reasonable time. However, Rayleigh waves and head waves are not revealed by this method.

Keywords: Ultrasound, NDT, Pulsed field, Isotropic Solid, Transducer.

1. Introduction

The theoretical problem of the calculation of the displacement field generated by a point source and normal harmonic force is known in the literature as the problem of Lamb, who was the first to propose its solution. The specific solution suggested is given in integral form. In the following some methods describing the field radiated by a transducer in a solid are reviewed.

2. Review of field calculation methods

The exact method of resolution suggested by Eason [1] allows the calculation of the field radiated by a contact transducer, considered as a source of normal, uniform and transient force. Numerical calculations are tedious but highlight four types of waves. Gakenheimer and Miklowitz [2] have solved the transient problem for a point source of normal constraint to the surface of the solid. The Green function is given in an integral form. The resolution of the problem uses a

transformation technique suggested by Cagniard and De Hoop [3, 4]. Djelouah and Baboux [5] used integral transformations to express the components of the displacement in the form of multiple integrals. Miller and Pursey [6] proposed an asymptotic solution of the Lamb problem in the case of a monochromatic source of normal constraint. A good far field approximation [7, 8] does not account for head waves or Rayleigh waves. Monochromatic approaches allow treating the equations of elasticity provide a simple analytical description. The transient problem can also be treated by Fourier analysis [9]. Gridin [10] calculated the field of a circular or a rectangular transducer a so-called high frequency asymptotic solution. By using the Cagniard–De Hoop method, Bresse and Hutchins [11] expressed the displacement as a convolution integral. Weight [12] proposed an empirical model for solids. Semi-analytical solutions permit, by using some approximations, the calculation of the field in a reasonable time. Gendreu [13] developed two formulations of the impulse response which have been obtained by integrating the Green functions suggested by Gakenheimer et al. [2]. According to the first one, the model is valid within the wave-fronts approximation for coupled L- and S-waves. In the second formulation the two kinds of waves are decoupled and the head waves are neglected. Such calculation, which is valid in the far field, has been carried out for the normal or tangential forces by Lhémery [14]. These two functions are integrated on the transmitting surface by using the Stepanishen method [15]. Purely numerical methods such as finite element method [16] and finite differences [17].

3. Description and assumptions of the selected models

We considered the ultrasonic field radiated at point M of an isotropic solid medium by a source at point R of the active surface of the transducer. The elastic tensor can be expressed versus Lamé coefficients λ and μ.

$\vec{u}$ Being the displacement field, the equation of propagation can be given by:

$$\rho_0 \cdot \frac{\partial^2 \vec{u}}{\partial t^2} = \mu \cdot \Delta \vec{u} + (\lambda + \mu) \cdot \vec{\nabla} \cdot \left(div \vec{u} \right) \tag{1}$$

where ρ_0 is the density of the propagation medium. The displacement can be decomposed as the sum of a longitudinal and transversal wave displacement:

$$\vec{u} = \vec{u}_L + \vec{u}_T \tag{2}$$

With

$$\begin{cases} \vec{u}_L = \vec{\nabla} \cdot \phi \\ \vec{u}_T = \vec{\nabla} \wedge \vec{\psi} \end{cases} \tag{3}$$

ϕ and $\vec{\psi}$ are the scalar and vector acoustic potential respectively. This leads to the uncoupled equations of propagation:

$$\nabla^2 \phi = \frac{1}{c_L^2} \frac{\partial^2 \phi}{\partial t^2} \tag{4}$$

$$\nabla^2 \vec{\psi} = \frac{1}{c_T^2} \frac{\partial^2 \vec{\psi}}{\partial t^2} \tag{5}$$

With $c_L^2 = \dfrac{\lambda + 2\mu}{\rho_0}$ and $c_T^2 = \dfrac{\mu}{\rho_0}$. c_L and c_T are the velocities of the longitudinal and shear waves respectively.

3.1. Boundary and initial conditions

In order to approach real conditions, the following assumptions are made:

- o   The surface of the sample in contact with the transducer is planar.
- o   The piece is assumed to be sufficiently large to avoid reflection of the boundaries.
- o   The stress and the displacements are initially null in the solid medium and on the boundaries.

3.2. Description of Lhémery model

With considering the free field Green function, the integral formulation of the displacement created by point force at field point $\vec{r}$ can be given by:

$$\begin{aligned} u_i(\vec{r},t,T_j(\vec{\xi},\tau)) = \iint\limits_R (T_j \frac{(3\gamma_i\gamma_j - \delta_{ij})}{4\pi\rho_0} \frac{1}{r^3} \int\limits_{r/c_L}^{r/c_T} \tau'\delta(t-\tau-\tau')d\tau \\ + T_j \frac{\gamma_i\gamma_j}{\rho_0 c_l^2} \frac{\delta(t-\tau-r/c_l)}{4\pi r} - T_j \frac{\gamma_i\gamma_j - \delta_{ij}}{\rho_0 c_t^2} \frac{\delta(t-\tau-r/c_t)}{4\pi r})ds_R \end{aligned} \tag{6}$$

where u_i is the displacement at point $\vec{r}$, which is due to the stress T_j applied at $\vec{\xi}$. γ_i is the cosine director defined by $\gamma_i = (r_i - \xi_i) / |\vec{r} - \vec{\xi}|$ and i and j indicate the components in the referential (Oxyz).

The last two terms of (Eq. 6) describe the (1/r) decrease of the amplitude of the two longitudinal and shear spherical volume waves. The behaviour of the first term of (Eq. 6) in $(1/r^2)$ is more complex since it is neither irrotational nor solenoidal. It expresses a coupling between the L-waves and the S-waves in the near field. This term is neglected by Lhémery (Eq. 6) becomes:

$$u_i(r,t) = \iint_R \frac{\gamma_i \gamma_j}{\lambda + 2\mu} \frac{T_j(r_R \cdot t - |r - r_R|/c_l)}{2\pi|r - r_R|} - \frac{\gamma_i \gamma_j - \delta_{ij}}{\mu} \frac{T_j(r_R \cdot t - |r - r_R|/c_t)}{2\pi|r - r_R|} ds_R \quad (7)$$

This formula allows the numerical evaluation of the displacement in much simpler way than the integration of the exact solution [1, 5, 9, 11 and 17]. The separation of time and space variables allows rewriting (Eq. 7) it in the form of a temporal convolution for the two components of the displacement vector. That is:

$$u_r(r,t) = -P_0 T(t) \otimes_t \iint_R \frac{\gamma_r \gamma_z}{\lambda + 2\mu} \frac{\delta(t - r/c_l)}{2\pi r} - \frac{\gamma_r \gamma_z}{\mu} \frac{\delta(t - r/c_t)}{2\pi r} ds_R$$
$$u_z(r,t) = -P_0 T(t) \otimes_t \iint_R \frac{\gamma_z^2}{\lambda + 2\mu} \frac{\delta(t - r/c_l)}{2\pi r} - \frac{(\gamma_z^2 - 1)}{\mu} \frac{\delta(t - r/c_t)}{2\pi r} ds_R$$

$$(8)$$

where $r = |r - r_R|$ and $\otimes_t$ represents the temporal convolution operator. The two integrals on R are the impulse responses respectively of the radial and axial components of the displacement. Each component of the displacement vector contains compressional waves and shear waves. By defining $h_l^r(r,t)$ and $h_t^r(r,t)$ the impulse responses for the radial displacement of the compressional wave and a shear wave respectively and, $h_l^z(r,t)$ and $h_t^z(r,t)$ those for the z component.

$$u_r(r,t) = -P_0 T(t) \otimes_t \left[h_l^r(r,t) + h_t^r(r,t) \right]$$
$$u_z(r,t) = -P_0 T(t) \otimes_t \left[h_l^z(r,t) + h_t^z(r,t) \right]$$

$$(9)$$

3.3. Description of Djelouah model

The most methods used to solve the partial derivative in (Eq. 1) are those which call for transformation techniques such as Laplace–Hankel or Fourier–Hankel

transforms [5]. The application of these integral transformations on ϕ and ψ respectively (Eqs. 4 and 5), leads to simple equations on their transforms ϕ^T and ψ^T. The solutions ϕ and ψ are then deduced by inverse integral transforms. Fourier transforms of displacement components can be written:

$$\overline{u}_r \; (\xi, z, \omega) \; = F(\omega) \, \overline{U_{ri}}(r, z, \omega) \tag{10}$$

$$\overline{u}_z \; (\xi, z, \omega) \; = F(\omega) \, \overline{U_{zi}}(r, z, \omega) \tag{11}$$

where $\overline{U_{ri}}(r, z, \omega)$ and $\overline{U_{zi}}(r, z, \omega)$ represent the transfer functions for the radial and axial components of the displacement respectively. These are given by:

$$\overline{U_{ri}}(r, z, \omega) = \frac{a}{\mu} \int_0^\infty \frac{\xi}{G(\xi)} \left(\begin{array}{l} \left(K_T^2 - 2\xi^2 \right) e^{-z\left(\xi^2 - K_L^2 \right)^{\frac{1}{2}}} + 2\left(\xi^2 - K_L^2 \right)^{\frac{1}{2}} \\ \left(\xi^2 - K_T^2 \right)^{\frac{1}{2}} \cdot e^{-z\left(\xi^2 - K_T^2 \right)^{\frac{1}{2}}} \end{array} \right) J_1(\xi a) J_0(\xi r) d\xi$$

$$\overline{U_{zi}}(r, z, \omega) = \frac{a}{\mu} \int_0^\infty \frac{\left(\xi^2 - K_L^2 \right)^{\frac{1}{2}}}{G(\xi)} \left(\begin{array}{l} \left(K_T^2 - 2\xi^2 \right) \cdot e^{-z\left(\xi^2 - K_L^2 \right)^{\frac{1}{2}}} + \\ 2\xi^2 \cdot e^{-z\left(\xi^2 - K_T^2 \right)^{\frac{1}{2}}} \end{array} \right) J_1(\xi a) J_0(\xi r) d\xi$$

$$\tag{12}$$

With:

$$G(\xi) = (2\xi^2 - K_T^{\,2})^2 - 4\xi^2 (\xi^2 - K_L^{\,2})^{1/2} (\xi^2 - K_T^{\,2})^{1/2} \tag{13}$$

4. Results

To simulate the displacement provided by the two models, the situation of a circular transducer of radius a, transmitting ultrasonic waves in a semi infinite block of steel is examined. (Figs. 1 and 2) compare the results predicted by Lhémery with the exact solution obtained of Djelouah for the axial and radial components of the particle velocity, υ_z and υ_γ respectively. The field is calculated at the axial distance " $z = 15\,\text{mm}$ " at various radial distances. In order to interpret these results, the following notations in (Figs. 1 and 2) are used. Op indicates the compressional direct plane wave which arrives at instant t_0^l. OB$_l$ (respectively OB$_t$) indicates the compressional edge (respectively shear) wave on the axis

($r=0$). OB$_{l1}$ indicate the contribution of the compressional waves (respectively shear waves) resulting from the nearest edge of the source, which arrives at the observation point at instant t_1^l.

OB$_{l2}$ indicates the contribution of the compressional waves (respectively shear waves) resulting from the farthest edge of the source arriving at the observation point at instant t_2^l. In the field region $\left(0 \le r \le a\right)$, so-called "region of direct radiation", and on axis ($r=0$), the axial component of the particle velocity v_z obtained by the application of the two models is the sum of three components (Fig. 1a): the first one, which has the same waveform as the "excitation" arrives at instant t_0^l and is called "compressional plane wave".

Fig. 1. Temporal variation of the axial components of the particle velocity radiated by a circular transducer ($a = 10$ mm), at $z_0 = 15$ mm and (**a**): $r = 0$ mm, (**b**): $r = 5$ mm and (**c**): $r = 15$ mm

The second component, of low amplitude compared to the plane wave and of opposite polarities is called "compressional edge wave". The third component which has the lowest amplitude and the same polarity as the plane wave is called "shear edge wave". Out of axis ($r = 5$ mm), the velocity field is constituted of three edge waves of small amplitudes in addition to the plane wave which interfere with the first longitudinal edge wave (Fig. 1b).

In the region ($r \geq a$), so-called the "shadow region", the ultrasonic field is constituted of four edge waves (longitudinal and transversal) of small amplitudes (Fig. 1c). Note the existence of a wave of small amplitude (encircled) at instant $t_{min} = t_0^t$ (Fig. 1a, b) and which corresponds to a "transversal plane wave", which has no physical significance. In Fig. 2 and for the two models, in the region $(0 \leq r < a)$ and on axis, the radial particle velocity is the sum of two components.
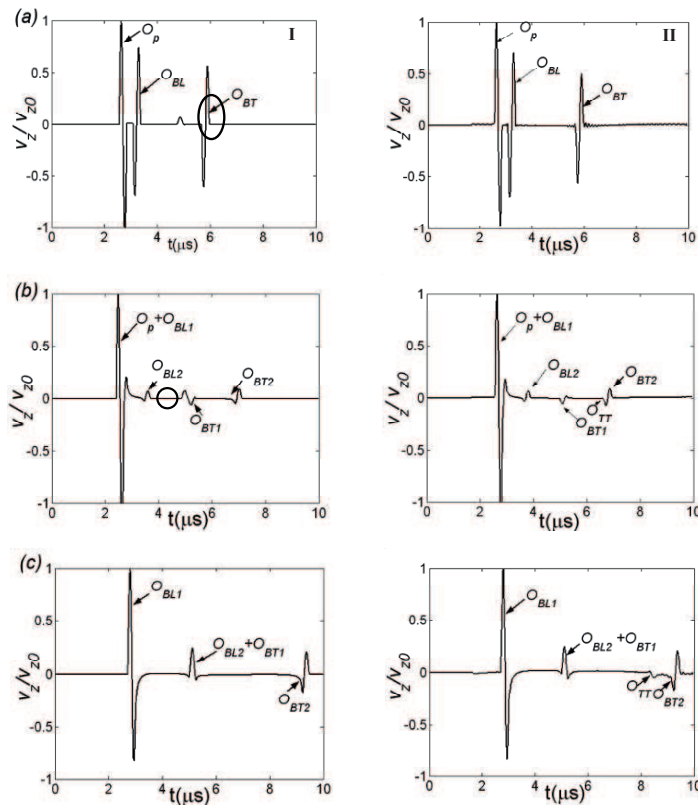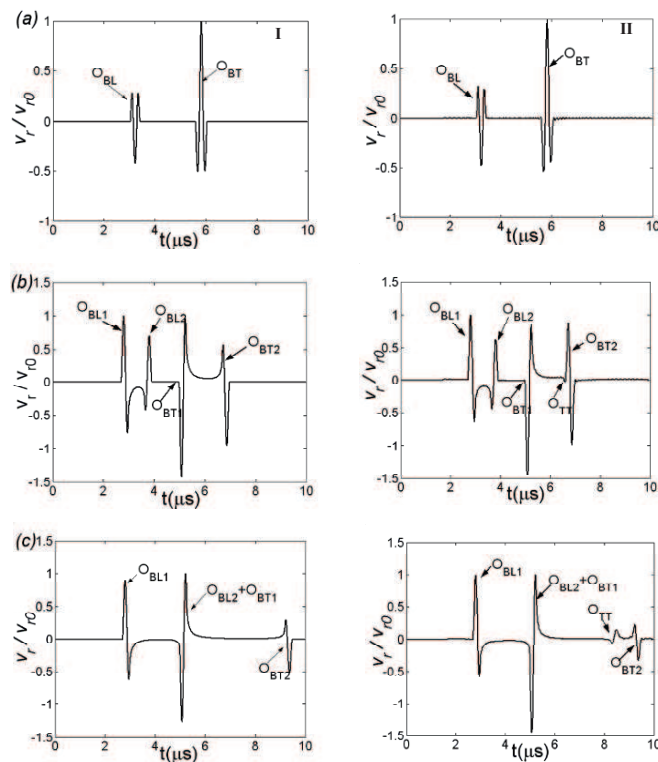

Fig. 2. The temporal variation of the radial components of the particle velocity by a circular transducer ($a = 10$ mm), at $z_0 = 15$ mm and (**a**) $r = 0$ mm, (**b**) $r = 5$ mm and (**c**) $r = 15$ mm

The first one is called "compressional edge wave" and the second one "transversal edge wave" (Fig. 2a). Note that the radial component of the particle

velocity is null on axis. At $r = 5$ mm, a radial component of the particle velocity consists of four visible pulses corresponding to two edge waves (longitudinal and transversal) respectively. For the region ($r > a$) and at $r = 15$ mm, one can notice an interference between the second edge longitudinal wave and the first edge transversal wave resulting from the nearest and farthest edge of the transducer respectively.

5. Discussion and conclusions

The objective of our work is to model the impulse ultrasonic field radiated in the isotropic solids in all points of the solid. In this order, the first step was to recall the theoretical bases of the propagation in an elastic medium and to choose the model which approaches reality and permits field calculation in a reasonable time. The great advantage of the Lhémery method remains the computation time (much less than one second on a personal computer for the two axial and radial components). Efficient calculation of the ultrasonic field can be included in a more general program of calculation to predict radiation, propagation and reception of the short pulses resulting from defects in solids.

Numerical calculations based on exact solutions are very tedious but allow the interpretation of physical phenomena and show all four types of waves propagating in the solid. The temporal variations of the velocity field predicted by Lhémery and those calculated by using the exact theory are overall in good agreement. According to the approximations made by Lhémery the ultrasonic field radiated close to the solid surface such Rayleigh and head waves are not revealed. This is not the case for the "exact" model. Lhémery model predicts the behaviour of the longitudinal and transversal volume waves. A small pulse arriving at instant t_0^t corresponding to a time of flight of a "shear plane wave" to the field point is observed. This shear wave has no physical explanation.

References

[1] Eason G (1966) The displacements produced in an elastic half space by a suddenly applied surface force. J Inst Maths Applics 2:299–326.
[2] Gakenheimer DC, Miklowitz J (1969) Transient excitation of an elastic half space by a point load travelling on the surface. J Appl Mech 36:505–515.
[3] Cagniard L (1939) Réflexion et réfraction des ondes séismiques progressives: Gauthiers-Villars, Paris.
[4] De Hoop (1956) AT A modification of Cagniard's method for solving seismic pulse problems. Appl Sci Res B8:349–356.
[5] Djelouah H, Baboux (1990) Transient ultrasonic field radiated by a circular transducer in a solid medium. J Acoust Soc Am 92:2932–2941.
[6] Miller GF, Pursey H (1954) The field and radiation impedance of mechanical radiators on the free surface of a semi-infinite isotropic. I: solid Proc R Soc, London, A223, pp 521–541.

[7] Lord Jr AE (1966) Geometric diffraction loss in longitudinal and shear-wave attenuation measurements in an isotropic half space. J Acoust Soc Am 39(4):650–662.

[8] Hutchins DA, Dewhurst RJ and Palmer SB (1981) Directivity patterns of Laser generated ultrasound in aluminium. J Acoust Soc Am 70(5):1362–1369.

[9] Kawashima K (1984) Quantitative calculation and measurement of longitudinal and transverse ultrasonic wave pulses in solid IEEE Trans Son & Ultras: SU-41(2).

[10] Gridin D, Fradkin LJ (1998) High-frequency asymptotic description of pulses radiated by a circular normal transducer into an elastic half-space. J Acoust Soc Am 104(6):3190–3198.

[11] Bresse LF, Hutchins DA (1989) Transient generation of elastic waves in solids by a disk-shaped normal force source. J Acoust Soc Am 86:810–817.

[12] Weight JP (1987) A model for the propagation of short pulse of ultrasound in a solid. J Acoust Soc Am 81:815–826.

[13] Gendreu P (1995) Étude des champs ultrasonores impulsionnels générés dans les liquides et les solides par des transducteurs piézo-composites: Application à la focalisation dans les solides : Barrettes de phase en contact. Thèse de Doctorat, Université Paris VII.

[14] Lhémery A (1994) A model for the transient ultrasonic field radiated by an arbitrary loading in a solid. J Acoust Soc Am 96(6):3776–3786.

[15] Stepanishen PR (1971) Transient radiation from pistons in an infinite planar baffle. J Acoust Soc Am 49(5):1629–1638.

[16] Ilan A, Weight JP (1990). The propagation of short pulses of ultrasound from a circular source coupled to an isotropic solid. J Acoust Soc Am 88:1142–1151.

[17] Laturelle (1989) Finite element analysis of wave propagation in an elastic half-space under step loading. Comput Struct 32:721–735.

Investigation of Ag Doping Effects on $Na_{1.5}Co_2O_4$ Elastic Parameters

Ibrahim Al-Suraihy, Abdellaziz Doghmane and Zahia Hadjoub

Laboratoire des Semi-Conducteurs, Université Badji-Mokhtar, BP12, Annaba 23000, Algérie

Abstract   In this work, we investigate elastic properties of intrinsic $Na_{1.5}Co_2O_4$ and Ag-doped $Na_{1.5}Co_{2-x}Ag_xO_4$ with $0 < x \leq 0.5$. Such properties, seldomly investigated, are very importance in many device applications and in fundamental understanding of inter-atomic forces and varying bonding structures. Hence, we first deduce the values of propagating surface acoustic wave velocities as well as bulk and Poisson ratio for intrinsic and doped structures. It was found that as Ag doping increases, longitudinal velocities vary form 4057 to 5620 m/s whereas shear velocities from 2338 to 3268 m/s. The calculated reflectance functions put into evidence that critical angles correspond to the excitation of longitudinal and Rayleigh modes depend on Ag doping. Moreover, the deduced acoustic materials signatures exhibited periodic behaviors; they were also shown to be very sensitive to the Ag addition that lead to an increase in Rayleigh velocities accompanied with an enhancement of the curves amplitude.

Keywords: Mechanical Properties, $Na_{1.5}Co_2O_4$, Acoustic Signatures, SAW Velocities, Doping Effects.

1. Introduction

Cobalt oxide systems are new materials which have recently attracted increased attention due to their superconductivity. The most promising synthesized sodium cobalt oxide $Na_xCo_2O_4$, formed out of oxide sheets (O_2 and Co atoms) having Na atoms in between, can be doped by the introduction of Ag atoms. The investigation of layered cobalt oxides concerns both solid-state physicists and chemists because of various unusual physical properties and their technologically important properties, such as fast-ion conduction for battery materials and large thermopower in thermo-electric coolers [1, 2]. In particular, unconventional superconductivity found in $Na_{0.35}CoO_{2\ 1.3}H_2O$ much stimulates our intellectual curiosity, because the origin of the superconductivity seems to be associated with rather unusual spin-triplet-type electron pairing with ferromagnetic spin-fluctuation [3, 4]. Another interesting property of $NaCo_2O_4$ is the relatively high carrier concentration in spite of being an oxide; oxides in general have been regarded as unsuitable for thermoelectric application because of their poor mobility. A large thermoelectric power is an important factor from the point of view of application of compounds to high-performance thermoelectric device. The physical properties of such materials have been widely studied but their elastic properties are poorly investigated despite

their great importance in many device applications and in fundamental understanding of inter-atomic forces and varying bonding structures. In this context, we investigate intrinsic $Na_{1.5}Co_2O_4$ and Ag-doped_$Na_{1.5}Co_{2-x}Ag_xO_4$ with $0 < x \leq 0.5$. We first deduce their mechanical properties such as bulk modulus, B, Poisson ratio, ν, as well as longitudinal and shear surface acoustic wave, SAW, velocities. Then calculate reflection coefficients as well as acoustic materials signatures for all intrinsic and doped materials. Finally, Rayleigh velocity on Ag doping is also reported.

2. Materials and methodology

2.1. Materials

Thermoelectric materials of $Na_{1.5}Co_{2-x}Ag_xO_4$ ($x = 0$, 0.1, 0.2, 0.3, 0.4, 0.5) were prepared from the powder precursors obtained from the polymerized complex (PC) method [5]. Figure 1 shows the schematic view of the oxygen network of the CoO_2 block in $NaCo_2O_4$. Edge-shared distorted octahedra (and Co in the center of them) form a triangular lattice. Na cations and CoO_2 blocks alternately stack along the c axis to make a layered structure. To study, nondestructively, the mechanical properties of these structures, the best method would be scanning acoustic microscopy, SAM, which distinguishes between modulation of the signal by the viscous properties of a material and its elastic properties. The first is represented by acoustic attenuation, the latter by the acoustic impedance. Deformation by the ultrasound waves is extremely small (in the subnanometer range). Hence, elastic properties of a variety of materials may be determined, qualitatively and/or quantitatively, via the scanning acoustic microscopy technique based on the emission and reflection of surface acoustic waves.
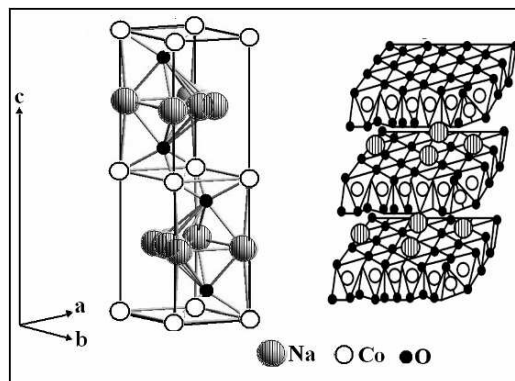
Fig. 1. Schematic representation of oxygen networks of CoO_2 block in $NaCo_2O_4$

2.2. Formulation of elastic parameters

Elastic properties of isotropic materials of density, ρ, can be expressed in term of independent parameters, shear modulus, G, Young's modulus, E, bulk modulus, B, and Poisson ratio, ν. These parameters can be determined by ultrasonic longitudinal sound velocity V_L and shear sound velocity V_S as follows:

$$G = \rho V_S^2 \tag{1}$$

$$E = \frac{G \cdot \left(3V_L^2 - 4V_S^2\right)}{V_L^2 - V_S^2} \tag{2}$$

$$B = \rho \cdot \left(V_L^2 - \frac{3}{4}V_S^2\right) \tag{3}$$

$$\upsilon = \frac{E}{2 \cdot \left(\rho V_S^2\right)} - 1 \tag{4}$$

2.3. Acoustic signatures

The most important property of quantitative scanning acoustic microscopy is the so-called $V(z)$ signatures. These acoustic signatures show the variation of the voltage, V, generated by an acoustic microscope as the distance, z, between the microscope lens and the specimen when the latter is displaced in the z direction towards the lens. $V(z)$ curves are used for measuring different properties of materials: evaluation of velocity and attenuation of surface waves [6, 7], measurement of coating thickness [8], anisotropy investigations [9, 10] crack detections [11] surface hardening measurement [12], determination of residual stress patterns in materials [13]. To better clarify the SAM instrumentation and principle, we illustrate its schematic diagram in Fig. 2 together with the ray trajectories in the system. The acoustic lens is located above the specimen while the coupling fluid ensures good SAW transmission in between. It is now well established [14, 15] that, after being reflected by the object, principally two types of rays can reach the transducer, which is mounted at the top of the lens rod. One type of rays is critically reflected rays, generally at Rayleigh angles, ray 1 in Fig. 2. This ray undergoes some horizontal shift. The second types are centrally reflected rays which strike the object vertically. Ray 2 comes back to lens after being reflected by the top surface of the specimen.

Then by keeping the lens and the sample at a fixed (x, y) position whereas translating the lens towards the object in the z direction; one observes a series of oscillations in the transducer output as a function of z. This is because the axial and Rayleigh rays that contribute to signal at the transducer will alternate between being in phase and out of phase.
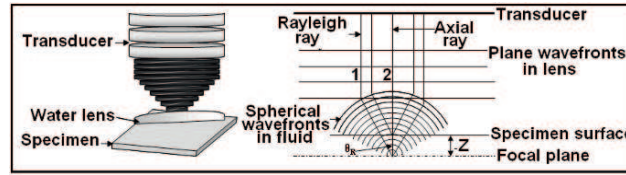
Fig. 2. Schematic diagram of the acoustic microscope experimental setup

The dependence of the variation of the signal output, V, on the defocus z can be modeled and expressed as [16]:

$$V(z) = \int_{0}^{\pi/2} R(\theta)P^2(\theta)e^{i2kz\cos\theta}\sin\theta\cos\theta \cdot d\theta \tag{5}$$

where θ is the angle between a wave vector (k) and the lens axis (z), $P(\theta)$ is the pupil function of the lens, and $R(\theta)$ is the reflection function of the specimen.

From the spatial period, Δz, of the resulting oscillations in $V(z)$, Rayleigh velocity, V_R, can be deduced [17]:

$$V_R = \frac{V_{Liq}}{\sqrt{1 - (^{1-V_{Liq}}\!/_{2f.\Delta z})^2}} \tag{6}$$

where, V_{Liq} is the velocity in the coupling fluid and f the operating frequency.

2.4. Reflectance function

The reflectance function, $R(\theta)$, which is a complex function admitting a modulus $|R|$ and a phase φ, is calculated by solving the acoustic Fresnel law and can be written in terms of the angles $\theta, \theta_L, \theta_S$ that the incident ray make with the normal to the surface [14, 15, 18, 19]; subscripts L and S stand for layer and substrate. It depends on the coupling liquids-isotropic solid boundary conditions (impedance Z, density, incidence angle θ and velocity of different wave modes).

$$R(\theta) = \frac{Z_L \cos^2 2\theta_S + Z_S \sin^2 2\theta_S - Z}{Z_L \cos^2 2\theta_S + Z_S \sin^2 2\theta_S + Z} \tag{7}$$

Moreover, the choice of the coupling liquid is an important point that has to be mentioned. Several characteristics are involved in the choice of the liquids studied as coupling fluids. The main factors are the velocity of the acoustic waves and their attenuation in the liquid, as well as the chemical reactivity of the liquid with the materials constituting the lens and the sample. The velocity of the longitudinal mode of acoustic waves in liquids increases with the interactions between molecules [20]. The choice of fast coupling fluids should be directed towards polar liquids. Water is one of the more polar solvents. In the present work, we used water as coupling liquid whose $V_L = 1,500$ m/s and $\rho = 1,000$ kg/m^3.

3. Results and discussions

3.1. Acoustic parameters

It should be stressed that only few results were reported on $Na_{1.5}Co_2O_4$ elastic properties; very recently Seetawan et al. [21] published some measured results of E and G of Ag doped material. In this work, making use of such results and relations 1 to 4, we first determine the whole set of acoustic parameters (ν, B, V_L and Vs) of doped $Na_{1.5}Co_{2-x}Ag_xO_4$ (with x = 0; 0.1; 0.2; 0.3; 0.4; 0.5). Summarised in Table 1 are the calculated values of Poisson ratio, bulk modulus, longitudinal and shear velocities. The effect of varying the Ag concentration is clearly observable due to density changes in the material structures as well as to atomic bounding. In fact, the microstructure of the non-doped sample is composed of significantly coarse grains about 10–20 μm in size and it leads to low density. On the other hand, the microstructure of the Ag-doped sample is composed of significantly fine grains and Ag particles around 10 μm in size that precipitate on the grain boundary and it leads to high density.

Table 1. Measured and calculated parameters of $Na_{1.5}Co_{2-x}Ag_xO_4$ with $0 < x \leq 0.5$

Sample composition	Experimental [21]			Calculated			
	ρ (kg/m^3)	E (GPa)	G (GPa)	ν	B (GPa)	V_L (m/s)	V_S(m/s)
$Na_{1.5}Co_2O_4$	3640	49.8	19.9	0.251	33.68	4057	2338
$Na_{1.5}Co_{1.9}Ag_{0.1}O_4$	3870	67.4	27.0	0.248	44.61	4564	2641
$Na_{1.5}Co_{1.8}Ag_{0.2}O_4$	4030	91.5	36.6	0.250	61.00	5220	3014
$Na_{1.5}Co_{1.7}Ag_{0.3}O_4$	4040	81.7	32.7	0.249	54.30	4923	2845
$Na_{1.5}Co_{1.5}Ag_{0.5}O_4$	4250	113	45.4	0.245	73.71	5620	3268

3.2. Ag-doping effects on |R(θ)|

As mentioned above the reflection coefficient is complex-valued function; therefore we separately calculate its amplitude (modulus) |R(θ)| and phase from Eq. 7 for waves incident on the structure: water half-space/$Na_{1.5}Co_{2-x}Ag_xO_4$. The results obtained for the amplitude are illustrated in Fig. 3 for undoped (x = 0) and other different Ag doping (0.1; 0.3; 0.4 and 0.5). It can clearly be noticed that, when the incident angle increases, all the curves exhibit similar behaviour: (i) a saturation, (ii) a sharp peak, (iii) another saturation, (iv) a smooth increase and (v) a final saturation with $|R| = 1$ corresponding to the case where no energy can be propagated. However, we also notice that as Ag doping increases several features can be observed:

Fig. 3. Amplitude of reflection coefficient as function of incident angle, with water coupling, of Ag-doped $Na_{1.5}Co_{2-x}Ag_xO_4$; (x = 0, 0.1, 0.3, 0.4 and 0.5)

   I.   The displacement of all these critical angles is towards lower values (with water coupling) when the amount Ag doping increases.

  II.   The value for zero angle of incidence θ = 0 varied by small amount from undoped compound. This small variation corresponds to the slight change in the crystal structure due to adding Ag.

 III.   The cusps near ($θ_L$ = 21°; 19°; 17.9°; 17.5° and 15.2°) where $|R|$ for all curves first rises to one, which corresponds to the longitudinal-wave critical angle of $Na_{1.5}Co_{2-x}Ag_xO_4$ (x = 0; 0.1; 0.3; 0.4 and 0.5) respectively.

 IV.   The kink near ($θ_S$ = 38.5°; 34°; 31.2°; 30° and 27.2°) where the value of $|R|$ next rises to one, which corresponds to the shear-wave critical angle for $Na_{1.5}Co_{2-x}Ag_xO_4$; (x = 0; 0.1; 0.3; 0.4 and 0.5) respectively.

  V.   The constancy near ($θ_R$ = 40.5°; 35°; 32.3°; 31° and 28°) just past the kink, which corresponds to the Rayleigh-wave critical angle for water-$Na_{1.5}Co_{2-x}Ag_xO_4$; (x = 0; 0.1; 0.3; 0.4 and 0.5) respectively.

3.3. Ag-doping effects on R(θ) phase

The phase of reflection coefficient is illustrated in Fig. 4 as a function of incident angles for water/$Na_{1.5}Co_{2-x}Ag_xO_4$; at different Ag doping levels (x = 0; 0.1; 0.3; 0.4 and 0.5).

The phase of R(θ), experiences several small fluctuations around the longitudinal critical angle ($\theta_L = 21°$ to $15.2°$), but its most dramatic behavior (a 2π transition) occurs around the Rayleigh-wave critical angle ($\theta_R = 40.5$ to $28°$). The deduced variations of critical angles (θ_L and θ_R) with Ag doping are regrouped in Table 2 whose analysis confirms all the above behaviors obtained with amplitude $|R|$.
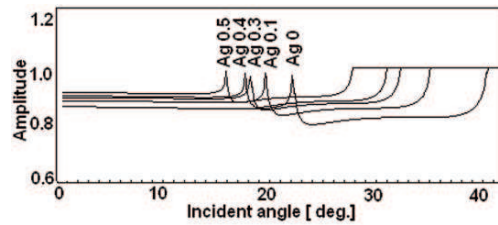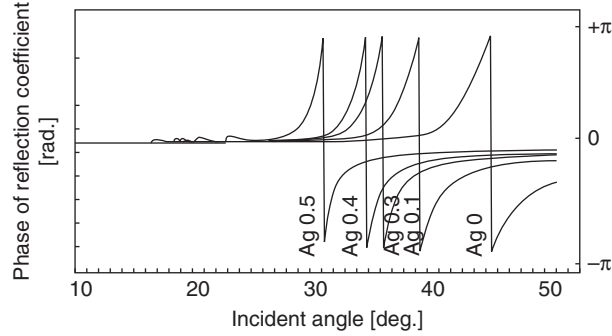

Fig. 4. Phase of reflection coefficient as function of incident angle, with water coupling, of Ag-doped Na$_{1.5}$Co$_{2-x}$Ag$_x$O$_4$; ($x = 0$; 0.1; 0.3; 0.4 and 0.5)

Table 2. Deduced critical angels and velocities of longitudinal and Rayleigh modes for different Ag-doping in Na$_{1.5}$Co$_{2-x}$Ag$_x$O$_4$

x	0	0.1	0.3	0.4	0.5
θ_L [deg.]	21	19	17.9	17.5	15.2
θ_R [deg.]	40.5	35	32.3	31	28
V_L [m/s]	4045	4558	5193	4911	5036
V_R [m/s]	2217	2402	2633	2698	3009

3.4. Doping effects on V(z) curves

Acoustic signatures, or V(z), can be either measured experimentally or determined theoretically. In the present investigation, we considered the latter case via the application of Eq. 5 deduced by the angular spectrum model [16].

In Fig. 5, we illustrate the calculated acoustic signatures for a 50° lens opening angle, a frequency of 140 MHz and water coupling. It can be seen that there are strong oscillations, where a series of periodic maxima and minima occurs, characterized by a period $\Delta(z)$.

This region is characteristic of the sample's acoustic properties. The patterns vary with the material doping, as do the depths of the minima and the relative magnitude of the maxima which on Ag doping as well.
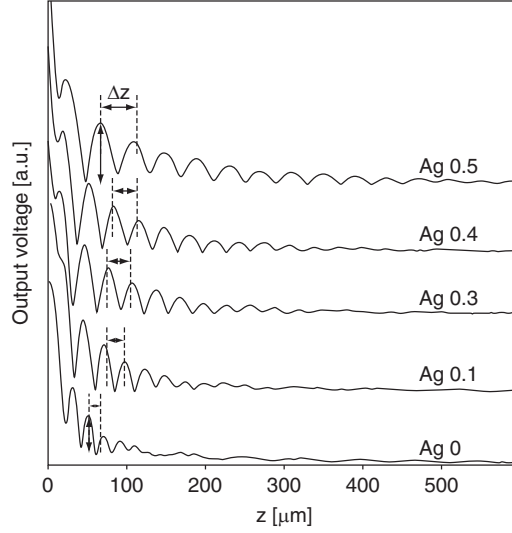
Fig. 5. V(z) of Ag-doped $Na_{1.5}Co_{2-x}Ag_xO_4$ (x = 0; 0.1; 0.3; 0.4 and 0.5)

3.5. Analysis of V(z) curves

To analyze and quantify acoustic signature of Fig. 5, we first subtract the effect of the acoustic lens signal from these curves to obtain the real material signatures as shown in Fig 6a. Then, these periodic signals can be quantified through fast Fourier transform (FFT), a spectral method used in numerical signal processing. Figure 6b displays the obtained spectra; it clearly puts into evidence the evolution of the shape of the FFF curves, deduced from the acoustic signature of the $Na_{1.5}Co_{2-x}Ag_xO_4$ with $0 < x \leq 0.5$ and its related attenuation of the propagation mode.
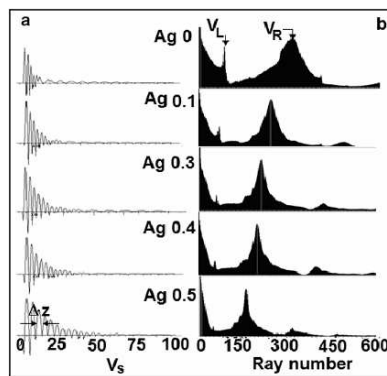
Fig. 6. Analysis of acoustic signatures plotted in Fig. 5

The peak corresponding to the longitudinal mode appears for all Ag doping concentration. The magnitude of V$_L$ peaks is weakened with increase of the doping amount. The Rayleigh mode, V$_R$, merges in a single widened peak. As a consequence; the velocity V$_R$ of the Rayleigh mode is obtained and moved to the lower value of ray number which means that V$_R$ increase with increase Ag.

3.6. Doping effects on velocities

Since, under the present simulation conditions, Rayleigh mode dominates all other types of propagating surface acoustic waves. From Eq. (6) we were able to deduce the dependence of Rayleigh velocities, V$_R$, of Na$_{1.5}$Co$_{2-x}$Ag$_x$O$_4$. After FFT analysis, it was found that (see Table 2, last two lines) as the doping amount increases from 0 to 0.5 the Rayleigh velocities vary form 2,217 m/s to 3,009 m/s; similarly longitudinal velocities vary form 4,045 m/s to 5,591 m/s. Hence, all investigated acoustic parameters (Young's and shear moduli as well as longitudinal, shear and Rayleigh velocities) exhibit an identical increase with additional Ag doping.

4. Conclusions

Elastic properties of intrinsic and Ag doped Na$_{1.5}$Co$_{2-x}$Ag$_x$O$_4$ with $0 < x \leq 0.5$ were deduced. The parameters of the former case were found to be B = 19.9 GPa, $\nu = 0.251$, $V_L = 4057$ m/s, $V_S = 2338$ m/s and $V_R = 2217$ m/s. Whereas, it was shown that the introduction of Ag doping atoms lead to some variations in the above parameters. These variations are the result of the microstructure of the Ag-doped sample that is composed of significantly fine grains and Ag particles that precipitate on the grain boundary. Moreover, these changes were also put into evidence via the calculation of reflectance function and acoustic signatures.

References

[1] Braconnier J J, Delmas C, Fouassier C, Haggenmuller P (1980) Comportement électro-chimique des phases Na$_x$CoO$_2$. Mat Res Bull 15: 1797–1804.

[2] Terasaki I, Sasago Y, Uchinokura K (1997). Large thermoelectric power of NaCo$_2$O$_4$ single crystals. Phys Rev B 56: 12685–12687.

[3] Chen D P, Chen H C, Maljuk A, Kulakov A, Zhang H, Lemmens P, Lin C T (2004) Single crystal growth and investigation of Na$_x$CoO$_2$ and Na$_x$CoO$_2$ $_v$H$_2$O. Phys Rev B 70: 024506.

[4] Singh D J, (2003) Quantum critical behavior and possible triplet superconductivity in electron-doped CoO$_2$ sheets. Phys Rev B 68: 020503.

[5] Seetawan T, Amornkitbamrung V, Burinprakhon T, Maensiri S, Kurosaki K, Mutab H, Unob M, Yamanaka S (2006) Thermoelectric power and electrical resistivity of Ag-doped Na$_{1.5}$Co$_2$O$_4$. J Alloys Compd 407: 314–317.

[6] Kushibiki J, Ohkubo A., Chubachi N (1982) Effect of leaky SAW parameters on V(z) curves obtained by acoustic microscopy. Electron Lett 18: 668–670.

[7] Bouhedja S, Hadjoub I, Doghmane A, Hadjoub Z (2005) Investigation of Rayleigh wave attenuation via annular lenses in acoustic microscopy. Physical Status Solidi a, 202: 1025–1032.

[8] Weglein R D, Mal A K (1991) Elastic characterization of diamond films by acoustic microscopy. Surf Coating Tech 47: 677–686.

[9] Kushibiki J, Ohkubo A, Chubachi N (1982) Material characterization by acoustic line-focus beam. Acoust Imaging Plenum Press, New York. 12: 101–111.

[10] Gomez-Moralez J, Rodrigues R, Durand J, Ferdj-Allah H, Hadjoub, Attal J , Doghmane A (1991), Characterisation and identification of berlinite crystals by acoustic microscopy. J Mater Sci 6: 2448–2489.

[11] Daft C M W, Weaver J M, Briggs G A (1985) Phase contrast imaging of tissue in the scanning acoustic microscope. J Microscopy 139: RP3–RP4.

[12] Yamanaka K, Enomoto Y, Tsuya Y (1982), Application of accoustic microscope to the study of fracture and wear. Acoust Imaging Plenum Press, New York.12: 79–87.

[13] Liang K, Khuri-yakub B T, Bennett S D, Kino G S (1983) Phase measurements in acoustic microscopy. Proc Ultrasonics Symp 2: 591–604.

[14] Briggs A (1992) Acoustic Microscopy. Clarendon : Oxford.

[15] Yu Z, (1995) Scanning acoustic microscopy and its applications to material characterization. Rev Mod Phys 67: 863–891.

[16] Sheppard C J R, Wilson T (1981) Effects of high angles of convergence on V(z) in the scanning acoustic microscopy. Appl Phys Lett 38: 858–859.

[17] Kushibiki J, Chubachi N (1985) Material characterization by line focus-beam acoustic microscope. IEEE Trans Sonics Ultrason 32:189–212.

[18] Doghmane A, Hadjoub Z (1997) Theoretical and experimental investigation of acoustic signatures of materials using scanning microscopes with variable lens illumination. J Phys D Appl Phys 30: 2777–2782.

[19] Beldi I, Hadioub Z, Doghmane A (2008) Etude de la Réflexion des ondes acoustiques de surface aux Interfaces dans le Système Liquide/Couche Mince/Substrat. Phys Chem News 41: 30–35.

[20] Cros B, Gigot V Despaux G (1997) study of the coupling fluids for acoustic microscopy. Appl Surf Sci 119: 242–252.

[21] Seetawan T, Amornkitbamrung V, Burinprakhon T, Maensiri S, Kurosaki K, Mutab H, Unob M, Yamanaka S (2005) Mechanical properties of Ag-doped $Na_{1.5}Co_2O_4$. J Alloys Compd 403: 308–311.

The Dynamics of Compressible Herschel–Bulkley Fluids in Die-Swell Flows

F. Belblidia[1], T. Haroon[2] and M.F. Webster[1]

[1]Institute of non-Newtonian Fluid Mechanics, School of Engineering, Swansea University, Singleton Park, Swansea, SA2 8PP, UK

[2]Visiting researcher, COMSATS Institute of Information Technology, Abbottabad, Pakistan

Abstract   In a variety of industrial applications, modelling compressible inelastic free-surface flows remains a numerical challenge. This is largely due to the physical phenomena involved and the computational cost associated with the simulations of such flows. In particular, the die-swell benchmark problem is characterised by specific features. These are related to the presence of a sharp separation point at the die-exit, the location and the shape of the free-surface, and additionally the consideration of fluid compressibility under various forms of material modelling. In this article, a time-marching pressure-correction scheme is considered to solve both incompressible and compressible inelastic flows. This is achieved via a pressure-based approach within a finite element framework employing efficient high-order time-stepping schemes. A Tait-type model is utilised to express the equation of state that links density to pressure, so that pressure is retained as a primary variable. Various material models are considered in this numerical study for the die-swell problem, where the material rheological characteristics have a direct impact upon the location and form of the free-surface. Initially, unyielded material is considered through Newtonian and power-law assumptions. Further complication is then introduced through the Bingham model, where fluid yield stress is taken into account. More general rheological modelling is constructed via the Herschel–Bulkley model, combining inelastic behaviour with yield stress presence. This is complimented by relaxing incompressible assumptions, allowing the effects of compressibility to enter the problem. Results are presented for steady and transient flow scenarios and numerical solutions are validated against published data. There is Focus upon on the effect of variation in compressibility parameter setting, inertia level, power-law index and yield stress level, with regard to the evolving shape/location of the free-surface and the response in extrudate swell. Extrudate swell is observed to decline with decrease in power-law index. With increase in Reynolds number, extrudate swell decreases before finally reaching a plateau at high Reynolds number, in agreement with experimental results. Swelling also decreases with rise in yield stress levels. The combination of these parameters within the compressible Herschel–Bulkley model renders it difficult to predict, a priori, the outcome in terms of die-swell behaviour.

Keywords: Die-Swell, Inelastic, Power-Law, Bingham, Herschel–Bulkley Model, Yield Stress.

1. Introduction

Nowadays, extruded materials include metals, ceramics, polymers, paints, coatings and food products. Much research has focused attention on low-pressure, high-flow

extrusion processes in an effort to better understand and prevent interfacial instabilities. The die-swell problem naturally introduces free surface modelling, provocative transient evolution states, material rheology and influence of compressibility. In spite of a variety of industrial applications, modelling compressible free surface flows itself remains a numerical challenge, largely due to the physical phenomena involved. For example, the *free surface* of the jet introduces mixed-type boundary conditions on the flow. Various slip (velocity) conditions may be pertinent on the tube wall, while the jet itself supports traction (or stress) boundary conditions. This local and sudden change in the type of boundary conditions will generate a singular stress field, accompanied with steep velocity gradients. There are many approaches to treat free surface computations, such as the volume of fluid technique (VOF), marker and cell method (MAC) and the arbitrary Lagrangian Eulerian (ALE) scheme. Most studies have assumed incompressible flow and unyielded material through Newtonian or power-law model. A yield stress response may be adapted through the Bingham model, or with inelastic effects, through the Herschel–Bulkley model. To date, the extrusion problem has attracted much interest within the literature. Beverly and Tanner [1] analysed the effects of yield stress on extrudate swell in a tube, and found that yield stress inclusion reduced the degree of swell. Mitsoulis and co-workers [2] studied entry and exit flows of Bingham fluids, observing the presence of unyielded regions within the flow. Compressible viscoelastic domain remains relatively uncharted in the literature, Georgiou [3] has addressed non-Newtonian inelastic fluid modelling for compressible flows, expressing interest in slip effects. In addition, compressible flow computations were covered by Webster and co-workers [4, 5].

2. Governing equations

For compressible Newtonian fluid flow under isothermal setting, the governing equations may be expressed in non-dimensional form as:

$$\frac{\partial \rho}{\partial t} + \nabla \cdot (\rho\, u) = 0 \tag{1}$$

$$\mathrm{Re}\,\frac{\partial u}{\partial t} = \nabla \cdot t - \mathrm{Re}\, u \cdot \nabla u - \nabla p \tag{2}$$

where field variables are ρ, u, τ, p, for density, velocity, stress and pressure, respectively. $\mathrm{Re} = \rho_0\, U \cdot l / \mu_0$ represents the conventional dimensionless Reynolds number.

Stress is related to field kinematics through a constitutive law, which is defined for compressible Newtonian fluids as:

$$\tau_{ij} = \mu\left(d_{ij} - 2/3\left(\nabla \cdot u\right)\delta_{ij}\right) \tag{3}$$

where μ is the viscosity (constant or function of shear-rate, see on), δ_{ij} is the Kronecker tensor, $2d = \nabla u + \nabla u^T$ is the rate of deformation tensor, and the 2/3 term vanishes under incompressible assumptions. Further equations are necessary (see below), relating to free surface computation, material modelling and compressibility considerations.

2.1. Compressibility considerations

Under compressible flow settings, the modified two-parameter (B,m) Tait equation [6], is considered to relate density to pressure. Thus,

$$\left(p + B\right)/B = \rho^m \tag{4}$$

By differentiating the equation of state, one gathers [4]:

$$\frac{\partial p}{\partial \rho} = \frac{m \cdot \left(p + B\right)}{\rho} = c_{(x,t)}^2 \tag{5}$$

where $c_{(x,t)}$ is the derived speed of sound. Such dependencies have influence upon transient evolution.

2.2. Free surface considerations

Under the extrusion flow problem, no-slip boundary conditions are assumed along the wall, and free kinematic conditions on the free surface. This generates a singular stress field at the die-exit. On the free surface, zero normal velocity, zero shear stress and normal stress are set. We appeal to the evolving free surface equation:

$$\frac{\partial h}{\partial t} = u_r - \upsilon_z \frac{\partial h}{\partial z} \tag{6}$$

where $u = \left(u_r,\, v_z\right) = \left(\partial r / \partial t,\, \partial z/\partial t\right)$ is the velocity vector and $h = h(x,t)$ is the radial height. The die-swell ratio is defined as $\chi = h_f / h_0$, where h_f and h_0 are the final extrudate radius and die radius, respectively (see Fig. 1).

An ALE-technique is performed to radially adjust mesh.

2.3. Material modelling considerations

The so-called 'yield stress τ_0' (first introduced by [7]), governs the transition from solid-like to liquid-like response. It is the presence of yielded and unyielded regions across the domain, which provides the intrinsic discontinuity within the model. To overcome this deficiency, several modifications have been proposed (see on). The power-law model allows for a degree of deviation from Newtonian behaviour ($n = 1$). Thus, shear-thinning is observed for $n < 1$, and $n > 1$ corresponds to shear-thickening. The generalised Herschel–Bulkley (HB) model provides further rheological richness, incorporating both power-law type and Bingham type.

2.4. Flow equations

For non-Newtonian fluids, the viscosity is considered as a nonlinear function of the second invariant (Π_d) of the rate-of-strain tensor (d_{ij}), which modifies (3) accordingly. A Bingham material remains rigid when the shear-stress is below the yield stress τ_0, but flows like a Newtonian fluid when the shear-stress exceeds τ_0:

$$\tau = \left(\mu + \frac{\tau_0}{2|\Pi_d|^{\frac{1}{2}}} \right) \cdot \dot{\gamma} \ \text{ for } |\Pi_\tau| > \tau_0^2 \text{ ; and } \dot{\gamma} = 0 \ \text{ for } |\Pi_\tau| \le \tau_0^2 \quad (7)$$

Papanastasiou [8] proposed a modified Bingham model, by introducing a regularisation stress growth exponent (m) to control the rate-of-rise in stress, in the form:

$$\tau = \left(\mu + \tau_0 \frac{1 - e^{-m|\Pi_d|}}{2|\Pi_d|^{\frac{1}{2}}} \right) \cdot \dot{\gamma} \qquad (8)$$

Other rheological derivations to accommodate for shear characteristics, may be considered through power-law model:

$$\tau = \left(k \cdot |\dot{\gamma}|^{n-1} \right) \cdot \dot{\gamma} \qquad (9)$$

where k is the consistency parameter.

It is the Herschel–Bulkley (HB) model that incorporates both a yield stress and shear behaviour. To address the shortcoming of infinite apparent viscosity at vanishing shear-rates, Mitsoulis [9], Alexandrou et al. [10] introduced the modified HB-model, viz:

$$\tau = \left(k\, \Pi_d^{\frac{n-1}{2}} + \tau_0 \frac{1-e^{-m|\Pi_d|}}{|\Pi_d|^{\frac{1}{2}}} \right) \text{ for } |\Pi_\tau| > \tau_0^2 \text{ ; and } \dot{\gamma} = 0 \text{ for } |\Pi_\tau| \le \tau_0^2 \quad (10)$$

3. Numerical discretisation

A time fractional-staged Taylor-Galerkin incremental pressure-correction (TGPC) framework is considered (see [4, 5] for derivation). The *first phase* involves a predictor-corrector doublet (Lax-Wendroff) for velocity and stress. The *second phase* is a pressure-correction scheme that ensures second-order accuracy in time. A *third phase* recaptures the velocity field at the end-of-time step loop. Triangular tessellation is employed based on a quadratic velocity and linear pressure interpolations. For density, a piecewise-constant interpolation is employed, with recovered density gradients, over an element. The discrete compressible TGPC may be expressed via Eqs. (11–14). Note, the equations for compressible and incompressible flows differences appear mainly under the continuity equation (13).

Stage 1a :

$$\left[\frac{M_\rho}{\Delta t/2} + \frac{1}{2} S_u \right]\left(\Delta U^{n+\frac{1}{2}} \right) = -\left[S_u U + N_\rho(U)U - L^{\mathrm{T}}\left\{ P^n + \theta_1\left(P^n - P^{n-1} \right) \right\}P \right]^n \quad (11)$$

Stage 1b :

$$\left[\frac{M_\rho}{\Delta t} + \frac{1}{2} S_u \right]\left(\Delta U^* \right) = -\left[S_u U - L^{\mathrm{T}}\left\{ P^n + \theta_1\left(P^n - P^{n-1} \right) \right\}P \right]^n - \left[N_\rho(U)U \right]^{n+\frac{1}{2}} \quad (12)$$

Stage 2 :

$$\left[\frac{M_C}{\Delta t^2} + \theta \cdot K \right]\left(\Delta P^{n+1} \right) = -\frac{1}{\Delta t} L_P \cdot U^* \quad (13)$$

Stage 3 :

$$\frac{M_\rho}{\Delta t}\left(U^{n+1} - U^* \right) = \theta\, L^{\mathrm{T}}\left(P^{n+1} - P^n \right) \quad (14)$$

4. Numerical results and discussion

Our approach is to start by analysing an incompressible Newtonian fluid and then systematically introduce further complexity through inertia, compressibility, genera-lised Newtonian and HB representation. The capillary radius is held constant (unity) and only half of the die-swell domain is analysed (symmetry). Applied boundary conditions and die-swell dimensions are supplied in Fig. 1.
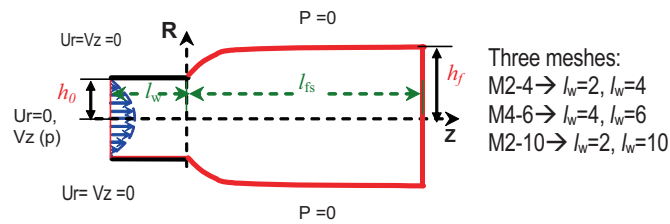
Fig. 1. Die-swell schema

4.1. Newtonian case

4.1.1. Effect of die-swell design and mesh consistency analysis

Effects of mesh refinement, extrudate length and capillary length on the swelling ratio are analysed. During the transient development, one observes a common maximum swelling at the same location followed by different swelling ratio steps in the jet, being larger with longer jet-lengths.

Once a steady development is achieved, swelling height reaches the ratio of 1.13, independent of the level of refinement used. The transient pressure response is achieved instantaneously, following a linear development trend in pressure-drop.

4.1.2. Effect of inertia

A generally accepted finding is that under incompressible assumptions, the jet swelling reduces as inertia (Re) increases, see Georgiou and co-workers [11]. This is clearly illustrated in Fig. 2, when based on mesh M2-4, we detect two distinct regions: below Re = 7.5, there is expansion through jet swelling, whilst, above this Re-level, we observe compression of the jet, reaching a plateau of $\chi = 0.91$ at larger levels of Re > 40. There is a clear evidence of pressure-drop reduction as Re-increases.

4.1.3. Influence of compressibility

For Newtonian fluids and various compressible settings (Ma = 0.0 to Ma_{max} = 0.55), the free surface shape and extrudate swell-ratio are insignificantly affected by the three proposed die-swell designs and mesh refinements. This fact was also highlighted by Georgiou [12]. This is mainly due to the imposition of no-slip boundary conditions on the wall. Detailed analysis of various slip conditions is the subject of a future study.
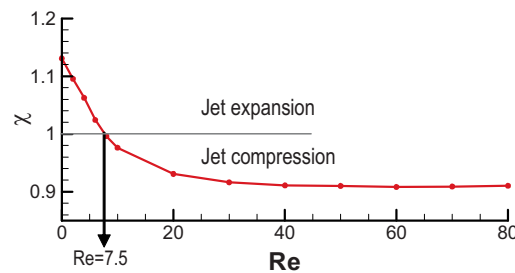
Fig. 2. Inertial effect on jet swelling; incompressible, Newtonian

4.2. Inelastic power-law representation

4.2.1. Effect of power-index (n)

The variation of swelling ratio with power-index is depicted in Fig. 3. , under $k = 1.0$. Here, a longer channel length (M4-6) is selected to allow for the full development of the velocity profile from its parabolic inlet state. In agreement with Mitsoulis [13] findings, the general trend is that die-swell increases with the increase of power-law index n, except in the range $0 < n < 0.2$, where a slight contraction or negative swell is observed.
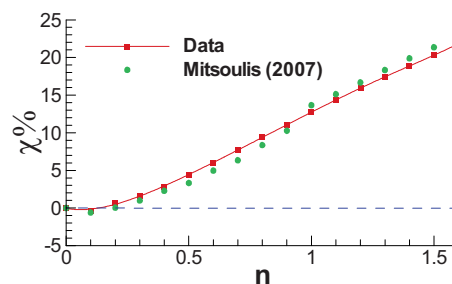
Fig. 3. Die-swell as a function of power-law index n for the power-law model

4.3. Viscoplasticity-Bingham yield stress

We analyse the effect of yield stress on the flow based on the modified Bingham model. The (χ)-response against Bn is shown in Fig. 4.
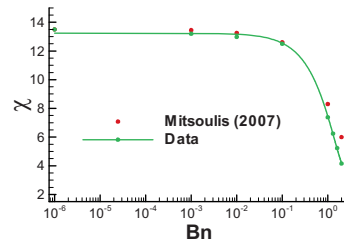
Fig. 4. Swelling ratio as function of yield stress with modified Bingham model

We observe a substantial decrease of swelling for levels of yield stress above 0.1, whilst there is a sustained plateau in swelling for *Bn* below 0.01, as in [13]. Similarly, the pressure-drop increase with increased yield stress, as the increase is more pronounce for *Bn* > 0.1, whilst, pressure remains relatively constant over the low *Bn*-range.

4.4. Herschel–Bulkley modelling

Swelling under the HB-model is governed by the variation of both power-law index *n* and yield stress τ_0. At steady-state, the swelling under $n = 0.9$ and $\tau_0 = 0.1$ reaches a level of $\chi = 1.1$, as already observed under power-law modelling (Fig. 3). This position is not affected by the yield stress level over this plateau range of *Bn*-value (see Fig. 4). Steady-state shear-rate and viscosity contour plots for *n*=0.9 and two levels of *Bn*=10^{-3} and 10^{-1} are depicted in Fig. 5. The shear-rate contours are similar for both levels of yield stress, whilst there is a clear increase in the maximum viscosity attained at larger τ_0 applied.
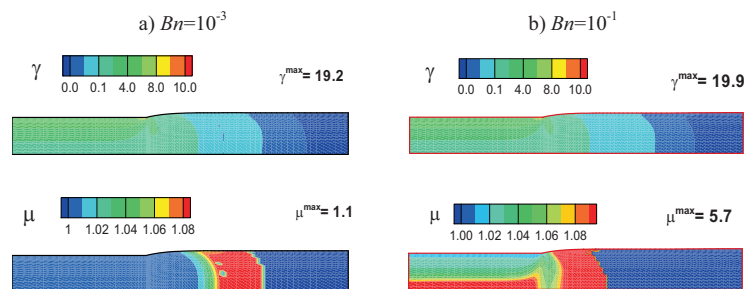
Fig. 5. Shear-rate and viscosity contours for a) *Bn* = 0.001 and b) *Bn* = 0.1

5. Conclusions

The die-swell benchmark problem naturally introduces free surface modelling, sharp separation point at the die-exit, provocative transient evolution states and material modelling. Focus is placed on the jet shape dynamic evolution and the free surface location. Steady and transient flow situations are presented under incompressible and compressible assumptions, with findings validated against recent published data. Initially, unyielded material is considered through Newtonian and power-law assumptions. Further complication is then introduced through the Bingham model, where fluid yield stress is taken into account. Subsequently, a more rheological generalisation is built via the Herschel–Bulkley model.

The study demonstrated that extrudate swell is unaltered by compressibility considerations under no-slip wall conditions. However, it is expected that this position will be altered under slip-wall settings. The swelling is observed to decline with decrease in power-law index. Swelling also decreases with rise in yield stress levels. Therefore, predictions remain difficult, a priori, under the parameters combination within the Herschel–Bulkley model. Further challenges posed will be elevated from its generalised Herschel–Bulkley model, to a novel visco-elasto-plastic material modelling, permitting a direct comparison across regimes for compressible representation, ranging from viscoplastic, to viscoelastic, to visco-elasto-plastic alternatives.

References

[1] C.R. Beverly and R.I. Tanner. Numerical Analysis of Extrudate Swell in Viscoelastic Materials with Yield Stress. *J. Rheol.* 33 (1989) 989–1009.

[2] S.S. Abdali, E. Mitsoulis and N.C. Markatos. Entry and exit flows of Bingham fluids. *J. Rheol.* 36 (1992) 389–407.

[3] G.C. Georgiou. The time-dependent, compressible Poiseuille and extrudate-swell flows of a Carreau fluid with slip at the wall. *J. Non-Newt. Fluid Mech.* 109 (2003) 93–114.

[4] M.F. Webster, I.J. Keshtiban and F. Belblidia. Computation of weakly-compressible highly-viscous liquid flows. *Eng. Comput.* 21 (2004) 777–804.

[5] I.J. Keshtiban, F. Belblidia and M.F. Webster. Numerical simulation of compressible viscoelastic liquids. *J. Non-Newt. Fluid Mech.* 122 (2004) 131–146.

[6] P.G. Tait, Physics and Chemistry of the Voyage of H.M.S. Challenger, 2, Part IV (1888), HMSO, London, England.

[7] E.C. Bingham. Fluidity and Plasticity. McGraw-Hill, New York, 1922.

[8] T.C. Papanastasiou. Flows of materials with yield. *J. Rheol.* 31 (1987) 385–404.

[9] E. Mitsoulis. Numerical simulation of planar entry flow for a polysobutylene solution using an integral constitutive equation. *J. Rheol.* 37 (1993) 1029–1040.

[10] A.N. Alexandrou, T.M. McGilvreay and G. Burgos. Steady Herschel–Bulkley fluid flow in three-dimensional expansions. *J. Non-Newt. Fluid Mech.* 100 (2001) 77–96.

[11] E. Taliadorou, G.C. Georgiou and E. Mitsoulis. Numerical simulation of the extrusion of strongly compressible Newtonian liquids. *Rheol. Acta* 47 (2008).
[12] G.C. Georgiou. The compressible Newtonian extrudate swell problem. *Int. J. Num. Meth. Fluids* 20 (1995) 255–261.
[13] E. Mitsoulis. Annular extrudate swell of pseudoplastic and viscoplastic fluids. *J. Non-Newt. Fluid Mech.* 141 (2007) 138–147.

Numerical Simulation of the Behaviour of Cracks in Axisymmetric Structures by the Dual Boundary Element Method

N. Amoura[1], H. Kebir[2], S. Rechak[3] and J.M. Roelandt[2]

[1]Mechanical Department, Centre Universitaire de Médéa, 26001, Algeria

[2]Roberval laboratory, UMR UTC/CNRS 6253, BP 20529, 60205 Compiègne, France

[3]LGMD laboratory, ENP, 10 H. Badi 16200 EL-Harrach, Algeria

Abstract   The study of defected axisymmetric structures is among important industrial applications. Detection of such defects, and or the evaluation of intrinsic parameter leads to a better design of those mechanical parts. The first part of the conducting research concerns the evaluation of the stress intensity factors (SIF) in axisymmetric elastic structures with internal or circumferential edge crack using the dual boundary element method (DBEM). Its application to axisymmetric problems requires a stress (hypersingular) boundary integral equation together with the displacement (standard) boundary integral equation, one applied to each side of the crack. This process requires a great algebraic handling due to the complexity of the axisymmetric kernels. Crack surfaces are discretized with discontinuous quadratic boundary elements to satisfy the existence of the finite-part integrals and the continuity of the unit outward normal at corners. SIF evaluation is done using displacements extrapolation at the crack tip. Examples of axisymmetric geometries are analyzed and obtained results are compared to others researchers.

Keywords: Boundary Element Method, Cauchy Principal Value, Hadamard Finite-Part, Fracture Mechanics, Hypersingular Integrals, Linear Elasticity.

1. Introduction

The boundary element method has been successfully applied to axisymmetric elasticity during several years, starting with the works of Kermanidis [1], Mayr [2] and Cruse et al. [3]. Dual integral equations were introduced by Watson [4], in a formulation based on the normal derivative of the displacement equation in plain strain. Hong and Chen [5] presented a general formulation, which incorporates the displacement and the traction boundary integral equations. An effective numerical implementation of the two dimensional DBEM for solving general linear elastic fracture mechanics problems with finite-parts defined was presented by Portela et al. [6]. An axisymmetric hypersingular boundary integral formulation for elasticity problems was developed in De Lacerda and Wrobel [7, 8]. Hypersingular boundary integral equations (HBIE) are derived from a differentiated version of the standard BIE, considering the asymptotic behaviour of their singular and hypersingular

kernels with evaluation of stress intensity factors in, and propagation of cracks inside cylinder. The strongly singular and hypersingular equations in this formulation are regularized by De Lacerda and Wrobel by employing the singularity subtraction technique. Mukherjee [9] has revisited the same problem and interpreted the HBIE in a finite part sense [10]. The DBEM is a well-established method for the analysis of crack problems [11–14]. Its application to axisymmetric geometries requires the use of the stress boundary integral equation together with the displacement boundary integral equation.

2. Standard and hypersingular boundary integral equations for axisymmetric elastic solid

Axisymmetric geometry is obtained by a 2π rotation of a two-dimensional body about z-axis. Under an axisymmetric loading, displacements and stresses are independent of the hoop direction. As consequence of this axisymmetry, a 3-D domain is reduced to a 2-D one, and directions r and z are sufficient to define the problem. In the absence of body forces, the axisymmetric elasticity equation for an internal point of a linear elastic solid Ω with boundary Γ has the following form:

$$u_i(P) = \int_\Gamma \alpha(Q) U_{ij} \cdot (P,Q) t_j(Q) d\Gamma - \int_\Gamma \alpha(Q) T_{ij} \cdot (P,Q) u_j(Q) d\Gamma \qquad (1)$$

With i, j= r, z, $\alpha(Q)=2\pi r(Q)$.

P is the internal source point where the ring unit load is applied; Q is the integrating field point. r(Q): is the radial distance from the field point to the axis of symmetry and u_r, u_z and t_r, t_z are the radial and axial displacements and tractions respectively. U_{ij} and T_{ij} are the axisymmetric displacement and traction kernels, which are functions of the complete elliptic integrals of the first and second kind K and E [15]. Details on the singular behaviour of U and T are presented in reference [7]. When the source point is on Γ and out of the axis of symmetry, U is a combination of regular and weak-singular (O $\ln \bar{r}$) terms, whereas T includes regular, weak, and strong singular terms (O $\bar{r}^{-1}$). The case where P is on the axis of symmetry is still discussed in [7], but not reported here, since we consider an axial hollow geometry. For a source point P on the boundary Γ, the displacement boundary integral equation (Eq. 1), in a limiting process, can be written for a smooth boundary:

$$\frac{1}{2} u_i(P) = \int_\Gamma \alpha(Q) U_{ij} \cdot (P,Q) t_j(Q) d\Gamma - \int_\Gamma \alpha(\overline{Q}) T_{ij} \cdot (P,Q) u_j(Q) d\Gamma \qquad (2)$$

The first integral on the right-hand side of Eq. (2) is of Riemman type since the integrand has at most a logarithmic singularity, while the second one is evaluated as a Cauchy Principal Value integral, (the sign on the second integral indicates CPV). An alternative approach to the solution of axisymmetric elasticity problems comes from the Somigliana identity for stresses. Differentiating the displacement equation (Eq. 2) with respect to directions r and z, substituting into the linear strain-displacement equations and applying Hook's law, an integral equation for stresses at boundary points can be obtained:

$$\frac{1}{2}\sigma_{ij}(P) = \int_\Gamma \alpha(\overline{Q}) D_{ijk}\cdot(P,Q)\,t_k(Q)\,d\Gamma - \int_\Gamma \alpha(\overline{\overline{Q}}) S_{ijk}\cdot(P,Q)\,u_k(Q)\,d\Gamma \qquad (3)$$

With i, j, k = r, z. Kernels D_{ijk} and S_{ijk}, are linear combinations of derivatives of U_{ij} and T_{ij}, and consequently, complete elliptic functions K and E. The first integral on the right-hand side of Eq. (3) is evaluated in the CPV sense, while the second one is also improper and must be evaluated in the Hadamard Finite-Part sense, (the sign on the second integral indicates HFP). Multiplying both sides of Eq. (3) by the normal components at the source point $n_j(P)$ leads to the traction equation:

$$\frac{1}{2}t_i(P) = n_j\int_\Gamma \overline{\alpha}(Q) D_{ijk}\cdot(P,Q)\,t_k(Q)\,d\Gamma - n_j\int_\Gamma \overline{\overline{\alpha}}(Q) S_{ijk}\cdot(P,Q)\,u_k(Q)\,d\Gamma \qquad (4)$$

3. The dual boundary element method

The advantage of the DBEM in solving fracture mechanics problems comes from the fact that only boundaries are discretized, which considerably reduces the size of systems to be solved. Crack propagation analysis is integrated without difficulties since only crack increments are added to the mesh. Discontinuous quadratic elements are employed for the discretization of both geometries (non-crack boundaries, and the crack itself). Discontinuous elements have their edge nodes shifted towards the centre of the element in order to satisfy, smoothness at the boundary nodes, continuity of the displacement derivatives, and boundary curvature at these points. Every crack element has two sides on witch equations (2) and (4) are applied to the elements of each side. A discretized system of equations is obtained where integrals over each element are evaluated.

4. Numerical treatments

The evaluation of different integrals that arise in Eqs. (2) and (4) depends on their singularity. For regular integrals, Gaussian quadrature is straightforward, whereas for singular ones, special treatments are required depending on the singularity type. For weak singular integrals, a local transformation with Gaussian quadrature is employed to improve the accuracy of their evaluation [16]. The singularity subtraction method [6] is used for improper integrals (strong singular and hyper-singular). In the neighborhood of a collocation node, the regular part of the integrand is expressed as a Taylor's expansion of sufficient terms to isolate the singularity. The original improper integral is thus transformed into a sum of regular integral and an integral of a singular function. Standard Gaussian quadrature is then used for numerical evaluation of the regular integral, while the singular function is evaluated analytically. Elliptic functions K and E are approximated by polynomial expressions [15].

4.1. The stress intensity factors evaluation

Near the crack tip, the elastic field is defined by an infinite series expansion that can be decoupled into mode I and II components [17]. Considering only the first term of the expansion, the displacement field on the crack surfaces is identical to the plane strain one. In a polar coordinate system centred at the crack tip, one can write:

$$u_2(\theta = \pi) - u_1(\theta = -\pi) = \frac{4(1-\nu)}{G} K_I \sqrt{\frac{r}{2\pi}} \qquad (5)$$

$$u_1(\theta = \pi) - u_1(\theta = -\pi) = \frac{4(1-\nu)}{G} K_{II} \sqrt{\frac{r}{2\pi}} \qquad (6)$$

where G is the shear modulus, and ν the Poisson's ratio, K_I and K_{II} are the stress intensity factors for the deformation modes I and II respectively, they can be computed from Eqs. (5) and (6), when the displacements on the crack surfaces are known.

4.2. Crack propagation

The crack growth direction is determined by the maximum principal stress criterion, which stipulates that the crack will grow perpendicularly to the principal stress direction at the crack tip. If K_I and K_{II} are known, this direction is calculated by the following expression:

$$\theta = 2tg^{-1}\left[\frac{1}{4}\left(k \pm \sqrt{k^2 + 8}\right)\right] \qquad k = K_I / K_{II} \tag{7}$$

where θ is measured from the crack axis in front of the crack tip.

Once the growth direction is known, an increment of length δa is added to the crack at each tip. This procedure constitutes an extremely easy re-meshing approach, since the new increments contributes with a few extra rows and columns to the global system of equations, quickly assembled.

5. Numerical applications

5.1. Evaluation of the convergence of the method

Different cases of axisymmetric cracks in a thick-walled cylinder are considered, using *KSP* code [19], with implementation of a new module for axisymmetric DBEM. The convergence of results using the crack displacement extrapolation is apparent from Fig. 1 as the number n of boundary elements increase. Less than 1% error was achieved with $n = 32$ for the two cases (internal and external circumferential crack) confirming the possibility to carry out good results using smutty meshes.
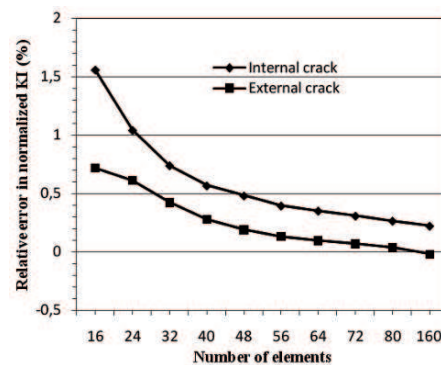
Fig. 1. Evaluation of the error according to the full number of elements used to discretize the geometry

5.2. Axially loaded thick-walled cylinder with circumferential crack

Consider a thick-walled cylinder with internal radius R_i, external radius R_e, height H and material properties E = 70,000 MPa and $\nu = 0.3$, subjected to a tensile axial

stress σ = 1.0. The cylinder contains a circumferential crack (internal or external), with radius *a* perpendicular to the axis of symmetry at mid-height position.

Normalized K_I is computed for three values of the ratio R_i/R_e and results are compared to those of the reference [18].
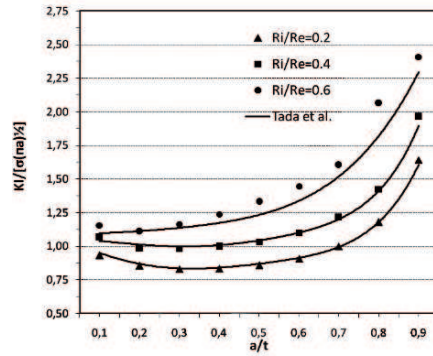
Fig. 2. Comparison of normalized stress intensity factor of an internal circumferential crack in a thick-walled cylinder
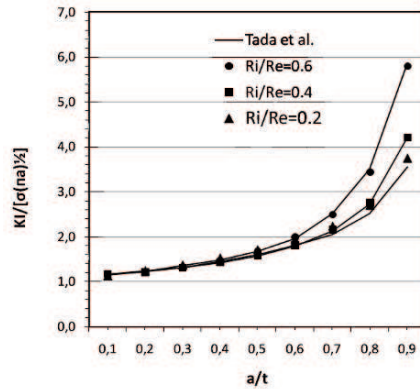
Fig. 3. Comparison of normalized stress intensity factor of an external circumferential crack in a thick-walled cylinder

A very close agreement can be seen for the two smaller values of the ratio, but the difference tends to increase as the thickness of the cylinder decreases for internal crack case (Figs. 2 and 3).

5.3. Cone crack propagation

In this example, simulation of the propagation of a centred internal cone crack, in a thick-walled cylinder is illustrated under different static loading conditions. Data for this example are: $R_i/R_e = 0.4$, $H = 4a$, initial crack length $a/t = 1/12$ and the cone crack is at $45°$, $E = 70,000$ and $\nu = 0.3$.

The boundary mesh includes 20 discontinuous quadratic elements at each segment. At the crack, 10 equal discontinuous quadratic elements were initially located on each side. At each increment, the crack grows by two elements (one at each tip) of the same type and size of those used for the initial crack. For each load case, a crack trajectory is obtained, for a total of 20 crack increments (Fig. 4a–c). Similar previous results could not be found in literature for comparison but the present results are regular with each applied load.
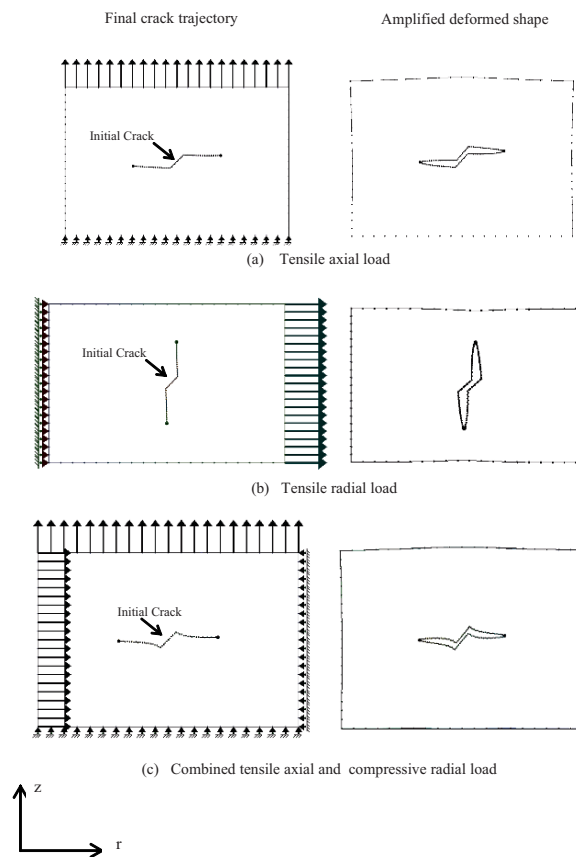
Fig. 4. Crack propagation of a cone crack inside a thick-walled cylinder under three different loading conditions

6. Conclusions

Cracked axisymmetric elastic solids have been analyzed using the dual boundary element method. The DBEM incorporates two independent boundary integral equations with their corresponding fundamental solutions.

Monomial transformation was applied to weak singular integrals, to improve precision with a reduced number of Gauss points. Singularity subtraction technique was applied to strong singular and hypersingular kernels, to allow evaluation of the Hadamard and Cauchy principal Value integrals.The use of discontinuous quadratic boundary element ensure continuity of the strains at the collocation nodes and then, the existence of the finite-part integrals. Stress intensity factors for circumferential or internal cracks were evaluated using the displacement extrapolation technique, and results were compared to analytical solutions. Accurate results were obtained for all treated applications.

References

[1] Kermanidis T (1975) A numerical solution for axially symmetrical elasticity problems. Int J Solids Struct 11:493–500.
[2] Mayr M (1976) The numerical solution of axisymmetric problems using an integral equation approach. Mech Res Commun 3:393–398.
[3] Cruse T, Snow DW, Wilson RB (1977) Numerical solutions in axisymmetric elasticity. Comput Struct 7:445–451.
[4] Watson JO (1986) Hermitian cubic and singular elements for plain strain. In Banerjee and Watson (eds.), Develop in boundary elt meth 4, Elsevier ASP, 1–28.
[5] Hong H, Chen J (1988) Derivations of integral equations of elasticity. J Eng Mech, ASCE; 114:1028–1044.
[6] Portela A, Aliabadi MH, Rooke DP (1991) The DBEM: effective implementation for crack problems. Int J Num Meth Eng 33:1269–1287.
[7] De Lacerda LA, Wrobel LC (2001) Hypersingular boundary integral equation for axisymmetric elasticity. Int J Num Meth Eng 52:1337–1354.
[8] De Lacerda LA, Wrobel LC (2002) DBEM for axisymmetric crack analysis. Int J Frac 113:267–284.
[9] Mukherjee S (2002) Regularization of hypersingular boundary integral equations: a new approach for axisymmetric elasticity. Eng Anal Bound Elem 26: 839–844.
[10] Mukherjee S (2000) CPV and HFP integrals and their applications in the boundary element method. Int J Solids Struct 37:6623–6634.
[11] Portela A, Aliabadi MH, Rooke DP (1993) DBEM: Incremental analysis of crack propagation. Comput Struct 46:237–247.
[12] Kebir H, Roelandt JM, Foulquier J (1996) Dual boundary element incremental analysis of crack growth in bolted joints. Improvement of materials, Mat-Tec. 223–230.
[13] De Lacerda LA, Wrobel LC (2002) An efficient numerical model for contact-induced crack propagation analysis. Int J Solids Struct 39:5719–5736.
[14] Gaiech Z, Kebir H, Chambon L, Roelandt JM (2007) Computation of fracture mechanics parameters for structures with residual stresses. Eng Anal Bound Elem 31:318–325.
[15] Becker AA (1986) The Boundary Integral Equation Method in Axisymmetric Stress Analysis Problems. Springer eds, Berlin.

[16] Johnston PR, Elliott D (2002) Transformations for evaluating singular boundary element integrals. J. Comp App Math 146: 231–251.

[17] Williams ML. Stress singularities resulting from various boundary conditions in angular corners of plates in extension. J Appl Mech ASME, 1952; 19:526–528.

[18] Tada H, Paris PC, Irwin GR (2000) The Stress Anal of Cra Handbook, 3rd ed. ASME, NY.

[19] Kebir H (2008) Kernel Simulation Program. DBEM C++ code, V 2.0, Roberval Laboratory, Université de Technologie de Compiègne, France.

Numerical Evaluation of Energy Release Rate for Several Crack Orientation and Position to the Bi-Material Interface Plates

N. Kazi Tani[1], T. Tamine[1] and G. Pluvinage[2]

[1]Laboratory LCGE, Faculty of Mechanical engineering, University of Sciences and Technology of Oran, USTO MB, BP 1505 El-M'nauer, 31000 Oran, Algeria

[2]Laboratoire de Fiabilité Mécanique ENIM, 57040 Metz, France

Abstract   The finite element method and fracture mechanics concept were used to study the interfacial fracture of bimaterial structure. The effects of mechanical materials properties, position and orientation between crack and the bimaterial interface are developed. The numerical results show that the energy release rate of the interface crack is influenced considerably by these parameters. For the several examples studied, a good agreement is obtained with different authors in term of normalised stress intensity factor and the energy release rate.

Keywords: Bi-material, Interface Crack, Mixed Mode, Stress Intensity Factor, Energy Release Rate, Finite Element.

1. Introduction

Many authors have studied the cracks in complex media as non-homogeneous materials. Recently, some researchers have been interested by the problems of the interfacial cracks in bimaterial plates. Marur and Tippur [9] have solved the interfacial crack problems in bimaterial plates analytically by the development of the stress field formulations into analytical series. Using the boundary element method (BEM), Liu and Nan Xu [13] have determined the stress intensity factors for a curved interfacial cracks. The same parameters have been expressed analytically by J.P. Shi [6] using the variational approach. In their paper, Bjerken and Persson [3] have used the crack closure integral method to determine the complex formulation of the stress intensity factors for the cracks at the interface in bimaterial plates. For the cracks perpendicular to the interface, Wang and Stahle [12] have determined the stress field near the crack tip by using the Muskhelishivili's potentials. Yilan and Hua [7] have calculated the stress intensity factors from the displacement equations near the crack tip for an edge crack perpendicular to the interface where the position of crack tip is at the interface. Using the photoelasticity experimental techniques, Cirello and Zuccarello [1] have studied the effect of crack propagation perpendicular to the interface in non homogenous media which

contains two dissimilar materials. The aim of this present study is to describe the effects of the position and the crack orientation with the presence of interfaces in bimaterial plates on the fracture parameters, especially the stress intensity factor (K) and the restitution energy rate (G). The influence of the crack length (a) and fracture mixed modes have been developed in this paper for the both cases when the crack is parallel and perpendicular to the interface. The results obtained numerically have been compared to recent research works.

2. Basic formula

2.1. Stress field for the crack parallel to the bimaterial interface
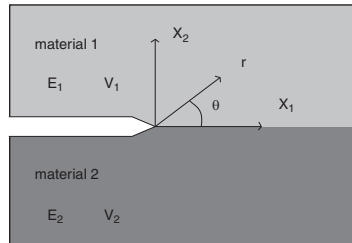
Fig. 1. Geometry of the crack and coordinate system in bimaterial plate

The complex form of the stress field near the crack tip for a crack at the interface (Fig. 1) can be expressed as follows [8]:

$$\sigma_{\alpha\beta} = \frac{\Re e\left[Kr^{i\varepsilon}\right]}{\sqrt{2\pi r}}\Sigma_{\alpha\beta}^{I}(\theta,\varepsilon) + \frac{\Im m\left[Kr^{i\varepsilon}\right]}{\sqrt{2\pi r}}\Sigma_{\alpha\beta}^{II}(\theta,\varepsilon) \tag{1}$$

(r,θ) are the polar coordinates system and α, β are the material indices 1 and 2. ε is the parameter that characterized the bimaterial specimen defined by the equation:

$$\varepsilon = \frac{1}{2\pi}\ln\left(\frac{1-\beta_D}{1+\beta_D}\right) \tag{2}$$

With: β_D is the Dundur's parameter [5].

The complex stress intensity factor K is defined as:

$$K = K_1 + i \cdot K_2 = |K| \cdot e^{i\kappa} \tag{3}$$

where: κ, is the phase angle, which depends of the bimaterial constant ε.

The functions $\Sigma_{\alpha\beta}^{I}(\theta,\varepsilon)$ and $\Sigma_{\alpha\beta}^{II}(\theta,\varepsilon)$ are equal to unity along the interface ahead of the crack tip $(\theta = 0)$. For $(\theta \neq 0)$, the angular functions can be found in [10]. For $\varepsilon = 0$, Eq. (1) reduces to the expression for the stress field close to a crack tip in a homogeneous material. For $\theta = 0$, the stresses σ_{22} and σ_{12} at the interface directly ahead of the tip are given by:

$$\sigma = \sigma_{22} + i\sigma_{12} = \frac{K_1 + iK_2}{\sqrt{2\pi r}} r^{i\varepsilon} \tag{4}$$

The associated crack surface displacements, δ_1 and δ_2, at a distance r behind the tip, $(\theta = \pi)$ are given by [3] as:

$$\delta = \delta_2 + i\delta_1 = \frac{8(K_1 + iK_2)}{(1 + 2i\varepsilon)\cosh(\pi\varepsilon)} \sqrt{\frac{r}{2\pi}} \frac{r^{i\varepsilon}}{E^*} \tag{5}$$

$$\frac{1}{E^*} = \frac{1}{2}\left(\frac{1}{\overline{E}_1} + \frac{1}{\overline{E}_2}\right) \tag{6}$$

$\overline{E}_j = \dfrac{E_j}{\left(1 - \upsilon_j^2\right)}$ in plane strain, $\overline{E}_j = E_j$ in plane stress, j = 1, 2.

When the possibility of crack advance is considered, the energy release rate is often used as a measure of the driving force. For an interfacial crack, Malyshev and Salganik [2] showed that the energy release rate G, in terms of the complex stress intensity factor K is:

$$G = \frac{|K|^2}{\cosh^2(\pi\varepsilon)E^*} \tag{7}$$

2.2. Stress field for the perpendicular crack to the bimaterial interface

Consider the plane elastic problem as shown in Fig. 2. A finite crack is perpendicular to a bimaterial interface. A Cartesian coordinate system oxy is attached on the interface.

The x axis is along the interface and the y axis is normal to the interface and coincident with the crack elongation direction [12]. Both materials are isotropic and homogeneous. The material I is occupied by the upper half plane S_1 and the materials II is occupied by the lower half plane S_2.
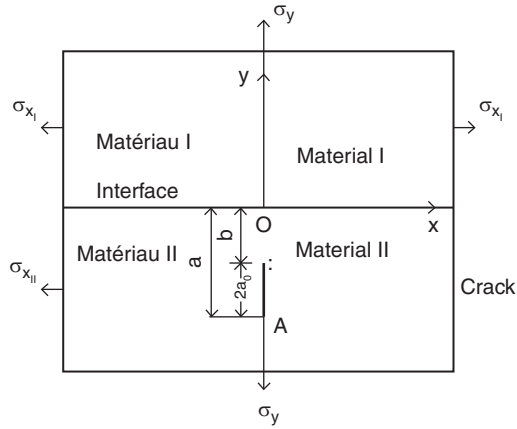
Fig. 2. A finite crack perpendicular to a bimaterial interface

Stress and displacement in an elastic solid can be represented by two Muskhelishivili potentials:

$$
\begin{aligned}
\sigma_x + \sigma_y &= 4\Re_e\big(\Phi(z)\big) \\
\sigma_y - i\tau_{xy} &= \Phi(z) + \Omega(\bar{z}) + (z - \bar{z}) \cdot \overline{\Phi'}(z) \\
2\mu\big(u_x + iu_y\big) &= \kappa\Phi(z) - \omega(\bar{z}) - (z - \bar{z}) \cdot \overline{\Phi'}(z) \\
\Phi(z), \Omega(z) & \; complex \; potentials
\end{aligned}
\tag{8}
$$

The complex potentials for an edge dislocation at $z = s$, in an infinite elastic solid can be expressed as follows:

$$
\begin{aligned}
\Phi_0(z) &= \frac{B}{z - s} \\
\Omega_0(z) &= \frac{B}{z - s} + \overline{B}\,\frac{s - \bar{s}}{(z - s)^2} \\
B &= \frac{\mu}{\pi\, i(\kappa + 1)}\big(b_x + ib_y\big)
\end{aligned}
\tag{9}
$$

where b_x and b_y are the x- and y-components of the dislocation, $\kappa = 3 - 4\nu$ for plane strain, ν Poisson's ratio and μ is the shear modulus.

If the edge dislocation is embedded in material II and according to [11], the complex potentials are:

$$\Phi(z) = \begin{cases} (1+\Lambda_1)\Phi_0(z) & z = S_1 \\ \Phi_0(z) + \Lambda_2\Omega_0(z) & z \in S_2 \end{cases} \tag{10}$$

$$\Lambda_1 = \frac{\alpha_D + \beta_D}{1 - \beta_D} \quad \text{and} \quad \Lambda_2 = \frac{\alpha_D - \beta_D}{1 + \beta_D} \tag{11}$$

where α_D and β_D are two Dundur's [5] parameters.

The crack can be considered as a continuous distribution of dislocations. Hence for this problem, we have:

$$\Phi_0(z) = \frac{\mu_2}{\pi i \cdot (1 + \kappa_2)} \int_a^b \frac{(bx + iby)}{z + it} dt \tag{12a}$$

$$\Omega_0(z) = \frac{\mu_2}{\pi i (1 + \kappa_2)} \int_a^b \frac{(bx + iby)}{z + it} dt + \frac{\mu_2}{\pi (1 + \kappa_2)} \int_a^b \frac{t(bx - iby)}{(z + it)^2} dt \tag{12b}$$

$T_m(\xi)$, is the first Chebyshev polynomial [12].

a and b are the distances from the crack tips A and B to the interface, respectively.

3. Numerical simulations of cracks in bimaterial plates

3.1. Cracks normal to the interface in bimaterial plates

In this following application, we consider a bimaterial cracked specimens aluminium/ PSM-1 ($W = L = 15$ mm, $t = 5.5$ mm) as the ones used in [1] Fig. 3 by Cirello and Zuccarello. Different crack lengths have been chosen according to the geometric ratio (a/w = 0.1, 0.2, 0.3, 0.4, 0.5, 0.6, 0.7, 0.8, 0.9, 0.99).

The specimens are subjected to a global tensile force F = 6,600 N that it yields a stress field at the upper and lower edge of the plate as shown in Fig. 4.

Due to the symmetry according to the both axis of (x, y) reference, we have considered only the quart of the plate in the modelisation of the specimen as shown in Fig. 4.
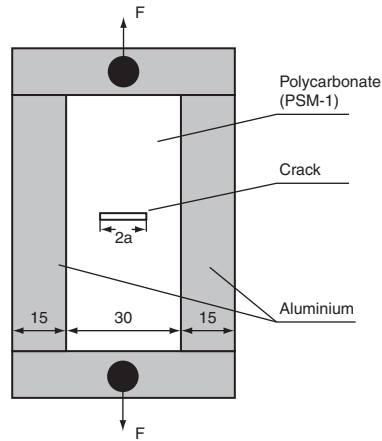
Fig. 3. Geometry of the cracked specimen subjected to the tensile loading [1]
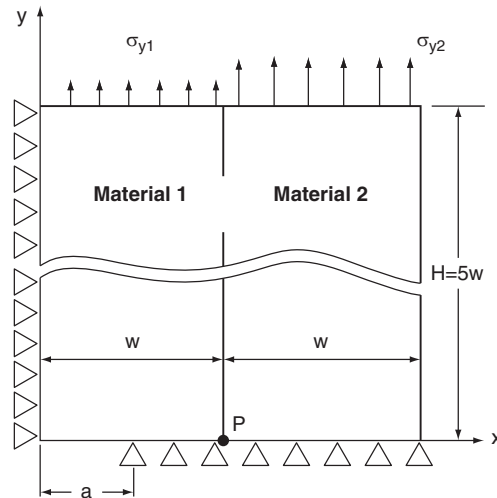
Fig. 4. Modelisation of bimaterial plates [1]

Figure 5 shows the results of the stress intensity factors obtained numerically by FEM and those obtained by Cirello and Zuccarello in [1] using experimental *RGB* photoelasticity and a semi analytic relationship defined as:

$$\overline{K}_I = 1 - \frac{\lambda_1(\alpha_D - \beta_D\lambda_1)}{2\alpha_D} Tan\left[\frac{\pi}{2}\lambda_1(\alpha_D + \beta_D\lambda_1)\cdot\left(\frac{a}{w}\right)^{\alpha_D + \beta_D\lambda_1}\right] \qquad (13)$$

where α_D, β_D are the Dundur parameters and λ_1 is the order of singularity.
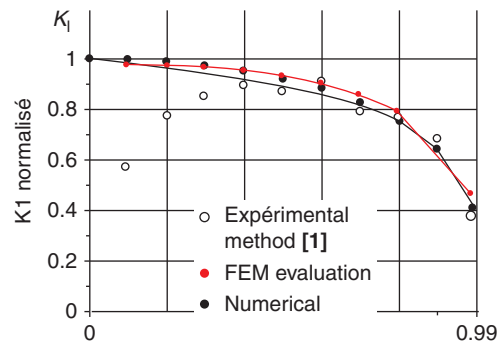
Fig. 5. Numerical FEM evaluation of normalised stress intensity factor vs. crack length

$$\overline{K} = \frac{K_I}{\sigma_y\sqrt{\pi a}} \qquad (14)$$

The values of the normalised stress intensity factor obtained numerically by the FEM [4] are in a good agreement with the ones evaluated in [1] by *RGB* experimental photoelasticity and Eq. (13). In the Fig. 5, the presence of the crack in the less stiffened material and the effect of interface materials mismatch, yield a "closing" bridging stress intensity factor that decreases the stress intensity factor resulting from the external loading with the crack length i.e. when the crack tip is close to the interface.
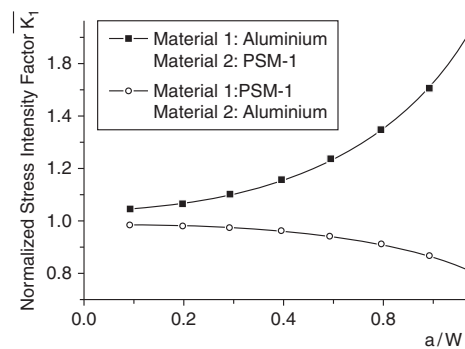
Fig. 6. Evaluation of the normalised SIF with the crack propagation and material properties

The numerical simulation in Fig. 6 shows the decreased tendency of the normalised stress intensity factors when the crack propagation is in the domain of material 1 (PSM-1, $E = 3050$ MPa, $\nu = 0.39$). The same evaluation has been considered when the crack propagation is in the more stiffened domain of the bimaterial plate (Aluminuim, $E = 64{,}300$ MPa, $\nu = 0.33$).

In this case, the normalized stress intensity factor increases with the geometric ratio a/w. It is important to note that the ratio of the evolution of the $\overline{K}_I$ parameter in Fig. 6 will be more significant when the geometric crack ratio is greater than $a/w = 0.4$; it means that when the crack tip is close to the interface.

3.2. Cracks parallel to the interface

In the following simulation, we try to show the effect of lateral position of the crack on the restitution energy rate G when the crack is located at a distance h from the interface. The evolution of parameter G is plotted in Fig. 7. The obtained results in Fig. 7 show that the G parameter increases when the crack is too far from the interface. The evolution ratio of this tendency depends on the material elastic constants of the domain containing the crack and the geometric factor a/w.
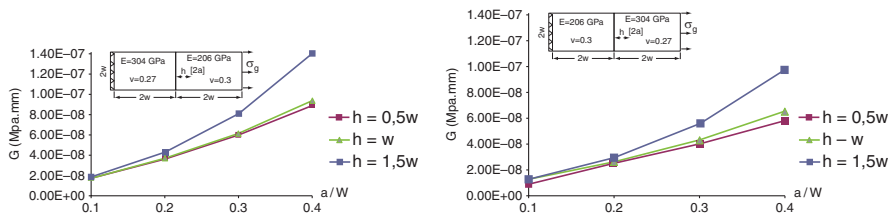
Fig. 7. Evolution of G with the lateral position h of the crack

The greater values of G are noted when the crack evolution is in the less stiffened domain ($E = 206$ GPa, $\nu = 0.30$).

3.3. Interface cracks in mixed mode

This section concerns the effect of mixed mode and the mechanical properties of the bimaterial on the fracture parameters, especially on the restitution energy rate G. The specimen used in this application is a bimaterial plate containing an inclined edge crack with various geometric ratio ($a/w = 0.1, 0.2, 0.3, 0.4, 0.5, 0.6$) and inclination angles. The cracked plate is subjected to a tensile loading ($\sigma_g = 1$ MPa), Fig. 8. A finite element method is used for the modelisation of the specimen Fig. 9. The problem has been solved in plane stress.
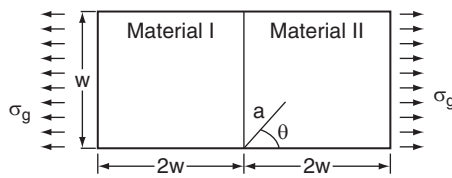
Fig. 8. Inclined edge crack in bimaterial plate
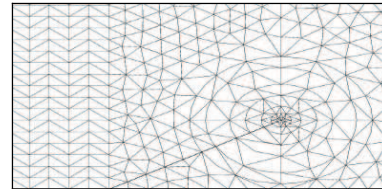
Fig. 9. Finite element modelling of the crack tip near the interface

After numerical resolution, the restitution energy rate values are plotted for several crack orientations and material positions in Fig. 10 in term of G_{eq} given by Eq. (15).

$$G_{eq} = \sqrt{G_I^2 + G_{II}^2} \tag{15}$$

The graphs of G_{eq} in Fig. 10 show that this parameter increases with the crack length. It is important to note that when the crack propagation is located in the more stiffened domain of the specimen (E = 304 GPa, ν = 0.27), the values of the restitution energy rate G_{eq} decreased Fig. 10 for all studied inclination crack angles.
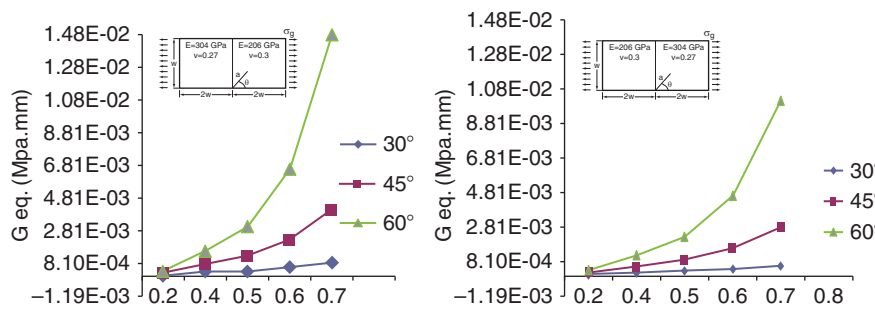
Fig. 10. Restitution energy rate *Geq* vs. crack inclination angle and the ratio *a/w*

4. Conclusions

In this paper, the stress field near the crack tip has been studied for several orientations and positions of crack by means of numerical analysis. The oscillatory singularity of the stress and its complication for cracks along the interface has been considered in the evaluation of energy restitution rate *G*. When the crack is perpendicular to the interface, the decreased evolution of the normalised stress intensity factor $\overline{K}_I$ obtained by Cirello and Zuccarello [1] is confirmed for all the

geometric ratio *a/w* (Fig. 5). This decreased tendency is explained in [1] by the significant presence of "bridging effect". The graphs plotted in Fig. 6 show that the influence of the "bridging effect" is negligible when the crack propagation is in the aluminium domain, i.e., the normalized stress intensity factor increases with the crack length. In this present study, the crack eccentricity from the interface and its position are considered for both cases i.e when the crack is in the material I (E = 304 GPa, ν = 0.27) and in the material II (E = 206 GPa, ν = 0.30). The obtained graphs in Fig. 7 show that *G* increases with the distance *h* from the interface. It is important to note that the values of restitution energy rate are significantly higher when the crack is located in the less stiffened domain (E = 206 GPa, ν = 0.30). It seems that the crack needs more extension force in this weak domain. For the inclined edge crack emanating form the interface, the results in Fig. 10 shows that *G* parameter increases with the crack inclination angle, this increased tendency is more significant when $a/w \geq 0.4$ and (θ = 60°). The elastic mismatch effect on the restitution energy rate is more important when the crack tip orientation is closed to the interface. As mentioned above, the elastic constants of the domain containing the crack has the same effect on the restitution energy rate *G*.

References

[1] A Cirello, B. Zuccarello (2006) On the effects of a crack propagating toward the interface of a bimaterial system. Journal of Engineering Fracture Mechanics 73: 1264–1277.
[2] B M Malyshev, R L Salganik (1965) The strength of adhesive joints using the theory of cracks. International Journal of Fracture Mechanics 5: 114–128.
[3] Christina Bjerken, Christer Persson (2001) A numerical method for calculating stress intensity factors for interface cracks in bimaterials. Engineering Fracture Mechanics 68: 235–246.
[4] Code CASTEM 2000. Commissariat à l'Energie Atomique CEA-DEN/DMSS/SEMT.
[5] J Dundur (1969) Edge-bonded dissimilar orthogonal elastic wedges under normal and shear loading. Journal Applied Mechanics 36: 650–652.
[6] J P Shi (1998) Stress intensity factors for interface crack in finite size specimen using a generalised variational approach. Theoretical and Applied Fracture Mechanics 28: 223–230.
[7] Kang Yilan, Lu Hua (2002) Investigation of near-tip displacement fields of a crack normal to and terminating at a bimaterial interface under mixed-mode loading. Engineering Fracture Mechanics 69: 2199–2208.
[8] Nao Aki Noda, Takao Kouyane, Yositomo Kinoshita (2006) Stress intensity factors of an inclined elliptical crack near a bimaterial interface. Engineering Fracture Mechanics 73: 1292–1320.
[9] P R Marur, H V Tippur (1999) A strain gage method for determination of fracture parameters in bimaterial systems. Engineering Fracture Mechanics 64:87–104.
[10] J R Rice, Z Suo, J-S Wang (1990) Mechanics and thermodynamics of brittle interfacial failure in bimaterial systems. Pergamon, New York, 269–294.
[11] Z Suo (1989) Singularities interacting with interface and cracks. International Journal of Solids and Structures 25: 1133–1142.
[12] T C Wang, P Stahle (1998) Stress state in front of a crack perpendicular to bimaterial interface. Engineering Fracture Mechanics 59: 471–485.
[13] J Yijun, Liu & Nan Xu (2000) Modeling of interface cracks in fiber-reinforced composites with the presence of interphases using the boundary element method. International Journal Mechanics of Materials 32: 769–783.

Numerical Simulation of the Ductile Fracture Growth Using the Boundary Element Method

Gaëtan Hello[1], Hocine Kebir[1] and Laurent Chambon[2]

[1]Laboratoire Roberval, UTC, BP 20529–60205 Compiègne Cedex

[2]EADS IW,18 rue Marius Terce BP 13050–31025 Toulouse Cedex 3

Abstract   This work aims at simulating the ductile fracture phenomenon occurring in thin cracked structures thanks to the boundary element method. A process based on the dual integral formulation of the problem has been developed so as to solve elastoplastic cracked problems. Since this method provides accurate mechanical fields at the crack tip, the Rice and Tracey criterion for ductile fracture can be evaluated during the post-processing step. The validity of the method is at last addressed with the comparison between numerical and experimental results for a test on a CCT specimen.

Keywords: Boundary Element Method (BEM), Non-Linear Fracture Mechanics, Local Approach of Ductile Fracture, R-Curve.

1. Introduction

Taking into account the resistance to fracture is a mandatory aspect of the design process for aeronautical structures. Indeed the mass gain imperatives must conciliate efficiently both economical aspects and security requirements. Thus the behaviour of a cracked structure under loading has to be predicted with a good accuracy. Dealing with thin metallic structures, this issue is handled thanks to the classical R-curve notion. This curve links the energy release rate with the progressive crack advance. In fact, contrary to thick cracked structure which break down as soon as the K-factor reaches a critical value, the thin ones on the opposite may exhibit a stable propagation of the defect before the occurrence of the final collapse. This stability is due to the competition opposing the irreversible mechanisms of dissipation taking place simultaneously at the crack tip, namely the crack propagation and the plastic dissipation. On a micro-mechanical point of view, the ductile fracture phenomenon is based on the creation of micro-voids around inclusions or flaws in the metallic matrix, their progressive growth and finally their coalescence leading to macro-cracks [1]. Two main classes of models have been developed. The first one includes models where the damage does not modify the constitutive equations [2–4]. This uncoupled strategy has the advantage to be easily implemented into an existing numerical tool since it only requires the update of fracture parameters at a post-processing step.

On the other hand, coupled models [5–7], incorporate damage parameters into the constitutive equations so as to describe the altered behaviour of the damaged zones. These more sophisticated models lead to specific numerical developments since the elasticity and plasticity are now explicitly dependant on fracture parameters. For a given structure, the R-curve has the interesting property to be solely dependant on the material and thickness parameters. In this it is possible to extrapolate the behaviour of a complete structure from the curve obtained with a simple specimen of the same thickness and material.

2. Context and objectives

For the moment, the determination of the curve relies on experimental tests made on normalized specimens. Previous works carried out by the UTC and EADS IW (formerly EADS CCR) has shown that it was nevertheless possible to use the finite elements method to predict the answers of specimens and even of full structures [8]. The strategy presented in this paper intend to take advantage of the qualities of the boundary element method (good representation of the fields at the crack tip, liberty toward (re)meshing issues, simplified programming of the propagation) so as to determine numerical R-curves with precision.

The direct industrial application aims at reducing the number of experimental tests that may be pretty expensive especially in the case of large structures. The first step of the works has consisted into developing an efficient method for the solving of plasticity problems in cracked structures. The boundary element formulation of the problem is based on dual integral formulation presented in [9]. The material non linearity is taken care of by the mean of a classical radial-return algorithm enabling the integration of the elastoplastic behaviour [10]. The mechanical fields at the crack tip being especially accurate, it is therefore possible to use them in order to evaluate the ductile fracture criterion of Rice and Tracey [3] during a post-processing step. The final determination of the R-curve then requires only a correlation of the fracture parameter critical value with experimental tests.

3. Solving elastoplastic problems in cracked structures

3.1. Dual boundary element formulation

If an elastoplastic problem has to be solved in a cracked structure, the classical integral formulation has to be extended. This classical solution is based on two equations, the first one in displacement for the points of the boundary (1), the other one in stress for points strictly inside the domain (2). In both equation can be found the unknown mechanical fields: displacement u and tension t on the

boundary, plastic deformations ε^p in the domain. These fields are multiplied by the known kernels U, T, D, S, σ et Σ of the Kelvin fundamental solution [11].

$$\frac{1}{2}\cdot u_i\left(\underline{X}\right)=\left[\begin{array}{c}\displaystyle\int_{\partial\Omega}U_{ij}\left(\underline{X};\underline{Y}\right)\cdot t_j\left(\underline{Y}\right)\cdot d\Gamma\left(\underline{Y}\right)-\int_{\partial\Omega}T_{ij}\left(\underline{X};\underline{Y}\right)\cdot u_j\left(\underline{Y}\right)\cdot d\Gamma\left(\underline{Y}\right)\\[2mm]\displaystyle+\int_{\Omega}\sigma_{ijk}\left(\underline{X};\underline{Y}\right)\cdot\varepsilon_{jk}^p\left(\underline{Y}\right)\cdot d\Omega\left(\underline{Y}\right)\end{array}\right] \tag{1}$$

$$\sigma_{ij}\left(\underline{X}\right)=\left[\begin{array}{c}\displaystyle\int_{\partial\Omega}D_{ijk}\left(\underline{X};\underline{Y}\right)\cdot t_k\left(\underline{Y}\right)\cdot d\Gamma\left(\underline{Y}\right)-\int_{\partial\Omega}S_{ijk}\left(\underline{X};\underline{Y}\right)\cdot u_k\left(\underline{Y}\right)\cdot d\Gamma\left(\underline{Y}\right)\\[2mm]\displaystyle+\int_{\Omega}\Sigma_{ijkl}\left(\underline{X};\underline{Y}\right)\cdot\varepsilon_{kl}^p\left(\underline{Y}\right)\cdot d\Omega\left(\underline{Y}\right)+f_{ij}\left(\varepsilon_{kl}^p\left(\underline{X}\right)\right)\end{array}\right] \tag{2}$$

This formulation has proven its efficiency when the structure does not contain any defect [12]. Nonetheless, the introduction of the crack, whose lips are geometrically confounded, leads to a singular matrix that cannot be used numerically. Among the different methods permitting to get rid of the singularity, it has been chosen to use the dual formulation described in [9]. This method has both the advantages to be quite close to the classical formulation and to require just a few extra numerical developments. It is based on the two previous equations that are completed by two new ones for the crack points: another displacement equation for the upper lip (3) and a tension equation for the lower lip (4).

$$\frac{1}{2}\cdot\left[u_i\left(\underline{X}^+\right)+u_i\left(\underline{X}^-\right)\right]=\left[\begin{array}{c}\displaystyle\int_{\partial\Omega}U_{ij}\left(\underline{X}^-;\underline{Y}\right)\cdot t_j\left(\underline{Y}\right)\cdot d\Gamma\left(\underline{Y}\right)-\int_{\partial\Omega}T_{ij}\left(\underline{X}^-;\underline{Y}\right)\cdot u_j\left(\underline{Y}\right)\cdot d\Gamma\left(\underline{Y}\right)\\[2mm]\displaystyle+\int_{\Omega}\sigma_{ijk}\left(\underline{X}^-;\underline{Y}\right)\cdot\varepsilon_{jk}^p\left(\underline{Y}\right)\cdot d\Omega\left(\underline{Y}\right)\end{array}\right] \tag{3}$$

$$\frac{1}{2}\cdot\left[t_i\left(\underline{X}^+\right)-t_i\left(\underline{X}^-\right)\right]=n_j\left(\underline{X}^+\right)\cdot\left\{\begin{array}{c}\displaystyle\int_{\partial\Omega}D_{ijk}\left(\underline{X}^+;\underline{Y}\right)\cdot t_k\left(\underline{Y}\right)\cdot d\Gamma\left(\underline{Y}\right)-\int_{\partial\Omega}S_{ijk}\left(\underline{X}^+;\underline{Y}\right)\cdot u_k\left(\underline{Y}\right)\cdot d\Gamma\left(\underline{Y}\right)\\[2mm]\displaystyle\int_{\Omega}\Sigma_{ijkl}\left(\underline{X}^+;\underline{Y}\right)\cdot\varepsilon_{kl}^p\left(\underline{Y}\right)\cdot d\Omega\left(\underline{Y}\right)+\frac{1}{2}\cdot\left[f_{ij}\left(\varepsilon_{kl}^p\left(\underline{X}^+\right)\right)-f_{ij}\left(\varepsilon_{kl}^p\left(\underline{X}^-\right)\right)\right]\end{array}\right\} \tag{4}$$

3.2. Boundary elements and linear systems

Starting from the integral equations (1) to (4), the obtainment of the discrete form of the problem consists into a first step of decomposition of integrals on subdomains and a second step of local approximation for the unknown mechanical fields [13]. The displacement and tension fields on the boundary are locally represented with 1D quadratic non conformal polynomials.

The plastic deformations in the domain are approximated with 2D linear non conformal polynomials. This choice of non-conformal representation of the fields has the advantage to permit the collocation of integral equations on points with a suitable level of continuity.

These steps of discretisation of the geometry and the fields lead to two different linear systems (5) and (6) of discrete unknowns {u}, {t}, {ε^p}, respectively the displacement vector, the tension vector and the plastic deformations vector.

$$[A] \cdot \{u\} = [B] \cdot \{t\} + [D] \cdot \{\varepsilon^p\} \tag{5}$$

$$\{\sigma\} = -[A'] \cdot \{u\} + [B'] \cdot \{t\} + [E] \cdot \{\varepsilon^p\} \tag{6}$$

3.3. Algorithm for the integration of the elastoplastic behavior

The effective solving of the problem relies on an implicit elastoplastic algorithm which involves the systems (5) and (6). The local integration of the behaviour is made by the mean of the classical Simo and Taylor radial return technique [10] for each plastified domain point. In this the algorithm shows at the same time an incremental aspect linked with the gradual increase of the load (either displacement or stress driven) and an iterative aspect due to a convergence process on each load step.

3.4. Numerical results

The validation of the method will be achieved with the comparison, for a given problem, of the numerical results obtained by the BEM code with those given by the commercial FEM code ABAQUS. Here the problem considered is the thin cracked plate depicted on Fig. 1.

The meaningful parameters retained for the comparison are the displacement components on the crack lips. The quantities have the double interest to be a pertinent proof of the precise representation of the plastic field and to be immediately accessible in both BEM and FEM results. Concretely the FEM model is composed of 4350 CPS6 elements (quadratic plane stress) (Fig. 2). The BEM model on its side has 60 boundary elements and 492 2D cells.

The comparison between the BEM solver and ABAQUS is done for different level of stress: 100, 120, 140 and 160 MPa. It has to be noticed that for this last load the plastic zone is definitely not confined to the crack tip, it has almost propagated to the whole BEM discretisation of the surface (Fig. 3). On Fig. 4 are summarized the deformed cracks obtained by both codes for the different levels of loading. The predictions given by the two codes are in very good agreement.

Fig. 1. Problem   **Fig. 2**. FEM mesh   **Fig. 3.** BEM discretisations

Fig. 4. Comparison of deformed cracks between BEM and FEM
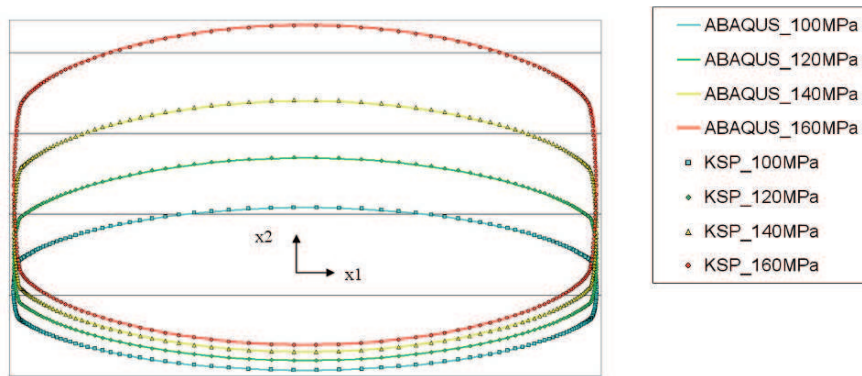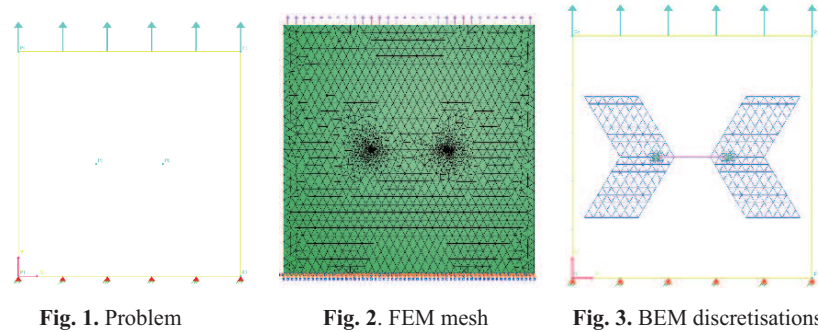
4. Numerical simulation of the ductile fracture

Since the BEM solver for elastoplastic cracked problem has proven its efficiency to predict the fields at the crack tips, it is now possible to add a post-processing step dealing with the evaluation of the Rice and Tracey fracture parameter. This fracture criterion (7) depends on the stress and plastic deformations fields and describes the growth of micro-cavities leading to the propagation of the crack.

$$\frac{\dot{R}}{R} = 0.283\, exp\left(\frac{3}{2} \cdot \frac{\sigma_h}{\sigma_{VM}} \right) \cdot \dot{p} \tag{7}$$

This fracture parameter is incremented at the end of each load step and compared to its critical value so as to determine a potential crack advance. The evaluation of this numerical critical value is based on a comparison with experimental curves (resulting load versus crack length and crack opening measures obtained by optical captors).

In this it is now possible to simulate simultaneously the irreversible processes of plasticity and crack propagation. Considering a CCT160 specimen under a progressive displacement load, a stable propagation phase can be observed before the breakdown occurs (Fig. 4). Finally the desired R-curve can be obtained (Fig. 5).

Fig. 5. Total load versus crack opening curves – comparison between experimental and numerical results for different values of the fracture parameter

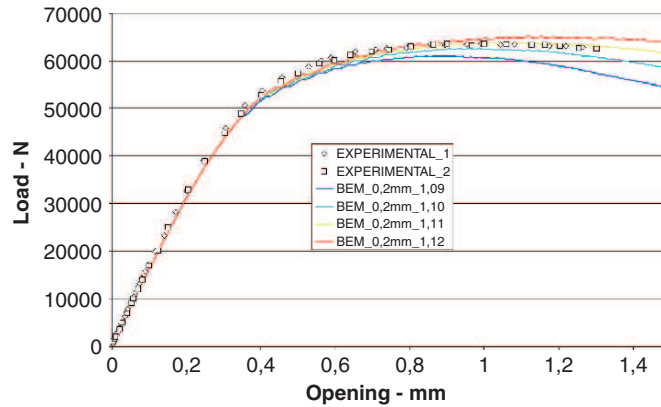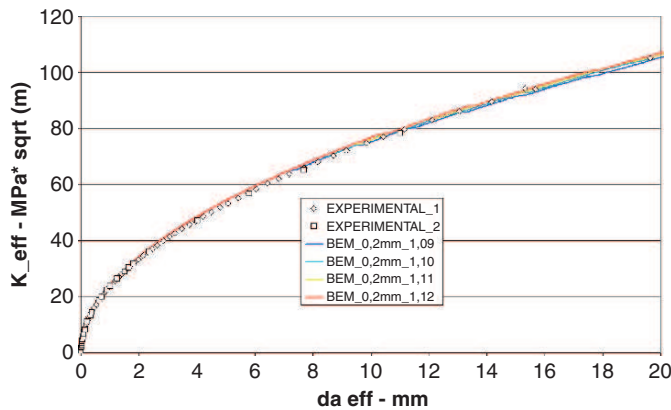**Fig. 6.** Effective K-factor versus effective crack-length curves – comparison between experimental and numerical results for different values of the fracture parameter

5. Conclusions

The boundary element method has proven its efficiency in simulating elastoplastic crack problems. The stress and plastic strains fields are described with a very good accuracy.

The local fracture criterion of Rice and Tracey, function of these two fields, can therefore be evaluated precisely near the crack-tip. The ductile fracture phenomenon is hence modelled numerically with a BEM solver for elastoplatic cracked structures combined with a post-processor based on the uncoupled damage model. An appropriate fitting of the fracture parameter with experimental results leads to numerical R-curves overlapping the experimental ones (Fig. 6). The efficiency of the strategy is thus proven. The next step will deal with the determination of the numerical parameters conditioning the extrapolation of specimens' results to real aeronautical structures.

References

[1] T.L. Anderson. Fracture Mechanics: Fundamentals and Applications. Second edition, 1995, CRC Press.

[2] F.A. McClintock. A criterion for ductile fracture by growth of holes. J. Appl. Mech. 35, 1968, pp. 363–371.

[3] J.R. Rice and D.M. Tracey. On the ductile enlargement of voids in triaxial stress fields. J. Mech. Phys. Solids 17, 201.

[4] W.H. Tai and B.X. Yang. A new damage mechanics criterion for ductile fracture. Eng. Fract. Mech. 27 (4), 1987, pp. 371–378.

[5] A.L. Gurson. Continuum theory of ductile rupture by void nucleation and growth: part 1-yield criteria and flow rules for porous ductile media. J. Eng. Mat. Tech. 99, 1977, pp. 2–13.

[6] Tvergaard and A. Needleman. Analysis of the cup-cone fracture in around tensile bar. Acta Metall. 32, 1984, pp. 157–169.

[7] G. Rousselier. Ductile fracture models and their potential in local approach of fracture. Nucl. Eng. Des. 105, 1987, pp. 97–111.

[8] J. Delmotte. Modélisation numérique de la déchirure ductile en milieu bidimensionnel à l'aide d'une approche locale. Simulation des courbes de résistance à la fissuration. Thèse de doctorat, Université de Technologie de Compiègne.

[9] Y. Mi and M.H. Aliabadi. Dual boundary element method for three-dimensional fracture mechanics analysis. Eng. Anal. Bound. Elem. 10 (2), 1992, pp. 161–171.

[10] M. Bonnet. Boundary Integral Equations Methods for Solids and Fluids. Wiley, New York, 1999.

[11] M.H. Aliabadi. The boundary element method, volume 2: applications in solid and structures. Wiley, 2002, ISBN: 978-0-470-84298-0.

[12] G. Hello. Application de la méthode des éléments de frontière à la résolution de problèmes élastoplastiques. Actes Giens 2005, Hermès, pp. 445–450.

[13] H. Kebir, J.M. Roelandt and J. Foulquier. A new singular boundary element for crack problems: application to bolted joints. Eng. Fract. Mech. 62 (6), April 1999, pp. 497–510.

Enriched Finite Element for Modal Analysis of Cracked Plates

M. Bachene[1], R. Tiberkak[2], S. Rechak[3], G. Maurice[4] and B.K. Hachi[5]

[1]Mechanical physics and mathematical modeling Laboratory, University of Medea, Algeria

[2]Department of Mechanical engineering, University of Blida, Algeria

[3]Mechanical Engineering and Development Laboratory, National Polytechnic School of Algiers, Algeria

[4]LEMTA/ENSEM-INPL, 2 avenue de la Forêt de Haye BP 160 F-54504 Vandœuvre-lès-Nancy, France

[5]Department of Electromechanical Engineering, CUD, BP 3117 Ain-Cheih, 17000 Djelfa, Algeria

Abstract   In this Paper, the extended finite element method (X-FEM) is adopted then numerically implemented for the analysis of the vibratory behaviour of isotropic homogeneous plates having a through crack located at various positions. The mathematical model includes the effects of rotary inertia and transverse shear deformation. Various applications including plates with central crack and edge crack are considered. The results obtained in terms of Eigen frequencies with respect to the crack length show a net decrease in the frequency with an increase in the crack length. This physical effect is more pronounced for particular vibratory modes as it also depends on the nature of the crack. Overall, the present results compare well with the experimental, analytical, and numerical results consulted in the literature.

Keywords: Vibratory Behavior, Natural Frequencies, X-FEM, Cracked Plates.

1. Introduction

The development of numerical techniques for the analysis of cracked structures still attracts many researchers. The presence of discontinuities in these structures poses the problem in their numerical representation. The vibratory phenomenon of cracked rectangular plates was first reported by Lynn and Kumbasar [1]. In their work, a Fredholm integral equation is obtained using a Green's function approach. Stahl and Keer [2] reported the vibration and stability of cracked rectangular plates. Their development is based on a dual series equation to reach the solution in terms of a Fredholm integral equation of the second kind. Liew et al. [3] used domain decomposition in determining frequencies of cracked plates. Khadem et al. [13] introduced a modified comparisons functions (MCFs) to analyze vibration

of a rectangular cracked plate. Those MCFs are derived using the Rayleigh–Ritz method.

The finite element method has been employed to analyze vibration problems of cracked plates [5–7]. Krawczuk and Ostachowicz [5] calculated the flexibility matrix of a plate with the crack as a sum of the noncracked plate and an additional flexibility matrix caused by the crack. The extended finite element method (X-FEM) applied to various fracture mechanics problems shows to be a promising alternative, and thus all discrepancies on the standard finite element method are alleviated. In the X-FEM, the crack is independently represented of the mesh by adding functions on discontinuity nodes to the standard finite element. Those added functions take into account of the singularities due to the crack. The main objective of the present work is to analyze the vibratory behavior of cracked plates and demonstrate as well the efficiency of the X-FEM in the analysis of such physical problem. This paper continues previous work conducted by the authors [11]. Up to our knowledge, the usage of the X-FEM in the modal analysis of cracked plates has not yet been reported in the literature. The methodology presented by Moës et al. [9] is followed in the development of the numerical model. Cases of plates with through central cracks and side cracks, and under various boundary conditions, are considered.

2. X-FEM formulation

The extended finite element method analysis consists at a first stage to mesh the domain (2D or 3D) regardless of the crack. The effect of the crack is then introduced into the expression of the displacement field for nodes in the neighborhood of the crack. Those nodes are thus enriched by functions taking into account of discontinuities and peculiarities due to the crack. Let us consider a through cracked rectangular plate of sides a, b and thickness h. A Cartesian coordinate system (x, y, z) is taken in such way that the (x, y) plane coincide with plate's midsurface. In the X-FEM approximation, the displacement field of an arbitrary point x within the plate can be expressed as:

$$\Delta(x) = \sum_{i \in I} N_i(x)\delta_i + \sum_{j \in J} N_j(x)f(x)\delta'_j \qquad (1)$$

where N_i and δ_i are the classical shape function, and the classical nodal displacement at node i, respectively. I is the set of all nodal points of the plate, while J represents the set of nodes of the elements located on the discontinuity. $\delta'_j \; j \in J$ are the nodal degrees of freedom to be enriched, and f is the enrichment function. However, with regard to Fig. 1, two kinds of discontinuities can be presented: (i) the element is completely cut by the crack, in this case the Heaviside function $H(x)$ is used to enrich the nodes of element; (ii) the second case of

discontinuity is when the element contains the crack tip, in this case the asymptotic function is used. More details of the enrichment can be found in [9, 10].
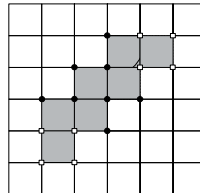
Fig. 1. Plate with an arbitrary crack nodes in square are enriched with an asymptotic function

In the present study, we impose in the finite element discretization that the crack stops at the edge of elements, i.e. there are no elements containing crack tip, and therefore only the Heaviside function is used for enrichment. Equation (1) can thus be rewritten as:

$$\Delta(x) = \sum_{i \in I} N_i(x)\delta_i + \sum_{j \in J} N_j(x)H(x)\delta'_j \tag{2}$$

The Heaviside function $H(\text{x})$ takes the value $+1$ above the crack and -1 otherwise.

3. Elements of stiffness and mass matrices

In this section, elements of stiffness matrix and mass matrix will be derived from the expression of potential energy and kinetic energy. The FEM formulation is based on the Mindlin–Reissner plate theory in which the effects of shear deformation and rotatory inertia are taken into account. Each node possesses three degrees of freedom w, θ_x and θ_y. In conjunction with Eq. (2), the displacement field in the X-FEM formulation can be written as:

$$\begin{Bmatrix} w_0 \\ \theta_x \\ \theta_y \end{Bmatrix} = \sum_I N_i(x)\delta_i + \sum_J N_j(x)H(x)\delta'_j \tag{3}$$

where $\delta_i = \{w_{0i} \quad \theta_{xi} \quad \theta_{yi}\}^T$ and $\delta'_j = \{w'_{0j} \quad \theta'_{xj} \quad \theta'_{yj}\}^T$

The strain fields in term of curvature and transverse shear is derived from Eq. (3) and can be expressed as:

$$\varepsilon = \sum_I B_i \delta_i + B'_j \delta'_j \tag{4}$$

Where $\quad B_i = \begin{bmatrix} 0 & N_{i,x} & 0 \\ 0 & 0 & N_{i,y} \\ 0 & N_{i,y} & N_{i,x} \\ N_{i,x} & N_i & 0 \\ N_{i,y} & 0 & N_i \end{bmatrix} \quad$ and $\quad B'_j = HB_j$

The x and y subscript denotes the first derivative about the x and y directions respectively. Equation (4) can be rewritten in a compact form as:

$$\varepsilon = B\delta + B'\delta' \tag{5}$$

The stress field in term of moments and transverse shear force is:

$$\sigma = CB\delta + CB'\delta' \tag{6}$$

where C is the matrix of elastic rigidities, and σ is the generalized stresses. When the plate is discretized with the usual finite element method, the potential energy for an element e of the plate can be written as follows:

$$U^e = \frac{1}{2} \int_{A_e} \sigma^T \varepsilon dA = \frac{1}{2} \left\{ \delta^T \quad \delta'^T \right\} K^e \left\{ \begin{matrix} \delta \\ \delta' \end{matrix} \right\} \tag{7}$$

A_e is the element area and K^e is the element stiffness matrix, expressed as follows: $K^e = \int_{A_e} \begin{bmatrix} B^T CB & B^T CB' \\ B'^T CB & B'^T CB' \end{bmatrix} dA$

The kinetic energy for an element e of the plate is:

$$T^e = \frac{1}{2} \int_{A_e} \dot{\Delta}_e^T \rho \dot{\Delta}_e h dA = \frac{1}{2} \left\{ \dot{\delta}_i^T \quad \dot{\delta}_j'^T \right\} M^e \left\{ \begin{matrix} \dot{\delta}_i \\ \dot{\delta}_j' \end{matrix} \right\} \tag{8}$$

The dot point indicates the first derivative of the displacement field with respect to time and ρ is the material density of the plate, M^e is the element mass matrix:

$$M^e = \int_{A_e} \begin{bmatrix} N_i N_i & N_i(N_j H) \\ N_j(H N_i) & (N_j H)(N_j H) \end{bmatrix} \rho h dA \tag{9}$$

The free vibration problem can then be formulated as follows:

$$(K - \lambda M)\delta = 0 \tag{10}$$

where K is the global stiffness matrix, M is the global mass matrix, λ are eigenvalues and δ are eigenvectors.

4. Numerical studies and results

The numerical computations are carried out via a self FORTRAN computer code developed for this purpose. In order to check the validity of results, a comparative study is made on the first fundamental frequencies, where the actual results are compared to those obtained by analytical solutions. The subspace iteration method [12] is used when calculating eigenvalues and eigenvectors.

In all cases, we present the non-dimensioned natural frequencies as $\varpi = \omega a^2 (\rho h / D)^{1/2}$, where D is the bending rigidity of the plate.

4.1. Simply supported rectangular plate with an edge crack

The first application deals with an isotropic simply supported rectangular plate possessing an edge crack. The dimensions of the plate are such that, the ratio of the lengths a/b = 2.0, the aspect ratio h/a = 0.001, and its Poisson's ratio ν = 0.3. The crack is at the middle of side b, and parallel to the *x*-axis (Fig. 2). A nine node isoparametric element is used in the discretization and the plate is subdivided into 400 elements i.e.; 20 × 20 elements. We impose that the crack path is aligned with the boundary of the element (Fig. 3).
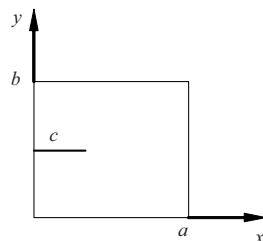
Fig. 2. Square plate with a side crack
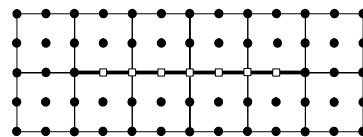
Fig. 3. Crack position with respect to the meshing (only nodes in square are enriched)

This hypothesis permits the usage of the classical numerical scheme without any numerical locking problem. Nevertheless, in the present paper reduced integration technic is used for its efficiency for the case of thin Mindlin's plate's theory including transverse shear deformation and rotatory inertia effects. Table 1 shows adimensional fundamental frequency as a function of the crack length.

On the same table are also presented the results given by Stahl and Keer [2], and Liew et al. [3]. The values in parenthesis are the percent errors with respect to Stahl's and Keer's solution. One can observe a severe drop in the fundamental frequency of about 44%, demonstrating the effect of an edge crack. We will see in the next section that a central crack has less effect than the edge crack does. The accuracy of the present method is very high as compared to the analytical solution given in reference [2]. The maximum percentage error is about 0.11%. One can conclude that the X-FEM is efficient in the dynamic analysis of cracked plates.

Table 1. Dimensionless fundamental frequencies ϖ of a simply supported isotropic rectangular plate with a side crack (a/b = 2.0, ν = 0.3 and h/a = 0.001)

c/a	Present	Analytical solution in Ref. [2]	Stahl and Keer [2]	Liew et al. [3]
0.0	49.348	(0.00)	49.348	49.35
0.2	48.971	(0.03)	48.953	49.05
0.4	44.486	(0.06)	44.512	45.40
0.6	36.158	(0.04)	36.172	37.44
0.8	29.874	(0.11)	29.905	30.50
1.0	27.508	(0.10)	27.536	27.52

4.2. Simply supported square plate with a central crack

The second application is the one of an isotropic simply supported square plate and possessing a through central crack (Fig. 4). It's Poisson's ν = 0.3, and its aspect ratio (thickness to the plate length) is equal to 0.001. Table 2 shows numerical results for the first three adimensional natural frequencies for a simply supported square plate centrally cracked for various values of the crack ratio c/a (crack length/plate length). For sake of comparison, we present on the same table, the analytical results given by Stahl and Keer [2], and the numerical results given by Liew, Hung and Lim [3]. As far as the accuracy is concerned, one can say that the present numerical results compare very well with those of [2, 3].

One can observe that the frequency of all modes decreases as the crack length increases. This physical fact is more pronounced for the antisymmetrical mode in y-axis. In fact, the drop in the adimensional frequency of this mode is about 60%. However, the drop in the adimensional fundamental frequency is 44% meaning that the central crack has less effect on the fundamental frequency than the edge crack does. For example, with reference to Stahl's and Keer's results, the maximum errors when omitting the case of c/a = 1.0, are 0.06%, 0.07%, and 0.13% for mode1, mode2, and mode3, respectively.
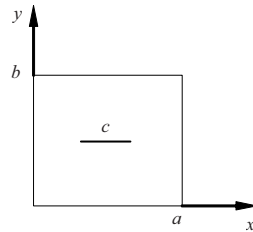
Fig. 4. Square plate with a centrally located crack

Table 2. Dimensionless fundamental frequencies ϖ of a simply supported isotropic square plate with an internal crack

c/a		0.0	0.2	0.4	0.6	0.8	1.0
Mode 1	Present	19.74	19.31	18.28	17.18	16.41	16.13
	Ref. [2]	19.74	19.30	18.28	17.19	16.40	16.13
	Ref. [3]	19.74	19.38	18.44	17.33	16.47	16.13
	Present	49.35	49.18	46.64	37.99	27.75	17.83
Mode 2	Ref. [2]	49.35	49.17	46.62	37.98	27.77	16.13
	Ref. [3]	49.35	49.16	46.44	37.75	27.43	16.13
	Present	49.35	49.32	49.03	48.21	47.20	46.73
Mode 3	Ref. [2]	49.35	49.33	49.03	48.22	47.26	46.74
	Ref. [3]	49.35	49.31	49.04	48.26	47.27	46.74

4.3. Clamped-free-clamped-free rectangular plate centrally cracked

The third application is a rectangular plate (*a*, *b*) containing a central crack parallel to the *x-axis*. The sides parallel to *x*-axis are fixed while the two others are free (Fig. 5). The plate configurations as given in [3] are:

- Plate sides ratio *a/b* = 0.5
- Aspect ratio (plate thickness to plate length) *h/a* = 0.001
- Ratio (crack length to plate length) *c/a* = 0.4
- And a Poisson's ratio ν = 0.31

Table 3 shows adimensional frequencies of the five modes of vibration. Along with the present results and for sake of comparison, results given by Liew, Hung and Lim [3], and Fujimoto and Sumi [8] are also presented on the same table. Compared to the experimental results [8], the present once are satisfactory with a maximum percentage error of 2%.

Figure 6 shows the first five eigenfunctions obtained for the cases *c/a* = 0.4 and *c/a* = 1.0, where the crack is visible for mode 1 and mode 5 (symmetric about *x*, symmetric about *y*).

For the ratio $c/a = 0.4$, the frequency drops up to 21% and 14% for mode 1 and mode 5, respectively. On the other hand the crack has no big effect on the other three eigenfunctions.

Table 3. Comparison of Non-dimensional fundamental frequencies ϖ for a FCFC rectangular plate with a centrally located crack $a/b = 0.5$, $c/a = 0.4$ and $\nu = 0.31$

N° Mode	Present	Experiment [8]	Liew [3]
1	5.31	5.3	5.26
2	8.98	9.0	8.98
3	15.15	15.6	15.11
4	20.58	20.6	20.50
5	26.75	26.3	26.56
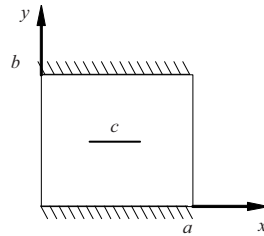
Fig. 5. FCFC square plate with a centrally located crack

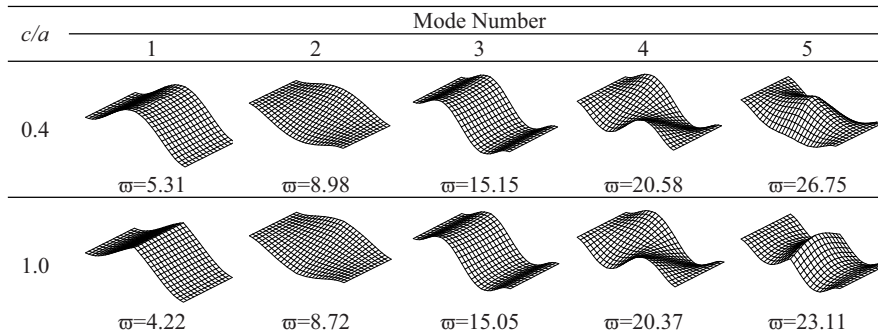**Fig. 6.** Eigenfunctions for the first five modes of a FCFC rectangular plate with a centrally located crack $a/b = 0.5$, $c/a = 0.4$ and $\nu = 0.31$

5. Conclusions

The effects of crack on the dynamic response of plates have been considered using the extended finite element method (X-FEM). The mathematical model includes transverse shear deformation and rotatory inertia. Based on this model a self

contained computer code written in FORTRAN has been developed and validated through applications reported by previous researchers. It is shown that the crack has significant effects on frequencies of vibration. In fact, results show a net decrease in all the frequency modes while the crack increases. These physical facts more pronounced for typical modes of vibration, as it depends on the crack peculiarities. Overall, the X-FEM is suitable in the dynamic analysis of cracked plates.

References

[1] Lynn PP, Kumbasar N (1967) Free vibration of thin rectangular plates having narrow cracks with simply supported edges. *Proceedings of the 10th Midwestern Mechanics Conference Colorado State University, Fort Collins CO*, pp 911–928.
[2] Stahl B, Keer LM (1972) Vibration and stability of cracked rectangular plates. *Int J Solids Struct,* 8: 69–92.
[3] Liew KM, Hung KC, Lim MK (1994) A solution method for analysis of cracked plates under vibration. *Eng Fract Mech*, 48(3): 393–404.
[4] Qian GL, Gu SN, Jiang JS (1991) A finite element model of cracked plates and application to vibration problems. *Comput Structs*, 39(5): 483–487.
[5] Krawczuk M, Ostachowicz WM (1993) A finite plate element for dynamic analysis of a cracked plate. *Comput Meth Appl Mech Eng*, 115: 67–78.
[6] Krawczuk M (1993) Natural vibration of rectangular plates with a through crack. *Arch Appl Mech*, 63: 491–504.
[7] Lee HP, Lim SP (1993) Vibration of cracked rectangular plates including transverse shear deformation and rotary inertia. *Comput Struct*, 49(4): 715–718.
[8] Fujimoto T, Sumi S (1987) Vibration characteristics of center cracked plates under tension. *Bull Jpn Sot Mech Engrs*, 53: 1124–1131.
[9] Moës N, Dolbow J and Belytschko T (1999) A finite element method for crack growth without remeshing. *Int J Numer Meth Eng*, 46: 131–150.
[10] Belytschko T, Moës N, Usui S et al. (2001) Arbitrary discontinuities in finite elements. *Int J Numer Meth Eng*, 50: 993–1013.
[11] Bachene M, Tiberkak R, Rechak S, Hachi BEK (2007) Analyse du comportement vibratoire des plaques fissurées par la X-FEM. *18th French Congress on Mechanics, Grenoble, France*, August.
[12] Bathe KJ, Wilson EL (1996) Finite element procedures. Prentice Hall, Upper Saddle River, New Jersey, 07458.
[13] Khadem SE, Rezaee M (2000) Introduction of modified comparison functions for vibration analysis of a rectangular cracked plate. Journal of Sound and Vibration, 236(2): 245–258.

A New Generation of 3D Composite Materials: Advantage and Disadvantage

Z. Aboura[1], K. Khellil[1], M.L. Benzeggagh[1], A. Bouden[2] and R. Ayad[3]

[1]Laboratoire ROBERVAL UMR - CNRS 6263, Université de Technologie de Compiègne, Centre de Recherches de Royallieu, BP 20529 - 60205 Compiègne cedex, France

[2]L3M IUT de Tremblay en France, Rue de la Rapperie 93290 Tremblay-en-France

[3]Group of Mechanic for Materials and Structures (GMMS, EA 2617), ESIEC/Université de Reims Champagne-Ardenne, Esp. Roland Garros, BP1029, 51686 Reims, France

Abstract   The advent of a new generation of materials composite, known as three-dimensional composite, raises as many hopes as new scientific challenges. Indeed, the reinforcement in the third direction allows the reduction of the interlaminar stresses, the improvement of the impacts behavior and the increase of the performances in the third direction. However, the complexity of architectures imposes a modification of the experimental and theoretical approaches used until now for traditional composite materials. This article proposes a summary of the work carried out within the Roberval laboratory of the University of Technologie of Compiègne on this type of material. It aims to highlight the advantages and the disadvantages of this new generation of composite materials as well as the weaknesses of the experimental and theoretical used approaches.

Keywords: 3D Composite Materials, Impact, Behaviour, Mode I.

1. Introduction

The development of the techniques of weaving allowed, these ten last years, the development of new architectures of three-dimensional reinforcements. Thus was born a new generation of composite materials whose elastic and rupture performances in the third direction are not any more to show (Dransfield et al., 1994). Moreover the reinforcement in the third direction allows a clear improvement of the inter-laminar resistance which remains one of main concerns with respect to laminated composite materials [1, 2]. However this reinforcement presents certain disadvantages. Indeed, in the case of the stitched reinforcements for example, the passageway of the seam in the basic 2D fabric involves a bursting of the yarn and generates areas rich in resin [3]. Moreover the ringlet of weaving at the foot of the seam is a zone of weakness (yarn strongly twisted). Thus the tensile properties can be faded during the introduction of a stitch [4]. With regard to bending behaviour, the works listed in the literature is rather contradictory.

Indeed certain authors [5] find that the stitch introduction allows the enhancement of the elastic modulus and the stress failure in the case of 4 points bending tests. On the contrary, other authors, such as Mouritz [6], indicate that the bending properties can be degraded with the introduction of a seam. In fact the properties are strongly related to the density and the nature of the seam. The experimental analysis of these new materials requires a sophistication of the means due to the complexity of their architectures. Thus, recent work [7] showed that it was essential to crosschecking several investigation techniques (acoustic emission, strain fields analysis, in-situ and post mortem microscopic observations) in order to understand the ruin process of interlock composite material. Concerning the behaviour modelling approaches of these materials, some attempts are proposed but remain limited to the elastic behaviour and in the case of simple solicitation [8, 9]. It is obvious that this aspect of the problem remains very complex more especially as it is far from being solved in the case of composite materials with 2D reinforcement. It comes out from this short introduction that these new materials raise as many hopes as new scientific challenges. Through this article, we will present two cases of figures. The first relates to the behaviour of these materials under Mode I solicitation where we will reveal the great advantage of these materials. The second case relates to the impact and post-impact behaviour where the contribution of reinforcement in the third direction is mitigated and remains dependant on the architecture of the reinforcement.

2. Materials presentation

The study concerns seven families of materials made up of the same RTM 6 epoxy resin. Two groups will be distinguished. First is consisted of the 3 mm thickness materials whose basic reinforcement is a carbon T300 5-satin weave. This reinforcement is then stitched either with T900 and 5 mm step (A2) or with the same stitch and 7 mm step (B2) or with a 5 mm step and a T300 stitch (C2). The not stitched material (2D) will be used as reference. Second consists of materials which differ by nature of the reinforcements. It concern a stitched (A3) an orthogonal 3D fabric (G3) and an interlock (H3), Table 1.

Table 1. Presentation of materials

Reference	Type of reinforcement
2D	5-weave satin
A2	Stitch T900, 5 mm step, 3 mm thickness
B2	Stitch T900, 7 mm step, 3 mm thickness
C2	Stitch T300, 5 mm step, 3 mm thickness
A3	Stitch T900, 5 mm step, 6 mm thickness
G3	Orthogonal 3D fabric T300, 8 mm thickness
H3	Interlock fabric T300, 8 mm thickness

3. Mode I interlaminar fracture of stitched textile composite materials

Few works have been done on interlaminar fracture of stitched composites and no specific methodology is proposed. We will thus base on the compliance method. The data reduction will be refined by observations carried out during the tests followed by microscopic analyzes. Let start by studying the load/displacement curves of materials A2, A3, B2 and B3 (Figs. 1 and 2).
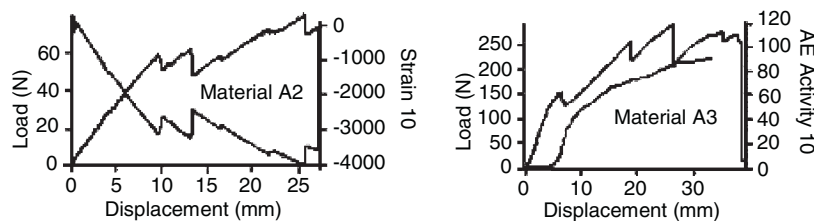
Fig. 1. Curves load/displacement respectively of materials A2 and A3
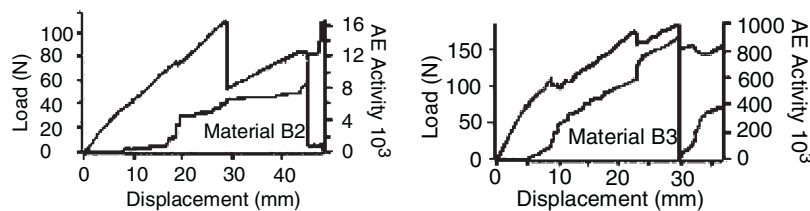
Fig. 2. Curves load/displacement respectively of materials B2 and B3

Table 2 summarizes the main behaviour observed during the tests.

Table 2. Behaviours observed during tests

Ref.	Behaviours observed during the tests.
A2	Few samples present seams debonding. For the majority of samples there is rupture of the sample upper arm by bending around the first row of seam.
B2	Delamination and washing away of the seams.
A3	Delamination and washing away of the seams.
B3	Delamination and washing away of the seams.

Another important fact is noted. It relates to the position of the pre defect compared to the first seam. Thus for the materials A2, A3, and B3 the crack front is to 15 mm of the first stitch row whereas it is only to 5 mm for material B2. Thus, the firsts parts of the load/displacement curves of the materials A2, A3 and

B3 correspond to the delamination of 5-weave satin produced on the first 15 mm (between the first row of the stitches and the crack front of the pre defect) who is characterized by a load fall. This phase is followed by a load increases which corresponds to a stitches solicitation. As regards the load / displacement curve of the B2 material, it does not present a first load fall because the stitches are directly requested. The following diagram summarizes these remarks (Fig. 3). As regards the determination of the strain energy release rate for the basic 2D material, the problem is simple. It is enough to use the compliance method introduced by Benzeggagh [10] on the first part of the load/displacement curve. Concerning the of the strain energy release in the presence of the seams two possibilities exist (Fig. 3):

o   To measure the compliance on area 2–3, thus we will consider that the crack is directly in the presence of the stitches and we will disregard all initial damage.
o   To measure the compliance from the first point (point 0) up to point 3. This compliance must be including the whole of the phenomena produced at the beginning of the loading.

The second method should be more representative of the behaviour of materials, nevertheless the two methods will be used and a comparison of the results will be carried out.
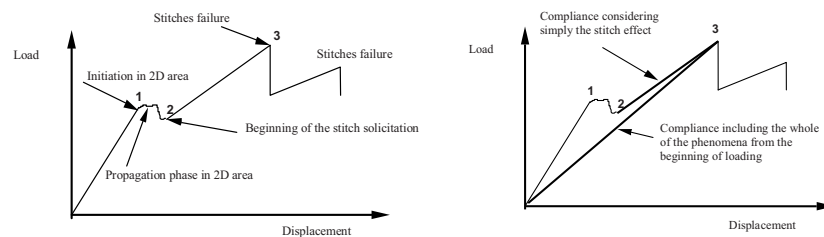
Fig. 3. Fracture scenery for specimens A2, A3 and B3 and compliance selection

The histogram of Fig. 4 presents the main results. They indicate a considerable difference between the energy values issue from the two methods for the materials B3 and C3. In fact the first method which does not take account of the damages establish by the cracking of the 2D, over-estimates the energy of delamination of stitched composite. The second method which includes the whole of damages phenomena must be more reliable, more especially as between the material B2 and C3 the value of energy is practically the same one. With regard to the performances of various materials, it appears that A3 material with a T900 seam and a 5 mm stitch step, offers the best performances. Thus the stitch step has an influence on the Mode I energy value. A difference of 20% is observed between average GImax A3 material (5 mm stitch step) and B3 material (7 mm stitch step). The influence of the nature of the stitch is even stronger. Indeed for the same step, the seam in T900 offers performances definitely higher (56%) than those of the T300.

This first part shows the unquestionable interest of the reinforcement in the third direction for mode I solicitation. On the other hand the data reduction techniques seem to be insufficient. Thus the determination the crack energy propagation remains impossible in the current state of knowledge. Much remains to be made in order to control the behaviour of these materials. In the second part, we will show that the 3D composite materials do not have only advantages. In the case of the impact behaviour, for example, the introduction of reinforcement into the third direction can prove, in certain cases, harmful.
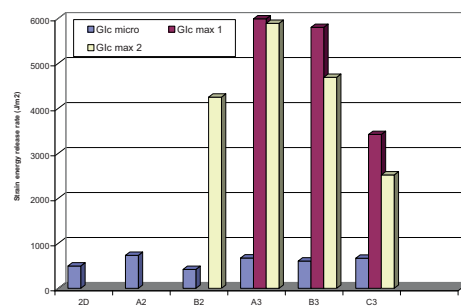

Fig. 4. Strain energy release rate obtained by the two methods

4. Analysis of post-impact bending behavior

The experimental protocol adopted for this study is declined in four stages:

- Carry out impact Charpy tests until failure in order to analyze the influence of the geometrical and mechanical parameters of the reinforcement.
- Introduce, by the means of various levels of impacts, the damages within materials.
- Identify the nature of the damages by microscopic observations.

Post impact three points bending test and follow-up of the damage by the technique of acoustic emission. The results of the first stage are shown on Fig. 5. Two main parameters are measured: the failure energy E_r (at maximum load) and the maximum energy E_{max} (area under load / displacement curve). The introduction of reinforcement into the third direction is not inevitably synonymous with performance enhancement. Indeed, with regard to the maximum energy absorptive, the material not strengthened 2D offers the best performances. It preserves this capacity to dissipate energy by delamination which is abolished in other materials by the effect of the introduction of the seam. It also presents the failure energy higher of 10% than stitched material A2. On the other hand the B2 material, whose stitch step is 7 mm, makes it possible to improve of 16% the energy of failure compared to 2D material not stitched.

The C3 material presents the weakest performances due to a stitch step of 5 mm and a less powerful stitch (T300 compared with T900). As regards the second group, we will compare the performances due to different architectures of weaving. The comparison of material A3 to the materials G3 and H3 cannot be made because of the difference the thicknesses. Concerning the materials G3 and H3, we note that generally, the G3 material with 3D orthogonal reinforcement presents the higher energy absorption. The gap between energies of failure is about 40%. However this difference is reduced to 8% if maximum energies are compared. Thus, it appears that the difference between the energy of failure and the energy maximum of the G3 material is very reduced whereas this gap is very important for the material with interlock reinforcement (H3). The G3 material probably dissipates practically the whole energy during the first fall of load, whereas the H3 material continues to dissipate energy, probably by delamination, beyond the first damages.
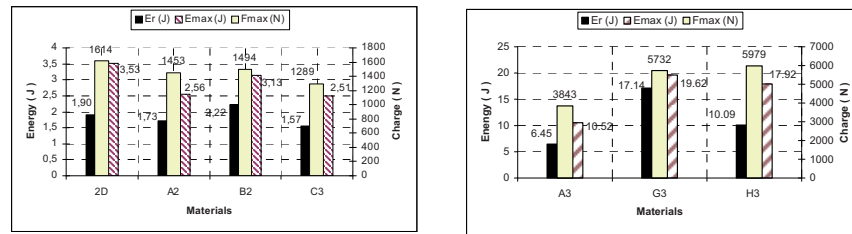
Fig. 5. Results of impact until failure

4.1. Bending and post-impact bending tests

The three points bending tests were carried out in accordance with the ISO standard 179NF-035. The distance between supports is 40 mm (conditions identical to those of Charpy). In the case of the materials of the first group, the state of stress generated by these conditions would be combined: bending + shearing. On the other hand the materials of the second group will be subject to a pure shearing because of their thickness.A comparison criterion, independent of the geometry of the specimens, was retained: the parameter R which is the ratio between the slope P of the curve charge–displacement (rigidity) and the specimen section (R = P/A). Table 3 presents the value of this parameter for the study materials. It appears that the not stitched material (5-weave satin) is the most rigid material among materials of the first group. This material has a higher rigidity R of 10%. Rigidities of the materials A2 B2 and C3 are almost identical.

It is clear that, neither the density nor nature of the stitches affect the value of R. As regards materials of the second group, architecture H3 and G3 offer similar performances.

Three points bending tests were conducted following the introduction of damage into materials by the means of impacts to energy levels ranging between 25% and 75% of failure energy. Figure 6 shows an example of the load / time curve superposed to energy/time curves. The load diagrams are presented in the form of typical bell of a resilient contact.

Table 3. R values for the different materials

Materials	2D	A2	B2	C2
$R(N/mm^3)$	32.46	28.41	29.07	29.08

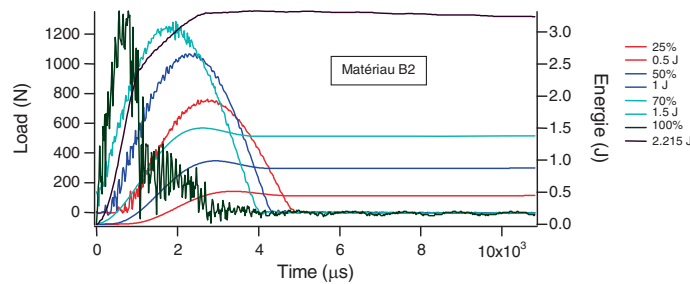| Materials	A3		G3	H3
$R(N/mm^3)$	77.25		86.58	85.59

Fig. 6. Impact at different energies levels

If we analyze the results of Table 4, relating to materials of the first group, it is noted that for the same energy level of impact, the materials stitched with a T900 seam (A2 and B2) present the less important stiffness loosing. They are followed by the materials 2D and C3. This maximal loss of 10% of rigidity remains acceptable. The thickening of the specimens and the change of the nature of the stress (shearing) increase this stiffness loosing as it showing by material A3 (compared to A2). This loss reaches 14% for a level of impact of 62% of failure energy. This phenomenon is accentuated by changing the nature of the architecture of the reinforcement. Indeed, in the case of the orthogonal material G3, a loss being able to reach the 70% for a level of impact of 75% of failure energy. The loss of rigidity in the case of the H3 material is a little less but reaches neverthe-less 41% for a level of impact of 75%. The explanation of such phenomena will be provides by the microscopic analysis correlated to acoustic emission technique. During the bending tests all specimens were instrumented by an acoustic emission (AE) sensor. Previous works [2] allotted the ranges of amplitudes recorded to physical phenomena occurring during the damage process. In this paper, the case of the G3 materials will be discussed (Table 5). The Fig. 7a, b illustrate the distributions of amplitudes recorded to the beginning and at the end of the loading, on the H3 material not impacted. A superposition with the load diagram makes possible to have an outline on the level of loading.

The beginning of damage is related to the cracking of the matrix corresponding to the range of amplitude between 40 and 55 dB. This phenomenon is classical because of the architecture of orthogonal materials present important areas rich in resin. This phenomenon continues with the emergence of damage at the interfaces for a loading level close to the 2100 N. The fibres failure occurs at the end of the loading when the whole of the interfaces is damaged. This phenomenon is showing on the Fig. 4b where signals of AE amplitudes higher than 80 dB appear. The stiffness of material is 8726 N/mm. The impact of material with 25% of the failure energy introduces damages mainly localized into the areas rich in resin. Thus, as the Photo 1a shows it, these damages appear in the form of 45° inclined crack synonymous of a shear stress state. Moreover interfaces around the vertical reinforcement are also strongly degraded. An impact with a stronger energy. The layers in the stratification plane are crossed by a tilted crack beginning on a vertical reinforcement and reaching the following (Photo 1b).

Table 4. Stiffness loosing in the case of materials of the first group

Materials	Thickness (mm)	Impact energy in % of failure energy	Percentage of stifness loosing
2D	3.04	26	4.4
		52	8
		79	9
A2	3.07	29	<1
		58	2
B2	3.10	23	<1
		47	2
		70	8
C3	2.98	32	8
		64	10

Table 5. Stiffness loosing in the case of materials of the second group

Materials	Thickness (mm)	Impact energy in % of failure energy	Percentage of stifness loosing
		16	7
A3	6.08	31	13
		62	14
		25	36
G3 (3D)	8.14	50	50
		75	70
		30	6
H3 (Interlock)	8.17	50	13
		75	41

The introduction of these damages completely amends the failure process after takeover the sample on three points bending. The Fig. 8a, b present the distributions of AE amplitudes. They were recorded at the beginning and the end of loading for a material impacted at 75% of rupture energy. The appearance of the first acoustic events is much earlier and rich in phenomena compared to the material which does not have undergoes impact.

The main phenomena relate to the resin but also to the fibers. The resin and the interfaces having been damaged by the impact the fibers support directly the efforts. The shape of the load curve presents an important nonlinearity (Fig. 8b). Compared to Fig. 7b, the falls of brutal load are replaced by a more stable propagation of the damages. Rigidity passes to 2645 N/mm and the maximum load to 4465 N against 6346 N in the case of the material not impacted.

The impact involved a dissociation of the vertical reinforcements of those existing in the plan. The residual behavior is strongly affected. We can summarize the performances of the two groups of materials, according to the nature of reinforcement, by Table 6. It appears that the reinforcement in the third direction is not necessary synonym of increasing properties. Here again the composite is synonym to compromise.
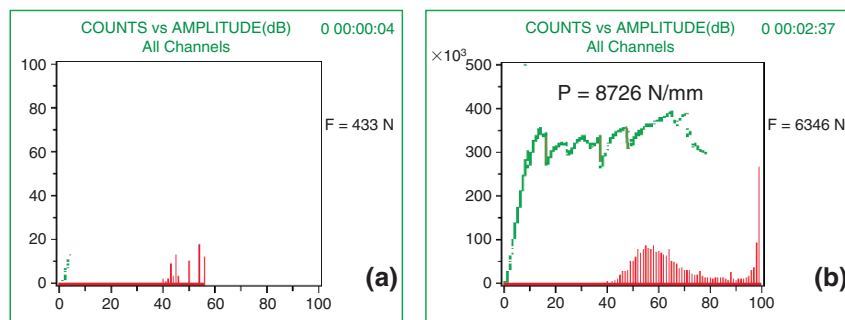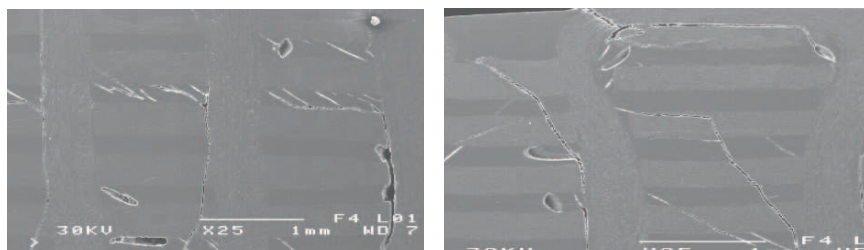

Fig. 7(a) and (b). Amplitudes distributions at the beginning and the end of the test

Photos 1(a) and (b). Material G3 impacted at 25% and 75% of failure energy
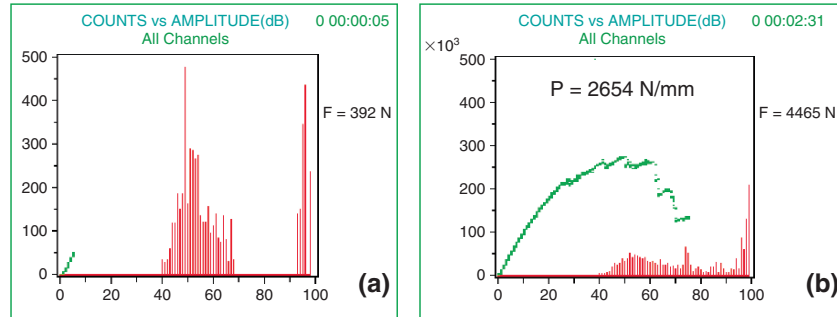
Fig. 8(a) and (b). Amplitudes distributions in the case of impacted specimen

Table 6. Summary of performances

Ref.	E_r	E_{max}	Rigidity (R)	Percentage of rigidity loosing after impact
2D	++	+++	++	++
A2	++	+	+	+++
B2	+++	++	+	+++
C2	+	+	+	+
A3	+	++	++	++
G3	+++	+++	+++	+
H3	++	+++	+++	+

5. Conclusions

This work made it possible to give an outline on the mechanical behaviour of 3D composites material. This reveals that the reinforcement in the third direction is not synonymous with enhancement of mechanical properties. Thus in the case of the Mode I behaviour, the reinforcement in the third direction takes all its interest. Energy is multiplied by factor 10 compared to the 2 D conventional composite materials. Whereas in the case of bending and impact behaviour, the composite material not strengthened in the third direction presents the best performances. In this case of figure we note well that the presence of reinforcement in the third direction is regarded as a disadvantage. On the other hand as regards to post impact behavior, the contribution of the reinforcement in the thickness makes it possible to improve rigidity and to delay the ruin of the specimen. These two cases illustrate well the broad field of investigation which this new generation of materials requires. Moreover, as we saw, the data reduction methods of these materials remain, in certain cases, insufficient. Many works remain to make in this field. More than ever, composite materials with three-dimensional reinforcements remain synonymous with a compromise between the performances in the third direction and the performances in the plan.

References

[1] Aboura Z, et al. (1995) Mode I Interlaminar Failure of Stitched Textile Ccomposites Materials: Proposition of predictive Reinforcement Model. *10ème Conférence Internationale des Matériaux Composites. ICCM 10 Vancouvert.*

[2] Aboura Z, et al. (2002) Sur la pertinence de l'utilisation de l'émission acoustique comme moyen de suivi des endommagements dans les matériaux composites. *Sigma 2002 1er Congrès international de mécanique, Oran, Algérie.*

[3] Benzeggagh ML [1980] *Application de la mécanique de la rupture aux matériaux composites. Exemple de la rupture par délaminage d'un stratifié.* Thèse de l'UTC 1980.

[4] Ch. EL Hage, et al. (2008) Analytical and numerical modeling of mechanical characteristics of orthogonal 3D CFRP. *Compos. Sci. Technol.*, V 69, pp 111–116.

[5] Chung WC, Jang BZ, Chang TC, Hwang LR and Wilcox RC (1989) Fracture behavior of stitched multidirectional composites. *Mat. Sci. Eng.* A112, pp 157–173.

[6] Dransfield K, Baillie C et Mai, YW (1994) Improving the delamination resistance of CRFP by Stitching-a review. *Comp. Sci. Tech.* V 50, pp 305–317.

[7] Herszberg I et al. (1996) The residual tensile strength of stitched and unstitched carbon/ epoxy laminates impacted under tensile load. *Congress on Applied Mech.* pp 309–314, Melbourne, Australia.

[8] Lascoup B, Aboura Z, Khellil K and Benzeggagh ML (2006) On the mechanical effect of stitch addition in sandwich panel. *Compos. Sci. Technol.* 66, pp 1385–1398.

[9] Mouritz AP (1996) Flexural properties of stitched GRPlaminates. *Composites* 27A, pp 525–530.

[10] Mouritz AP, et al. (1997) Flexural and interlaminar shear properties of stitched GRP laminate following reapeated impacts. *Compos. Sci. Technol.* V 57, pp 509–522.

Benefit from Embedded Sensors to Study Polymeric Composite Structures

Francis Collombet[1], Matthieu Mulle[1], Hilario-Hernandez Moreno[1, 2], Redouane Zitoune[1], Bernard Douchin[1] and Yves-Henri Grunevald[3]

[1]Université de Toulouse; INSA, UPS; LGMT (Laboratoire de Génie Mécanique de Toulouse); 133C, avenue de Rangueil, 31077 Toulouse, France

[2]Instituto Politécnico Nacional, ESIME Unidad Ticomán, Av. Ticomán No. 600, Col. San José Ticomán, 07340, México D.F., México

[3]Composites Expertises Solutions (CES), 31320, Castanet Tolosan, France

Abstract The present paper deals with the use of optical fibers with Bragg gratings for the identification of process-properties relations for composite structures. This study relates a 7 year-experience in the field of process and mechanical characterization of composite parts. It highlights some major topics in terms of technological issues such as sensor integration, information discrimination and measurement accessibility. Results of process monitoring concerning autoclave cure and filament winding are shown through which initial states are identified. Finally, structural tests of instrumented parts are presented, showing the efficiency of the embedded sensors to allow test-calculation dialogues and thus properties identification.

Keywords: Composites, Optical Fibers, Process and Mechanical Characterization, Properties Identification.

1. Introduction

This paper concerns themes associated to the processing of composite materials using the main industrial manufacturing means such as an autoclave, a resin transfer molding unit (RTM) and a filament winding machine. Diverse and numerous research programs are undertaken around topics concerned with the influence of process parameters over material properties variability. Physico-chemical and mechanical studies of cured parts and structures may bring an important knowledge on the influence of the manufacturing conditions but they won't be able to precisely trace the material elaboration history. Indeed, the specific operating modes of these manufacturing means (high pressures, high temperature, rotation…) present technological difficulties to undertake in situ measurement acquisitions during the fabrication phase. This research activity has been involved for many years in the use of optical fibre technologies to take on this challenge [1–3]. Advantage is taken of the composite material integration

potential so that composite parts are instrumented with embedded optical fiber Bragg gratings (OFBG).

The present paper starts by relating our finding and positioning over some of the major issues concerning OFBG embedment and measurement understanding. It is then shown how technological issues related to each manufacturing means are solved in order that OFBGs deliver exploitable information. Some curves of strain assessment during manufacturing process are presented. Finally, themes concerned with material properties identification taking into account the influence of process parameters [4–6] are approached. They are based on experiments which are carried out over elementary coupons and also on representative industrial composite specimens. Instrumenting this kind of specimen is obviously more difficult because they present geometrical singularities and complex staking sequences but the knowledge of the material properties within these structures is the final target.

2. Preliminary issues

A first preliminary aspect concerns the sensor integration in the host material. The interface OFBG/matrix quality and the effective load transfer were estimated experimentally through a series of SEM observations (Fig. 1), and standard elementary tests including Interlaminar Shear Stress (ILSS) tests (Fig. 2, left) which are most revealing to detect any defect or weakness.

Numerical simulations (Fig. 2, right) are also undertaken in order to estimate the thermo mechanical influence of the OFBG on its environment. Results show that the invasive character of the sensor is negligible and that the structural integrity of the instrumented part is not altered if the optical fibers are deployed parallel to the reinforcement fibers [7].
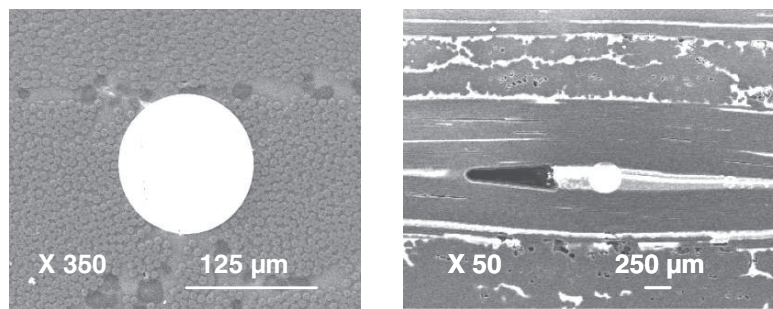

Fig. 1. SEM observations of an optical embedded with OF parallel to the reinforcements (*left*) and OF transverse to reinforcements (*right*)

The second major point of interrogation concerns the understanding of information delivered by the fiber Bragg grating (FBG) sensor. Indeed, during

manufacturing processes or mechanical tests, several quantities (mainly strain and temperature) may be acting on the embedded sensor at the same time.
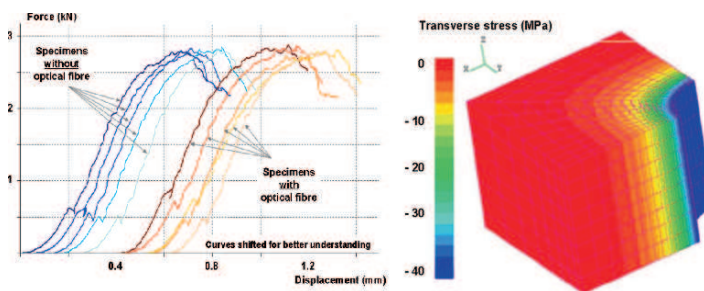

Fig. 2. Standard ILSS tests for carbon-epoxy coupons with and without optical fiber (*left*) and thermo mechanical numerical 3D simulations about effect of OF embedded parallel to reinforcements of UD carbon epoxy laminate with transverse stress cartography (*right*)

The Bragg wavelength-shift λ_B, in response to a strain change ε, and a temperature change ΔT, is given in a simplified way by equation 1:

$$\Delta\lambda_B = K_T\Delta T + K_\varepsilon\varepsilon \tag{1}$$

where, K_T and K_ε are the temperature and strain sensitivities of the FBG respectively [6].

Various discrimination methods have thus been used and analyzed. Our work has focused on two different techniques. The first one is an association of a bare FBG with an encapsulated FBG (Fig. 3, left). The second technique is an association of an FBG with a thermocouple. In both cases the second sensor delivers the thermal component of the total information. The first technique gives very accurate results in condition of varying temperature but the tube is to invasive to envisage mechanical studies. In case both thermal and mechanical studies are envisaged then, the second technique is more appropriated.
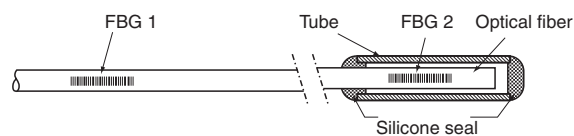

Fig. 3. Bare FBG associated to "encapsulated" FBG in order to discriminate strain and temperature (*left*) and scheme of the experimental set-up for the FBG calibration (*right*)

However, it requires a very precise calibration procedure of the temperature and strain sensitivities characterizing the FBG employed. This is undertaken in an oven equipped with an upper and bottom hole through which may go the OF, as described in Fig. 3 (right).

There is a third point of interrogation. Indeed, prior to any exploitation of FBG results, it was found necessary to validate the embedded optical sensor information. This phase was carried out through a series of comparisons with other techniques of analysis. Thermal expansion measurements are considered with Thermo Mechanical Analysis (TMA) or high temperature resistive strain gages. Mechanical measurements are also considered with traditional strain gages and with digital image correlation techniques (DIC). Finally, both thermal and mechanical situations are simulated with numerical models. Results show overall good match, however some slight discrepancies are observed between surface measurements (strain gages and DIC) and in-core measurements [6] whereas the latter present an excellent correlation with numerical results. This emphasizes the importance to capture the experimental information inside the material [7, 8]. The structural specimen in Fig. 4 is respectively made of 36 plies in the current part (9 mm thick) with a stacking sequence of $[0/45/0/-45/0/90/\ 0/45/0/-45/0/90/0/45/0/-45/0/0]_s$ and 72 plies in the reinforced zone (18 mm thick); the complementary stacking sequence is the same as above. This leads to the following reinforcement distribution: 55.6% at 0°, 33.3% at +/−45° and 11.1% at 90° [8].
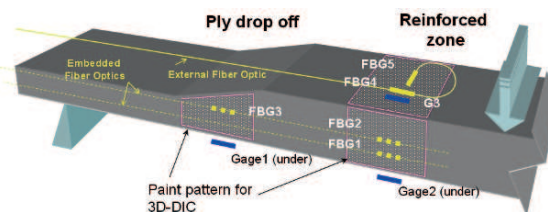

Fig. 4. Multi-instrumented structural specimen submitted to a three-point bending test with surface instrumentation (3D-DIC, strain gages and FBGs) and embedded FBGs

3. Process monitoring

3.1. Autoclave cure

Many stages of this manufacturing process present situations that are a risk for the integrity of FO. Compacting, vacuuming, pressurizing is likely to subject OFs to more or less important folding. Some may attenuate the reflected signal in some critical extend, but they may even be responsible of fiber ruptures. The OF curvatures must be reduced as much as possible. Figure 5 (left) shows a solution to minimize them by using beveled silicone foam. For similar reasons a specific

device was especially conceived to allow the passage of optical fibers through the wall of the autoclave (Fig. 5, right).

The major difficulty is to ensure a perfect sealing without breaking the optical fibers.
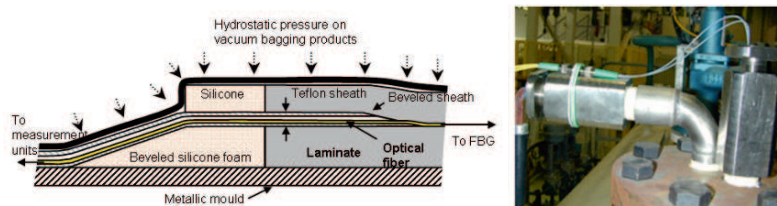

Fig. 5. Optical fibre ingress protection in prepreg before the autoclave curing process (*left*) and OF gate device of the autoclave (*right*)

The adopted solution is a silicone stopper placed in a tube crossing the wall of the autoclave. The stopper may be finely squeezed by means of a hollow screw. The autoclave manufacturing process is particularly effective for high performance structures. This elaboration mode is largely used in the aeronautical and aerospace fields. The quality of the parts is obtained thanks to the association of three process parameters: pressure, vacuum and temperature. Each one of them has an important influence on the initial properties of the structure, such as the fiber content ratio, presence of porosity, degree of advance or level of cure residual stresses (CRS) which may have a considerable influence on the damage sensitivity of composite structure under loading and Rupture. CRSs are closely related to the strain evolution within the material throughout the process. Thus, the capacities of FBGs are exploited to undertake the cure monitoring of various specimens and to analyze the various phases of the autoclave curing process. The assessment of process induced strains in two structural specimens is shown in Fig. 6 (bottom). The FBG is positioned in the middle of the third ply of the thin zone of the structural specimen which counts a total of 20 plies stacked in a typical aeronautical way (50/40/10) (Fig. 6, top). Looking at Fig. 6 (bottom), it may be observed that, at the beginning of the cycle, the setting under pressure and vacuum phase is clearly marked by a strong positive deformation. At this stage prepregs are relatively rigid and the stress fields which are exerted on the FBGs are not easily identifiable if one sticks to the optical answer. During the rise in temperature, the tensions on OFs seem to be released. Then strains stabilize until the beginning of the 180°C isothermal shelf. There, an increase in the strain appears and corresponds to the beginning of gelation. During the isothermal shelf, the strains are stabilized again even if one distinguishes a light reduction (contraction) which could be associated to chemical contraction. The evolution of strain during the cooling phase is not made in a linear way. The material seems to contract with variable progressions. The mould expansion, on which the specimens are placed, is certainly not foreign to this irregular change. A brutal change of orientation of the strain curves appears towards the end of cooling, at the moment when the pressure and the vacuum are

released. This is explained by the relaxation of the interfacial constraints between mould and specimen.

At the end of the curing process, residual strain is estimated for both specimens (respectively −80 and −50 μm/m). This example highlights how FBGs are able to translate specific manufacturing phases such as temperature change, pressurization, vacuum setting up, gelation, mould-part interaction and build up of residual strains [3, 4, 6].
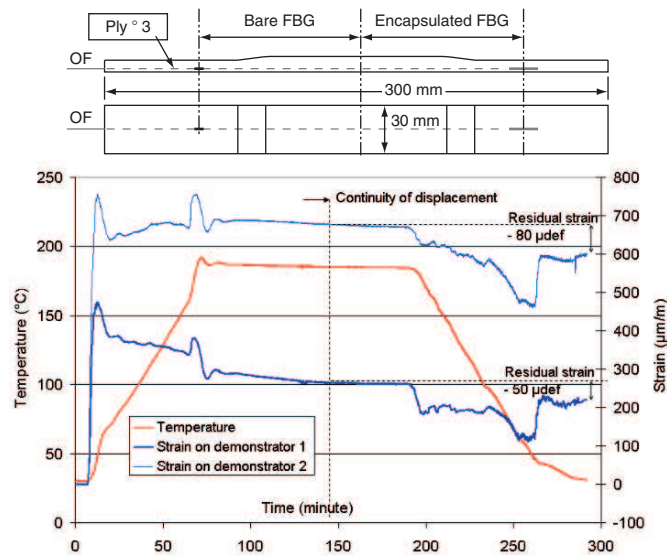

Fig. 6. Geometry of the structural specimen and FBG positioning (*top*) and strain changes vs. cure cycle for two structural specimens (*bottom*)

3.2. Filament winding and cure

It deals with the technological challenge and the development of specimens instrumented with embedded FBGs and thermocouples. The aim is to monitor the temperature and strain changes during the cylinder manufacturing process. Specimens are filament wound glass reinforced epoxy composites. Two technological problems have to be solved: the first question is to collect data during fabrication and the second is to withdrawn the specimen from the mandrel without damaging sensors. This first issue is solved through the development of a rotating interface between the filament winding machine and the composite cylinder in fabrication (Fig. 7, left). The second issue is solved thanks to a specially designed split mandrel (Fig. 7, right). The filament winding machine rotary-static cable interface design leads signal transmission from rotary sensors (embedded sensors in the rotary specimen) to the static reading instruments (Fig. 7, centre). Cylinders are thin walled having a 4.42 mm thick, the reinforcement fiber is continuous glass roving (1200 tex),

with a 3.5 mm width. The matrix system is a mixture of araldite LY 5052 and hardener HY 5052.

Combined rotational and axial movements produce double helical trajectories and a rhomboid shape pattern. The winding has a pattern of 5 rhomboids in the circumferential direction. The 350 mm long is obtained with a machining operation. The number of layers is 7. At both ends of the cylinder, there are zones of reinforcing fibers with an angle of 90°. Fiber orientation has an angle of ±55°, which is a classical winding angle used for pressure vessels. Layer patterns are placed to be stacked coincident in order to have the same material pattern through the thickness direction. Winding angles are strictly maintained for all layers, this produces a slight increase in cell size with thickness. Mean measured thicknesses are 4.4 ± 0.16 mm. The specimens are wound and cured, at 50 °C for 15 h to save rotating connectors. Fiber content ratios were obtained by burn off method giving a mean of 51% ± 2.1%. Detailed information can be found in [4].
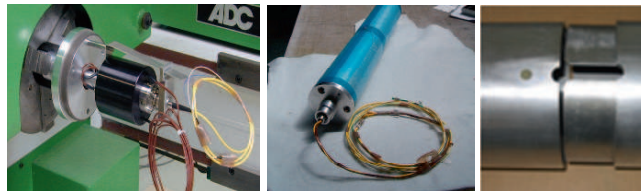

Fig. 7. Connector system on winding machine (*left*), mandrel-connector system (*centre*) and cable passage of the split mandrel (*right*)

In such cylinders, FBGs are aligned in axial and circumferential directions, with a thermocouple placed next to each Bragg grating. Once the conditioned mandrel with the rotary interface and sensors is installed in the filament winding machine, the placement of the first layer is carried out. Next, sensors are placed over the first layer, one Bragg grating and one thermocouple in the circumferential direction and in the axial direction respectively. The second layer is carefully wound over the first layer covering sensors, and then the rest of the layers are wound like any other non instrumented specimen. As indicated on Fig. 8 (left), the circumferential strain evolution during winding is a historical file of the winding process, where the most important events occurring during winding are recorded. The number of the waves and the period of them correspond to the number of layers and the time spent for winding layers. Tests are performed to measure in situ strain and temperature during cure (here for six nominally identical filament wound cylinders). Several points and events of the curing process are identified; these points can be grouped in two classes, one group is formed by points limiting the different phases, the second group is formed by points where material transformations occur. The characteristic points and event explanations are shown in Tables 1 and 2. Axial and circumferential mean strains of all specimens from optical sensors are plotted on Fig. 8 (right). Strain values at the end of winding segment are almost zero, this situation is expected because during winding resin is still

liquid and no bound is present between resin and the optical fiber, so Bragg grating is only exposed to thermal excitation. At the beginning of the curing cycle (in oven), both strains climb as the temperature rise during curing cycle warm up.

It corroborates the fact that during the test, incipient polymerization is observed at the end of the winding phase. A characteristic point is noticed before the end of the warm up segment (point a), where axial strain changes from a positive slope to negative, even if the warm up segment is not finished yet.
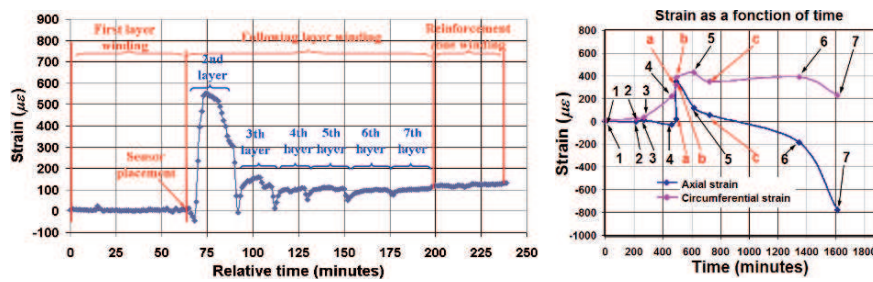

Fig. 8. Event detections during winding phase (*left*) and mean strains delivered by FBGs and characteristic points during curing phase (*right*)

Table 1. Process characteristic phase identification

Process phase identification	Phase description
1–2	Winding
3–4	Waiting between winding and curing cycle
4–5	Heating
5–6	Curing constant temperature phase
6–7	Cooling

Table 2. Phenomena and transformation identification

Characteristic point identification	Point description and occurring transformation
A	Point from which elastic response and thermo-elastic behavior begin to appear during heating
B	Point where axial strain shows a fast decrease, and may indicate a transformation. From this point there is no elastic response nor thermo-elastic behavior
C	Point at which a transformation occurs from semi liquid or liquid state in to a solid state. Material shows again an elastic and thermo-elastic behaviors

This means that in axial strain the beginning of a material transformation is detected. This point is coincident with the gelation temperature of the resin system (58°C). On the contrary, in circumferential strain this characteristic point is not detected, and circumferential strain follows temperature tendency to climb. It can

be noted here, that the composite cylinder over the cylindrical mandrel is free of constrain in axial direction, but in circumferential direction the composite cylinder has to follow mandrel expansion during warm up, this may be the reason why the characteristic point a is not detected by circumferential strain response. During constant temperature segment, in the curing cycle (5–6), axial strain decreases until zero, while circumferential strain remains almost constant, this response indicates a transformation within the material (axial strain releasing), which is supposed to be related with the polymerization process. During cooling down segment (6–7) both strains follow temperature evolution and one can suppose that polymerization has finished and strain evolution is due to thermo elastic behavior.

After the curing cycle, strain values are different from zero, which reveals the presence of residual strains within the material. In axial direction specimens follow a contraction (negative strain mean value: −995 με) and in circumferential direction positive values indicate an expansion (mean value: 134 με), which is related to mandrel expansion because composite elongation in circumference is imposed by mandrel expansion (Fig. 8, right).

4. Property identifications

As it has been shown the initial state of a structure may be approached thanks to FBG. Once the composite part is cured, the embedded sensors may be used to identify experimental values. It may be a basis to elaborate test-calculation dialogues in order to identify material properties.

4.1. Thermo-mechanical testing of autoclave cured structures

In an economical way [5], a test-calculation dialogue can be undertaken successfully using as few FBGs as possible. However, for a deeper and more precise investigation on the material properties it is possible to increase the number of sensors. Such study was undertaken using a similar structural specimen than that described in Section 5.2. Four OFBGs were embedded and superimposed in the reinforced zone of the specimen in order to estimate the through-thickness strain distribution during thermo mechanical tests. FBGs are disposed as shown in Fig. 9. This zone is composed of 28 plies, stacked in a typical aeronautical way (50/40/10) and FBGs are one on top of each other in plies 3, 10, 19 and 26.
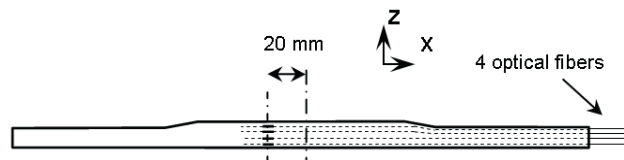

Fig. 9. Distributed instrumentation in the reinforced zone of the structural specimen in plies 3, 10, 19 and 26

Once embedded in composite parts, FBGs may be used to study the thermal behavior of the material. This has been done for the above mentioned structural specimen, thanks to the 4 FBGs embedded in the reinforced zone (Fig. 10, left). Through reheating procedures in oven, expansion coefficients have been identified though the thickness of the reinforced zone. Surprisingly, a variability of thermal elastic properties values is determined [6]. The specimen was submitted to a four-point bending and a numerical FEM simulation was carried out. A test-calculation dialogue enabled to identify a set of properties that correlates much better than the given manufacturer's data (Fig. 10, right).
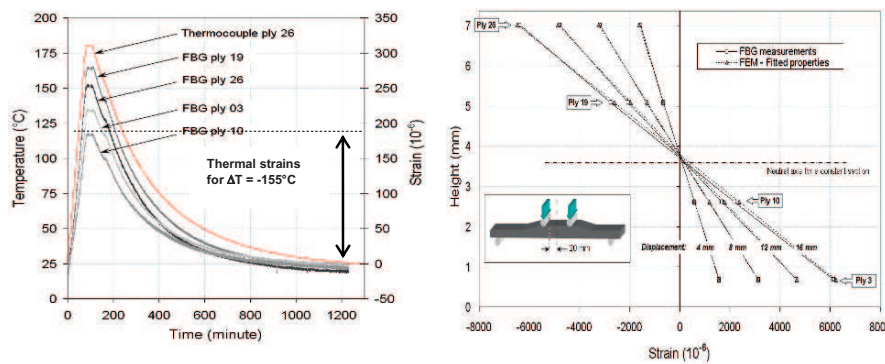

Fig. 10. Thermally induced strain distribution vs. heating cycle in the structural specimen (*left*) and strain distribution in the reinforced zone of a structural specimen during a four-point bending test (comparison between FBG measurements and numerical FEM results, *right*)

4.2. Filament wound cylinders under external pressure until rupture

Specimen was tested under external pressure to validate embedded instrumentation during service and to continue the monitoring of a composite filament wound structure until failure. The test was performed in the IFREMER facilities at Plouzané (France), using the hyperbaric testing chamber. For this test, one closure is provided with a sealed passage tube to connect the optical fibers in the specimen interior to the chamber cover (Fig. 11).
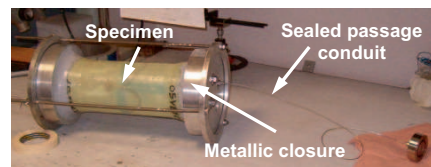

Fig. 11. Bragg grating and strain gage multi instrumented specimen conditioned for external pressure testing

This device was designed by IFREMER. Additionally specimen was instrumented with strain gages to compare with the Bragg grating results. These are bonded on the inner surface, three of them in the circumferential direction and one in the axial direction. Test is carried out by applying loading and unloading pressure cycles, having increments in pressure of 10 bar, starting at 10 bar. Results from this test show that specimen implosion pressure is 6.7 MPa, a 3 lobe buckling circumferential failure mode is observed, which is coincident with values obtained in previous tests of non-instrumented specimens [4] from which a mean value of a 6.5 MPa was determined with a standard deviation of 0.4 MPa.

This result indicates that the embedded instrumentation has no significant influence on mechanical strength at implosion. Bragg grating strain responses and strain gage responses show similar evolution. Bragg grating strain during the last three cycles presents a deviation compared with strain gages. As far as pressure-strain diagrams are concerned (Fig. 12), critical pressure can be observed around 5.5 MPa (the pressure at which the pressure versus strain plot becomes non-linear). Beyond this point a Bragg grating hysteresis response is noted which is not detected by strain gages.

A particular aspect of this phenomenon is that both gratings recorded it, and reacted in the same way, even though both are embedded in different places, both in the central section (half length of the cylinder), but at different circumferential positions. If this phenomenon is a local event (for instance optical fiber and resin interface debonding), each grating would react independently.
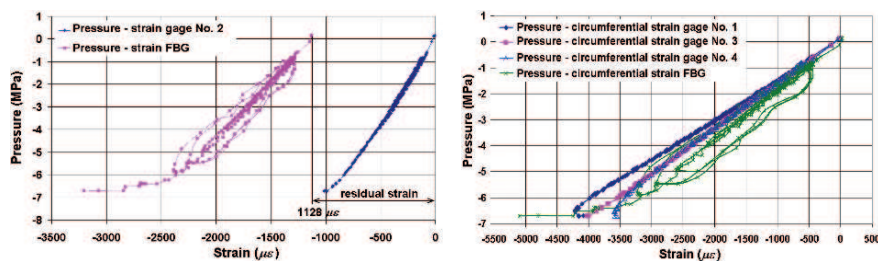
Fig. 12. Pressure - axial strain (*left*) and pressure – circumferential strain (*right*) diagrams during external pressure testing

5. Conclusions

Although the recognized capacities of FBGs are expected to be employed for Structural Health Monitoring (SHM), we show in this paper that the optical sensors represent a precious advanced tool for the identification of composite material properties. Furthermore, FBGs give the possibility to identify the material properties within the structure itself.

Our studies are undertaken on structural specimens that present singular zones (reinforced zone, ply drop off) or filament wound cylinders. FBGs are extremely useful and reliable sensors for process monitoring and further cured part analysis as long as optical fibers are deployed and tested in the appropriate direction and in non significant transverse and/or non uniform stress fields. FBGs give the possibility to estimate initial state, in terms of residual stresses and strains. They may be exploited to investigate thermal elastic behaviours and determine expansion coefficients. Moreover, when mechanical tests are carried out, the gathered experimental information turn out to be very precious in a test-simulation dialogue.

References

[1] Guemes J.A., Menéndez J.M., Response of Bragg grating fiber-optic sensors when embedded in composite laminates. Composites Science and Technology, Vol. 62, Issue 7–8, pp. 959–966, 2002.

[2] Botsis J., Humbert L., Colpo F., Giaccari P., Embedded fiber Bragg grating sensors for internal strain measurements in polymeric materials. Optics and lasers in Engineering, Vol. 43, pp. 491–510, 2005.

[3] Okabe Y., Yashiro S., Tsuji R., Mizutani T., Takeda N., Effect of thermal residual stress on the reflection spectrum from fiber Bragg grating sensor embedded in CFRP laminates. Composite Part A, Vol. 33, pp. 991–999, 2002.

[4] Hernández-Moreno H., Monitoring de la fabrication de tubes composites réalisés par enroulement filamentaire et comportement mécanique sous pression externe. PhD thesis of Paul Sabatier University (in French), Toulouse, France, 2006.

[5] Collombet F., Mulle M., Grunevald Y.-H., Zitoune R., Contribution of embedded optical fiber with Bragg gratings in composite structures for tests-simulations dialogue. Mechanics of Adv. Materials and Structures, Vol. 13, Issue 5, pp. 429–439, 2006.

[6] Mulle M., Zitoune R., Collombet F., Olivier P., Grunevald Y.-H., Thermal expansion of carbon–epoxy laminates measured with embedded FBGS – comparison with other experimental techniques and numerical simulation. Composites Part A: Applied Science and Manufacturing, Vol. 38, Issue 5, pp. 1414–1424, 2007.

[7] Mulle M., Eprouvettes technologiques instrumentées à cœur par réseau de Bragg pour l'analyse du matériau composite dans la structure. PhD thesis of Paul Sabatier University (in French), Toulouse, France, 2007.

[8] Mulle M., Collombet F., Périé J.N., Grunevald Y.-H., Instrumented Technological Specimen: Curing Process and Mechanical Characterization Using Embedded Fiber Bragg Gratings. ECCM11, Rhodes (Greece), CD Rom of the Proc.: C137.pdf, 10 pages May 31–June 3, 2004.

Effect of Temperature and Initiator on Glass Fibre/Unsaturated Polyester Composite: Cross-linking, Mechanical Properties

Nabila Belloul[1], Ali Ahmed-Benyahia[2], Aicha Serier[1] and Nourdine Ouali[2]

[1]Laboratoire Revêtement, Matériaux et Environnement, Université M'Hamed Bougara de Boumerdes, Avenue 1er Novembre 35000 Boumerdes – Algérie

[2]Laboratoire de Mécanique Avancée (LMA), Université Houari Boumediène, BP 32 El-Alia 16100 Bab Ezzouar, Algérie

Abstract   The influence of temperature (20–60°C) and initiator ratio (1–3%) on the cross-linking and mechanical properties of the matrix resin and of glass fibre/unsaturated polyester composite; prepared by hand lay-up process and used in marine structures, is studied. Reactivity tests have shown that the effect of temperature increase is similar to that of initiator ratio. They increase reaction rate and reduce the gelation time and exothermic peak. Conversely, the Fourier transform infrared spectroscopy analyses have shown that the final conversions of styrene and polyester vinyl groups are almost complete, and that whatever the chosen operating conditions. Tensile and bending tests have shown that the mechanical properties (Elastic modulus, tensile strength…) are optimal for the samples operated at 40°C with 1% of initiator and those operated at 20°C with 2% of initiator.

Keywords: Glass Fibre/Unsaturated Polyester Composite, Temperature, Initiator, Cross-Linking, Mechanical Properties.

1. Introduction

The composites based on polyester reinforced with glass fibers are widely used in naval construction due to their light weight, their resilience and their ease of implementation. Generally, the manufacturing process more used is the hand lay-up process which consists in posing glass fiber coupons (mat and woven) on a mould then to soak them with resin until obtaining desired thickness of the laminated part. However, the non mastery of operating conditions of this kind of materials such as the temperature and the concentration of initiator will cause certainly falls of the general properties of the finished product.

In the literature treating of the behaviour of the resin polyester, it is largely established that when the concentration of initiator increases, the reaction rate increases and the time of gelation decreases [1]. It is established, also, that when the operating temperature increases, the reaction rate and the final conversion

increase and time to reach this final conversion decrease [2, 3]. Adami [4] noted the same thing, but from a certain critical temperature estimated at 32°C, the final conversion decreases. As regards the mechanical properties, it is established that they depend primarily on the chemical structure of the resin [5, 6], of the type of the three-dimensional network which is formed after hardening as well as nature of the reinforcements used and their distribution in the material [7].

This article is part of a work by which we want to help our manufacturers to better understand their products, establish technical data sheets and define the development process to follow. We will study the influence of the operating temperature and the concentration of initiator on the cross-linking and on the mechanical properties of the polyester resin and the composite glass/polyester used in the construction of fishing vessels.

2. Experimental

2.1. Materials

The composites materials glass/polyester are moulded in the form of laminated plates $(300 \times 300 \times 3.4 \text{ mm}^3)$ of sequence [mat300/mat450/mat600/woven500]. The plates are prepared by hand lay-up process with considering the operating conditions summarised in Table 1. The average porosity is of 2.3% with diameters varying mainly between 1 μm and 50.88 μm.

Table 1. Operating conditions of resins and laminates

Samples n°	1	2	3	4	5	6	7
Initiator ratio (%)	1	2	3	1	1	1	1
Temperature (°C)	20	20	20	30	40	50	60

The resin used in this work is pre-accelerated unsaturated polyester (RESIMER 55 E-1323) supplied by EUROMERE with a content styrene of 32wt%. A methyl ethyl ketone peroxide solution (PMEC 50) is used to initiate the hardening reaction. The analysis by x-ray fluorescence of the resin reveals the presence of several additives based of Si, Mg, Na…, and who are added by the producer with an aim of making improvements specific to its product. The Cobalt (Co) which is, in theory, the accelerator of the reaction of cross-linking, is detected with a rate of 0.06%. The viscosity of the resin is of 764 cps at 20°C and it decreases with the increase in the temperature. The fibres are E-glass with a textile/plastic finish compatible with polyester resins supplied by AHLSTROM. The reinforcement is mat of 300, 450 and 600 g/m^2 surface weight and taffeta woven of 500 g/m^2 surface weight.

The composite specimens are cut from the plates described above, according to the size recommended by the standards ISO 527 for the tensile test and standards NF T 51-001 for the bending test (Fig. 1).
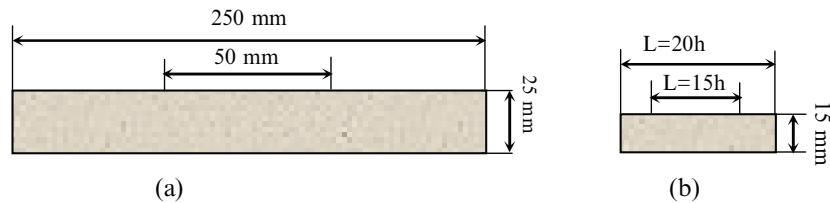

Fig. 1. Specimen dimensions for: (**a**) tensile tests, (**b**) bending tests

Some virgin resin specimens are also prepared by casting in glass moulds, under the same conditions given in Table 1. The shape and dimensions of specimens are recommended by ASTM D 638-77a for tensile tests and standard NF T 51-001 for the bending tests (Fig. 2).
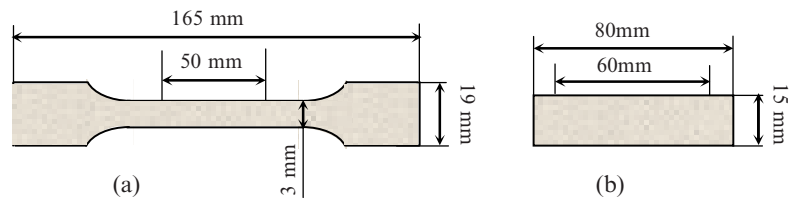
Fig. 2. Specimen dimensions for: (**a**) tensile tests (h = 3 mm), (**b**) bending tests (h = 4 mm)

2.2. Techniques

2.2.1. Reactivity measurement

The tests of the reactivity are carried out according to the standard ISO 2535 under the same conditions of temperatures and concentration of initiator previously chosen.

The procedure consists in immersing a thermometer in a beaker containing 50 g of resin, catalyzed and carried at the chosen temperature with using a Marie bath. The stopwatch is launched immediately after addition of the initiator, and that, to follow the change of the temperature of the reaction according to time.

2.2.2. Fourier transform infrared spectroscopy (FT-IR)

Identification of various chemical transformations occurred during the curing of the resin is realized by an FT-IR analysis with a resolution of 8 cm^{-1} in absorbance at room temperature. This analysis is done on a drop of resin with no additional initiator and tough in the form of films elaborated in the conditions of temperature and concentration of initiator such as defined in Table 1.

2.2.3. Mechanical tests

Tensile and bending tests are performed on a series of five samples (Zwick/Roell Z050 machine) at controlled displacement mode with a speed of 2 mm/min. For tensile tests, the displacement is measured by using an extensometer placed on the calibrated portion of the specimen. For the bending test, the distance between support ensures a twinge l/h = 15 (length between support/thickness values). The examination of the results enabled us to determine the elastic modulus, strength and elongation at fracture.

3. Results and discussion

3.1. Reactivity measurement

The addition of the PMEC to the pre accelerated resin leads to an exothermic reaction. Since the gel initiation, the resin temperature starts to increase gradually to a maximum afterwards; it decreases slowly until the room temperature.

The determination of the gelation time and the exothermic peak is very important for the construction of a composite because they correspond respectively to the maximum processing time of the resin and that one necessary to remove from the mould of the part. We established thermograms showing the behaviour of the resin mixtures for various temperatures and various initiator concentrations (Fig. 3).

The gel of mixtures prepared in ambient temperature starts at 36°C according to Adami [4]. For resins prepared at temperatures above 30°C we have considered that the gel starts at the beginning of the temperature increase. We note that the point of gelation and the exothermic peak are reached more quickly during hot hardening and for important concentrations of initiator. This phenomenon leads to an increase of the reaction rate of cross-linking. These results agree well with those of the literature [1–3].
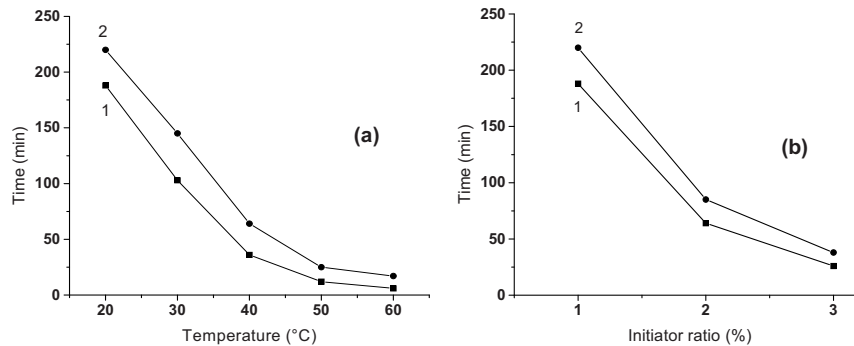
Fig. 3. Effect of temperature (a) and initiator ratio (b) on the gelation time and exothermic peak:
1: gelation time; 2: exothermic peak

3.2. Fourier transform infrared spectroscopy

The polyester and styrene vinyl groups, responsible for the resin hardening, are detected respectively at 982 and 915 cm^{-1} (Fig. 4). The spectra of the polyester films obtained by FT-IR analysis are presented in Figs. 5 and 6. All the spectra reveal the almost total disappearance of the characteristic peaks corresponding to the reactive polyester and styrene vinyl groups detected before the hardening of the resin (Fig. 4). It is therefore deduced that the cross-linking is obtained with high conversions into polyester and styrene. The increase of the curing temperature and initiator concentrations has little effect on the final conversion rate. However, this analysis did not inform us about the mode of combination between polyester and styrene knowing that one can have copolymerization UPS and homo-polymerisation UPUP and SS.
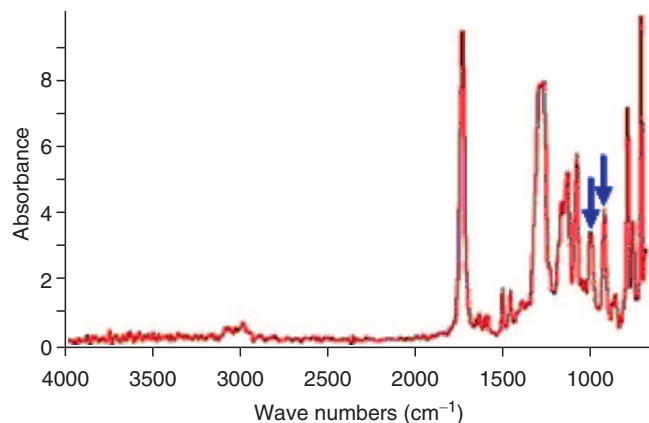

Fig. 4. IR spectra of the RESIMER 55 E-1323 resins without initiator
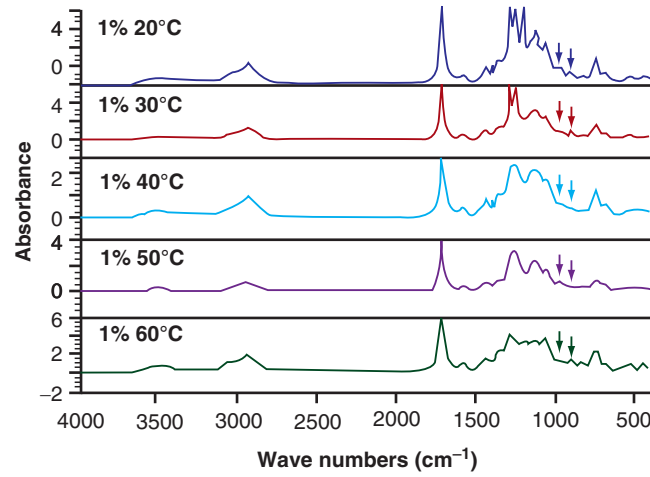
Fig. 5. Spectra comparisons of resin films elaborated in various temperatures
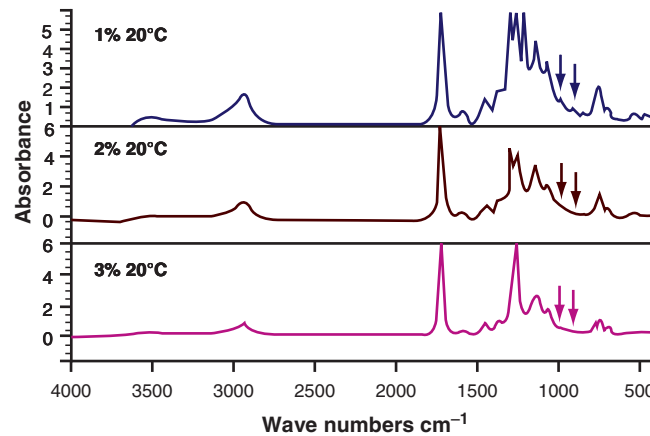
Fig. 6. Spectra comparisons of resin films elaborated in various initiator concentrations

3.3. Mechanical tests

Tensile and bending tests showed that the resin and the laminate of the study have a linear elastic behaviour with an almost fragile fracture. The results for the optimal mechanical properties are represented in Table 2 (the results of tests conducted on bending resin without reinforcements were not considered due to their dispersal). In order to better illustrate the effect of the increase in temperature and initiator concentrations on the mechanical behaviour of the resin and the laminate, the results obtained (for the elastic modulus) are represented in the form of diagrams (Fig. 7).

Table 2. The results for the optimal mechanical properties vs. resins and laminates

Samples	Elastic modulus (GPa)	Fracture strength (MPa)	Fracture elongation (%)
[a]Resin [1]	4.12 ± 0.15	39.41 ± 9.87	1.52 ± 0.18
[a]Resin [2]	4.08 ± 0.19	41.10 ± 2.73	1.42 ± 0.08
[a]Laminate [1]	17.20 ± 0.82	172.18 ± 15.52	5.40 ± 0.00
[a]Laminate [3]	17.65 ± 0.76	171.13 ± 0.70	4.69 ± 0.05
[b]Laminate [2]	12.59 ± 0.30	345.38 ± 27.38	3.82 ± 0.12
[b]Laminate [3]	11.95 ± 0.23	344.61 ± 25.15	4.17 ± 0.06

[a]Tensile test, [b]Bending test.
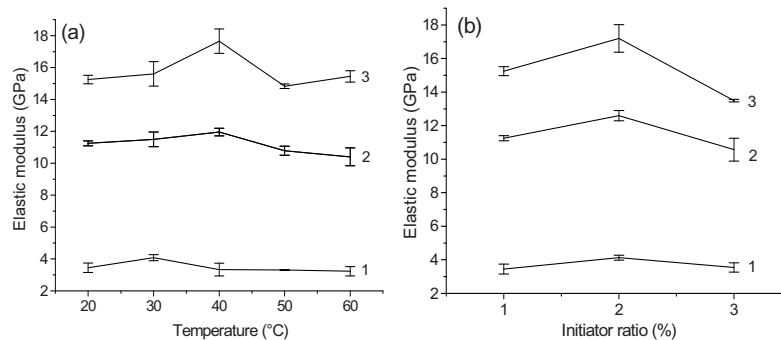[1] (2%–20°C), [2] (1%–30°C), [3] (1%–40°C)

Fig. 7. Evolution of elastic modulus vs. temperature and initiator, 1 Resins (traction), 2 Laminates (Flexion), 3 Laminates (Flexion)

Figure 7 shows that the increase in the curing temperature and the initiator concentrations generate an optimal value of the tensile elastic modulus corresponding respectively to a temperature of 30°C for the resin and 40°C for the laminate and a rate 2% of initiator for the resin and the laminate (see Table 2). These results are confirmed by the bending test in the case of the laminate. The same evolution is recorded for the diagrams of strength at fracture according to the temperature and for this of the initiator concentration.

While referring to the results of FT-IR analysis, we can deduce that we have a three-dimensional network which offers better mechanical properties corresponding to the optima obtained by the mechanical tests. We can say that the increasing of curing temperature and the initiator concentrations influence directly the combination mode between polyester and styrene. It should be also noticed that there is a difference between the optimal temperature of the resin and the laminate. This difference is due probably to the presence of the reinforcement in the composite because, it was established that the glass fibers slightly influences the progression of the cross-linking reaction by delaying it [8].

The whole results analysis leads us to conclude in the existence of equivalence between the effect of the curing temperature increase and that of the initiator concentration. Moreover, it should be noticed that the laminate elaborated at 20°C with 2% of initiator has the same behaviour as that elaborated at 40°C with 1% of initiator.

4. Conclusions

The aim of this work was the study of the influence of the curing temperature and the concentration of peroxide initiator on the cross-linking and the mechanical properties of the resin and the composite materials glass/polyester elaborated by hand lay-up process.

The reactivity measurement of the polyester resin showed that the increase in the curing temperature and the initiator concentrations have a similar effect on the chemical and rheological characteristics (faster reaction, shorter gelation time of and exothermic peak). The FT-IR analysis showed that the cross-linking occurred with high enough conversions for all the samples. This is deduced from an almost total disappearance of the peaks characteristic of polyester and styrene.

The results of the mechanical characterization revealed that the mechanical properties are optimal for samples prepared at 40°C with 1% of catalyst and for those prepared at 20°C with 2% catalyst.

References

[1]   J.L. Vilas, J.M.Laza, M.T. Garay, M. Rodriguez, L.M. Leon (2001) J. Appl. Polym. Sci., Vol 79, pp. 447–457.
[2]   K. De La Caba, P. Guerero, A. Eceiza, I. Mondragon (1997) Eur. Polym. J., Vol 33, No 1, pp. 19–23.
[3]   H. Yang, L.J. Lee (2001) J. Appl. Polym. Sci., Vol 79, pp. 1230–1242.
[4]   Julien Adami (2004) Thèse, Lyon, 189 p.
[5]   E.Bureau, k. Chebli, C. Cabot, J.M. Saiter, F. Dreux, S. Marais, M. Metayer (2001) Eur. Polym. J., Vol 37, pp. 2169–2176.
[6]   Jean-Claude Jannel (1992) Technique de l'ingénieur, traité Plastique et Composites, AM 3445, pp. 1–19.
[7]   M. Hildebrand (1992) Ifremer, Actes de colloques n° 15, communication n° 21, pp. 214–223.
[8]   H. Ng, I. Manas- Zloczower (1989) Polym. Eng. Sci, Vol 29, pp. 302–307.

Theoretical and Experimental Investigations of the Plane Strain Compression of Amorphous Polymers in the form of a Flat Plate

Nourdine Ouali, Krimo Azouaoui, Ali Ahmed Benyahia and Taoufik Boukharouba

Laboratoire de Mécanique Avancée (LMA), Département de Construction Mécanique & Productique. USTHB, B.P. 32 El-Alia, 16111 Bab-Ezzouar, Alger/Algérie.

Abstract   This paper studies a test method which overcomes some of the disadvantages of the tensile test. It is based on the plane-strain compression test, initially developed by Green, and is suitable for large strains. The experimental investigation of plane-strain compression test is carried out on Polymethylmethacrylate (PMMA) in the form of a flat plate, over a wide range of experimental conditions which cannot be reached in tensile tests owing to the brittle nature of the material. Over the whole range investigated, load-compression curves exhibit a well-defined maximum followed by a part where the load is minimum. The maximum is taken as the yield point and the minimum corresponds to the stationary plastic flow mode. The Stress analysis is made on the basis of plasticity theory, taking into account the influences of geometry and friction at the interfaces dies-sample. The equivalent yield stress is shown equal to the one obtained with other stress systems (uniaxial compression, uniaxial extension, simple shear). The plot of the stationary value of equivalent plastic flow stress normalized to the shear modulus versus the temperature normalized to Tg, formally illustrates the existence of two deformation regimes. After plane-Strain compression test, the grid dug by scanning electron microscope into the sample on the surface normal to the longitudinal axis of the dies allows visualization of the deformation state under optical microscope.

Keywords: Plane-Strain Compression Test, Yield Stress, Plastic Flow, Amorphous Polymers, PMMA.

1. Introduction

The majority of former work on the plastic deformation of vitreous polymers used modes of stress in uniaxial stresses (traction, compression) or in any case rather simple (shearing). If the materials studied are presented in the form of flat plate the uniaxial compression test is not applicable to the latter (the analysis of the state of deformation is very complex: triaxial deformation). The tensile test does not offer a solution of replacement since the amorphous polymers, at a temperature lower than Tg-20, under this stress presents a rupture at weak deformation (before reaching the plastic range). The plane-strain compression test is compatible with the condition related to the sample geometry in the shape of flat plate.

2. Plane strain compression test and material

The schematic representation of the plane-strain compression test is shown in Figs. 1 and 2. The specimen in the form of a flat plate is placed between two parallel dies (Fig. 2), which are forced the plate from either side. The two parallel faces are highly polished in order to minimize interfacial friction between the sample and the dies. The specimen suffers no constraint to elongation in the direction normal to the dies. The deformed material under the tools is restrained from moving in a parallel direction to the dies by the friction at the interfaces dies-sample and by the constraint of the undeformed material on either side of the deformed section and resulting in zero strain in this direction. This test has the advantage that the area under load remains constant and no instability due to reduction in area can occur. In order to apply a plane-strain compression, flat plates of PMMA 1.90 mm thick, 14 mm width, 25 mm length were selected.
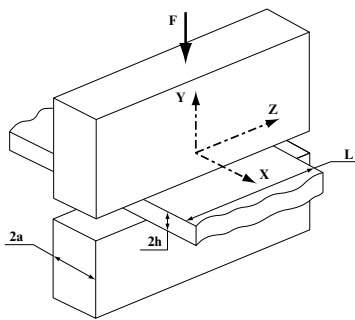

Fig. 1. Principle of the plane-strain compression test
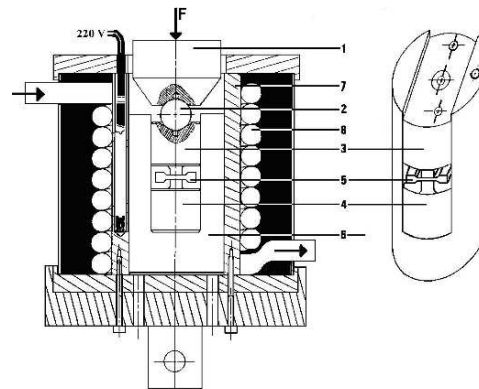
Fig. 2. Experimental setup for plane-strain compression test

3. Theoretical considerations

Two principal noted to help theoretical analysis:

o   If the length of the specimen L is larger than the dies width 2a, the deformation along axis 0Z is negligible compared to those which occur in plan X0Y (friction prevent deformation of the material along Z axis): conditions of a plane-strain, which notably simplifies the mechanical analysis of problem;

o   This deformation has two symmetry planes: planes X0Z and Y0Z. In experimental study, the application of the load on the mobile dies results reducing in the thickness of plate. At any time, during plane-strain compression test, there exists a relationship between the specific conditions of the test (load and speed of plane-strain compression, the geometry contact of the dies

(width 2a) and specimen (length L and thickness 2h) and two unknown parameters related to material under plane strain compression: its equivalent stress σ and the friction force τ at the interface dies-specimen.

That is relationship which the various methods for mechanics of continuous mediums and, in our case, the plasticity mechanics make it possible to establish. In order to adapt the theory of plasticity to the stress analysis of polymers a number of assumptions will be considered. These assumptions are:

o   The deformation occur at the constant volume.
o   The deformation occur at the constant strain rate.
o   The material is assumed to be isotropic. Anisotropy only becomes apparent after considerable deformation has occurred.

With these assumptions, the problem to be solved is that of large strains deformation with a non-linear relationship between stress and strain for constant conditions of loading, strain rate and temperature. Yielding is assumed to occur according to the Maxwell–Von Misses criterion [1]:

$$\left(\sigma_y - \sigma_x\right)^2 + \left(\sigma_x - \sigma_z\right)^2 + \left(\sigma_y - \sigma_z\right)^2 = 2k^2 \tag{1}$$

where k, is a parameter depending on the amount of prior strain. The variation of k with strain can be described by means of a curve relating σ^* an equivalent stress and ε^* an equivalent strain defined in terms of principal stress as:

$$\sigma^* = \frac{1}{\sqrt{2}} \sqrt{\left(\sigma_y - \sigma_x\right)^2 + \left(\sigma_x - \sigma_z\right)^2 + \left(\sigma_y - \sigma_z\right)^2} \tag{2}$$

And:

$$\varepsilon^* = \frac{\sqrt{2}}{3} \sqrt{\left(\varepsilon_y - \varepsilon_x\right)^2 + \left(\varepsilon_x - \varepsilon_z\right)^2 + \left(\varepsilon_y - \varepsilon_z\right)^2} \tag{3}$$

The Prandtl–Reuss relationship between these functions and the stress–strain components is expressed in the follows form:

$$\varepsilon_x = \frac{\varepsilon^*}{\sigma^*}\left[\sigma_y - \frac{1}{2}\left(\sigma_x + \sigma_z\right)\right] \tag{4}$$

Let σ_y be the stress applied to the dies being forced into the material. The stress along the dies axis may be assumed to be zero [1, 2] and $\sigma_x = 0$. The material undergoing deformation is restricted from moving along the dies axis and there is, therefore, zero strain in this direction and $\sigma_z = 0$.

Substitution in Eq. (3) gives: $\sigma_x = -\sigma_y$. From Eq. (6): $\sigma_x = 0.5\ \sigma_y$. Substituting in Eqs. (2) and (3) gives: $\sigma^* = \dfrac{\sqrt{3}}{2}\left(\sigma_y - \sigma_x\right)$. The analysis of strain is carried out in terms of contraction ratios defined in logarithmic terms, and: $\varepsilon^* = \dfrac{2}{\sqrt{3}}\ln\dfrac{h_0}{h}$. h_0 is the half thickness of simple before testing, and h is the half thickness of the simple during the test. The geometry of the specimens verifies a ratio h/a <1, consequently, the analysis will be carried by the method of the vertical sections [3]: for this purpose, we cut fictitiously our material into vertical slices infinitely thin along the X axis (Fig. 3).
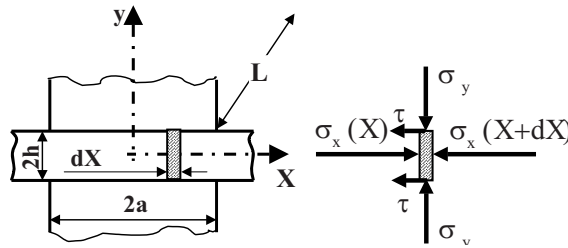

Fig. 3. Analysis by the method of the vertical sections

The friction dies – specimen results only in one friction force τ at the interface dies – sample. Computation can be carried out by using the follows Tresca friction law:

$$\tau = C_f\,\frac{\sigma^*}{\sqrt{3}} \tag{5}$$

With C_f is the Tresca friction coefficient, which in the case of a perfectly plastic material leads to a constant friction force on the entire interface. Let us consider half of the plate where $x > 0$ (Fig. 3). The force balance for one vertical slice along the X axis is written with $\tau > 0$.

At the second order: $\sigma_x\left(X + dX\right) = \sigma_x\left(X\right) - \dfrac{d\sigma_x}{dX}\,dX$

The force balance is: $-2hL\cdot\left(\sigma_x\left(X\right) + \dfrac{d\sigma_x}{dX}\,dX\right) + 2hL\cdot\sigma_x\left(X\right) - 2L\cdot\tau\,dX$

From where, $\dfrac{d\sigma_x}{dX} = -\dfrac{\tau}{h}$. Since τ does not depend on X, the integration of equation gives: $\sigma_x = \sigma_x\left(a\right) + \dfrac{\tau}{h}\left(a - X\right)$. At $X = a$, normal surface to the X axis is

free (no longer in contact with the dies) and therefore: $\sigma_x(a) = 0$ and $\sigma_x = \dfrac{\tau}{h}(a - X)$. We deduce the values of The maximum stress,

$$\sigma_{max} = \frac{2}{\sqrt{3}}\sigma^* + \frac{a}{h}\tau .$$

The plane-strain compression force:

$$F = 2L \cdot \int_0^a \sigma_y(X)dX = 2La \cdot \left(\frac{2}{\sqrt{3}}\sigma^* + \frac{a}{2h}\tau\right).$$

The average plane-strain compression stress:

$$\sigma_{app} = \frac{F}{2La} = \frac{2}{\sqrt{3}}\sigma^* + \frac{a}{2h}C_f \cdot \frac{\sigma^*}{\sqrt{3}} .$$

From above equation the equivalent stress σ^* can be written:

$$\sigma^* = \frac{\dfrac{\sqrt{3}}{2}\sigma_{appl}}{\left(1 + C_f \dfrac{a}{4h}\right)}$$

4. Results and discussion

The plane-strain compression force developed Figure 4a shows the equivalent stress-equivalent strain curves during plane-strain compression tests at a constant deformation rate, $\dot{\varepsilon}$, of 7.10^{-4} s^{-1}, measured at several temperatures, T, between 292 and 363 K. Figure 4b also present the equivalent stress-equivalent strain curve during plane-strain compression test measured at T = 233 K, but by using a constant deformation rate lower than that before used and $\dot{\varepsilon} = 9.10^{-5}$ s^{-1}; because at low temperatures under deformation rate $\dot{\varepsilon} = 7.10^{-4}$ s^{-1}, the specimen fractured before arriving the yield zone. These curves results resemble to those usually found in the literature for glassy polymers [4] and can be divided into four parts:

- An initially linear part corresponding to the elasti response
- A part where the curve reaches a maximum in stress, indicating a softening of material with an accompanying drop in stress
- A minimum stress part, corresponding to the stationary plastic flow mode;
- A final part where the stress increases, corresponding to homogeneous deformation with increasing work hardening

The σ value corresponding to stationary conditions is referred as σ_{stat}. It is instructive to compare results of the plane-strain compression test with those obtained at the same conditions of temperature and deformation rate in uniaxial compression and simple shear tests.

The yield equivalent plane-strain compression stress (Fig. 5a), in the same conditions of temperature and deformation rate, is shown equal to the yield compression stress (Fig. 5b) [5]. Furthermore, and as shows it the Figs. 6a and b, the yield compression stress is equal to the double of the yield shear stress.
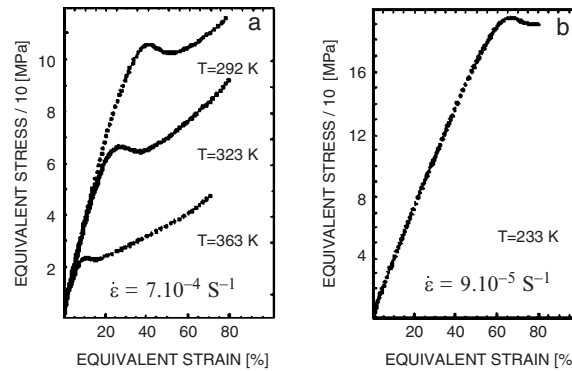

Fig. 4. Effect of the temperature on the plastic behavior of the PMMA
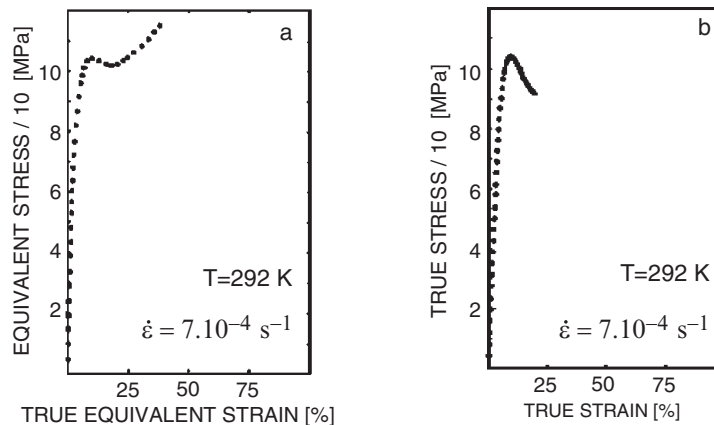
Fig. 5a. Plane strain compression stress–strain curve **Fig. 5b.** Compression stress–strain curve

Figure 7 where the stationary value of plane-strain compression plastic flow stress σ_{stat} normalized to the shear modulus G (G = 2,500 MPa) is plotted as a function of temperature T normalized to the glass transition Tg (Tg = 380 K). The data points are obtained from Fig. 4a, b and the hatched area represents the area that contains experimental points from the literature [2, 6–11]. The stress corresponding to published experimental points that were obtained using a different deformation rate was extrapolated in order to allow its comparison with our own data corresponding to a deformation rate of $7 \; 10^{-4} \; s^{-1}$.

Figure 7 shows that $\text{Log}\left(\sigma_{stat}/G\right)$ initially linearly decreases with increasing temperature and then decreases increasingly more rapidly as temperature approaches Tg and the temperature separation formally separates the low from the high temperature behavior.
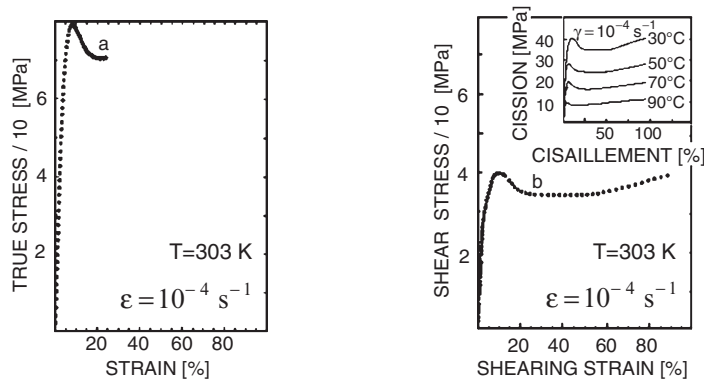
Fig. 6a. Compression stress–strain curve   **Fig. 6b.** Shear stress–shearing strain curve [6]
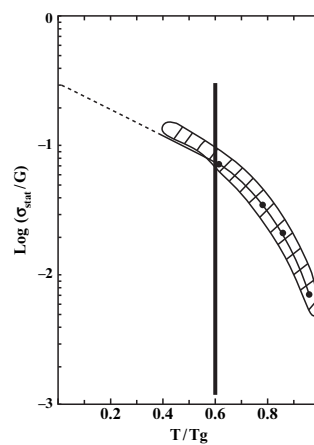
Fig. 7. Experimental ratio of the plastic flow plane-strain compression stress over the unrelaxed modulus plotted against normalized temperature [2, 6–11]

It is instructive to see the state of deformation of a sample after plane-strain compression test at room temperature: Photography of Fig. 8 taken under optical microscope shows the grid dug by scanning electron microscope into the sample on the surface normal to the longitudinal axis of the dies (surface perpendicular to the axis OZ, see Fig. 1) before the test. The irradiated path is depolymerised, then dissolved using an appropriate solvent: Propanol 70–30% Methyl ethyl ketone.

The line pitch of the grid is 50 μm. After deformation (to ε^* true = 0.2), the photography of Fig. 9 makes it possible to evaluate the deformation locally and to thus distinguish the zones presenting strong deformation ratio of those remaining neutral or slightly distorted. Thus, we can clearly distinguish five deformation zones: (i) zones A and E: where the grid does not distort (neutral zones), in agreement with the analysis of this type of test [1]; (ii) zone B, where the deformation is mainly of shear; (iii) zone C, where the deformation is of tensile; (iv) finally, the zone D, revealing at the same time tensile and shearing strains.
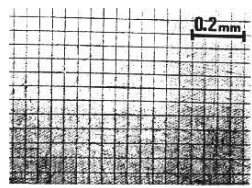

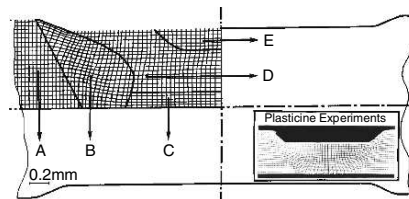**Fig. 8.** Grid dug on the PMMA with scanning electron microscope

Fig. 9. Grid after plane-strain compression test; the in with a serted figure corresponds to the plasticine (Green [1])

5. Conclusions

In this work we adapted the plane–strain compression test to the study of the mechanical behavior of sub-Tg PMMA under varying conditions of temperature and deformation rate. The equivalent yield stress is shown equal to those obtained in uniaxial compression and uniaxial tensile stresses systems. The temperature which separates the two deformations regimes, the low from the high temperature behavior, is formally identified. The grid dug into the sample allows, after plane-Strain compression test, visualisation of the deformation state under optical microscope.

References

[1]   Green, A.P., 1951, Phil. Mag., Vol. 42, series 7, p. 900.
[2]   Bowden, P.B., 1976, Edited by Haward, R.N., London, p. 279.
[3]   Daignieres, P., 1976, Métaux et alliages. Paris, Edition CNRS. p. 245.
[4]   Ward, I.M., 1971, London: Wiley Interscience, 375 p.
[5]   Williams, J.G. and Ford, H.J., 1964, Mec. Eng. Sci., Vol. 6, N°4, p. 405.
[6]   Bouton-Rochelle, C. and G'sell, C., 1991, The Plastics and Rubber Institute, 8th International Conference on deformation yield and fracture of polymers, p. 67/1.
[7]   Lefebvre, J.M., 1982, Ph. D. Thesis, Université des Sciences et Techniques, Lille, France.
[8]   Bauwens-Crowet, C., 1973, J. Mater. Sci., Vol. 8, p. 968.
[9]   Ouali, N., 1992, Ph. D. Thesis, INSA-Lyon, France.
[10] Perez, J., 1992, Physique et Mécanique des Polymères Amorphes., Edt. Lavoisier, 384 p.
[11] Ouali, N., Mangion, M.B.M., and Perez, J., 1993, Phil. Mag. A, Vol. 67, p. 827.

Wavelet-Based Multifractal Identification of Fracture Stages

Djedjiga Ait Aouit and Abdeldjalil Ouahabi

Ecole Polytechnique de l'Université de Tours, 7 avenue Marcel Dassault, 37200 Tours, France

Abstract   Because fracture phenomena are highly nonlinear and non-stationary, the classical analyzis of fracture lines development is not adapted for their characterization. Multifractal analysis is now increasingly used to characterize these irregular patterns. In this investigation, multifractal analyzis based on the continuous Wavelet Transform Modulus Maxima method (WTMM) is proposed to give a multifractal discrimination of the profile lines development at different fracture stages: fracture initiation, fracture propagation and final rupture. This multifractal analyzis makes it possible to take into account the local regularity of fracture profiles. The degree of these fluctuations is quantified by Hölder exponent α, computed from WTMM coefficients of the signal. The proposed wavelet-based multifractal approach is mainly compared to standard multifractal one based on the box-counting method (BCM). We noted that WTMM describes reasonably well the scaling properties of fracture patterns distributions at three distinct fracture stages. The results suggest that parameters of the multifractal spectrum such as the capacity dimension D_0, the average singularity strength α_0, the aperture of the left side $\alpha_0 - \alpha_q$ and the total width $(\alpha_{max} - \alpha_{min})$ of the $f(\alpha)$ spectra may be useful as parameters characterizing the different fracture stages and mechanisms of elastomeric material.

Keywords: Fracture, Profile, Roughness, Wavelet, Singularity, Multifractal Spectrum.

1. Introduction

The concept of fractal XE "fractal" geometry has been proved to be very useful in describing fracture XE "fractal" morphology of materials [1]. Much greater abilities of a multifractal XE "fractal" description of simulated and real fracture lines development are shown by Stach's works [2–4], essentially based on the box-counting method (BCM). That consists to vary the square box sizes to give multi-scale analysis. Except that, an oscillate box gives the best multi-scale analysis and the best singularity detection of fluctuate signals. This oscillate box called wavelet was introduced by Morlet and Grossmann for seismic signals study [5]. The wavelet transform (WT) is a mathematical used for the decomposition of a signal (or surface) into a set of functions characterized by position and scale parameters [6]. Arneodo and his team [7] present the continuous WT as a mathematical microscope which is well suited for characterizing the local regularity of rough surfaces. However, a new approach of multifractal XE "miltifractal" analysis of

irregular XE "irregular"signals was born [8]. It is based on the Wavelet XE "Wavelet". Transform Modulus Maxima (WTMM). Indeed, the WTMM representation is emphasized as a very efficient and accurate numerical tool for scanning the singularities of mathematics or physical signals. The principle of this novel approach is to determine the singularity spectrum XE "singularity spectrum" (or multifractal XE "miltifractal" spectrum) of the studied signal. That consists of associating to each Hölder exponent XE "Hölder exponent" α (local regularity exponent) the dimension of the sets of points which exhibit the same value of α. The Hölder exponent estimation is given by the local maxima modulus of continuous wavelet transform WTMM of the signal [9]. We refer the reader to references [10, 11] for rigorous mathematical description. Created by The purpose of the present work is to generalize the canonical WTMM method from 1D fracture XE "fracture" profiles XE "fracture profiles" of an elastomeric XE "elastomeric" material in order to give best characterization of three different fracture stages: fracture initiation, fracture propagation and final rupture.

2. Materials and methods

In this study, crack propagation tests using a Dynamic Mechanical Analyzer system (a TA instrument DMA 2980) have been carried out under following fatigue mechanical conditions: frequency f = 5 Hz and strain ε = ±20%.
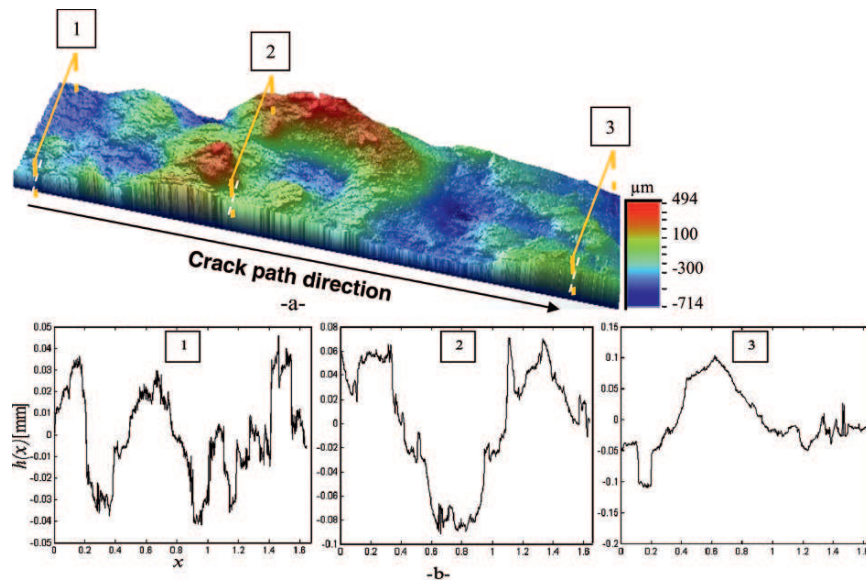

Fig. 1. Examples of digitized fracture surface; (**a**) 3D roughness profile, (**b**) three different fracture profiles extracted at (1) crack initiation zone, (2) crack propagation one and (3) final rupture

For the crack propagation study, we used an edge cracked simple tension specimen. The elastomeric XE "elastomeric" sample dimensions are: 13 mm of length × 9 mm of width × 2 mm of thickness. In order to make a global study of the fracture XE "fracture" surface roughness, we have digitized the obtained fracture surfaces with a white light optical profiling using vertical scanning interferometer (Wyko NT 1100 profilometer). The time of the entire surface scan (with the given above dimensions) is about 5 to 6 h. The obtained image covers more than 2,000 different profiles. An example of 3D and 1D fracture profiles XE "fracture profiles" is given by Fig. 1. The extraction process of the 1D profile is carried out in the direction of the crack propagation.

2.1. Fourier spectra analysis of the fracture XE "fracture" profiles

Spectral analysis provides an essential tool for understanding the frequency components of a surface roughness. It has been used to study different topics such as the upper and lower limits of fractal XE "fractal" dimensions of a fracture XE "fracture" surface and the selection of a proper sampling bandwidth for 3D surface topography measurement. The power spectral method can simply be realized by means of the fast Fourier transformation and it leads to useful results. As demonstrated in Fig. 2, an example of fracture XE "fracture" surface displays a $f^{-8/3}$ power-law shape over a range of frequencies (f = spatial frequency (mm^{-1})). This decrease of power-law corresponds to a scale-invariance by anisotropic transformation. This phenomenon is observed for all the fracture surfaces obtained from the same fracture condition (20%–5Hz). The average Hurst exponent XE "Hurst exponent" (roughness exponent) obtained from the fracture surfaces of ten samples equals to $H = 0.7955 \pm 0.0103$. This result is close to the universal exponent of the self-affine fracture surface, $H = 0.8$. This parameter confirms the self-affine nature of the fracture XE "fracture" surfaces of the studied material.
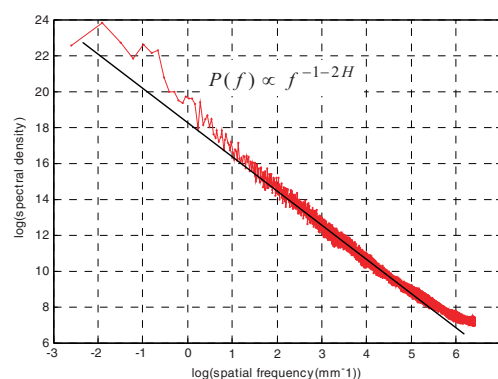

Fig. 2. Log–log plot of the power spectral density of the fracture profiles resulting from: (**a**) 20%–5Hz fracture conditions

Unfortunately, it presents global quantity that do not account for the possible local fluctuations of the fracture surface morphology. So, we propose a multifractal XE "multifractal" description of the acquired profiles, to give a locale description.

2.2. Multifractal spectrum calculation

Fractals are rough or fragmented geometric shape that can be subdivided in parts, each of which is a reduced copy of the whole. These fragmented patterns can be characterized using the increase of a measure $\mu(B_x(r))$ at different scales, where $B_x(r)$ is the volume element of size r and centered at x, this element is square box in the case of box-counting method. If $r \rightarrow 0^+$, the measure $\mu(B_x(r))$ is defined as:

$$\mu(B_x(r)) \sim r^{\alpha(x)} \tag{1}$$

$\alpha(x)$ is the local singularity strength of the measure μ at a given x.

The singular spectrum (or multifractal XE "multifractal" spectrum 'MS') $f(\alpha)$ describes the statistical distribution of the singularity α, it is defined with the Legendre transform as:

$$f(\alpha) = \inf_{q \in R}(q\alpha - \tau(q)) \tag{2}$$

Multifractal measures given by the formula (2) describe the behavior of the objects not only at different scales r, but also for different statistical moments q. Thus, the idea of covering the support μ is also applied in different moments, which leads to the definition of partition function:

$$z(q,r) = \sum_{i=1}^{N(r)} \left(\mu(B_i(r))\right)^q \tag{3}$$

And the partition function behaves:

$$z(q,r) \sim r^{\tau(q)} \tag{4}$$

One of the powerful properties of the continuous wavelet transform CWT is that we can detect and measure the strength of the singularities points in the signal at multiple scales through the local maxima coefficients (WTMM) [12]. The other fundamental advantage of using CWT is that the skeleton defined by the WTMM, provides an adaptative space-scale partitioning from which we can extract the $f(\alpha)$ singular spectrum. This specification of the WTMM is related to the partition function given by the formula (3), replaced by:

$$z(q,s) = \sum_{l \in L(s)} \left(\sup_{(u,s') \in l, s' \le s} \left| W_\psi(X)(u,s') \right|^q \right) \tag{5}$$

where $W_\psi(X)$ is the wavelet transform of the signal X, using mother wavelet of type ψ at a location u and a scale s:

$$\forall u \in R, \forall s > 0, W_\psi(X)(u,s) = \frac{1}{\sqrt{s}} \int_R X \psi \left(\frac{x-u}{s} \right) dx \tag{6}$$

The major implementation steps of the MS computation based WTMM can be formulated as follows:

i. Calculate the continuous wavelet transform (CWT) of the signal at multiple scales.
ii. Find the local maxima of the absolute values of wavelet transforms in each scales.
iii. Chain the wavelet maxima points from the coarse scales to fine scales.
iv. Compute the partition functions.
v. Compute $\alpha, f(\alpha), and \tau(q)$.

This procedure is illustrated by Fig. 3. That relates to the fracture XE "fracture" profile analysis given by Fig. 3a. We notice that the WTMM chains which are prolonged almost on all scales (see Fig. 3c) are pointed towards the strong singularities (or the strong fluctuations) of the profile. The applied wavelet can be any wavelet with the number of vanishing moments defined by the formula (7) that are one degree higher than highest vanishing moment of the signal. The best wavelet examples are the derivatives of the Gaussian, such as the first derivative of Gaussian.

$$\forall k = 0,1,\cdots, N-1 \quad \int_R x^k \psi(x) dx = 0 \tag{7}$$

2.3. Multifractal Analysis of fracture XE "fracture" profiles

In this section, we present an illustration of multifractal XE "multifractal" analysis applied on fractographic study of elastomeric XE "elastomeric" material. It is reasonable to assume that different fracture XE "fracture" stages on the material should affect both the morphology and the scaling of the fracture surface [13]. Therefore, a special interest is to achieve multifractal XE "multifractal" discrimination of different fracture stages on the material: fracture initiation, fracture propagation and final rupture. To ensure a good reproducibility on the average multifractal XE "multifractal" spectrum parameters, it was necessary to extract at least ten profiles per zone (crack initiation zone, crack propagation zone and final rupture zone, see

Fig. 1), from ten digitized fracture XE "fracture" surfaces obtained from the same fracture conditions. The range of q in our work was selected by taking into account coefficients of determination, R^2, of the fitted straight line equal to or greater than 0.90. Thus, $f(\alpha)$ spectra were computed in the range $-10 < q < 10$ for successive 0.2 steps. The selected parameters values obtained for the two methods are the average of 100 spectra per zone (one spectrum by fracture XE "fracture" profile).
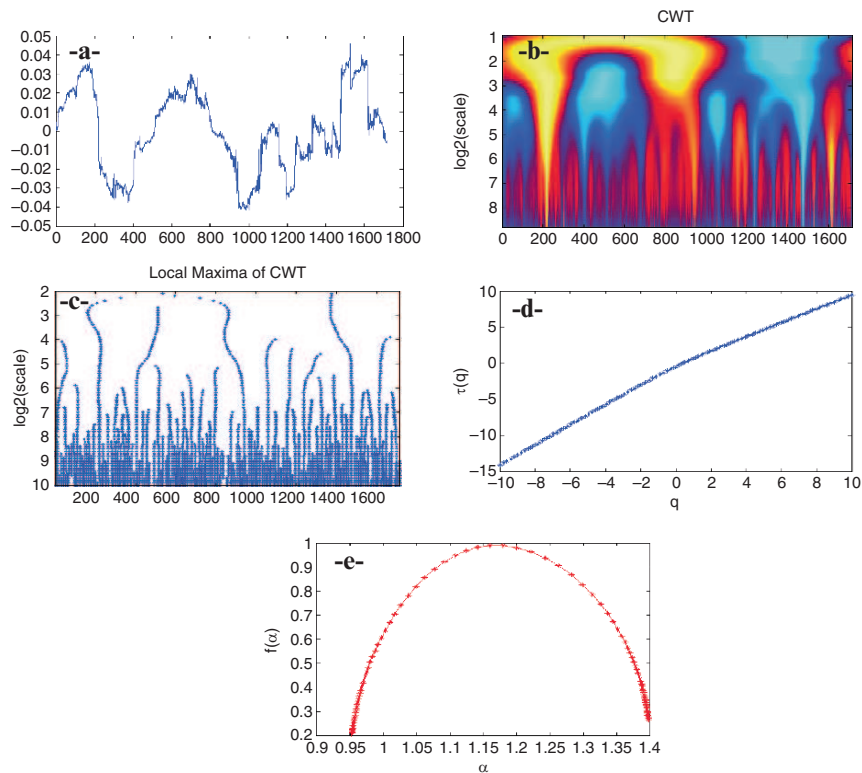
Fig. 3. The different steps of the MS computation based WTMM of the fracture profile given by graph (**a**). (**b**) continuous wavelet transform (CWT) of the profile, (**c**) local maxima of CWT, (**d**) τ(q) graph and (**e**) multifractal spectrum

2.4. Based box-counting method

The average multifractal XE "multifractal" spectra estimated on the three crack zones with the BCM are shown in Fig. 4. All plots are characterized by a typical concave parabolic shape, but exhibit very different symmetry features.

At first sight, we note that the discrimination of the three crack zones through the spectra position is difficult. Especially, the spectra estimated at the crack propagation and final rupture zones tend to be superimposed. Hölder exponents of order zero, α_0, and order q, α_q, are parameters that can be used to distinguish between fracture XE "fracture" patterns distribution at the three crack zones.

Average values of the $\alpha_{\max}$, $\alpha_{\min}$ and α_0 computed respectively with the most positive, negative and the zero order moments are listed in Table 1. The value of α_0 quantifies the average scale or mass density (or probability); in other terms; it is the average of the singularity strength of the fracture XE "fracture" patterns distribution. The crack zone with the maximum α_0 exhibited on average the lowest degree of mass concentration, and the opposite, such that the crack zone with minimum α_0 presented on average the highest degree of local density. Starting from this description, the values of this parameter obtained with BCM are not appropriate for an efficient characterization of the three crack zones seen that they are very close (see Table 1).

The total width $\Delta\alpha = \alpha_{\max} - \alpha_{\min}$ and the left side one $\alpha_0 - \alpha_{q+}$ of the $f(\alpha)$ spectra are also evaluated and may be useful as predictive parameters that capture some of the inner details of the whole singularity of the fracture XE "fracture" lines development. These parameters showed significant differences between crack zones (Table 1). The range of the left side $\alpha_0 - \alpha_{q+}$ of the $f(\alpha)$ spectra was highest for crack propagation profiles zone, $\alpha_0 - \alpha_{q+} = 0.4989$, and lowest for final rupture profiles zone, $\alpha_0 - \alpha_{q+} = 0.3325$. The same characterization is given by the total width $\Delta\alpha$ estimated on the crack path direction, $\Delta\alpha = \{0.5877, 0.6364, 0.4764\}$ at crack initiation, crack propagation and final rupture zone, respectively. Values of the capacity dimension D_0 were not significantly different for the three spectra.

Table 1. Main parameters from multifractal XE "multifractal" analysis based BCM of fracture XE "fracture" profile line development

Multifractal features	Crack initiation	Crack propagation	Final rupture
$\alpha_{\max}$	1.2027 ± 0.015	1.1703 ± 0.011	1.1791 ± 0.017
$\alpha_{\min}$	0.6150 ± 0.013	0.5339 ± 0.019	0.7027 ± 0.008
α_0	1.0335 ± 0.008	1.0328 ± 0.012	1.0352 ± 0.005
$\alpha_0 - \alpha_{\min}$	0.4185 ± 0.010	0.4989 ± 0.015	0.3325 ± 0.009
$\Delta\alpha = \alpha_{\max} - \alpha_{\min}$	0.5877 ± 0.011	0.6364 ± 0.016	0.4764 ± 0.010
D_0	0.9998 ± 0.002	0.9999 ± 0.001	0.9998 ± 0.001

2.5. Based wavelet modulus maxima method

We notice on the Fig. 4 that the positions of the spectra corresponding to the three crack zones are definitely separable, both the α_{max} and the α_{min} exhibit a trend to increase on the crack path direction. This finding of the multifractal XE "multifractal" spectra based WTMM allows a better characterization and differentiation of these zones (Fig. 5).

Fig. 4. Average multifractal spectra (MS) estimated with BCM of different profiles extracted at three zones: crack initiation, crack propagation and final rupture zones
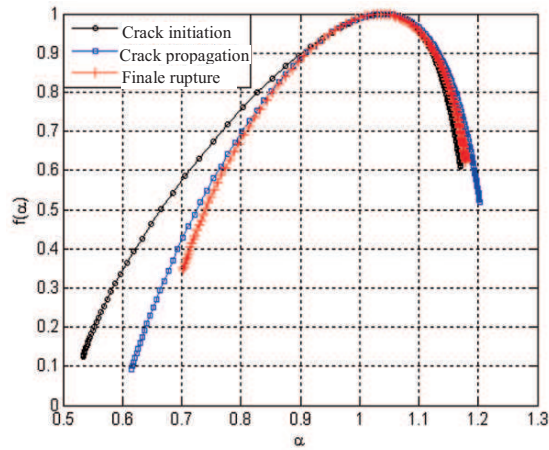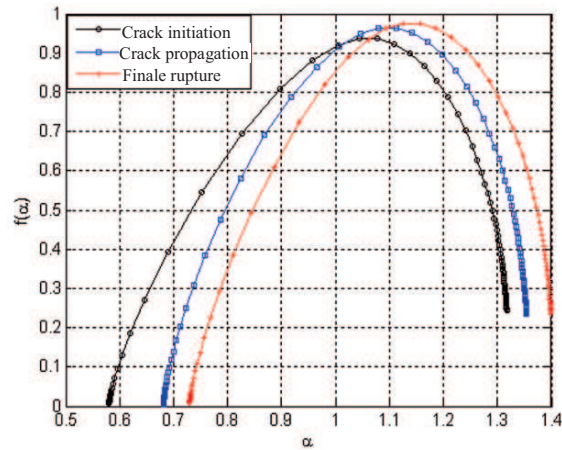

Fig. 5. Average multifractal spectra (MS) estimated with WTMM of different profiles extracted at three zones: crack initiation, crack propagation and final rupture zones

Now, if we analyze the features extracted from these spectra listed in Table 2, we observe that the determination coefficients in estimating α_0 allow discrimination between crack initiation zone with $\alpha = 1.0967$, crack propagation with $\alpha_0 = 1.0608$ and final rupture profiles with $\alpha_0 = 1.1309$. We can also say that the profiles extracted upon crack propagation zone develop a strong singularity than other profiles. Concerning the left side $\alpha_0 - \alpha_{q+}$ and total width $\Delta\alpha$ of the spectra, crack propagation zone profiles exhibit a higher width or aperture than those of the crack initiation and final rupture one. Heterogeneity can also be assessed by the magnitude of changes around D_0, seen that this parameter presents an important difference between the three zones (Table 2). The whole of the features estimated with multifractal XE "multifractal" analysis based WTMM shows significant difference between fracture XE "fracture" profiles complexity on the three crack zones.

Table 2. Main parameters from multifractal XE "multifractal" analysis based WTMM of fracture XE "fracture" profile line development

Multifractal features	Crack initiation	Crack propagation	Final rupture
α_{max}	1.3540 ± 0.023	1.3173 ± 0.019	1.3987 ± 0.028
α_{min}	0.6811 ± 0.017	0.5805 ± 0.045	0.7305 ± 0.025
α_0	1.0967 ± 0.021	1.0608 ± 0.033	1.1309 ± 0.012
$\alpha_0 - \alpha_{min}$	0.4156 ± 0.019	0.4803 ± 0.027	0.4004 ± 0.020
$\Delta\alpha = \alpha_{max} - \alpha_{min}$	0.6729 ± 0.015	0.7368 ± 0.030	0.6682 ± 0.019
D_0	0.9642 ± 0.006	0.9771 ± 0.005	0.9376 ± 0.002

3. Conclusions

The degree of the profile line development depends on the mechanical resistance of the material and on its physico-chemical properties. However, the study of the fracture XE "fracture" morphology complexity allows a better understanding of the material behaviour at the fatigue state. The self-affinity of the fracture XE "fracture" surfaces of the elastomeric XE "elastomeric" studied material is revealed. The global roughness exponents H are found to be similar values close to the Hurst universal exponent of the self-affine fracture surfaces, $H = 0.8$.

Several multifractal XE "multifractal" attributes such as capacity dimension, D_0, the width of the left side $\alpha_0 - \alpha_{q+}$ of the $f(\alpha)$ spectra, and the width of the $f(\alpha)$ spectra itself $\alpha_{max} - \alpha_{min}$ showed significant differences between fracture XE "fracture" surface morphology at different fracture stages. Notably, with the multifractal analysis based WTMM, the whole of the estimated features $\{\alpha_{max}, \alpha_0, \alpha_{min}, \alpha_0 - \alpha_{q+}, \alpha_{max} - \alpha_{min}, D_0\}$ can be very useful to characterize and to describe the irregularity evolution on the crack path direction.

Through theses results we can easily isolate and identify the crack initiation on the studied material. With the multifractal XE "multifractal" analysis based BCM, we noted that the results of the estimated parameters evolve according to the same tendency as those obtained with WTMM method, except that some parameters such as α_0 and D_0 are not exploitable for an apparent discrimination. These two parameters are very close in the case of the three crack zones. We conclude that the choice of multi-scale tool is very important for the multifractal XE "multifractal" features estimation.

References

[1] Mandelbrot BB, Passoja DE and Paulay AJ (1984) Fractal character of fracture XE "fracture" surfaces of metals. Nature, vol. 308, pp. 721–722.

[2] Stach S et al (2004) Multifractal or fractographic fracture XE "fracture" line description. Materials Characterization'04, vol. 140(3), pp. 440–443.

[3] Stach S, Cybo J and Chmiela J (2001) Fracture surface‐fractal XE "fractal" or multifractal XE "multifractal". Materials Characterization'01, vol. 26, pp. 163–167.

[4] Stach, S. and Cybo J (2003) Multifractal description of fracture XE "fracture" morphology: theorical basis. Materilas Characterization'03, vol. 51(1), pp. 79–86.

[5] Grossmann A and Morlet J (1984) Decomposition of Hardy functions into square integrable wavelets of constant shape. SIAM Journal on Mathematical Analysis, vol. 15, pp. 723–736.

[6] Mallat S (1998) A wavelet tour of signal processing. New York: Academic Press.

[7] Arneodo A, Decoster N and Roux SG (1999) A wavelet-based method for multifractal XE "multifractal" image analysis I. Methodology and test applications on isotropic and anisotropic random rough surfaces. The European Physical Journal B, vol. 15, pp. 567–600.

[8] Abry P, Goncalves P and Levy Vehel J (2002) Lois d'échelle, fractales et ondelettes. Paris, Hermes Science Publications, vol. 1, ISBN : 2-7462-0409-6, p. 270.

[9] Jaffard S (2004) Wavelet XE "Wavelet" techniques for pointwise regularity. Proceedings of Symposia in Pure Mathematics, pp. 91–151.

[10] Mallat SG and Hwang WL (1992) Singularity detection and processing with wavelets. IEEE Transactions on Information Theory, vol. 38, pp. 617–643.

[11] Jaffard S (1997) Multifractal formalism for functions part I: Results valid for all functions. SIAM Journal on Mathematical Analysis, vol. 28, pp. 945–970.

[12] Jaffard S (2004) Wavelet XE "Wavelet" techniques in multifractal XE "multifractal" analysis. Fractal Geometry and Applications: A Jubilee of Benoit Mandelbrot. Eds. M. Lapidus et M. van Frankenhuysen. Proc. of Symp. in Pure Mathematics.

[13] Ouahabi A and Ait Aouit D (2008) Wavelets and fractals for signal and image analysis. In: Siarry P., editor, Optimization in Signal and Image Processing, France: ISTE, HERMES Science & Lavoisier Company, ISBN: 9781848210448, p.352.

Characterization of Mixed Mode Delamination Growth and Thresholds

M. Kenane[1] and M.L. Benzeggagh[2]

[1]USTHB, Faculté GM-GP, LSGM, BP32, El Alia, 16111, Bab Ezzouar, Alger, Algerie

[2]Université de Technologie de Compiègne, laboratoire Roberval 1505, BP649 Compiègne Cedex, France

Abstract   Interlaminar fracture is the dominant failure mechanism in most advanced composite materials. The delamination behaviour of materials is quantified in terms of the strain energy release rate G. In this paper, the measured growth rates, *da/dN*, were correlated with the corresponding strain energy release rates, ΔG_I, ΔG_{II} and ΔG_T. The strain energy release rate thresholds ΔG_{Tth}, below which no delamination would occur, were also measured. Three specimen types were tested: Double cantilever beam (DCB), end-loaded split (ELS), and mixed-mode bending (MMB), for mode I, mode II, and mixed-mode (I+II) loading, respectively. A large number of mode ratios have been used in order to cover the maximum number of cases in the range from 0 to 100%.

Keywords: Composite, Fatigue, Mixed mode Fracture, Crack Growth Rate Threshold.

1. Introduction

A considerable amount of current research activity is devoted to the study of failure mechanisms in laminated composite materials. The most common failure mechanism in laminated composites is the interlaminar damage. It results generally from mode I, mode II, or mixed-mode (I+II). Double cantilever beam (DCB), end-loaded split (ELS), and mixed-mode bending (MMB) specimens are used in this experiments. In this study of cyclic tests, experimental results are used to predict delamination growth rate through the Paris' power law: $\dfrac{da}{dN} = B(\Delta G_T)^d$. Thus for each value of the mode ratio $\dfrac{G_{II}}{G_T}$ there are corresponding values of d and B.

However, it was assumed that if the delamination had not begun to grow after 1 million cycles, the applied load and, hence, the corresponding ΔG_T could be considered below a threshold value. Then, no delamination growth behaviour was investigated for mode I, mode II, and mixed-mode (I+II) loadings in terms of the total strain energy release rate threshold ΔG_{Tth} .

2. Experimental procedure

2.1. Material

The laminates used in this study were an M10 epoxy resin (Vicotex) reinforced with 52% by volume of E-glass fibres, 5% of which are woven perpendicularly to hold the parallel fibres together and they could set a limit to the crack shifting. This material was made by compression of 16 quasi-unidirectional plies of prepeg, which were stacked in a sheet 6mm thick. The starter crack was formed by inserting a 0.06 mm thick Teflon film at mid-thickness.

The elastic constants obtained experimentally [1] were (Table 1):

Table 1. Elastic constants for E-glass/M10-epoxy composite

$E_{11} = 36.2$ GPa	$G_{12} = 5.6$ GPa	$\nu_{12} = 0.26$
$E_{22} = 10.6$ GPa	$G_{13} = 3.7$ GPa	$\nu_{13} = 0.33$
$E_{33} = 7.2$ GPa	$G_{23} = 3.2$ GPa	$\nu_{23} = 0.48$

2.2. Specimen

The configuration of double cantilever beam (DCB) specimen was used to determine the mode I interlaminar fracture toughness G_I.
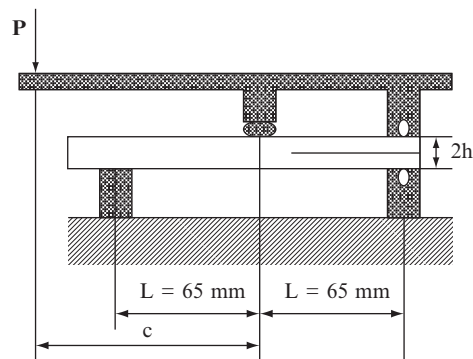

Fig. 1. MMB test configuration

The metallic hinges were attached to both sides of the DCB specimen at the end adjacent to the starter notch to allow for unconstrained rotation at the end during load introduction.

The end-loaded split (ELS) specimen was used for characterizing mode II fracture toughness G_{II}. The toughness for mixed-mode was evaluated using the mixed-mode bending (MMB) configuration developed by Reeder and Crews [2, 3]. This test is a simple combination of the DCB (mode I) specimen and the ENF (mode II) specimen (Fig. 1). Actually, the MMB is included in the ASTM standards [4].

2.3. Test conditions

The experiments were carried out in a 1 kN, computer-controlled, servo-hydraulic testing machine (Instron 1341). They were conducted under constant-amplitude fatigue tests at a minimum to maximum cyclic load ratio (R) of 0.1 and a frequency of 4 Hz. During tests, the maximum and the minimum strain-energy release rates, G_{max}, G_{min} and delamination growth rate $\dfrac{da}{dN}$, were monitored.

The threshold was found by reducing the applied load with level of 10–15% until the crack growth arrests, and when the delamination had not begun to grow after 10^6 cycles. Then, the applied load and, hence, the corresponding ΔG_{th} could be considered below a threshold value.

2.4. Energy release rates

The delamination strain energy release rate can be expressed as:

$$G = \frac{P^2}{2b}\frac{dC}{da} \tag{1}$$

where b is the width of the specimen (mm), P is the applied load (N) and C is the compliance (N mm^{-1}). The compliance of the DCB can be shown to be equal to a power law function of the delamination length of the form:

$$C = \frac{\delta}{P} = \frac{a^n}{h} \tag{2}$$

where n and h are determined experimentally ($n = 1.89$, $h = 24.78 \times 10^5$).

An analysis similar to that for mode I was adopted for mode II and mixed-mode (I+II), for which the compliance can be expressed as $C = \alpha + \beta^3$.

The constants α and β can be found by plotting experimental values of C versus a^3 the $\dfrac{G_{II}}{G_T}$ modal ratio considered (Table 2).

Table 2. Constants for compliance fits

G_{II}/G_I (%)	28	53	82	ModeII
α (10^{-3} mm.N^{-1})	33.86	15.38	11.48	1.85
β (10^{-7} N^{-1}.mm^{-2})	3.52	1.11	1.05	1.06

The critical strain–energy release rates, G_{IC} and G_{IIC}, from mode I and mode II tests, respectively, and the total critical strain-energy rate, G_{TC}, from mixed mode considered in this work can be calculated [5] and results are given in Table 3.

Table 3. Total strain energy release rate values

G_{II}/G_I (%)	0	28	53	82	100
G_{TC}(J/m^2)	118.02 (2.72)	340 (37.26)	579.62 (58.66)	1822 (84.47)	2906 (224.55)

3. Results

3.1. Delamination growth rate determination

As a delamination grows at a constant cyclic load, the cyclic ΔG_T changes; hence, the delamination growth rate changes. A plot of $\dfrac{da}{dN}$ versus ΔG_T may be obtained for each over $\dfrac{G_{II}}{G_T}$ mode ratio, pure mode I and pure mode II, as shown in Figs. 2, 3, and 4 and the results may be fitted by Eq. (3). The coefficients B and d, obtained by least-squares fitting of the fatigue-crack growth rate curve, are presented in the Table 4.

Table 4. Experimental values of d and B parameters

G_{II}/G_I (%)	0	28	53	82	100
d	1.9	2.13	2.62	3.33	4.2
B		21.6 10^{-12}	1.02 10^{-12}	0.29 10^{-12}	1.04 10^{-16}	1.73 10^{-23}

The results published in the literature show that the d exponent for graphite/epoxy composites is generally much higher than that for glass/epoxy composites [6–8]. For glass/epoxy composite, the d value found by Prel et al. [8] is closer to what we have obtained. However Bathias and Laksimi [9] have studied glass-cloth-reinforced epoxy under similar loading conditions, and obtained a high d

values for mode I ($d = 3.71$) and mode II ($d = 7$). In this case a crack can be confronted locally with several rigidities, unlike in unidirectional composites where the crack propagates in the plane in which the rigidity is relatively homogeneous. However, contrarily to graphite/epoxy composite, results obtained for glass /epoxy in this study show that the d exponent increases with $\dfrac{G_{II}}{G_T}$.
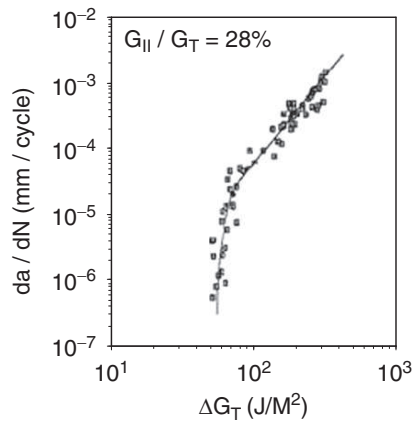

Fig. 2. da/dN versus the strain-energy release rate, ΔG_T, for $G_{II}/G_I = 28\%$
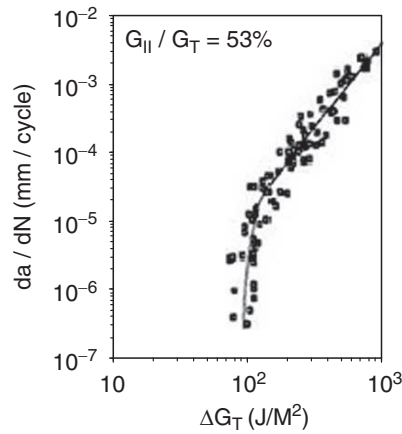

Fig. 3. da/dN versus the strain-energy release rate, ΔG_T, for $G_{II}/G_I = 53\%$
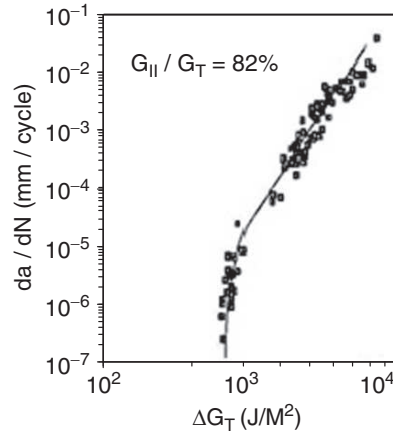
Fig. 4. da/dN versus the strain-energy release rate, ΔG_T, for G_{II}/G_I = 82%

3.2. Threshold total strain energy release rate

The total strain energy release rate threshold ΔG_{Tth} is characterized by a very weak delamination growth rates $\dfrac{da}{dN}$ ($<10^{-6}$ mm/cycle). Therefore, a crack can't propagate during a test which can last during many thousands of cycles. The ΔG_{Tth} values are obtained by the decreasing load method. Three to five specimens were tested for each G_{II}/G_T mode ratio considered. In this study, the ΔG_{Tth} values correspond to ($10^{-6} < \dfrac{da}{dN} < 10^{-7}$).

As shown in Figs. 2, 3, and 4, the threshold value is progressively reached after having described a curve representing the transition between the curve linear part (Paris' law) and the threshold value. This is a characteristic of the glass–fibre composites. However, for the carbon–fibre composites, the threshold value is suddenly reached just after the curve linear part.

Table 5 summarises the results of the ΔG_{Tth} values as function of G_{II}/G_T mode ratio. The obtained results show a logical development. The higher the G_{II}/G_T mode ratio, the greater the value of ΔG_{Tth}.

Table 5. Threshold total strain energy release rate results

G_{II}/G_I (%)	0	28	53	82	100
ΔG_{Tth} (J/m^2)	56.17 (5.65)	78.90 (4.81)	115.52 (12.11)	243.88 (10.37)	281.11 (18.05)

Studies presenting the measured delamination growth $\dfrac{da}{dN}$ as function of the strain release rate ΔG_T (Paris law), have proposed by numerous investigators. But, few studies including the threshold for no delamination growth are presented in the literature.

However, for unidirectional carbon-fibre reinforced epoxy composites, many authors Mall et al. [6], Russell and Street [10], Gustafson and Hojo [11] have shown that the total strain energy release rate ΔG_{Tth} decreases when $\dfrac{G_{II}}{G_T}$ mode ratio increases. In the case of unidirectional glass-fibre reinforced epoxy composites, the opposite phenomenon is noted.

Numerous fatigue studies Mall et al. [6], Russell and Street [10] have shown that the total strain energy release rate threshold increases when the matrix toughness decreases in mode I, mode II, and mixed mode (I+II).

4. Conclusions

The present investigation has examined the delamination mode I, mode II and mixed-modes (I+II) delamination growth and threshold in unidirectional laminates of E-glass/epoxy composite under fatigue conditions. This entailed the use of DCB, ELS, and MMB fracture mechanics coupons. The conclusions of this study may be summarised as follows:

For each G_{II}/G_T mode ratio considered in this study, results are presented in the form of ΔG_T versus $\dfrac{da}{dN}$ plots which fit the Paris law. Threshold values of the total strain energy release rate below which no initiation of delamination growth occurs were determined for both mode I, mode II, and mixed mode (I+II). In order to propose a semi-empirical threshold fatigue criterion, the study of a large number of G_{II}/G_T mode ratios is necessary.

References

[1] Gong X.J. (1992) Rupture interlaminaire en mode mixte (I+II) du composite stratifié verre/epoxy unidirectionnel et multidirectionnel. Thèse de docteur de l'UTC, France.
[2] Crews J.H. & Reeder J.R. (1988) A Mixed Mode Bending apparatus for delamination testing. NASA TM 100662 Report.
[3] Reeder J.R. & Crews J.H. (1991) Non linear analysis and redesign of the Mixed Mode Bending delamination test. NASA TM 102777 Report.
[4] ASTM D 6671-01 (2004) Standard test method for mixed mode I-mode II interlaminar fracture toughness of unidirectional fiber-reinforced polymer matrix composites.

[5]   Benzeggagh M.L. & Kenane M. (1996) Measurement of mixed-mode delamination fracture toughness of unidirectional glass/epoxy composites with mixed-mode apparatus. Composite Science and Technology, 56, pp 439–449.

[6]   Mall S., Yun K.T. & Kochhar N.K. (1989) Characterization of Matrix Toughness Effect on Cyclic Delamination Growth in Graphite Fiber Composite. ASTM STP 1012, pp 296–310.

[7]   Martin R.H. & Muri G.B. (1990) Characterization of Mode I and Mode II, Delamination Growth and Threshold in AS4/PEEK Composite. ASTM STP 1059, pp 251–270.

[8]   Prel Y., Davies P., Benzeggagh M.L. & De charentenay F.X. (1989) Mode I and Mode II Delamination of Thermosetting and Thermoplastic Composites. ASTM STP 1012, pp 251–269.

[9]   Bathias C. & Laksimi A. (1985) Delamination Thershold and Loading Effect in Fiber Glass Epoxy Composite. ASTM STP 876, pp 217–237.

[10] Russell A.J. & Street K.N. (1987) The Effect of Matrix Toughness on Delamination: Static and Fatigue Fracture Under Mode II Shear Loading of Graphite Fiber Composites. Toughened Composites, ASTM STP 937, pp 275–294.

[11] Gustafson C.G. & Hojo M. (1987) Delamination Fatigue Crack Growth in Unidirectional Graphite/Epoxy Laminates. Journal of Reinforced Plastics and Composite, pp 36–52.

Modification of Cellulose for an Application in the Waste Water Treatment

Lamia Timhadjelt, Aicha Serier, Karima Boumerdassi, Mohamed Serier and Zoubir Aîssani

Laboratory of Coating, Materials and Environment (LRME); University M'Hamed Bougara of Boumerdes; Avenue of the Independence, 35000 Boumerdes, Algeria

Abstract   Today's dramatic shortage of water resources and alarming pollution has recently triggered a lot of research for alternative water resources. This study consists in modifying cellulose by grafting of the amidoxime groups for its use in the adsorption of the Cu^{2+}, Cr^{3+} and sulphide ions present in industrial waste waters. Cellulose is an abundant biodegradable polymer. The amidoxime groups are strong complexans of metal ions. The grafting is achieved in two steps: cyanoethylation and amidoximation, confirmed by FT-IR. The optimum conditions and the parameters influencing the two reactions are determined by the kjeldahl's method and by FT-IR. The amidoxime quantity is determined by measuring the quantity of the amine functions by HCl proportioning. The implementation of the modified cellulose is intended for the adsorption of the metal ions Cu^{2+} and Cr^{3+} and sulphide ions S^{2-} in a double adsorption. The FT-IR analysis reveals that the fixing of metal cations is based on the complexation of the latter with the ligands of the adsorbent. The optimum adsorption was recorded at pH = 6 for a contact time of 5 h and an initial concentration of 10^{-1}M in metals. The desorption of fixed metals is possible by the EDTA, and the re-use of the adsorbent confirms the effectiveness of recycling.

Keywords: Cellulose, Modification, Sorption, Heavy Metals, Waste Water Treatment.

1. Introduction

The fast changes of polymeric materials due to technological and industrial practices have made their use more effective and less expensive. Thus, new implementations are regularly carried out with chemically modified polymers such as in the waste water treatments. However, the biopolymers and particularly cellulosics was the subject of these modifications. Indeed, during these last years, works of research were about the possibility of finishing controlled changes in the properties of the cellulosic materials [4] as cotton and cellulose [1, 5, 6] and bagasse [2, 3].

These last are very often chemically modified by amino groups. This alternative has the advantage of increasing the value of some natural products and sub-products [7]. In addition, the re-use of used waters represents a solution to the problem of water shortage, and takes part in the reduction of the pollution generated by the industrial effluents. The economic limits of the traditional techniques of metal processing liquid waste resulted in developing new processes implementing

properties of adsorption and complexation of biomaterials, particularly those based on the cellulose [4]. Indeed, in this field, the lignocellulosic materials seem promising by the adsorption of toxic heavy metals [8].

The objective of our work thus consists of the introduction of the amidoxime groups, complexants, into cellulose for an application in the field of the waste water treatments by the adsorption of heavy metals and with sulphide ions. The latter are eliminated by fixing in the second adsorption on the metals already trapped on amidoximated cellulose.

2. Material and methods

Pure cellulose powders some (60–65% crystalline) (Sigma-Aldrich Chemistry limited liability company, France), Acrylonitrile (Aldrich), hydroxylamine (Fluka Chimie, France). The heavy metal ions (Cu^{2+} and Cr^{3+}) were obtained starting from the metal salts ($CuCl_2$, $2H_2O$) and ($CrCl_3$, $6H_2O$) adjusted with pH between 3 and 6 using the solutions of Clarck-Lubs [6], by using the potassium hydrogenophthalate (Table 1).

Table 1. Clarck-Labs buffer solutions [6]

pH	Metals Solution (ml)	Potassium Hydrogeno-Phthalate 0.2 M (ml)	HCl 0.2 M (ml)	NaOH 0.2 M, (ml)	Deionized water
3	250	250	101.6	2	Dilute for 1,000 ml
4	250	250	/	119.25	Dilute for 1,000 ml
5	250	250	/	227.25	Dilute for 1,000 ml
6	250	250	/	/	Dilute for 1,000 ml

The products are characterized by a spectrometer FT-IR of Thermo-Nicolet Nexus series at ambient temperature. After drying under 40°C during 48 h, 3 mg of the sample is crushed with 150 mg of KBr then pressed. The pastille of $\emptyset = 6$ mm is analyzed.

The influence of the various parameters on the reactions was expressed by the degree of substitution (DS) determined by the Kjeldahl's method (Eq. 1) and by FT-IR. The proportioning of the metal ions in solution is carried out by an atomic adsorption spectrometer, SOLAAR M6, after acidification, dilution and filtration of the solutions.

The spectrometer UV, JASCO 3200, is used to highlight the effectiveness of the regeneration of Amidoxime Cellulose (Am-Cel). The solutions are introduced into a basin of optical way of 1cm. The quantity of the sulphide ions fixed is determined by iodic proportioning.

2.1. Modification of cellulose

Obtaining the amidoxime cellulose (Am-Cel) passes by the preparation of the cyanoethyl cellulose (CE-Cel) like first stage. The latter is obtained by the action of the acrylonitrile (AN) on the cellulose (Cel) in alkaline medium, NaOH with 36% in weight, in the presence of tetramethylammonium chloride (TMAC) [3, 6]. The Degree of substitution (DS) of the CE-Cel is obtained from the ultimate analysis of nitrogen rate N (%) using the following relation [6]:

$$DS = \frac{M_{Cel}N(\%)}{100M_N - M_{AN}N(\%)} \tag{1}$$

The CE-Cel prepared is then treated by an aqueous hydroxylamine hydrochloride solution [6] at constant temperature (60–80°C) for variant time (90–180 min). The modified cellulose obtained is washed with deionized H_2O and filtered under vacuum. The results are expressed by the quantity of amidoxime Q_A, obtained by the absorption of *HCl* by the amidoxime groups [6].

2.2. Adsorption and desorption of the heavy metal ions

The experiments of adsorption were carried out in a batch for a ratio of mass of adsorbent/volume of solution of 1/100 (g/ml), with the variation successively of the pH of the solution between 3 and 6, the contact time from 0 to 48 h and the initial heavy metal (Cu^{2+} and Cr^{3+}) concentrations from 0 to 10^{-1} M. For the same ratio of mass of adsorbent/volume of solution, a well defined mass of Am-Cel was immersed in an adequate volume of solution containing Cu^{2+} and Cr^{3+} ions for 24 h at ambient temperature under continuous agitation. The suspension is then filtered. The quantities of the Cu^{2+} and Cr^{3+} ions were determined by atomic absorption spectroscopy. The Am-Cel was regenerated by desorption of the metal ions adsorbed by a solution of EDTA at 0.1 N. A quantity of 0.1 g of Am-Cel is immersed in this last solution at ambient temperature during 24 h. The suspension is then washed by deionized H_2O, filtered and finally analyzed by UV spectroscopy. After the adsorption of the metal ions on the Am-Cel, the sulphide ions are eliminated in the second adsorption by immersing 0.005 g of the powder not regenerated in a sulphide solution with various concentrations: $2 \cdot 10^{-2}$, $4 \cdot 10^{-2}$ and $8 \cdot 10^{-2}$ M in closed bottles with continuous agitation.

3. Results and discussions

The CE-Cel and the Am-Cel are characterized by FT-IR. The comparison of the respective spectra (Fig. 1) shows the appearance of a peak characteristic of the $C \equiv N$

groups to 2254 cm^{-1} on the spectrum of the CE-Cel, while on that of the Am-Cel, we observe a considerable reduction in the peak characteristic of the $C{\equiv}N$ groups and the appearance of a peak characteristic of double bond $C = N$ to 1,666 cm^{-1}, thus indicating the formation of the CE-Cel and the Am-Cel respectively. Tables 2 and 3 indicate the influence of the conditions of cyanoethylation and amidoximation reactions respectively on DS and quantity of amidoxime (Q_A).
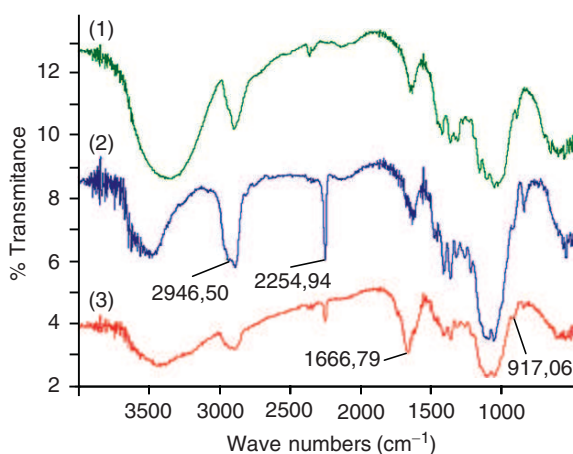

Fig. 1. Cellulose (1), CE-Cel (2) and Am-Cel (3) infrared spectrum

Table 2. Parameters influencing the cyanoethylation reaction

TMAC	Time (min)	(NaOH) (%)	DS
Without	90	36	1,510
With	90	36	2,297
With	45	36	0,847
With	150	36	2,385
With	90	10	0,391
With	90	20	0,739

Table 3. Parameters influencing the amidoximation reaction

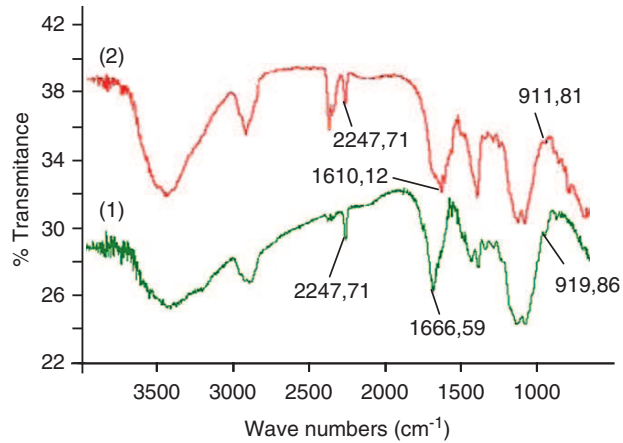| Temp (°C)	Time (min)	(NH$_2$OH) (%)	DS of CE-Cel	Q_A (mmol/g)
80	90	5	2.297	3.80
80	90	10	2.297	4.27
80	60	10	3.385	3.73
80	90	10	3.385	4.10
80	150	10	3.385	4.40
80	180	10	3.385	5.00
60	90	10	3.385	3.37

Fig. 2. Am-Cel (1) and Cu^{2+}-Am-Cel (2) infrared spectrum

We note an increase in the DS of the CE-Cel with the presence of tetramethylam-monium chloride (TMAC), time and the NaOH concentration up to an optimal value of 20% of the later. Q_A contained in the Am-Cel, increases with the temperature and time until 180 min (Fig. 2). According to authors [2, 5, 6], obtaining a stage beyond 180min indicates a maximum of conversion. The amidoximation is privileged by a concentration in NH_2OH of 10%. These results agree with literature works [2, 3, 5, 6]. Contrary to the Cel and the CE-Cel, the Am-Cel showed a great affinity for heavy metals (Cu^{2+} and Cr^{3+}). An octahedral complex which is characterized by the FT-IR analysis (Fig. 3) tends to be formed between the latter and the Am-Cel in the presence of the phthalates anions [8] at ambient temperature. The results (Fig. 3) show that the quantity of (Cu^{2+} and Cr^{3+}) ions adsorbed increases with their initial concentration.
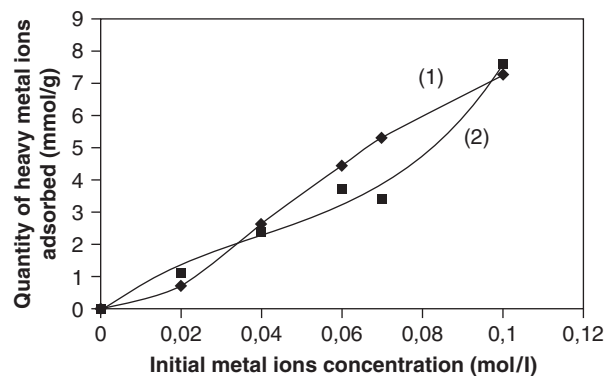

Fig. 3. Variation of the quantity of Cu^{2+} (1) and Cr^{3+} (2) ions adsorbed with their initial concentration

Figure 4 shows that the quantity of (Cu^{2+} and Cr^{3+}) ions increases with the time of contact, the equilibrium time is 5 h; the curves tend then towards a stage in accordance with the theory, indicating the saturation of the adsorption sites. The reduction recorded after 24 h can be explained by a light desorption due to the molecular collisions.
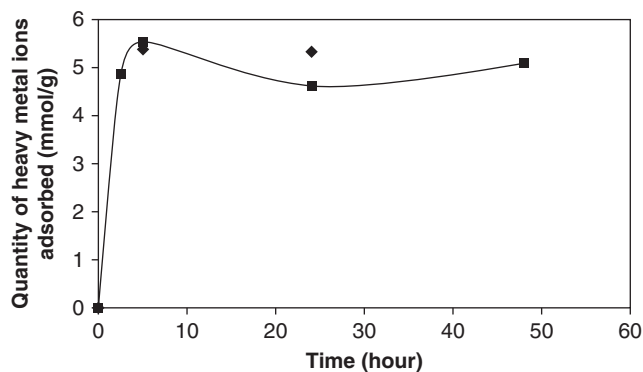

Fig. 4. Variation of the quantity of Cu^{2+} and Cr^{3+} ions adsorbed with the contact time

The results represented on Fig. 5 show in the case of chromium, that the quantity of the Cr^{3+} ions adsorbed increases with the solution pH. A small quantity was recorded towards pH = 3, this is due to the inhibiting effect. On another side, with pH = 6, we observe the precipitation of the metal ions with the OH^- ions.
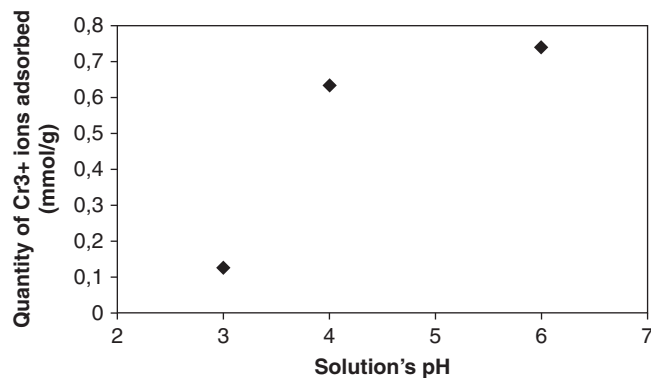

Fig. 5. Variation of the quantity of Cr^{3+} ions adsorbed with solution's pH

Figure 6 shows an increase in the quantity of Cu^{2+} ions adsorbed with Q_A contained in the adsorbent. This is foreseeable because the amidoxime groups represent the sites of adsorption.
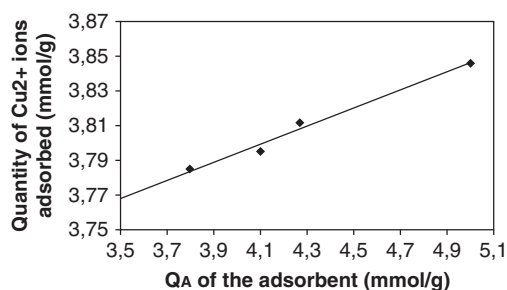
Fig. 6. Variation of the quantity of Cu^{2+} ions adsorbed with the quantity of the amidoxime

The results deferred on Table 4, show that the Cu^{2+} ions is selectively adsorbed on the amidoxime cellulose. This result agrees with works of Gauthier and al. [6] and EL-Wakil et al. [2].

Table 4. Determination of the quantity of Cu^{2+} and Cr^{3+} ions adsorbed for evaluation of their selectivity

Sample	Initial Concentration (mol/l)	Metal ion non adsorbed content (mol/l)	Metal ion adsorbed content (mol/l) = metal ion adsorbed quantity (mmol/0.01 g)	Metal ion adsorbed quantity (mmol/g)
Cu^{2+}	$7\ 10^{-2}$	$0.885\ 10^{-2}$	$6.114\ 10^{-2}$	6.11(4)
Cr^{3+}	$7\ 10^{-2}$	$3.782\ 10^{-2}$	$3.218\ 10^{-2}$	3.21(8)

It is carried out by desorption of the Cu^{2+} and Cr^{3+} ions by a solution of EDTA 0.1 N. In the presence of the latter, the Am-Cel doesn't show any affinity towards the metal ions. The effectiveness of regeneration is proven by the re-use of the treated powder. It is highlighted by the change of color *green → yellow* obtained by immersion of the powder in a sulphide solution during t = 30–60 min. Figure 7 shows that the quantity of the sulphide ions fixed increases with their initial concentration.
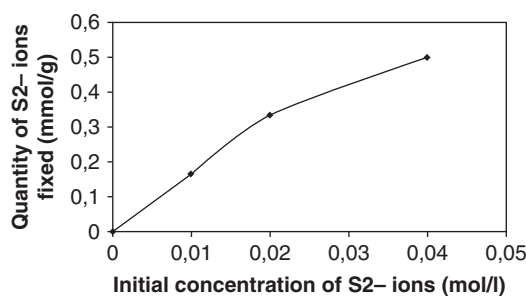

Fig. 7. Variation of the quantity of S^{2-} ions fixed with their initial concentrations

4. Conclusions

The cellulose was modified into Am-Cel while passing by the CE-Cel. The amidoxime groups can be chelated with heavy metals by formation of an octahedral complex metal-Am-Cel, which make them useful in the waste waters treatment. The operating conditions of preparation are simple. The adsorption of heavy metals is influenced by several parameters. It increases with their initial concentration, the time of contact and the pH of the solution. The sulphide ions are fixed on the heavy metals adsorbed beforehand on the Am-Cel. The regeneration of the Am-Cel is possible using a solution of EDTA at 0,1N.

References

[1] Gustaro Rocha de Castro, Ilton Luiz de Alcântara, Paulo dos Santos Roldan (2004) Synthesis, characterization and determination of the metal ions adsorption capacity of cellulose modified with p-aminobenzoic groups. Mat. Res., 7(2): 12.

[2] Hassan M. L., EL-Wakil N. A. (2003) Heavy metal ion removal by amidoximated bagasse. Wiley Periodicals. J. Appl. Polym. Sci., 87: 666–670.

[3] Hassan M. L., EL-Wakil N. A., Sefain M. Z. (2001) Thermoplasticization of Bagasse by cyanoethylation. Inc. J. Appl. polym. Sci., 79: 1965–1978.

[4] Hebeish A., Guthrie J. T. (1981) The chemistry and Technology of cellulosic copolymers. Springer, Berlin Heidelberg, New York, 342p.

[5] Kuboka H., Shigehisa Y. (1995) Introduction of amidoxime groups into cellulose and its ability to adsorb metal ions. Inc. J. Appl. Polym. Sci., 56(2): 147–151.

[6] Saliba R., Gauthier H., Gauthier R., Petit-Ramel M. (2000) Adsorption of copper (II) and chromium (III) ions onto Amidoximated cellulose. Inc. J. Appel. Poly. Sci., 75: 1624–1631.

[7] Satge Céline (2002) Etude de nouvelles stratégies de valorisation de mono et polysaccharides. Ph.D. thesis, Limoges University, 137p.

[8] Seko N., Tamada M., Yoshii F. (2004) Current status of adsorbent for metal ions with radiation grafting and crosslinking techniques. 6th International Symposium on Ionising Radiation and Polymers, IRAP.

A Full 3D Simulation of Plastic Forming Using a Heuristic Generalised Contact Algorithm

Tewfik Ghomari[1], Rezak Ayad[2] and Nabil Talbi[3]

[1]University of Sciences and Technology of Oran (USTO), Mechanical Department, BP 1505 El-Mnaouar, Oran, Algeria

[2]University of Reims Champagne-Ardenne, Group of Research in Sciences for Engineers Mechanics (GRESPI), Reims, France ESIEC, Esp. Roland Garros, BP 1029, Reims, France

Abstract A full 3D contact approach is proposed for simulating forming processes of plastic bodies. It uses a new local searching procedure which is based on the product of the geometrical positions of the "Slave" node before and after having crossed a plan "master". Coupling with the finite element method is achieved by using a classical 8-node hexahedral element. The use of a Mooney-Rivlin constitutive model allows getting a final simulation tool in order to optimise the mechanical behaviour of plastic bodies during their forming processes. Applications are essentially focused on 3D problems involving contact between solids, with a particular attention to the thermoforming process.

1. Introduction

The contact problems are very frequently encountered in industry. The codes of market such as ABAQUS, LS-DYNA, MARC, PAM-CRACH etc., take into account the problem of contact with or without friction. That made it possible to solve a rather vast number of industrial problems considered difficult. The main difficulties of a contact problem come owing to the fact that the boundary conditions related to the contact are not known in advance and they depend on the solution (boundary conditions evolutionary). Thus, the real contact surface and the contact reactions belong to the unknown factors of the problem. In case of great transformations, nonlinearities coming from the contact are added to the geometrical and material nonlinearities, making the forming problem quite difficult to solve. The general problem of the balance of a linear elastic solid in contact without friction with a rigid foundation, it was necessary to wait the Sixties so that Duvaut and Lions [1] proposed the variational inequations making it possible to establish the existence and the unicity of the solution. This obviously made it possible during the Seventies many numerical methods to be born. The first algorithm allowing making leave the nodes "Master" and "slave", in the case of the problems 2D and 3D, was established by Hallquist [2]. It is based on the concept of Bucket-sorting (sorting of limp).

In 1994, Oldenbourg and Nilsson [3] simplified the preceding algorithm while bringing back the search for three dimensions to only one dimension, thanks to an approach called "position codes" making it possible to codify all the nodes according to the positions of the nodes and of the numbers of limp circumscribed.

This technique allows to simplify the search of the areas of contact by examining the "position codes" (codified position of the nodes) of each node, after a binary sort as a preliminary. By using this algorithm, the cost of total search is thus reduced to ($NLog_2N$) operations of permutations. It does not remain about it less than the process of total search is not very effective. To improve it, Zhong [4] proposed the algorithm unified by combining the technique of "position codes" with a labellized approach "HITA" (Hierarchy Territories and Contact Territories). Although these methods and/or algorithms, proposed and developed for total search, remain in their globality rather effective, it does not remain about it less than effective algorithms for the local research of contact remain rather little developed [5]. The local research is employed to determine with precision so yes or not a node slave is in contact. The algorithms of local contact available in the literature are based on the algorithm known as "of node to segment" or "node on surface [6]. The method of Raphson Newton is often employed to determine the distances from penetration of the "Slave" node through the segment "master". In the majority of the problems with contact, the iteration count can strongly increase for small values of tolerance (lower than 10^{-3} test of stop), or if the geometry of the segment "master" presents sharp angles. Moreover it is unstable in certain case when the nodes candidates are opposite several segments. To improve the algorithm of "node slave/segment master", Wang [5] proposed the "Inside–outside" algorithm. The aforementioned is based on the orientation of the normal vectors carried by the element "master" and the trajectory of the "Slave" node between iteration I and i + 1. This method is considered to be fast because no iteration is added. However, from the problems can emerge at the edge between two segments or two or several bilinear surfaces called "areas of dead angle", because there is no more continuity of the normal between two segments. The areas of dead angles are the weak points of the local algorithms of search. To overcome these difficulties Ju [7], an algorithm of local research proposed which eliminates the sharp angles by making a smoothing from the points of the cubic segments using splines.

But the possibility of multiple solutions of the contact of a node by several segments affects the effectiveness of the search for contact. Heinstein and al. [8] could develop an algorithm of search for total contact able to treat the contact impact (Crash landing of car). It was implemented on Software PRONTO 3D. The aforementioned belonged to the algorithms of search for contact based on the technique "bucket sorting". A formula thus makes it possible to calculate the code of limp unbounded, which distinguishes the algorithm from that Zhong (position codes). The algorithm of search for contact developed in our work rests on this technique with a new algorithm of search local which is based on the product of the geometrical positions of the "Slave" node before and after having crossed a plan "master".

2. Basis 8 node hexahedral element in total lagrangian formulation (FLT)

We present the main equations used for the implementation of a behavior law in a classical three-dimensional solid element (8-node hexahedral element H8). A Total Lagrangian displacement Formulation is used.

2.1. Geometrical approximation and displacement formulation

The position vector of a point in the meridian plan, expressed in the Cartesian coordinate system, is given by:

$$\vec{x}_p = x\,\vec{i} + y\,\vec{j} + z\,\vec{k} \quad with \quad x = \sum_{i=1}^{Nodes} N_i x_i \;;\; y = \sum_{i=1}^{Nodes} N_i y_i \;;\; z = \sum_{i=1}^{Nodes} N_i z_i \qquad (1)$$

The 3D displacement field of point p is defined by the following classical trilinear approximation:

$$U = \sum_{i=1}^{8} N_i U_i \;;\; V = \sum_{i=1}^{8} N_i V_i \;;\; W = \sum_{i=1}^{8} N_i W_i \qquad (2)$$

The shape functions and their derivatives are those of a conventional 8-node hexahedral element (H8) (Fig. 1). $2 \times 2 \times 2$ gauss points are sufficient to get an exact integration of the stiffness tangent matrix.
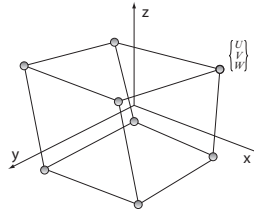

Fig. 1. 3D 8-node hexahedral element

$$\begin{Bmatrix} U,_x \\ U,_y \\ U,_z \\ V,_x \\ V,_y \\ V,_z \\ W,_x \\ W,_y \\ W,_z \end{Bmatrix} = \begin{bmatrix} N_{1,x} & \dots N_{8,x} & \\ N_{1,y} & \dots N_{8,y} & \\ N_{1,z} & \dots N_{8,z} & \\ & N_{1,x} & \dots & N_{8,x} \\ & N_{1,y} & \dots & N_{8,y} \\ & N_{1,z} & \dots & N_{8,z} \\ & & N_{1,x}\dots & N_{8,x} \\ & & N_{1,y}\dots & N_{8,y} \\ & & N_{1,z}\dots & N_{8,z} \end{bmatrix} \begin{Bmatrix} U_1 \\ V_1 \\ W_1 \\ \vdots \\ U_8 \\ V_8 \\ W_8 \end{Bmatrix} \qquad (3)$$

2.2. Green–Lagrange deformation tensor

The displacement gradient tensor [F] and the Cauchy Green Right stress tensor [C] are written in the Cartesian co-ordinate system as:

$$[F] = \begin{bmatrix} 1+U_{,x} & U_{,y} & U_{,z} \\ V_{,x} & 1+V_{,y} & V_{,z} \\ W_{,x} & W_{,y} & 1+W_{,z} \end{bmatrix} \quad [C] = [F^T][F] = \begin{bmatrix} C_{11} & C_{12} & C_{13} \\ C_{21} & C_{22} & C_{23} \\ C_{311} & C_{32} & C_{33} \end{bmatrix} \quad (4)$$

$$[C] = \begin{bmatrix} (1+U_{,x})^2+V_{,x}^2+W_{,x}^2 & (1+U_{,x})U_{,y}+(1+V_{,y})V_{,x}+W_{,x}W_{,y} & (1+U_{,x})U_{,z}+V_{,x}V_{,z}+(1+W_{,z})W_{,x} \\ (1+U_{,x})U_{,y}+(1+V_{,y})V_{,x}+W_{,x}W_{,y} & U_{,y}^2+(1+V_{,y})^2+W_{,y}^2 & U_{,y}U_{,z}+(1+V_{,y})V_{,z}+W_{,y}(1+W_{,z}) \\ (1+U_{,x})U_{,z}+V_{,x}V_{,z}+(1+W_{,z})W_{,x} & U_{,y}U_{,z}+(1+V_{,y})V_{,z}+W_{,y}(1+W_{,z}) & U_{,z}^2+V_{,z}^2+(1+W_{,z})^2 \end{bmatrix} \quad (5)$$

I_1, I_2 and I_3 are the invariants of tensor [C]:

$$\begin{aligned} I_1 &= C_{11} + C_{22} + C_{33} \\ I_2 &= C_{11}C_{22} + C_{22}C_{33} + C_{33}C_{11} - C_{12}^2 - C_{23}^2 - C_{13}^2 \\ I_3 &= C_{11}C_{22}C_{33} + 2C_{12}C_{23}C_{13} - C_{11}C_{23}^2 - C_{22}C_{13}^2 - C_{33}C_{12}^2 \end{aligned} \quad (6)$$

The Green-Lagrange tensor is written as:

$$[E] = \frac{1}{2}([C]-[I]) \quad (7)$$

2.3. Minimum total potential energy principle

The total potential energy is defined by:

$$\Pi = \sum_k \left(\Pi_{int}^k - \Pi_{ext}^k \right) \quad (8)$$

Π_{int}^k is the elementary internal potential energy which can be written as:

$$\Pi_{int}^k = \int_{v^0} W\left(\bar{I}_{21}, \bar{I}_2, J\right) dv^0 \quad (9)$$

W represents the deformation energy per unit of no-deformed volume, accumulated in the structure during the deformation:

$$W(\bar{I}_1, \bar{I}_2, J) = W_d(\bar{I}_1, \bar{I}_2) + W_s(J) \tag{10}$$

For a Mooney-Rivlin law [9], W is given by Crisfield [10]:

$$W(\bar{I}_1, \bar{I}_2, J) = C1(\bar{I}_1 - 3) + C2(\bar{I}_2 - 3) + \frac{1}{2}\kappa(J-1)^2 \tag{11}$$

$\bar{I}_1$ and $\bar{I}_2$ are modified invariants. The first variation of the external potential energy Π_{ext}^k is given by:

$$\delta\Pi_{ext}^k = \iint_{S^0} \langle \delta u \rangle \{p\} dS^0 \tag{12}$$

$\langle \delta u \rangle$ is the displacement vector in the local base $\langle \vec{t}_1, \vec{t}_2, \vec{n} \rangle$ and $\{p\}$ the compressive distributed forces. Residual vector:

$$\delta\Pi_{int}^k = \iint_{S^0} \langle \delta u \rangle \{p\} dS^0 \tag{13}$$

where $\delta\Pi_{int}^k$ represents the first variation of the internal elementary energy.

$$\delta\Pi_{int}^k = \int_{V^0} \delta W(\bar{I}_1, \bar{I}_2, J) \, dV^0 \tag{14}$$

We obtain the vector of the internal forces:

$$\delta\Pi_{int}^k = \langle \delta U_n \rangle \int_\xi \int_\eta \int_\zeta \{\bar{r}\} \det J d\xi d\eta d\zeta \quad with \langle \delta U_n \rangle = \langle \delta U_1 \, \delta V_1 \, \delta W_1 \, \ldots \, \delta U_8 \, \delta V_8 \, \delta W_8 \rangle \tag{15}$$

$$\delta\Pi_{int}^k = \langle \delta U \rangle \{f_{int}^k\} \tag{16}$$

Introducing a Mooney-Rivlin law leads to:

$$\delta\Pi_{int}^k = \int_{V^0} (A_1 \, \delta\bar{I}_1 + A_2 \, \delta\bar{I}_2 + A_3 \, \delta\bar{I}_3) dV^0 \tag{17}$$

With:

$$A_1 = C_1 I_3^{-\frac{1}{3}}, A_2 = C_2 I_3^{-\frac{2}{3}}, A_3 = -\frac{1}{3}C_1 I_1 I_3^{-\frac{4}{3}} - \frac{2}{3}C_2 I_2 I_3^{-\frac{5}{3}} + \frac{1}{2}\frac{\kappa(J-1)}{J} ; j = \sqrt{I_3} \tag{18}$$

$\delta \bar{I}_1$, $\delta \bar{I}_2$ and $\delta \bar{I}_3$ The variations of the invariants of the right tensor represent.

$$
\begin{aligned}
\delta \bar{I}_1 &= tr(\delta [C]) = \delta C_{11} + \delta C_{22} + \delta C_{33} \\
\delta \bar{I}_2 &= (C_{22} + C_{33})\delta C_{11} + (C_{11} + C_{33})\delta C_{22} + (C_{11} + C_{22})\delta C_{33} - 2C_{12}\delta C_{12} - 2\,C_{13}\delta C_{13} - 2C_{23}\delta C_{23} \\
\delta \bar{I}_3 &= (C_{22}C_{33} - C_{23}^2)\delta C_{11} + (C_{11}C_{33} - C_{13}^2)\delta C_{22} + (C_{11}C_{22} - C_{12}^2)\delta C_{33} + \\
&\quad 2(C_{13}C_{23} - C_{12}C_{33}) + 2(C_{12}C_{23} - C_{22}C_{13})\delta C_{13} + 2(C_{12}C_{13} - C_{11}C_{23})\delta C_{23}
\end{aligned}
\tag{19}
$$

These theoretical developments allows getting the following expression of $\delta \Pi_{\text{int}}^k$:

$$
\delta \Pi_{\text{int}}^k = \int_{V^0} \sum_{i=1}^{Nodes} \left(f_1 \delta U + f_2 \delta V + f_3 \delta W \right) dV^0
\tag{20}
$$

$$
\begin{aligned}
f_1 &= 2(1 + U_{,x})N_{,x} B_1 + 2U_{,y} B_2 + 2U_{,z} N_{i,z} B_3 + (U_{,y} N_{,x} + (1 + U_{,x})N_{,y})B_4 \\
&\quad + (U_{,z} N_{i,x} + (1 + U_{,x})N_{i,z})B_5 + (U_{,z} N_{i,y} + U_{,y} N_{i,z})B_6
\end{aligned}
\tag{21a}
$$

$$
\begin{aligned}
f_2 &= 2V_{,x} N_{i,x} B_1 + 2(1 + V_{,y})N_{,y} B_2 + 2V_{,z} N_{i,z} B_3 + (V_{,x} N_{i,y} + (1 + V_{,y})N_{i,x})B_4 \\
&\quad + (V_{,x}N_{,z} + V_{,z} N_{i,x})B_5 + ((1 + V_{,y})N_{i,z} + V_{,z} N_{i,y})B_6
\end{aligned}
\tag{21b}
$$

$$
\begin{aligned}
f_3 &= 2W_{,x} N_{,x} B_1 + 2W_{,y} N_{i,y} B_2 + 2(1 + W_{,z})N_{,z} B_3 + (W_{,x} N_{i,y} + W_{,y}N_{i,x})B_4 \\
&\quad + (W_{,x}N_{i,z} + (1 + W_{,z})N_{i,x})B_5 + (W_{,y}N_{,z} + (1 + W_{,z})N_{i,y})B_6
\end{aligned}
\tag{21c}
$$

And:

$$
\begin{aligned}
B_1 &= A_1 + (C_{22} + C_{33})A_2 + (C_{22}C_{33} - C_{23}^2)A_3 \\
B_2 &= A_1 + (C_{11} + C_{33})A_2 + (C_{11}C_{33} - C_{13}^2)A_3 \\
B_3 &= A_1 + (C_{11} + C_{22})A_2 + (C_{11}C_{22} - C_{12}^2)A_3 \\
B_4 &= -2\left(C_{12}A_2 + (C_{12}C_{33} - C_{13}C_{23})A_3\right) \\
B_5 &= -2\left(C_{13}A_2 + (C_{13}C_{22} - C_{12}C_{23})A_3\right) \\
B_6 &= -2\left(C_{23}A_2 + (C_{11}C_{23} - C_{12}C_{13})A_3\right)
\end{aligned}
\tag{22}
$$

The final internal force vector $\left\{ f_{\text{int}}^k \right\}$ is written as:

$$
\delta \Pi_{\text{int}}^k = \langle \delta U_1 \delta V_1 \delta W_1 \cdots \delta U_8\ \delta V_8\ \delta W_8 \rangle \int_\xi \int_\eta \int_\zeta \langle f_1 f_2 f_3 \cdots f_1 f_2 f_3 \rangle^T \det J\, d\xi\, d\eta\, d\zeta
\tag{23}
$$

$$\delta\Pi_{\text{int}}^k = \langle\delta U\rangle\left\{f_{\text{int}}^k\right\}\tag{24}$$

3. Tangent matrix

The calculation of the elementary tangent matrix can be explicitly defined by expressing the second variation of the elementary virtual work or by a perturbation technique. We have adopted the last technique which usually used. It is based on a finite difference scheme:

$$\left\{K_{T_j}\right\} = -\frac{\left\{R\left(\{U\} + \{\delta U_j\}\right)\right\} - \left\{R\left(\{U\} - \{\delta U_j\}\right)\right\}}{2\delta U_j}\tag{25}$$

We present a searching algorithm for the analysis of 3D contact. It's based, on the one hand, on the work of Heinstein et al. [8], and, on the other hand, on a local searching algorithm with a penalty method that we've developed in this work. There are other searching techniques of contact areas, which make it possible to avoid a systematic sweeping of the whole of the nodes to each step of time. The principle rests on a space division using a virtual mesh (Figs. 2 and 3). The lists of objects containing nodes in each zone are updated at each new introduction of object. The simplest structure is the regular mesh covering the field. Each box of mesh is indexed by an entirety. This structure is described on the Figs. 2 and 3.
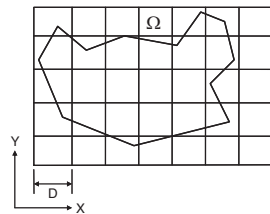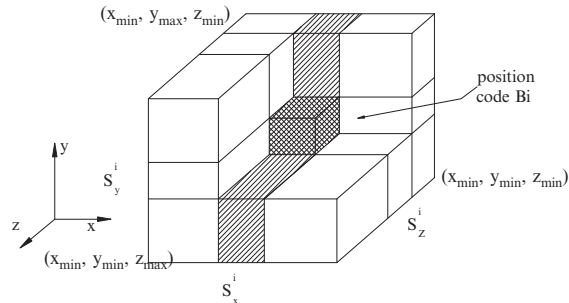

Fig. 2. Virtual mesh   **Fig. 3.** The position code buckets

In order to cure the need for locating the nodes candidates in contact with an arbitrary manner, a total strategy is adopted which consists in the following:

- Initialize the vector (nbox) which contains the numbers of the nodes in each bucket of a virtual mesh (Figs. 2 and 3).
- Find the code Bi for each node.
- Store the codes of all nodes i in a vector (lbox): lbox (I) = Bi.
- Increment the storyteller for the codes of such kind: nbox (Bi) = nbox (Bi) +1.

- Calculate the pointer of each code j in a list of nodes.
- Npoint (1) = 1, npoint (j) = npoint (j-1) + nbox (j-1).
- Initialize nbox with zero.
- Find the nodes slaves in agreement with the numbers of code in a list (ndsort).
- Ndsort (nbox (lbox (I))+npoint (lbox (I)))=Inbox (lbox (I))=nbox(lbox (I))+1.

The code of each bucket is determined by the expression below:

$$B_i = \left(S_Z^i - 1\right)S_X\,S_Y + \left(S_Y^i - 1\right)S_X + S_X^i \tag{26}$$

$$
\begin{array}{ll}
S_X = \mathrm{int}\left[(x_{\max} - x_{\min})/b_S\right]+1 & S_X^i = \mathrm{int}\left[(x_i - x_{\min})/b_S\right]+1 \\
S_Y = \mathrm{int}\left[(y_{\max} - y_{\min})/b_S\right]+1\,; & S_Y^i = \mathrm{int}\left[(y_i - y_{\min})/b_S\right]+1 \quad b_s : width\ of\ bucket \\
S_Z = \mathrm{int}\left[(z_{\max} - z_{\min})/b_S\right]+1 & S_Z^i = \mathrm{int}\left[(z_i - z_{\min})/b_S\right]+1
\end{array} \tag{27}
$$

The cutting which contains any node is calculated as follows:

$$
\begin{aligned}
ibox_{\min} &= \min\left(S_X, \mathrm{int}\left((xc_{\min} - x_{\min})/b_S\right)+1\right) \\
jbox_{\min} &= \min\left(S_Y, \mathrm{int}\left((yc_{\min} - y_{\min})/b_S\right)+1\right) \\
kbox_{\min} &= \min\left(S_Z, \mathrm{int}\left((zc_{\min} - z_{\min})/b_S\right)+1\right) \\
ibox_{\max} &= \min\left(S_X, \mathrm{int}\left((xc_{\max} - x_{\min})/b_S\right)+1\right) \\
jbox_{\max} &= \min\left(S_Y, \mathrm{int}\left((yc_{\max} - y_{\min})/b_S\right)+1\right) \\
kbox_{\max} &= \min\left(S_Z, \mathrm{int}\left((zc_{\max} - z_{\min})/b_S\right)+1\right)
\end{aligned} \tag{28}
$$

$X_{C,\min}$, $X_{C,\max}$, $Y_{C,\min}$, $Y_{C,\max}$ and $Z_{C,\min}$, $Z_{C,\max}$ are the ends of buckets widened in the direction of X, Y and Z.

Identification of the code of each bucket widened while determining arranged in three directions X Y and Z:

$$
\begin{aligned}
&Loop\ from\ ibox = ibox_{\min}\ to\ ibox_{\max} \\
&\quad Loop\ from\ jbox = jbox_{\min}\ to\ jbox_{\max} \\
&\quad\quad Loop\ from\ kbox = kbox_{\min}\ to\ kbox_{\max} \\
&\quad\quad\quad B_i = (kbox-1)S_x S_y + (jbox-1)S_x + ibox \\
&\quad\quad End\ Loop \\
&\quad End\ Loop \\
&End\ Loop
\end{aligned} \tag{29}
$$

All the codes of the nodes calculated are able potentially to interact with the main segment. On the level of the search for local contact, an algorithm is worked out to detect the Slave nodes which can crossed the segment master by checking

the product the positions before and after if it is negative indeed node A crosses if the product is positive two cases can the this presented either node does not have crosses the segment or the node has cross-piece the segment before and after this last case can generates some concern (Fig. 4), before curing it one needs an additional checking of the product the position of the node in its initial position and its final position.
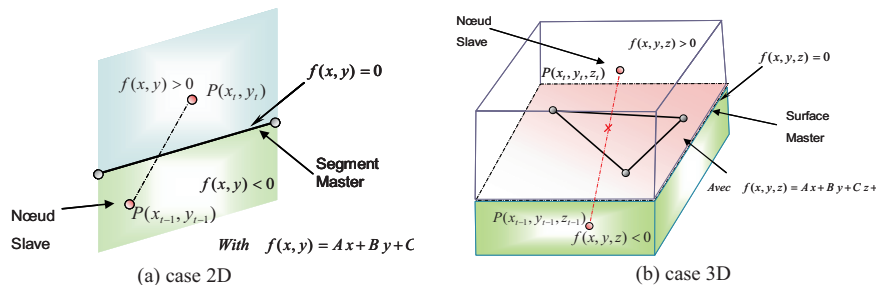

(a) case 2D   (b) case 3D

Fig. 4. Detection of the passage of the node compared to the line

4. Discretization

The local reference mark is defined on the element (1-2) by the base $(\vec{t}, \vec{n})$ with $\vec{t}$ tangent vector and $\vec{n}$ the normal vector whose components in the total reference mark with two dimensions such as:

$$\{t\} = \frac{1}{L}\left(\{X_2\} - \{X_1\}\right) = \begin{Bmatrix} c \\ s \end{Bmatrix} \; ; \; \{n\} = \begin{Bmatrix} -s \\ c \end{Bmatrix} \quad with \; L = \|X_2 - X_1\| \quad \begin{matrix} c : \cos \\ s : \sin \end{matrix} \tag{30}$$
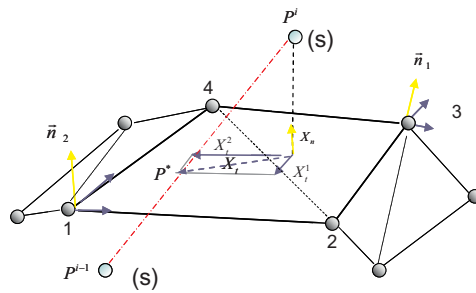

Fig. 5. Local State 3D

That is to say ξ the standardized curvilinear coordinate of p (the projection of S on the segment (1-2)) for the case two dimensional:

$$\xi = (1/L)\langle X_S - X_1\rangle\{t\} \; with \; 0 \le \xi \le 1 \tag{31}$$

The normal gap is the distance from penetration of the node S through the element (1-2) or a surface is expressed in the local reference (Fig. 5) mark like; the tangential gap is defined by:

$$\{x_n\} = \langle X_S - X_1 \rangle \{n\} \quad and \quad \{x_t\} = \langle X^s - X^* \rangle \{t\} \tag{32}$$

The reactions are calculate by Coulomb law and are given by the following expressions:
Tangential reaction

$$If \ x_n \geq 0 \ no \ contact \Rightarrow r_n = 0; \ If \ x_n < 0 \ contact \Rightarrow r_n = k_n x_n \tag{33}$$

Tangential reaction

$$r_{t_{cri}} = \mu \, r_n \ critical \ reaction \ and \quad r_t = k_t \, x_t \quad tangential \ reaction \tag{34}$$

where µ represents the friction coefficient:

$$if \ |r_t| < r_{t_{cri}} \ adhering \ contact \Rightarrow r_t = k_t \, x_t \ ; \ if \ |r_t| \geq r_{t_{cri}} \ slipping \ contact \Rightarrow r_t = r_{t_{cri}} \frac{x_t}{|x_t|} \tag{35}$$

The contribution of the reactions of a node of contact in the residue of total balance is written:

$$\{F_{cnt}\}^n = [Q]^T \begin{Bmatrix} r_n \\ r_t \end{Bmatrix} \tag{36}$$

The tangent matrices of contact are evaluated in the following:

$$[K_{cnt}]^n = [Q]^T \begin{bmatrix} k_t & 0 & 0 \\ 0 & k_t & 0 \\ 0 & 0 & k_n \end{bmatrix} [Q] \Rightarrow adhering \ contact \tag{37a}$$

$$[K_{cnt}]^n = [Q]^T \begin{bmatrix} 0 & 0 & 0 \\ 0 & 0 & 0 \\ 0 & 0 & k_n \end{bmatrix} [Q] \Rightarrow contact \tag{37b}$$

With [Q] is the matrix of passage of the local at total reference.

The algorithm search for contact must be able to manage ambiguous situations which can occur at the time of the procedure of search for contact (see Fig. 6):

- ▪ The free node, or in contact, is opposite a dead angle, and does not have any projection on the close main elements; in that case two situations present themselves (see Fig. 6) case 2D.
- ▪ The node active slave free, in contact or penetrating, is opposite a valley and thus has several projected on main elements in this case, we associate one of the main elements to him nearest from which the distance from the point candidate and its projection on this element is smallest.
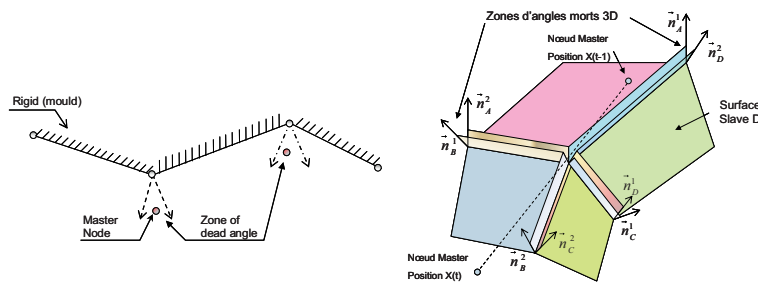

Fig. 6. Ambiguous cases 2D and 3D trajectories met

4.1. Numerical experiments

All our geometry and results have been drawn and visualized using the educational version of GID software (www.gidhome.com).

4.2. Circular plate under uniform pressure

We consider a circular plate treated by Hughes et al. [11], Radius L and thickness h are respectively 190.5 and 12.7 mm. The plate is fixed on its circumference and subjected to a pressure on one of its faces (Fig. 7).
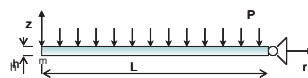

Fig. 7. Geometry of plate under pressure

We use a quasi-incompressible hyperelastic material represented by the Mooney-Rivlin's model [9] with the constants $C_1 = 0.55$ MPa and $C_2 = 0.14$ MPa. The penalty factor κ used to penalize the internal energy is taken equal to K = 68.9 MPa. The curve of loading of the pressure is obtained by controlling the extreme node of the plate (Figs. 8 and 9).
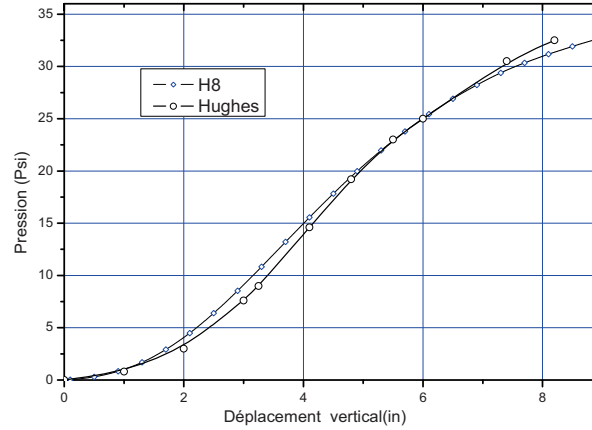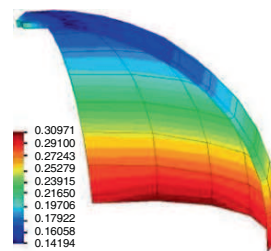
Fig. 8. Courbe de charge Pression déplacement

Fig. 9. Circular plate under pressure

4.3. Thermoforming of a cup

A second example treats the thermoforming of a cup. In this problem we consider a plastic paraison thickness 2.54 mm simply pressed on a cup cylindrical and subjected to a uniform pressure. The geometry is illustrated on Fig. 10. This example was treated by DeLorenzi [12]. Calculation is made on a material hyper-elastic (type Mooney Rivlin): with the constants $C1 = 0.142$ MPa, $C2 = 2.2\,e\text{-}4$ MPa and $k = 68.94$ MPa (Bulk Modulus). The resolution is carried out using an implicit scheme of type Newton Raphson. The contact of paraision is supposed sticking and the coefficient of penalty taken equal to 10^7. The objective of this test, famous to be severe, is to study the thicknesses distribution of the cup at during time forming (Fig. 11). The pitches of loading will have to be very small for better attenuating the strong numerical oscillations observed. A comparison with the element SFR-Axi is made for a better examination of the performances and precision on the distribution thicknesses. Figure 12 shows the shape of the curve of thicknesses distribution along the generator of the cup.

The results provided by the two models are in agreement with the experimental tests. A pressure of 0.0716 MPa proved to be necessary to completely plate the preform against the mould. It should be noted that calculation in round background areas (bottom of the cup) requires a considerable CPU time. To cure it, it is completely possible that a mending of meshes localized of the areas with round

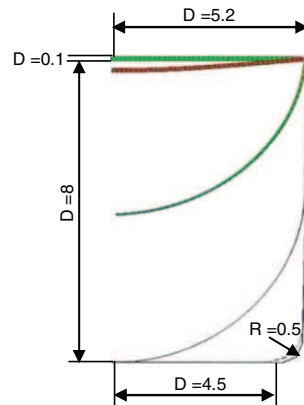cavities is carried out. Another solution consists in applying load factors of strong value for implicit calculation.
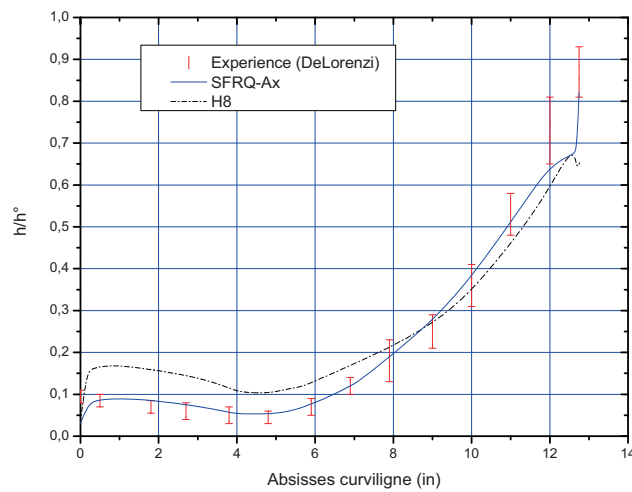

Fig. 10. Thermoforming of a cup

Fig. 11. Distribution thickness according to the curvilinear coordinate

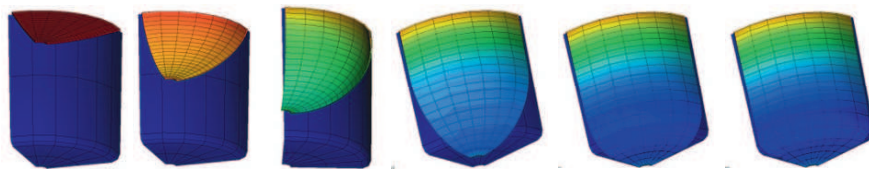**Fig. 12.** Plastic forming process

References

[1] Duvaut G. and Lions J.L. (1976) Inequalites in mechanics and physics. Springer, Berlin.

[2] Hallquist J.O. (1993) LS-DYNA3D Theoretical Manual. Livermore Software Technology Corporation, Livermore, Rev. 2.

[3] Oldenburg M. and Nilsson L. (1994) The position code algorithm for contact searching. Int. J. Numer. Meth. Eng., 37:359–386.

[4] Zhong Z.H. and Nilsson L.A. (1996) Unified contact algorithm based on the territory concept. Comput. Method. Appl. Mech. Eng., 130:1–16.

[5] Wang S.P. and Nakamachi E. (1997) The inside–outside contact search algorithm for finite element analysis. Int. J. Numer. Meth. Eng., 40(19):3665–3685.

[6] Hallquist J.O., Goudreau G.L. and Bension D.J. (1985) Sliding interfaces with contact–impact in large-scale lagrangian computations. Comput. Method. Appl. Mech. Eng., 51:107–137.

[7] Ju S.H. (1998) Cubic-spline contact element for frictional contact problems. J. Chin. Inst. Eng., 21(2):119–128.

[8] Heinstein M.W., Mello F.J., Attaway S.W. and Laursen T.A. (2000) Contact-impact modeling in explicit transient dynamics. Comput. Method. Appl. Mech. Eng., 187:621–640.

[9] Rivlin R.S. (1948) Large elastic deformation of isotropic materials. i. Fundamental concepts. Philos. T. Roy. Soc., 240:459–490.

[10] Crisfield M.A. (1991) Non-linear finite element analysis of solids an structures, vol. 2. Wiley, England.

[11] Hughes T.J.R. and Carnoy E. (1983) Non linear finite element shell formulation accouting for large membrane strains. Comp. Meth. Appl. Mech. Eng., 39:69–82.

[12] DeLorenzi H.G., Nied H.F. and Taylor C.A. (1988) Blow molding and thermoforming of plastics: finite element modeling. Comput. Struct., SPE, Tech. (34):797–799.

A Novel Approach for Bone Remodeling After Prosthetic Implantation

Habiba Bougherara[1], Václav Klika[2], František Maršík[3], Ivo A. Mařík[4] and L'Hocine Yahia[5]

[1]Department of Mechanical and Industrial Engineering, Ryerson University, 380 Victoria street, Toronto, Ontario, Canada, M5B 3K2

[2]Faculty of Nuclear Sciences & Phys. Eng. CTU, Zikova 4, 166 36 Prague 6, Czech Republic

[3]Institute of Thermomechanics CAS, Dolejškova 5, 182 00 Prague 8, Czech Republic

[4]Ambulant Centre for Defects of Locomotor Aparatus, Olsanska 7, Prague 3, Czech Republic

[5]Laboratory for Innovation and Analysis of Bioperformance (LIAB), École Polytechnique, Montréal, Québec, Canada, H3T 1J4

Abstract   The aim of the present study is to predict the functional adaptation of bone in response to changes in mechanical loading using a new biothermodynamic model for bone remodeling. In our approach, which fits into the framework of open systems, changes in the density are governed by balance of mass and balance of entropy supplemented by additional mass and entropy sources. The governing equations of bone remodeling process are based on irreversible thermodynamics and kinetics of chemical reactions. The key feature of this model is its ability to simulate the coupling between the mechanical and biochemical parameters that control bone remodeling, in particular the effect of dynamical loading, frequency of load and nutrition. Besides, the model can be used to predict some skeletal diseases such as bone fractures and osteoporosis. In the present paper, a biothermodynamic model was applied to the design of prosthetic implants. Numerical computations of bone density distributions after Total Hip Replacement (THR) using 3D finite element analysis showed that the biomimetic composite stem exhibit a better density patterns compared to the conventional titanium stem, indicating that the biomimetic prosthesis promotes higher remodeling rate and consequently less stress shielding. Furthermore, the model showed that the concentration of a new bone strongly depends on the history and intensity of loading and also on nutrition.

Keywords: Bone Remodeling, Dynamical Loading, FEM, Stem Cells, Composite Hip Stem.

1. Introduction

The process of bone remodeling has attracted the attention of researchers for many decades. Theories of bone adaptation begin in the XIXth century. Wolff [1] stated that bone structure could adapt in response to ever changing mechanical environment. This change is related to the mechanical stimulus history and the underlying physiologic mechanisms. Early 1970s, several mathematical theories of bone adaptation were developed to predict changes in bone shape and density based on

strain, stress and damage [2–9]. Generally, these models derive the rate of change of bone structure in response to stress, strain or damage. Despite the success achieved with these biomechanical models to predict normal bone architecture, they involve three major limitations, as Huiskes [5] pointed out. First, they have their empirical nature in common, by relating stress or strain in bone to adaptive remodeling behavior, without considering the relationship between the mechanical and biological mechanisms. Second, they considered bone as a continuum material, for which the theories of linear elasticity are valid. Third, these models are (quasi) static ones, effects of loading rates, visco-elastic effects and inertial effects are not considered. Therefore, the biomechanical models don't correspond to reality. Over the past decade the interest has shifted from biomechanics to mechanobiology. There have been several attempts to investigate bone remodeling process using mechanostat theory introduced by Frost [10]. This theory relates cellular activity in bone modeling and remodeling to external forces and explains adaptive behavior of bone at a microscopic level. Osteocytes were assumed to be mechanosensitive and capable of translating signals to the bone surface to attract the called basic multicellular units BMU's, which control the net apposition or removal of bone tissue [11–14]. While, mechanobiological models are suitable to investigate the morphological consequences of alternative loading conditions, metabolic disorders, as well as their pharmaceutical interventions, they involve two main limitations. Obviously, the metabolic effects of mechanical loading on bone are expressed through biochemical signals. However, bone physiology is not included in such theories. Second, theses models can provide valuable information on the morphological phenomena of bone at a microscopic level, unluckily, all of them consider a unique governing equation for the whole process of bone remodeling. Furthermore, they are characterized by single phase continuum model of bone. Currently, new theories based on the activities of osteoclasts and osteoblasts were developed to obtain some insight in bone remodeling processes. There are a few papers published that define, from a mathematical point of view, the dynamics of bone remodeling at the cellular level. Two of them propose a mathematical model accounting for the differential activity of PTH administration on bone accumulation [15, 16]. The third one suggests a mathematical model of autocrine and paracrine interactions among osteoblasts and osteoclasts [17]. The last model incorporates the RANK-RANKL-OPG pathway [18]. According to the latter model, it is possible to simulate skeletal diseases by inserting dysfunctional connections in the coupling network to explore different disease hypotheses. Although these new models give some insights into bone remodeling at the molecular level, none of them considered the bone as an open system. Limitations with these models are related to the formulation of the remodeling theory itself. Many simplifications and assumptions were made including the reduction of cell interaction equations, model's variables and parameters. For instance, in Lemaire model, cell interaction for the whole bone remodeling process were only described by the set of three differential equations [19], while it should be, at least, described by five equations as mentioned in the work of Petrtýl and Danešová [20]. In addition the dynamical loading, which is crucial for bone remodeling was not included. Thus, further work is clearly needed in this area.

The objectives of the study are twofold. The first is to predict the functional adaptation of bone around total hip stems made of Ti and HA-coated composite, using a new thermodynamic algorithm combined with the finite element analysis method. The second is to investigate the influence of the model parameters on bone remodeling.

2. Materials and methods

2.1. Biochemical description of bone remodeling processes

Bone resorption and formation involves the activity of two types of cells: osteoclasts and osteoblasts. Osteoclasts are coupled to multinuclear cells according to the following correlation:
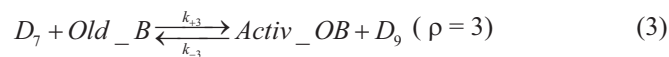
$$D_1 + MCELL \underset{k_{-1}}{\overset{k_{+1}}{\rightleftharpoons}} MNOC + D_4 \ (\rho = 1) \tag{1}$$
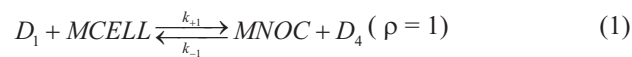
where D_1 is mixture of substances that are initiating the reaction with mononuclear cells (*MCELL*). *MNOC* referrers to multinucleated osteoclasts and D_4 is a remaining product from the ρth reaction. The osteoclasts cells break down bone by acting on trabecular bone surface to erode minerals and matrix. This action is described by the following chemical reaction:

$$MNOC + Old\_B \underset{k_{-2}}{\overset{k_{+2}}{\rightleftharpoons}} D_6 + D_7 \ (\rho = 2) \tag{2}$$
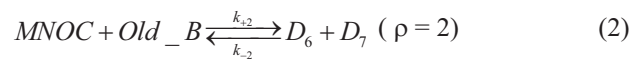
where *Old_B* is the abbreviation for old bone, and D_6 and D_7 are products made during bone decomposition. The product D_7 participates in the activation of osteoblasts.

Before osteoblasts (*OB*) repair and fill the eroded cavities, they need to be activated by the activator (*Activ OB*), which is produced after bone resorption. The action of osteoblasts can be described as follows:

$$D_7 + Old\_B \underset{k_{-3}}{\overset{k_{+3}}{\rightleftharpoons}} Activ\_OB + D_9 \ (\rho = 3) \tag{3}$$

$$Activ\_OB + OB \underset{k_{-4}}{\overset{k_{+4}}{\rightleftharpoons}} Osteoid + D_{12} \ (\rho = 4) \tag{4}$$

where D_{12} is a remaining substratum.

The final stage of remodeling is bone calcification. The bone surface is restored and covered by a layer of lining cells according to:

$$D_{13} + Osteoid \underset{k_{-5}}{\overset{k_{+5}}{\rightleftharpoons}} New\_B + D_{15} \quad (\rho = 5) \tag{5}$$
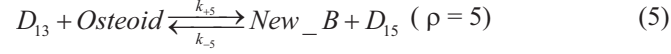
where D_{13} is is the substratum, that initializes mineralization of osteoid, *New_B* is the abbreviation of new bone formed by remodeling process and D_{15} is the residue of bone formation reaction. The above chemicals equations $(\rho = 1) - (\rho = 5)$ have a common form (i.e., Menten–Michaelis reaction) and describe the two most important stages in bone remodeling formation and resorption.

2.2. Thermodynamical description of bone remodeling process (BRT)

Bone remodeling, a coupled process, can be viewed as an irreversible thermodynamic system that operates far away from equilibrium. In this way, non-equilibrium thermodynamics [21] can be applied to describe interactions between the mechanical loading and chemical reactions (see Fig. 1). According to the second law of thermodynamics, the entropy production of bone remodeling process is always positive.

$$T\sigma(S) = pd_{(1)} + w_\rho A_\rho + \sum_\alpha \mathbf{j}_\alpha . \nabla \mu_\alpha (n_\alpha, p, \varphi) \geq 0, \tag{6}$$

where $d(1) = \dfrac{\partial v^1}{\partial x^1} + \dfrac{\partial v^2}{\partial x^2} + \dfrac{\partial v^3}{\partial x^3} = -\dfrac{\dot{\rho}}{\rho}$ is the trace of deformation rate tensor, p is a mechanical energy concentration or pressure, w_ρ and A_ρ are the chemical reaction rate and affinity of ρ-the reaction respectively. The sum $\sum_\alpha \mathbf{j}_\alpha . \nabla \mu_\alpha (n_\alpha, p, \varphi)$ is the rate of entropy production and $\mathbf{j}_\alpha \equiv (\mathbf{j}_{D_\alpha}, \mathbf{j}_c, \mathbf{j}_e)$ represents the fluxes of chemical component α which include the diffusion fluxes, $\mathbf{j}_{D_\alpha}$, mass flux $\mathbf{j}_c$ and bioelectrical current $\mathbf{j}_e$. Cowin et al. (1995), showed that all fluxes are driven by the gradients of concentrations n_α, pressure p and bioelectrical potential φ according to the following relation:

$$\left(\mathbf{j}_{D_\alpha}, \mathbf{j}_c, \mathbf{j}_e \right)^T = \mathbf{L} (\nabla n_\alpha, \nabla p, \nabla \varphi), \tag{7}$$

where L is the matrix of phenomenological coefficients.

These coefficients have to be determined experimentally or estimated on the base of corresponding biophysical models using Onsager symmetrical rules.

The cross coupling effects between the pressure (p) and chemical reactions rates (w_p) are expressed by Onsager's relations:

$$p = l_{vv}d_{(1)} + l_{v\rho}A_\rho \tag{8}$$

$$w_\rho = l_{\rho v}d_{(1)} + l_{\rho\rho}A_\rho, \tag{9}$$

Here l_{vv} represent the viscosity and $l_{\rho\rho}$ is the constant of chemical reaction rate. Onsager has shown that for fluxes and affinities, the cross effects in Eqs. (8) and (9) must satisfy the Osanger's reciprocal relation $l_{v\rho} = l_{\rho v}$.

These cross effects must also satisfy the second law of thermodynamics. By substituting Eqs. (8) and (9) into Eq. (6), the following conditions must be considered:

$$l_{vv} > 0 \ \ \& \ \ l_{\rho\rho} > 0 \tag{10}$$

and:

$$q = \frac{l_{v\rho}}{\sqrt{l_{vv}l_{\rho\rho}}} \in (-1,1) \tag{11}$$

where q denote the coupling parameter.

2.3. The role of coupling between mechanical loading and chemical reaction

To illustrate the importance of the mechanical loading, let us define the efficiency of interaction H, which represent the ratio of the mechanical loading to the chemical reaction:

$$H = \frac{w_\rho A_\rho}{pd_{(1)} + w_\rho A_\rho} \tag{12}$$

The relationship between the efficiency H and the coupling parameter q is thus:

$$H = \frac{\delta q + \delta^2}{1 + 2\delta q + \delta^2} \tag{13}$$

With:

$$\delta = \sqrt{\frac{l_{\rho\rho}}{l_{vv}}} \frac{d_{(1)}}{A_\rho} \tag{14}$$

In nature, all systems including living tissues are optimized [22]. Accordingly, we can assume that the efficiency described by Eq. (12) should have the absolute highest value. This value is reached when: $\delta = -\frac{1}{q} \pm \frac{1}{q}\sqrt{1-q^2}$. The most effective interaction corresponds to:

$$H_{max} = 1 \pm \frac{1}{2} \frac{q^2}{\sqrt{1-q^2}\left(1 \pm \sqrt{1-q^2}\right)} \tag{15}$$

The physical meaning of the above Eqs. (6–15) can be interpreted as follows:

- In the case of coupling $(q \neq 0)$, the chemical reactions are driven by mechanical loading if the chemical reaction rate is positive and the affinity is negative.
- If both parameters the chemical reaction rate the affinity are positive the chemical reactions are running spontaneously.
- Without coupling $(q = 0)$, the efficiency $H_{max} = 1$, the mechanical loading has a stimulatory effect on bone remodeling even when the affinity is negative.

2.4. Mathematical formulation of the host tissue biochemistry

The host tissue (i.e. bone) is a considered as a self organizing system (open system) that exchanges matter energy and entropy with its surroundings. Time evolution of the concentrations of all biochemical components of the bone is described by the set of differential equations, which are formulated, on the bases of chemical kinetics theory and non-equilibrium thermodynamics. The change of the concentration of chemical substances in the point $x \equiv (x^1, x^2, x^3)$ and time t can be expressed by the following differential equations:

$$\dot{n}_i = \sum_{\rho=1}^{5}\left(v'_{\rho i} - v_{\rho i}\right)w_\rho, \tag{16}$$

where $i = 1,2,\ldots,15$ and refers to the chemical substances. $MCELL$, $MNOC$…, D_7…, D_{15}, $\nu_{\rho i}$ is the stoichiometrical coefficient of ith chemical component for substrates and $\nu'_{\rho i}$ is the stoichiometrical coefficient of ith chemical component of products. The differential equation (16) can be expressed in dimensionless by scaling variables according to:

$$\tau = tk_{+2}n_{B0}, \; N_i = n_i/n_{B0}, \; \delta_\rho = k_{+\rho}/k_{+2}, \; \beta_i = B_i/n_{B0},$$
$$\mathfrak{D}_\rho = l_{\rho\nu}d_{(1)}/k_{+2}n_{B0}^2, J_j = j/k_{+2}n_{B0}^2 \tag{17}$$

where τ is time, N_i is the rate of concentration of the ith substance, δ_ρ is the ratio of rate of ρth reaction to second reaction, D_ρ is the parameter that describes the influence of dynamical loading on rate of ρth chemical reaction, β_i is the concentration of the ith substance and n_{B0} is the sum of initial molar concentration of relevant substances, one gets the set of equations. All parameters involved in equations ($\rho = 1,\ldots5$) can be calculated by solving the kinetic chemical equations and the time evolution of concentrations of substances (Eq. 18).

$$\frac{\partial N_{MCELL}}{\partial \tau} = -\delta_1\left(\beta_1 + N_{MCELL}\right)N_{MCELL} + J_3 + J_{New\_B} - \mathfrak{D}_1,$$

$$\frac{\partial N_{Old\_B}}{\partial \tau} = -\left(\beta_3 - N_{MCELL} + N_{Old\_B} + N_{Activ\_B} + N_{Osteoid} + N_{New\_B}\right)N_{Old\_B}$$
$$-\delta_3\left[\beta_7 - N_{Old\_B} - 2\left(N_{Activ\_OB} + N_{Osteoid} + N_{14}\right)\right]N_{Old\_B} + 2J_{New\_B} - \mathfrak{D}_2 - \mathfrak{D}_3, \tag{18}$$

$$\frac{\partial N_{Activ\_B}}{\partial \tau} = \delta_3\left(\beta_7 - N_{Old\_B} - 2(N_{Activ\_B} + N_{Osteoid} + N_{New\_B})\right)N_{Old\_B}$$
$$-\delta_4\left(\beta_{10} - N_{Osteoid} - N_{New\_B}\right)N_{Activ\_OB} + \mathfrak{D}_3 - \mathfrak{D}_4,$$

$$\frac{\partial N_{Osteoid}}{\partial \tau} = \delta_4\left(\beta_{10} - N_{Osteoid} - N_{New\_B}\right)N_{Activ\_OB} - \delta_5\left(\beta_{13} - N_{New\_B}\right)N_{Osteoid} + \mathfrak{D}_4 - \mathfrak{D}_5,$$

$$\frac{\partial N_{New\_B}}{\partial \tau} = \delta_5\left(\beta_{13} - N_{New\_B}\right)N_{Osteoid} - J_{New\_B} + \mathfrak{D}_5,$$

2.5. Simulation of thermodynamic bone remodeling (BRT) after total hip replacement (THR)

To conduct the finite element analysis the commercially available software (ANSYS 10; Ansys, Inc., Montreal, CA) is used with the implantation of Runge-Kutta 4 program to solve the system of differential equations (Eq. 18). The bone remodeling algorithm is tested first in a standard proximal femur. The idea is to qualitatively observe the results from the remodeling model due to a rather realistic environment.

3D geometry of a proximal femur was reconstructed from CT scan slices of a composite femur [23]. For structural analysis, cortical and cancellous bones were both simplified as homogeneous linear-elastic materials with transversely isotropic behavior. The second model of application is the proximal femur implanted with conventional stem made of Ti-base alloy ($E = 110$ GPa, $\nu = 0.3$), whereas, in the third model, a biomimetic composite stem is used. The latter (composite stem) is extensively described in previous work [24, 25]. It is composed of a 3 mm-thick sub-structure made of several layers of a carbon fiber/polyamide 12 (CF/PA12) polymer composite laminate with pre-determined fiber orientation, an internal polymeric core and a 100 microns thick bioactive HA coating in the proximal section to enhance bone ingrowth and increase the fixation strength.

The first and the second FE models are meshed with eight-nodded brick type element (SOLID45) with three degrees of freedom attributed to each node. For the third model, the sub-structure is meshed with eight nodded shell type element (SHELL 99). The bone-implant interface (HA coating) was modeled using surface-to-surface contact elements (CONTA174 and TARGE170). The three FE models are loaded with the most critical load case of gait of a body weight of 88 kg (a single limb stance phase). It consisted of a 1.9 kN force applied to the femoral head and a 1.24 kN abductor muscle force [26, 27]. This load is distributed over several nodes to avoid stress concentration and the displacement of all nodes at the distal end of the femoral bone is rigidly constrained.

3. Results and discussion

3.1. Validation of the FE model

The system of differential equations (Eq. 18) is solved using both MATLAB and ANSYS software. The iterative process for the thermodynamic model of (BR) outlined on figure is obtained when no changes in the time evolution of bone density occur.

Figure 1 represents the variation of the time evolution of the elastic modulus in the z direction (E_{ZZ}) in two different zones of the bone versus the number of iterations (N). As can be seen, with the increase of (N), values of (E_{ZZ}) decrease and the steady state is reached after approximately 35 iterations. To validate the FE model, the bone configuration obtained using the BRT model is compared to the frontal longitudinal midsection of upper femur (Fig. 2a), as well as the diagram of the lines of stress from Henry Gray Anatomy [28]. Prediction of bone remodeling in normal healthy bone (Fig. 2b) shows similar bone density patterns to those the inner structure of proximal femur (Fig. 3b). This result is also supported by numerous clinical investigations (Fig. 3a).
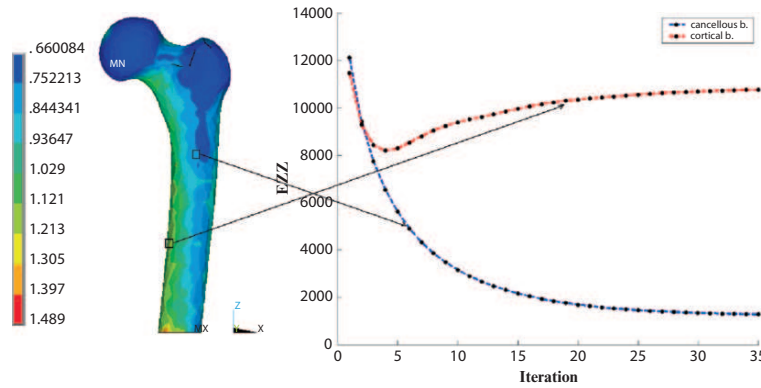
Fig. 1. Elastic modulus in z direction (EZZ) in two different zones of the bone vs
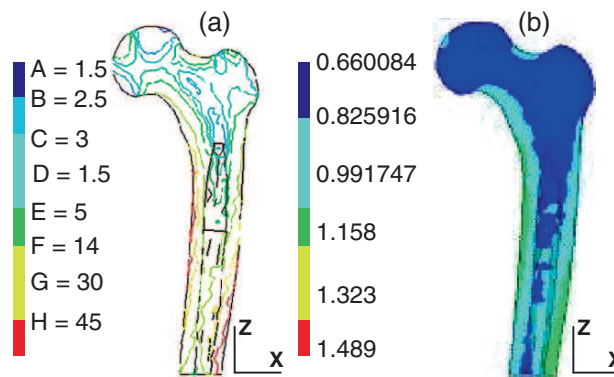

Fig. 2. Cuts of a proximal femur (**a**) isovalues of Von Mises stress (**b**) bone density evolution

The thermodynamic model is also compared to the classical adaptive bone remodeling model developed previously by Huiskes et al. [29] and Weinans et al. [6]. This model uses the strain energy density (SED) as the mechanical stimuli that lunches and controls bone remodeling process. By comparing bone density distributions in the two models (Fig. 4), it can be said that the structure of the femur are comparable. We can notice the clear formation of cortical and cancellous bone in both models. However, difference in the range values of bone density can be observed. This is due, on one hand, to the boundary conditions used in the model. In the classical model, values of starting and end points for the predicted apparent density are constant (i.e., the apparent density varies between 00.1 and 1.74 g/cm^3) while, in the thermodynamic model, these limits are calculated and depend strongly on the model parameters (see Fig. 3a).

On the other hand, it can also be attributed to the fact that the classical model considers only the mechanical loading as the driving force for remodeling process and neglects the effect the chemical reactions which, however, is included in the thermodynamic model.
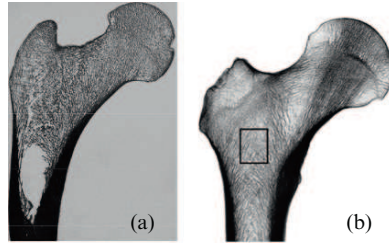
Fig. 3. Frontal longitudinal midsection of the upper adapted from (**a**) grey anatomy atlas [28] and (**b**) X-rays [30]
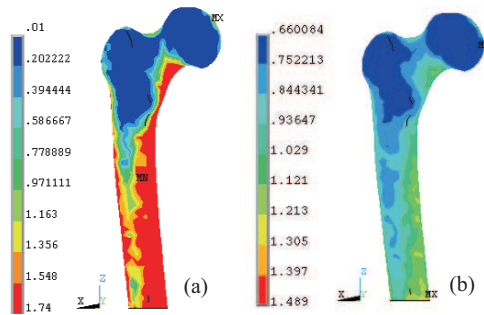

Fig. 4. Predicted bone density in the femur using

3.2. Time evolution of bone density after total hip replacement

As initial state an isotropic homogenous density was used for the whole femoral bone. The impact of bone remodeling in each part of the bone was then calculated at each step. Figures 5 and 6 illustrated the time evolution of bone density under a physiological load using both Ti and biomimetic composite stems.
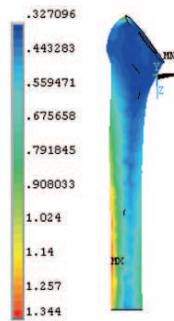

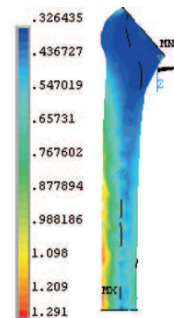**Fig. 5.** Bone density distribution using CF/PA12 stem after 46 iterations

Fig. 6. Bone density distribution using Ti stem after 46 iterations

The time evolution of bone density distributions using Ti stem (Fig. 5) were lower and ranged between 0.32 and 1.29 g/cm^3, with a peak density of 1.29 g/cm^3 than those obtained when the biomimetic composite was used (Fig. 6) (bone density ranged between 0.32 and 1.34 g/cm^3 and a peak density of 1.34 g/cm^3), demonstrating that the biomimetic prosthesis promotes higher remodeling rate and consequently less stress shielding.

3.3. Influence of the locomotion (dynamical loading)

Locomotion or dynamical loading is crucial for proper bone development and remodeling. To illustrate the effect of dynamic loading we varied the parameters Dρ of the model. If no stimulus is present, the bone resorbs (i.e., concentration of both old bone and new bone is decreasing) and after some period of time reaches equilibrium where almost no new bone is being produced (Fig. 7a, blue line).

On the other hand if proper exercise is applied (yet not possible to determine what type of exercise it represents) we may observe a moderate decrease in density at first. This decrease is soon shifted into significant rise where formation predominates resorption. When the activity is increased furthermore (by higher frequency or higher load) the stationary solution may become unreal (negative value of the concentration of the old bone black line in Fig. 7a). According to model, there is a threshold for dynamic loading. Exceeding this threshold leads to breaking of bone.
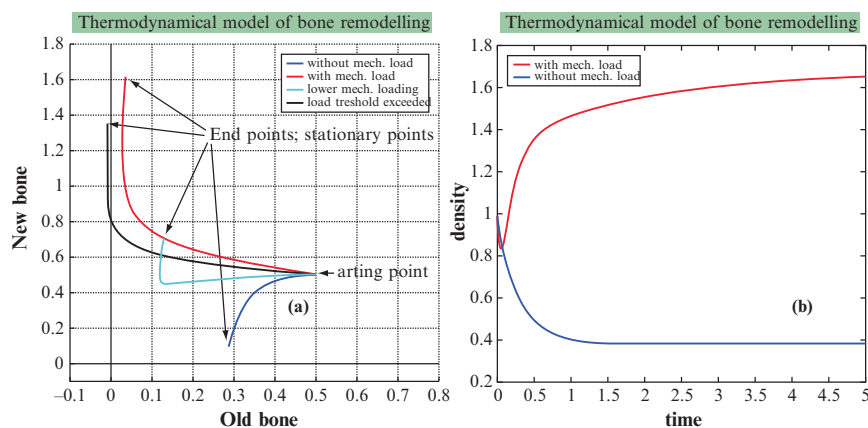

Fig. 7. Influence of locomotion on bone density

4. Conclusions

The thermodynamic bone remodeling model (BRT) proposed combine both – the mechanical stimulus and also the biological background. Using FEM software we were able to calculate the density distribution throughout the whole bone which is great agreement with knowledge of bone anatomy. Using this approach we may simulate different loading cases (exercise, patients) as well as nutrition or other biological features (e.g., the influence of several hormones involved in bone remodeling). These simulations and possible predictions for skeletal diseases are currently being studied.

References

[1] Wolff J. Das Gesetz der Transformation der Knochen, translated as: The law of bone remodeling: Hirschwald, Berlin; 1892.
[2] Cowin SC, Hegedus DH. Bone remodeling I: Theory of adaptive elasticity. J. Elasticity 1976; 6(3):313–326.
[3] Carter D, Hayes WC. The behavior of bone as a two-phase porous structure. J. Bone Joint Surg. 1977; 59A:954–962.
[4] Cowin SC, Hart RT, Balser JR, Kohn DH. Functional adaptation in long bones: establishing in vivo values for surface remodeling rate coefficients. J. Biom. 1985; 18:665–864.
[5] Huiskes R, et al. Adaptive bone-remodeling theory applied to prosthetic-design analysis. J. Biomech. 1987; 20:1135–1150.
[6] Weinans H, Huiskes R, Grootenboer HJ. The behavior of adaptive bone-remodeling simulation models. J. Biomech. 1992; 25:1425–1441.
[7] Prendergast PJ, Taylor D. Prediction of bone adaptation using damage accumulation. J. Biomech. 1994; 27:1067–1076.
[8] Wang X, Dumas GA. Simulation of bone adaptive remodeling using a stochastic process as loading history. J. Biomech. 2002; 35(3):375–380.
[9] Levenston ME, Carter DR. An energy dissipation-based model for damage stimulated bone adaptation. J. Biomech. 1998; 31(7):579–586.
[10] Frost HM. The mechanostat: a proposed pathogenetic mechanism of osteoporoses and the bone mass effects of mechanical and nonmechanical agents. Bone and Min 1987; 2:73–85.
[11] Mullender M, Huiskes R. Proposal for the regulatory mechanism of Wolff's law. J. Orthop. Res. 1995; 13(4):503–512.
[12] Huiskes R, Ruimerman R, van Lenthe GH, Janssen JD. Effects of mechanical forces on maintenance and adaptation of form in trabecular bone. Nature 2000; 405:704–706.
[13] Ruimerman R, Huiskes R, van Lenthe GH, Janssen JD. A Computer-simulation model relating bone-cell metabolism to mechanical adaptation of trabecular architecture. Comp. Meth. Biomech. Biomed. Eng. 2001; 4:433–448.
[14] Taylor D, O'Brien F, Lee TC. A theoretical model for the simulation of microdamage accumulation and repair in compact bone. Meccanica 2002; 37:397–406.
[15] Kroll MH. Parathyroid hormone temporal effects on bone formation and resorption. B. Math. Biol. 2000; 62(1):163–188.
[16] Rattanakul C, Lenbury Y, Krishnamara N, Wollkind DJ. Modeling of bone formation and resorption mediated by parathyroid hormone: response to estrogen/PTH therapy. Biosystems 2003; 70(1):55–72.

[17] Komarova SV, Smith RJ, Dixon SJ, Sims SM, Wahl LM. Mathematical model predicts a critical role for osteoclast autocrine regulation in the control of bone remodeling. Bone 2003; 33(2):206–215.

[18] Lemaire V, Tobin FL, Greller LD, Cho CR, Suva LJ. Modeling the interactions between osteoblast and osteoclast activities in bone remodeling. J. Theor. Biol. 2004; 229(3):293–309.

[19] Lauffenburger DA, Linderman JJ. Receptors: Models for Binding, Trafficking, and Signaling. New York: Oxford University Press; 1996.

[20] Petrtýl M, Danešová J. Principles of bone remodelling – the limit cycles of bone remodelling. Acta Bioeng. Biomech. 2001; 3(1):75–91.

[21] Nicolis G, Prigogine I. Selforganization in Nonequilibrium Systems. Wiley, NewYork; 1977.

[22] Bejan A. Shape and Structure from Engineering to Nature. Cambridge University Press; 2000.

[23] Papini M, Zalzal P. Thirdgen.zip, from the International Society of Biomechanics (ISB) Finite Element Mesh Repository, Istituti Ortopedici Rizzoli. Italy, Available from: http://www.cineca.it/hosted/LTM-IOR/back2net/ISB_mesh/isb_mesh.html.

[24] Bougherara H, Bureau MN, Campbell M, Vadean A, Yahia L’H. Design of a biomimetic polymer-composite hip prosthesis. J. Biomed. Mater. res. 2007; 81A(1):27–40.

[26] Bergmann G, Graichen F, Rohlmann A. Hip joint loading during walking and running, measured in two patients. J. Biomech. 1993; 27(8):969–990.

[27] Terrier A, Rakotomanana RL, Ramaniraka AN, Leyvraz FP. Adaptation model for anisotropic bone. Comput. Method. Biomech. Biomed. Eng. 1997; 1(1):47–59.

[28] Gray H. Anatomy of the Human Body. Available from: http://www.bartleby.com. 1918.

[29] Huiskes R, Weinans H, Grootenboer HJ, Dalsra M, Fudala B, Sloof TJ. Adaptive bone-remodeling theory applied to prosthetic-design analysis. J. Biol. 1987; 20(11 12):135–1150.

[30] Truong L-H, Kuliwaba J, Tsangari H, Fazzalari N. Differential gene expression of bone anabolic factors and trabecular bone architectural changes in the proximal femoral shaft of primary hip osteoarthritis patients. Arthritis Research & Therapy 2006; 8(6):R188.

Hybrid Composite-Metal Hip Resurfacing Implant for Active Patient

Habiba Bougherara[1], Marcello Papini[1], Michael Olsenb[2], Radovan Zdero[2], Paul Zalzal[3] and Emil H. Schemitsch[2, 4]

[1]Department of Mechanical and Industrial Engineering, Ryerson University, Toronto, ON, Canada

[2]Martin Orthopaedic Biomechanics Lab, St. Michael's Hospital, Toronto, ON, Canada

[3]Department of Surgery, McMaster University, Toronto, ON, Canada

[4]Department of Surgery, Faculty of Medicine, University of Toronto, Toronto, ON, Canada

Abstract Hip resurfacing technique is a conservative arthroplasty used in the young patient in which the femoral head is reshaped to accept metal cap with small guide stem. In the present investigation, a hybrid composite-metal resurfacing implant is proposed. The cup is made of carbon fibre/polyamide 12 (CF/PA12) covered with a thin layer of (Co-Cr). Finite element (FE) method was applied to analyze and compare the biomechanical performances of both composite and Co-Cr implants. Results of the finite element analysis showed that the composite implant leads to stresses in the cancellous bone16% higher than Co-Cr, indicating a lower potential for stress shielding and higher potential for bone apposition with the hybrid resurfacing implant.

1. Introduction

The successful reintroduction of the improved Metal-On-Metal (MOM) bearings has led to a resurgence of interest for hip resurfacing procedure as a viable alternative to conventional arthroplasty for younger, active patients [1, 2]. The reported benefits of hip resurfacing (HR) include reduced dislocation rate and increased function compared to total hip arthroplasty (THA) [3–5]. Other advantages of HR compared with THA include minimal bone resection, easier revision, and reduction in the stress shielding in the proximal femur [2]. Femoral neck fracture and stress shielding remain a concern with resurfacing hip prostheses [6, 7]. Most implants for hip joint replacements including resurfacing implants are manufactured from stiff materials (i.e., stainless steel, Co-Cr etc.). These materials undergo stress shielding that may lead to implant failure, including implant loosening and femoral neck fracture [8]. A new hybrid composite-Co-Cr resurfacing implant is proposed to prevent stress shielding and bone fracture.

The aim of this article is thus to present the concept design for the hybrid resurfacing implant and secondly, to compare its performance with conventional hip resurfacing (Fig. 1).

Fig. 1. Birmingham Metal-on-Metal hip resurfacing implant

2. Material and methods

2.1. 3D geometries and concept design

Computerized tomography (CT) scan sections were performed every 0.5 mm along the length of the composite femur (Sawbones 3rd generation composite bone models) and used to generate the 3-D solid model of the proximal femur [9] (Fig. 2a). The original density and the elastic modulus of the simulated cortical (short fibre filled epoxy) and cancellous (rigid polyurethane foam) based on CT scan and ASTM D-638, D-695, D-1621 tests were equal to 1.64 g/cm^3, 16.7 (GPa) and 0.32 g/cm^3, 137 (MPa).

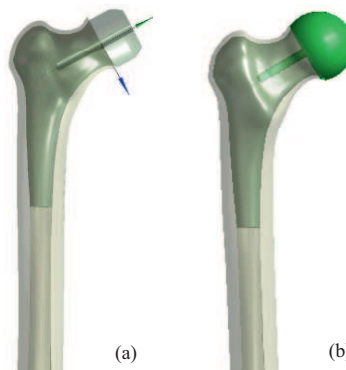(a)   (b)

Fig. 2. 3D geometry of the femur: (**a**) reamed bone and (**b**) bone with hybrid HR implant

The concept and geometry of the hybrid resurfacing component are shown in Fig. 3. The femoral cup with a diameter of 46 mm (Birmingham) is composed of

2 mm-thick shell structure made of several layers of a continuous Carbon Fibre/ Polyamide 12 (CF/PA12) composite fabric, onto which a 1 mm layer of Co-Cr is overlaid in order to avoid wear debris formation. The guide stem is composed of the same material as the cup (i.e. CF/PA12-Co-Cr).
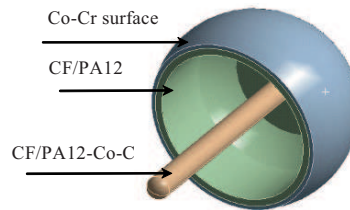

Co-Cr surface
CF/PA12
CF/PA12-Co-C

Fig. 3. Concept design of the hybrid composite-metal HR implant

2.2. Details of the FE models and loading conditions

3D FE-Models of a composite femur were meshed and analyzed using ANSYS 11.0 software. The femoral head was reamed and embedded with two types of hip resurfacing implants. The first was a model of the femoral bone in which the implanted stem was made of a Cr-Co-base alloy (E = 200 GPa, ν = 0.3) (Fig. 4), while the second was the hybrid composite (CF/PA12) – metal (Co-Cr) stem. The properties of the composite are shown in Table 1.

Table 1. Mechanical properties of the composite prosthesis

Material	Modulus of elasticity (MPa)	Shear modulus (MPa)	Poisson's ratio
CF/PA12 composit (±45°)	$E_x = 15{,}400$	$G_{xy} = 3{,}000$	$\nu_{xy} = 0.3$
	$E_y = 15{,}400$	$G_{xz} = 3{,}500$	$\nu_{xz} = 0.25$
	$E_z = 3{,}500$	$G_{yz} = 3{,}200$	$\nu_{yz} = 0.2$

Bonded conditions were assumed at bone-femoral head component interface, while bone-femoral stem interface was left unbonded (frictionless contact was used) (Fig. 4). For each FE model, the load corresponded to 8 running and consisted of a 3704 kN load applied to the femoral head and a 1085 kN great trochanter muscles load [10].

The loads were distributed over several nodes to avoid stress concentration, and for all FE analyses, the displacement of all nodes at the distal end of the femoral bone was rigidly constrained (Fig. 5).
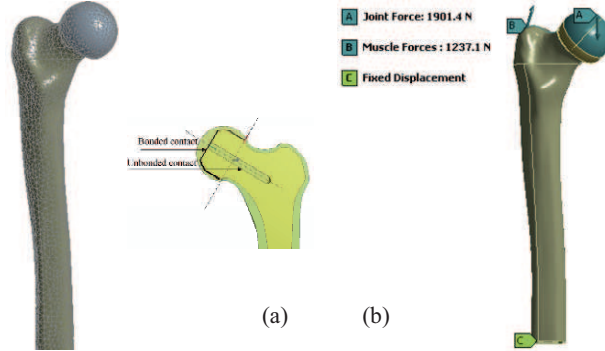
Fig. 4. (**a**) Finite element model and types of contact used, (**b**) Load conditions

3. Results

3.1. Stresses in the trabecular bone

The Von Mises stresses in the trabecular bone with the Cr-Co and CF/ PA12 resurfacing implants are shown in Fig. 6. The stress inside the trabecular bone was higher for the conventional Co-Cr resurfacing implant (Von Mises stress of between 0 and 4.7 MPa, than the one using the hybrid CF/PA12-Co-Cr, Von Mises stress level ranged between 0 and 4.1 MPa). The highest stress patterns were noted in the posteroinferior region near the rim of the implant. Peak stresses were 6.13 MPa for the Co-Cr prosthesis and 5.26 MPa for the hybrid HR.
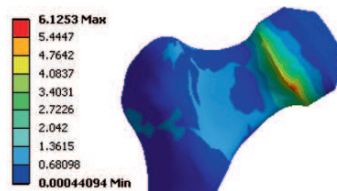

Fig. 5. Von Mises stress in the cancellous bone using the metallic HR implant
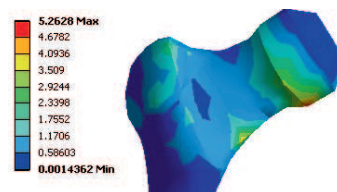

Fig. 6. Von Mises stress in the trabecular bone using the hybrid composite HR implant

3.2. Stresses in the implant

The values of stresses in the conventional Co-Cr implant were ranged between 0 and 77 compared to 0 and 68 MPa when the hybrid implant is used. The peak stress in the conventional implant was higher (173.2 MPa) than that found in the hybrid implant (152.9) (Figs. 7a and 7b).
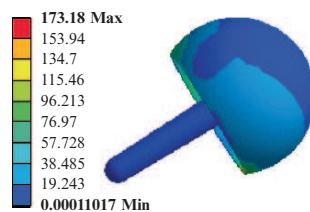

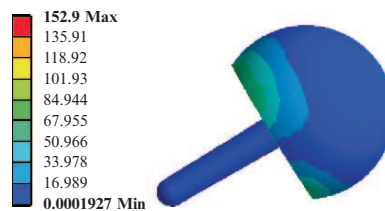**Fig. 7a.** Von Mises stress in the metallic Co-Cr implant

Fig. 7b. Von Mises stress in the trabecular bone using the hybrid composite-Co-Cr HR implant

4. Discussion

The new concept design for hip resurfacing using a hybrid composite-metal was described. Finite element analysis has been performed to evaluate and analyse the potential of the proposed design concept.

In the case of the hybrid implant, numerical results have shown that the von Mises stresses were more uniform and higher by more than 15% in the cancellous bone. This indicates the potential of the hybrid composite implant to reduce stress shielding, especially in the great trochanter region. Also higher peak stress in the cancellous bone was found when the Co-Cr is used, which may lead to one fracture. Again the use of the hybrid implant reduced considerably the peak bone stress in the cancellous bone and thus prevent from bone fracture.

Results of simulation indicate also that the hybrid implant reduced the stress in the femoral cup by approximately 10–20%. Therefore more loads are transferred to the bone with the hybrid composite-Co-Cr resurfacing implant than the conventional ones.

5. Conclusions

The outcome of this study shows that the hybrid composite-metal hip resurfacing has the potential to reduce stress shielding, preserve bone stock and prevent from bone fracture compared to conventional metallic hip resurfacing implants.

References

[1] Back DR, Young D, Shimmin A. Early results of primary Birmingham hip resurfacings. An independent prospective study of the first 230 hips. J. Bone Joint Surg. 2005;87(B):324–329.

[2] Daniel J, Pynsent, PB, McMinn, D. Metal-on-metal resurfacing of the hip in patients under the age of 55 years with osteoarthritis. J. Bone Joint Surg. 2004;86(B):177–188.

[3] Adams D, Quigley S. Hip resurfacing: Past, present and future. J. Orthop. Nur. 2005;9(2):87–94.

[4] Beaule PE, Le Duff M, Campbell P, Dorey FJ, Park SH, Amstutz HC. Metal-on-metal surface arthroplasty with a cemented femoral component: A 7-10 year follow-up study. J. Arthroplasty 2004;19(8, Supplement 1):17–22.

[5] Ebied A, Journeaux S. (iv) Metal-on-metal hip resurfacing. Curr. Orthopaed. 2002;16(6):420–425.

[6] Ramakrishnan R, Jaffe WL, R. Kennedy W. Metal-on-metal hip resurfacing: radiographic evaluation techniques. J. Arthroplasty 2008;23(8):1099–1104.

[7] Hayaishi Y, Miki H, Nishii T, Hananouchi T, Yoshikawa H, Sugano N. Proximal femoral bone mineral density after resurfacing total hip arthroplasty and after standard stem-type cementless total hip arthroplasty, both having similar neck preservation and the same articulation type. J. Arthroplasty 2007;22(8):1208–1213.

[8] Pearson AM, Foguet P, Little C, Murray D, McLardy-Smith P, Krikler S. Can we prevent fractures in hip resrfacing? J. Bone Joint. Surg. Br. 2005;87-B(SUPP_I):41.

[9] Papini M, Zalzal P, Thirdgen.zip, from the International Society of Biomechanics (ISB) Finite Element Mesh Repository, Istituti Ortopedici Rizzoli. Available from: http://www.cineca.it/hosted/LTM-IOR/back2net/ISB_mesh/isb_mesh.html.

[10] Bergmann G, Graichen F, Rohlmann A. Hip joint loading during walking and running, measured in two patients. J. Biomech. 1993;27(8):969–990.

Anisotropic and Unilateral Damage Application to Concrete

O. Bélaidi Chabane Chaouche[1], N.E. Hannachi[1] and Y. Labadi[2]

[1]Laboratoire lamons, Faculté du Génie de la Construction, Université Mouloud Mammeri, BP 17 RP, Route de Hasnaoua, Tizi Ouzou, Algérie

[2]CFAI de l'Aube, 12 rue Québec, 10430 Rosières-Près-Troyes, France

Abstract   The effect of the nucleation and growth of microvoids and/or microcracks (damage) on the overall response behavior of a wide class of materials is now clearly understood. The damage of materials occurs when atomic bonds break at the microstructural level. These microscopic alterations react upon the macroscopic thermomechanical materials properties, elastic softening, decreased conductictivity, plastic yield surface alteration, etc. For concrete, the experimental behavior analysis (concrete is assumed initially isotropic) let us say the principal following phenomena:

- A loss of stiffness beyond a certain stress point due to damage which is strongly anisotropic due the directionality of the defects (induced anisotropy)
- A permanent or irreversible strains with the loss of material stiffness (which are due to growth of damage)
- A stiffness recovery with the change from the damaging loading in traction to a compression loading called "unilateral bahavior" (the damage can be active or inactive, when the microcracks are respectively open or closed)
- A dissymetric behavior between traction and compression and a softening behavior during traction and compression.

In many engineering situations, concrete can be considered as an elastic material susceptible of damage. Continuum Damage Mechanics (CDM) is intended to interpret and describe the phenomena connected with the deterioration of materials before the macroscopic rupture. However, the behaviour of this material is of most complexes and its modelling can generate numerous variables. In this survey we present a local simple model of anisotropic damage, to traduce phenomena of deterioration of the concrete. We endeavored to describe the damage by one alone variable, making call that restricts intrinsic parameters of the material easily accessible by the experimentation. The final objective being to drive calculations of structures, the implantation being returned of this comfortable fact.

Keywords: Elasticity, Damage, Non Linear Behaviour, Concrete, Numerical Aspects.

1. Introduction

It is well known that the deformation of most engineering materials is often accompanied by irreversible changes in their internal structures. The nucleation and the growth of distributed microscopic cavities and cracks do not only induce

the occurrence of macro-cracks, but also lead to the deterioration of material properties due to internal microstructural changes. Therefore, understanding and knowledge of the damaging process and its effects on the macroscopic behaviour of materials are very important prerequisites for accurate analysis of structural integrity of practical problems. An approach to these problems can be provided by the recently developed theory of continuum damage mechanics (CDM), which involves irreversible micro structural changes implicitly. Several CDM models have been proposed for brittle materials. For example, the Chow and Yang model 1991 [1], is based on the hypothesis of damage surface that is similar to the yield function in plasticity theory and uses one scalar valued internal variable to represent the damage state. The Chaboche model [2] assumes anisotropic damage basically and introduces tensorial damage variables. Therefore, it can be considered that there exists a relationship between small cracks (damage) and strain direction. However, a detailed method to apply this model to anisotropic damage in any direction is still under development. Moreover CDM theories, which incorporate vectors [3], scalars [4], second-order tensors [5, 6, 19, 20], and fourth-order tensors [7] have been proposed. But these theories show either a discontinuous stress–strain response when the unilateral condition takes place or an unacceptable non-symmetric elastic behaviour for some loading conditions [21]. In this paper, we attempt to describe the non-linear elastic constitutive equation using CDM and evaluate the structural integrity of brittle material components by the damage parameter introduced in this type of theory.

Strength and stiffness degradation can be effectively modelled in the framework of CDM: isotropic damage models with a single damage variable [8] or a tension damage variable and a compression damage variable [3, 9], anisotropic damage models [6, 10, 11], to cite a few. The aim of the paper is to propose a thermodynamically consistent model, which accounts for some anisotropy induced by damage, and which includes unilateral effects related to crack closure. Attention is paid to limiting the complexity of the model, and especially the number of parameters, in order to make the model a viable candidate for practical engineering computations.

2. The damage model

2.1. Generality

Introduced in 1958 by Kachanov [12] for creep failure of materials under uniaxial loads, and proposed a creep damage evolution model. Later Rabotnov (1969) [13] improved Kachanov's creep model by introducing an extra coefficient to show that the damage rate is influenced more strongly by the degree of damage than by the global mechanical behavior. Continuum damage mechanics has been applied in the 1980 for simulating the non linear behaviour of concrete [8, 14, 15].

Thermodynamics of irreversible processes gave the framework to formulate the adapted constitutive laws (e.g., [16]). Considering the material as a system described by a set of variables and a thermodynamic potential, constitutive laws are systematically derived along with conditions on the kinematics of damage. However, an adequate choice of the potential and of the damage variable (scalar, tensor, etc.) remains to be made. Several anisotropic damage models have already been proposed by Dragon and Mroz [17] and Mazars and Pijaudier-Cabot [18]. Possible applications cover also dynamic problems [11, 12], porous materials [22] and chemical damage [23]. A recent literature review on damage mechanics can be found in ref. [24].

2.2. Elasticity modelling

The model is formulated within a strain space framework. In order to make the subsequent implementation in finite element code easier, Helmotz's strain based free energy has been chosen. The Cauchy strain tensor, $\underline{\varepsilon}$, will be split into a volumetric part, ε_v, and a deviator part $\underline{e}$, so that:

$$\underline{\varepsilon} = \varepsilon_v.\underline{1} + \underline{e} \tag{1}$$

The stress-strain relation:

$$\underline{\sigma} = 2G.\underline{e} + K.Tr[\underline{\varepsilon}]\underline{1} \tag{2}$$

where K and G, are the bulk and shear modulus of the undamaged material.

2.3. Elasticity coupled with anisotropic damage

To traduce the damage, two independent variables are chosen:

- A scalar variable δ representing the volumetric damage of material, i.e., the reduction, in effective volume of a damaged unit element volume compared with a virgin one. The material behaviour is due to the effect of a strong hydrostatic pressure applied to the micro porous structure of the concrete.
- A second order symmetric damage tensor $\underline{D}$. This tensor is meant to be representative of 'surface damage', i.e., the reduction in effective area of surface elements with different orientations from the undamaged to the damaged state.

The damage and the inelastic strains evolve simultaneously. These micro voids are the cause of the inelastic strains. The thermodynamic forces associated to $\underline{e}$, $\underline{D}$ and δ have as expressions:

$$\underline{\sigma} = 2G.Tr\left[(1-\underline{D})^{1/2}.\underline{e}(1-\underline{D})^{1/2}\right] + K.(1-\delta)Tr[\underline{\varepsilon}]\underline{1} + \frac{1}{2}\left(2G\beta(\underline{D}\cdot\underline{D}) + \gamma K\delta^2\underline{1}\right) \qquad (3)$$

$$\underline{Y}_D = G\underline{e}.\underline{e} - 2\beta G\left[\underline{D}\cdot\underline{e} + \underline{e}\cdot\underline{D}\right] \qquad (4)$$

$$Y_\delta = \frac{1}{2}KTr^2[\underline{\varepsilon}] - \gamma K\delta Tr[\underline{\varepsilon}] \qquad (5)$$

From Relation [3] one deduces the inelastic stress which is written:

$$\underline{\sigma}_{an} = \frac{1}{2}\left(2\beta G(\underline{D}\cdot\underline{D}) + \gamma K\delta^2\underline{1}\right) \qquad (6)$$

We can observe that the total stress is divided into two parts:

- An isotropic contribution, relating to the volumetric damage variable δ : $\gamma K\delta^2\underline{1}$
- An anisotropic contribution, relating to the surface damage variable $\underline{D}$: $2\beta G(\underline{D}\cdot\underline{D})$

2.4. Unilateral damage modelling

This unilateral damage effect usually leads to complex models when damage anisotropy is considered, One writes.

$$\underline{e} = \underline{e}^t + \underline{e}^c \qquad (7)$$

In the same way one postulates the existence of two independent internal variables, $\underline{D}^t$ and $\underline{D}^c$ for traction and compression respectively. Allowing for unilaterality, the following expression is proposed for the Helmotz's the stress-strain relationship of the material:

$$\underline{\sigma} = 2G.Tr\left[(\underline{1}-\underline{D}^t)^{1/2}\cdot\underline{e}^t\cdot(\underline{1}-\underline{D}^t)^{1/2}\right]+$$
$$G.Tr\left[(\underline{1}-\underline{D}^c)^{1/2}\cdot\underline{e}^c\cdot(\underline{1}-\underline{D}^c)^{1/2}\right]+K(1-\delta)Tr[\underline{\varepsilon}]\cdot\underline{1} \qquad (8)$$

Derivation of equation with respect to the damage variables yields the damage driving forces conjugate to and:

$$\underline{Y}_D^t = -\frac{\partial(\rho\psi)}{\partial\underline{D}^t} = G.\underline{e}^t.\underline{e}^t \qquad (9a)$$

$$\underline{Y}_D^c = -\frac{\partial(\rho\psi)}{\partial\underline{D}^c} = G.\underline{e}^c.\underline{e}^c \qquad (9b)$$

$$Y_\delta = -\frac{\partial(\rho\psi)}{\partial\delta} = \frac{1}{2}K.Tr^2[\varepsilon] \qquad (9c)$$

3. Damage evolution laws

3.1. Evolution law of tensile damage

In each principal direction i, the level of damage is governed by positive strains the formulation of the behaviour law one writes the law of damage in explicit form:

$$D_i^t = 1 - \left[\left(\frac{e_{D0}}{e_i^t}\right)\exp\left[-b(e_i^t - e_{D0})\right]\right] \qquad (10)$$

b is a material parameter driving the slope of the softening branch.

3.2. Evolution law of compressive damage

Compressive damage in a particular direction is considered only as a consequence of the tensile behaviour of the material and, is taken equal to a function of the state of tensile along the orthogonal directions [25], i.e., the increase in cracking in

compression is induced by the transverse and positive extensions [26]. One uses a law power of the form:

$$D_i^c = \left(\frac{D_j^t + D_k^t}{2} \right)^\alpha \tag{11}$$

α is a material parameter.

3.3. Evolution law of volumic damage

This variable of damage can be interpreted like a macroscopic effect of volumetric damage. To define the evolution of the damage variable, one poses a relation between the absolute value of the trace of the strain and δ.

$$\delta = 1 - \left[\left(\frac{\varepsilon_{D0}}{\langle Tr[\varepsilon] \rangle} \right) \exp\left[-b(\langle Tr[\varepsilon] \rangle - \varepsilon_{D0}) \right] \right] \tag{12}$$

4. Numerical results

To examine the utility of the constitutive and damage evolution equations formulated in the preceding section, the process of elastic and brittle fracture of concrete will be analysed. The capabilities of the proposed model in reproducing the mechanical response of material elements subjected to different stress histories in the nonlinear field are illustrated in next sections.

4.1. Uniaxial tension test

The analysis is performed at the material level. We present here, the response of concrete representative volume element (RVE) submitted to a uniaxial tension under controlled displacement.

The calculation is carried out under the hypothesis of two dimensional plane strains. The material parameters used for the analysis are: (The data of the tested specimen are the following): E = 20,000 MPa, $\nu = 0.2$, $f_t = 2.5$ MPa, $f_c = 25$ MPa, $G_f = 0.05$ Nmm/mm^2, $\varepsilon_{Do} = 0.0001$, Hypothetical values of: $\beta = 8.10^{-4}$, $\gamma = -3 .10^{-4}$.

The numerical results obtained from the simulation of the uniaxial tensile test are reported below. The response in tension is represented on the Fig. 1. The model returns the principal characteristics of the material:

- A loss of stiffness beyond a certain stress point due to damage which is strongly anisotropic due the directionality of the defects (induced anisotropy)
- A permanent or irreversible strains with the loss of material stiffness (which are due to growth of damage)
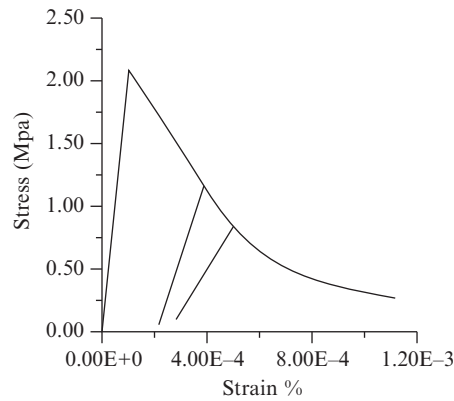

Fig. 1. Tension test

4.2. Response of the model under compressive loadings

A unit volume of material is loaded in uniaxial compression under controlled displacement. The analysis is performed at the material level. The material parameters used for the analysis are: E = 20,000 MPa, ν = 0.2 f_t = 2.5 MPa, f_c = 25 MPa, G_f = 0.05 Nmm/mm^2, ε_{Do} = 0.0001.
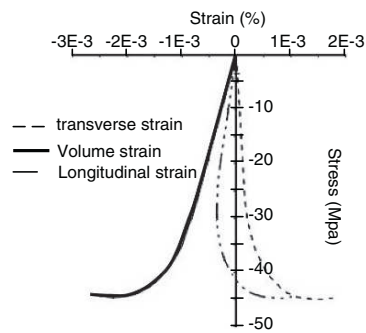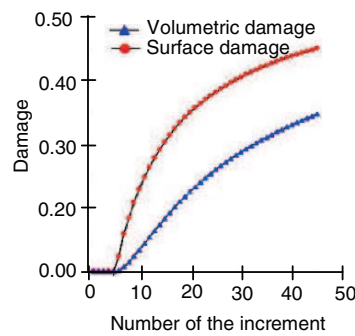

Fig. 2. Compression test

Fig. 3. Surface and volumetric damage evolution

In Fig. 1 the stress–strain plot in uniaxial compression is shown. The asymmetric behaviour in compression typical of brittle materials is correctly described. The response of the model in terms of stress versus the longitudinal and transverse strain is represented on the Figs. 2 and 3. One can observe that the model is able to describe the volumetric response of the material satisfactorily.

4.3. Response of an RVE under cyclic loading

For instance, Fig. 4 shows the numerical simulation of a uniaxial tension followed by compression on one element.

The dissymmetric behavior between traction and compression and a softening behavior during traction and compression is captured by the model. A Fig. 4 show that the unilateral condition applied to the anisotropic damage model preserve the continuity of the response and gives a stiffness recovery with the change from the damaging loading in traction to a compression loading.
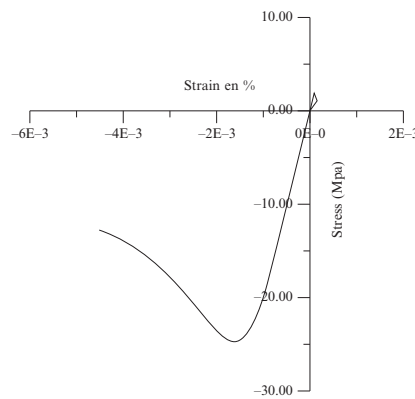

Fig. 4. Unilateral effect

5. Conclusions

A new anisotropic damage model is proposed for brittle materials such as concrete. The model is formulated in the framework of the continuum damage mechanics. A second-rank symmetric tensor is used to characterize material surface damage due to oriented microcracks; the volumic damage is characterized by a scalar damage variable. This anisotropic model is combined with a unilateral condition in order to take into account the crack closure phenomenon and elastic moduli recovery. The validity of the model is tested through numerical predictions in various loading conditions.

The overall performance of the model is evaluated. The proposed damage model is capable of capturing several aspects of the nonlinear behaviour of brittle solids, namely, the damage-induced anisotropy, the unsymmetric behaviour in tension and compression, the 'unilateral' behaviour of the material (i.e., stiffness recovery upon crack closure) and the development of irreversible strain. Extensions are still required to incorporate in the model important phenomena, such as the hysteresis loops at fixed level of damage during cyclic loadings, which were neglected in the present version.

References

[1] Chow CL, Yang F (1991). On one-parameter description of damage state for brittle material. Eng. Fract. Mech., Vol 40, no. 2, pp. 335–343.

[2] Chaboche JL, Lesne PM, Maire JF (1995). Continuum damage mechanics, anisotropy and damage deactivation for brittle materials like concrete and ceramic composites. Int. J. Damage Mech., Vol 4, no. 1, pp. 5–22.

[3] Krajcinovic D, Fonseka GU (1981). The continuous damage theory of brittle materials, parts II and I. J. Appl. Mech. ASME, Vol 48, pp. 809–882.

[4] Ladeveze P, Lemaitre J (1984). Damage effective stress in quasi-unilateral material conditions, IUTAM Congress, Lyngby, Denmark.

[5] Cordebois C, Sidoroff F (1979). Endommagement anisotrope en élasticité et plasticité, Journal de Mécanique appliquée, Vol 25, pp. 45–60.

[6] Ramtani S (1990). Contribution à la modélisation du comportement multiaxial du béton endommagé avec description de l'effet unilatéral", thèse de doctorat de l'université Paris VI, France.

[7] Ju LW (1989). On energy-based coupled elastoplastic damage theories: constitutive modelling and computational aspects, Int. J. Solids Struct., Vol 25, no. 7, pp. 803–833.

[8] Lemaitre J, Mazars J (1982). Application de la théorie de l'endommagement au comportement non linéaire et à la rupture du béton de structures, Annales de l'ITBTP, Vol 401.

[9] Comi C (2001). A non local model with tension and compression damage mechanisms. Eur. J. Mech. A-Solid., Vol 20, pp. 1–22.

[10] Ghrib F, Tinawi R (1995). Non linear behaviour of concrete dams using damage mechanics. J. Eng. Mech., Vol 121, no. 4, pp. 513–527.

[11] Ragueneau F, La Borderie Ch, Mazars J (2000). Damage model for concrete like materials coupling cracking and friction, contribution towards structural damping: first uniaxial application. Mechanics cohesive frictional materials, Vol 5, pp. 607–625.

[12] La Borderie Ch (1991). Phénomènes unilatéraux dans un matériau endommageable: modélisation et application à l'analyse des structures en béton", thèse de doctorat, Université Paris 6.

[13] Rabotnov YN (1968). Creep rupture. Proc. XII Int. Appl; Mech. Conference, ed by M Htenyi and H Vicinti, Stanford University, pp. 342–349.

[14] Krajcinovic D (1983). Constitutive equations for damaging material. J. Appl. Mech. ASME, Vol 50, pp. 355–360.

[15] Ladevèze P (1983). Sur une théorie de l'endommagement anisotrope. Int. Report No. 34, Laboratoire de Mécanique et Technologie, Cachan, France.

[16] Lemaitre J, Chaboche JL (1985). Mécanique des matériaux solides, ed Dunod-Bordas, Paris, France.

[17] Dragon A, Mroz Z (1979). A continuum model for plastic-brittle behaviour of rock and concrete. Int. J. Eng. Sci., Vol 17, pp. 121–137.

[18] Mazars J, Pijaudier-Cabot G (1989). Continuum damage theory: application to concrete. J. Engrg. Mech., ASCE, Vol 115, no. 2, pp. 114–122.

[19] Mazars J, Berthaud Y, Ramtani S (1990).The unilateral behaviour of damaged concrete. Engineering Fracture Mechanics, Vol 35, Issues 4-5, pp. 629–635.

[20] Mazars J, Berthaud Y, S Ramtani S (1990). The unilateral behaviour of damaged concrete. Eng. Fract. Mech., Vol 35, Issues 1–3, pp. 607.

[21] Chaboche JL (1992). A new unilateral condition for the description of the behavior of materials with anisotropic damage. Académie des Sciences (Paris), Comptes Rendus, Série II - Mécanique, Physique, Chimie, Sciences de la Terre et de l'Univers (ISSN 0764-4450), Vol 314, no. 13, June 18, 1992, pp. 1395–1401.

[22] Pijaudier-Cabot G, Burlion N (1996). Damage and localisation in elastic materials with voids, Int. J. Mech. of Cohes.-Frict. Mat., Vol 1, pp. 129–144.

[23] Gérard B, Pijaudier-Cabot G, La Borderie C (1998). Coupled diffusion-damage modelling and the implications on failure due to strain localisation, Int. J. Solids & Structures, Vol 35, pp. 4107–4120.

[24] Burlion N, Gatuingt F, Pijaudier-Cabot G, Daudeville L (2000). Compaction and tensile damage in concrete: constitutive modelling and application to dynamics. LMT-Cachan, ENS Cachan/CNRS/Université P. et M. Curie Comput. Methods Appl. Mech. Engrg. 183, 291–308

[25] Fichant S, Pijaudier-Cabot G, Laborderie C (1997). Continuum damage modelling: Approximation of crack induced anisotropy. Mechanics Research Communications, 24(2): 109–114.

[26] Mazars J (1984) Application de la mécanique de l'endommagement au comportement non linéaire et à la rupture du béton de structure, Thèse de Doctorat ès Sciences, Université Paris 6, France.

The Behaviour of Self-Compacting Concrete Subjected to an External Sulphate Attack

Riçal Khelifa[1, 2], Xavier Brunetaud[1], Hocine Chabil[2] and Muzahim Al-Mukhtar[1]

[1]Centre of Research on Divided Matter, University of Orléans, CNRS-CRMD, 1 b, rue de la Férollerie, 45071 Orléans Cedex 2, France

[2]Civil Engineering Department, University Mentouri of Constantine, Route de Ain El-Bey 25000 Constantine, Algeria

Abstract   The research presented in this communication relates to the effect of external sulphate attack on self-compacting concretes. In this aim, four types of self-compacting concretes were made out of Algerian cements, aggregates and adjuvants. Each concrete has been subjected to three external sulphate attack protocols: total immersion, immersion-drying at 105°C and immersion-drying at 60°C. Although all behaviours are not fully stabilized, it is already possible to identify the main conclusions. Two different behaviours of our concretes were distinguished: some concrete samples were damaged by the external sulphate attack whereas other concretes samples were damaged by the salts precipitation.

1. Introduction

Many current structures are characterized by the complexity of their architecture (variable shapes and multiple bends) and a high concentration of reinforcements, which often makes it difficult to use concrete with conventional plasticity. Recent researches have been conducted in order to adapt concrete to these structures [1, 2]. The resulting concrete formulations are characterized by better workability, while remaining stable with good mechanical properties and durability. These new types of concrete can fit in place under the influence of gravity (without any vibration), hence the term Self-Compacting Concrete "SCC". Some regions of the world have very few rivers, thus considerably reducing the availability of alluvial aggregates (rolled), which are commonly used to produce a good self-compacting concrete "SCC". However, in these regions there are plenty of quarries that can produce crushed limestone aggregates. The aim of our study is to demonstrate the feasibility of using crushed aggregates in the manufacture of a stable and durable self-compacting concrete. Research carried out here aims at proposing formulas for durable SCC with respect to an external sulphate attack, by simulating a soil or air pollution.

In fact, the external sulphate attack occurs only if sufficient amounts of sulphate are supplied in liquid or gas form. Sulphates can react with some concrete hydrated phases (including portlandite and calcium monosulfoaluminate) to produce gypsum or secondary ettringite. The precipitation of large amounts of these new hydrated phases can lead to the swelling of concrete and its cracking. The obtained results led to select the most durable concrete with respect to an external sulphate attack and to propose reliable acceleration protocols.

Finally, the selected type of concrete formulation, may represents a strong interest for the development of the building industry.

2. Experimental programs

Four types of self compacting concrete satisfying all tests on fresh state have been prepared with Algerian aggregates and admixtures (adjuvants). They are based on two types of cement and two different Water/Cement (W/C) ratios (see Table 1). The different types of concrete are almost similar in terms of slump, yield stress and spread. Concrete samples (11×22 cm cylinders) and mortar samples ($4 \times 4 \times 16$ cm prisms) were made. After being immersed in water for a maturation period of 28 days, the 11×22 cm cylinders underwent a core sampling to produce smaller cylinders (4×8 cm). Three protocols of sulphate attack were applied:

- Total immersion in a solution of Na_2SO_4, $10H_2O$
- Cycles of drying at 105°C-immersion in a solution of Na_2SO_4, $10H_2O$
- Cycles of drying at 60°C-immersion in a solution of Na_2SO_4, $10H_2O$

Table 1. Composition of different types of self-compacting concrete (SCC)

SCC	CEMII/59	CEMI/59	CEMII/49	CEMI/49
Cement (42,5)	CEM II/A	CEM I	CEM II/A	CEM I
Water/Cement	0.590	0.590	0.490	0.490
super plasticizer	1.4% C	1.1% C	2.0% C	1.6% C
Colloidal agent	0.05% C	0.05% C	–	–

2.1. Total immersion

The immersion of the concrete and mortar specimens in water with 5% of Na_2SO_4, $10H_2O$ as specified in literature [3], is renewed every 30 days. Each week, all samples are weighed and the speed of sound through the samples is measured. In addition, the expansion of mortar specimens is measured, since only those specimens are equipped with expansion plots. This protocol is the most common in the bibliography; it simulates the typical case of a sulphate attack on the concrete through soil pollution such as gypsum soil [4, 5].

2.2. Cycles of immersion-drying at 105°C

This protocol was chosen to accelerate the ageing of concrete caused by the total immersion; it is based on 24-h cycles of immersion/drying. The specimens are immersed in water with 5% of Na_2SO_4, $10H_2O$ during 4 h until saturation and then dried in an oven at 105°C for 20 h. This protocol is based on standardized ageing test of stones under the effect of salts precipitation [6].

2.3. Cycles of immersion-drying at 60°C

This protocol is identical to the previous one except that samples are dried at 60°C instead of 105°C. The idea is to accelerate the effect of total immersion, without making the test as severe as drying at 105°C. The choice of a 5% concentration of Na_2SO_4, $10H_2O$ is based on the bibliography [5, 7]. Concerning the chosen temperatures:

- The first one, 105°C, was selected to maximize the effect of immersion-drying cycles and thus obtaining the fastest ageing process. The only drawback is the risk of an internal sulphate attack, hence the choice of a second lower temperature.
- The second one, 60°C, was selected because the combination of both internal and external sulphate attacks is impossible. The delayed formation of the ettringite has never been diagnosed below 65°C [8].

3. Experimental results

Only mortar specimens were equipped with plots to measure any expansion and no mortar samples were affected by an external sulphate attack. Cases of damage diagnosed on mortar samples were due to salts precipitation and not to a chemical interaction between sulphates and cement hydrates. This kind of damage does not generate any significant swelling.

The small cylinders of concrete that were affected by a significant external sulphate attack were not equipped with expansion plots. However, it was possible to measure a local variation of the sample diameter of about 10% for concrete CEMII/59 that was subjected to a complete immersion and cycles of immersion-drying at 60°C.

The dynamic modulus G (in N/m²) is related to the speed of sound V (in m/s) by the following relation: $G = \rho \cdot V^2$, where ρ is the density (in kg/m s²). This dynamic modulus characterizes the rigidity of the cement material and thus estimates the damage induced in it.

3.1. Total immersion

The 11×22 cm concrete cylinders and mortar samples behaved rather well in general, and the changes in the dynamic modulus were insignificant. Regarding small cylinders, the self-compacting concrete CEMII/59 was considerably affected compared to the other three types. The mass increase associated with a localized swelling (Fig. 3) along with a very important decrease in the dynamic modulus due to cracking of the sample (Figs. 1 and 2) proved that these specimens were affected by an external sulphate attack [9].

3.2. Cycles of immersion-drying at 60°C

Small cylinders of concrete CEMII/59 exposed to cycles of immersion-drying at 60°C were affected by an external sulphate attack. In fact, in this case too, we noticed a simultaneous increase in mass with a swelling of the sample and a decrease in the dynamic modulus (Figs. 4, 5 and 6). So far, no macroscopic signs of damage have been observed on the mortar specimens.

3.3. Cycles of immersion-drying at 105°C

All samples of CEMII/59 – small cylinders and mortar – were partially damaged at the surface, generating a loss of matter around the edges (Figs. 7 and 8). The dynamic modulus, which reflects the state of damage of the sample's core, showed no variation. Moreover, there was no mass increase associated with the opening of deep cracks.

In fact, it was a phenomenon that affected only a few millimetres at the surface of the samples. This corresponds to the symptoms of degradation of stones by the crystallization of salts. The damage is not due to an external sulphate attack but to salts precipitation.
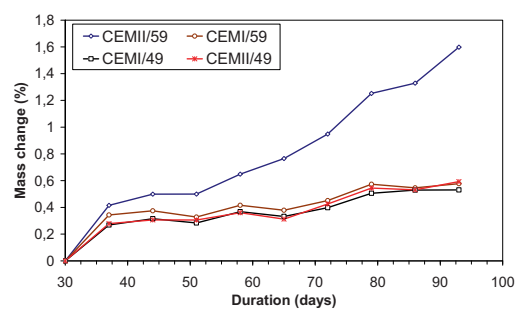

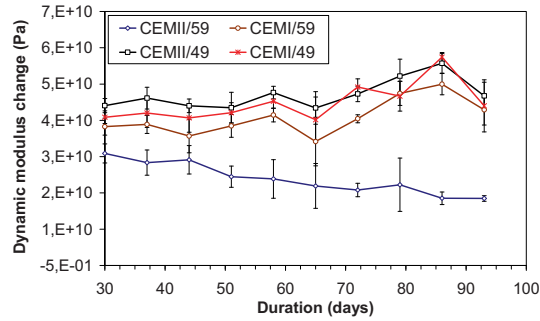**Fig. 1.** Mass variation of small cylinders subjected to total immersion

Fig. 2. Evolution of dynamic modulus of small cylinders subjected to total immersion

Fig. 3. Photographs of a small cylinder of concrete CEMII/59 subjected to total immersion at the end of test

Fig. 4. Photograph of a small cylinder of concrete CEMII/59 subjected to cycles of immersion-drying at 60°C
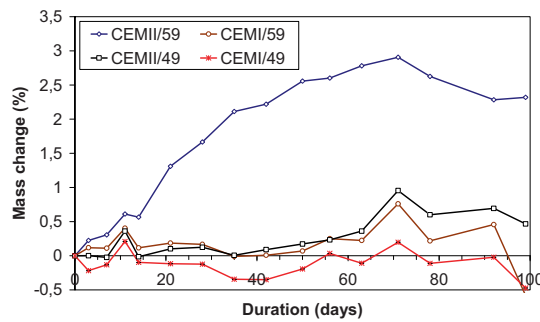

Fig. 5. Mass change of small cylinders subjected to cycles of immersion-drying at 60°C
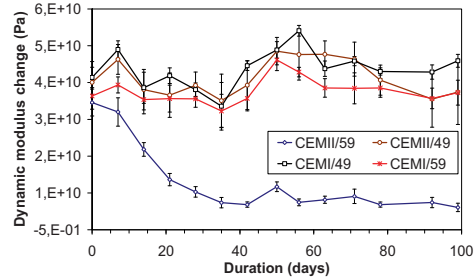
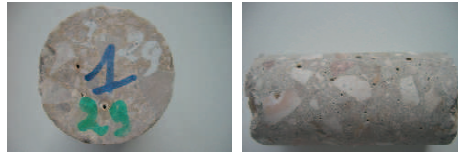**Fig. 6.** Evolution of dynamic modulus of small cylinders subjected to cycles of immersion-drying at 60°C

Fig. 7. Photographs of a small cylinder subjected to cycles of immersion-drying at 105°C at the end of test

Fig. 8. Photographs of a mortar sample subjected to cycles of immersion-drying at 105°C at the end of test

4. Discussions and conclusions

The concrete CEMII/59 prepared with cement CEM II/A 42.5 is the most damaged under the various exposure conditions. Both types of concrete CEMI/59 and CEMI/49, prepared with cement CEMI 42.5 "sulphate resistant" do not show any sign of damage subsequent to the three protocols. A lower sulphate resistance of CEMII/59 compared to CEMII/49, prepared with the same cement, can be explained by the effect of the W/C ratio: 0.59 for CEMII/59 and 0.49 for CEMII/49. A lower W/C ratio with sulphate resistant cement ensures a better durability. The cycles of immersion-drying at 105°C induces the precipitation of salts, not an external sulphate attack on our types of concrete. There is no swelling or cracking of samples exposed to this protocol; it does not fit the objectives of our study. The two protocols, total immersion and the cycles of immersion-drying at 60°C protocols show that samples are damaged by an external sulphate attack; there is swelling and cracking of samples.

Damage takes much time to occur in the case of total immersion compared to immersion/drying at 60°C whereas final damage to samples subjected to total immersion is greater. As a consequence, cycles of immersion-drying at 60°C are the protocol which gave in this study the fastest response, while remaining fully consistent with the total immersion test.

This protocol may therefore be an alternative acceleration test with regard to a simple immersion. The behaviour of mortar samples and cylinders is different from that of small cylinders; so far the latter have been the only samples undergoing an external sulphate attack.

The initial dynamic modulus of small cylinders is lower than that of mortar specimens; this could be due to coring. The fact that these samples are mechanically weaker may be the cause of their higher sensitivity to sulphates. Another difference is that the cored samples do not have any skin layer, unlike the cylinders of concrete or mortar. Initially, the paste/aggregate interfaces, which are the preferential precipitation zone for ettringite, are peeled off for small cylinders. This could explain their higher sensitivity to sulphates.

Finally, results obtained demonstrate clearly the feasibility to use crushed aggregates in the manufacture of stable and durable self-compacting concrete. Different types of self-compacting concrete were formulated. Variable test conditions that simulated a sulphate attack were applied. Three of the prepared types of concrete showed a good resistance to aggressive environments containing high levels of sulphates. Further studies, in progress, deal with the durability of different types of prepared concrete:

- Macroscopic tests concerning the porosity, permeability, and mechanical resistance at different testing periods.
- Microscopic tests concerning mineralogical changes (via X-ray diffraction and thermo-gravimetric tests), microstructure and texture changes (scanning electron microscope and mercury porosimetry tests).

References

[1] Olivier JP et al. (2008) La durabilité des bétons. Ecole nationale des ponts et chaussées, Paris.
[2] Khayat K (1997) Les bétons autonivelants-Les bétons bases et données pour leur formulation. Eyrolles France.
[3] Sahmaran M, Erdem TK, Yaman IO (2006) Sulphate resistance of plain and blended cements esposed to wetting–drying and heating–cooling environments. Construction and Building Materials 10.1016/j.
[4] Merida A, Talah A, Kharchi F, Chaid R (2005) Contribution à l'étude de la corrosion des BHP de pouzzolane en milieu sulafaté (in French). Colloque CMEDIMAT 2005, Algeria.
[5] Ghrici M, Kenai S, Meziane E (2006) Mechanical and durability properties of cement mortar with Algerian natural pouzzolana. Journal of Material Science, Springer 101007/s.
[6] EN 12370 (1999) Natural stone test methods – determination of resistance to salt crystallization. Comié Européen de Normalisation (CEN).

[7] Sideris KK, Savva AE, Papayianni J (2005) Sulphate resistance and carbonation of plain and blended cements. Cement and Concrete Composites 28: 47–56.

[8] Brunetaud X (2005) Etude de l'influence de différents paramètres et de leurs interactions sur la cinétique et l'amplitude de la réaction sulfatique interne au béton. PhD. Thesis (in French), Ecole Centrale des Arts et Manufactures – Ecole Centrale de Paris.

[9] Bonnet S and Khelidj A (2004) La durée de vie des ouvrages en béton armé situés sur la façade atlantique. MEDACHS, Iterreg IIIB Atlantic Space – Project N°197, Report N°2-1.

Mixed Finite Element for Cracked Interface

S. Bouziane[1], H. Bouzerd[1] and M. Guenfoud[2]

[1]Civil Engineering department, University of Skikda, Skikda, Algeria

[2]Laboratory of Civil Engineering and Hydraulics, University of Guelma, Guelma, Algeria

Abstract   Several disorders observed in an existing work on civil engineering may have their origin in local phenomena which reveal the weak points of this work. These critical zones are located, on the one hand in the links between materials or interfaces, on the other hand in singularly formed areas such as cavities, angles and cracks, seats of strong stress concentrations. In this paper, the finite element method (mixed formulation) is used for the study of the interfacial cracks in bimaterials. A special finite element based on the mixed formulation, able to take into account the continuity of the interface on the coherent part (mechanical and geometrical continuity), and the discontinuity of this one on the cracked part (edge effect), is used to model at best this type of interface. This element was developed by H. Bouzerd using a direct formulation: the shape functions of the displacement and stress fields are built directly starting from the real configuration of the element in a reference (x, y). In this purpose, this element was reformulated starting from a reference element in a natural plan (ξ, η). This formulation presents, in addition to the simplification of calculations, the enormous advantage of modelling the types of cracks and their orientations. This interface element was associated with the virtual extension–crack to evaluate the energy release rates using only one meshing by finite elements. Several numerical examples concerning the interfacial cracks are analysed to assess the validity of this element by comparing with an available analytical solution or numerical ones obtained from others finite elements.

Keywords: Mixed Finite Element of Interface, Cracked Interface, Energy Release Rate, Virtual Crack Extension, Bimaterial, Brittle Fracture.

1. Introduction

Disorders observed in an existing civil engineering structure, have generally their origin in local phenomena which reveal the weak points of this structure. These critical zones are located, on the one hand in the links between materials or interfaces, on the other hand in singularly formed areas such as cavities, angles and cracks, locations for strong stress concentrations.

In this paper, the mixed finite element method is used for the study of the interfacial cracks in bimaterials. The mixed variational formulation has several advantages [2] over the conventional finite element formulations, including direct evaluation of nodal stresses along with nodal displacements and improved accuracy of both displacements and stresses.

The mixed finite element method developed by Herrmann [10] for plate bending analysis has been extended to plane elasticity problems by Mirza and Olson [12]. Aivazzadeh [1] developed a family of rectangular mixed interface element using Reissner's mixed variational principle. Habib [9] presented various axisymmetric mixed element for studying bonded assemblies and laminate structure. Bichara [3] and Sarhan-Bajbouj [17] developed mixed finite elements for one or multi interfaces. Wu and Lin [19] presented a two dimensional mixed finite element scheme based on a local high-order displacement model for the analysis of sandwich structure. Carrera [5, 6] also presented various mixed models based on Reissner's mixed variational principle. Ramtekkar et al. [15] developed a three dimensional mixed finite element model using the minimum potential energy principle. Desai and Ramtekkar [7] presented a mixed finite element based on displacement theory satisfying fundamental elasticity relations. In this work a mixed finite element model has been presented using Reissner's mixed variational principle. The model takes into account the continuity of the interface on the coherent part (mechanical and geometrical continuity) and the discontinuity of this one on the cracked part (edge effect). This mixed finite element was developed by Bouzerd [4] using a direct formulation: the shape functions of the displacement and stress fields are built directly starting from the real configuration of the element in a physical (x, y) plane. In the present paper, this element was reformulated starting from a parent element in a natural (ξ, η) plane. This interface element was associated with the virtual crack extension method to evaluate the energy release rates using only one meshing by finite elements.

2. Formulation of the interface element

The stages of construction of the proposed interface element are schematized on Fig. 1. The RMQ-7 (Reissner Modified Quadrilateral) element is a quadrilateral mixed element with 7 nodes and 14 degrees of freedom [4]. Three of its sides are compatible with linear traditional elements and present a displacement node at each corner. The fourth side, in addition to its two displacement nodes of corner (node 1 and node 2), offers three additional nodes: a median node (node 5) and two intermediate nodes in the medium on each half-side (nodes 6 and 7), introducing the components of the stress vector along the interface. The Continuity of the displacement and stress vectors can be taken into account on the level on this particular side, which must be placed along the interface.

2.1. Construction of the parent element RMQ-5

The RMQ-5 element is obtained by adding a displacement node to the Reissner mixed element. It has a side (associate with the interface) presenting three nodes, the medium node (displacement node) characterizes the crack tip in the final version of the element.

The RMQ-5 and the Reissner elements present the same static behaviour. The stress field is expressed by the same shape functions. The element displacement component is approximated by:

$$\{u\} = [N]\{q\} \tag{1}$$

where $\{q\}$ is the vector of nodal displacements and $[N]$ is the matrix of interpolation functions for displacements.

The shape functions are:

$$N_1 = -\frac{1}{4}(1-\xi)(1-\eta)\xi \quad, \quad N_2 = \frac{1}{4}(1+\xi)(1-\eta)\xi \quad, \quad N_3 = \frac{1}{4}(1+\xi)(1+\eta)$$

$$N_4 = \frac{1}{4}(1-\xi)(1+\eta) \quad, \quad N_5 = \frac{1}{2}(1-\xi^2)(1-\eta) \tag{2}$$

The stress field in any point is written:

$$\{\sigma\} = [M]\{\tau\} \tag{3}$$

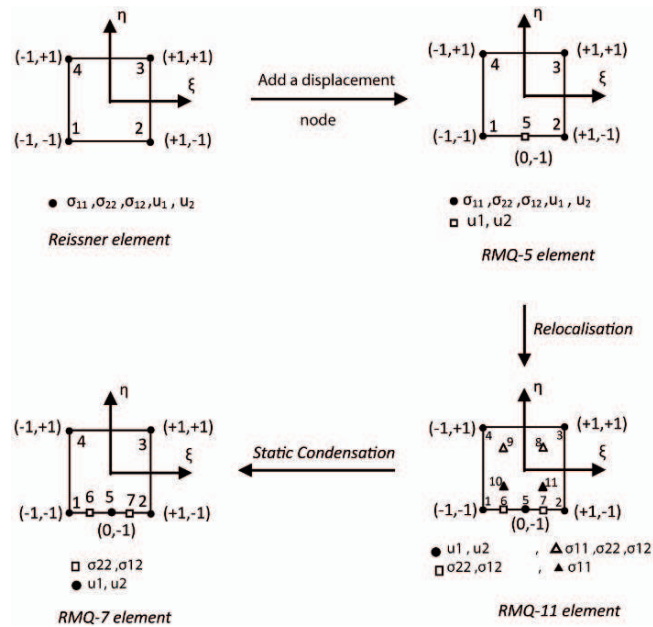where $[M]$ is the matrix of interpolation functions for stresses and $\{\tau\}$ vector of nodal stresses.

Fig. 1. Stages of construction of RMQ-7 element

The element matrix [K$_e$] is given by:

$$[K_e] = \begin{bmatrix} [K_{\sigma\sigma}] & [K_{\sigma u}] \\ [K_{\sigma u}]^t & [0] \end{bmatrix}$$

(4)

Here:

$$[K_{\sigma\sigma}] = -e \int_{A^e} [M]^t [S][M] dA^e$$

(5)

And:

$$[K_{\sigma u}] = e \int_{A^e} [M]^t [B] dA^e$$

(6)

where: e is the thickness, [S] is the compliance matrix, A^e is the element area and [B] is the strain-displacement transformation matrix.

2.2. Construction of the RMQ-11 element

The RMQ-11 element is obtained starting from the parent element RMQ-5 by relocalisation [18] of certain variables inside the element and by displacement of static nodal unknown of the corners towards the side itself.

The displacements nodes are still unchanged either by number sum, or in position. Do the elements RMQ-5 and RMQ-11 present the same shape functions. In the configuration of Fig. 1, the shape functions used to approximate σ_{22}, σ_{12} are given as follows:

$$M_{i2}^6 = \frac{1}{6}(1 - 2\xi)(1 - 2\eta), \quad M_{i2}^7 = \frac{1}{6}(1 + 2\xi)(1 - 2\eta), \quad M_{i2}^8 = \frac{1}{3}(1 + 2\xi)(1 + \eta),$$
$$M_{i2}^7 = \frac{1}{3}(1 - 2\xi)(1 + \eta)$$

(7)

The element stiffness matrix is written in the form given by the Eqts. 4, 5 and 6. This matrix can be evaluated by Gauss numerical integration scheme, with four points (2x2) on the element.

2.3. Construction of the RMQ-7 element

The four intern's nodes of RMQ-11 element complicate the operation of setting in data, and increase the size half-width of band during the assembly, which causes an increase of the computing time. The method used for condensation of the internal degrees of freedom to contour is related to the general concept of reduction of the size of an equations system per elimination of a certain number of variables. Gallagher [8] used this type of procedure in structural analysis.

3. Virtual crack extension method

The virtual crack extension method proposed by Parks [14] can calculate the energy release rate as:

$$G = -\frac{dU}{da} = -\frac{1}{2} \sum_{i=1}^{ne} \{u\}_i^t \frac{\Delta K_i}{\Delta a} \{u\}_i \tag{8}$$

where U is the potential energy of the system, a is the length of a crack, Δa is the length of the virtual crack extension, and ΔK_i and $\{u\}_i$ are the difference of the stiffness matrixes and the nodal displacements vectors of the elements i, surrounding a crack tip at the virtual crack extension, respectively.

4. Numerical examples

4.1. Example 1

In order to evaluate the validity and the credibility of the present element, a study of the convergence on a cantilever beam in bending is carried out. A cantilever beam, with dimensions and loading as shown in Fig. 2, is subjected to two types of loading. This problem has been solved by the present mixed element (for various meshes) to compare our result with the literature result.

Table 1 presents a comparison of deflections at the point A. Table 1 shows the good results obtained with the present mixed element compared with those of the analytical solution. Indeed, with a number of degrees of freedom definitely lower than those retained in the other comparative elements, excellent results are obtained. To see the convergence rapidity of the deflection at point A, several meshes are used.

Figure 3 represents the convergence of the deflection. It is noted that the interface mixed element converges very quickly for a number relatively low of degrees of freedom.
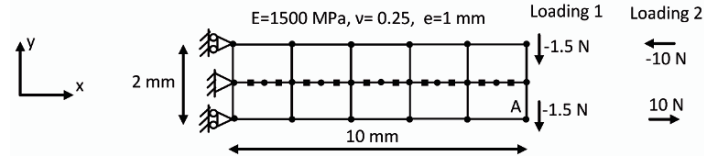
Fig. 2. Test of cantilever beam – Mesh

Table 1. Deflection in a cantilever problem solved by various elements

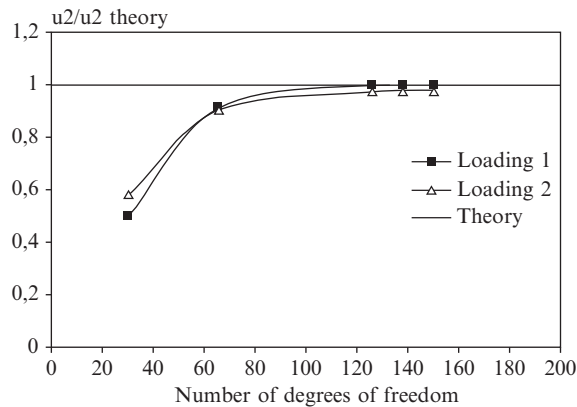| Element type	Number of degrees of freedom	Deflection at point A (mm)	
		Loading 1	Loading 2
Displacement (4 nodes)	728	0.961	0.922
Reissner (4 nodes)	1431	1.023	0.998
Quad-1 Bichara [3]	498	1.029	1.000
Present mixed element	150	1.000	0.976
Classical theory	–	1.000	1.000
Timoshenko theory	–	1.030	1.000

Fig. 3. Convergence of deflection in a cantilever beam

4.2. Example 2

Simply supported sandwich beam has been considered. This beam presents three isotropic layers and presenting coherent interfaces. A sandwich beam, with dimensions and loading as shown in Fig. 4, is subjected to uniform load and the interest is primarily centered on the study of transverse shear stresses and the deflection.
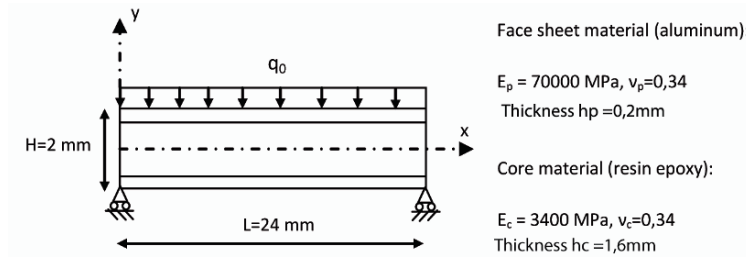
Fig. 4. Sandwich beam analyzed

To see the convergence rapidity of the transverse shear and deflection several meshes are used. Figures 5 and 6 show the variation of the deflection at x = L/2 and the transverse shear respectively with the number of degrees of freedom. It appears that the mixed interface element converges very quickly for a number relatively low of degrees of freedom. It can be seen that the results from the present mixed element are in very good agreement with the elasticity solution [13].
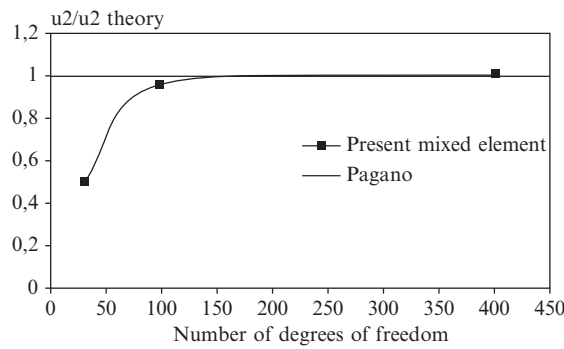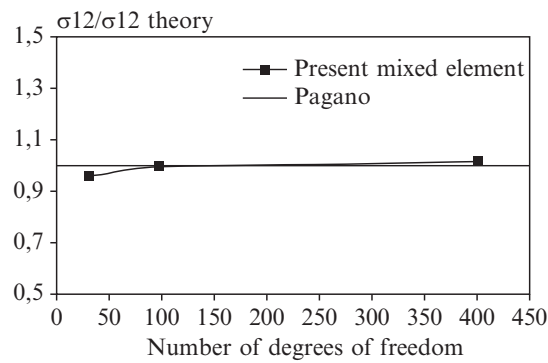

Fig. 5. Convergence of deflection at x = L/2

Fig. 6. Convergence of transverse shear at x = L/4 (y = −h_c/2)

4.3 Example 3

In this example, we analyzed a dissimilar square plate with a center crack in the interface plan between two isotropic materials [11] as shown in Fig. 7. In this problem, the present element is associated to the virtual crack extension method to evaluate the energy release rate G. During numerical calculation, the choice of the crack length variation Δa is very important. To see the influence of this variation on the precision of calculation, we considered only one mesh with 50 elements and 286 degrees of freedom and we varied the extension in the interval $\frac{\Delta a}{a} = \frac{1}{10} \div \frac{1}{500}$.

Results obtained with present interface element are compared with the values of the analytical solution [16] and the values of the numerical modelling of Lin and Mar [11]. These authors gave like results of their studies the stress intensity factors K_I and K_{II} from which we evaluated the energy release rate. Table 2 gives the values obtained according to E_1/E_2.

The results obtained confirm the importance of the choice of the extension and the validation of the present element for the cracked structure.

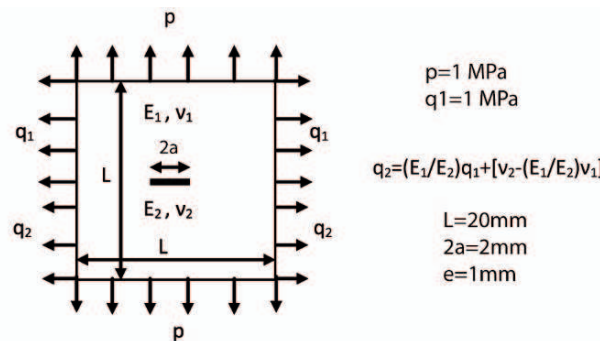**Fig. 7.** A center crack in a dissimilar square plate

Table 2. Energy release rate of center interface crack between dissimilar materials

E_1/E_2	Energy release rate G (N/mm)		
	Rice and Sih [16]	Lin and Mar [11]	Present mixed element
1	3.14	3.20	2.43
3	6.17	6.28	6.28
10	16.43	16.67	17.36
100	144.20	144.60	149.23

5. Conclusions

The mixed finite element method is used to derive a special interface element. The present mixed element was built in order to answer as well as possible the conditions of continuity of displacement and stress vectors in the coherent part, and of discontinuity of displacements and effect edge on the cracked part. In the formulation of this element, we used Reissner's mixed variational principle to build the parent element. The mixed interface finite element is obtained by successively exploiting the technique of relocalisation and the static condensation procedure in a natural plane.

This interface element was associated with the virtual crack extension method to evaluate the energy release rates using only one meshing by finite elements. Economy of analysis is achieved when the present elements are included with a relatively smaller mesh and present sufficiently accurate results.

The accuracy of the element has been evaluated by comparing the numerical solution with an available analytical solution or numerical ones obtained from others finite elements. Results obtained from the present mixed interface element have been shown to be in good agreement with the analytical solutions.

References

[1] Aivazzadeh S (1984) Eléments finis d'interface: Application aux assemblages collés et structures stratifiées. Thèse de docteur-ingénieur, Université de Technologie de Compiègne.
[2] Alturi SN, Gallagher S, Zienkiewicz OC (1983) Hybrid and mixed finite element method. Wiley, New York.
[3] Bichara M (1990) Formulation d'éléments d'interface. Application aux assemblages collés. Thèse de doctorat, Université Paris VI.
[4] Bouzerd H (1992) Elément fini mixte pour interface cohérente ou fissurée. Thèse de doctorat, Université de Claude Bernard (Lyon I).
[5] Carrera E (1996) C^0 Reissner-Mindlin multilayered plate elements including zig-zag and interlaminar stress continuity. Int. J. Num. Meth. Eng. 39:1797–1820.
[6] Carrera E (1998) Mixed layer-wise models for multilayered plates analysis. Compos. Struct. 43:57–70.
[7] Desai YM, Ramtekkar GS (2002) Mixed finite element model for laminated composite beams. Struct. Eng. Mech. 13:261–276.
[8] Gallagher RH (1976) Introduction aux éléments finis. Pluralis (traduction française).
[9] Habib M (1989) Eléments finis axisymétriques d'interface pour l'analyse des structures stratifiées et des assemblages collés. Thèse de doctorat, Université Claude Bernard (LyonI).
[10] Herrmann LR (1966) A bending analysis for plates. Proc. Conf. Matrix Methods in Structural Mechanics, AFFDL-TR-66-80, pp. 577–604.
[11] Lin KY, Mar JW (1976) Finite element analysis of stress intensity for cracks at a biomaterial. Int. J. Fracture 12:521–531.
[12] Mirza FA, Olson MD (1980) The mixed finite element method in plane elasticity. Int. J. Num. Meth. Eng. 15:273–289.
[13] Pagano NJ (1970) Exact solutions for rectangular bidimensionnal composite and sandwich plates. J. Compos. Mater. 4:20–35.

[14] Parks DM (1974) A stiffness derivative finite element technique for determination of elastic crack tip stress intensity factors. Int. J. Fracture 10:487–502.

[15] Ramtekkar GS, Desai YM, Shah AH (2002) Mixed finite element model for thick composite laminated plates. Mech. Adv. Mater. Struct. 9:133–156.

[16] Rice JR, Sih GC (1965) Plane problems of cracks in dissimilar media. J. Appl. Mech. 32 series E n°2:418–423.

[17] Sarhan-Bajbouj A (1990) Eléments finis d'interface pour le calcul des structures hétérogènes. Thèse de doctorat, Université de Claude Bernard (Lyon I).

[18] Verchery G (1987) Méthodes numériques de calcul des champs de contraintes dans les matériaux hétérogènes. Calcul des Structures et Intelligence Artificielle', Fouet J. M., Ladeveze P., Ohayon R., vol. 1, Paris, Pluralis, pp. 7–21.

[19] Wu CP, Lin CC (1993) Analysis of sandwich plates using mixed finite element. Compos. Struct. 25:397–405.

Three-Dimensional T-Stress to Predict the Directional Stability of Crack Propagation in a Pipeline with External Surface Crack

M. Hadj Meliani[1, 4], H. Moustabchir[4], A. Ghoul[2], S. Harriri[3] and Z. Azari[4]

[1]Department of Mechanics, FSS, University Hassiba Benbouali of Chlef. P.O.Box 151, Hay Salem, Chlef 02000, Algeria

[2]On leave from absence from the Hassiba BENBOUALI University of Chlef

[3]Department of Mechanics and comportment of Materials. Ecole des Mines de Douai, 941 rue Charles Bourseul B.P. 838 – 59508 Douai Cedex

[4]Laboratory of Mechanical Reliability, LFM-ENIM, Ilea of saulcy, 57045, University of Metz, France

Abstract   In industrial structures, the presence of cracks under critical loads leads to complete ruin. Fracture rupture mechanics allowed studying macroscopic defect harmfulness. This requires the knowledge of the stresses fields and the deformations near of the crack. Our work is an application of fracture mechanics into the domain of the pressurised structures with defects in the presence of the T-stress parameter. Design of this type of structures is subjected to standards, codes and regulations driven by the potential risk which they represent. The knowledge of the limit pressures in these structures allows appreciating the safety domain of. We present numerical solutions by the commercial code CASTEM2000 in three dimensional 3D and experimental results for the stress intensity factor SIF and the transverse stress noted T-stress, distribution at defect-tip in a Pipeline. The elastic structure modelling will be treated by the finites elements simulation. We study the influence of the geometrical parameters for surface notches and the measures of strains near defects in the studied model have been made by strain gauges. On the basis of the detailed 3D elastic FE analysis results, solutions presented are believed to be the most accurate, and thus provide valuable information for structural integrity assessment considering a notch-tip constraint. The experimental results validate allow numerical simulation.

Keywords: Crack, Pressure, T-stress, SIF, Finite element simulation, Strain Gauges.

1. Introduction

Despite of the T-stress solution's publication for a range of specimen geometries, the concept of the two-parameter approach to fracture problems did not seem to have received much attention until recently [1]. This increased interest in the application of T-stress to the assessment of structural integrity. Despite the numerous discussions

presented in literature on stress intensity factor solutions and T-stress for notches in Pipelines, the available results are based on crude estimates, and their accuracies in predicting crack growth are even less known. On the other hand, numerical solutions for surface cracks have diverged so widely from authors to authors that they present problems in themselves. Several methods or techniques resolve this problem. The basic disciplines are fracture mechanics, and generally reliability of components of the structures. These scientific basic techniques, don't often give regrettably an easy analytical solution for the complex structures, so we have to resort to the numerical methods. The finites elements method gives a good solution to industrial problems. This paper is focused on the *K-T* approach which was derived from a rigorous asymptotic solution and has been developed for a two-parameter fracture. With K being the driving force and *T* a constraint parameter, this approach has been successfully used to quantify the constraints of notch-tip fields for various proposed geometry and loading configurations. Note that the parameter *T* is almost independent of its position near the notch-tip. Experimental tests which were realized on gas Pipelines, confirm the values given by the numerical modelling.

2. Bibliography reviews

2.1. Stress intensity factors (SIF) in pipeline

The local fracture criterion presumed that the fracture process requires a certain fracture volume [2] or a distance from a crack-tip. Therefore, the notch stress intensity factor (NSIF) is defined as a function of effective distance and effective stress. In the case of a crack, the stress intensity factor is given by Irwin [3] formula. For finite element (FE) results, we obtained a distance x_{eff} corresponding to the value of the yielding stress σ_e. Creager and Paris [4] propose that the stress distribution at the notch is identical to that of a crack, but is moved in the direction of the crack-tip by a distance of $\rho/2$.

Table 1. Recapitulation of the stress intensity factor for different methods

Author's	Effective stress, effective distance	Stress intensity factor equation
Crack [30]	$\sigma_{\max}(x=0, r=0)$	$K_{I,Irwin} = k_t \sigma_n \sqrt{\pi a} = \sigma_{\max}\sqrt{\pi a}$
FE	$\sigma_{\max}(x=x_{eff}, r=0)$	$K_{I,FE} = \sigma_{eff}\sqrt{2\pi x_{eff}}$
Creager [4]	$\sigma_{eff}(x=\rho/2, r=0)$	$K_{I,Creager} = (\sigma_{eff}/2)\sqrt{2\pi(\rho/2)}$
Panasyuk [5]	$\sigma_{eff} = \sigma^*, x_{eff} = d^*$	$K_{I,Panasyuk} = 0.886\sigma_y^* \sqrt{d} = \sigma_{eff}\sqrt{2\pi(\rho/8)}$

Panasyuk et al. [5] proposed a parametric equation σ_y, which determines the stress intensity factor K_I [5]. The stress intensity factors (SIFs) and the notch stress intensity factors (NSIFs) for different used methods are presented in Table 1.

2.2. Effect of transverse stress

A second fracture parameter, the T-stress, is used in order to understand the effect of structural and loading configuration at the crack tip, even though the physical significance of the parameter is unknown. In order to correlate the higher term effects to an appropriate physical parameter, some authors [6–9] simplified the higher terms to define the T term. T-stress is defined as constant stress acting parallel to the crack and its magnitude is proportional to the nominal stress in the vicinity of the crack. In an isotopic linear elastic body containing a three-dimensional crack subject to symmetric loading, the stresses for each of the fields can be written as a series expansion [10]. Near the tip of the crack, where the higher order terms of the series expansion are negligible, stresses for mode I write:

$$\sigma_{xx} = \frac{K_I}{\sqrt{2\pi r}} \cos\frac{\theta}{2}\left(1 - \sin\frac{\theta}{2}\sin\frac{3\theta}{2}\right) + T \tag{1a}$$

$$\sigma_{yy} = \frac{K_I}{\sqrt{2\pi r}} \cos\frac{\theta}{2}\left(1 + \sin\frac{\theta}{2}\sin\frac{3\theta}{2}\right) \tag{1b}$$

$$\sigma_{zz} = \frac{K_I}{\sqrt{2\pi r}} 2\upsilon\cos\frac{\theta}{2} + E\varepsilon_{zz} + \upsilon T \tag{1c}$$

$$\sigma_{xy} = \frac{K_I}{\sqrt{2\pi r}} \sin\frac{\theta}{2}\cos\frac{\theta}{2}\cos\frac{3\theta}{2} \tag{1d}$$

The subscripts x, y and z suggest a local Cartesian co-ordinate system formed by the plane normal to the crack front and the plane tangential to the crack front point; r and θ are the local polar co-ordinates, K_I is the mode I local stress intensity factor, E is the Young's modulus and ε is the Poisson's ratio. T is the T-stress, representing a tensile/compressive stress. In the mode (I) loading, equation (1) shows that σ_{xx} comprises the singular term and T. This implies that T can be determined along any direction where the singular term of σ_{xx} vanishes or can be set to zero by superposing with a fraction of σ_{yy}. This corresponds to mode I positions around the crack tip.

$$T_{xx} = \left(\sigma_{xx} - \sigma_{yy}\right)_{r=0,\theta=0} \qquad (2)$$

Various studies have shown that T-stress has significant influence on crack growth direction, crack growth stability, crack tip constraint and fracture toughness [11–16]. In addition, crack path direction has received attention beginning by Larsson and Carlsson [17] and Rice [18] showed that the sign and magnitude of the T-stress substantially change the size and shape of the plane strain crack tip plastic zone at finite load levels. Kirk et al. [19] and Sorem et al. [20], in their experimental studies, have also shown that the fracture toughness of a given material can be considerably dependent on the size and geometry of the crack body. Analytical and experimental studies have shown that T can be used as a measure of constraint for contained yielding; see for example Hancock at al. [21] and Sumpter [22]. Recently, Ganti and Parks [23], Zhang et al. [24] and Jayadevan et al. [25] investigated the effect of the T-stress on the constraint of elastic interface crack. Very recently, Li and Xu [26] extensively discussed the T-stresses across static crack kinking.

3. Experimental tests

The aim of theses experimental tests is to measure the strain near defect tip in a Pipeline. In the following the experimental devices and the equipments used in the different tests are presented subsequently: (i) Test Parameters: tube geometry, loading…etc, (ii) Material characterizations: chemical composition and mechanical properties, (iii) The different devices used to control crack evolution. The experimental study is done on a specimen made with cylinder closed at the end by two tore spherical shell with large radius.

Figure 1 gives the geometrical parameters of the studied structure. Figure 2 presents the experimental conventional stress strain curve evolution and indicates clearly the ductile behaviour of the material. The mechanical properties are: Young's modulus of 2,07,000 MPa, Poisson's ratio of 0.3, Yield stress of 360 MPa, Ultimate strength is 440 MPa and Elongation of 35%. The chemical composition of the material is given in Table 2.
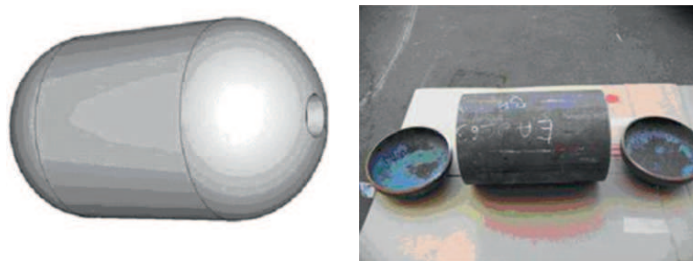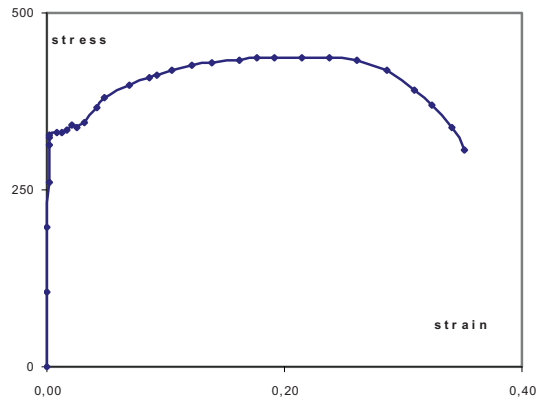

Fig. 1. Specimen geometry

Fig. 2. Stress–strain curve of the material

Table 2. Chemical compositions (mass%)

%	C	Min	S	Yew	P	Al
Material	0.135	0.665	0.002	0.195	0.013	0.027
Standard (max)	0.18	1	0.015	0.4	0.025	0.02

The pipe is submitted to an internal water pressure which induces nominal stress $\sigma_n = 48.3$ MPa. The studied specimen is Pipeline with including semi elliptical surface cracks. The defect is characterized by a ratio a/t = 0.2, with crack depth measured in radial direction, 2c is the crack length, a thickness $t = 10$ mm and $R_i = 193.2$ mm the internal radius. Figure 3 represents the geometries of longitudinal notches and by the same technique of measure are represented the circumferential notches.
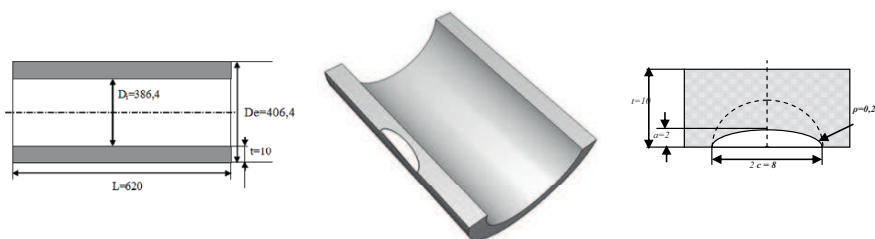

Fig. 3. Cylindrical geometries and specimen dimensions

For the second step, we aim to determine the experimental strain distribution near of the crack tip (elastic domain), in order to validate our numerical models. The specimens are instrumented by some gauges in the defect zone. For an optimal comparison with numerical computation, a total of 90 gauges were necessary (see Fig. 4).
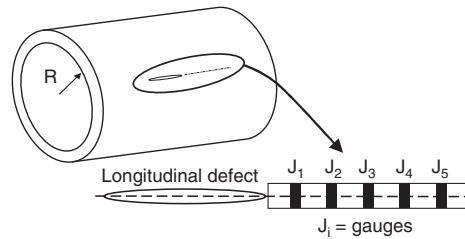
Fig. 4. Sight of the gauges in the vicinity of default and the position and orientation of the gauges in the vicinity

4. Finite element analysis

The finite element method was used to determine the crack-tip parameters stress intensity factor (K_I) and the transverse stress in the *xx* direction, noted $T_{xx,}$ for the pipe specimens. The structures were modeled by CASTEM 2000 code [27] in three dimensions under plane strain conditions using free-meshed isoperimetric 8-nodes elements. Only one half of the test apparatus was modelled due to symmetry in the geometry and loading conditions. The concept of the cylindrical structure with external surface notch is divided into several steps. The principle is to build a block of notch which rests on the extrusion of a grid 2D of a plane notch along the face of notch (curve of semi elliptic form). This operation makes it possible to generate an essential volume, Fig. 5a. The specimen is loaded by a uniform distribution of a pressure in elastic conditions. The support and symmetric boundary conditions are used in this model (see Fig. 5b). The material used was steel P264GH, the stress/strain curve is represented by the Ramberg–Osgood curve hardening expression:

$$\frac{\varepsilon}{\varepsilon_0} = \frac{\sigma}{\sigma_y} + \alpha \left(\frac{\sigma}{\sigma_y} \right)^n \tag{3}$$

In Eq. (3), ε_0, σ_y, α and *n* are constants, with $E\varepsilon_0 = \sigma_y$.

The deformation plasticity option with a small geometry change continuum model was invoked. We take $\alpha = 1$ and $\sigma_y = 340$ MPa. Two values of the strain hardening exponent *n* were selected, $n = 1$ and $n = 0.0446$. A series of finite element analyses was performed for different crack length ratios (a/t).
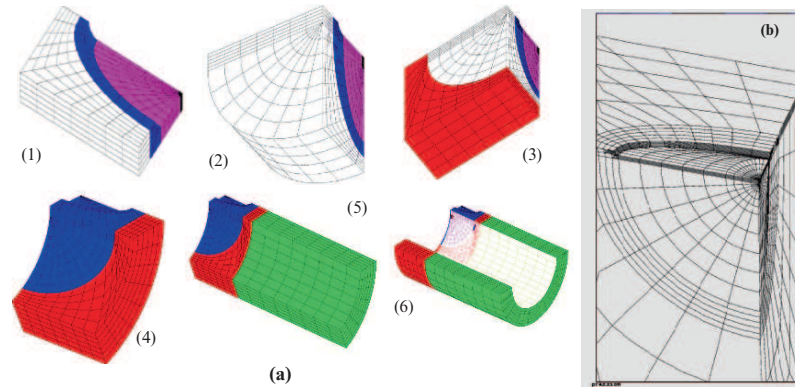
Fig. 5. (**a**) Various steps of design notched sample for simulation, (**b**) typical 3D finite-element mesh used to model the cracked a Pipeline for elastic analysis

5. Results and discussions

In the vicinity of the default, we stuck a chain of 5 gauges (J_1, J_2, J_3, J_4 and J_5) in the longitudinal direction. Figure 6a gives the circumferential deformation $\varepsilon_{\theta\theta}$ according to the pressure (in bars). It is noticed that the zone of measurement nearest to the defect passes in the plastic range to a pressure of about 42 bars. Figure 6b gives the circumferential deformations measured by the chain compared with the numerical results for crack and notch default, for an internal pressure of 25 bars. In the zone of disturbances of the default, the three results of deformations obtained numerically and in experiments are very close and the maximum variation is 5.2%. This deformation becomes constant when one moves away from the default and his zone of influence. The notch is characterized by a concentration stress factor K_t defined by Peterson [28]. The value of K_t equal to 7.2 with a pressure applied $\sigma = 48.3$ MPa and the maximum stress obtained by finite element is $\sigma_{max} = 360.33$ MPa. It is noted that the results obtained by our calculations are the closest to those obtained in literature. The finite element method treats various geometries of the structure studied and determines the distribution of the elastic stress at the notch-tip. We confronted the results of the calculation of the stress intensity factor, obtained by using the computer code CASTEM2000 [27], for the semi-elliptic notch and those obtained by simulation of N'Diaye [29].

The Pipeline, considered internal diameter of 193.2 mm and a thickness t of 10 mm, carries a two types of surface notches, noted D1 in the longitudinal sense and D2 in the circumferential sense, of depth a, an acuity $\rho = 0.25$ mm are subjected to an internal pressure of 25 bars (see Table 3). The values of SIFs, obtained by various authors, are shown in Table 4. The simulation by [30] shows a maximum variation of 10%. The SIF comprising a crack is larger than the stress intensity factor of pipe with notch.
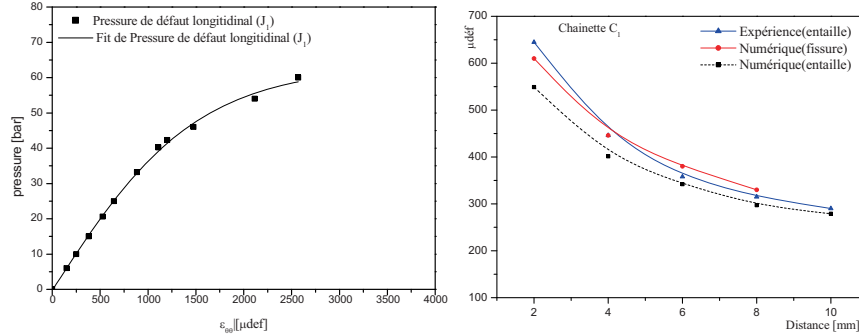
Fig. 6. (**a**) Deformation ($\varepsilon_{\theta\theta}$) according to the pressure in the first gauge (J_1) near the notch-tip, (**b**) circumferential deformations in the chain C1 according to the distance (P = 25 bar)

The maximum relative variation of the stress intensity factor between the approach method of finite elements and the method of Panasyuk remain lower than 29%. The stress difference method (SDM) proposed by Wang et al. [31, 32] is used to determine *T*-stress for a distance *x* behind the notch for different used methods. These results show the variation of the transverse stress (*T*-stress) with longitudinal surface notch at the deep point for a ratio a/t = 0.2. The results are influenced by numerical errors normally expected from FE results in highly stressed zones. The effects of the higher order terms in William's series expansion are significant along of the ligament.

Table 3. Dimensions of defaults

Default		a (mm)	2c (mm)	R (mm)	t (mm)	Pressure (bars)
Longitudinal circumferential	D1	2	8	193.2	10	25
	D2	2	8	193.2	10	25

Table 4. Determination of SIF and normalised T-stress by various authors

Methods of calcul	MEF (Notch)		Panasyuk [5]	MEF (crack) [30]	Creager and Paris [4]
Notch D1	SIF MPa·m$^{1/2}$)	3.370	2.380	3.810	3.350
	(T_{eff}/σ_e)	−0.246	−0.288	−0.289	−0.231
Notch D2	SIF(MPa.m$^{1/2}$)	0.729	0.724	2.023	0.717
	(T_{eff}/σ_e)	−0.053	−0.067	−1.889	−0.046

The test data adopted in this paper are from two specimen geometries. We have a project to extend for various specimen geometries and different loading with different dimensions and orientations of notches. It should be mentioned that, the two notches with the same configurations and the sense different in orientation, have different constraint levels. The constraint augmentation in percent between the longitudinal notch and the circumferential is about 80%.

These results prove that the longitudinally oriented notches are known to be more vulnerable than along the circumferential direction mainly because the hoop stress for closed-end vessels is twice of the longitudinal stress. Noted that, the constraint in a crack is always greater than in a notch in each direction. The maximum errors values of normalized T-stress between the three methods 'MEF, Creager and Panasyuk, is about 25%. The purpose of using multiple specimen geometries is to obtain different constraint levels such that a broad range of T-stress at fracture load can be achieved. For instance, we study the K-T approach for short notches (a<t = 0.2) and it's important to investigated for long notch. As noted, several study remarks that the next term may not be negligible for long notches (the order of the grain size).

6. Conclusions

In this elastic part, we studied the distribution of the stress at the notch-tip as reported by several authors. It is noted that the maximum stress decrease gradually to reach a minimum along the ligament. The stabilization of this distribution represents the nominal stress. We determined the stress intensity factors (SIFs) and the notch stress intensity factors (NSIFs) in a Pipeline with external surface default subjected to an internal pressure for various approaches. Analyses carried out on these approaches give that the maximum relative variation of the stress intensity factor is lower than 10% between the method of [30] and the approach used here. This shows that the stress intensity factor in pipeline with a crack is greater than the stress intensity factor in a pipe with a notch. On the other hand the maximum relative variation of the stress intensity factor obtained by the method of Creager [4] and the approach method of Panasyuk [5] remain lower than 30%. By the finite element method (FEM), we show that the adopted digital model gives results coherent with the model of Creager (E < 1%) and in conformity with those which exist in the literature. The ratio obtained from the numerical results by several researchers showed some difference from the predicted stress intensity factor in mode I with and without presence of T-stress. To study size effect, FEA was performed for the two defects presented above and made all the in plane dimensions ten times larger. It is shown that for a given specimen geometry and loading configuration, the relation between: K_{Ieff} and T_{eff}, represent the apparent or the effective FIC and T-stress, in the other hand, K_{IC}, T_{crit}, represent the stress intensity factor with the ASTM-E399 conditions and the critique T-stress.

$$\left(\frac{K_{Ieff}}{K_{IC}}\right)^2 + \alpha \cdot \left(\frac{T_{eff}}{T_{crit}}\right)^2 = 1 \qquad (4)$$

where α is an empirical constant, T_{crit} is the critical T-stress.

References

[1]   Bhuyan GS, Webster CTL (1997). Fracture performance of NGV cylinder designs. Project report, Powertech Laboratory Inc., 12388-88th Avenue, Surrey, BC Vancouver, V3W 7R7 Canada.

[2]   Pluvinage G. Fracture and fatigue emanating from stress concentrators. Dordrecht: Kluwer; 2003.

[3]   Irwin JR (1974). Limitations to the-scale yielding approximation for crack-tip plasticity. J. Mech. Phys. Sol. 22, 17–26.

[4]   Creager M, Paris PC (1967). Elastic field equations for blunt cracks with reference to stress corrosion cracking. Int J. Fracture 3:247–252.

[5]   Panasyuk VV, Ivanytska GS, Ostash OP (1993). A new approach to the determination of the macrocrack nucleation period near a stress concentrator. Fatigue Fract. Eng. Mater. Struct. 16(4):453–464.

[6]   Nakamura T, Parks DM (1991). Determination of elastic T-stress along three-dimensional crack fronts using an interaction integral. Int. J. Solids Struct. 29:1597–1611.

[7]   Bilby BA, Cardew GE, Goldthorpe MR, Howard ICA (1986). Finite element investigation of the effect of specimen geometry on the fields of stress and strain at the tips of stationary cracks. In: Size effects in fracture. London: Mechanical Eng. Publications Limited. p:37–46.

[8]   Betegon C, Hancock JW (1991). Two-parameter characterization of elastic. plastic crack tip fields. ASME J. Appl. Mech. 58:104–110.

[9]   Du ZZ, Hancock JW (1991). The effect of non-singular stresses on crack tip constraint. J. Mech. Phys. Solids 39:555–567.

[10] Fett, T (1998). T-stresses for components with one-dimensional cracks. Report FZKA 6170, Forschungs-zentrum Karlsruhe.

[11] Williams JG, Ewing PD (1972). Fracture under complex stress – the angled crack problem. Int. J. Fract. 8(4):416–441.

[12] Ueda Y, Ikeda K, Yao T, Aoki M (1983). Characteristics of brittle failure under general combined modes including those under bi-axial tensile loads. Eng. F. Mech. 18(6):1131–1158.

[13] Smith DJ, Ayatollahi MR, Pavier MJ (2001). The role of T-stress in brittle fracture for linear elastic materials under mixed-mode loading. Fatigue Fract. Eng. Mater. Struct. 24(2):137–150.

[14] Cotterell B, Rice JR (1980). Slightly curved or kinked cracks. Int. J. Fracture 16:155–169.

[15] Du ZZ, Betegon C, Hancock JW (1991). J-dominance in mixed mode loading. Int. J. Fracture 52:191–206.

[16] O'Dowd NP, Shih CF (1991). Family of crack tip fields characterized by a triaxiality parameter-I. Structure of fields. J. Mech. Phys. Solids 39:989–1015.

[17] Larsson SG, Carlsson AJ (1973). Influence of non-singular stress terms and specimen geometry on small-scale yielding at crack tips in elastic–plastic materials. J. Mech. Phys. Solids 21:263–278.

[18] Rice JR (1974). Limitations to the-scale yielding approximation for crack-tip plasticity. J. Mech. Phys. Sol. 22:17–26.

[19] Kirk MT, Koppenhoefer KC, Shih CF (1993). Effect of constraint on specimen dimensions needed to obtain structurally relevant toughness measures. Constraint in Fracture, ASTM

STP 1171 (edited by E.M. Hachett, K.-H. Schwalbe and R.H. Dodds), American Society for testing and Materials, Philadelphia, 79–103.

[20] Sorem WA, Dodds RH, Rolfe ST (1991). Effects of crack depth on elastic plastic fracture toughness. Int. J. Fracture 47:105–126.

[21] Hancock JW, Reuter WG, Parks DM (1993). Constraint and toughness parameterized by T. constraint effects in Fracture, ASTM STP 1171 (edited by E.M. Hackett, K.-H. Schwalbe and R.H. Dodds), American Society for Testing and Mat., Philadelphia, 21–40.

[22] Sumpter JDS (1993). An experimental investigation of the T stresses approach. Constraint effects in Fracture, ASTM STP 1171 (edited by E.M. Hackett, K.-H. Schwalbe and R.H. Dodds), American Society for Testing and Materials, Philadelphia, 492–502.

[23] Ganti and Parks DM (1997). Elastic–plastic fracture mechanics of strength-mismatch interface cracks. In: Mahudhara RK et al., editors. Recent advances in fract.. London, 13–25.

[24] Zhang ZL, Hauge M, Taulow C (1997). The effect of T -stress on the near tip stress field of an elastic–plastic interface crack. In: Karihaloo BL et al., editors. Proceedings of the Ninth International Conference on Fracture, vol.4.Amsterdam:Pergamon.vp.2643.50.

[25] Jayadevan KR, Thaulow C, Østby E, Berg B, Skallerud B, Holthe K, Nyhus B (2005). Structural integrity of pipelines: T-stress by line-spring. Fatigue Fract. Eng. Mater. Struct. 28:467–488.

[26] Li XF, Xu LR. T-stresses across static crack kinking. J. Appl. Mech, 74(2):181–190.

[27] Cast3M^{TM} (2006). Commissariat à l'énergie atomique CEA.

[28] Peterson RS (1989). Stress Concentration Factors. Wiley, New-York.

[29] N'Diaye A, Hariri S, Pluvinage G, Azari Z (2006). Stress concentration factor analysis for notched welded tubular T-joints. Int. J. Fatigue 29(8):1554–1570.

[30] Elhakimi A (2006). Etude numérique et expérimentale de la nocivité des défauts dans des coques cylindriques et sphériques sous pression. Thèse de doctorat, Ecole des Mines de Douai, France.

[31] Wang X (2003). Elastic T-stress solutions for semi-elliptical surface cracks in infinite thickness plates. Eng. Fract. Mech. 70:731–756.

[32] Wang X, Bell R (2004). Elastic T-stress solutions for semi-elliptical surface cracks infinite thickness plates subject to non-uniform stress distributions. Eng. Fract. Mech. 71:1477–1496.